

Luís André Ferreira de Deus da Rocha Duarte

PHOTOCHEMISTRY AND STRUCTURE OF AROMATIC AZO COMPOUNDS ISOLATED IN CRYOGENIC NOBLE-GAS MATRICES

Doctoral Thesis in Chemistry, Molecular Spectroscopy branch, supervised by Prof. Rui Fausto and Dr. Igor Reva, and presented to the Department of Chemistry of the Faculty of Sciences and Technology of the University of Coimbra

2014



UNIVERSIDADE DE COIMBRA

Dissertation submitted in order to obtain a Doctoral
Degree in Chemistry

**Photochemistry and Structure of
Aromatic Azo Compounds Isolated in
Cryogenic Noble-Gas Matrices**

Luís Duarte

Coimbra 2014



University of Coimbra
Faculty of Sciences and Technology
Department of Chemistry

It's a Long Way to the Top...

Contents

Acknowledgments	ix
Abstract	xi
Resumo	xiii
Preface	xv
1 Introduction	1
1.1 Aromatic Azo Compounds	1
1.1.1 <i>EZ</i> Photoisomerization	3
1.1.1.1 Structure	4
1.1.1.2 Electronic Spectra	5
1.1.1.3 $E \rightleftharpoons Z$ Isomerization Mechanism	6
1.1.2 Azo-Hydrazone Tautomerism	8
1.1.3 Studied Compounds	8
1.2 Matrix Isolation	10
1.2.1 Coupling with Infrared Spectroscopy	12
1.2.2 Matrix Effects	15
1.2.3 Photochemistry in Matrices	16
1.3 Computational Methods	17
1.3.1 Ab initio	18
1.3.2 Density Functional Theory	21
1.3.3 Basis Set	23
References	25
2 Methods and Materials	33
2.1 Samples	33
2.2 Experimental Details	33
2.2.1 Matrix Deposition	33

2.2.2	IR Absorption Measurements	34
2.2.3	UV Irradiation	36
2.3	Computational Details	37
	References	38
3	Results	41
3.1	Azobenzene	41
3.1.1	Isomeric Composition of Matrix-Isolated AB	42
3.1.2	Photoisomerization	44
3.1.3	Choice of the Model Chemistries	46
3.1.4	Vibrational Spectra	47
3.1.5	Potential Energy Surfaces of <i>E</i> -AB and <i>Z</i> -AB	52
3.1.6	Geometries of <i>E</i> -AB and <i>Z</i> -AB	55
3.2	4-Hydroxyazobenzene	59
3.2.1	Most Stable Structures	59
3.2.2	HAB Structure in a Matrix Shortly After Deposition	61
3.2.3	Photochemistry	65
3.3	4-(Cyclopropyldiazenyl)phenol	67
3.3.1	Potential Energy of CPDP	67
3.3.2	CPDP Structure in a Matrix Shortly After Deposition	70
3.3.3	Photochemistry	77
3.4	1-(Cyclopropyldiazenyl)naphthalen-2-ol	81
3.4.1	Potential Energy Surface of CPDNO	81
3.4.2	CPDNO Structure in a Matrix Shortly After Deposition	88
3.4.3	Photochemistry	93
	References	97
4	General Conclusions and Concluding Remarks	105
	References	109
A	Appendix	111
A.1	Saccharin / Tetrazole-saccharyl Papers	111
B	Appendix	131
B.1	Azobenzene Supporting Information	131
B.2	Azobenzene Paper	152

C Appendix	165
C.1 Hydroxyazobenzene Supporting Information	165
D Appendix	177
D.1 CPDP Supporting Information	177
E Appendix	195
E.1 CPDNO Supporting Information	195
E.2 CPDNO Paper	212
List of Figures	223
List of Tables	227

Acknowledgments

This work would not have been possible without the support of many people to whom I would like to express my appreciation in the following lines.

First and foremost, I thank to Professor Rui Fausto for the opportunity to work in his research group, for his supervision, and guidance from the very early stage of this project until the completion of this thesis.

I am also deeply grateful to Dr. Igor Reva for his meticulous comments and insightful discussions. Without his advices and persistent help this thesis would not have been possible.

Professor Ana Maria Oliveira-Campos from the University of Minho and Professor Lurdes Cristiano from the University of Algarve are thanked for generously providing some of the compounds studied in this work.

Special thanks to all my present and former colleagues at the Laboratory for Molecular Cryospectroscopy and Biospectroscopy, particularly to Barbara Michela Giuliano, Andrea Gómez-Zavaglia, Ana Borba and Amin Ismael for their contribution on part of the work herein reported.

The Portuguese Foundation for Science and Technology is acknowledged for the doctoral grant that financially supported this research work (SFRH/BD/62090/2009).

I would like also to thank the Advanced Computing Laboratory of the University of Coimbra for providing computing resources that have contributed to the research results reported within this thesis, and the GNU/Linux and Open-source communities for the time they dedicate to the development of free, high-quality operative systems and software applications that are suitable for both scientific and everyday use.

To friends and family for their unconditional support and understanding along all these years I spent at the laboratory and writing this dissertation.

Abstract

The molecular structure, spectroscopic properties, and photochemical transformations of four azo compounds (azobenzene, 4-hydroxyazobenzene and two mixed aliphatic-aromatic azo derivatives) isolated for the first time in cryogenic noble-gas matrices were investigated by means of infrared spectroscopy and quantum chemical calculations performed at the DFT and MP2 levels of theory.

Monomers of *E*-azobenzene, the thermodynamically most stable isomer of the compound, were isolated in argon matrices at 15 K. In an attempt to convert *E*-azobenzene into the *Z* isomer, the matrix-isolated *E*-monomers were irradiated either by broadband or narrowband UV-visible light of different wavelengths, in the 600-200 nm range. However, no *E*-to-*Z* transformation was observed under these conditions. In an alternative experiment, *E*-azobenzene was irradiated by UV-visible broadband light in the gas phase prior to trapping in a matrix. In this case, the *E*-to-*Z* photoisomerization occurred, and both *E*- and *Z*-azobenzene monomers were detected in the matrix sample. Subsequent irradiation of the matrix with narrowband tunable visible or UV light ($\lambda < 550$ nm) resulted in back conversion of *Z*-azobenzene into the *E*-form. The observed photoinduced *E* \leftrightarrow *Z* isomerization allowed for the reliable vibrational characterization of both azobenzene isomers. In addition, the two-dimensional potential energy surfaces of *Z*- and *E*-azobenzene were explored as functions of the torsional movement of the two phenyl rings. They exhibit large flat areas around the minima, for both isomers, allowing for large-amplitude zero-point torsional vibrations. For the *Z*-form, these vibrations were found to be responsible for significant changes in the equilibrium NN bond length (up to 0.3 pm). This allowed also to explain the experimentally observed frequency smearing of the N=N stretching vibration in this isomer.

Similar behavior was observed for 4-hydroxyazobenzene isolated in an argon matrix; only the most stable *E* forms were experimentally detected and, after narrowband irradiation, no *E*-to-*Z* isomerization was observed. On the other hand, performing the irradiation experiments for the compound trapped in xenon matrices annealed at 60 K, allowed the observation of the *E*-to-*Z* transformation. The con-

straining of the $E \rightarrow Z$ isomerization process of azobenzene and 4-hydroxyazobenzene, was attributed to steric effects imposed by the rigid matrix environment.

Two forms of the 4-(cyclopropyldiazenyl)phenol derivative (CPDP1 and CPDP2; both with E configurations) were found experimentally in the matrices samples of the compound. Upon irradiation in the 335-325 nm range, a different isomeric form (CPDPZ; with a Z configuration) was produced. These forms were shown to be photochemically interconvertible and further irradiations at longer wavelengths consumed CPDPZ and regenerated CPDP1 (460-440 nm) and CPDP2 (400 nm).

For the 1-(cyclopropyldiazenyl)naphthalen-2-ol derivative, which can have two distinct tautomeric structures, only azo-enol forms (E1 and E2; both with E configurations) having the OH group involved in a strong intramolecular hydrogen bond, forming a six-membered ring with the azo group, were found experimentally. The non-observation of the respective keto-hydrazone tautomers (K1 and K2) was explained with the aid of theoretical calculations describing the displacement of the hydrogen atom in the tautomeric azo-enol/keto-hydrazone systems. Irradiation with a narrowband source at 345 nm generated a different azo-enol form (E9; with a Z configuration), while upon irradiation at 325 nm, two different keto-hydrazone forms (K5 and K6) are produced. These phototransformations were shown to be reversible and, depending on the excitation light, the azo-enol or the keto-hydrazone forms can be produced.

Resumo

A estrutura molecular, propriedades espectroscópicas e transformações fotoquímicas de quatro compostos azo (azobenzeno, 4-hidroxi-azobenzeno e dois compostos azo envolvendo substituintes alifáticos-aromáticos) isolados pela primeira vez em matrizes criogênicas de gases nobres, foram investigadas por espectroscopia de infravermelho e cálculos de química quântica realizados ao nível DFT e MP2.

Foram isolados monómeros do isômero termodinamicamente mais estável do azobenzeno (forma *E*) em matrizes de árgon a 15 K. Com o intuito de converter o *E*-azobenzeno no respectivo isômero *Z*, os monómeros do isômero *E* isolados em matriz foram irradiados com luz UV-visível (banda larga e banda estreita) de diferentes comprimentos de onda entre 600 e 200 nm. Nestas condições, a transformação da forma *E* para a forma *Z* não foi observada. Numa experiência alternativa, o *E*-azobenzeno foi irradiado na fase gasosa, antes do seu aprisionamento na matriz, com luz UV-visível de banda larga. Neste caso, a fotoisomerização de *E*-para-*Z* ocorreu e monómeros de ambas as formas (*E* e *Z*) do azobenzeno foram detectados na matriz. Subsequente irradiação da matriz com luz UV ou visível ($\lambda < 550$ nm) de banda estreita resultou na conversão do *Z*-azobenzeno em *E*-azobenzeno. A observação da fotoisomerização $E \leftrightarrow Z$ permitiu a caracterização vibracional dos dois isômeros do azobenzeno. Foram também exploradas as superfícies de energia potencial bi-dimensionais das formas *Z* e *E* do azobenzeno em função do movimento torsional dos dois anéis fenilo. Verificou-se que essas superfícies exibem regiões alargadas quasi-planares em torno dos mínimos correspondentes aos dois isômeros, permitindo movimentos torsionais de grande amplitude. No caso do *Z*-azobenzeno, estas vibrações são responsáveis por mudanças significativas na ligação de equilíbrio NN (cerca de 0.3 pm), o que permite explicar a forma invulgar da banda observada nos espectros de infravermelho do composto correspondente à vibração de alongamento N=N deste isômero.

Para o 4-hidroxi-azobenzeno isolado em matrizes de árgon, verificou-se uma situação semelhante à do azobenzeno; apenas as formas mais estáveis (*E*) foram detectadas. Após irradiação com luz UV-visível de banda estreita, não foi também neste caso observada isomerização de *E*-para-*Z*. Irradiações para o composto isolado em

matrizes de xénon a 60 K, permitiram a observação da isomerização $E \rightarrow Z$. O constrangimento do processo de isomerização $E \rightarrow Z$ do azobenzeno e 4-hidroxi-azobenzeno foi atribuído a efeitos estéreis impostos pelas matrizes.

Para o composto 4-(ciclopropildiazenil)fenol foram detectadas duas formas (CPDP1 e CPDP2; ambas com configurações E) nas matrizes de gases nobres. Com irradiação na gama de comprimentos de onda compreendida entre os 335-325 nm, foi possível obter uma forma isomérica diferente (CPDPZ; com uma configuração Z). Verificou-se que estas formas podem ser fotoquimicamente interconvertidas umas nas outras e que irradiações com comprimentos de onda mais longos consomem a forma CPDPZ e regeneram as formas CPDP1 (460-440 nm) e CPDP2 (400 nm).

Para o 1-(ciclopropildiazenil)naftaleno-2-ol, de entre as várias possíveis estruturas tautoméricas, apenas foram encontradas experimentalmente formas azo-enol (E1 and E2; ambas com configurações E) com o grupo OH envolvido numa ligação de hidrogénio intramolecular forte, formando um anel quasi-aromático de seis membros com o grupo azo. A não observação dos respectivos tautómeros cetohidrazona (K1 e K2) foi explicada com o recurso a cálculos teóricos descrevendo o deslocamento do átomo de hidrogénio no sistema tautomérico azo-enol/cetohidrazona. Irradiação a 345 nm, produz uma forma azo-enol diferente das anteriores (E9; com uma configuração Z , enquanto que, com irradiação a 325 nm, são geradas duas formas cetohidrazona (K5 e K6). Demonstrou-se que estas transformações são reversíveis e que, consoante o comprimento de onda utilizado, podem ser produzidas as formas azo-enol ou cetohidrazona.

Preface

The work reported in this thesis was carried out in the Laboratory for Molecular Cryospectroscopy and Biospectroscopy (LMCB) of the Department of Chemistry of the University of Coimbra and arose from an initial more general research project: “FTIR Spectroscopic and Theoretical Study of Matrix-Isolated *2H*-Chromenes and Azobenzenes”. Due to the fact that the later class of compounds usually raises more theoretical and application-driven interest (as well as because of some other more practical reasons), the project naturally evolved to a systematic structural and photochemical investigation of aromatic azo compounds (or azobenzenes) isolated in cryogenic matrices.

This thesis is organized in a classical style and therefore is divided into four chapters. In the first chapter, an outlook of some of the more characteristic properties of aromatic azo compounds and the reasons they foment so much interest is given. The studied compounds are presented and the theoretical framework underlying the experimental and computational methods used during this work are briefly outlined. In the second chapter, the experimental apparatus and computational methods are described. The third chapter contains the results obtained for each of the compounds studied. Finally, general conclusions of this investigation are presented in the fourth chapter.

Additionally, in the time available during the waiting period associated with the synthesis and/or purchase of the compounds necessary to carry out part of the work mentioned above, the photochemistry of matrix-isolated saccharin and one saccharyl-tetrazole derivative was also investigated. Since the main purpose of this dissertation is to serve as a base for the evaluation and critical discussion of all activities performed during the doctoral program, this information is also included. Therefore, for the sake of simplicity, the two papers relative to the saccharin/saccharyl-tetrazole topic are given in Appendix A, without any reference or relation with the main body of the thesis and they should be seen as self-contained sections.

1

Introduction

1.1 Aromatic Azo Compounds

Azo compounds can be simply defined as compounds containing the azo functional group ($-N=N-$) in their molecular structures (Figure 1.1). According with the IUPAC definition,¹ they can be considered as “derivatives of diazene (diimide), wherein both hydrogens are substituted by hydrocarbyl groups.” Their structural diversity is enormous and there are families of organic and organometallic azo compounds.^{2,3} When one or both of the groups attached to the azo moiety are of aromatic nature, such as phenyl or naphthyl rings, they are generally called aromatic azo compounds.



Figure 1.1 Structural formula of diimide, a general azo compound, and the most common aromatic azo compound - azobenzene. R_1 and R_2 represent hydrocarbyl groups.

The parent molecule of most aromatic azo compounds - azobenzene (AB) - was discovered around the mid 1800's^{4,5} and approximately one century later, in 1937, the first studies reporting its behavior upon exposure to light were published by Hartley.⁶ Since then, the aromatic azo compounds (or azobenzenes) have established themselves as one of the most important and versatile classes of synthetic coloring agents in industry, accounting for approximately 50-60% of all commercial dyes, and have found a wide variety of applications in textiles, printing, food additives, pharmaceuticals, and optical materials.⁷⁻⁹ Moreover, during the last decade, the aromatic azo compounds have been receiving considerable attention due to their potential for the photocontrol of biological macromolecules and materials' properties.

They currently constitute a very dynamic and exciting research field* and ingenious azo-based molecular lifts, sensors, nanovehicles, and light-controlled peptides have been successfully achieved (Figure 1.2).^{10,11} Extensive reviews on the applications and strategies adopted in the development of azo-based photofunctional dynamic molecular devices, switches, liquid crystals, polymeric materials and photonic systems can be found elsewhere.^{12–24}

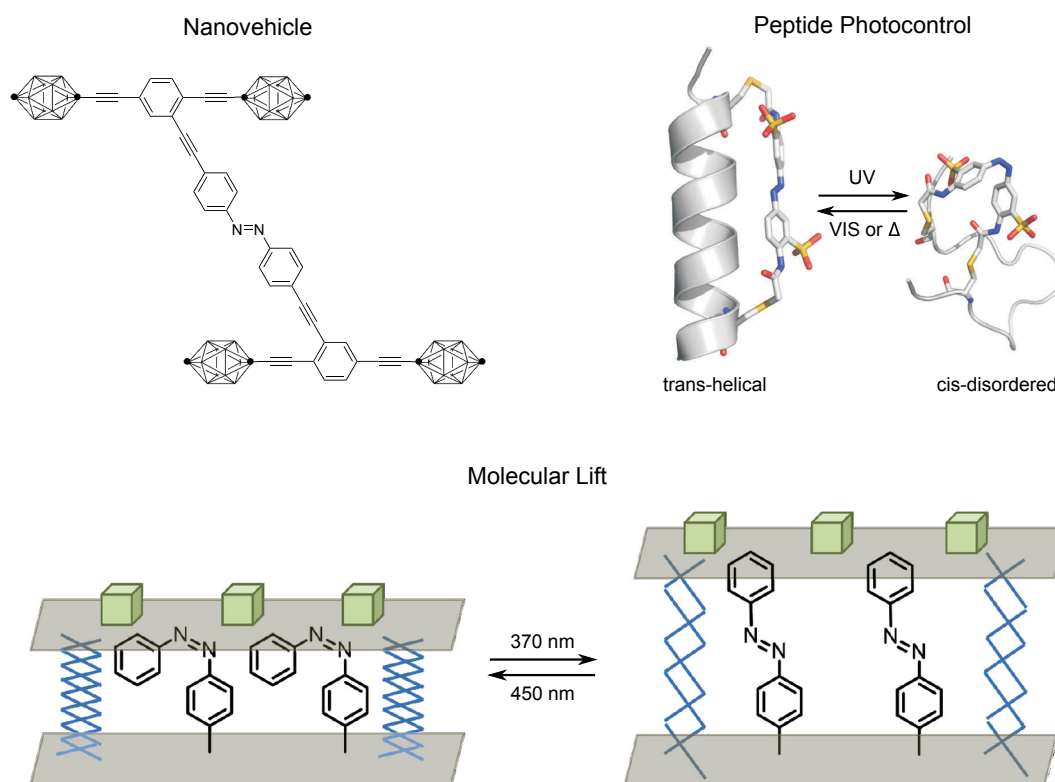


Figure 1.2 Schematic representation of some azo-based molecular applications. Adapted from references 10, 18 and 19.

Despite the plenitude of well-established applications, several aspects concerning the structure and photochemistry of aromatic azo compounds are still not fully understood. Therefore, detailed knowledge on their structural and photochemical behavior is crucial for understanding their reactivity and particularly important for the rational design of new azo-based technologies. In the following subsections, some of the more characteristic properties of azobenzenes will be summarized.

*A quick bibliography search in the ISI Web of Knowledge with the keyword “azobenzene” yields more than 10000 hits.

1.1.1 *EZ* Photoisomerization

Azobenzene is a typically photochromic molecule and can exist in two configurations, the *E* (*trans*) and *Z* (*cis*) forms, that can be interconverted either photochemically or thermally.^{25–28} Upon irradiation with wavelength between 300–350 nm, a change from the stable *E*-azobenzene (*E*-AB) to the metastable *Z*-azobenzene (*Z*-AB) is induced. The reaction is reversible and the *E* form can be regenerated when the *Z* form is irradiated with light of wavelength between 400–450 nm, or heated (Figure 1.3). Continuous irradiation of *E*-AB with either 313 nm or 436 nm radiation results in a photostationary state comprised of approximately 20% or 90% of *E*-AB, respectively.²⁹

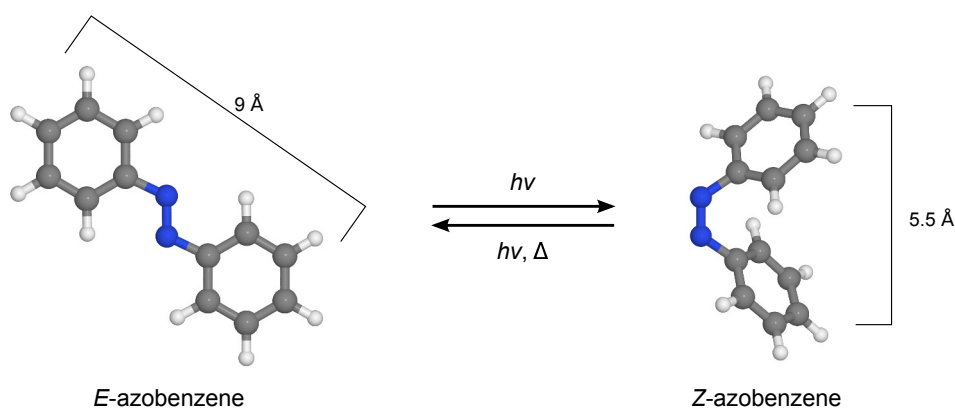


Figure 1.3 Photoisomerization of azobenzene. The two photochemical conversions occur on the picosecond timescale,³⁰ while the thermal relaxation of the *Z* isomer to the *E* isomer is much slower (milliseconds to days, depending on the molecule's particular substitution pattern and local environment).

The *E* isomer is about 58 kJ mol⁻¹ more stable than the *Z* form and the energy barrier for the thermal *Z* → *E* isomerization is ca. 96 kJ mol⁻¹.^{28,31–33} As a result, thermal isomerization occurs spontaneously, and under typical ambient illumination (or in the dark) azobenzene is found predominantly in the *E* form. The photoisomerization process causes a change of ~3.5 Å in the end-to-end distance between the carbon atoms of the benzene rings situated in the *-para* positions^{34–36} and leads to an increase of the molecular dipole from zero in the *E* form to approximately 3 D in the *Z* form.⁶

Essentially all aromatic azo compounds that share the azobenzene scaffold exhibit

similar photochemical behavior. It is the nature and particularities of the structural alterations resulting from irradiation with light, and the different chemical and physical properties of the interconverted isomers (molecular geometry, molecular shape, dipole moment or absorption spectrum) what makes them suitable and/or desirable for several distinct applications.

1.1.1.1 Structure

The first X-ray diffraction studies of *E*-AB^{34,35,37} suggested a structure slightly distorted from planarity and the existence of an orientational disorder at one of two crystallographically independent sites. At the disordered site, the molecules adopt two conformations that are related to one another by a 180° rotation around their longest axes. A later variable-temperature X-ray crystallographic analysis³⁸ of *E*-AB and three methylated derivatives revealed that the disorder is dynamic and confirmed the existence of two conformations with C_i symmetry in the crystal. It was found that the conformational interconversion takes place through a pedal motion and is facilitated by the large amplitude of the torsional vibration around the N–Ph bond.³⁹ In solution, Raman measurements⁴⁰ of *E*-AB and some of its isotopically substituted derivatives suggested the predominance of a distorted structure with C_i symmetry. Early gas electron diffraction (GED) measurements⁴¹ also indicated a non-planar molecular geometry with C_i symmetry. The phenyl groups were found to be twisted by approximately 30° around the N–Ph bonds. However, more recent GED measurements⁴² led to the conclusion that the structure in the gas phase is actually planar, with C_{2h} symmetry, and the discrepancies with the first GED study were attributed to the different treatment given to the phenyl torsions.

On the theoretical side, quantum-mechanical calculations also contributed to the controversy about the planarity of the structure. While the majority of the available theoretical works predict the planar *E*-AB structure as the most stable one in the gas-phase,^{33,43–46} investigations performed with the second-order Møller–Plesset (MP2) approach gave contradictory results. Kurita et al. obtained two imaginary vibrational frequencies for planar *E*-AB and found a low energy barrier between the twisted and planar forms at the MP2/6-31+G(d) level. On the other hand, Hättig and Hald⁴⁷ obtained a planar structure with C_{2h} symmetry from an MP2/cc-pVTZ optimization. This planar structure was latter confirmed by further theoretical calculations and the necessity of employing sufficiently extended basis sets was emphasized.^{48,49}

Therefore, despite some contradictory experimental and theoretical results, the

controversy about the planarity of *E*-AB structure seems to be resolved and it is most likely that different equilibrium structures exist in the condensed and gas phases.

There are less experimental results available for the *Z*-AB form. X-ray diffraction experiments indicated that the molecule has a bent geometry with C_2 symmetry.^{36,50,51} The CNNC dihedral angle is about 8° and the phenyl rings are rotated by approximately 54° out of the plane of the azo group. Density functional theory and ab initio theoretical predictions produced similar results to those obtained experimentally.^{33,43–46,48,52}

1.1.1.2 Electronic Spectra

The UV-visible absorption spectrum of *E*-AB in ethanol shows a weak band near 444 nm and a more intense one near 316 nm. The low-intensity band is attributed to the transition to the lowest singlet state, S_1 , of $\pi\pi^*$ nature and of B_g type in the C_{2h} symmetry group and the strong band to the transition to the S_2 state, of $\pi\pi^*$ nature and of B_u symmetry type. In a similar way, *Z*-AB has a $\pi\pi^*$ band near 437 nm and blue-shifted $\pi\pi^*$ bands at 270 nm and 247 nm (Figure 1.4).⁵³

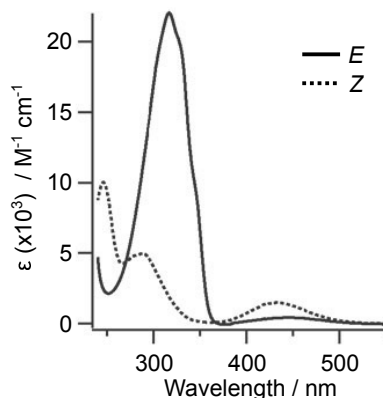


Figure 1.4 Electronic absorption spectra of the *E*- and *Z*- isomers of azobenzene dissolved in ethanol. Although for *E*-AB the $\pi^*\leftarrow n$ transition is symmetry-forbidden, vibrational coupling and nonplanarity make it observable.

By adding substituents to the azobenzene rings, the absorption spectrum can be changed to lie anywhere from the ultraviolet to the visible-red region.^{54,55} Based on the resulting absorptions, the aromatic azo compounds can be generally classified into three spectroscopic classes: the azobenzene type, the aminoazobenzene type and the pseudo-stilbene type of molecules.^{53,56} The azobenzene type, typically of yellow

color, exhibits similar behavior to the unsubstituted azobenzene and are characterized by a low-intensity $\pi^* \leftarrow n$ absorption band in the visible region, and much stronger $\pi^* \leftarrow \pi$ absorption band in the UV. The aminoazobenzene-type molecules are characterized by close-lying (or overlapping) $\pi^* \leftarrow \pi$ and $\pi^* \leftarrow n$ absorption bands in the UV-visible region. They are of orange color and contain electron-donor substituents (usually an amino group) in the *-ortho* or *-para* positions of the aromatic rings. The pseudo-stilbenes (in analogy to stilbene) are characterized by a low-lying red-shifted $\pi^* \leftarrow \pi$ transition that can be reversed in energy with respect to the $\pi^* \leftarrow n$ band. They are of red color and contain electron-donating and electron-withdrawing groups (such as an amino and a nitro group; the so called push-pull system) at the 4 and 4' positions, which leads to a strongly asymmetric electron distribution.

1.1.1.3 $E \rightleftharpoons Z$ Isomerization Mechanism

As noted above, the $E \rightleftharpoons Z$ azobenzene isomerization process involves excitation in the UV-visible range to either the $S_1(n\pi^*)$ or the $S_2(\pi\pi^*)$ states. The isomerization quantum yields display an unusual wavelength dependence. Photoisomerization occurs with a higher quantum yield when excitation is to the S_1 state than when it is to the S_2 state, which constitutes a violation of Kasha's rule. In sterically hindered azobenzenes this violation is not observed.⁵⁶⁻⁵⁸

Various ultrafast and time-resolved spectroscopic techniques have provided important information about azobenzene photophysical and photochemical decay.^{30,59-64} Excitation of E -AB from the S_0 ground state to the S_2 state is followed by rapid relaxation to the S_1 state and by a decay back to the S_0 state, either non-radiatively (*via* conical intersection) or by weak fluorescence. The process may however be even more complex, and the involvement of other states has also been suggested.^{33,65-68} Comparatively, the process following the $\pi^* \leftarrow n$ excitation is simpler as it involves only the S_1 state.^{60,64,69-71} Thus, contrary to what was initially believed,^{56,58,72} the isomerization process seems to always occur from the S_1 state, regardless of the excitation wavelength. Less experimental information is available for the $Z \rightarrow E$ photoisomerization, but similar conclusions were found for the excitation-relaxation dynamics.

The $E \rightleftharpoons Z$ isomerization itself has been addressed in a great number of studies and several possible mechanisms have been proposed (Figure 1.5).^{33,43,45,64-66,71,73-82} The two most frequently discussed mechanisms are rotation and inversion. The rotational pathway involves torsion around the central NN bond, while in the inversion pathway one of the two NNC angles increases to 180° , resulting in a semi-linear

transition state. Additional mixed mechanisms, such as the concerted inversion or the inversion-assisted rotation, have also been considered as possible pathways for the photoisomerization of azobenzene. In the concerted-inversion, both NNC bond angles increase to 180° generating a linear transition state, whereas the inversion-assisted rotation involves simultaneous changes in the CNNC dihedral angle and NNC angles. More recent studies predict that isomerization is dominated by pedal-like motion of the azo nitrogens.^{83–87}

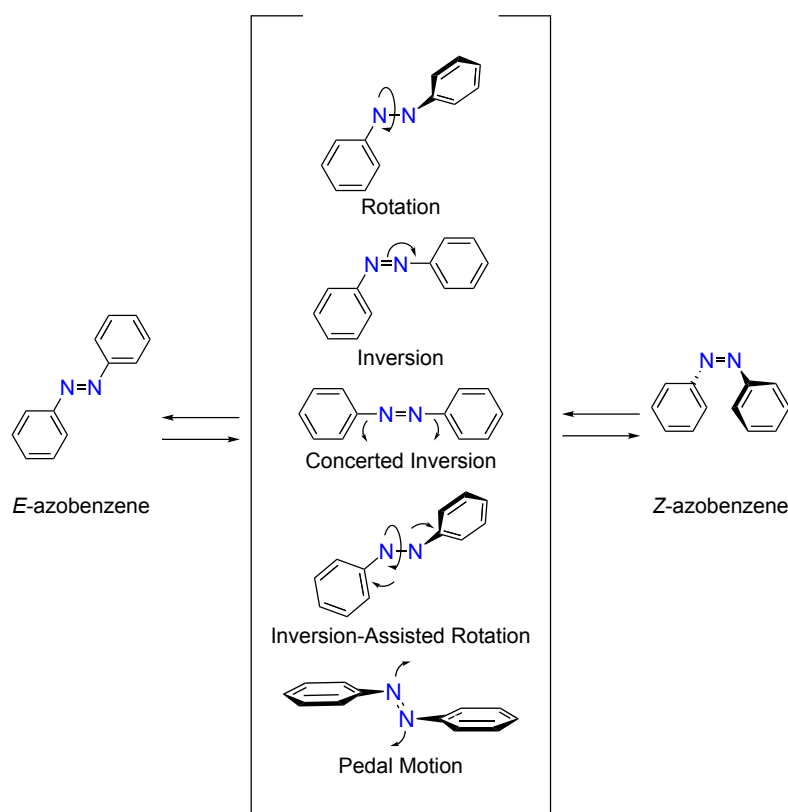


Figure 1.5 Proposed photoisomerization mechanisms for azobenzene. All mechanisms predict photostationary states consisting of both isomers.

Therefore, despite the considerable number of experimental and theoretical works carried out in the past three decades, the precise mechanism for the photoisomerization of azobenzene is still not completely clear and remains an active topic of investigation. Nevertheless, most works suggest a dominance of the rotational isomerization following excitation to either S_1 or S_2 for *E*-azobenzene in the gas-phase. In solution, the isomerization appears to occur by a multidimensional process with contributions from both the rotation and concerted-inversion pathways.^{64,78,79} For

Z-azobenzene, the available data suggest that photoisomerization occurs by rotation (clockwise or counterclockwise),^{76,81,88,89} following either S_1 or S_2 excitation, while thermal isomerization seems to occur by inversion.^{74,90} In other aromatic azo compounds, the presence of additional substituents influences the isomerization process, through steric and electronic effects, and other pathways may become relevant.^{78,90–92}

1.1.2 Azo-Hydrazone Tautomerism

Aromatic azo derivatives have more complex structures than azobenzene and many contain hydroxy substituents, that may show photochromism by intramolecular proton transfer. The aromatic compounds having azo and hydroxyl groups in *-ortho* or *-para* positions may give rise to two distinct tautomeric structures: azo-enol (OH) or keto-hydrazone (NH), which may coexist under certain experimental conditions. These tautomeric structures can be stabilized by intramolecular hydrogen bonds and the equilibrium between the two forms can also be explored in the functionalization of materials, signaling and switching.^{93–95}

Many theoretical and experimental studies on the azo-hydrazone tautomeric equilibrium can be found in the literature.^{96–106} However, due to the dependence of the tautomeric forms on the surrounding chemical environment, their structural and spectroscopic characterizations are not trivial. Indeed, many issues concerning the relative stability of these species and related with the intramolecular proton transfer that interconvert them into each other remain unclear. Therefore, understanding their reactivity and photochemical behavior is also particularly important from both the applied and fundamental points of view.

1.1.3 Studied Compounds

With the intent of contributing to the bulk of knowledge about the structural and photochemical properties of aromatic azo compounds, we studied by matrix isolation infrared spectroscopy four different (but still closely related) azo compounds (Figure 1.6). The set of model compounds consists of mixed aliphatic-aromatic and aromatic azo derivatives (some of them with the possibility of exhibiting azo-hydrazone tautomerism), and includes some of the most representative structures among the azo family of dyes (azobenzene and hydroxyazobenzene).

As we will see in the next section, the matrix isolation technique (together with infrared spectroscopy) emerges as a convenient way of obtaining information on the

1.1 Aromatic Azo Compounds

conformational and tautomeric (when applied) preferences of such systems and facilitates the interpretation of their photochemical processes. Surprisingly, the studies of aromatic azo compounds isolated in noble gas matrices are quite scarce and mainly concerned with the study of hydrogen bonding.^{107,108}

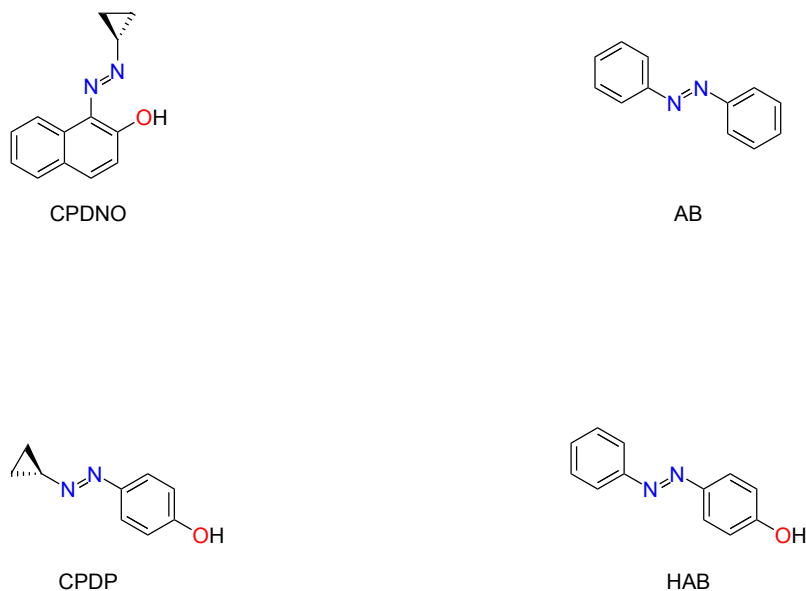


Figure 1.6 Compounds studied in this work. **AB**: azobenzene or 1,2-diphenyldiazenes; **HAB**: 4-hydroxyazobenzene or 4-(phenyldiazenyl)phenol; **CPDNO**: 1-(cyclopropyldiazenyl)naphthalen-2-ol; **CPDP**: 4-(cyclopropyldiazenyl)phenol.

1.2 Matrix Isolation

The term matrix isolation was introduced for the first time by George Pimentel, in 1954,¹⁰⁹ and refers to the technique where gaseous atoms or molecules are trapped in rigid host materials, usually solidified noble gases (or nitrogen)* at very low temperatures. The guest chemical species is mixed with a large excess of the host gas and is condensed onto a window cooled down to typically 4-30 K. At such temperatures, if the ratio of host to guest is high enough, the molecules or atoms of the chemical species to be studied are isolated from each other by layers of the host and prevented from diffusing and undergoing bimolecular reactions (Figure 1.7).

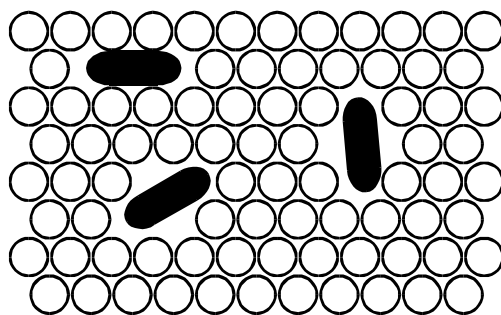


Figure 1.7 Schematic representation of a species isolated in a matrix host (usually neon, argon, and xenon). Adapted from reference 110.

The noble gases are transparent from the vacuum UV to the far-infrared spectral regions and provide a weakly-interacting trapping environment for stabilizing and characterizing both reactive and stable chemical species. Alternatively, specific host-guest reactions can also be studied by using reactive host gases such as carbon monoxide or oxygen. After deposition, the sample can be studied at leisure through the use of standard spectroscopic techniques and additional information can be obtained by irradiating or annealing the matrices.

In order to attain the low temperatures necessary to make the rigid matrices, specialized equipment has to be used. The experimental apparatus and its specific details may vary in consonance with the particular needs of each laboratory and the method of analysis chosen to be applied. Nonetheless, most matrix isolation setups usually include the components depicted in the schematic representation given in Figure 1.8.

*The matrix isolation term can also be applied in a more general sense, to include the range of all techniques where guest molecules are trapped in rigid host materials (e.g. crystals, zeolites, clays, polymers, glasses, etc.) and prevented from undergoing diffusion.

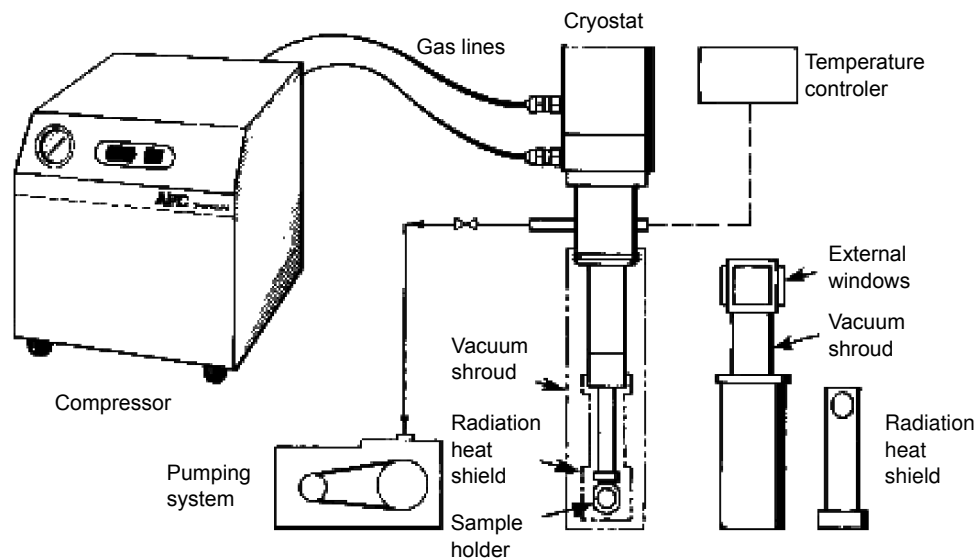


Figure 1.8 Schematic representation of a matrix isolation setup. Adapted from reference 111.

The compounds of interest are deposited from the gas phase and therefore must be volatile: liquids and solids with high enough vapor pressure can be premixed with the host gas in a vacuum line by standard manometric techniques or evaporated from glass tubes attached to the vacuum chamber; samples with low vapor pressure require heating and are usually vaporized from additional equipment designed for such effect (e.g. side arms, specialized mini ovens, Knudsen cells, etc.). The sample and host gas (or the mixture of both) enters the vacuum chamber of the cold cell through inlet port(s) at a controlled rate and condensates onto a window mounted into a sample holder, which in turn is attached to the cold finger of a cryostat (usually a closed-cycle helium refrigeration system). The cold window can be rotated in order to facilitate both the deposition and analysis processes, and is usually surrounded by a metallic shield that minimizes warming due to thermal background radiation. The vacuum chamber is connected to a pumping system and is maintained at very low pressures ($\leq 10^{-6}$ mbar), in order to provide thermal insulation of the cold window from the outside environment. After the deposition process is complete, the matrix-isolated sample can be probed through external windows fitted into the chamber. A complete description of the particular matrix isolation setup used in this work will be given in chapter 2. Comprehensive reviews concerning the matrix isolation technique and several matrix isolation studies can be found elsewhere.^{110–114}

1.2.1 Coupling with Infrared Spectroscopy

From all the possible spectroscopic methods that can be coupled with the matrix isolation technique, the most useful structural information is usually obtained with infrared (IR) spectroscopy. Features of an IR spectrum, such as the number of absorption bands, their intensities and shapes, constitute a molecule's unique physical property or "fingerprint". The atoms in a molecule vibrate constantly around their equilibrium positions, changing continuously the bond lengths and bond or dihedral angles. Energy of light from the mid-infrared region of the electromagnetic spectrum is sufficient to excite these vibrations and to promote the molecule to a state of higher energy, in which the vibrational amplitudes are increased. However, only absorptions corresponding to vibrational movements that result in changes in the molecular dipole moment, generating a permanent oscillating dipole with the same frequency of the oscillating electric field of the incident radiation, can be observed in the infrared spectrum.

According to the Born-Oppenheimer approximation, which allows us to consider the nuclear and electronic movements separately, a diatomic molecule undergoing vibrational motion may be simply represented as two masses connected by a spring and treated as an oscillator obeying Hooke's law - a harmonic oscillator. The potential energy, $V(x)$, associated with the vibrational coordinate is given by:

$$V(x) = \left(\frac{1}{2}\right) kx^2 \quad (1.1)$$

where $x = r - r_e$ is the displacement of the bond length, r , from its equilibrium value, r_e , and k is the force constant associated with the spring (bond) strength. The quantum mechanical treatment of the harmonic oscillator tell us that the energy associated with the vibration is quantized and that the molecule can have only discrete vibrational energy levels characterized by the quantum number v :

$$E_v = \left(v + \frac{1}{2}\right) h\omega \quad (1.2)$$

where v can take any integral value 0, 1, 2, 3, ..., and ω is the vibration frequency

given by:

$$\omega = \left(\frac{1}{2\pi} \sqrt{\frac{k}{\mu}} \right) \quad (1.3)$$

The quantity $\mu = m_1 m_2 / (m_1 + m_2)$ is the reduced mass. According to equation 1.2, the vibrational levels have equal spacing ($h\omega$) and in the lowest vibrational level the molecule still has the zero-point energy ($\frac{1}{2}h\omega$).

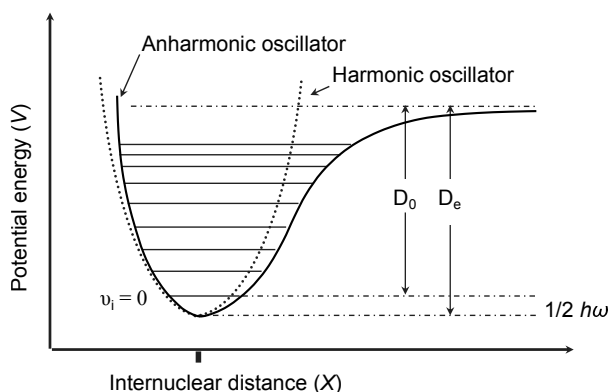


Figure 1.9 Potential energy diagrams for the harmonic (dotted line) and anharmonic (bold line) oscillator. D_0 is the energy necessary to break the bond.

This fairly simply approximation works well for small displacements near the bond length equilibrium value. However, when large displacements are involved, the vibration no longer behaves like that of a harmonic oscillator and anharmonic effects should be taken into consideration. As the distance between the nuclei decreases, the repulsion becomes stronger even for small bond length displacements. At longer bond lengths the bond becomes weaker and eventually dissociates. One approach that can be used to better account for this behavior is the Morse potential:

$$V(x) = D_e [1 - \exp(-\beta x)]^2 \quad (1.4)$$

where D_e is the depth of the potential well, $\beta = 2\pi c \bar{\omega} \sqrt{\mu/2D_e}$ is a measure of the curvature at the bottom of the well, and $\bar{\omega}$ the wavenumber. The allowed vibrational energy levels resulting from the quantum mechanical treatment of the

Morse potential are given by:

$$E_v/hc = \bar{\omega} \left(v + \frac{1}{2} \right) - \bar{\omega}x_e \left(v + \frac{1}{2} \right)^2 \quad (1.5)$$

where the parameter $\bar{\omega}_e x_e$ is an anharmonicity constant. The vibrational energy levels within an anharmonic potential curve are no longer equally spaced above the zero-point level and their smooth convergence can be taken into account by adding successively smaller terms to the expression of equation 1.5.

Whereas the vibration of diatomic molecules are restricted to single stretching modes, the vibrational modes of polyatomic molecules are more complex. A molecule with N atoms has $3N$ degrees of freedom corresponding to the variations of the Cartesian coordinates of each atom of the molecule. In a nonlinear molecule, 3 degrees of freedom correspond to rotation movements, other 3 to translation movements and the rest to fundamental vibrations ($3N - 6$); if the molecule is linear 2 degrees are rotational and 3 translational ($3N - 5$ fundamental vibrations). These normal modes, collectively, describe all possible vibrations of the molecule and can be grouped into two general classes: stretching and bending movements (which include dihedral and torsional angular deformations). After taking into consideration the symmetry of the vibration, the modes can be further subdivided in symmetric or anti-symmetric and, if the molecule has planar fragments, as in-plane or out-of-plane movements. Despite their inherent complexity, polyatomic molecules can also be treated by generalizations or extensions of the models described above for diatomic molecules.

Even though the IR spectrum and its features can provide useful structural information, its analysis with conventional techniques can be somewhat limited. Because the rotational energy levels of molecules are smaller than the vibrational energy levels, light energetic enough to excite vibrations can also excite the rotational movements of molecules. These rotation bands are generally superimposed on the vibration bands and can be easily observed in high-resolution spectra of gaseous samples. In solution, the molecular motion and frequent collisions, as well as a variety of intermolecular interactions leads to a broadening of the bands. On the other hand, in the low temperature matrices, the rotational motion is suppressed and the IR bands of matrix-isolated species tend to be very narrow and of increased simplicity, when compared with the ones in the gas phase or in solution. Thus, the recorded spectra shows minimal overlapping of bands and the identification of absorptions arising

from different species and their conformations, even when they differ by only a few wavenumbers, is facilitated. Moreover, the deviation of matrix IR frequencies from the gas-phase values is relatively small (~2%) and the experimental results can be directly compared with those obtained with theoretical quantum chemical methods, in general dealing with single molecules in vacuo.

1.2.2 Matrix Effects

The noble gases matrices provide a relatively inert trapping medium to preserve and study the chemical species of interest. However, they do exhibit some reactivity and several compounds containing covalently bound noble gases were shown to exist.¹¹⁴⁻¹¹⁷ Therefore, some extent of physical and chemical effects will always be exerted by the matrix host on the guest species. This effects, generally referred to as matrix effects, may contribute to the modification of the shape, intensity and frequency of vibrational bands and should be taken into account during the interpretation of the experimental spectra. Some of the more relevant matrix effects are summarized below:

Molecular rotation - As mentioned above, the matrix isolation, prevents molecules rotation and allows one to obtain spectra uncomplicated by the presence of rotational structure. However, the matrix environment will not fully prevent small molecules (*e.g.* water, ammonia) from rotating within the site and hindered rotation can occur, giving rise to spectroscopically observed characteristic features.

Matrix shifts - In the matrix environment, the isolated species are subject to interactions which disturb their vibrational levels and usually shift bands compared to gas-phase. In general, bands due to stretching modes are deviated to lower frequencies, while bending modes may show both red or blues shifts compared to gas phase. These shifts are relatively small and their magnitude depends on the polarizability of the chosen matrix material. Therefore, with neon or argon one obtains lower amount of interaction than with krypton and, in particular, than with the highly polarizable xenon.

Site splitting - The isolated molecules may be trapped by the matrix host in different orientations and in trapping sites with different morphology. This results in slightly different matrix-guest interactions within the possible matrix sites, and may cause a splitting of the vibrational bands into multiplets (the so called site-splitting effect). This effect may be confused with the splitting due to coexistence of different

conformers of the isolated molecule due to its temperature dependence. However, changing the matrix gas modifies the splitting pattern due to the matrix, while the components of the split bands which originate from different conformers are in principle independent of the nature of the matrix. Other common causes of band splitting are Fermi resonance and molecular aggregation. Fermi resonance is an intrinsic property of the molecule. It is observed when an overtone or a combination vibration interacts with a fundamental of nearly the same energy and bearing the same symmetry. This results in the appearance of two bands, of about equal intensity, on either side of the expected value. On the other hand, molecular aggregation results in several guest-guest interactions which may also cause band splitting and further complicate the spectrum. The splitting due to molecular aggregation can be identified by varying the matrix host-to-guest ratio.

Cage effects - These can influence the outcome of reactions occurring in the matrix and are particularly important for experiments where species are generated inside the same matrix cage, for example by photolysis. In some circumstances, the rigid low-temperature matrix may deactivate the excited molecules through collisional deactivation or cause the recombination of the cage generated fragments. In addition, since the mobility of the fragments resulting from photolysis of a given molecule is restricted by the matrix, cross-reaction involving fragments produced in different cages do not in general take place. Such simplification, compared to gas phase or solution studies, is very useful to extract mechanistic information about the photochemistry of the studied species.

1.2.3 Photochemistry in Matrices

The matrix-isolated species can be photochemically excited with light in the IR*, visible or UV range and the photogenerated products stabilized in the rigid matrices. With sequential irradiations of appropriate wavelengths it is possible to distinguish between different types of phototransformations. These usually are photoisomerization reactions or other photochemical transformations that involve bond breaking/bond forming processes, such as photodissociations. In this particular work, only the UV and visible ranges will be explored. *In situ* irradiation of the matrix with ultraviolet light provides the molecule with a large amount of energy and allows the observation of processes with high energy barriers such as, for example,

*when IR is used to excite the molecule and no electronic excited states are involved but just high-energy vibrational states, the expression “hot vibrational chemistry” should be used instead of “photochemistry,” to make a clear distinction between the two types of processes.

conformational changes leading to an increase in the population of one or more high energy conformers, tautomerizations, structural isomerizations and fragmentation processes.

1.3 Computational Methods

Computational chemistry can be viewed as a set of techniques for investigating chemical problems on a computer. It applies chemical, mathematical and computational skills in the resolution of chemical problems. In computational chemistry there is a variety of methodologies, based in classic and/or quantum mechanics, that can be employed (*e.g.*, molecular mechanics, semi-empirical, *ab initio*, density functional theory, molecular dynamics) according the problem at hands and the desired level of accuracy. The quantum mechanics methods rely on obtaining approximate solutions to the Schrödinger equation. The time dependent formulation of this equation is the following:

$$-\frac{\hbar^2}{2m}\nabla^2\Psi(r,t) + V(r)\Psi(r,t) = i\hbar\frac{\partial\Psi(r,t)}{\partial t} \quad (1.6)$$

where $\nabla^2 = \frac{\partial^2}{\partial x^2} + \frac{\partial^2}{\partial y^2} + \frac{\partial^2}{\partial z^2}$ is the Laplace operator, \hbar the Planck's constant divided by 2π and i the imaginary unity (the square root of -1). Equation 1.6 refers to a particle of mass m moving through time (t) and space (given by a position vector r) under the influence of an external field V . The wavefunction Ψ characterizes the movement of the particle and its square describes the probability of finding the particle at a certain location. Once a wavefunction has been determined, several properties of the particle can be derived. When the external potential is time independent, the wavefunction can be considered the product of a spacial part and a temporal part: $\Psi(r,t) = \Psi(r)T(t)$ and the Schrödinger equation can be written in its time-independent form:

$$-\frac{\hbar^2}{2m}\nabla^2\Psi(r) + V(r)\Psi(r) = E\Psi(r) \quad (1.7)$$

The left-hand side of the equation can be abbreviated and equation 1.7 written in its familiar reduced form $\hat{H}\Psi = E\Psi$, where \hat{H} is the Hamiltonian operator. To solve the Schrödinger equation it is necessary to find values of E and functions Ψ such

that, when the Hamiltonian operates on the wavefunction, it returns the function multiplied by the energy. It is an eigenvalue equation where Ψ is the eigenfunction and E the eigenvalue. The detailed definition of the Hamiltonian operator depends on the physical system to be described by the Schrödinger equation. There are several well known examples (particle in a box or the harmonic oscillator) for which the Hamiltonian has a simple form and the Schrödinger equation can be solved exactly. In the case of a molecular system, where multiple electrons interact with multiple nuclei, the situation is more complex. The problem can be simplified with the Born-Oppenheimer approximation, through the separation of the nuclear and electronic movement, and for a molecule with n electrons and μ atomic nuclei the electronic Hamiltonian (in atomic units) assumes the form:

$$\hat{H} = -\frac{1}{2} \sum_i^n \nabla_i^2 - \sum_{\text{all } \mu, i} \frac{Z_\mu}{r_{\mu i}} + \sum_{\text{all } i, j}^n \frac{1}{r_{ij}} \quad (1.8)$$

where i, j are the electron indices and Z_μ the nucleus charge. The first term represents the kinetic energy of electrons, the second term the potential due to the nucleus-electrons attraction and the third term the repulsion between electrons. The term for the repulsion between nuclei is added *a posteriori*. It is the third term that, by coupling the motion of the electrons, greatly complicates the problem and makes it impossible to exactly solve the Schrödinger equation for systems with more than one electron. Several ab initio or density functional theory based approaches can be used to obtain approximate solutions.

1.3.1 Ab initio

Ab initio calculations, as the name suggests (Latin: "from the beginning"), are derived directly from theoretical principles and a small number of fundamental physical constants (the speed of light, the masses and charges of electrons and nuclei, Planck's constant). The simplest ab initio approach for a system with n electrons is the Hartree-Fock (HF) method, in which the more complicated polyelectronic wavefunction can be broken down into simpler one-electron functions. The total molecular wavefunction Ψ is expressed by a single Slater determinant composed by occupied spin orbitals. Each spin orbital is the product of a conventional spatial

orbital (ψ) and a spin function (α, β) :

$$\Psi_{2n} = \frac{1}{\sqrt{2n!}} \begin{vmatrix} \psi_{1\alpha}(1) & \psi_{1\beta}(1) & \psi_{2\alpha}(1) & \psi_{2\beta}(1) & \cdots & \psi_{n\beta}(1) \\ \psi_{1\alpha}(2) & \psi_{1\beta}(2) & \psi_{2\alpha}(2) & \psi_{2\beta}(2) & \cdots & \psi_{n\beta}(2) \\ \vdots & \vdots & \vdots & \vdots & \vdots & \vdots \\ \psi_{1\alpha}(2n) & \psi_{1\beta}(2n) & \psi_{2\alpha}(2n) & \psi_{2\beta}(2n) & \dots & \psi_{n\beta}(2n) \end{vmatrix} \quad (1.9)$$

By inserting the explicit form of the Hamiltonian operator into the the Schrödinger equation and minimizing the energy, through the variational principle, relatively to the orbitals that compose the wavefunction (*i.e.*, relatively to the Slater determinant) the Hartree-Fock equations can be obtained:

$$\begin{aligned} \hat{F}\psi_1(1) &= \varepsilon_1\psi_1(1) \\ \hat{F}\psi_2(1) &= \varepsilon_2\psi_2(1) \\ \hat{F}\psi_3(1) &= \varepsilon_3\psi_3(1) \\ &\vdots \\ \hat{F}\psi_n(1) &= \varepsilon_n\psi_n(1) \end{aligned} \quad (1.10)$$

The Fock operator \hat{F} is a one-electron operator that acts on one-electron wavefunctions ψ_n to generate an energy value ε_n (*i.e.*, the energy of an electron in ψ_n subject to interaction with all the other electrons in the molecule), times ψ_n . However, the HF equations are not true eigenvalue equations because the Fock operator contains Coulomb and exchange operators that depend on the function ψ . In *ab initio* calculations *per se*, the orbitals are usually expanded by linear combinations of m basis functions:

$$\psi_i = \sum_{s=1}^m c_{si}\phi_s \quad i=1,2,3,\dots,m \quad (1.11)$$

where c are the coefficients of the s th basis functions ϕ of the i th molecular orbital. The equations resulting from this expansion are called the Roothaan-Hall version of the Hartree-Fock equations, and can be written in a matrix form:

$$FC = SC\varepsilon \quad (1.12)$$

where F , C , S and ε are the Fock matrix, coefficients matrix, overlap matrix and energy-levels matrix, respectively. This system of equations is then solved in an iterative self-consistent field procedure that involves diagonalization of the Fock matrix. At the end of the iterative procedure we have the molecular orbitals, their corresponding energies, and the total wavefunction. The molecular orbital energies can be used to calculate the total electronic energy of the molecule, while the total wavefunction can in principle be used to calculate several properties of the molecule, as the expectation value of some operator. Due to the variational nature of the Hartree-Fock SCF method, the energies from HF calculations are always greater than the exact energy and tend to a limiting value called the Hartree-Fock limit as the basis set is improved.

The main deficiency of the Hartree-Fock method is that it fails to adequately represent electron correlation: each electron is described as moving in an average electrostatic net field due to all the other electrons, while in reality the electrons are better able to avoid one another. In fact, an electron feels another moving electron and both mutually adjust (correlate) their movements in order to minimize the interaction energy. This correlation energy (E_{cor}) is defined as the difference between the exact energy of the system (E_{exa}) and the Hartree-Fock energy (E_{HF})

$$E_{cor} = E_{exa} - E_{HF} \quad (1.13)$$

Including correlation effects generally improves the accuracy of computed energies and molecular geometries. These can be incorporated into an ab initio calculation with post-HF methods such as, for example, the Møller-Plesset perturbation theory.

Møller-Plesset Perturbation Theory

The Møller-Plesset (MP) treatment of electron correlation is based on the Rayleigh-Schrödinger perturbation theory. The basic idea behind this theory is to treat a complex system as a small perturbation to a simpler or idealized version of that system. Accordingly, the Hamiltonian operator can be expressed as the sum of a zeroth-order Hamiltonian (H_0) and a perturbation H' :

$$H = H_0 + \lambda H' \quad (1.14)$$

where λ is a variable (from 0 to 1) parameter determining the strength of the perturbation. By using the Hartree-Fock wavefunction and energy (*i.e.*, the sum of the HF one electron-energies) as zeroth-order approximation to the exact wavefunction and varying the perturbation, the MP energy corrections can be obtained. There is a hierarchy of MP energy levels which successively account more thoroughly for electron-electron repulsion. The sum of the zeroth order and first-order energies corresponds to the Hartree-Fock energy and to improve this energy it necessary to use Møller–Plesset second order (MP2) perturbation theory or higher order corrections (MP3, MP4, etc). The corrections introduced by perturbation are essentially electronic terms that can be associated with the promotion of electrons from occupied to unoccupied (virtual) molecular orbitals: in MP2 calculations, doubly excited configurations interact with the ground state; in MP3, doubly excited states interact with one another; MP4 calculations involve singly, doubly, triply and quadruply excited states. In a way, the Møller–Plesset method gives electrons more space to move and makes it easier for them to avoid one another. The decreased electron-electron repulsion results in a lower electronic energy.

The MP n calculations generally improve the accuracy of computed energies and molecular geometries when compared to Hartree-Fock. They are also size-consistent, *i.e.*, they give the energy of a collection of n widely-separated atoms or molecules as being n times the energy of one of them. However, depending on the particular size of the system under study, this particular type of calculations can be computationally intensive. As an alternative, one may use density functional theory.

1.3.2 Density Functional Theory

Density functional theory (DFT) is one of the most commonly used methods of electronic structure determination in computational chemistry. Its success can be owed to the fact that it is less computationally intensive than other methods with similar accuracy: density functional theory is based on the electron density, ρ , which depends on just three coordinates, whereas in wavefunction based approaches a molecule with n electrons would have three spatial coordinates and one spin coordinate for each electron (total of $4n$ variables). Thus, while the complexity of the wavefunction increases with the number of electrons, the electron density maintains the same number of variables, independently of the system size.

The theoretical foundations of density functional theory were laid out in mid 1960s by Hohenberg, Kohn and Sham. The first Hohenberg-Kohn theorem proved that the ground-state energy of an atom or molecule are uniquely determined by its electron

density, *i.e.*, the ground-state energy and the correspondent electronic properties are a functional of the electron density, $E[\rho]$. Although this theorem proves that a functional of the electron density exists, it does not tell anything about the functional actual form. In a second theorem, Hohenberg and Kohn suggested that a variational approach could be used to calculate the energy and electron density, *i.e.*, if the exact functional form is used, then the electron density could be varied until the energy from the functional is minimized.

Kohn and Sham developed a formalism that lead to practical application of these theorems and, consequently, of density functional theory. They considered a system in which the electrons do not interact and in which the ground state electron density distribution is exactly the same as that in a real ground state system of interest, and separated the electronic energy into a part that can be calculated exactly (the one that concerns the idealized system) and a relatively small term accounting for electron-electron interaction. By expressing the electron density in terms of one-electron orbitals and following a variational approach the Kohn-Sham set of equations can be obtained:

$$\left[-\frac{1}{2}\nabla_i^2 - \sum_{\text{nuclei } A} \frac{Z_A}{r_{1A}} + \int \frac{\rho(r_2)}{r_{12}} dr_2 + V_{XC}(r_1) \right] \psi_i^{KS}(r_1) = \varepsilon_i^{KS} \psi_i^{KS}(r_1) \quad (1.15)$$

or

$$\hat{h}^{KS} \psi(r_1) = \varepsilon_i^{KS} \psi_i^{KS}(r_1)$$

where ψ_i^{KS} are the Kohn-Sham orbitals, ε_i^{KS} are the orbital energies and \hat{h}^{KS} the Kohn-Sham operator. The first term represents the kinetic energy of non-interacting electrons, the second term the electron-nuclei interactions, and the third term the electron-electron Coulombic repulsions between the electron being considered in one of the equations and the total electron density defined by all electrons. The fourth term, V_{XC} , is the exchange-correlation potential. The exchange-correlation term accounts for the correction to the kinetic energy term and corrections to the electron-electron repulsion energy. It can be defined as the functional derivative of the exchange-correlation energy:

$$V_{XC}(r) = \frac{\delta E_{XC}[\rho(r)]}{\delta \rho(r)} \quad (1.16)$$

Analogously to what happens in the Hartree-Fock method, the KS orbitals are then expanded as linear combinations of basis functions and the Kohn-Sham set of equa-

tions solved (in matrix form) in an iterative self consistent procedure.

The exchange-correlation term is the only unknown term in the expression for the DFT energy and finding the exact form of this functional remains one of the most important areas of active research in density functional theory. Several approaches for representing the exchange-correlation functional can be used. The simplest approximation, called a local density approximation (LDA), assumes that the exchange-correlation energy at any point in space is a function of the electron density at that point in space only and can be given by the electron density of a uniform electron gas of the same density. When electrons of opposite spin are placed in different KS orbitals, this is called the local spin density approximation (LSDA). Functionals that utilize both the electron density and its gradient are called gradient-corrected, or said to use the generalized-gradient approximation (GGA). Additionally, the recent meta-GGA (M-GGA) functionals also use the the second derivative of the electron density or the kinetic energy density. Finally, there are also hybrid methods (H-GGA, HM-GGA) that combine the exchange-correlation of conventional GGA or M-GGA methods with a percentage of Hartree-Fock (or exact) exchange. It has been found that the choice of “best” functional depends on the system and properties that one wants to describe and exhaustive reviews of the different types of available functionals, their applications and evaluations of their performance can be found in the literature.^{118–121}

1.3.3 Basis Set

As we saw before, when ab initio or density functional theory calculations are done, a basis set must be specified. A basis set is a set of basis functions that, when linearly combined, yield the molecular orbitals (Equation 1.11). The functions are usually (but not always) centered on atomic nuclei and they can be any set of mathematical functions convenient to manipulate and that give useful representations of molecular orbitals and the electron distribution in the molecule as a whole.

Two types of basis functions commonly used in molecular calculations are the Slater type orbitals (STOs; Equation 1.17) and the Gaussian type orbitals (GTOs; Equation 1.18):

$$\chi_{\xi,n,l,m}(r, \theta, \varphi) = NY_{l,m}(\theta, \varphi)r^{n-1} \exp(-\xi r) \quad (1.17)$$

$$\chi_{\xi,n,l,m}(r, \theta, \varphi) = NY_{l,m}(\theta, \varphi)r^{2n-2-l} \exp(-\xi r^2) \quad (1.18)$$

where r , θ and φ are spherical coordinates, N is a normalization constant, $Y_{l,m}$ are spherical harmonic functions, ξ is the orbital exponent, r is the radius in angstroms, and n , l , and m are the principal, angular momentum, and magnetic quantum numbers, respectively. Slater functions are good approximations to atomic orbitals (the exact solution to the Schrödinger equation for the hydrogen atom is a Slater type orbital) and would be the best choice for basis functions. However, the mathematical treatment involved by the use of STOs is more complex and their utility in molecular systems of large size is limited (but they can still be used for atomic and diatomic calculations). Gaussian type orbitals differ from the Slater functions in that the exponent involves the square of the distance of the electron from the point on which the function is centered. Due to this r^2 dependence in the exponential, the GTOs have problems representing the proper radial shape both near and far away from the nucleus. In order to overcome this problem, several Gaussians are usually used to reproduce as accurately as possible a Slater function. When a basis function is defined as a linear combination of Gaussians, it is referred to as a contracted basis function, and the individual Gaussians from which it is formed are called ‘primitive’ Gaussians.

Due to the nature of the computational methods, which scale at approximately m^x (m = basis functions; $x=3, 4$ and 5 for DFT, HF and MP2, respectively), it is of major importance to choose a basis set of adequate size, capable of providing a good compromise between accuracy and computational cost. Several types of basis sets are available in modern molecular ab initio programs. A minimal basis set contains just the number of functions that are required to accommodate all the electrons in each atom. This means that a single s -type function would be required for hydrogen and helium; for the first row elements, $1s$, $2s$ and $2p$ functions are used, and so on. Basis sets with the double, triple and quadruple of the number of functions in the minimal basis set are called double zeta, triple zeta and quadruple zeta, respectively. Because the core orbitals usually do not affect the chemical properties very much (chemical bonding occurs between valence orbitals), most practical calculations make use of split valence basis sets. In the split valence basis set, a single function is used for the core orbitals while the valence orbitals are represented by more than one basis function (split valence double zeta, triple zeta, and so on).

In addition, basis sets can include polarization and diffuse functions: polarization functions correspond to higher angular quantum number functions (p orbitals for hydrogen, d orbitals for the first and second-row elements, etc.) that give the wavefunction more flexibility by allowing the electron distribution to be displaced along a particular direction; diffuse functions are primitives with small exponents and they are often necessary for describing molecules containing lone pairs of electrons or electrons that are on average at larger distance from the nuclei. All these features of the basis sets are identified by notation schemes that can be somewhat different depending on the particular type of basis being used (Pople basis set, Dunning basis set, etc.). The functionals and basis set used in this work are given in chapter 2.

References

1. McNaught, A. D.; Wilkinson, A. *IUPAC Compendium of Chemical Terminology (the "Gold Book")*, 2nd ed.; Nič, M.; Jiráť, J.; Kořata, B.; Jenkins, A., Eds.; Blackwell Scientific Publications: Oxford, 1997.
2. Zollinger, H. *Diazo Chemistry I*; Wiley-VCH Verlag GmbH & Co. KGaA: Weinheim, FRG, 1994; Vol. 1.
3. Zollinger, H. *Diazo Chemistry II*; Wiley-VCH Verlag GmbH & Co. KGaA: Weinheim, FRG, 1995; Vol. 2.
4. Mitscherlich, E. *Ann. Phys. (Berlin)* **1834**, *108*, 225–227.
5. Noble, A. *Justus Liebigs Ann. Chem.* **1856**, *98*, 253–256.
6. Hartley, G. S. *Nature* **1937**, *140*, 281–281.
7. Hunger, K. *Industrial Dyes*; Wiley-VCH Verlag GmbH & Co. KGaA: Weinheim, FRG, 2003.
8. Bamfield, P. *Chromic Phenomena*, 2nd ed.; Royal Society of Chemistry: Cambridge, 2001.
9. Clark, M. *Handbook of textile and industrial dyeing*; Woodhead Publishing Limited, 2011; Vol. 1-2.
10. Sasaki, T.; Tour, J. M. *Org. Lett.* **2008**, *10*, 897–900.
11. Browne, W. R.; Feringa, B. L. *Annu. Rev. Phys. Chem.* **2009**, *60*, 407–428.

12. Feringa, B. L. *Molecular Switches*; Wiley-VCH Verlag GmbH: Weinheim, FRG, 2001.
13. Natansohn, A.; Rochon, P. *Chem. Rev.* **2002**, *102*, 4139–4175.
14. Yager, K. G.; Barrett, C. J. *J. Photochem. Photobiol., A* **2006**, *182*, 250–261.
15. Schnabel, W. *Polymers and Light*, 1st ed.; Wiley-VCH Verlag GmbH & Co. KGaA: Weinheim, 2007.
16. Zhao, Y.; Ikeda, T. *Smart Light-Responsive Materials*; John Wiley & Sons, Inc.: Hoboken, NJ, USA, 2009.
17. Russew, M.-M.; Hecht, S. *Adv. Mater.* **2010**, *22*, 3348–3360.
18. Beharry, A. A.; Woolley, G. A. *Chem. Soc. Rev.* **2011**, *40*, 4422–4437.
19. Merino, E.; Ribagorda, M. *Beilstein J. Org. Chem.* **2012**, *8*, 1071–1090.
20. García-Amorós, J.; Velasco, D. *Beilstein J. Org. Chem.* **2012**, *8*, 1003–1017.
21. Mahimwalla, Z.; Yager, K. G.; Mamiya, J.-i.; Shishido, A.; Priimagi, A.; Barrett, C. J. *Polym. Bull.* **2012**, *69*, 967–1006.
22. Sun, X.; Wang, W.; Qiu, L.; Guo, W.; Yu, Y.; Peng, H. *Angew. Chem. Int. Ed.* **2012**, *51*, 8520–8524.
23. Iqbal, D.; Samiullah, M. *Materials* **2013**, *6*, 116–142.
24. Zheng, Y. B.; Pathem, B. K.; Hohman, J. N.; Thomas, J. C.; Kim, M.; Weiss, P. S. *Adv. Mater.* **2013**, *25*, 302–312.
25. Hartley, G. S. *J. Chem. Soc.* **1938**, 633–642.
26. Corruccini, R. J.; Gilbert, E. C. *J. Am. Chem. Soc.* **1939**, *61*, 2925–2927.
27. Wolf, E.; Cammenga, H. K. *Z. Phys. Chem.* **1977**, *107*, 21–38.
28. Adamson, A. W.; Vogler, A.; Kunkely, H.; Wachter, R. *J. Am. Chem. Soc.* **1978**, *100*, 1298–1300.
29. Fischer, E. *J. Am. Chem. Soc.* **1960**, *82*, 3249–3252.
30. Lednev, I. K.; Ye, T.-q.; Hester, R. E.; Moore, J. N. *J. Phys. Chem.* **1996**, *100*, 13338–13341.

31. Schulze, F.-W.; Petrick, H.-J.; Cammenga, H. K.; Klinge, H. *Z. Phys. Chem.* **1977**, *107*, 1–19.
32. Mita, I.; Horie, K.; Hirao, K. *Macromolecules* **1989**, *22*, 558–563.
33. Cembran, A.; Bernardi, F.; Garavelli, M.; Gagliardi, L.; Orlandi, G. *J. Am. Chem. Soc.* **2004**, *126*, 3234–3243.
34. de Lange, J. J.; Robertson, J. M.; Woodward, I. *Proc. R. Soc. A* **1939**, *171*, 398–410.
35. Brown, C. J. *Acta Crystallogr.* **1966**, *21*, 146–152.
36. Hampson, G. C.; Robertson, J. M. *J. Chem. Soc.* **1941**, 409–413.
37. Bouwstra, J. A.; Schouten, A.; Kroon, J. *Acta Crystallogr., Sect. C* **1983**, *39*, 1121–1123.
38. Harada, J.; Ogawa, K.; Tomoda, S. *Acta Crystallogr., Sect. B* **1997**, *53*, 662–672.
39. Harada, J.; Ogawa, K. *J. Am. Chem. Soc.* **2001**, *123*, 10884–10888.
40. Kellerer, B.; Hacker, H. H.; Brandmüller, J. *Indian J. Pure Appl. Phys.* **1971**, *9*, 903–909.
41. Traetteberg, M.; Hillmo, I.; Hagen, K. *J. Mol. Struct.* **1977**, *39*, 231–239.
42. Tsuji, T.; Takashima, H.; Takeuchi, H.; Egawa, T.; Konaka, S. *J. Phys. Chem. A* **2001**, *105*, 9347–9353.
43. Cattaneo, P.; Persico, M. *Phys. Chem. Chem. Phys.* **1999**, *1*, 4739–4743.
44. Gagliardi, L.; Orlandi, G.; Bernardi, F.; Cembran, A.; Garavelli, M. *Theor. Chem. Acc.* **2004**, *111*, 363–372.
45. Crecca, C. R.; Roitberg, A. E. *J. Phys. Chem. A* **2006**, *110*, 8188–8203.
46. Klug, R. L.; Burcl, R. *J. Phys. Chem. A* **2010**, *114*, 6401–6407.
47. Hättig, C.; Hald, K. *Phys. Chem. Chem. Phys.* **2002**, *4*, 2111–2118.
48. Fliegl, H.; Köhn, A.; Hättig, C.; Ahlrichs, R. *J. Am. Chem. Soc.* **2003**, *125*, 9821–9827.

49. Briquet, L.; Vercauteren, D. P.; Perpète, E. A.; Jacquemin, D. *Chem. Phys. Lett.* **2006**, *417*, 190–195.
50. Robertson, J. M. *J. Chem. Soc.* **1939**, 232–236.
51. Mostad, A.; Rømming, C. *Acta Chem. Scand.* **1971**, *25*, 3561–3568.
52. Biswas, N.; Umaphathy, S. *J. Phys. Chem. A* **1997**, *101*, 5555–5566.
53. Helmut Knoll In *CRC Handbook of Organic Photochemistry and Photobiology, Volumes 1 and 2, Second Edition*; CRC Press, 2003.
54. Beharry, A. A.; Sadvski, O.; Woolley, G. A. *J. Am. Chem. Soc.* **2011**, *133*, 19684–19687.
55. Samanta, S.; Beharry, A. A.; Sadvski, O.; McCormick, T. M.; Babalhavaeji, A.; Tropepe, V.; Woolley, G. A. *J. Am. Chem. Soc.* **2013**, *135*, 9777–9784.
56. Rau, H. In *Photochromism: Molecules and Systems*, revised ed.; Dürr, H.; Bous-Laurent, H., Eds.; Elsevier Science: Amsterdam, 2003; pp 165–192.
57. Bortolus, P.; Monti, S. *J. Phys. Chem.* **1979**, *83*, 648–652.
58. Rau, H.; Lueddecke, E. *J. Am. Chem. Soc.* **1982**, *104*, 1616–1620.
59. Nägele, T.; Hoche, R.; Zinth, W.; Wachtveitl, J. *Chem. Phys. Lett.* **1997**, *272*, 489–495.
60. Lednev, I.; Ye, T.; Matousek, P.; Towrie, M.; Foggi, P.; Neuwahl, F.; Umaphathy, S.; Hester, R.; Moore, J. *Chem. Phys. Lett.* **1998**, *290*, 68–74.
61. Fujino, T.; Tahara, T. *J. Phys. Chem. A* **2000**, *104*, 4203–4210.
62. Fujino, T.; Arzhantsev, S. Y.; Tahara, T. *J. Phys. Chem. A* **2001**, *105*, 8123–8129.
63. Satzger, H.; Root, C.; Braun, M. *J. Phys. Chem. A* **2004**, *108*, 6265–6271.
64. Chang, C.-W.; Lu, Y.-C.; Wang, T.-T.; Diao, E. W.-G. *J. Am. Chem. Soc.* **2004**, *126*, 10109–10118.
65. Schultz, T.; Quenneville, J.; Levine, B.; Toniolo, A.; Martínez, T. J.; Lochbrunner, S.; Schmitt, M.; Shaffer, J. P.; Zgierski, M. Z.; Stolow, A. *J. Am. Chem. Soc.* **2003**, *125*, 8098–8099.

66. Conti, I.; Garavelli, M.; Orlandi, G. *J. Am. Chem. Soc.* **2008**, *130*, 5216–5230.
67. Yuan, S.; Dou, Y.; Wu, W.; Hu, Y.; Zhao, J. *J. Phys. Chem. A* **2008**, *112*, 13326–13334.
68. Bao, J.; Weber, P. M. *J. Am. Chem. Soc.* **2011**, *133*, 4164–4167.
69. Hamm, P.; Ohline, S. M.; Zinth, W. *J. Chem. Phys.* **1997**, *106*, 519–529.
70. Satzger, H.; Spörlein, S.; Root, C.; Wachtveitl, J.; Zinth, W.; Gilch, P. *Chem. Phys. Lett.* **2003**, *372*, 216–223.
71. Wei-Guang Diao, E. *J. Phys. Chem. A* **2004**, *108*, 950–956.
72. Monti, S.; Orlandi, G.; Palmieri, P. *Chem. Phys.* **1982**, *71*, 87–99.
73. Ishikawa, T.; Noro, T.; Shoda, T. *J. Chem. Phys.* **2001**, *115*, 7503–7512.
74. Ikegami, T.; Kurita, N.; Sekino, H.; Ishikawa, Y. *J. Phys. Chem. A* **2003**, *107*, 4555–4562.
75. Ciminelli, C.; Granucci, G.; Persico, M. *Chem. Eur. J.* **2004**, *10*, 2327–2341.
76. Shao, J.; Lei, Y.; Wen, Z.; Dou, Y.; Wang, Z. *J. Chem. Phys.* **2008**, *129*, 164111.
77. Dou, Y.; Hu, Y.; Yuan, S.; Wu, W.; Tang, H. *Mol. Phys.* **2009**, *107*, 181–190.
78. Bandara, H. M. D.; Friss, T. R.; Enriquez, M. M.; Isley, W.; Incarvito, C.; Frank, H. A.; Gascon, J.; Burdette, S. C. *J. Org. Chem.* **2010**, 4817–4827.
79. Tiberio, G.; Muccioli, L.; Berardi, R.; Zannoni, C. *ChemPhysChem* **2010**, *11*, 1018–1028.
80. Maurer, R. J.; Reuter, K. *J. Chem. Phys.* **2011**, *135*, 224303.
81. Pederzoli, M.; Pittner, J.; Barbatti, M.; Lischka, H. *J. Phys. Chem. A* **2011**, *115*, 11136–11143.
82. Harabuchi, Y.; Ishii, M.; Nakayama, A.; Noro, T.; Taketsugu, T. *J. Chem. Phys.* **2013**, *138*, 064305.
83. Böckmann, M.; Doltsinis, N.; Marx, D. *Phys. Rev. E* **2008**, *78*, 036101.

84. Böckmann, M.; Doltsinis, N. L.; Marx, D. *J. Phys. Chem. A* **2010**, *114*, 745–754.
85. Böckmann, M.; Marx, D.; Peter, C.; Site, L. D.; Kremer, K.; Doltsinis, N. L. *Phys. Chem. Chem. Phys.* **2011**, *13*, 7604–7621.
86. Gámez, J. A.; Weingart, O.; Koslowski, A.; Thiel, W. *J. Chem. Theory Comput.* **2012**, *8*, 2352–2358.
87. Neukirch, A. J.; Shamberger, L. C.; Abad, E.; Haycock, B. J.; Wang, H.; Ortega, J.; Prezhdo, O. V.; Lewis, J. P. *J. Chem. Theory Comput.* **2014**, *10*, 14–23.
88. Sauer, P.; Allen, R. E. *Chem. Phys. Lett.* **2008**, *450*, 192–195.
89. Ootani, Y.; Satoh, K.; Nakayama, A.; Noro, T.; Taketsugu, T. *J. Chem. Phys.* **2009**, *131*, 194306.
90. Wazzan, N. A.; Richardson, P. R.; Jones, A. C. *Photochem. Photobiol. Sci.* **2010**, *9*, 968–974.
91. Creatini, L.; Cusati, T.; Granucci, G.; Persico, M. *Chem. Phys.* **2008**, *347*, 492–502.
92. Bandara, H. M. D.; Burdette, S. C. *Chem. Soc. Rev* **2012**, *41*, 1809–1825.
93. Cheon, K.-S.; Park, Y. S.; Kazmaier, P. M.; Buncel, E. *Dyes Pigm.* **2002**, *53*, 3–14.
94. Antonov, L.; Deneva, V.; Simeonov, S.; Kurteva, V.; Nedeltcheva, D.; Wirz, J. *Angew. Chem. Int. Ed.* **2009**, *48*, 7875–7878.
95. Burdette, S. C. *Nat. Chem.* **2012**, *4*, 695–696.
96. Fischer, E.; Frei, Y. F. *J. Chem. Soc.* **1959**, 3159–3163.
97. Gilli, P.; Bertolasi, V.; Pretto, L.; Lyčka, A.; Gilli, G. *J. Am. Chem. Soc.* **2002**, *124*, 13554–13567.
98. Nedeltcheva, D.; Damyanova, B.; Popov, S. *J. Mol. Struct.* **2005**, *749*, 36–44.
99. Gilli, P.; Bertolasi, V.; Pretto, L.; Antonov, L.; Gilli, G. *J. Am. Chem. Soc.* **2005**, *127*, 4943–4953.

100. Matazo, D. R. C.; Ando, R. A.; Borin, A. C.; Santos, P. S. *J. Phys. Chem. A* **2008**, *112*, 4437–4443.
101. Filarowski, A.; Kochel, A.; Kluba, M.; Kamounah, F. S. *J. Phys. Org. Chem.* **2008**, *21*, 939–944.
102. Nedeltcheva, D.; Kamounah, F. S.; Mirolo, L.; Fromm, K. M.; Antonov, L. *Dyes Pigm.* **2009**, *83*, 121–126.
103. Nedeltcheva, D.; Kurteva, V.; Topalova, I. *Rapid Commun. Mass Spectrom.* **2010**, *24*, 714–720.
104. Almeida, M. R.; Stephani, R.; Dos Santos, H. F.; de Oliveira, L. F. C. *J. Phys. Chem. A* **2010**, *114*, 526–534.
105. Kurteva, V. B.; Antonov, L. M.; Nedeltcheva, D. V.; Crochet, A.; Fromm, K. M.; Nikolova, R. P.; Shivachev, B. L.; Nikiforova, M. S. *Dyes Pigm.* **2012**, *92*, 1266–1277.
106. Ferreira, G. R.; Garcia, H. C.; Couri, M. R. C.; Dos Santos, H. F.; de Oliveira, L. F. C. *J. Phys. Chem. A* **2013**, *117*, 642–649.
107. Pajak, J.; Rospenk, M.; Ramaekers, R.; Maes, G.; Glowiak, T.; Sobczyk, L. *Chem. Phys.* **2002**, *278*, 89–100.
108. Pajak, J.; Ramaekers, R.; Rospenk, M.; Alexandrov, V.; Stepanian, S.; Adamowicz, L.; Maes, G. *Chem. Phys.* **2003**, *286*, 193–204.
109. Whittle, E.; Dows, D. A.; Pimentel, G. C. *J. Chem. Phys.* **1954**, *22*, 1943.
110. Ian Dunkin In *CRC Handbook of Organic Photochemistry and Photobiology, Volumes 1 and 2, Second Edition*; CRC Press, 2003.
111. Willson, S. P.; Andrews, L. In *Handbook of Vibrational Spectroscopy*; John Wiley & Sons, Ltd, 2006.
112. Dunkin, I. R. *Matrix-Isolation Techniques: A Practical Approach*; Oxford University Press, USA, 1998.
113. Fausto, R.; Khriachtchev, L.; Hamm, P. In *Physics and Chemistry at Low Temperatures*; Khriachtchev, L., Ed.; Pan Stanford Publishing, 2011.

114. Fausto, R.; Gomez-Zavaglia, A. In *Photochemistry: Volume 39*; The Royal Society of Chemistry, 2011; Vol. 39, pp 1–29.
115. Nemukhin, A. V.; Khriachtchev, L. Y.; Grigorenko, B. L.; Bochenkova, A. V.; Räsänen, M. *Russ. Chem. Rev.* **2007**, *76*, 1085–1092.
116. Khriachtchev, L.; Räsänen, M.; Gerber, R. B. *Accounts of Chemical Research* **2009**, *42*, 183–191.
117. Khriachtchev, L.; Pettersson, M.; Runeberg, N.; Lundell, J.; Räsänen, M. *Nature* **2000**, *406*, 874–876.
118. Sousa, S. F.; Fernandes, P. A.; Ramos, M. J. *J. Phys. Chem. A* **2007**, *111*, 10439–10452.
119. Riley, K. E.; Op't Holt, B. T.; Merz, K. M. *J. Chem. Theory Comput.* **2007**, *3*, 407–433.
120. Zhao, Y.; Truhlar, D. G. *Acc. Chem. Res.* **2008**, *41*, 157–167.
121. Zhao, Y.; Truhlar, D. G. *Chem. Phys. Lett.* **2011**, *502*, 1–13.

2

Methods and Materials

2.1 Samples

The compounds CPDNO, CPDP and HAB were provided by Prof. Ana Maria Oliveira-Campos (University of Minho) and used as received. Azobenzene was purchased from *Fluka* (purity 98%) and used without any further purification.

2.2 Experimental Details

2.2.1 Matrix Deposition

The studied compounds were sublimated from a miniature glass oven placed in the vacuum chamber of the cryostat (or in the case of AB evaporated from a Pyrex glass tube connected to the cryostat through a needle valve), and the vapor of the compound deposited together with a large excess of matrix gas (argon N60 or xenon N48; both supplied by Air Liquide), onto a CsI window cooled to 15 K (Ar) or 30 K (Xe) by a closed-cycle helium refrigerator with an APD Cryogenics DE-202A expander. The temperature of the CsI window was measured directly at the sample holder by a silicon diode temperature sensor connected to a digital temperature controller (Scientific Instruments, Model 9650-1), which provides stabilization accuracy of 0.1 K (Figure 2.1).

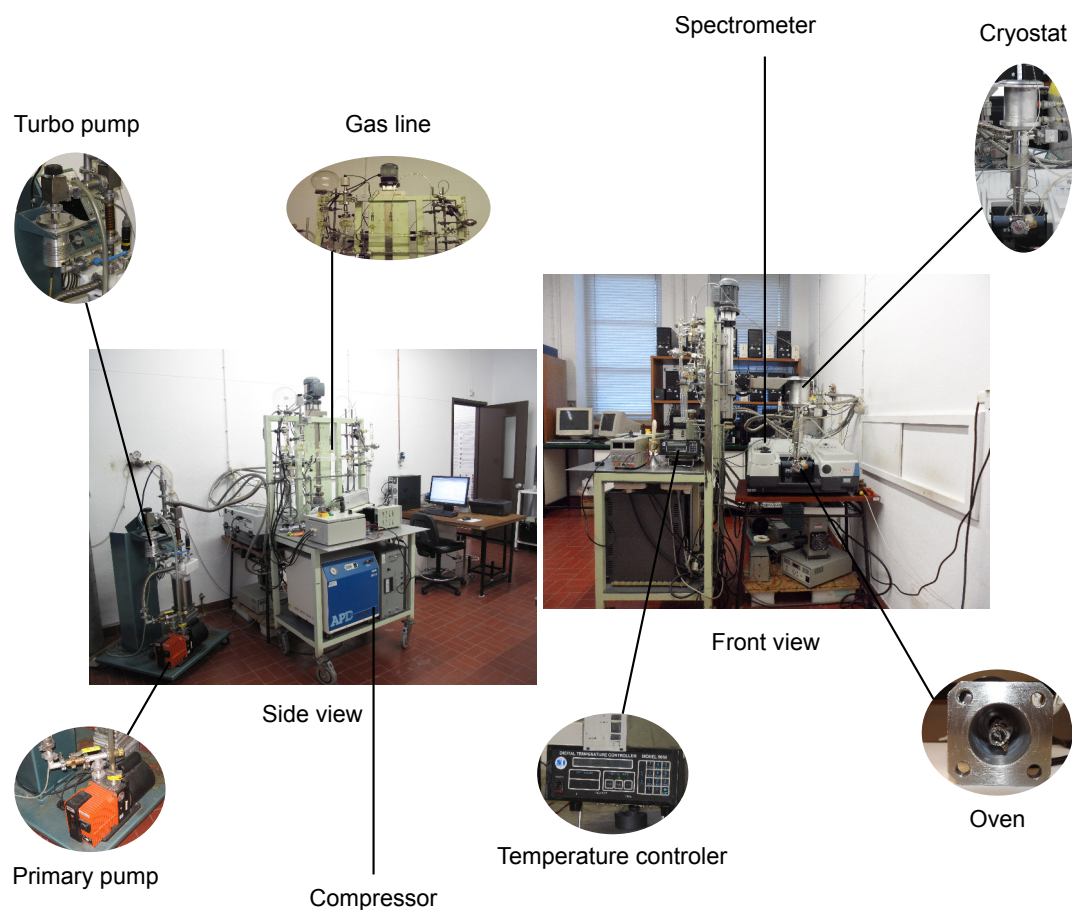


Figure 2.1 Matrix isolation experimental setup used during this work.

2.2.2 IR Absorption Measurements

The matrix isolation infrared spectra were recorded in the $4000\text{--}400\text{ cm}^{-1}$ range, using a Nicolet 6700 FTIR spectrometer equipped with a deuterated triglycine sulfate (DTGS) detector and a Ge/KBr beam splitter, with 0.5 cm^{-1} spectral resolution. Like most modern FTIR spectrometers, the Nicolet 6700 uses a Michelson interferometer to obtain infrared spectra (Figure 2.2). The infrared light emitted from the source is collimated and directed to the beamsplitter where is partially transmitted and reflected to the moving and fixed mirrors, respectively. The two IR beams are then reflected back to the beamsplitter ($\sim 50\%$ of the light is lost to the source), recombined and sent through a sample to the detector. Depending on the wavelength of the light and the optical path difference introduced by the moving mirror, the two combined beams may interfere constructively or destructively producing a

wavelength-dependent interference pattern - the interferogram - that contains the spectral information of the sample (*i.e.*, a superimposition of the data relative to all the different wavelengths scanned). The interferogram is then Fourier transformed and a plot of the IR signal versus wavelength - the single beam spectrum - is obtained. Finally, in order to account for the contributions relative to the instrumental noise and residual atmospheric absorptions from carbon dioxide and water vapors, the single beam sample spectrum is normalized against a single beam background spectrum measured without a sample and the final IR spectrum (in transmittance or absorbance form) is obtained.

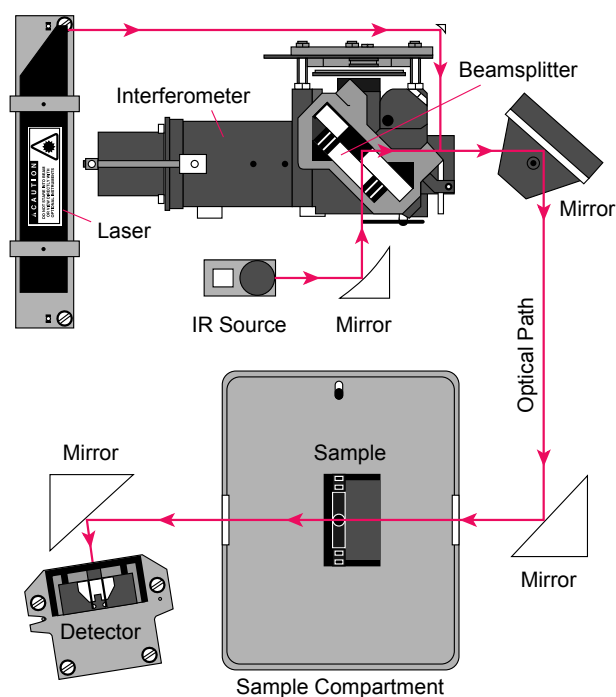


Figure 2.2 Schematic representation of a spectrometer layout. Infrared energy emitted from a ETC EverGlo* source enters the interferometer and the resulting interferogram is transmitted through the sample. The signal is then measured by the detector and sent to a computer where the Fourier transformation takes place. A HeNe laser is used as an internal wavelength calibration standard. Adapted from reference 1.

In all the performed experiments, the spectra were acquired after accumulating interferograms resulting from 64-128 scans. Necessary modifications of the sample compartment of the spectrometer were done in order to accommodate the cryostat head and allow purging of the instrument by a stream of dry, CO_2 filtered air (Figure 2.1).

2.2.3 UV Irradiation

The cryogenic matrices were irradiated through an outer quartz window of the cryostat using narrowband tunable (0.2 cm^{-1} spectral width) light provided by a Quanta-Ray MOPO-SL optical parametric oscillator (OPO), pumped with a pulsed (repetition rate = 10 Hz, duration = 10 ns) Nd:YAG laser (Figure 2.3). In the visible range (440-600 nm) the signal beam of the OPO was used as the light source (pulse energy of 30-40 mJ). In the UV range (230-440 nm), the frequency-doubled signal or idler beam was used (pulse energy $\sim 3 \text{ mJ}$).

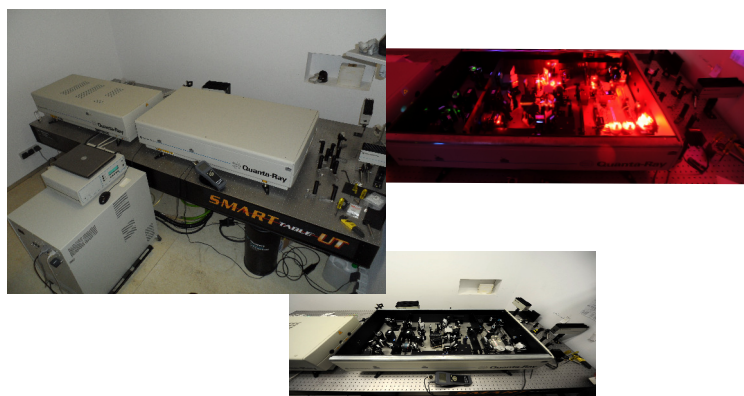


Figure 2.3 The Quanta-Ray Pro Pulsed Nd:YAG laser and MOPO-SL Optical Parametric Oscillator used in this work.

The Nd:YAG is a four-level laser that uses neodymium doped into a yttrium aluminum garnet solid host crystal ($\text{Y}_3\text{Al}_5\text{O}_{12}$) as a laser material. The electrons of the active lasing ions - Nd^{3+} - are optically pumped by a flash lamp from the ground state ($^4\text{I}_{9/2}$) to higher energy levels (Figure 2.4). These levels are characterized by a short lifetime and the excited electrons rapidly decay to the upper level of the lasing transition ($^4\text{F}_{3/2}$). The electrons remain in the upper laser level for a relatively long period of time (about $230 \mu\text{s}$) and a population inversion takes place. The transition to the lower laser level ($^4\text{I}_{11/2}$) is stimulated by the interaction with a light photon and the laser fundamental (1064 nm) is produced. The lower laser level then quickly relaxes back to the ground state.

The laser fundamental output can be converted by an internal harmonic generator system to the second (532 nm) and third (355 nm) harmonic waves. The optical wave resulting from the third harmonic generation can then be used to pump the optical parametric oscillator system (through the nonlinear interaction with a Beta Barium Borate crystal).

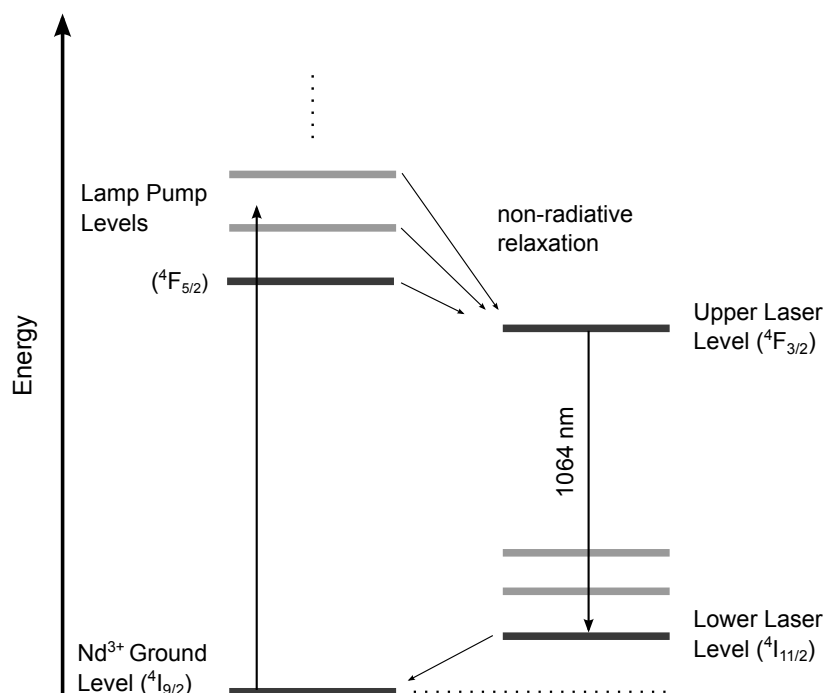


Figure 2.4 Simplified energy-level scheme of a Nd:YAG laser. All electronic transitions in the neodymium laser occur within the 4f shell.

Additionally, broad-band UV/vis irradiation, provided by a 500 W Hg(Xe) arc lamp (Spectra-Physics, model 66142), adjusted to have an output power of 200 W, was also used in some preliminary experiments and during deposition of azobenzene in the irradiation experiments performed on this molecule (see Section 3.1.1).

2.3 Computational Details

Azobenzene calculations were performed with the Gaussian 09² software package. The PW91, BP86, B97-1, B3LYP and OLYP functionals and the 6-311++G(3df,3pd) and cc-pVTZ basis sets were used. The equilibrium geometries were optimized with the default Berny optimization algorithm and a tight optimization criteria.³ The geometry optimizations were followed by harmonic frequency calculations at the same levels of theory, and the nature of the obtained stationary points was checked through analysis of the corresponding Hessian matrices. The theoretical normal modes were analyzed by carrying out potential energy distribution (PED) calculations. Transformations of the force constants with respect to the Cartesian coordinates to the force constants with respect to the molecule-fixed internal coordinates allowed the PED

analyses to be carried out as described by Schachtschneider and Mortimer.⁴ The internal symmetry coordinates used in these analyses were defined as recommended by Pulay et al.⁵

HAB, CPDP and CPDNO calculations were carried out at the DFT (B3LYP and PW91) and/or second order Møller-Plesset (MP2) levels using the 11 Aug 2011 (R1) version of the Gamess-US program.^{6,7} The Dunning's basis set cc-pVTZ and/or the 6-311+G(2df,2p) Pople basis set were used in these calculations. Geometrical parameters were optimized using the quadratic approximation optimization algorithm together with an SCF density convergence criterion of 1×10^{-5} Hartree and gradient convergence criterion of 1×10^{-4} Hartree/Bohr. The geometry optimizations were followed by harmonic frequency calculations at the same theory levels, and the nature of the obtained stationary points was checked through analysis of the corresponding Hessian matrices.*

References

1. *Introduction to Fourier Transform Infrared Spectrometry*; 2001; Thermo Nicolet Corporation.
2. Frisch, M. J.; et al.; *Gaussian 09 Revision A.02*; Gaussian Inc. Wallingford CT 2009.
3. Schlegel, H. B. *J. Comput. Chem.* **1982**, *3*, 214–218.
4. Schachtschneider, J. H.; Mortimer, F. S.; *Vibrational Analysis of Polyatomic-Molecules.VI. FORTRAN IV Programs for Solving the Vibrational Secular Equation and for the Least-Squares Refinement of Force Constants.*; 1969.
5. Pulay, P.; Fogarasi, G.; Pang, F.; Boggs, J. E. *J. Am. Chem. Soc.* **1979**, *101*, 2550–2560.
6. Schmidt, M. W.; Baldridge, K. K.; Boatz, J. A.; Elbert, S. T.; Gordon, M. S.; Jensen, J. H.; Koseki, S.; Matsunaga, N.; Nguyen, K. A.; Su, S.; Windus, T. L.; Dupuis, M.; Montgomery, J. A. *J. Comput. Chem.* **1993**, *14*, 1347–1363.

*For CPDNO, the Lebedev angular (nrad=96, nleb=590) grid,⁸ an SCF density convergence criterion of 1×10^{-6} Hartree and an gradient convergence criterion of 1×10^{-5} Hartree/Bohr were used instead. Anharmonic corrections for selected modes of isomers E1 and K1 were carried out with the vibrational self-consistent field method (VSCF)⁹ combined with the quartic force field approximation (QFF).¹⁰

7. Gordon, M.; Schmidt, M. In *Theory and Applications of Computational Chemistry: the first forty years*; Dykstra, C.; Frenking, G.; Kim, K.; Scuseria, G., Eds.; Elsevier: Amsterdam, 2005; pp 1167–1189.
8. Lebedev, V. I.; Laikov, D. N. *Dokl. Math.* **1999**, *59*, 477–481.
9. Chaban, G. M.; Jung, J. O.; Gerber, R. B. *J. Chem. Phys.* **1999**, *111*, 1823–1829.
10. Yagi, K.; Hirao, K.; Taketsugu, T.; Schmidt, M. W.; Gordon, M. S. *J. Chem. Phys.* **2004**, *121*, 1383–1389.

3

Results

3.1 Azobenzene*

As it was previously mentioned in Section 1.1, the photoisomerization reaction of azobenzene (Figure 3.1) is frequently employed in the development of photoresponsive systems. However, despite the abundance of well-established applications, some relevant aspects concerning the structure, spectroscopy and photochemistry of azobenzene still remain unclear.

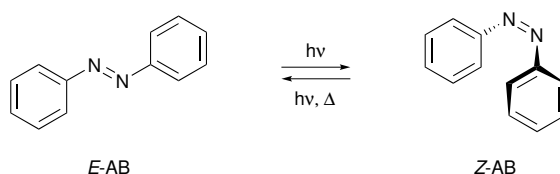


Figure 3.1 Structures of *E* and *Z* isomers of azobenzene.

In this regard, vibrational data have been shown to be particularly significant in the elucidation of structural properties and mechanistic questions in azo-based systems.¹⁻⁷ For example, examination of the NN stretching frequency of *E*-AB in both the ground state and first excited electronic states was used to gain some insight into the photoisomerization mechanism of azobenzene. Fujino and Tahara found that the NN stretching frequency in the S_1 state was very close to that of the ground state and concluded that the double bond nature of the NN bond is retained during the photoisomerization.⁸ Harabuchi et al. reported that the calculated (CASPT2) NN stretching frequency shows a slight decrease along the rotation pathway while it increases rapidly along the inversion pathway.⁴ In turn, Ikegami and co-workers studied the thermal isomerization reaction of *Z*-AB by direct molecular dynamics

*The content reported in this section was already published. The original paper (Duarte, L.; Fausto, R.; Reva, I. *Phys. Chem. Chem. Phys.* **2014**, DOI: 10.1039/C4CP00240G) can be found in Appendix B.

and calculated the vibrational spectra from the obtained trajectories. They showed that skeletal vibrations of the phenyl rings play an important role in the thermal isomerization reaction of the azobenzene molecule.⁹ Likewise, Jiang and Aida found that excitation of similar modes enhances the *Z*-to-*E* isomerization reaction of azo-dendrimers.¹⁰ Therefore, an accurate description of the vibrations of azobenzene is of value for improving the general understanding of azobenzene and derivatives.

A few studies dealing with the vibrational analyses of AB can be found in the literature.^{11–14} However, most of these studies rely on comparisons made with experimental spectra obtained for the compound in a KBr pellet or in solution.^{15–23} Furthermore, fewer experimental data have been reported for the *Z*-AB form, whose vibrational spectrum remains insufficiently characterized.

3.1.1 Isomeric Composition of Matrix-Isolated AB

Two types of experiments were carried out to obtain the monomers of azobenzene isolated in cryogenic matrices: (a) In the first type of experiment, crystals of AB were placed in a Pyrex glass tube maintained at room temperature, and the equilibrium vapors were introduced into the cryostat simultaneously with a large excess of argon and condensed together onto the cryostat optical window kept at 15 K. Since the *Z*-*E* energy difference in AB is very large [experimentally, it has been reported to be in the range 47–48 kJ mol⁻¹,^{15,24–26} in agreement with the calculated values obtained at various DFT (over 58 kJ mol⁻¹)²⁷ and also at CASSCF and MR-CIS (68 kJ mol⁻¹) levels],²⁸ the thermodynamically most stable *E*-AB form should be the only form detectable in the gas phase thermal equilibrium at room temperature. Accordingly, it was the only form observed to be present in the matrices prepared in this type of experiment (Figure 3.2a). (b) In the second type of experiment, the experimental layout of the deposition line was the same as in (a); the difference was that the vapors of AB prior to deposition were continuously irradiated through the walls of the Pyrex tube using broadband UV-visible light coming out of an Hg(Xe) arc lamp. Under these conditions, a set of new bands appeared in the experimental infrared (IR) spectrum of the matrix-isolated compound (Figure 3.2b). These new bands could be reliably assigned to the photogenerated *Z*-AB isomer.*

Selected regions of the infrared spectra of matrix-isolated azobenzene obtained in experiments of type (a) and (b) are shown in Figure 3.2, along with the theoretical

*Generation of *Z*-azobenzene in the present work is similar to the method discovered by Hartley, in 1937: when azobenzene placed in a glass bottle was exposed to sunlight for several days, *Z*-AB was generated. See: G. S. Hartley, *Nature*, 1937, v. 140, p. 281.

spectra of the *E*-AB and *Z*-AB isomers.*

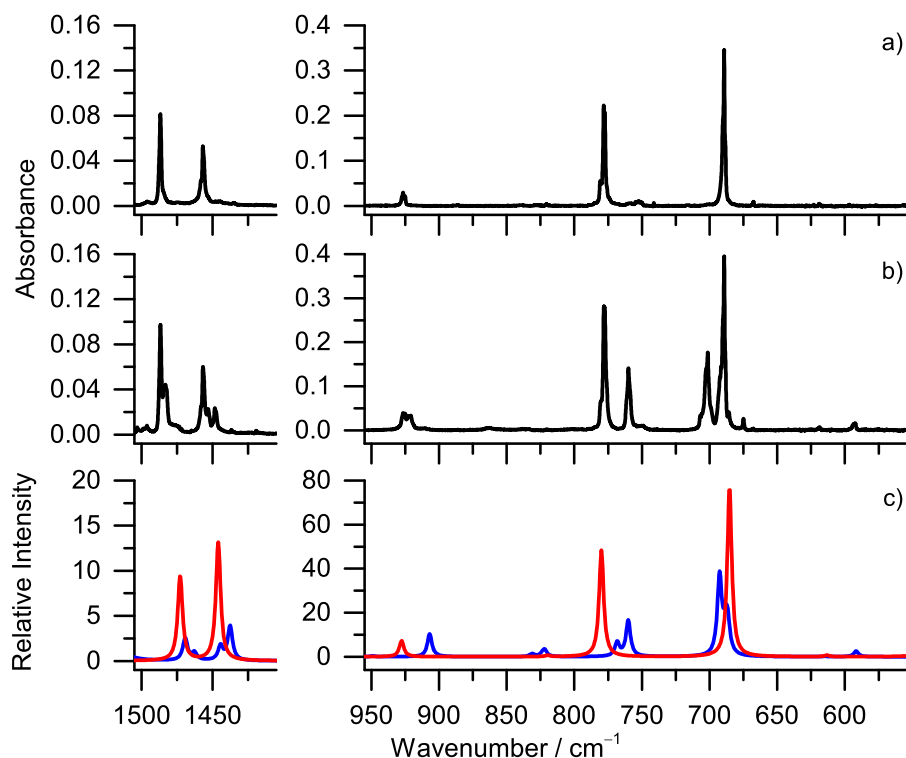


Figure 3.2 Selected regions of the experimental infrared spectra of azobenzene isolated in argon matrices at 15 K: (a) shortly after deposition of the equilibrium vapor existing over AB crystals at room temperature; (b) after trapping of the AB vapors subjected prior to deposition to broadband visible-UV irradiation by a Hg(Xe) lamp. (c) Spectra of *E* (red) and *Z* (blue) azobenzene forms simulated on the basis of the PW91/cc-pVTZ calculations. The calculated infrared intensities for *Z*-AB were scaled by 0.5, while those of *E*-AB were not scaled.

The above described observations deserve two comments, which are important for the following discussion: (i) The Pyrex glass (transmitting light above 290 nm) permits to induce the photochemical reaction and trigger the *E*→*Z* isomerization of AB in the gas phase. This is in accord with the energies of the lowest singlet excited states of *E*-AB (peak values: 2.78 and 4.10 eV, equivalent to 446 and 302 nm), measured in the gas phase by electron energy loss spectroscopy.²⁹ (ii) The photochemically generated *Z*-AB form does not thermally convert back to the *E* isomer, at room temperature, in the gas phase, on the time scale of the experiments (tens of minutes); it is stable enough to withstand collisions with the walls of the

*The choice of the model chemistry will be commented in the following section.

deposition line* and with other AB molecules, and can be successfully trapped in the matrix. This last observation can be reasonably explained by the value of the barrier for the thermal $Z \rightarrow E$ AB conversion, whose experimental^{30,31} measure is about 92-105 kJ mol⁻¹ (calculated DFT values, 80-100 kJ mol⁻¹, stay in the same range).²⁷

3.1.2 Photoisomerization

The E -AB monomers, trapped in the matrix in the first type of experiment, were irradiated with UV-visible light through an outer quartz window of the cryostat with the objective to induce *in situ* $E \rightarrow Z$ isomerization of azobenzene. Two types of irradiations were applied: (i) narrowband irradiation with light provided by an optical parametric oscillator (OPO) and tuned from 600 nm to 220 nm wavelength range, or (ii) broadband irradiation using light coming out of a Hg(Xe) arc lamp equipped with different longpass filters, with cut-off in UV or visible ranges, or without any filters, providing UV output down to 200 nm. The changes in the samples were followed by infrared spectroscopy after each irradiation. All performed irradiations were found not to cause any alterations in the IR spectrum of the irradiated samples.[†] On the other hand, when a matrix containing both E and Z isomers of azobenzene, obtained in the second type of the experiment described above, was irradiated with UV-visible light, almost complete conversion of the Z form into the E isomer was observed (Figure 3.3). In order to find out the longest wavelength at which the photoreaction starts, the samples were irradiated using the tunable output of the OPO, starting from 600 nm and gradually decreasing the wavelength (in steps of 10 nm). The first signs of phototransformation of AB were detected after irradiations at 550 nm, albeit tiny. The onset wavelength of the photoinduced $Z \rightarrow E$ conversion is thus in good agreement with the gas phase electronic absorption spectrum of Z -AB.^{31,33} When the irradiation was performed at 540 nm, the complete $Z \rightarrow E$ transformation occurred on a timescale of a few minutes. Irradiations at shorter wavelengths, in separate experiments, also led to consumption of Z -AB. When Z -AB was totally consumed, all subsequent irradiations at any wavelengths, whether using narrow- or broadband light sources, did not lead to additional changes.

*10-15 cm long, glass and stainless steel.

[†]The average relaxation time of the electronically excited azobenzene is 121 fs. See reference 32 and collection of references cited therein. For such a fast relaxation, the steady state spectroscopy allows only for detecting spectra of the electronically relaxed molecules.

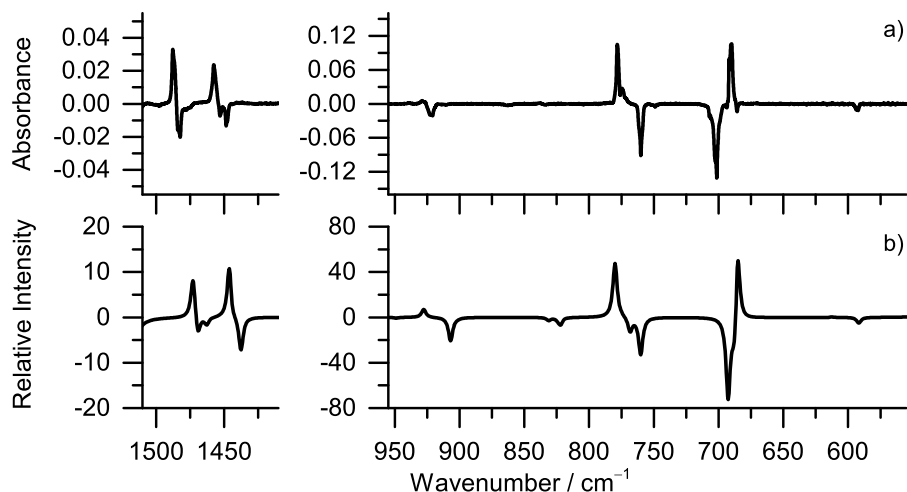


Figure 3.3 (a) Changes in the experimental infrared spectrum of AB in an Ar matrix at 15 K (second type of experiment, both *E*-AB and *Z*-AB are initially present) after 1 min irradiation at $\lambda = 440$ nm. Negative absorptions correspond to decreasing bands of the initially present *Z*-AB form. Positive peaks correspond to growing absorptions due to the *E*-AB form; (b) Simulated theoretical difference spectrum, representing quantitative transformation of *Z*-AB into *E*-AB, constructed as “*E* minus *Z*”.

The observed isomerization behavior of AB calls for an obvious conclusion. On one hand, the $E \rightarrow Z$ isomerization was successfully induced in the gas phase by UV-visible irradiation during the deposition of the matrices. On the other hand, no such isomerization could be induced when a similar irradiation was applied to the matrix-isolated *E*-AB monomers. The absence of the photoinduced $E \rightarrow Z$ transformation for matrix-isolated AB should then be attributed to the cryogenic matrix, restricting isomerization of the bulky phenyl substituent (C_6H_5) in the solid environment. Such situation was also recently found to occur for matrix-isolated stilbene, structurally similar to AB.³⁴ Interestingly, when one of the substituents linked to a double $N=N$ bond is reduced from phenyl to cyclopropyl (C_3H_5), the photochemical $E \rightarrow Z$ transformation could be successfully induced in the matrix (see Section 3.3 and Section 3.4). In this context, it appears also interesting to compare our observations with those from another recently published study, focusing on the photoisomerization of *E*-AB under high external pressures. Singleton *et al.* studied the photoswitching behavior of AB placed inside a diamond-anvil spectroscopic cell as a function of the external pressure.³⁵ They found that the *Z*-AB content of the photostationary state gradually decreased with pressure, with complete arrest of the $E \rightarrow Z$ photoisomerization above 1.5 GPa. The reverse, $Z \rightarrow E$ photoisomerization of

azobenzene was shown, however, still to be inducible at all the pressures investigated (up to 4 GPa). This was rationalized in terms of isomerization occurring in free volume pockets in the host material (that decrease with increase of pressure). Apparently, in the cryogenic argon matrix at 15 K, these free volume pockets are smaller than the $E \rightarrow Z$ isomerization requirement.

3.1.3 Choice of the Model Chemistries

Calculations for the structure and vibrational frequencies of azobenzene have been reported in the literature before. Biswas and Umaphy, ¹³ and Kurita *et al.* ³⁶ found that the BP86/6-31G* and PW91 (exchange and correlation functionals)/6-31+G* approaches, respectively, gave good results when used in the prediction of azobenzene vibrational frequencies. Fliegl and co-workers ¹⁴ performed RI-MP2 and DFT calculations, and showed that sufficiently extended basis set have to be employed for the correct description of the azo group. Klug and Burcl ^{27,37} found the geometrical parameters calculated with the OLYP and B97-1 functionals to be in excellent agreement with experimental geometries obtained by gas electron diffraction (GED). ³⁸ Thus, in order to find the most suitable approach for the interpretation of our experimental results, we carried out optimization of the structures of the two AB isomers followed by calculations of their vibrational spectra using the above mentioned functionals together with more complete basis sets. The widely used B3LYP functional was also included in the set of model chemistries investigated as a reference, and our results were also compared with other high-level calculations, such as RI-MP2. ¹⁴ A set of well-defined bands in the infrared spectrum of matrix-isolated AB was chosen, and the experimental frequencies were compared with their calculated counterparts, including the data available in the literature. The results are summarized in Table B.1. The best overall agreement was found for the PW91/cc-pVTZ and OLYP/cc-pVTZ approaches, both with a mean unsigned error (MUE) of 7 cm⁻¹. Between these two functionals, the OLYP presents the highest absolute error for the E and Z forms; hence we chose to use the PW91/cc-pVTZ method to carry out the vibrational calculations and normal mode analyses. From all the theoretical approaches, the widely used B3LYP functional and the second order Møller–Plesset (MP2) approximation gave the less satisfactory results. The vibrational frequencies and Cartesian coordinates of all optimized structures are given in Table B.2 and Table B.3, respectively.

3.1.4 Vibrational Spectra

The planar *E*-AB structure (C_{2h} symmetry) has 66 normal modes, 33 of which are infrared active (Table 3.1) while the remaining 33 modes are Raman active (Table B.5). The most intense infrared absorption bands in the *E*-AB spectrum, situated at 689.2 and 778.3 cm^{-1} have their calculated counterparts at 685.2 and 780.0 cm^{-1} (See Figure 3.4). They result essentially from the coupling of $\gamma(\text{CH})$ and $\tau(\text{ring})$ coordinates. The characteristic antisymmetric CN stretching mode was calculated at 1225.1 cm^{-1} and can be assigned to the experimental band observed at 1221.4 cm^{-1} . The NN stretching vibration is IR-inactive in *E*-AB and, therefore cannot be assessed by our experiment. It is predicted by the calculations at 1419.6 cm^{-1} , in good agreement with the previous reported Raman data ($\sim 1440 \text{ cm}^{-1}$).⁸

The planarity of the ground state structure of *E*-AB has been the subject of controversial reports. On the theoretical side, some reports indicate a non-planar structure with C_i symmetry.^{13,36,39} However, it was recently demonstrated that the inversion barrier at the planar structure is an artifact resulting from the use of deficient ab initio methods,⁴⁰ and, in accordance with this conclusion, the great majority of the previously described DFT and MP2 theoretical calculations carried out on *E*-AB led to a planar minimum energy structure, with C_{2h} symmetry.^{14,41,42} In our calculations, the optimized ground state *E*-AB geometry was also found to correspond to the planar C_{2h} structure, at all used theory levels (see Table B.3 in the supporting information for the Cartesian coordinates of *E*-AB). Experimentally, early GED experiments suggested a non-planar minimum energy structure (with either C_2 or C_i symmetry), with the phenyl groups rotated out of the CNNC plane.⁴³ However, a more recent GED study of *E*-AB yielded a C_{2h} planar structure for the compound, in agreement with the most recent theoretical results.³⁸ The absence of experimental reports on the microwave spectra of azobenzene should be related with the fact that the total molecular dipole moment of *E*-AB is equal to zero (for both the C_i and C_{2h} symmetries). Then, vibrational spectroscopy experiments on this molecule appear as a valuable experimental tool for probing its molecular geometry. Note also that in the previously reported experimental studies on crystalline AB and for the compound in solution,^{43–48} the molecular geometry may suffer significant distortions resulting from the effects of the environment. On the other hand, in the matrix isolation technique the effects of environment are minimized. The excellent agreement of the theoretical spectrum of *E*-AB with that obtained experimentally for the matrix-isolated compound (Figure 3.4) can be considered as an evidence for the planar structure of this species.

Table 3.1 Experimental wavenumbers (ν/cm^{-1}) of the absorption bands observed in the infrared spectrum of *E*-AB isolated in an Ar matrix at 15 K, and the theoretical wavenumbers (ν/cm^{-1}), absolute infrared intensities ($I/\text{km mol}^{-1}$) and potential energy distributions (PED, %) for the infrared-active A_u and B_u normal modes calculated at the PW91/cc-pVTZ level.^a

Ar (15 K)	Calculated			
ν	ν	I	Sym.	PED (%)
3104.0	3142.5	13.9	B_u	$\nu_{\text{as}}(\text{CH})$ (93)
3093.1, 3086.7	3133.3	40.5	B_u	$\nu(\text{CH})_2$ (83), $\nu(\text{CH})_4$ (12)
3075.6, 3070.4 , 3057.2	3123.9	30.6	B_u	$\nu(\text{CH})_4$ (57), $\nu(\text{CH})_8$ (30)
3046.35	3113.9	17.0	B_u	$\nu(\text{CH})_8$ (54), $\nu(\text{CH})_4$ (28), $\nu(\text{CH})_6$ (11)
3015.0	3103.8	5.0	B_u	$\nu(\text{CH})_6$ (82), $\nu(\text{CH})_8$ (14)
1595.1, 1592.8	1594.8	6.2	B_u	$\nu(\text{CC})_4$ (64), $\delta(\text{CH})_9$ (17)
1589.3, 1587.9	1577.6	3.8	B_u	$\nu(\text{CC})_6$ (64)
1486.7	1472.8	9.4	B_u	$\delta(\text{CH})_8$ (59), $\nu(\text{CC})_{10}$ (34)
1456.8	1446.0	13.1	B_u	$\delta(\text{CH})_2$ (50), $\nu(\text{CC})_8$ (38)
1307.4	1352.6	6.5	B_u	$\nu(\text{CC})_2$ (88)
1299.8, 1298.2	1295.2	1.7	B_u	$\delta(\text{CH})_6$ (75)
1221.4	1225.1	20.4	B_u	$\nu(\text{NC})$ (49), $\nu(\text{CC})_{12}$ (13), $\delta(\text{CH})_8$ (10)
1158.2	1149.9	0.4	B_u	$\delta(\text{CH})_4$ (76)
1151.6 , 1148.0	1139.6	32.1	B_u	$\delta(\text{CH})_9$ (68), $\nu(\text{CC})_4$ (16)
1071.8	1072.9	15.2	B_u	$\delta(\text{CH})_2$ (43), $\nu(\text{CC})_8$ (42)
1023.6, 1019.3	1017.1	13.5	B_u	$\nu(\text{CC})_{10}$ (50), $\delta(\text{CH})_8$ (27), $\nu(\text{CC})_{12}$ (21)
1000.8	993.4	3.4	B_u	$\delta(\text{ring}2)$ (64), $\nu(\text{CC})_{12}$ (32)
985.9	979.8	0.4	A_u	$\gamma(\text{CH})_1$ (110), $\gamma(\text{CH})_7$ (12)
n.o.	961.9	0.001	A_u	$\gamma(\text{CH})_7$ (99), $\gamma(\text{CH})_1$ (13)
926.6 , 925.1	927.6	7.2	A_u	$\gamma(\text{CH})_9$ (89), $\gamma(\text{NC})$ (10)
n.o.	831.3	0.04	A_u	$\gamma(\text{CH})_5$ (100)
820.6	819.7	0.6	B_u	$\nu(\text{CC})_{12}$ (29), $\nu(\text{NC})$ (26), $\delta(\text{ring}2)$ (19), $\delta(\text{ring}4)$ (11), $\nu(\text{CC})_{10}$ (10)
780.8, 778.3 , 777.5	780.0	48.3	A_u	$\gamma(\text{CH})_3$ (35), $\tau(\text{ring}1)$ (28), $\gamma(\text{NC})$ (23), $\gamma(\text{CH})_9$ (13)
689.2	685.2	76.8	A_u	$\tau(\text{ring}1)$ (67), $\gamma(\text{CH})_3$ (45)
618.8	613.3	0.6	B_u	$\delta(\text{ring}6)$ (79), $\nu(\text{CC})_6$ (10)
549.9, 547.0, 546.0	541.3	13.7	A_u	$\gamma(\text{NC})$ (31), $\tau(\text{ring}1)$ (25), $\tau(\text{ring}3)$ (22), $\tau(\text{CNCC})$ (19), $\gamma(\text{CH})_3$ (11)
536.4	532.1	6.3	B_u	$\delta(\text{ring}4)$ (66)
521.4	514.5	23.5	B_u	$\delta(\text{NCC})$ (38), $\delta(\text{NNC})$ (24), $\delta(\text{ring}4)$ (13)
n.o.	402.7	0.001	A_u	$\tau(\text{ring}5)$ (112)
n.i.	295.2	0.6	A_u	$\tau(\text{ring}3)$ (80), $\tau(\text{CNCC})$ (24)
n.i.	82.3	1.9	B_u	$\delta(\text{NNC})$ (62), $\delta(\text{NCC})$ (34)
n.i.	60.9	1.4	A_u	$\tau(\text{CNCC})$ (46), $\gamma(\text{NC})$ (41), $\tau(\text{ring}3)$ (10)
n.i.	14.8	0.03	A_u	$\tau(\text{NNCC})$ (95)

^a Theoretical wavenumbers are not scaled. The strongest components of split bands are given in bold. PED's lower than 10% not included. Definition of symmetry coordinates is given in Table B.4. ν , bond stretching; δ , in-plane-bending; γ , out-of-plane bending; τ , torsion; n.o., not observed; n.i., not investigated.

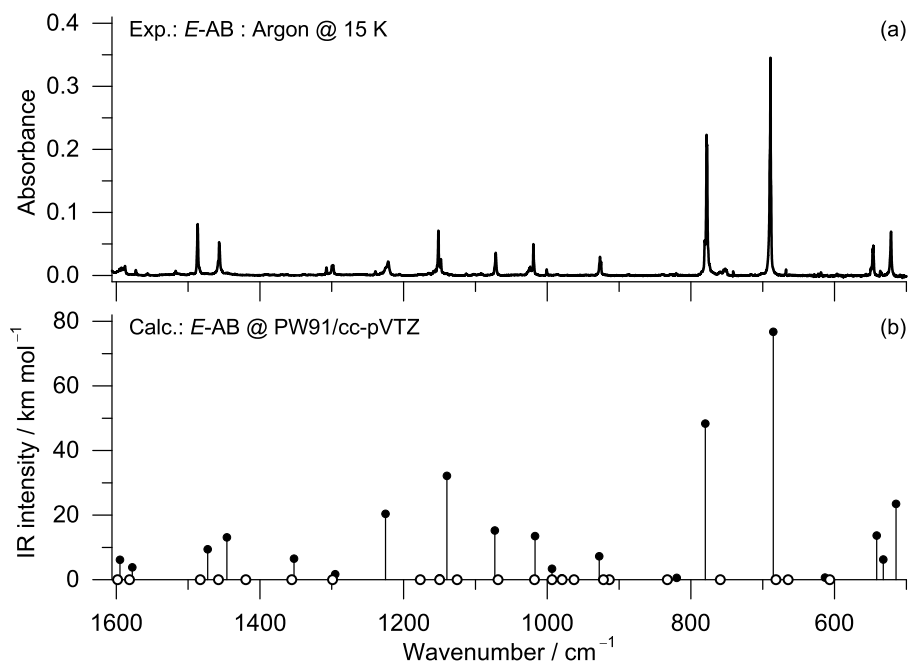


Figure 3.4 (a) Experimental infrared spectrum of *E*-AB isolated in an argon matrix at 15 K; (b) Theoretical infrared spectrum of the *E*-AB monomer calculated at the PW91/cc-pVTZ level of theory. Black circles represent the infrared-active (A_u and B_u) modes; white circles represent the infrared-inactive (A_g and B_g) modes.

Regarding the *Z*-AB isomer (C_2 symmetry), the 66 normal modes span 34 A and 32 B symmetry vibrations, which are both IR and Raman active (Table 3.2). Despite the fact of all modes being formally IR active, only 10 vibrations have absolute calculated infrared intensities above 10 km mol^{-1} and can be considered medium or strong IR absorbers (See Figure 3.5). On the other hand, 16 and 14 vibrations have absolute calculated infrared intensities in the ranges 10-4 and 4-1 km mol^{-1} , respectively, and can be regarded as weak IR absorbers, while almost a half of all vibrations (26 vibrational modes) were predicted to have very weak infrared absorptions (1 km mol^{-1} or less). The experimental spectrum of the *Z*-AB form was obtained as a result of post-processing spectra from the two types of experiments performed, where the bands due to *E*-AB were nullified by subtracting the spectrum of pure *E*-AB form (obtained in the experiment type 1) from the spectrum where both *E*-AB and *Z*-AB forms were present in the matrix (experiment type 2). The resulting spectrum is presented in Figure 3.5.

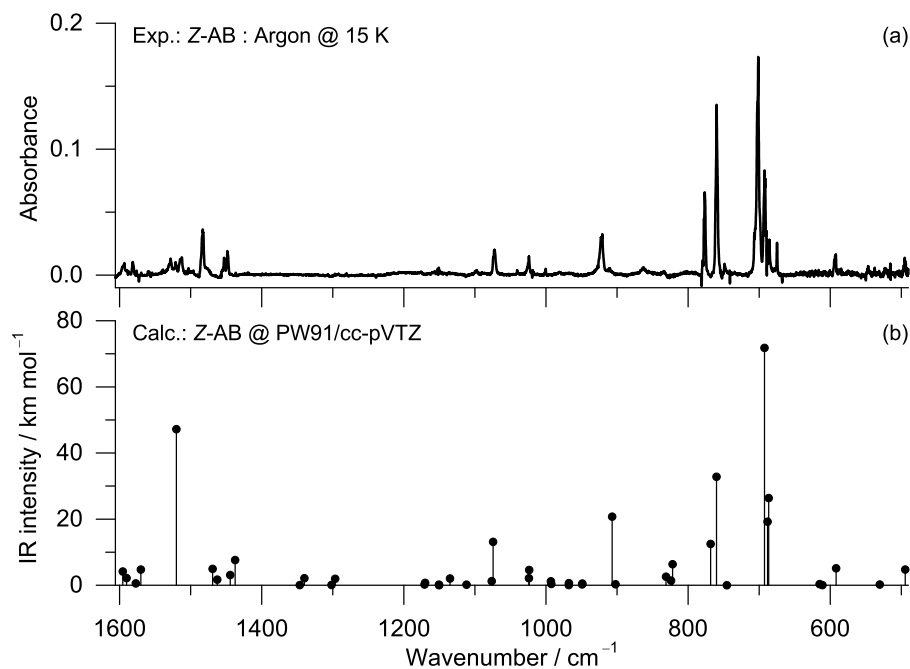


Figure 3.5 (a) Extracted experimental infrared spectrum of *Z*-AB obtained by subtraction of the spectrum recorded in the first type of experiment (deposition which yielded only *E*-AB) from the spectrum recorded in the second type of experiment (deposition which yielded *E*-AB + *Z*-AB), so that the bands due to *E*-AB are nullified; (b) Theoretical infrared spectrum of the *Z*-AB monomer calculated at the PW91/cc-pVTZ level of theory.

Five of the strongest IR bands of *Z*-AB are predicted between 780 and 680 cm^{-1} and are due to the $\gamma(\text{CH})$ and ring torsion modes. They appear in the experimental spectra as two multiplet features observed at 777-760 and 701-686 cm^{-1} . The ν_{NN} stretching mode is predicted to occur at 1520.1 cm^{-1} and, according to the calculations, should correspond to the second strongest absorption of *Z*-AB in the infrared (47 km mol^{-1}). The calculations predict a strong infrared band around 1520 cm^{-1} for the *Z*-AB form. However in the experimental spectrum (Figure 3.5), there is no any clearly defined band at this position. This apparent contradiction between theory and experiment will be addressed below in detail.

Note that there are much less experimental characterizations available for *Z*-AB than for the most stable *E*-AB form.^{1,15-23} In the previous vibrational analyses reported in the literature, the assignment of modes in the 1600-1570 cm^{-1} and 1200-1100 cm^{-1} regions was uncertain. The calculated bands at 1595.6, 1590.2 and 1570.2 cm^{-1} correspond to the ν_{CC} stretching modes and can be assigned to the experimental absorptions at 1595.6, 1593.2 and 1581.6 cm^{-1} , respectively. In

turn, the νCN stretching vibration calculated at the 1135.0 cm^{-1} (B symmetry) was assigned to the weak band at 1151.3 cm^{-1} , while the A-symmetry νCN stretching mode (calculated at 1111.9 cm^{-1}) has a very weak predicted infrared intensity and was not observed experimentally.

Table 3.2 Experimental wavenumbers (ν/cm^{-1}) of the absorption bands observed in the infrared spectrum of *Z*-AB isolated in an Ar matrix at 15 K, and the PW91/cc-pVTZ calculated wavenumbers (ν/cm^{-1}), absolute infrared intensities ($I/\text{km mol}^{-1}$) and potential energy distributions (PED, %) for the A and B symmetry modes.^a

Ar (15 K)	Calculated			
ν	ν	I	Sym.	PED (%)
3095.3	3136.0	5.2	A	$\nu(\text{CH})_1$ (87)
	3135.9	9.8	B	$\nu(\text{CH})_2$ (87)
3085.9	3131.5	0.2	A	$\nu(\text{CH})_7$ (68), $\nu(\text{CH})_9$ (14)
	3131.3	33.9	B	$\nu(\text{CH})_8$ (67), $\nu(\text{CH})_{10}$ (15)
3075.6, 3070.4 , 3057.2	3124.0	4.9	B	$\nu(\text{CH})_{10}$ (77), $\nu(\text{CH})_8$ (17)
	3123.9	14.2	A	$\nu(\text{CH})_9$ (78), $\nu(\text{CH})_7$ (16)
3038.0	3113.6	1.0	A	$\nu(\text{CH})_5$ (90)
	3113.5	8.4	B	$\nu(\text{CH})_6$ (91)
3028.4	3106.0	0.6	A	$\nu(\text{CH})_3$ (93)
	3105.9	1.9	B	$\nu(\text{CH})_4$ (93)
1595.6	1595.6	4.2	A	$\nu(\text{CC})_3$ (61), $\delta(\text{CH})_{10}$ (17), $\nu(\text{N=N})$ (11)
1593.2	1590.2	2.2	B	$\nu(\text{CC})_4$ (64), $\delta(\text{CH})_9$ (17)
n.o. ^b	1577.3	0.5	A	$\nu(\text{CC})_5$ (70)
1581.6	1570.1	4.7	B	$\nu(\text{CC})_6$ (63)
1514.8, 1512.6	1520.1	47.2	A	$\nu(\text{N=N})$ (77)
1482.3	1469.2	4.9	B	$\delta(\text{CH})_8$ (62), $\nu(\text{CC})_{10}$ (33)
1477.8	1462.8	1.7	A	$\delta(\text{CH})_7$ (60), $\nu(\text{CC})_9$ (31)
1453.1	1444.4	3.1	A	$\delta(\text{CH})_1$ (51), $\nu(\text{CC})_7$ (38)
1448.4	1437.6	7.6	B	$\delta(\text{CH})_2$ (49), $\nu(\text{CC})_8$ (35)
n.o.	1346.6	0.05	A	$\nu(\text{CC})_1$ (87)
n.o.	1339.9	2.1	B	$\nu(\text{CC})_2$ (82), $\delta(\text{CH})_4$ (11)
n.o.	1301.9	0.1	A	$\delta(\text{CH})_5$ (75)
n.o.	1296.7	1.9	B	$\delta(\text{CH})_6$ (70)
1176.4	1171.0	0.2	B	$\delta(\text{CH})_9$ (56), $\nu(\text{CC})_4$ (19), $\nu(\text{NC})$ (11)
	1170.2	0.7	A	$\delta(\text{CH})_{10}$ (66), $\nu(\text{CC})_3$ (21)
n.o.	1150.6	0.2	A	$\delta(\text{CH})_3$ (78)
n.o.	1150.4	0.02	B	$\delta(\text{CH})_4$ (78)
1151.3	1135.0	2.0	B	$\nu(\text{NC})$ (28), $\delta(\text{CH})_9$ (21), $\delta(\text{ring}2)$ (16), $\nu(\text{CC})_{12}$ (14)
n.o.	1111.9	0.2	A	$\nu(\text{NC})$ (29), $\delta(\text{ring}1)$ (21), $\nu(\text{CC})_{11}$ (18), $\delta(\text{CH})_{10}$ (11)
1074.6	1076.4	1.2	A	$\nu(\text{CC})_7$ (45), $\delta(\text{CH})_1$ (42)
1071.8	1074.4	13.1	B	$\nu(\text{CC})_8$ (45), $\delta(\text{CH})_2$ (40)
1025.3, 1024.1	1024.1	2.1	A	$\nu(\text{CC})_9$ (48), $\delta(\text{CH})_7$ (24), $\nu(\text{CC})_{11}$ (22)
	1023.7	4.6	B	$\nu(\text{CC})_{10}$ (48), $\delta(\text{CH})_8$ (24), $\nu(\text{CC})_{12}$ (22)
1000.7	993.2	1.2	B	$\delta(\text{ring}2)$ (58), $\nu(\text{CC})_{12}$ (38)
	992.5	0.4	A	$\delta(\text{ring}1)$ (58), $\nu(\text{CC})_{11}$ (39)
980.6	968.0	0.04	A	$\gamma(\text{CH})_1$ (118)
	967.8	0.6	B	$\gamma(\text{CH})_2$ (117)

Table 3.2 (Cont.)

Ar (15 K)		Calculated		
ν	ν	I	Sym.	PED (%)
963.1	949.2	0.3	A	$\gamma(\text{CH})_7$ (113)
	948.8	0.5	B	$\gamma(\text{CH})_8$ (111)
920.9	906.9	20.8	B	$\gamma(\text{CH})_{10}$ (78), $\gamma(\text{NC})$ (11)
910.0	902.2	0.3	A	$\gamma(\text{CH})_9$ (90)
862.7	831.1	2.6	B	$\delta(\text{NNC})$ (33), $\gamma(\text{CH})_{10}$ (17), $\nu(\text{NC})$ (13)
	824.0	1.4	A	$\gamma(\text{CH})_{a5}$ (98)
833.6	822.0	6.4	B	$\gamma(\text{CH})_6$ (89)
	776.6	768.3	12.5	A
760.0	760.1	32.8	B	$\nu(\text{NC})$ (19), $\gamma(\text{CH})_4$ (17), $\delta(\text{ring4})$ (17), $\nu(\text{CC})_{12}$ (11)
748.9	745.4	0.02	A	$\nu(\text{NC})$ (25), $\delta(\text{ring3})$ (25), $\nu(\text{CC})_{11}$ (11)
701.4	692.6	71.8	B	$\gamma(\text{CH})_4$ (55), $\delta(\text{NNC})$ (21), $\delta(\text{ring4})$ (11)
693.5	688.3	19.2	A	$\tau(\text{ring1})$ (68), $\gamma(\text{CH})_3$ (44)
685.7	686.6	26.4	B	$\tau(\text{ring2})$ (101), $\gamma(\text{CH})_4$ (15)
n.o.	614.9	0.3	A	$\delta(\text{ring5})$ (65), $\tau(\text{CNNC})$ (10)
n.o.	611.0	0.1	B	$\delta(\text{ring6})$ (35)
592.2	591.7	5.1	A	$\tau(\text{CNNC})$ (43), $\delta(\text{ring5})$ (23), $\tau(\text{ring1})$ (14)
531.3	530.4	0.2	A	$\delta(\text{ring3})$ (31), $\delta(\text{NNC})$ (15), $\gamma(\text{NC})$ (12), $\tau(\text{ring3})$ (12)
495.2	494.5	4.7	B	$\delta(\text{ring4})$ (43), $\gamma(\text{NC})$ (17), $\nu(\text{NC})$ (14), $\tau(\text{ring4})$ (11)
439.3	438.7	5.0	B	$\tau(\text{ring4})$ (51), $\gamma(\text{NC})$ (15), $\delta(\text{ring4})$ (12), $\delta(\text{NCC})$ (12)
419.6	416.8	3.1	A	$\tau(\text{ring3})$ (29), $\delta(\text{ring3})$ (18), $\nu(\text{NC})$ (17), $\tau(\text{ring5})$ (11),
				$\tau(\text{CNNC})$ (10)
n.o.	400.6	0.04	A	$\tau(\text{ring5})$ (102)
n.i.	396.7	4.4	B	$\tau(\text{ring6})$ (112)
n.i.	275.3	5.8	B	$\delta(\text{NCC})$ (67), $\tau(\text{ring4})$ (16)
n.i.	264.8	0.2	A	$\tau(\text{ring3})$ (47), $\delta(\text{NNC})$ (20), $\delta(\text{NCC})$ (15), $\tau(\text{CNNC})$ (10)
n.i.	168.9	0.2	A	$\tau(\text{NNCC})$ (55), $\delta(\text{NCC})$ (33), $\delta(\text{NNC})$ (12)
n.i.	151.3	4.0	B	$\gamma(\text{NC})$ (36), $\tau(\text{ring4})$ (33), $\delta(\text{NNC})$ (13)
n.i.	68.0	0.5	A	$\gamma(\text{NC})$ (33), $\tau(\text{CNNC})$ (27), $\tau(\text{NNCC})$ (21), $\tau(\text{ring3})$ (11)
n.i.	49.9	0.02	A	$\delta(\text{NNC})$ (40), $\tau(\text{NNCC})$ (35), $\delta(\text{NCC})$ (15), $\gamma(\text{NC})$ (10)
n.i.	41.1	1.4	B	$\tau(\text{NNCC})$ (103)

^a Theoretical wavenumbers are not scaled. The strongest components of split bands are given in bold. PED's lower than 10% not included. Definition of symmetry coordinates is given in Table B.6. ν , bond stretching; δ , in-plane-bending; γ , out-of-plane bending; τ , torsion; n.o., not observed; n.i., not investigated.

3.1.5 Potential Energy Surfaces of *E*-AB and *Z*-AB

A very large number of theoretical studies have been carried out to characterize the potential energy surfaces (PES) connecting the two possible isomers of azobenzene (*E*-AB and *Z*-AB).^{4,9,28,49–64} These potential energy surfaces deal with the necessity of transforming the *trans* CN=NC dihedral angle (in *E*-AB) into the *cis* CN=NC dihedral angle (in *Z*-AB), related to the *E*-*Z* isomerization around the central double bond. Such theoretical analyses must inevitably take into account structures very strongly distorted from the equilibrium geometry and enter high-energy regions (over 100 kJ mol⁻¹) of the PES. In such cases, the excited electronic states and conical

intersections must be considered, leading to the necessity of multireference calculations. On the other hand, in the context of the present work, we are interested in the characterization of PES in the “low-energy” domain, near the equilibrium geometries. Such analysis can be safely carried out within the single determinant approximation.

Near the energy minima, the PES of azobenzene is considerably flat along the phenyl rings’ torsional coordinates, with large geometrical modifications implying only small energy changes. As it will be shown below, accounting for these geometric changes permits to explain some peculiarities of the vibrational signatures of azobenzene observed in the present work. Considering an independent torsional motion for each phenyl ring, a two-dimensional (2D) PES can be constructed in the vicinity of each isomer, *E*-AB and *Z*-AB. Each phenyl ring will be named here as a “blade”, while the orientation of this blade relatively to the central CNNC fragment can be described by the value of the NNCC dihedral angle, which we shall call here “blade pitch”. To construct the 2D PES described below, two NNCC dihedral angles were incrementally fixed between 0° and 90° , with a step of 10° , while all other remaining geometrical parameters were fully optimized.

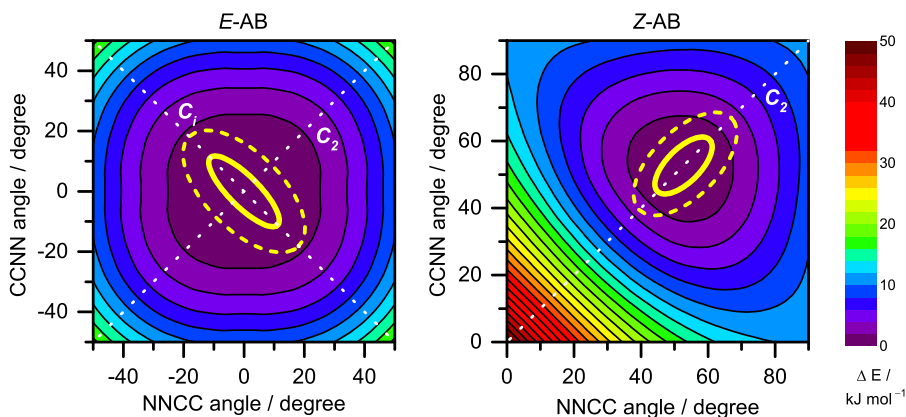


Figure 3.6 Relaxed 2D potential energy map of *E*- and *Z*-azobenzene isomers as a function of blade pitch variation, calculated at the B97-1/cc-pVTZ level of theory. The reaction coordinates were chosen as the two CCNN dihedral angles. The central CNNC dihedral angle was in the *trans*- and *cis*- orientations, respectively (and optimized). The relative zeroes were chosen to correspond to the energy of the respective minima. The dotted white diagonal lines indicate the cuts through the surfaces where the molecules conserve a particular overall symmetry (C_1 and C_2 for *E*-AB; C_2 for *Z*-AB). The solid and dashed yellow ellipses indicate the areas accessible to the molecules undergoing the zero-point vibrations and in their first excited vibrational states, respectively. These areas were projected from the frequencies of the two calculated $\tau(\text{CCNN})$ vibrations.

The 2D PES map calculated for *E*-AB is presented in Figure 3.6. The minimum energy geometry has two blade pitches equal to 0° and is in the center of the map. This structure has the C_{2h} symmetry. If both blades deviate from the equilibrium synchronously, by the same numeric value, and having the same sign of the blade pitch, the resulting set of geometries belongs to the C_2 symmetry point group. In terms of the map shown in Figure 3.6, these geometries lie on the diagonal designated C_2 . If the two blades deviate from the equilibrium synchronously, but have the opposite signs of the blade pitch, the resulting set of geometries conserves the C_i symmetry and corresponds to the second diagonal across the map (designated C_i). An important characteristic of the obtained potential energy map is that the central fragment of the map, within the 0 - 2 kJ mol^{-1} energy range corresponds to large blade pitch variations, up to 25° from the minimum (area of the map colored violet).

It is instructive to analyze the energy of the normal vibrations related with the coordinates of the potential energy map (τ NNCC coordinates), *i.e.* with the change of blade pitch. According to the normal mode analysis (Table 3.1 and Table B.4), there are two vibrations in *E*-AB with contribution from the τ NNCC coordinates. They belong to the B_g and A_u irreducible representations, which in terms of the 2D map (shown in Figure 3.6) means that they describe the vibrational movements along the C_i and C_2 diagonals, respectively. The corresponding vibrational frequencies calculated at the B97-1/cc-pVTZ level are 97.8 (B_g) and 22.0 cm^{-1} (A_u).* These frequencies correspond to the zero-point energy vibrations of 0.58 and 0.13 kJ mol^{-1} , respectively. The area accessible to the *E*-AB isomer, executing the zero-point vibrational movements, is defined by these two values and is shown in Figure 3.6 as a yellow ellipse (continuous line) with the major and minor axes oriented along the C_i and C_2 diagonals, respectively, and measuring to 0.58 and 0.13 kJ mol^{-1} . The larger (dashed) ellipse corresponds to the area on the map accessible to the *E*-AB isomer promoted to the first vibrational excited states (with the principal axes measuring to 1.75 and 0.39 kJ mol^{-1}).

The 2D PES map calculated for *Z*-AB as a function of the two blade pitches is also presented in Figure 3.6. The minimum energy geometry has the blade pitches equal to 49° and equal signs. This structure has the C_2 symmetry, and is situated on the C_2 diagonal. As compared to the *E*-AB 2D map, it can be seen that the potential energy surface of *Z*-AB near the minimum has a smaller flat area. This is manifested in larger frequencies of the normal modes related to the phenyl ring torsions in *Z*-

*The B97-1 and PW91/cc-pVTZ calculated frequencies coincide within 0.1 kJ mol^{-1} (or within 8 cm^{-1}), and then the choice of either B97-1 or PW91 functional gives similar quantitative results.

AB than in *E*-AB. In *Z*-AB, the two normal modes with dominating contribution from the τ NNCC coordinates belong to the A and B irreducible representations, and have the calculated frequencies equal to 174.0 (A) and 46.3 cm^{-1} (B), about twice as much as in *E*-AB. Similarly, as made above for *E*-AB, these frequencies were used to define the area available for the zero-point vibrational energy movements (solid ellipse in Figure 3.6), which extend to 1.04 kJ mol^{-1} along the C_2 diagonal and to 0.28 kJ mol^{-1} in the orthogonal direction. The dashed ellipse designates the area accessible for the *Z*-AB molecule in the first excited vibrational state.

3.1.6 Geometries of *E*-AB and *Z*-AB

It has been previously suggested that the variation of the phenyl dihedral angles is responsible for slight changes observed in the UV absorption spectrum of azobenzene in the 20-120 $^{\circ}\text{C}$ temperature range.⁶⁵ Here, we shall demonstrate that the phenyl ring torsions are also responsible for distinctive peculiarities observed in the vibrational spectra of the compound, even at cryogenic temperatures. The largest deviations of the AB molecule from the equilibrium geometry, related with the τ NNCC coordinates, correspond to the displacements along the C_1 diagonal in *E*-AB, and along the C_2 diagonal in *Z*-AB (Figure 3.6). The corresponding one-dimensional potential energy scans, calculated now at the PW91/cc-pVTZ level, are shown in Figure 3.7. In these scans, the C_1 and C_2 symmetries were conserved for *E*-AB and *Z*-AB, respectively. The blade pitches were incrementally fixed with a step of 5° , and the remaining coordinates fully optimized. At each point of these scans, the vibrational calculations were carried out. The resulting NN bond distances and the NN stretching frequencies are shown in parts (b, e) and (c, f) of Figure 3.7. In *E*-AB, the zero-point vibrational energy (ZPE) corresponds to the change of the blade pitch from -8.5° to $+8.5^{\circ}$ (the points where the ZPE line intersects the energy curve, Figure 3.7a). In *Z*-AB, the respective geometry variations within the ZPE energy level comprise the range of dihedral angles from 42° to 57° (Figure 3.7d). These pitch variations can be projected to the respective NN geometric and vibrational properties of AB. For *E*-AB, this projection shows that the change of the NN bond length, related with the ZPE vibrations of the pitch angles, is about 0.04 pm, which corresponds to the changes in the ν NN frequency of 2 cm^{-1} (Figure 3.7). The ZPE vibrations in *Z*-AB result in a change of NN bond length of about 0.28 pm, which correlates with a change in the ν NN frequency of 15 cm^{-1} (Figure 3.7). It is then clear that ZPE pitch variations of the same magnitude (17° in *E*-AB, and 15° in *Z*-AB) result in much larger changes of the NN bond length and the ν NN frequency

in the *Z*-AB form, as compared to *E*-AB.

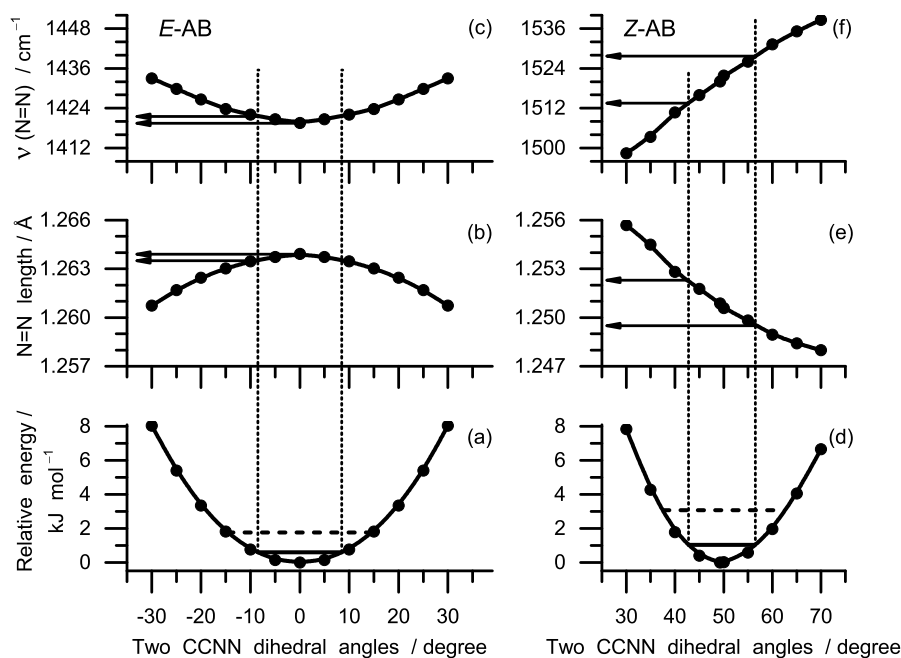


Figure 3.7 Relaxed potential energy scans in azobenzene as functions of the blade pitch variation, calculated at the PW91/cc-pVTZ level of theory for *E*-AB (a) and *Z*-AB (d). The reaction coordinates were chosen as the two CCNN dihedral angles having the same values and opposite signs (for *E*-AB, C_1 symmetry) or the same signs (for *Z*-AB, C_2 symmetry). The solid and dashed horizontal lines indicate energies of the ground states and the first excited vibrational levels along the reaction coordinates, respectively; (b) and (e) the optimized NN bond length; (c) and (f) the ν NN frequency, along the scans shown in parts (a) and (d). Note that the linear ordinate scales in pairs [(a), (d)], [(b), (e)] and [(c), (f)] were chosen the same.

The geometries where the ZPE levels in *E*-AB and *Z*-AB intersect the potential energy profiles were found from the corresponding normal vibrations (τ NNCC) and correspond to the following pitch variations: 8.5° (C_1 symmetry), 3° (C_2 symmetry) for *E*-AB; 42° and 57° (both C_2 symmetry) for *Z*-AB. For these points the pitch angles were fixed, all the remaining parameters optimized, and the vibrational calculations carried out. The corresponding vibrational frequencies, along with the vibrational data for the minima, are collected in Table B.7 (*E*-AB) and Table B.8 (*Z*-AB). These sets of calculations permitted to estimate the changes in the vibrational spectra, expected to occur in an AB molecule undergoing the zero-point vibrations along the τ NNCC coordinates. For *E*-AB, within the frequency range accessible in our experiments (above 400 cm^{-1}) all vibrational modes are predicted to keep their

frequencies within 3 cm^{-1} (Table B.7). From the seven calculated modes showing the largest variations of the predicted frequencies (between 2 and 3.3 cm^{-1}), four are infrared inactive, and three are weak infrared absorbers (the highest predicted infrared intensity is 6 km mol^{-1}). In practical terms, this means that the effects on other vibrational modes due to the zero-point torsional vibrations of the phenyl rings in *E*-AB are not detectable in the matrix-isolation experiments, where a typical full-width-at-half-maximum of the absorption bands is $\sim 2\text{ cm}^{-1}$. The situation is, however, significantly different for *Z*-AB. For this molecule, sixteen vibrations lying above 400 cm^{-1} are predicted to have frequency variations above 3 cm^{-1} (as compared to only one, IR inactive mode in *E*-AB). From these 16 vibrations, it is precisely the NN stretching mode (Table B.8) which undergoes the largest frequency shifts along with the zero-point torsional vibrations of the phenyl rings. This has been exemplified graphically in Figure 3.8, where the vibrational spectra of the *Z*-AB form, having pitch angles of 42, 49 and 57° are presented. The uncertainty of the NN stretching frequency with the pitch change in *Z*-AB will result in the smearing of the experimental band over a large frequency range, as designated in Figure 3.8a. Thus the broad experimental feature observed around $1500\text{-}1520\text{ cm}^{-1}$ is assigned to the NN stretching vibration. A similar phenomenon of frequency smearing has been previously observed for dimethyl oxalate.⁶⁶ Thus, *Z*-AB is yet another molecule where considering the large amplitude, low frequency vibrations permits a successful explanation of an apparent contradiction between the theory and experiment.

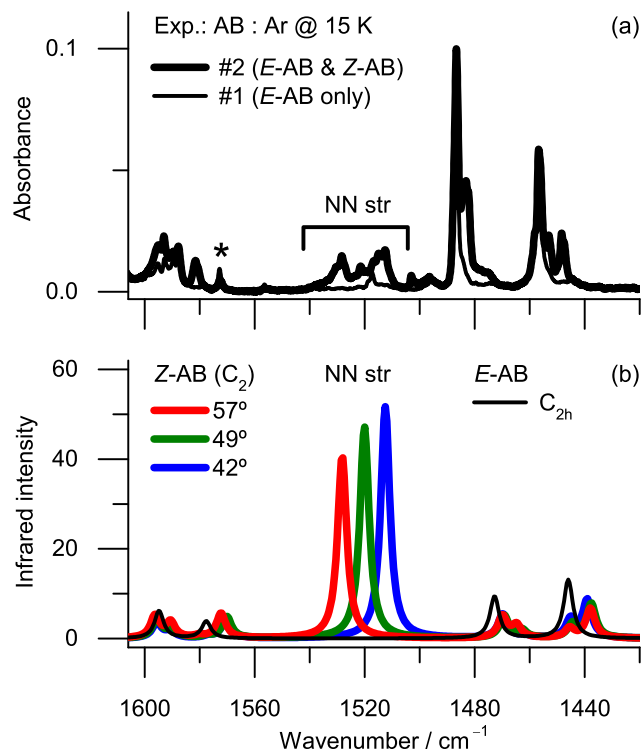


Figure 3.8 (a) Fragments of the infrared spectra of azobenzene isolated in argon matrices at 15 K observed in two types of experiments: #1 (thin line) only *E*-AB present; #2 (bold line) both *E*-AB and *Z*-AB present. Experimental intensities (#1 and #2) were normalized to the same amount of *E*-AB. The asterisk designates a band due to matrix-isolated water impurity; (b) Simulated spectra, for different *Z*-AB and *E*-AB geometries. Black line: *E*-AB at the minimum configuration (C_{2h} symmetry); Red, green, blue lines: *Z*-AB with the pitch angles fixed at 57° , 49° (minimum), and 42° , respectively, all within the C_2 symmetry. “NN str” refers to the *Z*-AB in both frames.

3.2 4-Hydroxyazobenzene

The azobenzenes substituted with one or more hydroxyl groups - hydroxyazobenzenes - can usually form hydrogen bonds, give rise to different tautomeric forms and exhibit a distinct isomerization behavior from other azo derivatives.⁶⁷ They can be used in the synthesis of novel aromatic azo compounds,^{68,69} fast optical switches,⁷⁰⁻⁷² and in the photocontrol of supramolecular assemblies.⁷³

Among the possible hydroxyazobenzenes, 4-hydroxyazobenzene (HAB), with one hydroxyl group in *para* position, is one of the simplest derivatives available for study (Figure 3.9). Therefore, in addition to the applications mentioned above, it has also been used to gain insight into the general isomerization mechanism of azobenzenes.

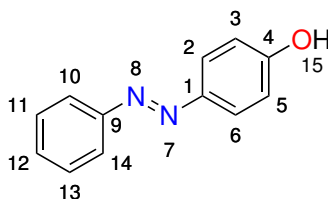


Figure 3.9 Structure of 4-hydroxyazobenzene (HAB), with numbering of heavy atoms.

The experimental and theoretical studies involving HAB are not so numerous as for azobenzene. The crystal structure of the *E* isomer has been determined by X-ray diffraction⁷⁴ and its Raman vibrational spectrum measured in solution at different pH values.^{75,76} Gabor *et al.*, reported the dependency of the thermal isomerization rate of HAB on temperature, concentration, and solvent.⁷⁷ They proposed that the formation of dimers occurs readily in nonpolar solvents, thereby affecting the isomerization kinetics, while in polar solvents, the solvent-solute interactions are strong enough to prevent aggregation. Kurita and co-workers, studied the solvent effects on the isomerization of HAB and calculated (DFT) the solvation complexes of several HAB dimers, supporting the role of dimerization on the isomerization rates.^{78,79}

3.2.1 Most Stable Structures

The four most stable azo-enol structures of 4-hydroxyazobenzene are presented in Figure 3.10. The *E*-HABt and *E*-HABc forms assume a planar geometry with the N=N double bond in the *E* configuration and the OH group positioned in a *trans* or *cis* orientation relatively to the azo group, respectively. The *Z*-HABt and *Z*-HABc

structures adopt a *Z* configuration in which the C14C9NN, C2C1NN and CNNC dihedral angles assume the values of approximately 60°, 38° and 9°, respectively. Analogously to the *E* forms, they can also have a *trans* or *cis* oriented OH group. The N=N bond length changes from *ca.* 125 pm in the *E* forms to 124 pm in the *Z* structures. The Cartesian coordinates of all optimized structures, from which all geometric parameters can be taken, are given in Appendix C (Table C.1).

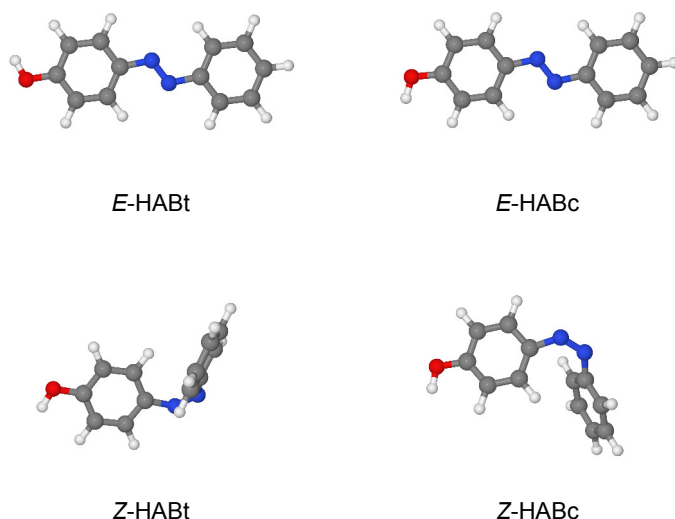


Figure 3.10 Most stable structures of HAB calculated at the B3LYP/6-311+G(2df,2p) level of theory.

The relative energy differences, including the zero-point vibrational contribution, calculated at different levels of theory are given in Table 3.3. The *E* forms are 50-66 kJ mol⁻¹ more stable than the *Z* ones. The relative populations, estimated from the calculated Gibbs free energies at 298.15 K and the Boltzmann distribution, indicate that only the *E*-HABt and *E*-HABc forms should be significantly populated in the gas phase and, consequently, expected to appear in the deposited low-temperature argon and xenon matrices.

In certain experimental conditions, HAB was reported to undergo tautomerization by solvent assisted proton transfer and give rise to keto-hydrazone forms.^{77,78} However, in the gas phase and the majority of organic solvents, HAB exists primarily in the the azo-enol form, and the keto-hydrazone tautomeric forms can be safely discarded.⁸⁰

Table 3.3 Calculated relative energies, with zero-point vibrational energy correction (ΔE_{ZPE}), of HAB conformers.^a

HAB	ΔE_{ZPE}			P (%)
	B3LYP		MP2	
	6-311+G(2df,2p)	cc-pVTZ	cc-pVTZ	
<i>E</i> -HABt	0.00	0.00	0.00	49
<i>E</i> -HABc	0.01	0.08	0.11	51
<i>Z</i> -HABt	65.30	66.40	50.01	0
<i>Z</i> -HABc	65.48	66.65	49.94	0

^a All energies in kJ mol^{-1} . Relative populations (P) estimated from the averaged Gibbs free energies calculated at 298.15 K at different levels of theory are also given.

3.2.2 HAB Structure in a Matrix Shortly After Deposition

The experimental infrared spectra of HAB isolated in argon and xenon matrices are presented in Figure 3.11. The experimental spectra are well reproduced by the spectrum simulated for *E*-HAB on the basis of the B3LYP/6-311+G(2df,2p) theoretical calculations and estimated relative populations for the **t** and **c** conformers (*i.e.*, simulated as the sum of **t**+**c**). The theoretically predicted spectra for the *E*-HABt and *E*-HABc conformers are very similar (with 1.5 cm^{-1} average maximum difference between homologous bands). Accordingly, it is very difficult to identify bands due to the individual conformers in the experimental IR spectra, where bands have full-widths at half-maximum between 2-4 cm^{-1}). Tentative band assignments are given in Table 3.4.

The characteristic N=N stretching frequency of aromatic azo compounds is usually strongly mixed with other vibrational modes and its assignment is not trivial.^{12,81} In addition, its theoretical prediction also shows considerable variation in function of the chosen method of theory.^{13,14,82} Our theoretical calculations, undertaken at the DFT [B3LYP and PW91, with the 6-311+G(2df,2p) and cc-pVTZ basis set] and MP2/cc-pVTZ levels, predict several bands in 1560-1400 cm^{-1} region with significant contributions from both the NN stretching and CH in-plane bending modes. The band with the largest contribution from the $\nu\text{N}=\text{N}$ mode is predicted to occur at approximately 1546, 1413 and 1409 cm^{-1} (unscaled values) by the B3LYP, PW91 and MP2 methods, respectively. Considering that the PW91 functional was previously found to give more reliable predictions for azobenzene (particularly in the azo region), we assigned the N=N stretching mode to the experimentally observed band situated at *ca.* 1429 and 1430 cm^{-1} in argon and xenon matrices, respectively.

This is in good agreement in the reported Raman data obtained for HAB in aqueous solutions ($\approx 1442 \text{ cm}^{-1}$).^{75,76}

Other characteristic absorption bands, such those due to the νCN_{as} , νOH , νCO and δOH modes, appear at *ca.* 1145, 3634, 1264, 1188 cm^{-1} , respectively (or 1145, 3612, 1264, 1188 cm^{-1} in Xe; average values; see Table 3.4) The calculated vibrational frequencies of all optimized structures (at all levels of theory used) are given in Table C.2.

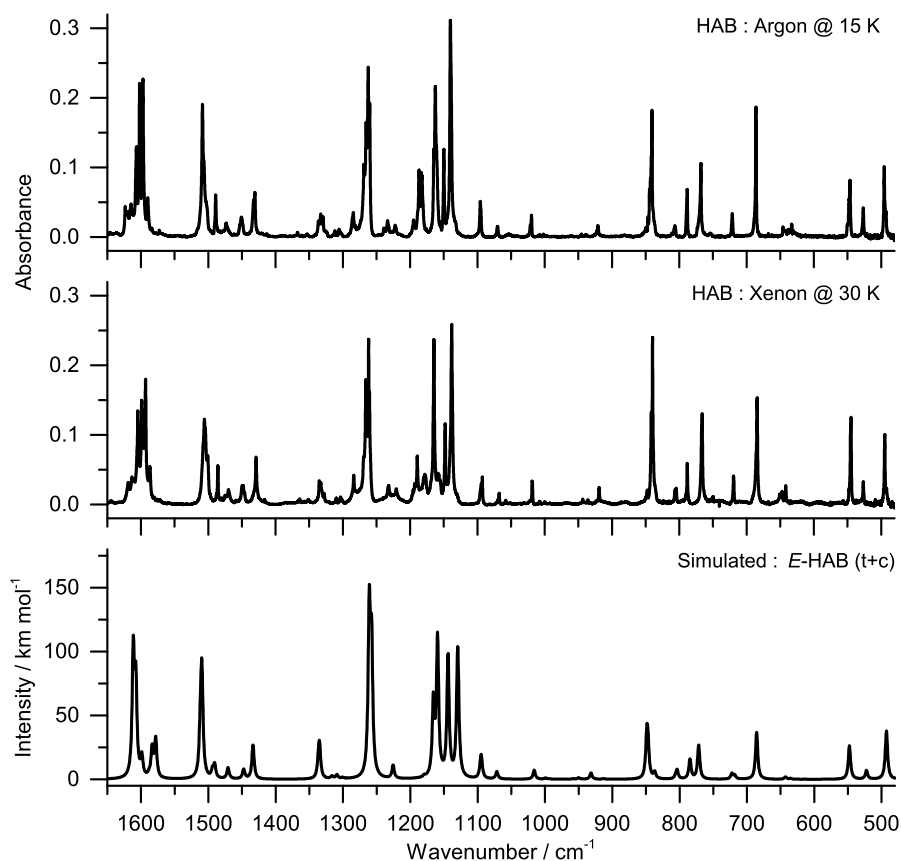


Figure 3.11 Experimental infrared spectra of HAB isolated in argon (15 K) and xenon (30 K) matrices compared with the theoretical spectrum of HAB (simulated as the sum of the *E*-HAB_t+*E*-HAB_c forms) calculated at the B3LYP/6-311+G(2df,2p) level of theory. The calculated harmonic frequencies were scaled by a factor of 0.976, obtained by least-squares linear fitting.

Table 3.4 Experimental observed wavenumbers (ν/cm^{-1}) and tentative assignments for the *E*-HAB conformers Isolated in argon and xenon matrices.

Ar (15K)	Xe (30K)		Calculated		Sym.	Appr. description
	ν	ν	<i>E</i> -HABt	<i>E</i> -HABc		
3640.7, 3633.1 , 3628.4	3621.8, 3619.1, 3602.1	3732.7	125.5	3736.3	115.9	A' $\nu(\text{OH})$
3090.4	3084.1	3133.1	3.5	3131.2	6.4	A' $\nu(\text{CH})$
3084.4	3069.6	3131.1	4.4	3131.1	0.1	A' $\nu(\text{CH})$
3068.6	3060.5	3116.9	14.4	3123.3	6.4	A' $\nu(\text{CH})$
3049.3	3048.8	3115.9	5.1	3116.7	16.2	A' $\nu(\text{CH})$
3040.6 , 3031.8, 3014.1	3032.8 , 3024.8, 3013.92	3111.0	5.6	3109.3	1.9	A' $\nu(\text{CH})$
1620-1585	1620-1585	3107.5	19.0	3107.4	19.0	A' $\nu(\text{CH})$
1508.7 , 1506.6, 1501.6	1505.8 , 1504.6, 1500.8	3096.7	10.1	3096.7	10.2	A' $\nu(\text{CH})$
1489.1	1485.7	3086.9	2.0	3087.0	1.9	A' $\nu(\text{CH})$
1473.6	1475.1, 1470.0	3080.7	21.4	3072.7	25.6	A' $\nu(\text{CH})$
1450.7	1448.5, 1446.1	1611.5	154.8	1607.7	188.3	A' $\nu(\text{CC}) + \delta(\text{CH})$
1432.3, 1430.7	1429	1599.2	7.9	1598.6	29.1	A' $\nu(\text{CC}) + \delta(\text{CH})$
1336.4, 1332.9, 1329.4	1335.0, 1332.8, 1327.8	1583.5	36.0	1588.0	5.1	A' $\nu(\text{CC}) + \delta(\text{CH})$
1311.9	1309.7	1578.1	46.3	1579.7	5.0	A' $\nu(\text{CC}) + \delta(\text{CH})$
1305.6	1303.4	1509.5	125.1	1511.7	93.7	A' $\nu(\text{N}=\text{N}) + \delta(\text{CH}) + \nu(\text{CC})$
1302.5	1300.7	1493.8	9.5	1490.6	27.3	A' $\delta(\text{CH}) + \nu(\text{N}=\text{N}) + \nu(\text{CC})$
1284.5, 1281.2, 1268.8,	1283.8, 1280.2, 1268.8, 1264.0,	1470.8	13.6	1467.9	1.1	A' $\delta(\text{CH}) + \nu(\text{N}=\text{N}) + \nu(\text{CC})$
1265.5, 1262.2 , 1260.12	1232.0 , 1220.6	1447.8	8.7	1446.9	6.2	A' $\delta(\text{CH}) + \nu(\text{CC})$
1233.5 , 1222.2	1195.5	1433.1	1.2	1433.7	69.5	A' $\delta(\text{CH}) + \nu(\text{CC})$
1195.0	1189.5	1334.8	38.0	1336.5	28.7	A' $\delta(\text{CH}) + \delta(\text{OH})$
1186.8, 1183.5, 1164.8, 1162.6	1185.5, 1178.4, 1164.7	1316.4	2.3	1316.3	1.8	A' $\nu(\text{CC}) + \delta(\text{CH})$
1156.6, 1154.5	1155.6	1309.0	4.4	1309.1	1.1	A' $\nu(\text{CC}) + \delta(\text{CH})$
1149.9	1148.0	1301.0	1.3	1299.2	0.4	A' $\delta(\text{CH})$
1140.2 , 1132.9	1138.2 , 1130.5	1261.0	206.6	1257.5	261.7	A' $\nu(\text{CO}) + \delta(\text{CH}) + \nu(\text{CC})$
1095.7	1094.2, 1092.7	1225.3	4.2	1225.7	21.0	A' $\nu(\text{NC}) + \nu(\text{CC}) + \delta(\text{CH})$
1070.0	1069.8, 1067.7	1179.5	0.7	1179.3	2.3	A' $\delta(\text{CH}) + \nu(\text{NC}) + \nu(\text{CC})$
1024.6, 1021.4, 1019.7	1022.9, 1018.7	1159.6	172.5	1165.7	154.8	A' $\delta(\text{OH}) + \delta(\text{CH})$
1009.2, 1007.6	1008.1 , 1007.0	1152.7	1.3	1152.6	1.0	A' $\delta(\text{CH})$
		1144.0	113.3	1144.1	63.4	A' $\delta(\text{CH}) + \nu(\text{CC}) + \delta(\text{OH})$
		1129.8	114.5	1129.0	91.6	A' $\delta(\text{CH}) + \nu(\text{NC}) + \delta(\text{ring})$
		1095.4	16.2	1094.4	27.3	A' $\delta(\text{CH}) + \nu(\text{CC}) + \delta(\text{OH})$
		1071.5	5.6	1071.4	6.2	A' $\delta(\text{CH}) + \nu(\text{CC})$
		1016.0	7.1	1015.9	7.3	A' $\nu(\text{CC}) + \delta(\text{CH})$
		999.5	0.8	999.0	1.4	A' $\delta(\text{ring}) + \nu(\text{CC})$

Table 3.4 (Cont.)

Ar (15K)	Xe (30K)	Calculated		Sym.	Appr. description
		E -HABt	E -HABc		
ν	ν	ν	I	ν	I
1002.2 , 1001.4	999.7	993.9	0.1	A ^o	ν (CH)
n.o.	n.o.	993.5	0.2	A ^o	δ (ring) + ν (CC)
n.o.	n.o.	979.9	0.1	A ^o	ν (CH)
n.o.	n.o.	979.3	0.01	A ^o	ν (CH)
945.3 , 939.2 , 937.9	943.5 , 935.9	950.0	2.0	A ^o	ν (CH)
925.6, 922.1, 921.01	923.3 , 919.2	931.7	5.0	A ^o	ν (CH)
916.6	911.7	911.6	0.2	A ^o	δ (NNC) + ν (CC) + δ (ring)
849.5, 846.6, 844.3, 841.5, 840.6	847.7, 841.7, 839.7	848.7	50.2	A ^o	ν (CH) + τ (ring) + ν (NC) + ν (CO)
		839.9	0.04	A ^o	ν (CH)
		837.1	5.3	A ^o	δ (ring) + ν (CC) + ν (CO)
811.3 , 806.6	806.2 , 804.5	803.8	11.2	A ^o	ν (CH)
788.3	788.2	784.7	15.6	A ^o	δ (ring) + ν (CC) + ν (CO) + ν (NC)
767.8	766.02	771.7	26.2	A ^o	ν (CH) + τ (ring) + ν (NC)
721.2	719.4	722.4	7.1	A ^o	ν (CH) + τ (ring) + ν (NC) + ν (CO)
686.1	684.4	685.7	37.7	A ^o	ν (CH) + τ (ring) + ν (NC)
645.9 , 642.8	650.6 , 647.3	643.0	0.5	A ^o	δ (ring) + ν (CC)
634.4, 633.0	643.2 , 641.8	635.5	0.8	A ^o	δ (ring) + δ (NNC)
n.o.	n.o.	614.1	0.1	A ^o	δ (ring)
550.4, 547.8, 546.3	547.8, 545.4, 544.7	547.9	26.6	A ^o	ν (NC) + τ (ring) + τ (CNNC) + ν (CH)
526.6	526.6	522.5	4.2	A ^o	δ (NCC) + δ (NNC)
n.o.	n.o.	495.7	0.8	A ^o	ν (NC) + τ (ring)
495.5 , 492.6	494.6 , 491.9	493.0	33.7	A ^o	δ (ring)
n.o.	n.o.	425.1	0.02	A ^o	τ (ring)
n.o.	n.o.	409.8	0.02	A ^o	τ (ring)
404.6	n.o.	401.3	23.3	A ^o	δ (CO)
n.i.	n.i.	382.4	2.9	A ^o	τ (ring) + ν (NC) + ν (OH)
n.i.	n.i.	366.7	101.4	A ^o	ν (OH)
n.i.	n.i.	279.1	0.5	A ^o	δ (NCC) + δ (NNC)
n.i.	n.i.	271.2	0.2	A ^o	ν (NC) + τ (ring) + τ (NCC)
n.i.	n.i.	202.3	1.1	A ^o	δ (NCC) + δ (NNC) + τ (ring)
n.i.	n.i.	192.6	0.2	A ^o	ν (NC) + τ (ring) + τ (CNNC)
n.i.	n.i.	94.9	0.1	A ^o	τ (CNNC) + τ (ring)
n.i.	n.i.	75.3	1.3	A ^o	δ (NCC) + δ (NNC)
n.i.	n.i.	46.3	1.1	A ^o	τ (CNNC) + ν (NC) + τ (ring)
n.i.	n.i.	6.3	0.02	A ^o	τ (NCC)

B3LYP/6-311+G(2df,2p) calculated wavenumbers (ν) in cm^{-1} and intensities (I) in km mol^{-1} are also given. The theoretical wavenumbers are scaled by a factor of 0.976. The strongest components of split bands are given in bold. ν , bond stretching; δ , in-plane-bending; γ , out-of-plane bending; τ , torsion; n.o., not observed; n.i., not investigated.

3.2.3 Photochemistry

The matrix-isolated 4-hydroxyazobenzene was irradiated with a narrowband UV laser light source through an outer quartz window of the cryostat. Preliminary selection of the wavelength for the applied UV light was guided by the absorption spectrum of HAB in acetonitrile (Figure C.1). Similarly to what happens with azobenzene, irradiations of HAB isolated in an argon matrix did not induce the isomerization process. On the other hand, by irradiating ($\lambda = 345$ nm) the compound isolated in a xenon matrix (30 K), two new weak absorptions around 756 and 693 cm^{-1} appear in the IR spectrum. By repeating the irradiations in xenon matrices annealed to 60 K, other bands also became evident (Figure 3.12). These bands can be assigned to *Z*-HAB form(s) (t+c).

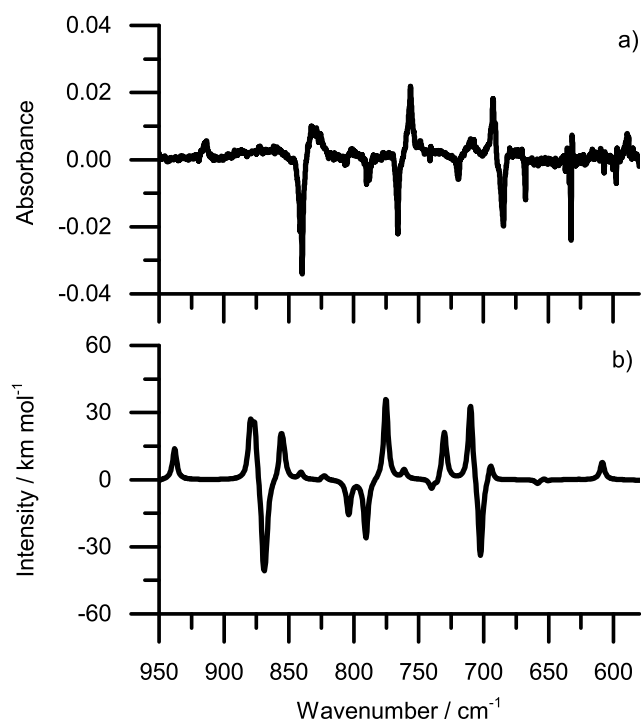


Figure 3.12 (a) Changes in the experimental infrared spectrum of HAB in an Xe matrix at 60 K after 5 min irradiation at $\lambda = 345$ nm. Negative absorptions correspond to decreasing bands of *E*-HAB forms (t+c). Positive peaks correspond to growing absorptions due to the *Z*-HAB forms (t+c); (b) Simulated theoretical difference spectrum, calculated at the B3LYP/6-311+G(2df,2p) level of theory, constructed as “*Z* minus *E*”. Theoretical wavenumbers were scaled by a factor of 0.976.

The N=N stretching mode of the *Z*-HAB form(s) is assigned to a band at 1515 cm^{-1} . This is also in good agreement with the PW91 calculations, which predict a blue shift of 100 cm^{-1} relatively to *E*-HAB form(s) (B3LYP and MP2 predict a blue shift of 39 and 53 cm^{-1} , respectively). It is also worth noting that in both argon and xenon matrices, irradiations with $\lambda \leq 300$ nm cause the appearance of bands in the 2145-2100 cm^{-1} region. These IR bands are consistent with the presence of ketene species (*i.e.*, they correspond to the antisymmetric vibrations of the ketene $-\text{C}=\text{C}=\text{O}$ group) and indicate the occurrence of decomposition. Similar behavior was observed by Giuliano *et al.* in the photochemical study of phenol.⁸³ By isolating monomers of phenol and pentadeuterated phenol in low-temperature argon matrices and irradiating with a narrowband tunable laser source, they were able to identify several photoproducts and possible photochemical channels. Among those, the observation of a open-ring conjugated ketene photogenerated ($\lambda = 275$ nm) from phenol via intramolecular hydrogen atom shift and through intermediacy of a 2,4-cyclohexadienone, was also reported.

Although the occurred spectral changes are relatively small, the fact that the *E*→*Z* isomerization process of HAB is only noticeable in xenon matrices, particularly in the less rigid higher temperature xenon matrix (60 K), seems to corroborate the assumption made before, during the azobenzene irradiation experiments (Section 3.1.2), that the *E*→*Z* isomerization in azobenzenes might be constrained by steric effects caused by the rigid matrix environment.

3.3 4-(Cyclopropyldiazenyl)phenol

The compound presented in this section, 4-(cyclopropyldiazenyl)phenol (CPDP), differs from the two compounds discussed previously (AB and HAB), because it bears a cyclopropyl ring substituent instead of one of the more usual aromatic substituents (Figure 3.13). It was synthesized⁸⁴ and provided by Professor Ana Maria Oliveira-Campos, from University of Minho, as a precursor of new possible azo dyes. The inclusion of the cyclopropyl group adds a different range of conformational possibilities that can be photochemically explored, and might present relevance in the development of azo-based systems. Additionally, the amount of information available for this particular type of mixed aliphatic-aromatic azo compounds is considerably smaller than for other more conventional azo compounds. The experimental characterization of this compound, as well as the description of its isomerization behavior can then be pertinent for future studies concerning the general isomerization mechanisms of azo compounds.

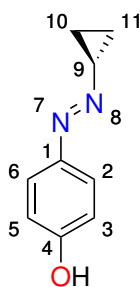


Figure 3.13 Structure of 4-(cyclopropyldiazenyl)phenol (CPDP).

3.3.1 Potential Energy of CPDP

The CPDP molecule has two rigid units, the cyclopropane ring and the aromatic phenol ring, that can show different relative arrangements around the azo group connecting them. A two-dimensional potential energy surface as a function of the $C_6-C_1-N=N$ and $N=N-C-H$ dihedral angles was calculated at the B3LYP/6-311+G(2df,2p) level of theory by letting the two specified angles assume all values between 0 and 360°, with increments of 20°, while all other remaining structural parameters were optimized (Figure 3.14).

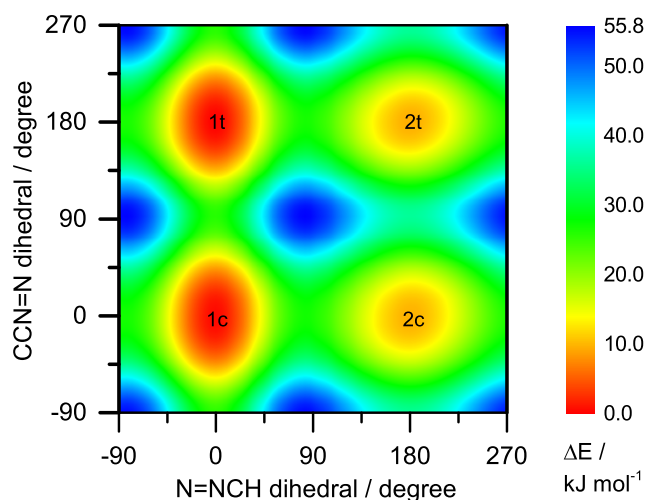


Figure 3.14 Contour map of the relaxed potential energy surface of CPDP calculated at the B3LYP/6-311+G(2df,2p) level of theory as a function of the $C_6-C_1-N=N$ and $N=N-C-H$ dihedral angles. Relative energy is calculated with respect to the lowest energy ground state form (**1t**).

Four energy minima were found on the potential energy surface. The two most stable **1t** and **1c** minima have the NNCH dihedral angle with a value of 0° while in the **2t** and **2c** structures this angle is rotated by 180° . For both type 1 and type 2 structures, the two conformers might also be interconverted by rotation of either the CCNN dihedral or the OH group by 180° . In addition to these relevant internal rotation degrees of freedom, the substituents at the $N=N$ double bond can also adopt the *Z* configuration, and two more structures (**Z1t** and **Z1c**) should be considered in the CPDP potential energy landscape (Figure 3.15). In contrast to the four *E* forms, the structures present a distorted non-planar geometry in which the CCNN, NNCH and CNNC dihedral angles assume the values of approximately 127° , 5° and 5° , respectively. The Cartesian coordinates of all optimized structures, from which all geometric parameters can be taken, are given in Table D.1. The relative energy differences, including the zero-point vibrational contribution, calculated at the B3LYP/6-311+G(2df,2p) and MP2/cc-pVTZ levels of theory are given in Table 3.5.

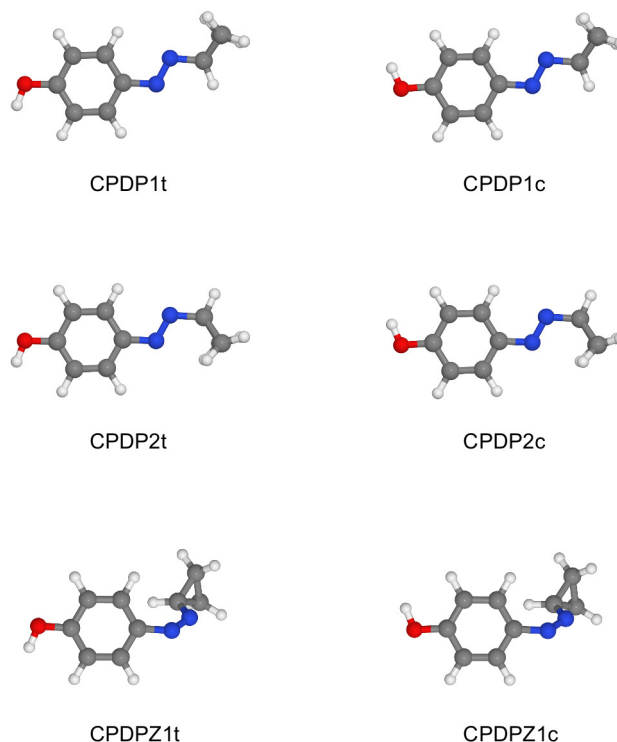


Figure 3.15 Most stable structures of CPDP optimized at the B3LYP/6-311+G(2df,2p) level of theory.

The CPDP1 conformers were calculated to be more stable than the CPDP2 and CPDPZ forms by approximately 5-10 and 44-51 kJ mol⁻¹, respectively. The higher stability of the CPDP1 (**1t** and **1c**) conformers relatively to the ones in which the cyclopropane group is rotated by 180° (**2t** and **2c**) can be explained by taking into account two factors: (i) the negative hyperconjugation that occurs when the lone pair on the nitrogen atom is anti co-planar to a *geminal* CH bond (*i.e.* both N and H atoms are attached to the same carbon atom);^{85,86} (ii) the additional stabilizing interaction between the lone pair of the nitrogen atom *vicinal* to the CH group and the positively charged hydrogen atom of the latter moiety. The **Z1t** and **Z1c** isomers are energetically unfavorable due to the repulsion between the lone electron pairs of the two adjacent nitrogen atoms and the sterically crowded arrangement created when the phenol and cyclopropane rings are brought into a close geometrical proximity. Relatively to the positioning of the OH group, the energy of 1, 2 and Z structures is not considerably affected by the different orientations.

The relative populations of **1t**, **1c**, **2t**, and **2c** at room temperature, estimated

from the calculated Gibbs free energies at 298.15 K and the Boltzmann distribution, suggests that these four conformers should be populated in the gas phase and, consequently, may be expected to appear in the deposited low-temperature argon and xenon matrices. The high energy **Z1t** and **Z1c** structures can be safely neglected.

Table 3.5 Calculated relative energies, with zero-point vibrational energy correction (ΔE_{ZPE}), of CPDP conformers.^a

CPDP	ΔE_{ZPE}			P (%)
	B3LYP		MP2	
	6-311+G(2df,2p)	cc-pVTZ	cc-pVTZ	
1t	0.00	0.00	0.00	45
1c	0.09	0.12	0.20	48
2t	9.51	9.22	4.58	3
2c	9.51	9.30	4.62	3
Z1t	50.99	51.70	43.51	0
Z1c	51.97	52.62	43.81	0

^a All energies in kJ mol^{-1} . Relative populations (P) estimated from the averaged Gibbs free energies calculated at 298.15 K at different levels of theory are also given.

3.3.2 CPDP Structure in a Matrix Shortly After Deposition

The experimental infrared spectra of CPDP isolated in argon and xenon matrices are presented in Figure 3.16 together with the relevant theoretical spectra calculated at the B3LYP/6-311+G(2df2p) level of theory. The experimental spectra are well reproduced by the spectrum simulated for CPDP1 on the basis of the theoretical calculations and estimated relative populations for the **1t** and **1c** conformers (*i.e.*, simulated as **1t+1c**). Analogously to the situation verified for HAB (see previous section), the theoretical spectra predicted for **1t** and **1c** are very similar, thus making difficult to distinguish between these forms in the experimental IR spectra. However, as it will be shown below, this conformational multiplicity of CPDP (*cis* and *trans*) seems to be of minor importance from the viewpoint of the photochemical properties of the compound, with both forms being equally consumed upon irradiation. Tentative band assignments are given in Table 3.6.

The DFT [B3LYP and PW91, with the 6-311+G(2df,2p) and cc-pVTZ basis set] and MP2/cc-pVTZ theoretical calculations predict the band with largest contribution from the $\nu_{\text{N}=\text{N}}$ coordinate at *ca.* 1572, 1477 and 1448 cm^{-1} (values not scaled), respectively. The N=N stretching frequency was assigned to the experimentally observed absorptions situated at approximately 1496 and 1491 cm^{-1} in argon and xenon matrices, respectively. Other characteristic vibrations, such as the ν_{OH} , ν_{CO}

and δOH modes, are observed at *ca.* 3634, 1261 and 1178 cm^{-1} in argon (3606, 1262 and 1177 cm^{-1} in xenon), and are relatively unperturbed when compared with the corresponding modes of matrix-isolated phenol (3636, 1259 and 1175 cm^{-1} ; argon matrix).⁸³

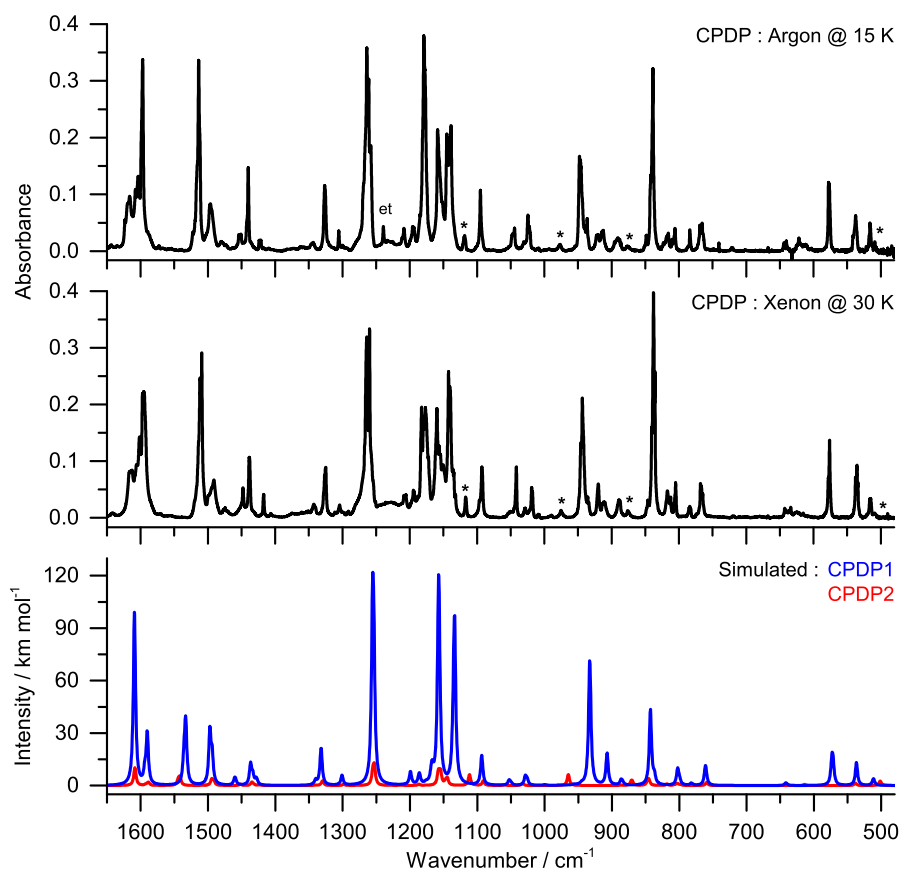


Figure 3.16 Experimental infrared spectra of CPDP isolated in argon (15 K) and xenon (30 K) matrices compared with the theoretical spectra of CPDP1 (simulated as **1t+1c**; blue color) and CPDP2 (simulated as **2t+2c**; red color) calculated at the B3LYP/6-311+G(2df,2p) level of theory. An asterisk (*) indicates the peaks corresponding to absorptions due to the CPDP2 forms. The band at 1239 cm^{-1} , marked as (et), is due to an ethanol impurity. The calculated intensities of CPDP1 and CPDP2 forms were scaled by 0.9 and 0.1, respectively. The calculated harmonic frequencies were scaled by a factor of 0.976 obtained by least-squares linear fitting.

Table 3.6 Experimental observed wavenumbers (ν/cm^{-1}) and tentative assignments for the CPDP1 conformers isolated in argon and xenon matrices.

Ar (15K)	Xe (30K)	Calculated				Sym.	Appr. description
		CPDP1t		CPDP1c			
ν	ν	ν	I	ν	I		
3634.4	3613.3, 3606.4	3736.3	100.6	3735.8	90.4	A'	νOH
3103.2	3103.2	3152.6	4.7	3151.8	6.8	A'	νCH ₂
n.o.	n.o.	3139.7	0.0	3138.8	0.1	A ^o	νCH ₂
3078.8	3074.0	3130.5	2.9	3128.8	2.2	A'	νCH _{Ph}
3069	3065.7	3114.2	3.3	3122.2	3.1	A'	νCH _{Ph}
3044.8	3041.1	3109.0	5.1	3108.1	4.7	A'	νCH _{Ph}
3034.5	3028.8	3078.8	18.7	3073.6	20.2	A'	νCH _{Ph}
3022.9	3019.7	3064.9	18.7	3064.9	24.1	A'	νCH ₂ + νCH _{CP}
3015.8	3011.6	3061.2	12.5	3060.9	14.7	A ^o	νCH ₂
3013.2	3006.1	3056.1	15.3	3056.9	12.9	A'	νCH _{CP} + νCH ₂
1619.1, 1616.5	1616.6, 1615.3, 1612.9	1609.3	100.9	1609.1	129.4	A'	νCC _{Ph} + νSCH _{Ph}
1603.7, 1597.0	1605.8, 1601.6, 1597.2, 1595.4	1590.2	49.4	1593.8	21.0	A'	νCC _{Ph} + νSCH _{Ph}
1513.7	1511.6, 1509.2	1497.2	50.8	1493.8	49.3	A'	νSCH _{Ph} + νCC _{Ph} + νCN _{Ph} + νN=N
1496.1	1491.14	1533.1	59.4	1535.6	40.7	A'	νN=N+ νCC _{Ph} + δNCC _{Ph} + δNCC _{CP}
1454.0, 1450.8	1447.9	1460.5	4.7	1459.2	7.3	A'	sci(CH ₂)+ νCC _{CP} + δCH _{CP}
1440.1	1438.7	1433.5	8.7	1436.8	37.4	A'	δCH _{Ph} + νCC _{Ph} + δOH
1423.8, 1421.4	1417.0	1428.4	4.9	1427.0	3.1	A ^o	sci(CH ₂)
1343.5	1342.5 , 1340.1	1340.0	4.6	1343.9	0.6	A'	δCH _{CP}
1326.5	1324.8	1331.8	27.0	1332.5	18.9	A'	δCH _{Ph} + νCC _{Ph} + δOH
1305.6	1304.3	1300.9	9.2	1301.8	0.9	A'	δCH _{Ph} + νCC _{Ph}
1263.9 , 1261.0, 1257.9	1263.7, 1259.8	1255.6	150.1	1253.7	194.0	A'	νCO+ δPh+ δCH _{Ph}
1211.7, 1208.7	1208.7, 1205.7	1199.2	9.0	1199.4	6.9	A'	νCN _{Ph} + δCH _{Ph} + δNCC _{CP}
1195.9 , 1193.8	1194.6 , 1193.5	1185.9	8.4	1187.0	5.4	A'	νCN _{Ph} + δCH _{Ph} + δCH _{CP}
n.o.	n.o.	1176.2	1.1	1174.7	0.4	A ^o	tw(CH ₂)
1184.8	1188.1	1166.4	8.0	1167.9	19.2	A'	δCH _{CP} + νCC _{CP} + νCN _{CP}
1179.2 , 1177.5	1182.5 , 1180.0, 11178.8,	1157.7	142.9	1156.5	147.9	A'	δOH+ δCH _{Ph}
1158.7 , 1144.9,	1176.8 , 1172.3	1133.6	139.5	1135.3	80.4	A'	δCH _{Ph} + νCN _{Ph} + νCC _{Ph} + δOH
1140.5, 1138.7	1159.7, 1156.5, 1142.4 , 1140.6,	1093.4	16.4	1093.5	23.4	A'	δCH _{Ph} + νCC _{Ph} + δOH
1095.0	1135.9, 1134.5, 1132.2	1092.1	0.1	1091.9	0.3	A ^o	tw(CH ₂)
	1096.6, 1092.8						

Table 3.6 (Cont.)

Ar (15K)	Xe (30K)		Calculated				Sym.	Appr. description
	ν	ν	CPDP1t		CPDP1c			
ν	ν	ν	ν	I	ν	I		
1047.0, 1044.31	1041.6	1052.8	4.7		1050.1	4.1	w(CH ₂)	
1024.4 , 1022.4	1018.8 , 1017.7	1028.7	8.3		1026.0	9.6	w(CH ₂)	
1010.6, 1008.6	1009.4, 1007.8	999.7	0.5		1002.2	0.3	ν CC _{Ph} + δ CH _{Ph}	
992.8	989.6	976.5	0.1		967.0	0.1	γ CH _{Ph}	
953.5	948.8	945.0	1.2		956.1	1.1	γ CH _{Ph}	
947.8 , 946.4, 945.4, 939.7, 936.3	945.6, 943.5 , 935.5, 934.1	933.3	85.2		932.2	82.1	ν CN _{CP} + δ CP	
921.5, 912.6	919.8, 911.9	907.0	20.8		907.6	20.3	δ CP	
895.71, 890.9 , 887.9, 886.3	889.0	886.5	4.3		884.4	5.4	γ CH _{CP}	
848.5, 841.9, 838.6	846.1, 840.4, 837.8 , 835.6	842.9	47.3		842.7	49.2	γ CH _{Ph}	
815.8 , 810.6	817.1 , 812.2	836.9	4.9		837.0	5.5	δ Ph	
805.9	805.0	802.2	13.6		803.3	4.9	γ CH _{Ph}	
783.9	784.0	800.1	1.0		799.5	6.2	γ CH _{Ph} + γ CH _{CP}	
768.4 , 765.6	768.0 , 767.0, 764.6	782.5	1.6		780.8	1.5	r(CH ₂) + δ Ph	
721.7 , 719.9	719.6	761.3	15.4		760.0	10.6	r(CH ₂) + δ Ph	
643.9	642.7	723.0	0.1		721.5	0.1	τ Ph	
577.7 , 576.5	577.9, 576.1	640.9	1.2		642.1	3.2	δ Ph	
541.4, 537.4	537.6, 535.4 , 534.0	573.3	22.4		571.5	30.5	δ NNCP _{Ph} + δ Ph	
516.1	516.1, 515.0	536.8	14.4		536.9	15.0	τ Ph + γ CH _{Ph}	
456.9	434.9	511.2	4.6		512.4	4.4	δ NCCCP+ δ Ph	
n.o.	n.o.	451.6	3.5		449.9	6.6	τ N=N + τ Ph	
n.i.	n.i.	422.8	1.1		421.9	0.1	τ Ph + τ CN _{Ph}	
409	410.5	405.0	14.7		406.3	6.1	δ CCO	
n.i.	n.i.	375.9	2.8		374.8	3.3	τ Ph + γ CN _{Ph}	
n.i.	n.i.	355.2	101.1		352.7	98.5	τ OH	
n.i.	n.i.	303.6	7.6		303.4	5.8	δ NNCCP	
n.i.	n.i.	275.7	1.2		274.1	1.2	δ NCCPh	
n.i.	n.i.	219.6	0.1		219.3	0.05	γ CN _{Ph} + γ CO	
n.i.	n.i.	127.9	0.9		125.3	0.6	γ CN _{CP}	
n.i.	n.i.	97.6	1.9		98.5	4.2	Skeletal	
n.i.	n.i.	86.4	1.0		81.7	1.0	τ CN _{CP}	
n.i.	n.i.	39.6	0.9		34.6	0.1	τ CN _{Ph}	

B3LYP/6-311+G(2df,2p) calculated wavenumbers (ν) in cm⁻¹ and intensities (I) in km mol⁻¹ are also given. The theoretical wavenumbers are scaled by a factor of 0.976. The strongest components of split bands are given in bold. ν , bond stretching; δ , in-plane-bending; γ , out-of-plane bending; w, wagging; sci, scissoring; r, rocking; τ , torsion; Ph, aromatic ring; CP, cyclopropane ring; n.o., not observed; n.i., not investigated.

A closer look to the CPDP experimental infrared spectra also reveals the presence of several absorptions (*e.g.*, 1118, 976, and 876 cm^{-1}) that can be promptly assigned to CPDP2 (**2t+2c**; see Figure 3.16). The barrier for intramolecular rotation of the cyclopropane moiety transforming CPDP2 into CPDP1 forms was calculated to be $\sim 16 \text{ kJ mol}^{-1}$ (at the B3LYP level). Such a high barrier can only be overcome at relatively high temperatures (above 50 K)^{87,88} and, after annealing the xenon matrix at 65 K, the bands relative to CPDP2 decreased and the ones of CPDP1 increased (Figure 3.17). Further confirmation that the decreasing bands indeed belong to CPDP2 was obtained during the irradiation experiments (see Section 3.3.3). The experimentally observed CPDP2 (**2t+2c**) wavenumbers are given in Table 3.7.

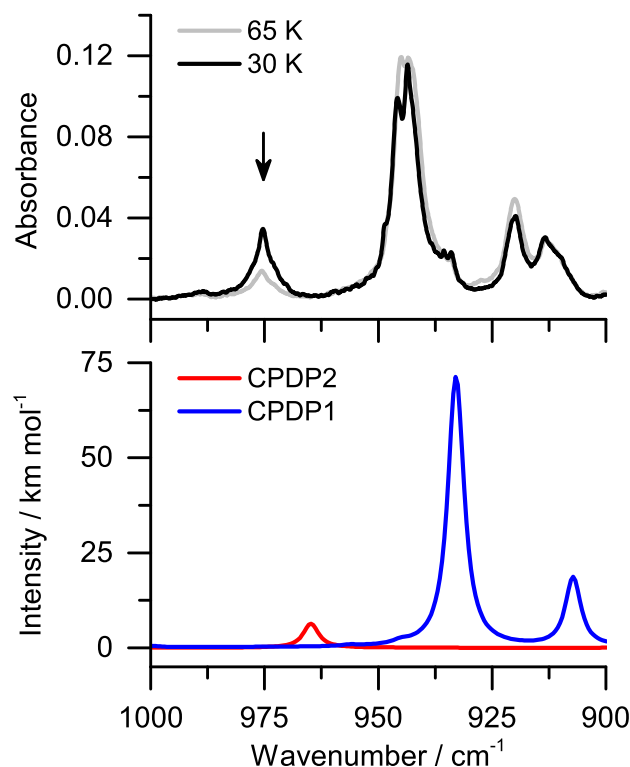


Figure 3.17 Selected region of the experimental infrared spectrum of CPDP in a xenon (30 K) matrix, compared with the theoretical spectra of forms CPDP1 (simulated as **1t+1c**; blue color) and CPDP2 (simulated as **2t+2c**; red color). A downward arrow (\downarrow) indicates one of the decreasing bands of CPDP2 upon annealing of the matrix. The calculated intensities of CPDP1 and CPDP2 were scaled by 0.9 and 0.1, respectively. All calculated frequencies were scaled by 0.976.

3.3 4-(Cyclopropyldiazenyl)phenol

Table 3.7 Experimental observed wavenumbers (ν/cm^{-1}) of the CPDP2 conformers isolated in argon and xenon matrices.

Ar (15K)	Xe (30K)	Calculated			
		CPDP2t		CPDP2c	
		ν	I	ν	I
3638.4	3616.3, 3611.2	3736.4	108.3	3734.9	89.8
3109.16	3106.5	3148.3	10.5	3148.6	10.4
n.o.	n.o.	3135.3	0.5	3135.6	0.6
3095.7	3097.1	3129.8	11.1	3128.5	2.4
n.o.	n.o.	3113.1	2.2	3121.5	6.3
		3109.2	17.1	3108.9	17.2
3074.1	3086.4	3108.7	5.9	3106.8	10.8
3041.7	3067.9	3078.6	17.6	3073.1	22.2
		3055.7	15.8	3055.9	15.8
3018.2 , 3009.0	3014.6 , 3008.4	3054.8	14.4	3055.0	14.5
1616.9, 1615.5	1613.6 , 1610.3	1609.0	89.7	1608.2	122.8
1604.2, 1599.6	1602.3, 1596.8, 1595.6	1588.4	36.3	1592.0	12.3
1522.8	1520.1, 1517.0	1541.6	86.6	1544.1	62.5
1497.6	1494.5	1494.4	69.0	1491.3	45.1
1442.7	1440.2	1451.1	3.5	1452.2	12.6
1435.6, 1432.5	1431.2	1432.6	8.5	1434.8	37.0
1410.9	1406.3	1422.6	4.5	1423.6	4.4
1352.6	1349.8	1341.2	2.2	1340.3	3.1
1325.7	1323.8	1329.7	42.7	1330.6	13.4
1303.7	1301.9	1298.5	13.4	1299.4	1.6
1269.0	1266.6, 1261.5	1255.2	134.4	1252.9	200.9
1214.3	1212.2	1212.3	0.6	1213.1	4.2
1195.3	1196.6	1186.8	3.9	1186.6	10.3
n.o.	n.o.	1177.2	0.7	1177.8	0.7
1182.4 , 1180.6	1180.9, 1176.9 , 1175.0	1157.8	149.8	1154.6	144.6
1151.8 , 1149.8	1150.5, 1147.8	1144.5	74.6	1147.2	38.1
1119.7	1117.1	1111.6	79.7	1111.5	46.1
n.o.	n.o.	1102.9	1.2	1102.9	1.1
1093.7	1093.1, 1091.9	1091.4	2.2	1091.1	51.4
1054.8	1050.3, 1049.4	1059.4	4.7	1059.4	4.5
1032.1 , 1030.6	1028.3 , 1026.7	1032.6	13.1	1032.5	14.0
n.o.	n.o.	997.6	1.3	999.3	0.3
n.o.	n.o.	979.1	0.02	969.1	0.02
976.4	975.3	964.5	74.0	965.2	55.9
n.o.	n.o.	948.2	1.2	958.2	0.8
896.0	894.3	886.3	2.6	886.5	2.8
877.2	876.1	869.8	33.3	871.2	38.7
839.9	838.3	846.9	47.7	845.1	52.9
816.7	814.5	818.3	7.8	818.6	11.9
		804.4	10.0	808.1	4.3
806.8, 805.3	804.9, 804.3	802.5	12.8	803.1	4.9

Table 3.7 (Cont.)

Ar (15K)	Xe (30K)	Calculated			
		CPDP2t		CPDP2c	
ν	ν	ν	I	ν	I
801.9	n.o.	797.8	5.0	798.0	4.8
773.9, 768.8	774.1 , 769.8	758.9	20.0	759.8	17.4
n.o.	n.o.	725.0	0.1	722.6	0.1
640.7	640.3	637.8	0.5	638.7	2.3
614.3 , 612.7	616.6, 615.4	613.9	7.3	613.7	6.4
537.7	535.4	538.6	14.1	538.4	14.3
508.8	509.2	502.4	15.6	501.4	38.1
454.5	451.9	449.8	2.5	448.6	4.3
n.o.	n.o.	420.1	1.1	419.6	0.2
420.9	421.0	416.1	20.3	417.4	0.4
n.i.	n.i.	364.8	9.7	363.9	4.7
n.i.	n.i.	350.2	36.0	348.3	10.0
n.i.	n.i.	340.2	69.0	326.7	92.9
n.i.	n.i.	209.9	0.3	210.3	0.1
n.i.	n.i.	186.9	0.1	186.8	0.0
n.i.	n.i.	148.5	0.7	149.3	0.9
n.i.	n.i.	107.9	3.0	109.6	4.6
n.i.	n.i.	62.8	0.8	63.2	0.2
n.i.	n.i.	34.8	0.02	34.9	1.5

B3LYP/6-311+G(2df,2p) calculated wavenumbers (ν) in cm^{-1} and intensities (I) in km mol^{-1} are also given. The theoretical wavenumbers are scaled by a factor of 0.976. The strongest components of split bands are given in bold. n.o., not observed; n.i., not investigated.

3.3.3 Photochemistry

CPDP isolated in the cryogenic matrices was irradiated with a narrowband UV laser light source. Preliminary selection of the wavelength for the applied UV light was guided by the absorption spectrum of the compound (Figure D.1). After each irradiation, the system was monitored by analysis of its IR spectrum. Upon irradiation in the 390-375 nm range, the bands initially assigned to CPDP2 increase while the bands of CPDP1 show a decrease in intensity. This increase in the intensity of the bands of CPDP2 allowed us to deconvolute its experimental spectrum (Figure 3.18) and unambiguously confirm (by comparison with the theoretical spectrum) the assignment made before, during the annealing experiments.

Upon irradiation in the 460-440 nm range, the bands of CPDP2 are consumed and those of CPDP1 show an increase in intensity. Further irradiation at 345 nm reverse this trend and, once again, the bands of CPDP1 and CPDP2 decrease and increase, respectively, clearly demonstrating that these two conformers can be photochemically interconverted, using appropriate excitation wavelengths.

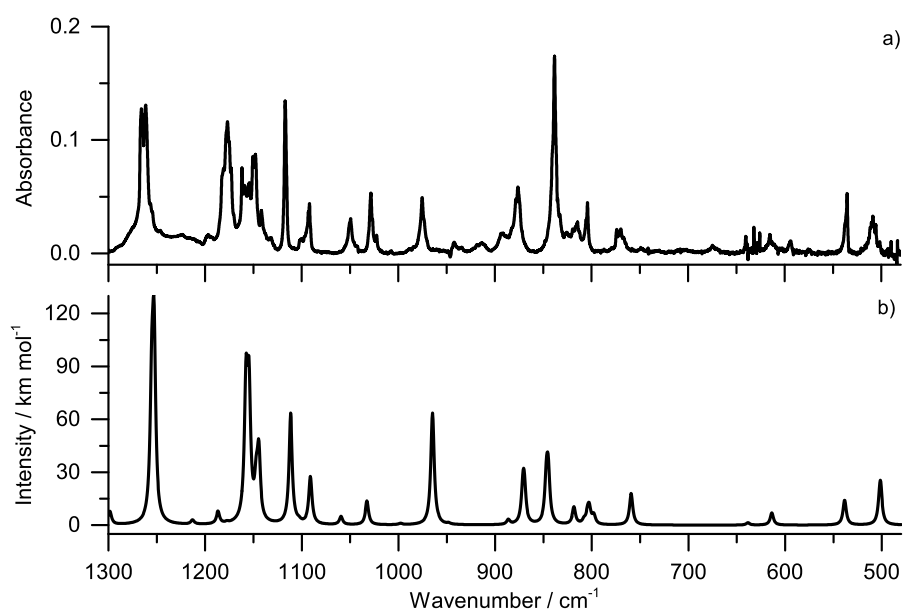


Figure 3.18 Extracted experimental infrared spectrum of CPDP2 obtained by subtraction of the spectrum recorded after irradiation at 460 nm (5 min) from the spectrum recorded after irradiation at 345 nm (5 min), so that the bands due to CPDP1 are nullified (a); Theoretical infrared spectrum of the CPDP2 (**2t+2c**) calculated at the B3LYP/6-311+G(2df,2p) level of theory (b).

During the interconversion between CPDP1 and CPDP2, an additional new set of bands (exhibiting a different growth behavior compared to the bands ascribable to CPDP2) also becomes noticeable. These bands become more evident upon irradiating the sample in the 335-325 nm range, while at the same time the bands of both CPDP1 and CPDP2 are consumed. After comparing the experimentally obtained difference spectrum with the theoretical calculated ones, this new set of bands could be assigned to the CPDPZ forms (Figure 3.19). Irradiations at longer wavelengths consume CPDPZ and regenerate both CPDP1 (460-440 nm) and CPDP2 (400 nm).

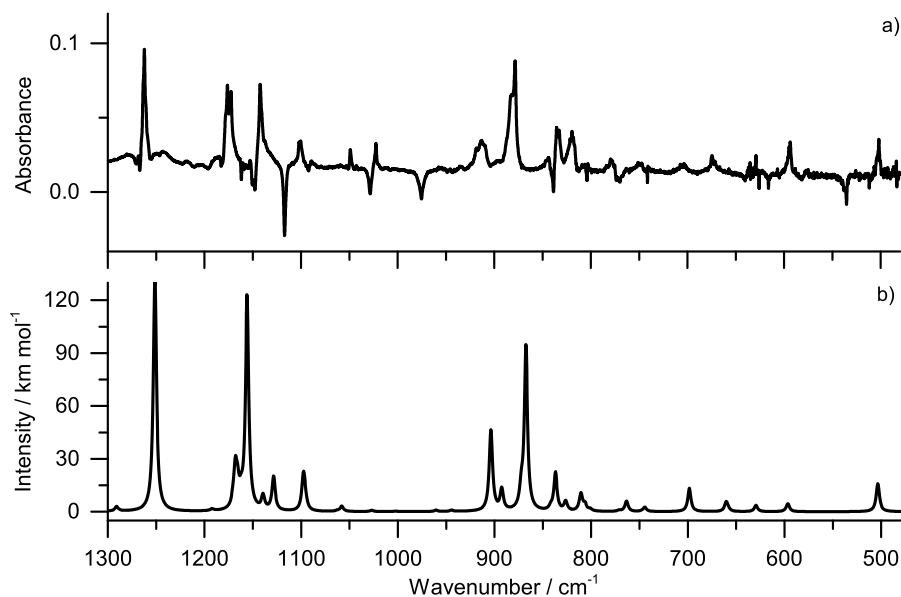


Figure 3.19 Extracted experimental infrared spectrum of CPDPZ obtained by subtraction of the spectrum recorded after irradiation at 345 nm (5 min) from the spectrum recorded after irradiation at 335 nm (5 min), so that the bands due to CPDP1 and CPDP2 are nullified or appear as negative peaks (a); Theoretical infrared spectrum of the CPDPZ (**Z1t+Z1c**) calculated at the B3LYP/6-311+G(2df,2p) level of theory (b). The experimentally observed CPDPZ (**Z1t+Z1c**) wavenumbers are given in Table 3.8.

The performed sequence of irradiations clearly indicates the reversibility of the photochemical interconversion between different CPDP forms, **1**, **2** and **Z**. By selecting the appropriate wavelength, these forms can be almost completely interconverted. However, the fact that they are never fully depleted during the different irradiations seems to suggest the existence of photostationary states. It should also be noted that a small extent of decomposition of the compound also occurs. This is indicated by the appearance of bands in the 2160-1990 cm⁻¹ region. These bands become more evident at shorter wavelengths and long irradiation times and suggest

3.3 4-(Cyclopropyldiazenyl)phenol

a decomposition behavior similar, to some extent, to the one observed for matrix-isolated phenol and 4-hydroxyazobenzene.⁸³

Table 3.8 Experimental observed wavenumbers (ν/cm^{-1}) of the CPDPZ conformers isolated in argon and xenon matrices.

Ar (15K)	Xe (30K)	Calculated			
		CPDPZ1t		CPDPZ1c	
ν	ν	ν	I	ν	I
3632.7	3612.7	3738.8	83.5	3741.9	97.9
n.o.	n.o.	3150.4	5.6	3152.0	5.4
n.o.	n.o.	3137.5	0.1	3138.9	0.3
n.o.	n.o.	3117.4	4.2	3118.7	5.4
n.o.	n.o.	3109.7	4.8	3106.0	3.1
n.o.	n.o.	3102.2	2.8	3102.9	1.6
n.o.	n.o.	3085.7	5.7	3085.8	5.1
3038.3	3036.4	3077.0	16.7	3073.0	18.0
3022.6 , 3014.1	3018.8	3061.1	10.4	3063.1	11.3
		3059.5	12.5	3060.6	11.3
1609.9 , 1606.2	1608.6, 1604.9	1609.6	47.0	1605.0	56.8
1594.4	1592.9	1581.9	18.0	1584.2	5.4
1527.5	1525.0	1557.5	55.1	1560.4	47.5
1501.5	1498.7	1493.4	86.4	1490.6	98.7
n.o.	n.o.	1460.7	0.9	1466.9	0.8
1428.0	1427.5	1428.1	14.1	1436.1	3.5
1420.1	1416.0	1423.6	3.0	1425.8	18.6
n.o.	n.o.	1335.3	0.1	1336.8	0.4
1327.2	1329.7	1327.1	25.5	1326.4	29.5
1305.6	1304.1	1290.9	2.8	1288.1	1.9
1261.7	1262.2	1251.4	135.1	1250.8	118.9
n.o.	n.o.	1192.1	1.1	1193.6	0.9
n.o.	n.o.	1170.7	3.4	1174.7	0.3
		1168.0	24.3	1165.7	112.4
1175.7	1176.2, 1172.5	1155.9	135.8	1162.1	60.1
1154.2	1152.7	1139.3	8.7	1141.4	2.4
1142.0	1142.2	1128.6	18.6	1128.4	26.2
1102.4	1102.1	1097.9	18.5	1097.1	2.8
1099.1	1100.5	1096.4	8.5	1094.5	14.7
1051.2	1049.0	1058.0	3.3	1063.0	4.2
1025.3	1022.5	1027.0	0.8	1036.6	0.4
n.o.	n.o.	1002.6	0.2	1000.9	0.3
n.o.	n.o.	960.5	0.9	961.9	0.2
n.o.	n.o.	944.6	0.8	937.4	1.1
914.3, 910.7	918.9, 913.4	903.8	45.9	903.0	51.5
900.6	898.3	892.5	13.3	898.9	1.4
886.2, 881.8	881.7, 878.4	867.5	104.0	872.3	104.5
836.6	832.8	837.0	24.2	841.8	18.7

Table 3.8 (Cont.)

Ar (15K)	Xe (30K)	Calculated			
		CPDPZ1t		CPDPZ1c	
ν	ν	ν	I	ν	I
822.2	819.5	826.4	4.6	826.6	12.2
809.1	805.8	810.6	10.6	812.0	5.1
n.o.	803.2	806.3	3.9	801.0	11.5
776.4	779.5 , 775.4	763.5	6.6	771.1	6.1
751.8, 748.9	750.5, 747.6	744.5	2.6	746.7	2.7
704.8	703.8	698.5	13.7	698.0	11.2
671.1	674.7 , 670.8	660.4	6.0	658.2	10.4
n.o.	629.2	629.6	3.7	629.5	2.4
595.4	594.8, 593.7	596.5	4.8	597.9	3.8
503.8	502.0	503.6	16.1	502.7	16.7
n.o.	n.o.	455.1	0.4	455.3	0.0
n.o.	n.o.	414.9	1.5	414.0	5.5
n.o.	n.o.	407.8	14.8	408.1	3.6
n.i.	n.i.	347.8	2.3	348.9	3.6
n.i.	n.i.	327.3	3.8	332.6	13.5
n.i.	n.i.	314.8	97.5	330.0	73.5
n.i.	n.i.	283.0	1.8	292.6	0.7
n.i.	n.i.	186.4	0.3	192.7	0.5
n.i.	n.i.	167.3	2.0	166.3	0.9
n.i.	n.i.	77.1	3.3	95.1	1.6
n.i.	n.i.	64.7	0.6	70.6	0.7
n.i.	n.i.	33.4	1.8	27.7	0.6

B3LYP/6-311+G(2df,2p) calculated wavenumbers (ν) in cm^{-1} and intensities (I) in km mol^{-1} are also given. The theoretical wavenumbers are scaled by a factor of 0.976. The strongest components of split bands are given in bold. n.o., not observed; n.i., not investigated.

3.4 1-(Cyclopropyldiazenyl)naphthalen-2-ol*

The compound discussed in this section (CPDNO) was also synthesized⁸⁹ by Prof. Ana Maria Oliveira-Campos (University of Minho) and differs from the previous one by having a 2-naphthol instead of a phenol ring (Figure 3.20). These particular type of aromatic azo compounds, with the azo and hydroxyl groups in *ortho* positions, have two distinct plausible tautomeric structures: azo-enol (OH) or keto-hydrazone (NH), which may coexist under certain experimental conditions. These tautomeric structures can be stabilized by intramolecular hydrogen bonds and the equilibrium between the two can be further explored in signaling and switching.^{90,91} Thus, detailed knowledge on the range of conformational/tautomeric possibilities introduced and photochemical behavior of such compounds is crucial for understanding their reactivity, and particularly important from the viewpoint of their applications.

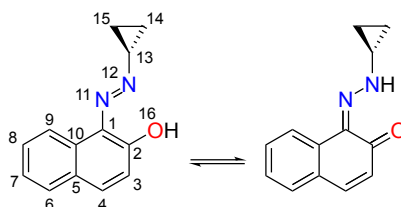


Figure 3.20 Structures for the azo-enol (**E**) and keto-hydrazone (**K**) forms of 1-(cyclopropyldiazenyl)naphthalen-2-ol (CPDNO), with numbering of heavy atoms.

3.4.1 Potential Energy Surface of CPDNO

The studied molecule, CPDNO, may adopt azo-Enol (**E**)[†] or Keto-hydrazone (**K**) tautomeric forms (Figure 3.20). For each tautomer, several conformers are possible due to the different relative arrangements of the two rings around the azo (or hydrazone) group. Additionally, in the case of the **E** tautomer, several conformers may arise due to the internal rotation of the hydroxyl group. Hereafter, the conformers will be named by letters **E** or **K** designating the respective tautomer, followed by numbers (in the increasing energy order) designating conformers within each tautomer.

*The content reported in this section was already published. The original paper (Duarte, L.; Giuliano, B. M.; Reva, I.; Fausto, R. *J. Phys. Chem. A* **2013**, 117, 10671–10680) can be found in Appendix E.

[†]Please note that designation “**E**” refers to azo-enol forms. Do not confuse with the “*E*” (from entgegen) used in the previous sections.

Taking into account both **E** and **K** tautomeric forms, the performed theoretical calculations predicted more than 20 minima on the ground electronic state potential energy surface of CPDNO. The optimized geometries and relative energies of the CPDNO isomers most relevant for the present discussion are shown in Figure 3.21 and Figure 3.22. All of the optimized structures, their energies, and Cartesian coordinates are given in Table E.1.

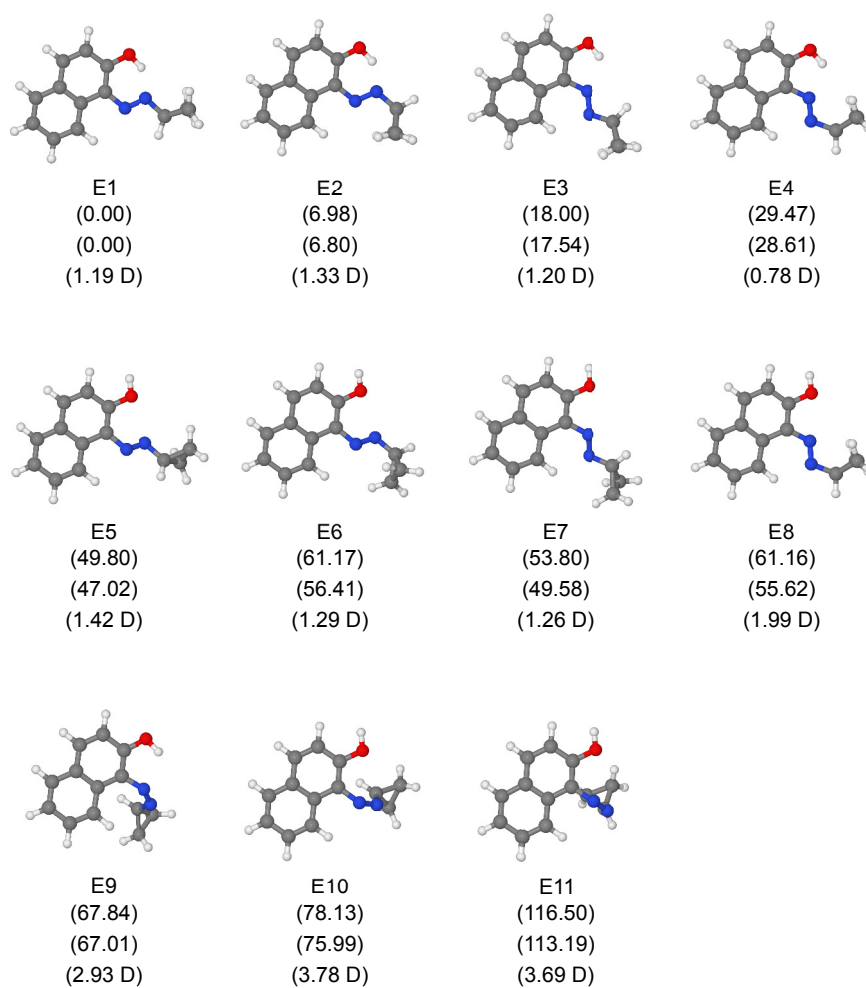


Figure 3.21 Structures of the calculated (B3LYP/6-311+G(2df,2p)) azo-enol forms of CPDNO. The relative energies, in kJ mol^{-1} , with zero point correction (top) and thermal correction to Gibbs free energy at 298 K (middle), and the dipole moments (bottom) are given below each structure.

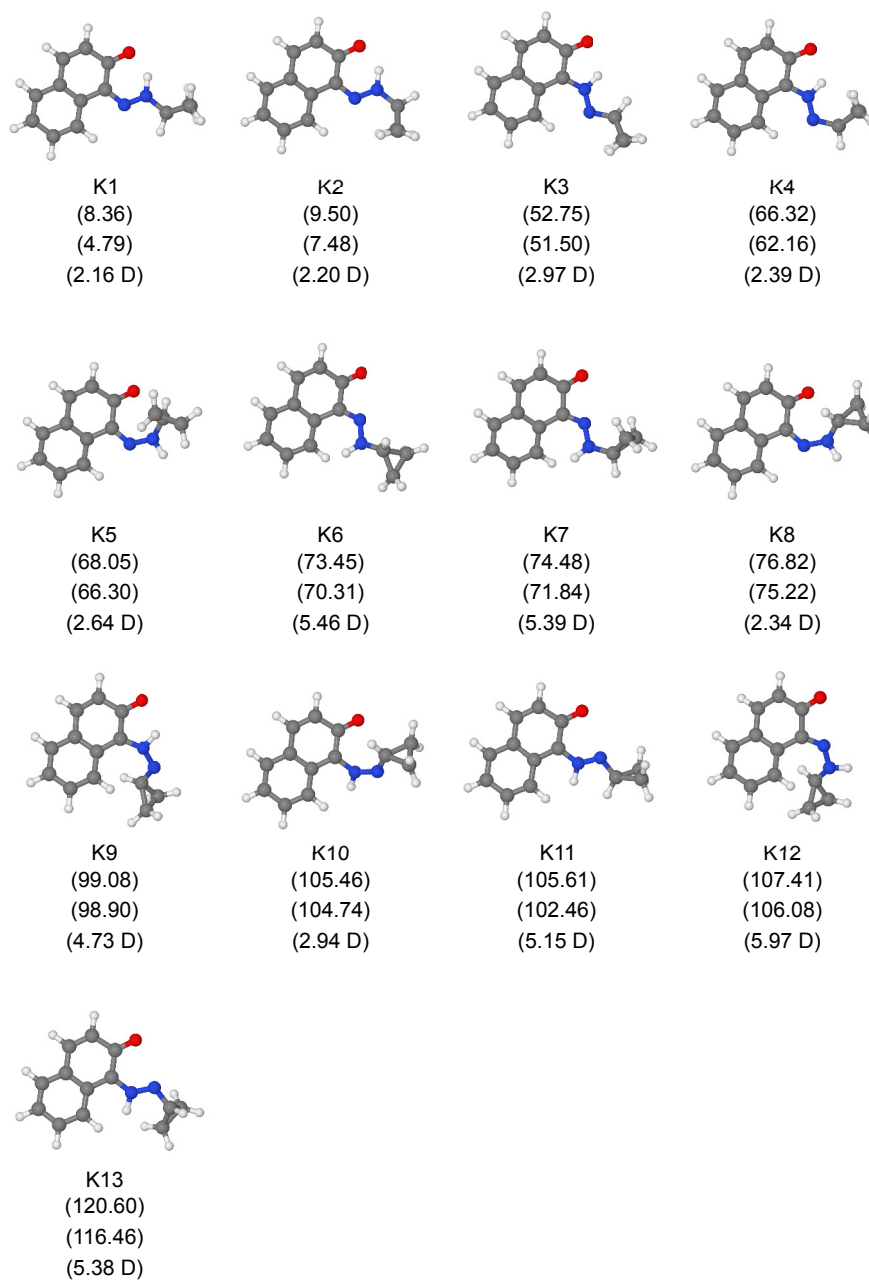


Figure 3.22 Structures of the calculated (B3LYP/6-311+G(2df,2p)) keto-hydrazone forms of CPDNO. The relative energies, in kJ mol⁻¹, with zero point correction (top) and thermal correction to Gibbs free energy at 298 K (middle), and the dipole moments (bottom) are given below each structure.

The two-dimensional potential energy landscape of the **E**-form of CPDNO as a function of the C–C–O–H and C–C–N=N dihedral angles is shown in Figure 3.23. This surface was calculated on a two-dimensional grid of 144 points where the reaction coordinates (the two dihedral angles specified above) assumed all values between 0 and 360°, with an increment of 30°. With the two dihedral angles incrementally fixed, all remaining parameters were optimized. Before focusing on these two structurally most relevant internal rotation degrees of freedom, we shall consider the relative energies of possible minimum energy structures differing in the arrangements about the CNNC and NNCH fragments.

The optimized values of the CNNC and NNCH dihedral angles conserved *trans* and *cis* orientations, respectively. Structures **E1**, **E3**, **E5**, and **E7** have the NNCH dihedral angle in the *cis* orientation. Their less stable **E2**, **E4**, **E6**, **E8** counterparts (not shown in Figure 3.23) have the NNCH dihedral angle in the *trans* orientation (*i.e.*, have the cyclopropane group rotated by $\approx 180^\circ$; see Figure 3.21). The higher stability of the NNCH *cis* forms can be explained by taking into account two factors: (i) negative hyperconjugation (Bohlmann effect). It occurs when the lone pair on the nitrogen is anti co-planar to a *geminal* CH bond (*i.e.*, both N and H atoms are attached to the same carbon atom);^{85,86} (ii) the additional stabilizing interaction between the lone pair of the nitrogen atom *vicinal* to the CH group and the positively charged hydrogen atom of the latter moiety. These two stabilizing interactions are present in **E1**, **E3**, **E5**, **E7** and absent in **E2**, **E4**, **E6**, **E8**, and are the same found to play also a crucial role in determining the stability of the different structures of CPDP, discussed in the previous section.

Regarding the CNNC dihedral angle: the azo group can adopt two orientations around the N=N bond, *trans* (or “entgegen”) and *cis* (“zusammen”). The *cis* structures are energetically unfavorable because of two reasons. First, the two adjacent nitrogen atoms having the same hybridization create repulsion of the lone electron pairs at both nitrogen atoms, inevitably augmenting the internal energy.⁹² Second, the *cis* arrangement brings the naphthol and cyclopropane rings into a close geometrical proximity, thus creating sterically crowded structures. In order to avoid the crowded geometries, the cyclopropane ring must be then moved away from the plane of the naphthol ring, at the expense of breaking the π -conjugation in the molecule. Though a few minima with a *cis* CNNC dihedral angle were indeed located for CPDNO, all of them have very high relative energies (≈ 65 kJ mol⁻¹ or above; see Figure 3.21).

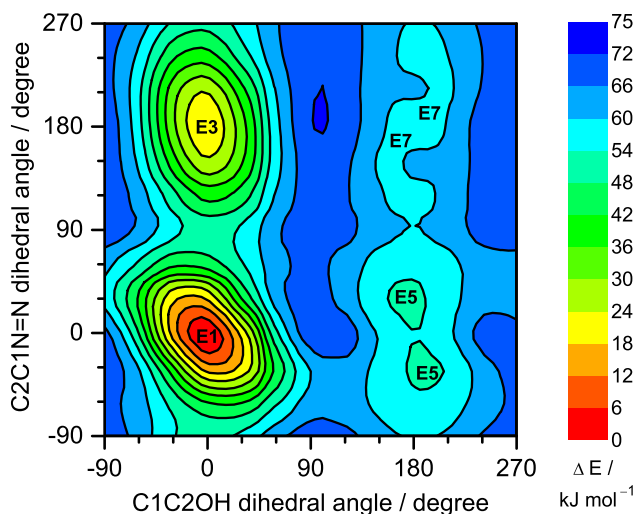


Figure 3.23 Contour map of the relaxed potential energy surface of CPDNO calculated at the B3LYP/6-311+G(2df,2p) level of theory as a function of the C–C–O–H and C–C–N=N dihedral angles. Relative energy is calculated with respect to the lowest energy ground state (**E1**) form. Atom numbering is shown in Figure 3.20.

The analysis of Figure 3.23 allows to extract the following conclusions regarding the dependence of the molecule's energy on the C–C–O–H and C–C–N=N dihedral angles: (i) all potential energy minima located on this surface are grouped along the two valleys where the CCOH dihedral angles assumes the *cis* (0°) or *trans* ($\approx 180^\circ$) orientations with respect to the C(1)C(2) bond. This means that hydroxyl group is essentially co-planar with the aromatic naphthol ring. This is also true for all other minima of the **E**-tautomer of CPDNO; (ii) the *trans*-OH minima (**E5** and **E7**) have very high relative energies ($\approx 50 \text{ kJ mol}^{-1}$ or above). This is explained by the unfavorable vicinity of the lone electron pair of the oxygen with the lone electron pairs of the azo group; (iii) the *cis*-OH minima (**E1** and **E3**) are stabilized due to the favorable orientation of the hydroxyl group establishing an intramolecular hydrogen-bond with one of the nitrogen atoms of the azo group; (iv) the minima along the CCNN dihedral angle also adopt positions close to the *cis* and *trans* orientations. This is dictated by the fact that the π -electron system of the N=N bond is stabilized due to the conjugative interaction with the π -electron system of the naphthol ring, which is maximized for co-planar arrangements of these two moieties.

Formation of the keto-hydrazone tautomer of CPDNO implies migration of the labile hydrogen from the OH group to one of the two nitrogen atoms. These two possibilities are depicted in Figure 3.21 and Figure 3.22, where the azo-enol forms **E1** and **E2** forming an intramolecular six-membered ring via OH...N bond give rise to the keto-hydrazone forms **K1** and **K2**, bearing a six-membered ring with an O...HN bond. Similarly, the **E3** form on one side and the **K3** form on the other side are the counterparts having a five-membered ring stabilized by an intramolecular OH...N\O...HN interaction. The azo-enol and keto-hydrazone isomers having the intramolecular H-bond inserted in a six-membered ring were found to be more stable by approximately 20 kJ mol⁻¹ and 50 kJ mol⁻¹, respectively, than their five-membered ring counterparts.

On the whole, the most stable isomer of CPDNO corresponds to **E1**. Among all of the calculated minima, only three other structures (**K1**, **E2**, and **K2**) fit into the 0-10 kJ mol⁻¹ interval of relative energies (see Figure 3.21 and Figure 3.22). The relative populations of **E1**, **K1**, **E2**, and **K2** at room temperature, estimated from the calculated Gibbs free energies at 298.15 K and the Boltzmann distribution (79, 12, 5, and 4%, respectively) suggest that only these four forms contribute non-negligibly to the gas phase equilibrium and, consequently, may be expected to appear in the deposited low-temperature matrices. All of the remaining structures have calculated energies above 17 kJ mol⁻¹, and their populations can be neglected from the viewpoint of the thermal equilibrium.

As it will be shown below in this work, only the signatures of two azo-enol conformers, **E1** and **E2**, were in fact identified in the experimental spectra. The nonobservation of the keto-hydrazone forms can be explained with the aid of the potential energy surfaces describing the displacement of the hydrogen atom in the [**E1**, **K1**] and [**E2**, **K2**] pairs (see Figure 3.24). The transition states for the proton shift in these two pairs were fully optimized and the remaining points were calculated with incrementally fixed OH distances on the **E**-side for **E1** and **E2** and with incrementally fixed NH distances on the **K**-side for **K1** and **K2**. Thus, each graph consists of two parts having two different abscissas (OH vs NH distance) that alternate at the transition state.

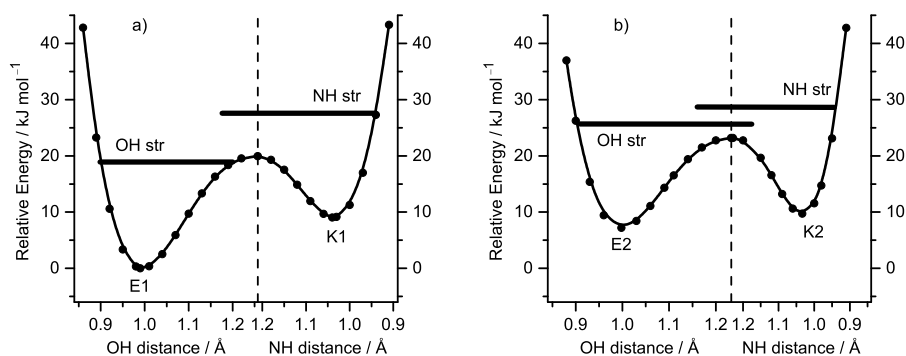


Figure 3.24 Relaxed potential energy surface for the proton shift between the E1-K1 (a) and E2-K2 (b) minima in CPDNO calculated at the B3LYP/6-311+G(2df,2p) level of theory. The lowest energy vibrational levels are designated by horizontal lines. The change in the reaction coordinate (OH vs NH distance) is designated by the vertical dashed line. The energy of E1 form was chosen as the relative zero.

The conclusions from these two surfaces are the following: (i) both **E1** and **E2** azo-enol minima are lower in energy than their **K1** and **K2** keto-hydrazone counterparts; (ii) even more important, the lowest (zero point) vibrational levels of these **E** forms are lower in energy than those in the respective **K** forms, that is, in both pairs the **E**-forms have lower internal energy (see Figure 3.24); (iii) both transition states for the proton movement in the [**E1**, **K1**] and [**E2**, **K2**] pairs are below the lowest vibrational states in **K1** and **K2**, which means these two **K**-forms cannot be treated as independent species. This dynamic behavior of the proton and its importance to the characterization of azo-enol/keto-hydrazone tautomeric forms was pointed out before by Gilli and co-workers in a series of X-ray crystallography and theoretical studies of phenyl-substituted 1-arylazo-2-naphthols.^{93,94}

From the viewpoint of the present experiments, at cryogenic temperatures, only the lowest vibrational states are relevant, and the system barrierlessly relaxes to the more stable **E1** and **E2** structures.* However, the geometries of these **E** tautomers shall be characterized by a very-large-amplitude motion of the labile proton between the O and N atoms. As a consequence, the corresponding vibrational frequencies (primarily due to the OH stretching) should then experience a large uncertainty, manifested by the broadening of absorptions in the experiment. It is indeed the fact, as will be shown in the next section.

*Estimative Conductor-like Polarizable Continuum Model (CPCM) calculations indicate that the relative energy of a more polar K1 form with respect to E1 decreases only slightly, from ≈ 9.06 (*in vacuo*) to 6.40 kJ mol^{-1} (in xenon). Therefore a solvation difference of the molecules with noticeably different dipole moments does not have an impact on our results.

3.4.2 CPDNO Structure in a Matrix Shortly After Deposition

The experimental FTIR spectra of CPDNO isolated in argon (15 K) and xenon (30 K) matrices are presented in Figure 3.25, together with the theoretical spectrum of the azo-enol form **E1**. With exception of the ν OH stretching region, there is a relatively good agreement between the experimental spectra and the theoretical spectrum predicted for the **E1** conformer. The absence of an absorption characteristic of a free OH group in the region around 3700-3600 cm^{-1} , together with the appearance of a broad absorption feature, with a large integrated intensity, between 2950-2570 cm^{-1} , indicates that the OH group of the **E1** azo-enol form is involved in a very strong intramolecular OH \cdots N hydrogen bond. Due to this strong intramolecular bond, the H \cdots N equilibrium distance in **E1** shortens to ≈ 1.69 Å (calculated value). This H \cdots N distance characterizes the strength of a hydrogen bond and can be related to the frequency shift of the OH stretching vibration in the H bonded OH group (relatively to the unperturbed OH group). According to the empirical relationship^{95,96} such a frequency shift in **E1** should amount to no less than 600-700 cm^{-1} , that is, fall below 3000 cm^{-1} (if the OH stretching mode of phenol 3634 cm^{-1} is considered as an unperturbed reference).⁸³ The OH stretching frequency in **E1** is predicted by the present harmonic calculations as low as at 3157.1 cm^{-1} . The anharmonic VSCF approximation was used also to locate the frequency for this particular mode more precisely. The calculated anharmonic OH stretching frequency (ca. 2701.6 cm^{-1}), even though obtained without taking in consideration the coupling between modes, still gives quite satisfactory agreement with the position of the broad absorption feature. This particular type of interactions, in which the H-bond encloses a pseudoaromatic ring and the coupling of the proton motion with the π -electron causes the appearance of lower frequency ν (OH) bands with huge integrated intensity, has been reported before.^{97,98}

Also, as suggested by the analysis of the potential energy surfaces for the proton shifts discussed above, there is no spectral evidence that the keto-hydrazone **K1** and **K2** (the calculated frequencies are given in Table E.2) tautomers are present in the deposited matrices. According to the calculations, if any of the K-forms (**K1** and/or **K2**) were to be present, two relatively strong absorptions due to C=O stretching (involved in the extensive conjugation and hydrogen bonding mentioned before) and N-H in-plane bending vibrations should be identifiable in the 1580-1505 cm^{-1} spectral region. Therefore, based on the absence of these characteristic absorptions in this particular region, the presence of the **K1** and **K2** forms can be ruled out.

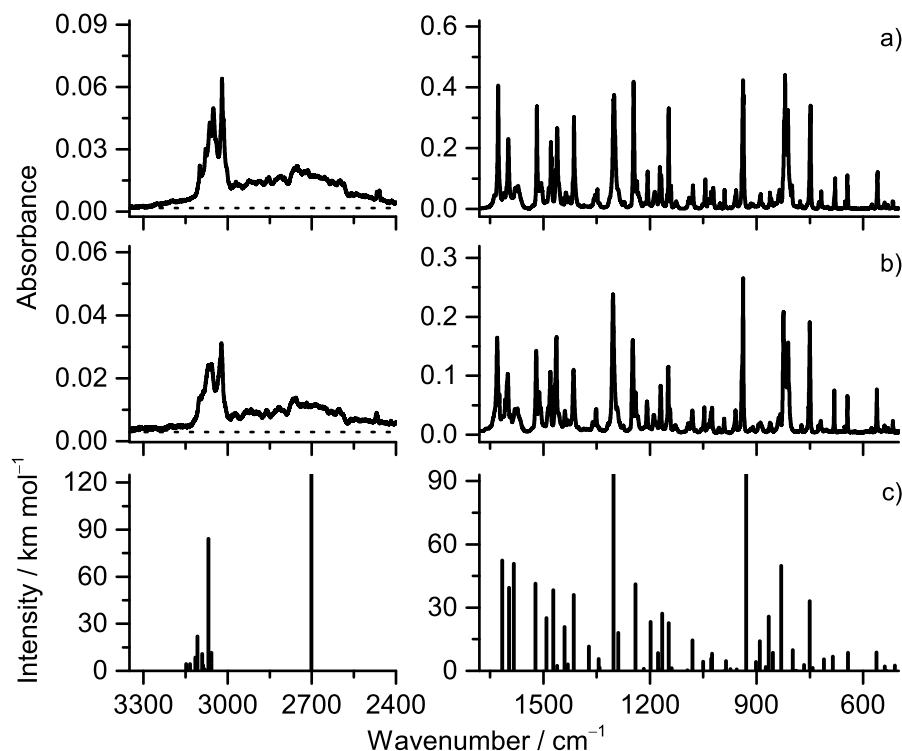


Figure 3.25 Selected regions of the experimental infrared spectra of monomeric CPDNO isolated in xenon at 30 K (a) and argon at 15 K (b) matrices compared with the theoretical spectrum of azoenol form **E1** (c). The calculated harmonic frequencies were scaled by a factor of 0.976 obtained by least-squares linear fitting. The OH stretching frequency at $\approx 2700\text{ cm}^{-1}$ was calculated within the VSCF anharmonic approximation and was not scaled.

The overall correspondence of the experimental spectrum and that calculated for the **E1** conformer is quite satisfactory. However, based on the theoretical predictions, it can be expected that the **E2** form contributes to the thermal equilibrium too. Its contribution should be about 6% if only **E1** and **E2** are participating in the thermal equilibrium. Alternatively, if **K1** and **K2** are also contributing to the thermal equilibrium at room temperature, and then collapse to **E1** and **E2**, respectively, upon deposition of the matrix, the **E2** fraction should be about 9%. Such an amount of **E2** (6-9%) should be detectable experimentally. The barrier for intramolecular rotation of the cyclopropane moiety transforming **E2** into **E1** was calculated to be $\approx 14\text{ kJ mol}^{-1}$. Such a high barrier can only be overcome at relatively high temperatures, above 50 K.^{87,88} Among noble gases, only Xe matrix permits attaining of such temperatures. Indeed, after annealing the xenon matrix at 55 K, a set of bands (see Table 3.10 and Table 3.9 for tentative assignments) initially present in

the spectrum of the deposited sample disappeared (see bands marked by arrows in Figure 3.26). These disappearing bands have frequencies that match infrared absorptions in the calculated spectrum of the **E2** conformer (and do not overlap with the **E1** absorptions).

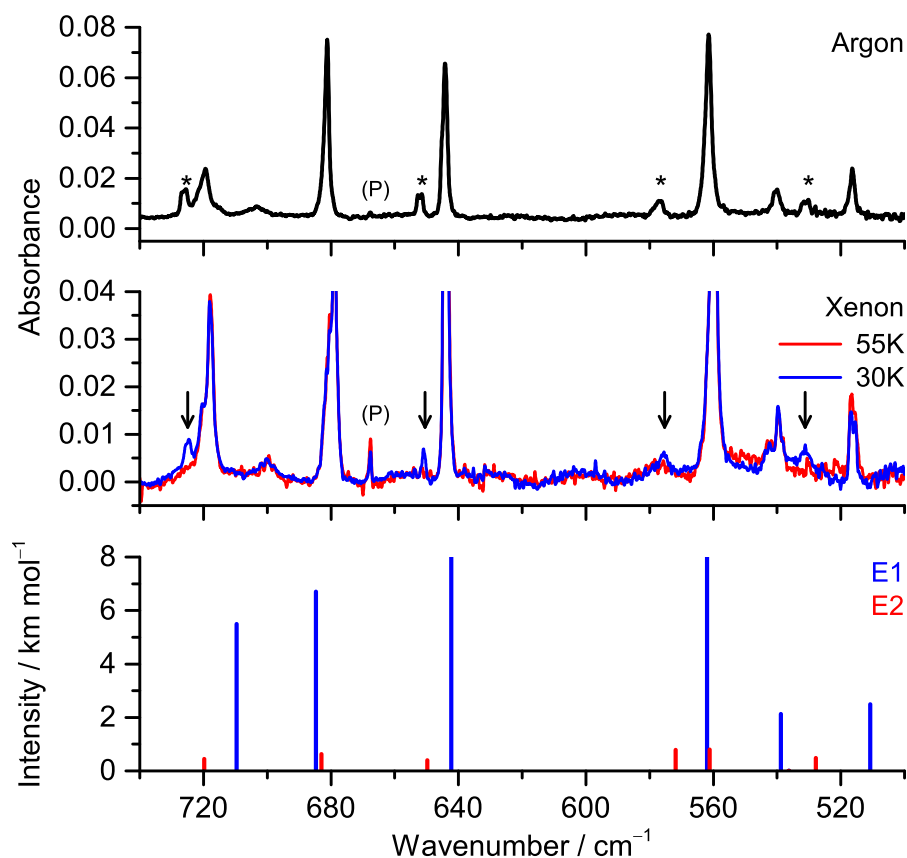


Figure 3.26 Selected region of the experimental infrared spectrum of CPDNO in argon (15 K) and xenon (30 K) matrices, compared with the theoretical spectra of azo-enol forms **E1** (blue) and **E2** (red). An asterisk (*) indicates the peaks corresponding to absorptions due to the **E2** form in an argon matrix. A downward arrow (↓) indicates the decreasing bands of **E2** form upon annealing in a xenon matrix. The band at 667 cm^{-1} , marked as (P), is due to atmospheric CO_2 . The calculated intensities of **E1** and **E2** were scaled by 0.9 and 0.1, respectively. All calculated frequencies were scaled by a factor of 0.976.

Annealing of argon matrices should not lead to relaxation of form **E2**, since a barrier of $\approx 14 \text{ kJ mol}^{-1}$ cannot be overcome in the temperature interval where argon is still rigid enough (up to 35 K). Then the population of **E2** should be efficiently trapped in an argon matrix, and the ratio of forms **E1** / **E2** trapped in argon should be similar to their ratio in the gas phase prior to deposition. In fact, if the

calculated intensities of **E1** and **E2** are scaled as 9:1 (as in the gas-phase equilibrium during sublimation), the simulated spectrum (Figure 3.26, bottom) provides a good match with the experiment (Figure 3.26, top). In such way, the presence of the **E2** conformer in the samples before annealing was reliably confirmed and some of its most prominent bands identified.

As a complement, the experimental infrared (in a KBr pellet) and the Raman spectrum of CPDNO powder were also obtained (see Figure E.2 and Figure E.3 in Appendix E). However, several factors, such as the presence of intermolecular interactions, contribute to the complexity of the experimental pattern of bands displayed and limit the amount of information that can be retrieved. Nevertheless, there is a fairly reasonable good overall agreement with the spectra simulated for azo-enol form **E1**, further suggesting that this form is also the predominant one in the solid state.

Table 3.9 Experimental observed wavenumbers (ν) and tentative assignments for the E1 azo-enol isomer isolated in argon and xenon matrices.

Ar (15K)	Xe (30K)	Calculated	Sym.	Appr. description	
ν	ν	ν	I		
3095.0	3099.4	3147.8	4.8	A'	$\nu_{\text{as}}(\text{CH}_2)_{\text{cp}}$
n.o.	3087.4	3134.5	0.1	A''	$\nu_{\text{as}}(\text{CH}_2)_{\text{cp}}$
3084.8	3078.0	3134.1	4.7	A'	$\nu(\text{CH})_{\text{ar}}$
3068.9	3063.3	3115.1	9.4	A'	$\nu(\text{CH})_{\text{ar}}$
3057.4	3051.2	3108.0	24.1	A'	$\nu(\text{CH})_{\text{ar}}$
n.o.	3040.6	3091.2	12.0	A'	$\nu(\text{CH})_{\text{ar}}$
n.o.	n.o.	3088.1	3.9	A'	$\nu(\text{CH})_{\text{ar}} + \nu(\text{OH})$
n.o.	n.o.	3081.6	1.1	A'	$\nu(\text{CH})_{\text{ar}}$
2850 - 2570	2850 - 2570	3079.7	163.7	A'	$\nu(\text{OH})$
3022.0	3020.2	3068.1	92.5	A'	$\nu(\text{CH})_{\text{cp}} + \nu(\text{OH})$
n.o.	3014.4	3058.8	5.2	A'	$\nu_{\text{s}}(\text{CH}_2)_{\text{cp}} + \nu(\text{CH})_{\text{cp}}$
n.o.	3004.9	3058.3	12.6	A''	$\nu_{\text{s}}(\text{CH}_2)_{\text{cp}} + \nu(\text{CH})_{\text{cp}}$
1630.0	1627.0	1615.9	57.5	A'	$\nu(\text{CC})_{\text{ar}} + \delta(\text{OH})$
1599.9	1598.6	1596.6	43.3	A'	$\nu(\text{CC})_{\text{ar}} + \delta(\text{OH})$
1572.8	1571.0	1583.5	55.9	A'	$\delta(\text{OH}) + \nu(\text{CC})_{\text{ar}} + \nu(\text{NN})$
1520.0 , 1511.4	1518.1 , 1508.8, 1505.9	1522.0	45.4	A'	$\delta(\text{OH}) + \nu(\text{CC})_{\text{ar}}$
1481.9, 1480.1	1478.9 , 1476.9	1491.3	27.5	A'	$\nu(\text{N}=\text{N}) + \nu(\text{CC})_{\text{ar}} + \delta(\text{OH})$
1467.6, 1463.0	1464.9, 1461.0	1471.9	42.1	A'	$\delta(\text{OH}) + \nu(\text{CC})_{\text{ar}}$
1449.2	1445.7	1461.3	2.7	A'	$\text{sci}(\text{CH}_2)_{\text{cp}} + \delta(\text{CH})_{\text{cp}}$ + $\nu(\text{CC})_{\text{cp}}$
1439.3	1437.0	1440.2	22.9	A'	$\delta(\text{CH})_{\text{ar}} + \nu(\text{NN}) + \nu(\text{CC})_{\text{ar}}$
1428.3	1424.6	1431.2	3.3	A''	$\text{sci}(\text{CH}_2)_{\text{cp}}$
1415.1	1413.4	1414.8	39.6	A'	$\delta(\text{CH})_{\text{ar}} + \delta(\text{OH}) + \nu(\text{CC})_{\text{ar}}$
1386.1	1386.4	1372.1	12.6	A'	$\nu(\text{CC})_{\text{ar}} + \nu(\text{CO}) + \delta(\text{CH})_{\text{cp}}$
1351.1	1347.7	1344.7	6.2	A'	$\nu(\text{CC})_{\text{ar}} + \delta(\text{CH})_{\text{cp}} + \nu(\text{CO})$
1345.0	1342.4	1341.4	1.8	A'	$\delta(\text{CH})_{\text{cp}} + \nu(\text{CC})_{\text{cp}} + \nu(\text{NCcp})$
1304.0	1302.6, 1300.8	1302.2	114.0	A'	$\nu(\text{CarN}) + \delta(\text{OH}) + \nu(\text{CC})_{\text{ar}}$
1292.5	1289.2	1289.3	19.8	A'	$\nu(\text{CO}) + \delta(\text{CH})_{\text{ar}} + \nu(\text{CC})_{\text{ar}}$
1248.5 , 1240.3	1246.1 , 1237.9, 1236.4	1240.9	45.1	A'	$\delta(\text{CH})_{\text{ar}} + \nu(\text{CO})$ + $\nu(\text{CC})_{\text{ar}} + \delta(\text{OH})$
1235.4	1233.1	1217.4	1.1	A'	$\delta(\text{CH})_{\text{ar}} + \nu(\text{NCcp})$ + $\nu(\text{CC})_{\text{ar}}$

Table 3.9 (Cont.)

Ar (15K)	Xe (30K)	Calculated		Sym.	Appr. description
ν	ν	ν	I		
1208.3	1206.6	1198.3	25.5	A'	$\nu(\text{NCcp}) + \delta(\text{CH})_{\text{ar}}$ + $\nu(\text{CC})_{\text{ar}}$
1188.4	1186.7	1177.6	9.2	A'	$\delta(\text{CH})_{\text{cp}} + \nu(\text{CC})_{\text{cp}}$ + $\nu(\text{NCcp})$
1180.9	1180.6	1170.3	0.5	A''	$r(\text{CH}_2)_{\text{cp}}$
1170.0	1172.2 , 1168.7	1165.8	29.9	A'	$\delta(\text{CH})_{\text{ar}} + \nu(\text{CarN})$
1149.5, 1148.3	1147.4	1147.6	24.9	A'	$\delta(\text{CH})_{\text{ar}}$
1143.4	1140.5	1139.2	1.4	A'	$\delta(\text{CH})_{\text{ar}}$
1091.7	1089.5	1094.9	0.3	A''	$\text{tw}(\text{CH}_2)_{\text{cp}} + \gamma(\text{CH})$
1080.7	1078.9	1080.7	16.0	A'	$\delta(\text{CH})_{\text{ar}} + \nu(\text{CarN})$
1047.0	1046.1, 1044.0	1050.7	4.8	A''	$w(\text{CH}_2)_{\text{cp}} + \gamma(\text{CH})_{\text{cp}}$
1028.5	1028.0	1027.7	6.3	A'	$w(\text{CH}_2)_{\text{cp}} + \delta(\text{CH})_{\text{ar}}$
1025.2	1021.9 , 1020.8	1024.9	9.0	A'	$\delta(\text{CH})_{\text{ar}} + \text{wag}(\text{CH}_2)_{\text{cp}}$
n.o.	n.o.	989.7	0.2	A''	$\gamma(\text{CH})_{\text{ar}}$
991.2	990.2	985.8	5.1	A'	$\delta(\text{ar}) + \gamma(\text{CH})_{\text{cp}}$
978.5	976.1, 974.6	973.8	0.9	A''	$\gamma(\text{CH})_{\text{ar}}$
n.o.	n.o.	956.3	0.8	A''	$\gamma(\text{CH})_{\text{ar}}$
937.8	938.0 , 936.6	929.3	107.8	A'	$\delta(\text{cp}) + \nu(\text{NCcp})$
910.3	915.0 , 909.4	902.0	4.7	A'	$\delta(\text{NNC}) + \delta(\text{cp})$
889.2	888.4	891.1	15.4	A''	$\tau(\text{OH}) + \gamma(\text{NCcp})$
866.5	865.0	874.5	2.0	A''	$\tau(\text{OH}) + \gamma(\text{CH})_{\text{ar}}$
862.14 , 860.01	862.4 , 858.7	865.8	28.3	A''	$\tau(\text{OH})$
n.o.	847.7	854.2	9.4	A'	$\delta(\text{ar}) + \delta(\text{cp})$
824.3 , 822.9, 818.7, 816.8, 811.1	822.5, 820.8, 819.6 , 817.3, 815.0, 813.3, 811.5	830.7	54.8	A''	$\gamma(\text{CH})_{\text{ar}}$
n.o.	800.3	798.5	10.9	A''	$\nu(\text{CC})_{\text{cp}}$
n.o.	n.o.	790.5	0.01	A''	$\gamma(\text{CH})_{\text{ar}}$
773.7	777.6	766.4	3.1	A'	$r(\text{CH}_2)_{\text{cp}}$
750.4	749.2 , 747.8	750.8	36.3	A''	$\gamma(\text{CH})_{\text{ar}}$
		742.1	1.5	A'	$\delta(\text{ar}) + r(\text{CH}_2)_{\text{cp}}$
719.4	720.6, 718.1	710.1	6.0	A'	$\delta(\text{ar})$
681.2	678.8	685.1	7.4	A''	$\tau(\text{ar})$
644.2	644.7 , 643.3	642.7	9.4	A'	$\delta(\text{ar}) + \delta(\text{CNN})$
561.5	560.1, 559.3	562.3	9.6	A''	$\tau(\text{ar})$
540.0	542.4, 539.7	539.1	2.3	A'	$\delta(\text{ar})$
n.o.	n.o.	536.6	0.02	A''	$\tau(\text{ar})$
516.4	517.2 , 515.5	511.1	2.7	A'	$\delta(\text{ar}) + \delta(\text{NNC})$
464.7	465.4, 466.4, 464.2	464.2	16.1	A'	$\delta(\text{NNC})$
450.2	453.1, 450.2	447.9	3.8	A''	$\gamma(\text{NNC})$
433.9	435.4, 433.3	429.9	2.7	A'	$\delta(\text{ar})$
n.o.	n.o.	408.8	0.3	A''	$\tau(\text{ar}) + \gamma(\text{NCcp})$
n.i	n.i	354.9	0.1	A''	$\tau(\text{ar}) + \gamma(\text{NCcp})$
n.i	n.i	351.5	3.3	A'	$\delta(\text{NNC}) + \delta(\text{CCO}) + \delta(\text{ar})$
n.i	n.i	332.8	9.4	A'	$\delta(\text{NNC}) + \delta(\text{CCO}) + \delta(\text{ar})$
n.i	n.i	270.3	≈ 0.0	A''	$\tau(\text{ar}) + \gamma(\text{NC})$
n.i	n.i	216.7	2.3	A'	$\delta(\text{NCC})_{\text{ar}} + \delta(\text{NCCcp})$
n.i	n.i	203.3	2.9	A''	$\tau(\text{ar}) + \gamma(\text{NC})$
n.i	n.i	135.7	0.3	A''	$\tau(\text{ar}) + \gamma(\text{CcpN})$
n.i	n.i	122.2	0.1	A''	$\tau(\text{ar}) + \gamma(\text{CO})$
n.i	n.i	94.4	1.1	A'	$\delta(\text{NNCcp})$
n.i	n.i	69.7	0.4	A''	$\tau(\text{ar}) + \gamma(\text{NCcp})$
n.i	n.i	47.9	0.5	A''	$\tau(\text{NCcp})$

B3LYP/6-311+G(2df,2p) calculated wavenumbers (ν) in cm^{-1} and intensities (I) in km mol^{-1} are also given. The theoretical wavenumbers are scaled by a factor of 0.976. The strongest components of split bands are given in bold. ν , bond stretching; δ , in-plane-bending; γ , out-of-plane bending; w, wagging; sci, scissoring; r, rocking; τ , torsion; ar, aromatic ring; cp, cyclopropane ring; n.o., not observed; n.i., not investigated. The OH stretching frequency of E1 calculated within the VSCF anharmonic approximation is 2701.6 cm^{-1} .

Table 3.10 Selected experimental wavenumbers (ν/cm^{-1}) of the absorption bands observed for the E1 and E2 azo-enol isomers, and the theoretical wavenumbers (ν/cm^{-1}) and absolute infrared intensities ($I/\text{km mol}^{-1}$) calculated at the B3LYP/6-311+G(2df,2p) level.^a

E2				
Ar (15 K)	Xe (30 K)	calculated		
ν	ν	ν	I	
2850-2570	2850-2570	3013.4	216.7	
1630 ^c	1627.8 ^b	1615.2	65.8	
1600 ^c	1599.8 ^b	1596.7	59.6	
1579.5	1579.4 ^b	1583.9	55.4	
1520 ^c	1518.5 ^b	1522.4	50.3	
1485.0	1484.5 ^b	1499.9	34.6	
1467.6	1465.0 ^b	1473.5	63.0	
1430.3	1427.5 ^b	1435.3	17.3	
1304 ^c	1303.6 ^b	1305.4	112.7	
1249 ^c	1247.1 ^b	1242.2	54.7	
1215.2	1213.7 ^b	1210.2	10.3	
1188 ^c	1186.7 ^b	1188.3	39.6	
1149 ^c	1151.0 ^b	1150.8	10.4	
1128 ^c	1126.3	1122.1	21.1	
1053.4	1051.5 ^b	1056.7	5.2	
1037.7	1035.2 ^b	1031.4	9.8	
n.o.	1028.6	1025.0	10.5	
1005.7	1003.2	1000.1	24.2	
959.4	957.5	951.6	65.4	
837.7	836.9	831.3	50.4	
833.5	835.4	823.0	31.9	
725.5	724.6	720.2	4.9	
651.5	650.8	650.2	4.4	
577.2	575.3	572.1	8.8	
530.2	530.8	528.1	5.4	
445.2	443.7	442.0	23.6	

^a The theoretical wavenumbers are scaled by a factor of 0.976. The OH stretching frequency of E2 calculated within the VSCF anharmonic approximation is 2657.9 cm^{-1} . ^bBands assigned based on annealing experiments. ^cEstimated values for E2 bands masked by E1 absorptions.

3.4.3 Photochemistry

CPDNO isolated in the cryogenic matrices was irradiated with a narrowband UV laser light source. The series of UV irradiations started at $\lambda = 375\text{ nm}$ and continued at shorter wavelengths (UV-visible spectrum of CPDNO is given in Figure E.4). After each irradiation, the sample was monitored by analysis of its IR spectrum. Immediately after the first irradiation at 375 nm the bands due to CPDNO decreased in intensity, and several new bands emerged in the spectrum (the new bands remained stable in the absence of irradiation). The bands due to **E1** and **E2** forms continued to decrease with irradiations at shorter wavelengths. The decrease of the broad absorption feature in the $3000\text{-}2400\text{ cm}^{-1}$ range (see Figure 3.27) suggests that the initial **E1/E2** structures stabilized by the $\text{OH}\cdots\text{N}$ hydrogen bond involved in a 6-membered ring are consumed. Simultaneously, the appearance of bands in the $3600\text{-}3400\text{ cm}^{-1}$

range of the spectrum indicates that new structures bearing OH or NH group not involved in a six-membered intramolecular interaction are generated. A similar spectroscopic behavior was observed for matrix-isolated *o*-hydroxybenzaldehyde (salicylaldehyde) and *o*-hydroxyacetophenone when new, non-hydrogen-bonded conformers of these compounds were photogenerated by UV irradiation.⁹⁹

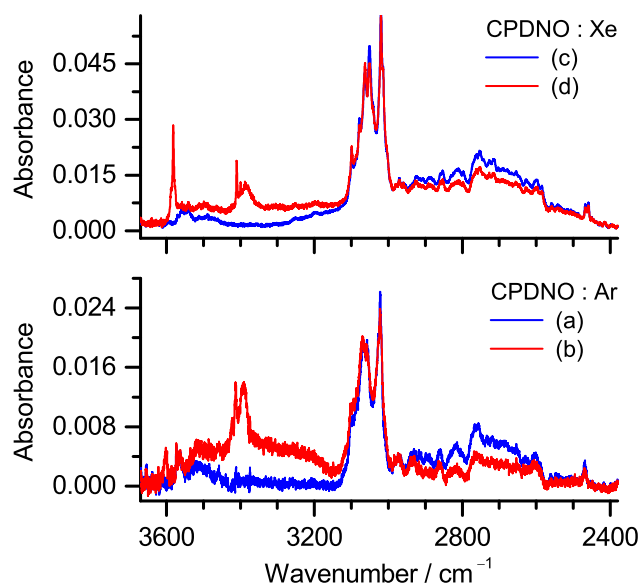


Figure 3.27 Experimental spectra of CPDNO isolated in argon (bottom) and xenon (top) matrices, before (blue) and after (red) 3 min of UV-irradiation at $\lambda = 340\text{-}345$ nm.

With the aid of irradiations at shorter wavelengths, it was possible to group the new bands in two distinct sets, indicated as P1 and P2 in Figure 3.28 and Figure 3.29, respectively. Upon irradiation at 345 nm, the intensity of bands belonging to the P1 set increased, while the bands of the P2 set showed a decrease in intensity. For irradiations at 325 nm, the opposite behavior is observed with the intensity of the bands of the P2 and P1 sets increasing and decreasing, respectively. This behavior clearly indicates a reversible phototransformation between, at least, two different forms. After comparing the experimental difference IR spectra with the spectra calculated for several rotameric and tautomeric forms (see Table E.2 in Appendix E), the P1 set of photoproduct bands could be assigned to the **E9** azo-enol form (see Figure 3.21). The **E9** azo-enol form most characteristic vibrations situated at *ca.* 3582, 1600, 1393, 1200 and 914 cm^{-1} (just to name a few) can be promptly identified. The photoinduced generation of conformer **E9** ($\text{N}=\text{N } Z$) from **E1** ($\text{N}=\text{N } E$) compares to the characteristic *E-Z* photoisomerization of azo compounds.^{100,101} In

this case, upon such isomerization, the intramolecular OH \cdots N hydrogen bond is broken, and therefore a band due to the OH stretching vibration emerges in the spectral range characteristic of free OH groups.⁹²

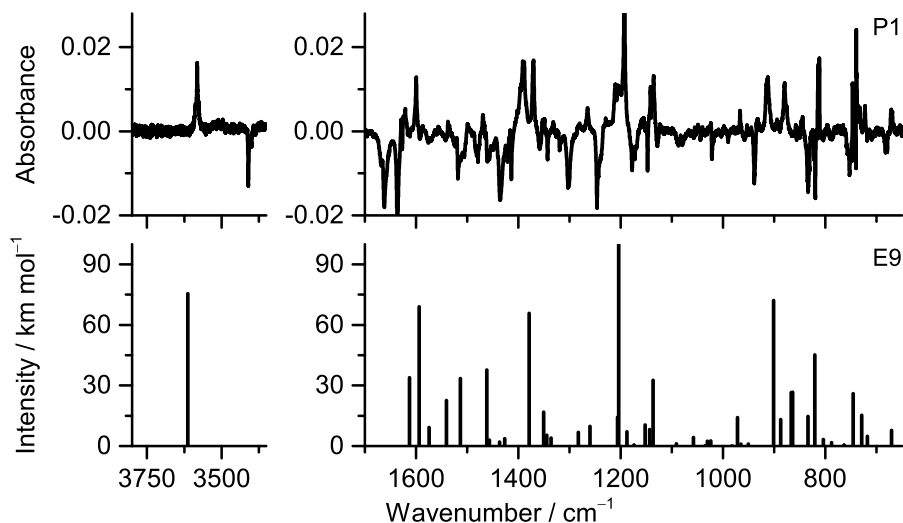


Figure 3.28 Changes in the experimental infrared spectrum of CPDNO isolated in a xenon matrix (top) after initial 6 min irradiation at $\lambda = 375$ nm and subsequent 3 min of UV irradiation ($\lambda = 345$ nm), compared with the theoretical infrared spectrum of the E9 form calculated at the B3LYP/6-311+G(2df,2p) level. Negative absorptions correspond to decreasing bands of the initially present E1 (and E2) form and to set P2 of photoproducts. Positive peaks correspond to growing absorptions due to the set P1 of photoproducts. Theoretical wavenumbers were scaled by a factor of 0.976.

On the other hand, the P2 set of photoproduct bands can be interpreted assuming the presence of two different keto-hydrazone forms. This is suggested by the observation of a band around 3410 cm^{-1} characteristic of a free NH stretching vibration.⁹² The most intense bands at *ca.* 3410 , 1636 , 1541 , 1435 , 1178 cm^{-1} can be assigned to the **K5** form, while the bands at *ca.* 1662 , 1523 , 1355 cm^{-1} suggest the presence of form **K6** (see Figure 3.22). The NH str vibration of form **K6** was not observed, since the calculated intensity ($\approx 3\text{ kmol}^{-1}$) for this mode is very low. Generation and stabilization of keto-hydrazone forms **K5** and **K6** appears possible due to the internal rotation around the C(1)N(11) bond which puts the newly formed N(12)H moiety away from the oxygen atom. The stability of keto-hydrazone tautomers, as individual structures, is already possible for forms where the O \cdots HN bond is involved in a 5-membered ring (like for **K3** and **K4**, see Figure E.1 in Appendix E), and even more so, when the NH bond is completely free from donor/acceptor interactions.

Table 3.11 Observed experimental and calculated wavenumbers for the E9 azo-enol photoproduct.^a

E9			
Ar (15 K)	Xe (30 K)	calculated	
ν	ν	ν	I
3601.8	3581.5	3615.7	75.4
1631.0	1628.9, 1625.7	1613.9	33.9
1602.1	1599.7	1594.9	68.9
1540.9	1534.9	1541.7	22.5
1522.7	1519.3	1514.2	33.4
1467.5	1465.3	1462.4	37.7
1401.4, 1395.4	1395.1, 1391.4	1379.7	65.7
1370.3	1370.2	1351.3	16.8
1211.1 , 1196.0	1209.9 , 1192.8	1204.7	206.9
n.o.	966.7	972.2	14.1
912.2 , 909.4	915.2, 912.4	901.7	72.1
896.5	894.3	887.5	13.2
880.7	879.5 {	867.2	26.5
815.9	814.2, 811.6	864.5	26.7
747.1	747.0	821.1	45.1
733.3	732.4	746.1	25.9
725.5	722.3	729.4	15.2
672.8	671.3 , 668.9	718.4	4.8
		670.8	7.8

^a B3LYP/6-311+G(2df,2p) calculated wavenumbers (ν) in cm^{-1} and intensities (I) in km mol^{-1} are also given. The theoretical wavenumbers are scaled by a factor of 0.976. The strongest components of split bands are given in bold.

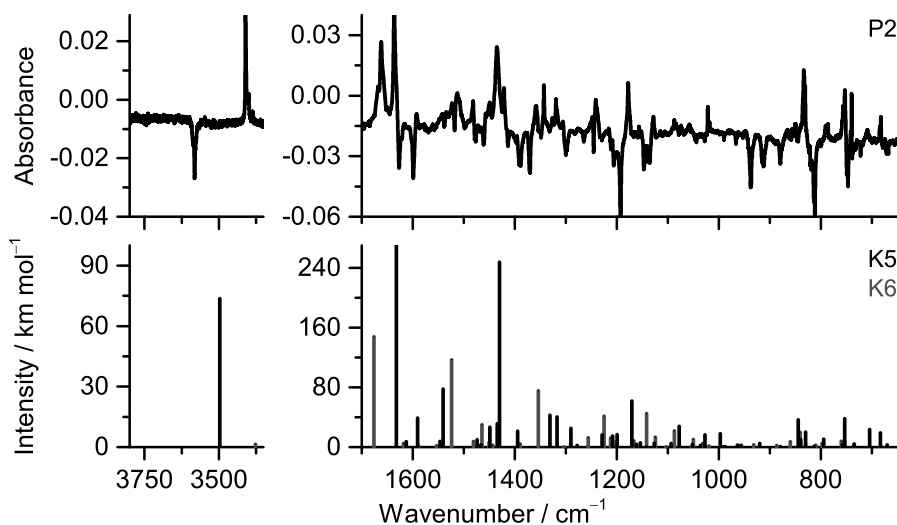


Figure 3.29 Changes in the experimental infrared spectrum of CPDNO isolated in a xenon matrix (top) after 6 min of UV irradiation ($\lambda = 325$ nm, preceded by irradiations described in caption of Figure 3.28) compared with the theoretical infrared spectra of forms K5 and K6 calculated at the B3LYP/6-311+G(2df,2p) level. Negative absorptions correspond to decreasing bands of the initially present E1 (and E2) form and to set P1 of photoproducts. Positive peaks correspond to growing absorptions due to the set P2 photoproduct(s). Theoretical wavenumbers were scaled by a factor of 0.976. The calculated intensity of forms K5 and K6 were scaled by 1 and 0.5, respectively.

Table 3.12 Observed experimental and calculated wavenumbers for the K5 and K6 keto-hydrazone photoproducts.^a

K5				K6			
Ar (15 K)	Xe (30 K)	calculated		Ar (15 K)	Xe (30 K)	calculated	
ν	ν	ν	I	ν	ν	ν	I
3414.1, 3412.6	3410.3 , 3399.82	3498.9	73.7	1674.4, 1666.4	1667.6, 1661.7	1677.3	295.8
1639.6	1636.4	1633.4	323.9	1526.7	1523.1	1524.9	234.1
1595.8	1592.5	1591.4	38.7	1360.1	1357.9	1354.9	150.9
1544.5	1540.8	1541.7	77.7	1243.3	1241.2	1225.7	82.7
1454.6	1449.1	1450.0	26.6	1133.2	1128.2	1142.5	90.2
1436.1 , 1427.3	1435.3 , 1421.1	1431.0	247.6	621.9	622.1	632.9	106.6
1339.8	1343.0	1332.1	42.7	n.o.	602.0	612.3	10.6
1317.5	1319.3	1318.3	40.3				
1177.6	1177.7	1171.5	61.8				
834.8	833.7	845.0	36.5				
788.6	786.1	794.7	10.5				
753.1	756.3, 753.1	753.6	37.9				
711.4	709.1	705.1	23.8				
684.6	682.4	683.5	19.0				
n.o.	616.5	629.0	35.6				

^a B3LYP/6-311+G(2df,2p) calculated wavenumbers (ν) in cm^{-1} and intensities (I) in km mol^{-1} are also given. The theoretical wavenumbers are scaled by a factor of 0.976. The strongest components of split bands are given in bold.

The fact that P1 and P2 photoproducts are structural isomers of CPDNO and not decomposition products was, confirmed by carrying out further irradiations of the sample using UV light in the 310-280 nm range. After these irradiations, the photoproducts P1 and P2 are consumed, and bands due to the **E1** and **E2** starting forms are partially growing back. However, most probably, some other new photoproducts (probably resulting from partial decomposition) are also appearing in the samples, and their experimental identification becomes complicated, since upon many irradiations the spectrum becomes very congested. The reversibility of the starting material (**E1** and **E2**-forms) upon UV-irradiations with shorter wavelengths in the present experiments is similar to the reversibility observed previously for salicylaldehyde and o-hydroxyacetophenone under similar conditions.⁹⁹

References

1. Hamm, P.; Ohline, S. M.; Zinth, W. *J. Chem. Phys.* **1997**, *106*, 519–529.
2. Tanaka, S.; Itoh, S.; Kurita, N. *Chem. Phys.* **2001**, *272*, 171–184.
3. Tanaka, S.; Itoh, S. *Chem. Phys. Lett.* **2002**, *362*, 467–475.

4. Harabuchi, Y.; Ishii, M.; Nakayama, A.; Noro, T.; Taketsugu, T. *J. Chem. Phys.* **2013**, *138*, 064305.
5. Gámez, J. A.; Weingart, O.; Koslowski, A.; Thiel, W. *J. Chem. Theory Comput.* **2012**, *8*, 2352–2358.
6. Furer, V.; Vandyukov, A.; Majoral, J.; Caminade, A.; Kovalenko, V. *Chem. Phys.* **2013**, *421*, 57–67.
7. Furer, V.; Vandyukov, A.; Majoral, J.; Caminade, A.; Kovalenko, V. *J. Mol. Struct.* **2013**, *1046*, 30–38.
8. Fujino, T.; Tahara, T. *J. Phys. Chem. A* **2000**, *104*, 4203–4210.
9. Ikegami, T.; Kurita, N.; Sekino, H.; Ishikawa, Y. *J. Phys. Chem. A* **2003**, *107*, 4555–4562.
10. Jiang, D.-L.; Aida, T. *Nature* **1997**, *388*, 454–456.
11. Klima, M.; Kotov, A.; Gribov, L. *J. Struct. Chem.* **1973**, *13*, 987–990.
12. Armstrong, D. R.; Clarkson, J.; Smith, W. E. *J. Phys. Chem.* **1995**, *99*, 17825–17831.
13. Biswas, N.; Umaphathy, S. *J. Phys. Chem. A* **1997**, *101*, 5555–5566.
14. Fliegl, H.; Köhn, A.; Hättig, C.; Ahlrichs, R. *J. Am. Chem. Soc.* **2003**, *125*, 9821–9827.
15. Hartley, G. S. *J. Chem. Soc.* **1938**, 633–642.
16. Le Fevre, J.; O'Dwyer, M.; Werner, R. *Aust. J. Chem.* **1953**, *6*, 341.
17. Kübler, R.; Lüttke, W.; Weckherlin, S. *Z. Elektrochem.* **1960**, *64*, 650–658.
18. Kellerer, B.; Hacker, H. H.; Brandmüller, J. *Indian J. Pure Appl. Phys.* **1971**, *9*, 903–909.
19. Gruger, A.; Le Calvé, N.; Dizabo, P.; Fillaux, J. *J. Chim. Phys. Phys. Chim. Biol.* **1972**, *69*, 291–298.
20. Gruger, A.; Le Calvé, N.; Fillaux, J. *J. Chim. Phys. Phys. Chim. Biol.* **1972**, *69*, 743–750.

21. Barker, I. K.; Fawcett, V.; Long, D. A. *J. Raman Spectrosc.* **1987**, *18*, 71–75.
22. Okamoto, H.; Hamaguchi, H.-o.; Tasumi, M. *Chem. Phys. Lett.* **1986**, *130*, 185–189.
23. Meić, Z.; Baranović, G.; Smrečki, V.; Novak, P.; Keresztury, G.; Holly, S. *J. Mol. Struct.* **1997**, *408*, 399–403.
24. Corruccini, R. J.; Gilbert, E. C. *J. Am. Chem. Soc.* **1939**, *61*, 2925–2927.
25. Wolf, E.; Cammenga, H. K. *Z. Phys. Chem.* **1977**, *107*, 21–38.
26. Adamson, A. W.; Vogler, A.; Kunkely, H.; Wachter, R. *J. Am. Chem. Soc.* **1978**, *100*, 1298–1300.
27. Klug, R. L.; Burcl, R. *J. Phys. Chem. A* **2010**, *114*, 6401–6407.
28. Pederzoli, M.; Pittner, J.; Barbatti, M.; Lischka, H. *J. Phys. Chem. A* **2011**, *115*, 11136–11143.
29. Dubecký, M.; Derian, R.; Horváthová, L.; Allan, M.; Štich, I. *Phys. Chem. Chem. Phys.* **2011**, *13*, 20939–20945.
30. Monti, S.; Orlandi, G.; Palmieri, P. *Chem. Phys.* **1982**, *71*, 87–99.
31. Lednev, I.; Ye, T.; Matousek, P.; Towrie, M.; Foggi, P.; Neuwahl, F.; Umaphathy, S.; Hester, R.; Moore, J. *Chem. Phys. Lett.* **1998**, *290*, 68–74.
32. Neukirch, A. J.; Shamberger, L. C.; Abad, E.; Haycock, B. J.; Wang, H.; Ortega, J.; Prezhdo, O. V.; Lewis, J. P. *J. Chem. Theory Comput.* **2014**, *10*, 14–23.
33. Andersson, J.-A.; Petterson, R.; Tegnér, L. *J. Photochem.* **1982**, *20*, 17–32.
34. Ünsalan, O.; Kuş, N.; Jarmelo, S.; Fausto, R. *Spectrochim. Acta. A. Mol. Biomol. Spectrosc.* **2013**, doi: 10.1016/j.saa.2013.10.050.
35. Singleton, T. A.; Ramsay, K. S.; Barsan, M. M.; Butler, I. S.; Barrett, C. J. *J. Phys. Chem. B* **2012**, *116*, 9860–9865.
36. Kurita, N.; Tanaka, S.; Itoh, S. *J. Phys. Chem. A* **2000**, *104*, 8114–8120.
37. Burcl, R. *J. Phys. Chem. A* **2011**, *115*, 3605–3606.

38. Tsuji, T.; Takashima, H.; Takeuchi, H.; Egawa, T.; Konaka, S. *J. Phys. Chem. A* **2001**, *105*, 9347–9353.
39. Kurita, N.; Ikegami, T.; Ishikawa, Y. *Chem. Phys. Lett.* **2002**, *360*, 349–354.
40. Lin, M. M.; Shorokhov, D.; Zewail, A. H. *J. Phys. Chem. A* **2009**, *113*, 4075–4093.
41. Hättig, C.; Hald, K. *Phys. Chem. Chem. Phys.* **2002**, *4*, 2111–2118.
42. Briquet, L.; Vercauteren, D. P.; Perpète, E. A.; Jacquemin, D. *Chem. Phys. Lett.* **2006**, *417*, 190–195.
43. Traetteberg, M.; Hillmo, I.; Hagen, K. *J. Mol. Struct.* **1977**, *39*, 231–239.
44. de Lange, J. J.; Robertson, J. M.; Woodward, I. *Proc. R. Soc. A* **1939**, *171*, 398–410.
45. Brown, C. J. *Acta Crystallogr.* **1966**, *21*, 146–152.
46. Bouwstra, J. A.; Schouten, A.; Kroon, J. *Acta Crystallogr., Sect. C* **1983**, *39*, 1121–1123.
47. Harada, J.; Ogawa, K.; Tomoda, S. *Acta Crystallogr., Sect. B* **1997**, *53*, 662–672.
48. Harada, J.; Ogawa, K. *J. Am. Chem. Soc.* **2001**, *123*, 10884–10888.
49. Cattaneo, P.; Persico, M. *Phys. Chem. Chem. Phys.* **1999**, *1*, 4739–4743.
50. Ishikawa, T.; Noro, T.; Shoda, T. *J. Chem. Phys.* **2001**, *115*, 7503–7512.
51. Schultz, T.; Quenneville, J.; Levine, B.; Toniolo, A.; Martínez, T. J.; Lochbrunner, S.; Schmitt, M.; Shaffer, J. P.; Zgierski, M. Z.; Stolow, A. *J. Am. Chem. Soc.* **2003**, *125*, 8098–8099.
52. Cembran, A.; Bernardi, F.; Garavelli, M.; Gagliardi, L.; Orlandi, G. *J. Am. Chem. Soc.* **2004**, *126*, 3234–3243.
53. Chang, C.-W.; Lu, Y.-C.; Wang, T.-T.; Diao, E. W.-G. *J. Am. Chem. Soc.* **2004**, *126*, 10109–10118.
54. Wei-Guang Diao, E. *J. Phys. Chem. A* **2004**, *108*, 950–956.

55. Ciminelli, C.; Granucci, G.; Persico, M. *Chem. Eur. J.* **2004**, *10*, 2327–2341.
56. Tiago, M. L.; Ismail-Beigi, S.; Louie, S. G. *J. Chem. Phys.* **2005**, *122*, 094311.
57. Crecca, C. R.; Roitberg, A. E. *J. Phys. Chem. A* **2006**, *110*, 8188–8203.
58. Conti, I.; Garavelli, M.; Orlandi, G. *J. Am. Chem. Soc.* **2008**, *130*, 5216–5230.
59. Shao, J.; Lei, Y.; Wen, Z.; Dou, Y.; Wang, Z. *J. Chem. Phys.* **2008**, *129*, 164111.
60. Dou, Y.; Hu, Y.; Yuan, S.; Wu, W.; Tang, H. *Mol. Phys.* **2009**, *107*, 181–190.
61. Bandara, H. M. D.; Friss, T. R.; Enriquez, M. M.; Isley, W.; Incarvito, C.; Frank, H. A.; Gascon, J.; Burdette, S. C. *J. Org. Chem.* **2010**, 4817–4827.
62. Tiberio, G.; Muccioli, L.; Berardi, R.; Zannoni, C. *ChemPhysChem* **2010**, *11*, 1018–1028.
63. Maurer, R. J.; Reuter, K. *J. Chem. Phys.* **2011**, *135*, 224303.
64. Cusati, T.; Granucci, G.; Martínez-Núñez, E.; Martini, F.; Persico, M.; Vázquez, S. *J. Phys. Chem. A* **2012**, *116*, 98–110.
65. De Boni, L.; Toro, C.; Zilio, S. C.; Mendonca, C. R.; Hernandez, F. E. *Chem. Phys. Lett.* **2010**, *487*, 226–231.
66. Lopes, S. B.; Lapinski, L.; Fausto, R. *Phys. Chem. Chem. Phys.* **2002**, *4*, 1014–1020.
67. Bandara, H. M. D.; Burdette, S. C. *Chem. Soc. Rev* **2012**, *41*, 1809–1825.
68. Merino, E. *Chem. Soc. Rev.* **2011**, *40*, 3835–3853.
69. Li, W.; Xu, D.; Zhang, Z.; Xu, Y. *Chinese J. Chem.* **2012**, *30*, 1819–1825.
70. Dunn, N. J.; Humphries, W. H.; Offenbacher, A. R.; King, T. L.; Gray, J. a. *J. Phys. Chem. A* **2009**, *113*, 13144–51.
71. Garcia-Amorós, J.; Sánchez-Ferrer, A.; Massad, W. a.; Nonell, S.; Velasco, D. *Phys. Chem. Chem. Phys.* **2010**, *12*, 13238–42.
72. Emond, M.; Le Saux, T.; Maurin, S.; Baudin, J.-B.; Plasson, R.; Jullien, L. *Chemistry* **2010**, *16*, 8822–31.

73. Liu, Y.; Zhao, Y.-l.; Chen, Y.; Guo, D.-s. *Org. Biomol. Chem.* **2005**, *3*, 584–91.
74. Shamuratov, E. B.; Batsanov, A. S.; Struchkov, Y. T.; Shukurov, A.; Makhsumov, A. G.; Sabirov, V. K. *J. Struct. Chem.* **1992**, *32*, 146–148.
75. Uno, T.; Lee, H.; Saito, Y.; Machida, K. *Spectrochim. Acta Part A Mol. Spectrosc.* **1976**, *32*, 1319–1322.
76. Machida, K.; Lee, H.; Saito, Y.; Uno, T. *J. Raman Spectrosc.* **1978**, *7*, 184–187.
77. Gabor, G.; Frei, Y. F.; Fischer, E. *J. Phys. Chem.* **1968**, *72*, 3266–3272.
78. Kojima, M.; Nebashi, S.; Ogawa, K.; Kurita, N. *J. Phys. Org. Chem.* **2005**, *18*, 994–1000.
79. Kurita, N.; Nebashi, S.; Kojima, M. *Chem. Phys. Lett.* **2005**, *408*, 197–204.
80. Sheban, G. V.; Zaitsev, B. E.; Dyumaev, K. M. *Theor. Exp. Chem.* **1980**, *16*, 207–211.
81. Tecklenburg, M. M. J.; Kosnak, D. J.; Bhatnagar, A.; Mohanty, D. K. *J. Raman Spectrosc.* **1997**, *28*, 755–763.
82. Minisini, B.; Fayet, G.; Tsobnang, F.; Bardeau, J. F. *J. Mol. Model.* **2007**, *13*, 1227–35.
83. Giuliano, B. M.; Reva, I.; Lapinski, L.; Fausto, R. *J. Chem. Phys.* **2012**, *136*, 024505.
84. Klimenko, I. P.; Korolev, V. A.; Tomilov, Y. V.; Nefedov, O. M. *Russ. J. Org. Chem.* **2006**, *42*, 1299–1306.
85. Wolfe, S.; Schlegel, H. B.; Whangbo, M.-H.; Bernardi, F. *Can. J. Chem.* **1974**, *52*, 3787–3792.
86. Lii, J.-H.; Chen, K.-H.; Allinger, N. L. *J. Phys. Chem. A* **2004**, *108*, 3006–3015.
87. Reva, I.; Simão, A.; Fausto, R. *Chem. Phys. Lett.* **2005**, *406*, 126–136.
88. Jesus, A. J. L.; Rosado, M. T. S.; Reva, I.; Fausto, R.; Eusébio, M. E. S.; Redinha, J. S. *J. Phys. Chem. A* **2008**, *112*, 4669–4678.
89. Tomilov, Y.; Kostyuchenko, I.; Shulishov, E.; Nefedov, O. *Mendeleev Commun.* **2002**, *12*, 104–105.

90. Antonov, L.; Deneva, V.; Simeonov, S.; Kurteva, V.; Nedeltcheva, D.; Wirz, J. *Angew. Chem. Int. Ed.* **2009**, *48*, 7875–7878.
91. Burdette, S. C. *Nat. Chem.* **2012**, *4*, 695–696.
92. Reva, I.; Almeida, B. J.; Lapinski, L.; Fausto, R. *J. Mol. Struct.* **2012**, *1025*, 74–83.
93. Gilli, P.; Bertolasi, V.; Pretto, L.; Lyčka, A.; Gilli, G. *J. Am. Chem. Soc.* **2002**, *124*, 13554–13567.
94. Gilli, P.; Bertolasi, V.; Pretto, L.; Antonov, L.; Gilli, G. *J. Am. Chem. Soc.* **2005**, *127*, 4943–4953.
95. Rozenberg, M.; Shoham, G.; Reva, I.; Fausto, R. *Phys. Chem. Chem. Phys.* **2005**, *7*, 2376–2383.
96. Rostkowska, H.; Nowak, M. J.; Lapinski, L.; Adamowicz, L. *Phys. Chem. Chem. Phys.* **2001**, *3*, 3012–3017.
97. Pajak, J.; Rospenk, M.; Ramaekers, R.; Maes, G.; Glowiak, T.; Sobczyk, L. *Chem. Phys.* **2002**, *278*, 89–100.
98. Pajak, J.; Ramaekers, R.; Rospenk, M.; Alexandrov, V.; Stepanian, S.; Adamowicz, L.; Maes, G. *Chem. Phys.* **2003**, *286*, 193–204.
99. Lapinski, L.; Rostkowska, H.; Reva, I.; Fausto, R.; Nowak, M. J. *J. Phys. Chem. A* **2010**, *114*, 5588–5595.
100. Beharry, A. A.; Woolley, G. A. *Chem. Soc. Rev.* **2011**, *40*, 4422–4437.
101. Merino, E.; Ribagorda, M. *Beilstein J. Org. Chem.* **2012**, *8*, 1071–1090.

4

General Conclusions and Concluding Remarks

The molecular structures and photochemistry of four azo compounds were investigated by a combined matrix-isolation IR spectroscopy and theoretical calculations approach. With the help of narrowband UV irradiation of the studied molecules, several relevant isomeric forms were experimentally produced (in some cases selectively), identified and characterized:

1. UV-visible broadband irradiation of *E*-azobenzene in the gas phase (at room temperature) allows for its partial conversion into the *Z*-isomer and trapping of both species in a cryogenic argon matrix (15 K). On the other hand, for matrix isolated azobenzene, UV-visible ($\lambda < 550$ nm) *in situ* irradiation could only induce the *Z*→*E* photoconversion, while the *E*→*Z* process was suppressed, presumably due to matrix steric constraints (Figure 4.1).

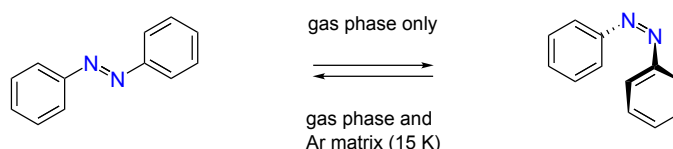


Figure 4.1 Experimentally observed photoisomerization behavior of azobenzene.

The observed photoinduced *E*↔*Z* isomerizations, together with a detailed theoretical characterization of the potential energy surfaces of the two isomers allowed for a reliable vibrational characterization of both forms, which appears particularly relevant for the higher energy *Z*-isomer, whose vibrational characterization had not yet been undertaken in detail hitherto. The calculated two-dimensional potential energy surfaces of *Z*-AB and *E*-AB revealed extensive flat areas around the minima, allowing for large-amplitude zero-point torsional movements of the rings. In the

case of the *Z*-form, these large amplitude ring torsional movements lead to significant changes of the equilibrium NN bond length (up to 0.3 pm), which, in turn, explain the experimentally observed frequency smearing of the N=N stretching vibration in this isomer. Both the theoretical and experimental results obtained in the present study are consistent with a planar C_{2h} structure for the minimum energy ground state *E*-AB.

2. The simplest studied azobenzene derivative, 4-hydroxyazobenzene (HAB), was trapped in argon and xenon matrices and its vibrational spectra investigated. The *E*→*Z* isomerization process of HAB was only noticeable in xenon matrices, particularly in those characterized by less rigidity (60 K) (Figure 4.2). Such results corroborate the assumption that the *E*→*Z* isomerization process in azobenzenes is constrained by the matrix environment.

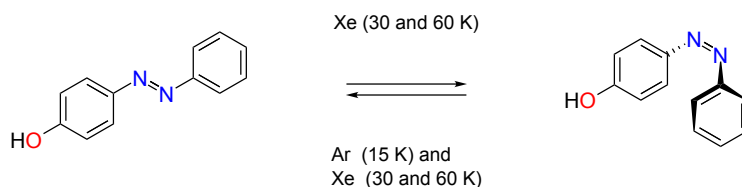


Figure 4.2 Experimentally observed photoisomerization behavior of 4-hydroxyazobenzene.

3. For 4-(cyclopropyldiazenyl)phenol (CPDP), two isomeric forms differing in the orientation of the cyclopropyl group (CPDP1 and CPDP2; with an *E* configuration), were experimentally detected in the cryogenic matrices. By irradiating in the 335-325 nm range, an isomeric *Z* form (CPDPZ) was also produced. By selecting the appropriate wavelength, these different forms were interconverted; irradiations at longer wavelengths consumed the CPDPZ form and regenerated the CPDP1 (460-440 nm) and CPDP2 (400 nm) forms. Comparatively to azobenzene and 4-hydroxyazobenzene, no constraints on the photoisomerization process were observed. These reactions are summarized in Figure 4.3.

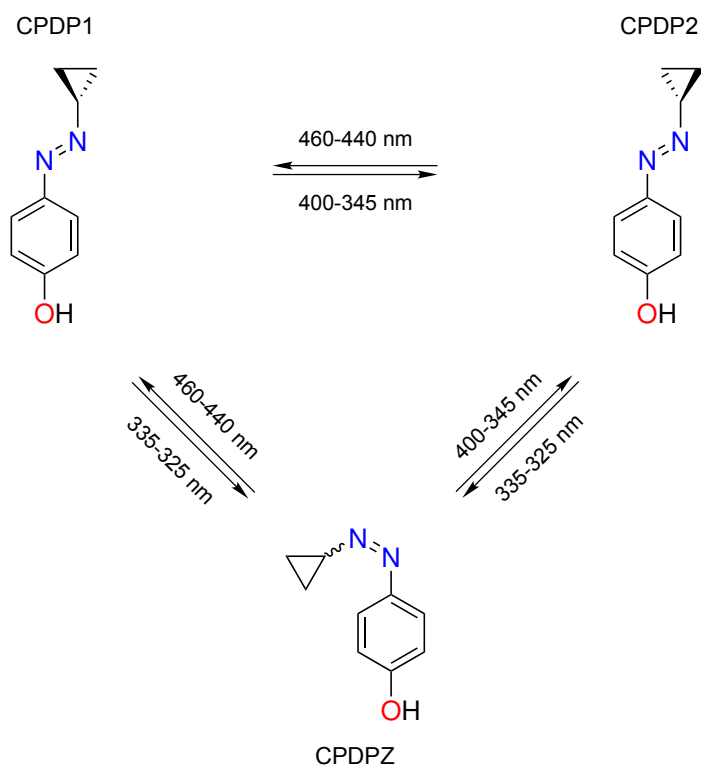


Figure 4.3 Photoisomerization reactions of 4-(cyclopropyldiazenyl)phenol.

4. Among the various possible rotameric and tautomeric forms of 1-(cyclopropyldiazenyl)naphthalen-2-ol (CPDNO), only the azo-enol forms having the OH group involved in a strong intramolecular hydrogen bond, forming a six-membered ring with the azo group (E1 and E2; both with *E* configurations) were found in the experiments. The nonobservation of the respective keto-hydrazone tautomers (K1 and K2) was explained with the aid of quantum chemical calculations describing the displacement of the hydrogen atom in the tautomeric azo-enol/keto-hydrazone system. Different isomeric forms without intramolecular H-bonding were photogenerated by UV irradiation of CPDNO at different wavelengths in the near-UV range. Irradiation at 345 nm generates the E9 azo-enol form (with a *Z* configuration), while upon irradiation at 325 nm, two keto-hydrazone forms (K5 and K6) are produced. These phototransformations were shown to be reversible, and depending on the excitation light, the azo-enol or the keto-hydrazone forms can be produced. Further irradiations using UV light in the 310-280 nm range partially regenerate the initial forms.

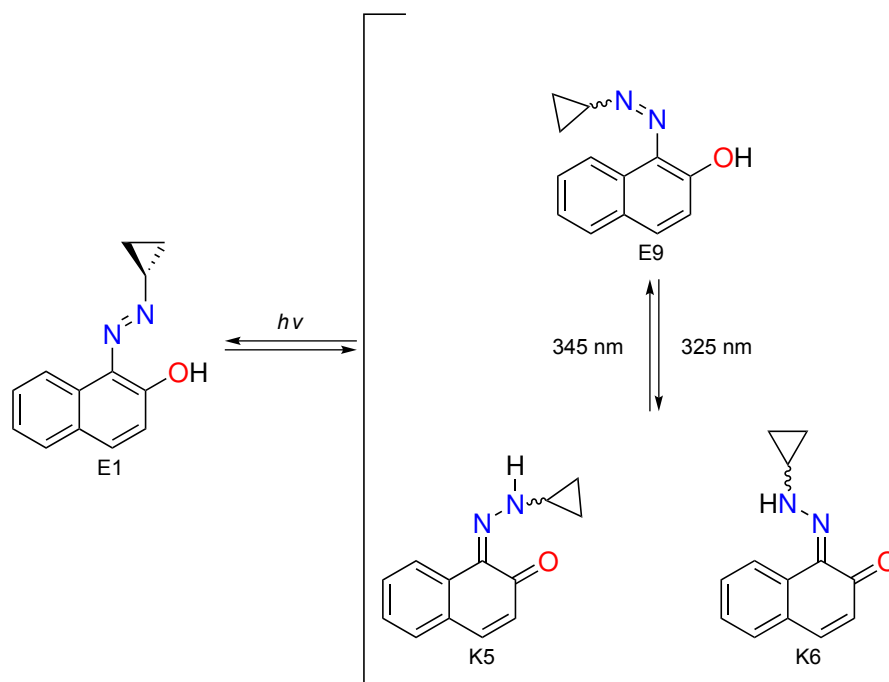


Figure 4.4 Photoisomerization reactions of 1-(cyclopropyldiazenyl)naphthalen-2-ol.

The most striking aspect of the results summarized above is the isomerization (or lack of it) observed for the different compounds studied in this work. This can be better rationalized by considering the nature of the cryogenic matrices and the free volume requirements of azobenzene(s).

Despite several studies on the subject, the exact morphology of solid cryogenic matrices is unknown. The most common matrix materials (Ne, Ar, Kr and Xe), in order to maximize the van der Waals forces between the atoms, adopt a simple close packed face centered cubic (fcc) arrangement, where different trapping sites are possible.¹⁻⁴ Atomic species and small molecules can be trapped in interstitial sites or substitutional holes resulting from the removal of matrix atoms. In the case of larger molecules, such as the ones studied in this work, multiple substitutional holes (resulting from the removal of two or more atoms) usually occur. However, due to the nature of the deposition process (rapid cooling from gas phase), the structure of the formed matrix is unlikely to be perfect and additional trapping sites resulting from lattice imperfections are also possible.

Therefore, the most probable scenario is thus that the planar azobenzene *E*-form is more densely packed between the matrix atoms layers, whereas the non-planar

kinked *Z*-form (with a free volume requirement⁵ larger than that of the *E* form) gets trapped inside matrix cages large enough to allow for the *Z*-to-*E* isomerization to occur. Since the atomic radii increase from argon to xenon, the size of both the substitutional and interstitial sites also increases, and it seems plausible to expect some extent of *E*-to-*Z*, as well as the *Z*-to-*E* isomerization to occur (as it is observed for 4-hydroxyazobenzene). In the case of the cyclopropylphenol and cyclopropylphenol derivatives, it is fair to assume that the change of one substituent from a phenyl group to a cyclopropyl group implies a reduction (comparatively to AB and HAB) on the free volume necessary for isomerization to occur, which results in the observation of photoisomerization (*E*-to-*Z* and *Z*-to-*E*) in both types of matrix.

As a final note, it appears also interesting to comment on the implications of these experimental observations from the viewpoint of the photoisomerization mechanism itself. Traditionally, the majority of the literature discussions concerning the prevailing photoisomerization pathways of azobenzenes are dominated by mechanisms involving some type of large amplitude movements of the phenyl groups (such as rotation and inversion; see Section 1.1.1.3). However, recent molecular dynamics simulations on AB show that other less explored mechanisms, such as the pedal motion, are also feasible.⁶⁻¹⁰ In this sense, although the results presented here are not sufficient to assert the exact isomerization pathway of AB, it is reasonable to expect that volume conserving mechanisms, such as the one involving a pedal-like motion of the CCNN group, are more likely to occur in the matrices. Indeed, there are several reports on the observation of similar types of movements for other classes of relatively large compounds (butadiene, octatetraene, styrene, etc.) isolated in cryogenic matrices.¹¹⁻¹³ Therefore, in order to obtain more conclusive insights into this issue, several other azo compounds (dihydroxyazobenzene, azotoluene, methyl red, sudan I, sudan orange G and azo violet), exhibiting different patterns of substitution, are currently under study.

References

1. Dobbs, E. R.; Jones, G. O. *Rep. Prog. Phys.* **1957**, *20*, 516–564.
2. Pollack, G. *Rev. Mod. Phys.* **1964**, *36*, 748–791.
3. Langel, W.; Schuller, W.; Knözinger, E.; Fleger, H.-W.; Lauter, H. J. *J. Chem. Phys.* **1988**, *89*, 1741.

4. Beattie, I. R.; Binsted, N.; Levason, W.; Ogden, J. S.; Spicer, M. D.; Young, N. A. *High Temp. Sci.* **1989**, *26*, 71–86.
5. Naito, T.; Horie, K.; Mita, I. *Polymer* **1993**, *34*, 4140–4145.
6. Böckmann, M.; Doltsinis, N.; Marx, D. *Phys. Rev. E* **2008**, *78*, 036101.
7. Böckmann, M.; Doltsinis, N. L.; Marx, D. *J. Phys. Chem. A* **2010**, *114*, 745–754.
8. Böckmann, M.; Marx, D.; Peter, C.; Site, L. D.; Kremer, K.; Doltsinis, N. L. *Phys. Chem. Chem. Phys.* **2011**, *13*, 7604–7621.
9. Gámez, J. A.; Weingart, O.; Koslowski, A.; Thiel, W. *J. Chem. Theory Comput.* **2012**, *8*, 2352–2358.
10. Neukirch, A. J.; Shamberger, L. C.; Abad, E.; Haycock, B. J.; Wang, H.; Ortega, J.; Prezhdo, O. V.; Lewis, J. P. *J. Chem. Theory Comput.* **2014**, *10*, 14–23.
11. Squillacote, M. E.; Sheridan, R. S.; Chapman, O. L.; Anet, F. A. L. *J. Am. Chem. Soc.* **1979**, *101*, 3657–3659.
12. Ackerman, J. R.; Forman, S. A.; Hossain, M.; Kohler, B. E. *J. Chem. Phys.* **1984**, *80*, 39–44.
13. Nakane, N.; Nicolaidis, A.; Tomioka, H.; Asato, A. E.; Liu, R. S. H. *Mol. Phys.* **2006**, *104*, 1009–1015.

A

Appendix

A.1 Saccharin / Tetrazole-saccharyl Papers

The papers relative to saccharin and one of its tetrazole derivatives are given in this appendix. As it was already mentioned in the Preface, this style of presentation was chosen in order to avoid mixing two distinct subjects, azo compounds and saccharin, that only have in common the fact that they were investigated during the time period encompassing the doctoral program and that they concern the photochemical study of species isolated in cryogenic matrices.

Photoisomerization of Saccharin

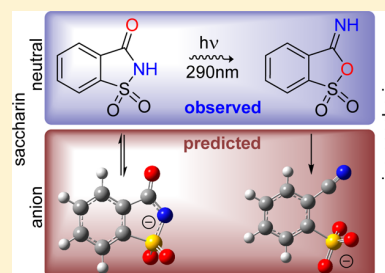
L. Duarte,[†] I. Reva,^{*,†} M. L. S. Cristiano,[‡] and R. Fausto[†]

[†]Department of Chemistry, University of Coimbra, P-3004-535 Coimbra, Portugal

[‡]CCMAR and Department of Chemistry and Pharmacy, University of Algarve, P-8005-139 Faro, Portugal

Supporting Information

ABSTRACT: Most known applications of saccharin and saccharyl derivatives and their potential for new uses rely on the thermal and photochemical stability of the saccharyl system. Here, we show that saccharin undergoes structural rearrangement when subjected to a narrow-band ultraviolet irradiation. Monomeric saccharin was isolated in low-temperature argon matrices and its photochemistry was characterized by means of infrared spectroscopy and DFT calculations. Among several DFT methods used, the O3LYP/6-311++G(3df,3pd) level gave the best match with the experimental spectra. Irradiation of matrix-isolated saccharin, with a narrow-band source (290 nm), generates a so far unknown isomer that we call iso-saccharin. The structures of the conjugate bases of saccharin and iso-saccharin were also computed theoretically. Their free energies and dipole moments suggest that both anions may be relevant in systems where saccharin participates, as is the case of the recently proposed saccharin-based ionic liquids.

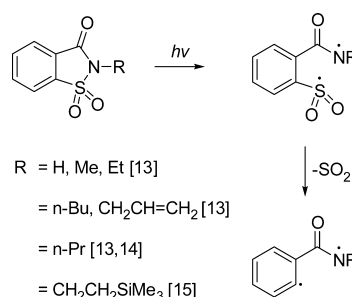


INTRODUCTION

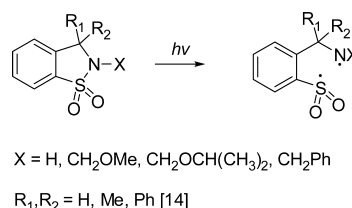
1,2-Benzisothiazol-3(2H)-one-1,1-dioxide (saccharin) and its derivatives have been extensively studied over the years, and in addition to their importance in the food industry,¹ they also find applications in the agricultural,² medical,³ and pharmaceutical areas.⁴ In organic and bioorganic synthesis, saccharin and saccharyl derivatives are known as cheap and versatile starting materials for the preparation of related heterocycles and as useful synthetic intermediates.⁵ Moreover, both saccharin and saccharinate act as ligands in coordination chemistry^{6,7} and have recently been considered for the formulation of amide-based ionic liquids.^{8–11} Most known applications of saccharin and saccharyl derivatives and their potential for new uses rely on the thermal and photochemical stability of the saccharyl system.

Regarding the photochemistry of benzisothiazoles, a literature search reveals that the information available is restricted to photolysis in solution. Early works on the photochemistry of *N*-propylsaccharin^{12,13} indicated that photolysis leads to cleavage of the S–N bond, ultimately resulting in formation of benzamide through extrusion of SO₂ (Scheme 1). Later, Döpp reported the photochemistry of 3,3-disubstituted 2,3-dihydro-1,2-benzisothiazole 1,1-dioxides in methanol and acetonitrile. Three reaction pathways were observed: in two cases, an initial S–N homolysis was suggested (Scheme 2) to be vital for these processes, and in the third, a formal oxygen shift from S to N, generating cyclic *N*-hydroxysulfonamides (sulfine hydroxamic acids), was proposed.¹⁴ Recently, Yoon, Mariano, and co-workers studied the photochemistry of *N*-[(trimethylsilyl)alkyl]saccharin in solution, reporting that, upon excitation, these compounds are involved in competitive silyl group transfer, homolysis of the S–N bond (Scheme 1), and H-abstraction processes, the relative contribution of each pathway depending on the

Scheme 1



Scheme 2



reaction conditions.¹⁵ Thus, the photochemistry of saccharyl derivatives in solution appears to be determined by the structure of the saccharyl ring, the nature of the substituents, and the reaction media. However, to the best of our knowledge, no information regarding the photochemistry of monomeric saccharin or its anion (conjugate base) is available.

In the present work, we report the photoisomerization of saccharin isolated in solid argon and discuss possible

Received: January 28, 2013

Published: March 11, 2013

implications of this reaction, namely those related to structural features of the conjugate bases that could be possibly formed from both isomers.

RESULTS AND DISCUSSION

Choice of the Model Chemistry. A fragment of the experimental infrared (IR) spectrum of matrix-isolated saccharin is shown in Figure 1, along with several calculated

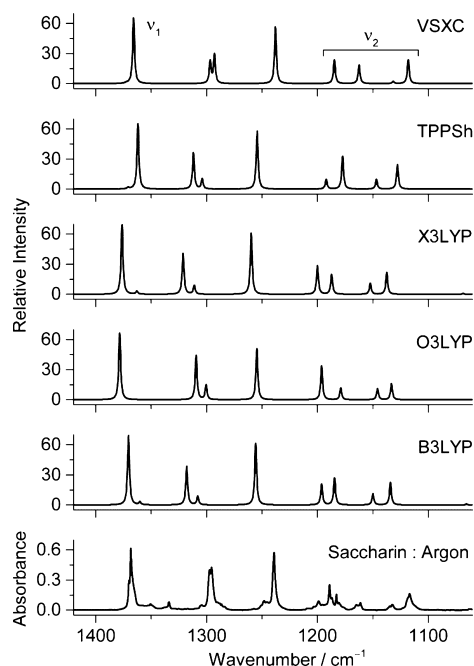


Figure 1. Fragment of the experimental infrared spectrum of saccharin isolated in an argon matrix at 15 K (bottom) compared with several simulated infrared spectra of saccharin in the region of the ν_{SO_2} vibrations. The 6-311++G(3df,3pd) basis set was used with all the functionals. Theoretical wavenumbers are not scaled. ν_1 : ν_{SO_2} *as*; ν_2 : mixed ν_{SO_2} *s* + δCH modes.

spectra for this molecule. Previous combined experimental and theoretical studies on saccharin derivatives showed that, due to the SO_2 moiety, the predicted vibrational frequencies and infrared intensities are very sensitive to the theoretical approach employed. It was found that the use of cost-effective density functional theory requires basis sets including extensive polarization and diffuse functions to provide the most suitable approach in attaining reliable structural and spectroscopic predictions.^{16,17} Taking into consideration some reviews on the general performance of DFT functionals,¹⁸ we carried out optimization of the structure followed by calculations of the vibrational spectrum of saccharin using the VSXC, O3LYP, X3LYP, and TPSSh functionals together with several basis sets. The widely used B3LYP functional was also included as a reference.

The prediction of the vibrational spectrum of saccharin is especially difficult due to the presence in this molecule of both the SO_2 moiety and the aromatic ring. The antisymmetric (*as*) and symmetric (*s*) stretching (ν) vibrations of the SO_2 group in inorganic molecules and in neat SO_2 isolated in cryogenic matrices occur around 1400 and 1200 cm^{-1} , respectively.¹⁹ On the other hand, in aromatic molecules, the CH in-plane bending (δ) vibrations fall within the 1200–1100 cm^{-1} range.²⁰

In saccharin, ν_{SO_2} *s* and four δCH vibrations occur at similar frequencies. The precise theoretical frequencies of these vibrations and their mixing pattern in the ν_2 range (see Figure 1) are very sensitive to the calculated equilibrium geometry.

Figure 2 shows the calculated values obtained at different levels of approximation in this study for selected geometrical

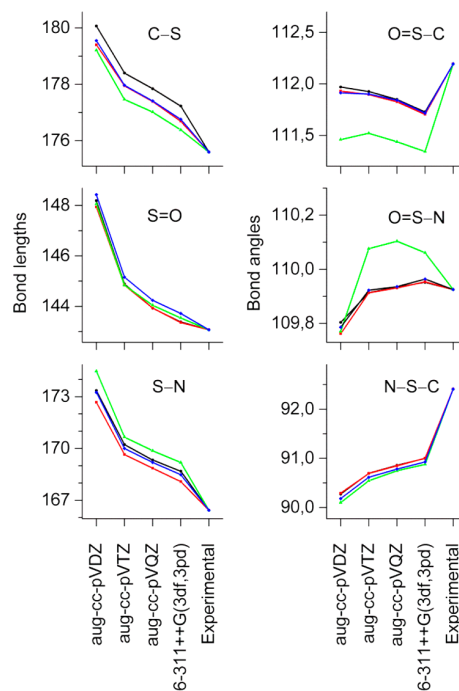


Figure 2. Selected geometrical parameters (bond lengths in pm and bond angles in degrees) calculated with the O3LYP (red), VSXC (green), TPSSh (blue), and B3LYP (black) functionals and different basis sets. Experimental data from ref 21.

parameters, compared with experimental values obtained from X-ray diffraction studies.²¹ The experimental geometries refer to the crystal structure, where saccharin forms centrosymmetric dimers stabilized by two $\text{C}=\text{O}\cdots\text{H}-\text{N}$ intermolecular hydrogen bonds. In this way, the $\text{HNC}=\text{O}$ moiety of saccharin crystal becomes more distorted comparing to a monomer in vacuum, while the geometry of the SO_2 fragment is less affected by crystal packing forces. Even though the calculations refer to isolated molecules in vacuo, the comparison with X-ray structures still appears very instructive. For example, the presence of a considerable number of polarization functions in the basis set for the accurate reproduction of bond lengths and angles where hypervalent sulfur atoms are involved is shown to be very important. It is also evident that the 6-311++G(3df,3pd) Pople-type basis set outperforms (in particular, for bond lengths) the more demanding Dunning-type aug-cc-pVTZ and aug-cc-pVQZ basis sets for this particular system, whichever functional was used (see Figure 2).

The quality of different DFT functionals combined with the 6-311++G(3df,3pd) basis set was then evaluated regarding their ability to predict vibrational data. A set of well-defined bands in the infrared spectrum of matrix-isolated saccharin (see Figure 3) was chosen, and the experimental frequencies were compared with their calculated counterparts (see Table 1). The best overall agreement was obtained for the O3LYP functional, with a mean unsigned error (MUE) of 8.55 cm^{-1} ,

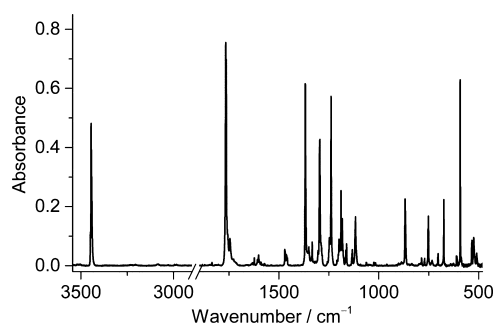


Figure 3. Experimental spectrum of monomeric saccharin isolated in argon at 15 K.

Table 1. Experimental and Theoretical Frequencies in the Infrared Spectrum of Saccharin Used in the Calculation of the Mean Unsigned Errors (MUE)

Ar (15 K) ^a	calculated/cm ⁻¹				
	VXSC	TPSSh	X3LYP	O3LYP	B3LYP
1765.8	1774.8	1784.7	1808.2	1801.7	1801.0
1471.5	1479.4	1491.2	1499.1	1483.5	1495.8
1463.3	1468.1	1482.9	1491.2	1473.1	1487.8
1368.4	1372.6	1370.8	1376.4	1378.4	1370.5
1239.1	1237.9	1254.4	1259.8	1254.7	1255.7
1132.7	1131.6	1146.9	1152.4	1145.9	1149.9
1116.7	1118.1	1127.9	1137.5	1133.2	1134.2
868.4	823.2	851.3	860.6	860.9	855.8
786.1	785.4	794.9	805.5	791.7	803.0
770.4	762.1	768.7	778.7	767.2	776.3
751.6	749.7	753.6	767.7	752.0	764.7
703.2	693.5	700.3	712.1	702.7	709.8
674.5	669.6	669.2	685.6	671.8	681.4
608.7	600.2	608.5	619.5	613.0	617.6
592.4	569.4	581.0	592.9	587.3	590.6
533.1	521.3	526.4	539.0	528.8	537.0
524.4	514.1	520.6	528.3	522.9	526.6
509.3	494.9	501.3	511.0	503.3	509.0
MUE/cm ⁻¹	9.33	9.39	14.54	8.55	12.05

^aThe experimentally observed band due to the NH stretching vibration of saccharin appears at 3445.8 cm⁻¹. This band was not used in the estimation of MUEs.

closely followed by the VXSC and TPSSh functionals, with MUEs of 9.33 and 9.39 cm⁻¹, respectively. The B3LYP functional shows a MUE of 12.05 cm⁻¹, while the largest deviation from the experiment was found for X3LYP (14.54 cm⁻¹). After consideration of all the different functionals and basis sets, the O3LYP/6-311++G(3df,3pd) level of theory arose as the best approach to be used in the vibrational characterization of new structures that might be generated from saccharin in the photochemical experiments. Also, along with the best overall agreement for the calculated frequencies, the O3LYP/6-311++G(3df,3pd) method reproduces the infrared intensities of the vibrational modes fairly well.

Narrow-Band UV-Induced Photochemistry of Matrix-Isolated Saccharin: First Observation of Iso-saccharin. In the present study, matrix-isolated saccharin was irradiated with narrow-band UV light provided by an optical parametric oscillator. Preliminary selection of the wavelength for the applied UV light was guided by the absorption spectrum of saccharin in ethanol.²² The series of UV irradiations of matrix-

isolated saccharin in the present study started at $\lambda = 300$ nm and continued at shorter wavelengths. After each irradiation, the reaction was monitored by analysis of the IR spectrum. The first phototransformations were observed for $\lambda = 295$ nm, and the effect became more pronounced when irradiation was performed at 290 nm. Upon these irradiations, the bands due to saccharin decreased in intensity, whereas a new set of bands at 1718.1, 1398.7, 1218.6, 973.4, 858.6, 800.5, 768.6, 607.2, and 553.2 cm⁻¹ emerged in the spectrum (Figure 4a). The IR spectrum of the photoproduct consists of sharp absorption bands, as narrow as the bands in the initial IR spectrum, which suggests occurrence of a photoisomerization.

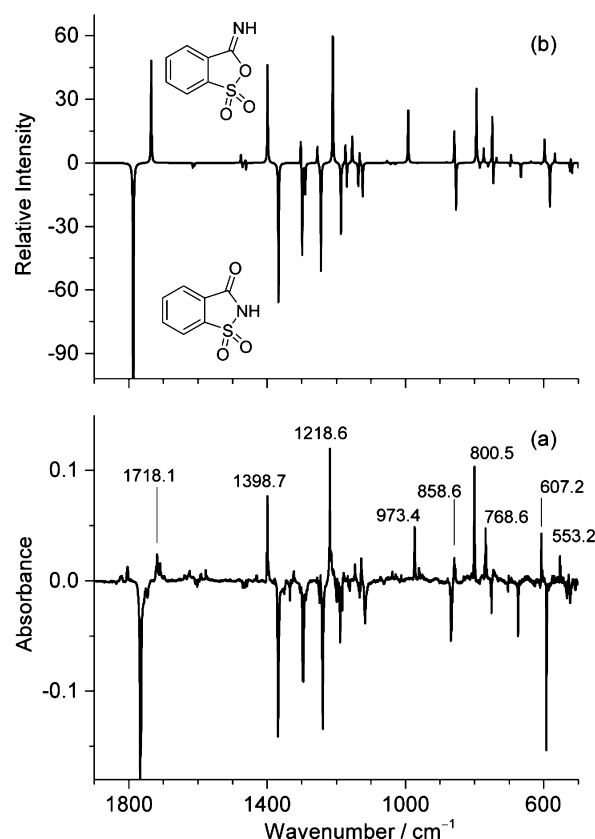


Figure 4. Difference infrared spectrum, obtained by subtraction of the spectrum recorded after the matrix deposition (negative bands) from the spectrum recorded after UV ($\lambda = 290$ nm; 78 min) irradiation (positive bands) of matrix-isolated saccharin (a), compared with the theoretical one obtained by subtraction of the simulated spectrum of saccharin from iso-saccharin (b). Theoretical wavenumbers were scaled by a factor of 0.992 obtained by least-squares linear fitting. In the simulation, the calculated intensities of iso-saccharin were scaled by 0.7.

Heterocyclic molecules bearing the HNC=O moiety, which is also present in saccharin, have been found to frequently undergo oxo-hydroxy photoisomerization.²³ On the other hand, as stated above,¹⁴ other conceptually possible isomerizations in saccharin may result from an oxygen atom shift from SO₂ to form *N*-hydroxysulfonamide or from homolysis of the S–N bond. The structures of these putative photoproducts were optimized in the present study and their vibrational spectra subsequently calculated at the O3LYP/6-311++G(3df,3pd) level of theory. These geometries and calculated spectra are

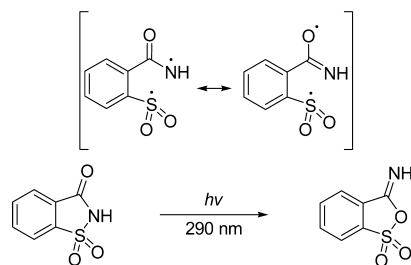
available in the Supporting Information (Scheme S1). After comparing the experimental difference IR spectrum (Figure 4a) with the simulated difference spectra built from saccharin and item-by-item examination of putative products, it could doubtlessly be concluded that the photoproduct bands indicate the formation of 3-imino-3*H*-2,1-benzoxathiole-1,1-dioxide (figure 4b), which we designate for brevity as “iso-saccharin”.

It can be estimated that about 70% of the consumed reactant has been converted to iso-saccharin (see Figure 4), while the remaining consumed material undergoes photofragmentation. Observation, in the spectrum of the irradiated matrix, of characteristic absorption bands due to an O=C=N moiety around 2260–2240 cm⁻¹ (see Figure S2, Supporting Information) suggests isocyanic acid or its derivatives as possible fragmentation photoproducts of saccharin. It is known that the antisymmetric O=C=N stretching vibration falls in this spectral range and the corresponding infrared intensity is huge (800–1100 km mol⁻¹).^{24,25}

It is also interesting to comment on the nature of the electronic states involved in the excitation of saccharin at 290 nm. In the experimental spectrum,²² a very weak oscillator strength can be observed around 290 nm, suggesting that this low intensity absorption is associated with an $n\pi^*$ transition. Time-dependent DFT (TD-DFT) calculations performed at the O3LYP/6-311++G(3df,3pd) level show that the first (vertical) excited singlet state of saccharin has a very low oscillator strength ($f = 0.0000$; at this level it does not have any significant digits in the standard Gaussian output) and is located at 293.62 nm, in excellent agreement with the onset of the photochemistry observed in this work. Moreover, natural bond orbital (NBO) calculations show that the HOMO and the LUMO of saccharin correspond to the lone-pair n orbital and the π^* orbital of the carbonyl group, respectively (see Figure S3, Supporting Information). Thus, all the experimental and theoretical data indicate that the observed isomerization is originated by the $n\pi^*$ excitation of the carbonyl moiety.

The proposed mechanism for the observed unprecedented photoisomerization of the saccharin system involves photo-induced homolysis of the S–N bond, producing a delocalized biradicaloid in the amide moiety that, upon rotation around the exocyclic C–C bond, affords the iso-saccharin product through ring closure (Scheme 3). A similar biradicaloid rearrangement

Scheme 3. Photoisomerization Reaction Observed for Saccharin

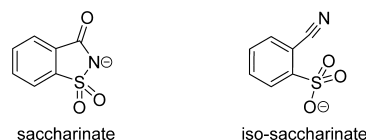


was recently proposed to take place in the photochemical conversion of diketene into cyclobutane-1,3-dione,²⁶ also occurring in argon matrices upon an $n\pi^*$ excitation of the reactant.

Structures of the Saccharinate and Iso-saccharinate Anions: Relevance to the Photochemistry of Saccharin. It is recognized that the saccharinate conjugate base, obtained

by deprotonation of the NH moiety in saccharin, is a very versatile and polyfunctional ligand in coordination chemistry.⁷ Here, we calculated the structures of the conjugate bases that result from deprotonation of both isomers, saccharin and iso-saccharin. Their optimized geometries are given in the Supporting Information. The saccharinate anion resembles very much its precursor, saccharin, and is a stable minimum in the calculations. On the contrary, deprotonation of the NH group in iso-saccharin induces barrierless cleavage of the CO bond, the resulting anion consisting of the cyano- and SO₃ groups linked to the aromatic ring at vicinal positions (formally 2-cyanobenzene sulfonate; Chart 1). To the best of our knowledge, 2-cyanobenzene sulfonate was never considered as a photoproduct of saccharin derivatives nor has it been described in the literature.

Chart 1. Structures of Saccharinate and Iso-saccharinate Anions (Conjugate Bases)



Interestingly, on moving from the neutral to anionic species, the iso-saccharinate becomes strongly stabilized compared to the saccharinate. The relative free energy of iso-saccharin (at room temperature) decreases from 50.8 (neutral) to 7.3 (anion) kJ mol⁻¹ only, calculated for monomers in vacuum. Taking into account that calculated net dipole moments of saccharinate and iso-saccharinate are 8.04 and 9.35 D, respectively, one could expect that the more polar iso-saccharinate will be further stabilized in polar environments,²⁷ such as ionic liquids.^{8–11} An exhaustive search of the online molecule databases did not retrieve any record for the iso-saccharin or its conjugate base; neither could we find any reference to these structures in the literature.

CONCLUSIONS

In this study, we have shown that saccharin undergoes structural rearrangement when subjected to narrow-band ultraviolet ($\lambda = 290$ nm) irradiation. The observed photoisomerization begins with an $n\pi^*$ excitation of the carbonyl moiety of the saccharin system and involves the homolysis of the S–N bond, generating a delocalized biradicaloid, which subsequently undergoes internal rotation and after ring closure produces the rearranged product. This photoisomerization of saccharin to iso-saccharin, never reported before, may have implications in the uses of saccharin, in particular when deprotonation is facilitated. In those cases, the present study shows that the iso-saccharinate anion (conjugate base) shall be promptly converted into 2-cyanobenzene sulfonate in a barrierless process. These changes in structure of the components shall imply important alterations in the properties of the saccharin- or saccharinate-based materials, in particular, the recently proposed saccharin-based ionic liquids.

EXPERIMENTAL AND COMPUTATIONAL METHODS

Samples were prepared by heating saccharin in a miniature glass oven placed inside the vacuum chamber of a cryostat and then depositing the saccharin vapors with a large excess of argon onto a CsI window

cooled to 15 K. Narrow-band (fwhm ~ 0.2 cm $^{-1}$) UV irradiation was provided by the frequency-doubled signal beam of a Quanta-Ray MOPO-SL optical parametric oscillator, pumped with a pulsed Nd:YAG laser (repetition rate 10 Hz, pulse energy ~ 3 mJ). Commercial saccharin (99%, Aldrich) and argon (N60, Air Liquide) were used.

All calculations were performed with the Gaussian 09 program package, and functionals and basis sets were applied as defined in Gaussian.²⁸ The equilibrium geometries reported here were optimized within the C_s symmetry point group, where applicable. The harmonic vibrational frequencies were then calculated at the optimized geometry. The nature of the obtained stationary points as true minima on the potential energy surface was confirmed through the analysis of the corresponding Hessian matrix.

■ ASSOCIATED CONTENT

■ Supporting Information

Figure S1, showing the 1900–600 cm $^{-1}$ region (an extension of Figure 1 to the whole fingerprint region); Figure S2, an extended version of Figure 4 showing the complete mid-IR region; Figure S3 showing the calculated frontier natural bond orbitals of saccharin; Scheme S1, showing structures of saccharin, iso-saccharin, and other isomeric forms considered in the analysis of the vibrational spectrum of the observed photoproduct; Tables S1 and S2, showing structures of anions derived from saccharin and iso-saccharin, optimized at the O3LYP/6-311++G(3df,3pd) level of theory, with Cartesian coordinates and APT charges. This material is available free of charge via the Internet at <http://pubs.acs.org>.

■ AUTHOR INFORMATION

Corresponding Author

*E-mail: reva@qui.uc.pt.

Notes

The authors declare no competing financial interest.

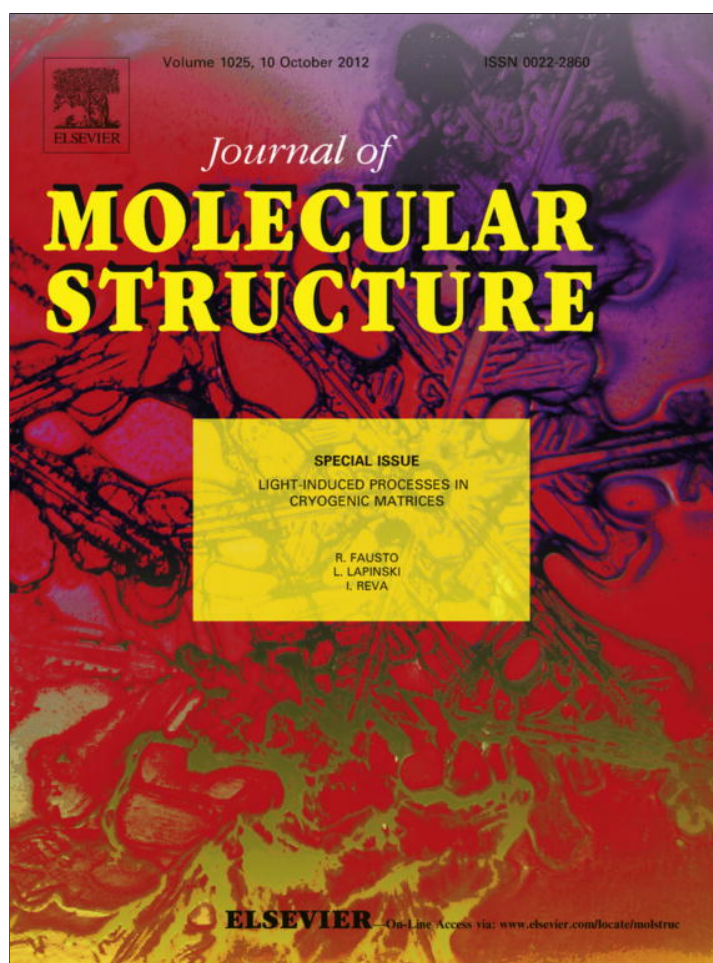
■ ACKNOWLEDGMENTS

This work was supported by the Portuguese “Fundação para a Ciência e a Tecnologia” (FCT) Research Projects PTDC/QUI-QUI/111879/2009 and PTDC/QUI-QUI/118078/2010, FCOMP-01-0124-FEDER-021082, cofunded by QREN-COM-PEETE-UE, and PEst-C/MAR/LA0015/2011. L.D. acknowledges FCT for the doctoral grant (No. SFRH/BD/62090/2009).

■ REFERENCES

- (1) George, V.; Arora, S.; Sharma, V.; Wadhwa, B. K.; Singh, A. K. *Food Bioprocess Technol.* **2010**, *5*, 323–330.
- (2) Wepplo, P. J.; Rampulla, R. A.; Heffernan, G. D.; Cossette, M. V.; Langevine, C. M.; Kameswaran, V.; Diehl, R. E.; Fiordeliso, J. J.; Haley, G. J.; Guaciaro, M. A. Herbicidal 3-heterocyclic Substituted Benzisothiazole and Benzisoxazole Compounds. US Patent US6706663 2004.
- (3) Wang, L. H.; Yang, X. Y.; Zhang, X.; Mihalic, K.; Fan, Y.-X.; Xiao, W.; Howard, O. M. Z.; Appella, E.; Maynard, A. T.; Farrar, W. L. *Nat. Med.* **2004**, *10*, 40–47.
- (4) Qiao, N.; Li, M.; Schlindwein, W.; Malek, N.; Davies, A.; Trappitt, G. *Int. J. Pharm.* **2011**, *419*, 1–11.
- (5) Ahn, K.; Baek, H.; Lee, S.; Cho, C. *J. Org. Chem.* **2000**, *65*, 7690–7696.
- (6) Baran, E. J.; Yilmaz, V. T. *Coord. Chem. Rev.* **2006**, *250*, 1980–1999.
- (7) Baran, E. J. *Quim. Nova* **2005**, *28*, 326–328.
- (8) Quentel, F.; Stankoska, K.; Grupče, O.; Jovanovski, G.; Mirčeski, V. *Electrochem. Commun.* **2011**, *13*, 1476–1478.
- (9) Zhang, Q.; Liu, S.; Li, Z.; Li, J.; Chen, Z.; Wang, R.; Lu, L.; Deng, Y. *Chem.—Eur. J.* **2009**, *15*, 765–778.
- (10) Carter, E. B.; Culver, S. L.; Fox, P. A.; Goode, R. D.; Ntai, I.; Tickell, M. D.; Traylor, R. K.; Hoffman, N. W.; Davis, J. H., Jr. *Chem. Commun.* **2004**, 630–631.
- (11) Shkrob, I. A.; Marin, T. W.; Chemerisov, S. D.; Hatcher, J.; Wishart, J. F. *J. Phys. Chem. B* **2012**, *116*, 9043–9055.
- (12) Ono, I.; Sato, S.; Fukuda, K.; Inayoshi, T. *Bull. Chem. Soc. Jpn.* **1997**, *70*, 2051–2055.
- (13) Kamigata, N.; Saegusa, T.; Fujie, S.; Kobayashi, M. *Chem. Lett.* **1979**, 9–12.
- (14) Döpp, D. *Int. J. Photoenergy* **2001**, *3*, 41–48.
- (15) Cho, D. W.; Oh, S. W.; Kim, D. U.; Park, H. J.; Xue, J. Y.; Yoon, U. C.; Mariano, P. S. *Bull. Korean Chem. Soc.* **2010**, *31*, 2453–2458.
- (16) Kaczor, A.; Almeida, R.; Gómez-Zavaglia, A.; Cristiano, M. L. S.; Fausto, R. *J. Mol. Struct.* **2008**, *876*, 77–85.
- (17) Almeida, R.; Gómez-Zavaglia, A.; Kaczor, A.; Ismael, A.; Cristiano, M. L. S.; Fausto, R. *J. Mol. Struct.* **2009**, *938*, 198–206.
- (18) Sousa, S. F.; Fernandes, P. A.; Ramos, M. J. *J. Phys. Chem. A* **2007**, *111*, 10439–10452.
- (19) Zeng, X.; Beckers, H.; Neuhaus, P.; Grote, D.; Sander, W. *Z. Anorg. Allg. Chem.* **2012**, *638*, 526–533.
- (20) Giuliano, B. M.; Reva, I.; Lapinski, L.; Fausto, R. *J. Chem. Phys.* **2012**, *136*, 024505.
- (21) Wardell, J. L.; Low, J. N.; Glidewell, C. *Acta Crystallogr., Sect. E: Struct. Rep. Online* **2005**, *61*, o1944–o1946.
- (22) Berci-Filho, P.; Quina, F. H.; Gehlen, M. H.; Politi, M. J.; Neumann, M. G.; Barros, T. C. I. *J. Photochem. Photobiol., A* **1995**, *92*, 155–161.
- (23) See, for example, Scheme 2 in: Reva, I.; Almeida, B. J. A. N.; Lapinski, L.; Fausto, R. *J. Mol. Struct.* **2012**, *1025*, 74–83.
- (24) Reva, I.; Lapinski, L.; Fausto, R. *J. Mol. Struct.* **2010**, *976*, 333–341.
- (25) Teles, J. H.; Maier, G.; Hess, B. A., Jr.; Schaad, L. J.; Winnewisser, M.; Winnewisser, B. P. *Chem. Ber.* **1989**, *122*, 753–766.
- (26) Breda, S.; Reva, I.; Fausto, R. *J. Phys. Chem. A* **2012**, *116*, 2131–2140.
- (27) Jakopin, Z.; Dolenc, M. S. *Curr. Med. Chem.* **2010**, *17*, 651–671.
- (28) Gaussian 09, Revision A.02: Frisch, M. J.; Trucks, G. W.; Schlegel, H. B.; Scuseria, G. E.; Robb, M. A.; Cheeseman, J. R.; Scalmani, G.; Barone, V.; Mennucci, B.; Petersson, G. A.; Nakatsuji, H.; Caricato, M.; Li, X.; Hratchian, H. P.; Izmaylov, A. F.; Bloino, J.; Zheng, G.; Sonnenberg, J. L.; Hada, M.; Ehara, M.; Toyota, K.; Fukuda, R.; Hasegawa, J.; Ishida, M.; Nakajima, T.; Honda, Y.; Kitao, O.; Nakai, H.; Vreven, T.; Montgomery, J. A., Jr.; Peralta, J. E.; Ogliaro, F.; Bearpark, M.; Heyd, J. J.; Brothers, E.; Kudin, K. N.; Staroverov, V. N.; Kobayashi, R.; Normand, J.; Raghavachari, K.; Rendell, A.; Burant, J. C.; Iyengar, S. S.; Tomasi, J.; Cossi, M.; Rega, N.; Millam, J. M.; Klene, M.; Knox, J. E.; Cross, J. B.; Bakken, V.; Adamo, C.; Jaramillo, J.; Gomperts, R.; Stratmann, R. E.; Yazyev, O.; Austin, A. J.; Cammi, R.; Pomelli, C.; Ochterski, J. W.; Martin, R. L.; Morokuma, K.; Zakrzewski, V. G.; Voth, G. A.; Salvador, P.; Dannenberg, J. J.; Dapprich, S.; Daniels, A. D.; Farkas, O.; Foresman, J. B.; Ortiz, J. V.; Cioslowski, J.; Fox, D. J. Gaussian, Inc., Wallingford, CT, 2009.

Provided for non-commercial research and education use.
Not for reproduction, distribution or commercial use.



This article appeared in a journal published by Elsevier. The attached copy is furnished to the author for internal non-commercial research and education use, including for instruction at the authors institution and sharing with colleagues.

Other uses, including reproduction and distribution, or selling or licensing copies, or posting to personal, institutional or third party websites are prohibited.

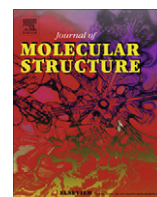
In most cases authors are permitted to post their version of the article (e.g. in Word or Tex form) to their personal website or institutional repository. Authors requiring further information regarding Elsevier's archiving and manuscript policies are encouraged to visit:

<http://www.elsevier.com/copyright>



Contents lists available at SciVerse ScienceDirect

Journal of Molecular Structure

journal homepage: www.elsevier.com/locate/molstruc

Structure and photochemistry of a novel tetrazole-saccharyl conjugate isolated in solid argon

A. Ismael^a, A. Borba^b, L. Duarte^b, B.M. Giuliano^b, A. Gómez-Zavaglia^{b,c,*}, M.L.S. Cristiano^{a,*}^a CCMAR and Department of Chemistry and Pharmacy, FCT, University of Algarve, P-8005-039 Faro, Portugal^b Department of Chemistry, University of Coimbra, P-3004-535 Coimbra, Portugal^c Center for Research and Development in Food Cryotechnology (CIDCA), La Plata, Argentina

H I G H L I G H T S

- ▶ A novel tetrazole-saccharyl conjugate (1-TE-BZT) was synthesised.
- ▶ 1-TE-BZT was isolated in argon matrices.
- ▶ The photochemistry of 1-TE-BZT was investigated.
- ▶ Three photofragmentation pathways involving both the cleavage of the tetrazole and the saccharyl moieties were proposed.
- ▶ On the basis of quantum chemical calculations, the proposed photoproducts could be assigned.

A R T I C L E I N F O

Article history:

Available online 8 May 2012

Keywords:

Saccharin
Tetrazole
Molecular structure
Matrix isolation
Photochemistry

A B S T R A C T

A combined matrix isolation FTIR and theoretical DFT/B3LYP/6-311++G(3df,3pd) study of the novel synthesised tetrazole-saccharyl conjugate 2-[1-(1H-tetrazol-5-yl)ethyl]-1,2-benzisothiazol-3(2H)-one 1,1-dioxide [1-TE-BZT] was performed. In the gas phase, at room temperature, the compound exists as a mixture of six isomeric forms (four conformers of 1H tautomer and two conformers of 2H tautomer). According to theoretical calculations, conformers 1H were the most stable and the relative energies among the three most stable forms are lower than 4 kJ mol⁻¹. These conformers benefit from stabilising intramolecular hydrogen bonds-like interactions involving the 1H of the tetrazole ring and the carbonyl oxygen of the saccharyl moiety.

The photochemistry of 1-TE-BZT in solid argon was investigated and theoretical DFT/B3LYP/6-311++G(3df,3pd) calculations also helped in assignment of the experimental bands. A quick consumption of the compound occurred after irradiation of the matrix with UV laser light at $\lambda = 275$ nm. Three photofragmentation pathways were proposed, one leading to 2-[1-(1H-diaziren-3-yl)ethyl]-1,2-benzisothiazol-3(2H)-one 1,1-dioxide and molecular nitrogen, a second one giving 2-(1,1-dioxide-3-oxo-1,2-benzisothiazol-2(3H)-yl)propanenitrile and azide, and a third one involving loss of azide from the tetrazole ring and decarbonylation of the saccharyl ring of 1-TE-BZT to give acrylonitrile and 7-thia-8-azabicyclo[4.2.0] octa-1,3,5-triene 7,7 dioxide. The comparison of the relative intensities of the bands of the photoproducts obtained from the three channels allowed us to consider the latter pathway, involving an unprecedented photocleavage of the benzisothiazole (saccharyl) ring, as the preferred photodegradation channel of 1-TE-BZT.

© 2012 Elsevier B.V. All rights reserved.

1. Introduction

Tetrazoles and benzisothiazoles are nitrogen heterocycles with important applications in major areas, such as medicine, agriculture, imaging technology and food chemistry. In the case of

tetrazoles, most of the applications derive from the acid/base properties of the tetrazolic acid fragment, —CN₄H, which acts as a metabolically stable surrogate for the carboxylic acid group [1]. These compounds can find wide applications in coordination chemistry, as ligands. It has been demonstrated that the heterocycle tetrazole is able to participate in at least nine distinct types of coordination modes with metal ions, in the construction of novel metal–organic frameworks. Furthermore, the coordination ability of the tetrazolyl ligand through four nitrogen electron-donating atoms allows it to serve as a bridging building block in supramolecular assemblies.

* Corresponding authors. Address: Center for Research and Development in Food Cryotechnology, La Plata, RA 1900, Argentina. (A. Gómez-Zavaglia).

E-mail addresses: angoza@qui.uc.pt (A. Gómez-Zavaglia), mcristi@ualg.pt (M.L.S. Cristiano).

1,2-Benzisothiazole-3-one 1,1-dioxide anions (deprotonated saccharines), also interact with metal centres, mostly through hydrogen bonding [2,3].

Tetrazolyl and saccharyl ethers have particularly important synthetic uses as intermediate compounds for reductive cleavage of the C–O bond in allyl- benzyl- and naphthyl alcohols and phenols catalysed by transition metals [4–7]. Much of the reactivity of these ethers is ascribed to changes in bond lengths around the central C_{HAR}–O–C_A ether bonds (HAR = heteroaromatic ring and A = alkyl allyl, benzyl, phenyl or naphthyl group), caused by the powerful electron-withdrawing effect of the benzisothiazole ring system. The neat result of these electronic changes determines a molecular structure in which the originally strong C_A–O bond in the alcohol or phenol lengthens becoming easily cleavable in the ether whereas the CH_{AR}–O bond acquires a considerable degree of double bond character. As such, thermal treatment of these compounds leads to easy cleavage of the C_A–O bond together with the formation of a C_{HAR}=O bond [8–12]. The thermally induced isomerisation of various allyloxy- and alkoxy-benzisothiazoles was investigated and proved to involve intramolecular migration of the allyl or alkyl groups from O to N and occur through an intramolecular sigmatropic rearrangement.

Considering the wide interest demonstrated in tetrazole and benzisothiazole heterocycles as multidentate nitrogen ligands [13,14], efforts were made to prepare tetrazole-saccharyl conjugates with various linkers and to investigate their structure and reactivity. Our previous works revealed that the benzisothiazole moiety is photochemically stable whereas tetrazoles are highly photoreactive [14–22]. Thus, combining the apparent photochemical inertness of the benzisothiazole moiety with the high reactivity of the tetrazole moiety appeared to us as a challenge for this investigation. If the benzisothiazole moiety proves photochemically inert upon photolysis, then new saccharyl derivatives resulting from photolysis of the tetrazole ring may be produced. Alternatively, if conditions for photocleavage of the benzisothiazole moiety are established, photolysis of the tetrazole-saccharyl conjugate will probably produce a set of new compounds, opening ways for the development of synthetic pathways to new scaffolds. Also, to the best of our knowledge the available information related to the photochemistry of benzisothiazoles is still very scarce and all published data report photochemistry in solution [23–26]. This scenario prompted us to explore the photolysis of the benzisothiazolyl-tetrazole conjugate by matrix isolation FTIR spectroscopy. The fact that in a cryogenic inert matrix the photochemical processes are cage-confined (molecular diffusion is inhibited) introduces a useful simplification to the study of the photochemical reactivity since no cross reactions can, in principle, take place and only primary unimolecular reactions are expected. Such

simplification is very useful for mechanistic elucidations and for the study of intermediates that are unstable at room temperature but that can be trapped in the matrices. Therefore, in this paper we describe the structure and scrutinise the photochemistry of a novel alkyl-linked tetrazole-saccharyl conjugate, 2-[1-(1H-tetrazol-5-yl)ethyl]-1,2-benzisothiazol-3(2H)-one (1-TE-BZT), isolated in solid argon. The experimental results are supported by quantum chemical calculations undertaken at the DFT(B3LYP)/6-311++G(3df,3pd) level of theory. As detailed below, unprecedented information concerning the matrix photochemistry of this tetrazole-saccharyl system was gathered.

2. Experimental and computational methods

2.1. Synthesis

The synthetic route to 2-[1-(1H-tetrazol-5-yl)ethyl]-1,2-benzisothiazol-3(2H)-one 1,1-dioxide (1-TE-BZT) is presented in Fig. 1. Experimental details for the compounds prepared are as follows.

2.1.1. 1-(1H-tetrazol-5-yl)ethanol, 2

Prepared from sodium azide (1.43 g; 22 mmol), zinc bromide (4.50 g; 20 mmol) and 2-hydroxy-propanenitrile **1** (1.45 mL; 20 mmol), in water (50 mL). The reaction mixture was refluxed for 20 h with vigorous stirring. White amorphous powder (1.70 g; 75% yield). IR ν_{\max} (cm⁻¹): 3390 (OH), 1696, 1624, 1243, 1123; ¹H NMR (CDCl₃): δ 7.55 (br, 1H), 7.22–7.35 (q, 1H), 7.35 (d, 3H); MS (EI), m/z 115 (33%) [M+H]⁺, 1 m/z 132 (100%) [M+NH₄]⁺. Acc. Mass (CI): found, 115.1145; calcd. for C₃H₇N₄O, 115.1134.

2.1.2. 3-Chloro-1,2-benzisothiazole 1,1-dioxide, 3

Prepared from saccharin (10.2 g; 56 mmol), and phosphorus pentachloride (14.0 g; 66 mmol) heated at 180 °C. Colourless needles from trichloromethane (7.00 g; 63% yield), m.p. 143–145 °C. IR ν_{\max} : 1724, 1654, 1603 (C=C), 1346 (SO₂), 775 (Ar–H) and 692 (C–Cl) cm⁻¹; ¹H NMR (CDCl₃): δ 7.85 (4H, m, Ar–H); Anal. calcd. for C₇H₄NO₂Cl: C, 41.7; H, 2.0; N, 7.0%, found: C, 41.5; H, 2.0; N, 6.9%; MS (EI), m/z 201 [M]⁺.

2.1.3. 2-[1-(1H-tetrazol-5-yl)ethyl]-1,2-benzisothiazol-3(2H)-one 1,1-dioxide 5

A mixture of 1-(1H-tetrazol-5-yl)ethanol **2** (0.20 g; 1.75 mmol), 3-chloro-1,2-benzisothiazole 1,1-dioxide (0.35 g; 1.75 mmol) and potassium tert-butoxide (0.65 g; 5.25 mmol, in dry THF (50 mL), was stirred at 60 °C under a nitrogen atmosphere, until TLC analysis (DCM/toluene 3:1) indicated the absence of starting material (48 h). Work-up afforded a pale yellow powder (0.28 g; 58% yield), m.p. 210–211 °C identified as 1-TE-BZT, **5**. IR ν_{\max} : 3091, 2974, 1721, 1593, 1463, 1336 (SO₂), 1177 cm⁻¹; ¹H NMR (CDCl₃): δ 8.05–8.08 (d, 1H), 7.91–7.95 (m, 2H), 7.86–7.90 (d, 1H), 5.26 (1H, d), 1.39–1.41 (d, 3H); MS (EI), m/z 279 [M]⁺; Acc. Mass (CI): found = 280.1089, calcd. for C₁₀H₁₀N₅O₃S: 280.1022.

2.2. Infrared spectroscopy and photochemical experiments

The infrared (IR) spectra of 1-TE-BZT were obtained using a Nicolet 6700 Fourier transform infrared spectrometer equipped with a deuterated triglycine sulphate (DTGS) detector and a Ge/KBr beam splitter, with 0.5 cm⁻¹ spectral resolution. Matrices were prepared by co-deposition, onto the cooled CsI substrate of the cryostat, of the matrix gas (argon 99.9998%, obtained from Air Liquide) and vapours of the compound under study produced by evaporation in a specially designed temperature variable mini-oven assembled inside the cryostat. The temperature of the

Table 1

Zero point corrected relative energies (ΔE_0 /kJ mol⁻¹) obtained at the DFT(B3LYP)/6-311++G(3df,3pd) level of theory of the various conformers of 1-TE-BZT^a and average energies ($-\Delta H$ /kJ mol⁻¹) for intramolecular interactions involving the NH group in 1H conformers of 1-TE-BZT, calculated using equations 1 and 2 (see text).^b

Tautomer	Conformer	ΔE_0 DFT(B3LYP)/6-311++G(3df,3pd)	NH...O=X (nm)	$\Delta\nu_{\text{NH}}$ (cm ⁻¹)	$-\Delta H$ (kJ mol ⁻¹)
1H	G'Sk'	0.0 (–3370201.670) ^c	0.2047	175.4	16.1
	GSK'	2.59	0.2012	194.5	17.2
	G'Sk	4.25	0.2150	129.8	13.1
	GSK	8.30	0.2179	119.8	12.4
2H	G'G'	7.12			
	GG'	8.60			

^a Energies in kJ mol⁻¹; conformers are depicted in Fig. 3.

^b See Fig. 1 for atom numbering.

^c Total energies with zero point vibrational energy contribution.

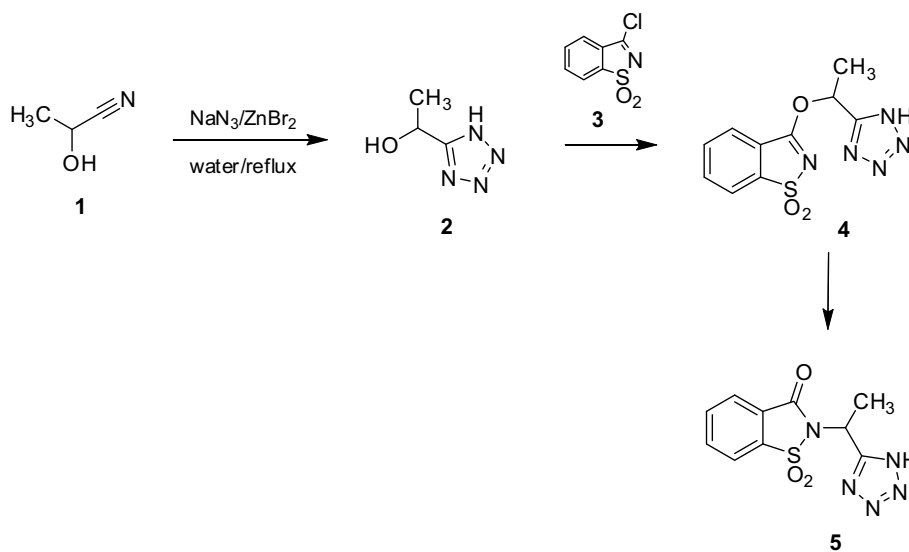


Fig. 1. Synthetic approach to 2-[1-(1H-tetrazol-5-yl)ethyl]-1,2-benzisothiazol-3(2H)-one 1,1-dioxide.

mini-oven used for evaporation of the compounds was *ca.* 335 K. The low temperature experiments were done on the basis of an APD Cryogenics close-cycle helium refrigeration system with a DE-202A expander. The temperature of the CsI substrate during deposition was 15 K.

The matrices were irradiated through the outer quartz window of the cryostat, with the frequency-doubled signal beam of the Quanta-Ray MOPO-SL pulsed (10 ns) optical parametric oscillator (FWHM $\sim 0.2\text{ cm}^{-1}$, repetition rate 10 Hz, pulse energy $\sim 2.5\text{ mJ}$) pumped with a pulsed Nd:YAG laser.

2.3. Computational methods

The quantum chemical calculations were performed at the DFT level of theory using the standard 6-311++G(3df,3pd) basis set [27–31] and the three-parameter density functional abbreviated as B3LYP, which includes Becke's gradient exchange correction [32] and the Lee, Yang, Parr correlation functional [33]. Geometrical parameters were optimised using the Direct Inversion in the Iterative Subspace (DIIS) method [34]. The optimisation of geometries was followed by harmonic frequency calculation at the same theory level. The nature of the obtained stationary points was checked through analysis of the corresponding Hessian matrix. Calculations were carried out using the Gamess program [35].

The calculated harmonic frequencies (scaled with the factor 0.978 [14]) were used to assist the analysis of the experimental spectra and to account for the zero-point vibrational energy (ZPVE) corrections.

3. Results and discussion

3.1. Synthesis of 2-[1-(1H-tetrazol-5-yl)ethyl]-1,2-benzisothiazol-3(2H)-one 1,1-dioxide

The synthetic route to 1-TE-BZT is presented in Fig. 1 and involves a convergent strategy whereby the tetrazolyl and saccharyl building blocks, **2** and **3**, are prepared separately and then coupled to form the ethyltetrazole-saccharyl ether **4** that subsequently isomerises to the required target compound **5**. Sigmatropic isomerisation in saccharyl ethers has been studied by our groups. An earlier investigation of the thermal isomerisation of allyl-saccharyl ethers in solution, revealed that migration of the allyl group from O to N

may occur through both [3,3']- and [1,3']-processes [8,10], the relative proportion of isomerisation products depending on structural features of the starting ether such as electron density and steric hindrance on the allylic system, polarity of the reaction medium and temperature. It was also observed that the saccharyl derivative of the cyclic allyl alcohol myrtenol isomerises at room temperature with exclusive formation of the [1,3']-product. This behaviour was interpreted on the basis of steric constraints imposed by the cyclic myrtenyl system, which destabilise the transition state required for concerted [3,3']-migration, preventing its formation [10]. It was further demonstrated that the [3,3']-products undergo inversion to the thermochemically more favourable [1,3']-isomers upon extended heating [8]. It is not clear whether the [1,3']-rearrangement in these ethers occurs through a fragmentation-recombination process or through a pseudo-pericyclic mechanism. Recently, the thermal isomerisation of neat 3-allyloxysaccharin was investigated in the liquid phase, combining matrix-isolation FTIR spectroscopy, differential scanning calorimetry and quantum chemical calculations. From the results, a [3,3']-sigmatropic shift mechanism for the isomerisation in the liquid phase was proposed [36]. We have also demonstrated that the isomerisation of 3-methoxy-saccharin in the solid-state and in the gas phase occurs through a Chapman-type mechanism [11,12]. Considering this scientific background, it was reasonable to expect that compound **4** would easily isomerise to the target conjugate **5**, and a synthetic approach making use of this reaction was therefore devised. Furthermore, migration of the alkyl group from O to N in ether **4** was expected to be easier than in the case of 3-methoxy-saccharin due to increased stabilisation of the carbocation-like migrating moiety. In fact, ether **4** could not be isolated because it readily isomerises to conjugate 1-TE-BZT, **5**, as could be demonstrated by FTIR and NMR (see Section 2.1.3).

3.2. Geometries and energies of 1-TE-BZT

Before the discussion of geometries and energies of 1-TE-BZT, it must be underlined that for compounds containing sulphur–oxygen linkages, such as benzisothiazoles, it is relatively difficult to obtain reliable predictions of their fundamental properties. More specifically, most of the standard computational methods and basis sets have been found unable to correctly predict the values of the S=O bond lengths and of the vibrational frequencies associated with it [37–40]. To overcome this problem, we decided to use

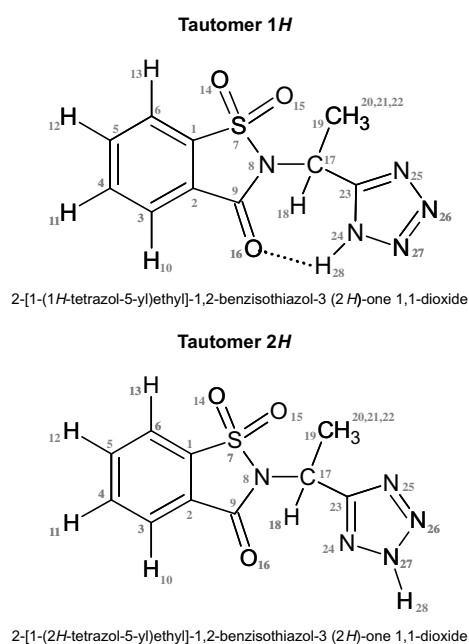


Fig. 2. Schematic representation of the two tautomeric forms of 1-TE-BZT with adopted atom numbering.

the B3LYP functional together with an extensive set of polarisation functions. As demonstrated in our previous work, this approach correctly reproduces both the geometry and frequencies of the polyvalent S=O bonds [41].

1-TE-BZT has a chiral centre, the two enantiomers (R and S forms) being spectroscopically equivalent. In the present study we will focus on the R form. The compound may exist in two tautomeric forms (Fig. 2), both having two conformationally relevant internal degrees of rotation, which are defined by the N₈–C₁₇ and C₁₇–C₂₃ bonds. Other tautomers, such as hydroxy benzisothiazole forms, could, in principle, be considered. These forms involve transfer of H₁₈ to O₁₆ (the carbonyl oxygen in the saccharin ring), forming and imino linkage between both heterocycles (keto–enol tautomerisation). However, taking into account the lower stability of enol forms and considering the high computational efforts required for the optimisation of benzisothiazole derivatives, the enol tautomers have been *a priori* ruled out [16].

The theoretical calculations at the B3LYP/6-311++G(3df,3pd) level predicted a total of six minima on the ground state potential energy surface of 1-TE-BZT. Four minima belong to the conformers of 1H tautomer and the remaining two correspond to the two conformers of 2H tautomer. The full set of conformers found for each tautomer and their calculated relative energies (including zero point energy corrections) are represented in Fig. 3 and Table 1. Geometrical parameters for the various isomers are given in Table S1 (Supporting information). The following systematic rules were used to attribute names to the different isomeric forms: C₉N₈C₁₇C₂₃ is indicated by the first letter (*G* = *gauche*, ca. 60°; *G'* = *gauche'*, ca. –60°); N₈C₁₇C₂₃N₂₄ is indicated by the second letters (*Sk* = *skew*, ca. 120°; *Sk'* = *skew'*, ca. –120° in tautomer 1H and *G'* = *gauche'*, ca. –60° in tautomer 2H). 1H and 2H refer to the position of H₂₈ in the tetrazole ring.

According to calculations, the conformers belonging to the 1H tautomer were found to be the most stable forms. The stabilisation of these forms results from the presence of an intramolecular hydrogen bond-like (NH···O=X, where X = S, C), that is absent in all the 2H conformers. The oxygens acting as electron donors are those bound to C₉ and S₇ of the saccharine ring (O₁₄, O₁₅ and

O₁₆) (see Fig. 1). All 1H conformers are close in energy and the slight energy differences can be understood mainly by considering the distances H₂₈···O=S or H₂₈···O=C. Table 1 shows the theoretically calculated NH···O=X distances for all 1H conformers. Iogensen, Rozenberg and coworkers proposed two empirical Eqs. (1) and (2) allowing the estimation of the hydrogen bond or hydrogen bond-like interaction strengths [42]. The first correlation (1) allows estimating the redshift of the νNH involved in hydrogen bonds or hydrogen bond-like interactions.

$$\Delta\nu\text{NH}/\text{cm}^{-1} = 0.011[r_{\text{H}\cdots\text{H}}/\text{nm}]^{-6.1} \quad (1)$$

where ΔνNH is the redshift induced by the hydrogen bond and $r_{\text{H}\cdots\text{H}}$ is the hydrogen bond distance (NH···O=X in 1-TE-BZT). The second Eq. (2) correlates the redshift estimated in equation 1 with the interaction enthalpy, thus describing the energies of the intramolecular hydrogen bondings involving the NH group of 1H conformers.

$$\Delta H^2 = 1.92 * [\Delta(\nu\text{NH}) - 40] \quad (2)$$

where ΔH is the interaction enthalpy (in kJ mol⁻¹) and ΔνNH, the redshift obtained from Eq. (1). Table 1 also shows the values corresponding to ΔνNH) and –ΔH. When compared the hydrogen bond energies of 1-TE-BZT with those of other compounds [42], it can be concluded that hydrogen bonds in 1-TE-BZT are rather weak. Eventhough, the hydrogen bond-like interactions in 1-TE-BZT are the main factors contributing for the stabilisation of the 1H conformers, and the relative energies of 1H conformers can be mainly explained in terms of hydrogen bonds distances. However, other factors such as repulsions between negatively charged atoms or slight sterical hindrances (i.e.: the methyl group addressed to the SO₂ is a slightly destabilising factor if compared with the hydrogen atom) should also be considered.

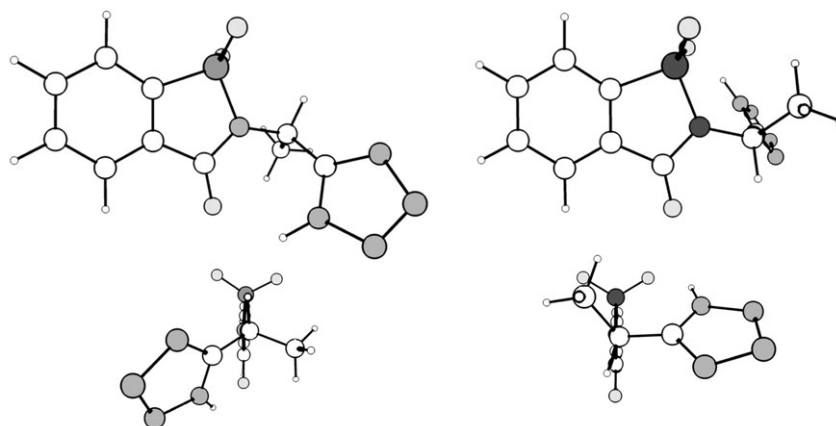
According to preliminary calculations (not presented) performed at a lower level of theory, all the barriers of interconversion between the 1H conformers were higher than 30 kJ mol⁻¹. Hence, considering the low relative energies between the three most stable 1H conformers and the high barriers of interconversion, these three forms can in principle be isolated experimentally in the argon matrices (note that due to the higher relative energy, 1H_GSk form does not have experimental relevance).

As explained in the previous paragraph, none of the conformers of 2H tautomer bears hydrogen bonds-like interactions. The position of H₂₈ in the tetrazole ring (2H position), oriented to the opposite side of the benzisothiazole ring precludes the formation of these stabilising forces, thus explaining the higher relative energies of 2H conformers and consequently, their non-experimental relevance.

3.3. Infrared spectra of the matrix-isolated compound

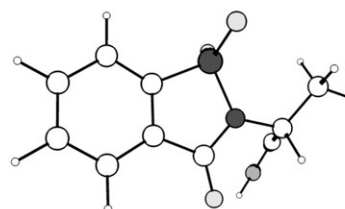
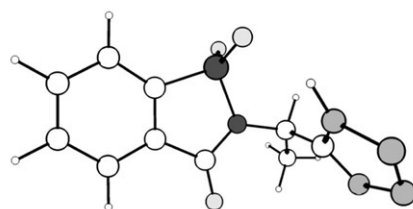
1-TE-BZT has 78 fundamental vibrations, all active in the infrared. The infrared spectrum of 1-TE-BZT isolated in an argon matrix with the substrate kept at 15 K during the matrix deposition is presented in Fig. 4, together with the calculated spectrum of the 1H_GSk' form. It must be considered that 1-TE-BZT is a molecule composed of 28 atoms, 16 of them belonging to the rigid benzisothiazole ring. This explains the reason why the bands corresponding to this ring are in general highly overlapped for the different 1H conformers, with the exception of the infrared modes relative to the oxygen atoms, for which the position strongly depend on the strength of the hydrogen bonds they establish. This fact makes especially difficult the assignment of bands to each of the most stable conformers. For this reason, we decided to simplify the

Tautomer 1H



1H_G'Sk'
0.00 kJ mol⁻¹
(-66.0°; -129.0°)

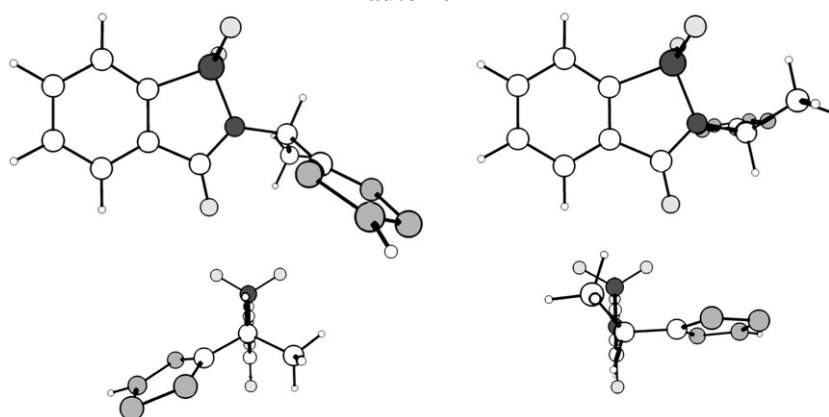
1H_GSk'
2.59 kJ mol⁻¹
(92.5°; -142.9°)



1H_G'Sk
4.25 kJ mol⁻¹
(-71.1°; 135.3°)

1H_GSk
8.30 kJ mol⁻¹
(73.7°; 118.8°)

Tautomer 2H



2H_G'G'
7.12 kJ mol⁻¹
(-63.1°; -16.8°)

2H_GG'
8.60 kJ mol⁻¹
(89.1°; -22.8°)

Fig. 3. DFT(B3LYP)/6-311++G(3pd,3df) optimised structures of the conformers of 1-TE-BZT. Two perspectives are provided, one with the viewpoint placed above the ring and the other with the viewpoint along the major axis of the molecule. The C₉–N₈–C₁₇–C₂₃ and N₈–C₁₇–C₂₃–N₂₄ dihedral angles are indicated in parentheses and zero point corrected relative energies are also shown.

assignments of bands in the freshly deposited matrix and, considering the nice fitting of the calculated 1H_GSk' spectrum with the

deposited compound in an argon matrix we performed the assignment of experimental bands to this low energy form (Table 2). In

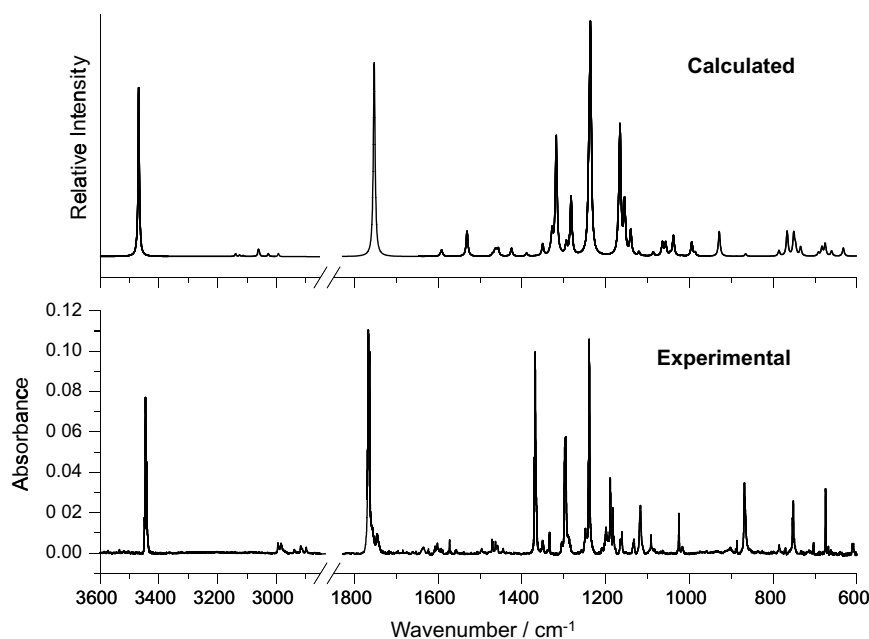


Fig. 4. Experimental infrared spectra (3600–600 cm^{-1} spectral range) of 1-TE-BZT in argon matrix (15 K), and DFT(B3LYP)/6-311++G(3pd,3df) calculated spectrum for conformer (*1H_GSk'*). The calculated spectrum was simulated using Lorentzian functions with full width at half maximum of 5 cm^{-1} with wavenumbers being scaled by 0.978.

agreement with the estimations reported in Section 3.2, the experimental observation of the ν_{NH} band at frequencies higher than 3400 cm^{-1} (Table 2) also indicates that the hydrogen bond-like interaction is relatively weak.

It must be underlined that the conformation of 1-TE-BZT as reagent does not influence the nature of the photoproducts observed after irradiation. Table S2 provides the complete set of frequencies of all the 1-TE-BZT isomers.

3.4. UV-irradiation experiments

The photochemistry of different matrix isolated benzothiazoles and tetrazoles has been addressed by our groups. Photodecomposition of tetrazoles involves cleavage of the tetrazolyl ring, leading to a variety of photoproducts, including azides, isocyanates or aziridines. The photochemistry of tetrazoles was also shown to be influenced by the chemical nature and conformational flexibility of substituents linked to the heterocycle, which may favour or exclude certain reaction channels, and also determine the relative amount of the final photoproducts [15–21].

In order to investigate the photochemical decomposition, the as-deposited compound was irradiated with UV light as described in Section 2.2 (Infrared spectroscopy and photochemical experiments). The wavelength used for irradiation has been chosen on the basis of the UV–Vis spectrum of 1-TE-BZT, which shows two absorption maxima at 275 and 385 nm (see in Fig. S1, the UV–Visible spectra of the compound in ethanol solution at room temperature). Irradiation at 385 nm did not stimulate any photofragmentation. After each irradiation, the sample was monitored by recording its infrared spectrum.

Irradiation at 275 nm induces a prompt decrease of the 1-TE-BZT bands with a concomitant observation of other new bands corresponding to the photoproducted species. Fig. 5 shows the spectroscopic results, obtained by subtracting the spectrum of the as-deposited matrix from the spectrum of the matrix irradiated during 40 min with laser ($\lambda = 275 \text{ nm}$), when almost all reagent was consumed. In Fig. 5, negative bands correspond to the

consumed reagent (1-TE-BZT) and the positive ones, to the photoproducts.

The calculated spectra for *1H_GSk'* and those of the photoproducts are also shown for comparison. A schematic summary of the observed photoprocesses is given in Fig. 6. The following photochemical pathways are proposed: (a) N_2 extrusion with the concomitant production of 2-[1-(1*H*-diaziren-3-yl)ethyl]-1,2-benzisothiazol-3(2*H*)-one 1,1-dioxide (BZT-DZ); (b) production of azide (N_3H) and 2-(1,1-dioxido-3-oxo-1,2-benzisothiazol-2(3*H*)-yl)propanenitrile (BZTC $\equiv\text{N}$); (c) decarbonylation and ejection of azide (N_3H) to give 7-thia-8-azabicyclo[4.2.0] octa-1,3,5-triene 7,7 dioxide (TAOTD) and propene–nitrile. The complete assignment of the bands observed for the different photoproducts is given in Table 3, together with available previously reported values for the isolated compounds [43–45] and calculated data.

In Pathway (a), 1-TE-BZT ejects molecular nitrogen to give BZT-DZ. The ejection of molecular nitrogen is a common photodecomposition pathway in tetrazoles isolated in rare gas matrices [15–21]. BZT-DZ has two rotational axes [N–C, and C–C(N_2H)] that can give rise to at least six different conformers (I, II, III, IV, V, VI), all of them with relative energies below 1.14 kJ mol^{-1} (Table S3). The most distinctive bands of this photoproduct could be identified in the irradiated matrices. As mentioned before for 1-TE-BZT, also in BZT-DZ, 16 out of 26 atoms belong to the benzothiazole ring. This means that 42 out of 72 vibrational modes are related with this ring. This fact explains the high overlap of bands corresponding to the different conformers of BZT-DZ, and also the overlap with bands corresponding to BZTC $\equiv\text{N}$ [produced in Pathway (b)]. However, the observation of some bands in relatively clean regions, such as those corresponding to $\nu(\text{N}=\text{N})$ of conformers I and V, at 1822 and 1803 cm^{-1} provides evidence for the photoproduction of BZT-DZ. Note also that the most intense band of the BZT-DZ is that of $\nu(\text{C}=\text{O})$ vibrational mode. This band fits nicely the calculated spectrum and represents another proof of the presence of BZT-DZ in the irradiated matrix. However, the low intensity of the $\nu(\text{C}=\text{O})$ experimental band indicates that Pathway (a) is not a major photodecomposition pathway of 1-TE-BZT. The assignment of the most relevant bands corresponding to this photoproduct is

Table 2

Experimental and calculated [B3LYP/6-311++G(3df,3pd); scaled by 0.978] vibrational frequencies (ν ; cm^{-1}) and calculated IR intensities (I , km mol^{-1}) for the 1H_GSk' form of 1 TE-BZT isolated in argon matrix.^a

Approximate description	Calculated 1H_GSk'		Observed ^b
	ν	I	
$\nu(\text{N-H})$	3468.5	262.6	3449.1/3445.6/3442.2
$\nu(\text{C-H})\text{ph}$	3138.8	4.2	2995.3/2984.7
$\nu(\text{C-H})\text{ph}$	3135.8	0.1	2939.2/2917.2
$\nu(\text{C-H})\text{ph}$	3125.0	2.2	2913.0/2899.5
$\nu(\text{C-H})\text{ph}$	3112.9	1.3	
$\nu(\text{CH}_3)\text{as}''$	3061.3	8.1	
$\nu(\text{CH}_3)\text{as}'$	3058.8	5.8	
$\nu(\text{CH}_{18})$	3027.3	4.3	
$\nu(\text{CH}_3)\text{s}$	2983.8	5.0	
$\nu(\text{C=O})$	1753.6	302.4	1766.9/1764.4
$\nu(\text{CC})\text{ph}$	1595.3	1.7	1602.0
$\nu(\text{CC})\text{ph}$	1591.6	9.6	1593.2
$\delta(\text{N-H}) + \nu(\text{C}_{17}-\text{C}_{23})$	1531.1	39.2	1573.1
$\gamma(\text{CH}_3)''$	1470.1	3.5	1496.2
$\delta(\text{C-H})\text{ph}$	1464.4	8.0	1471.4/1470.3
$\delta(\text{CH}_3)\text{as}''$	1461.0	7.3	1469.6
$\delta(\text{C-H})\text{ph}$	1456.5	10.9	
$\text{sci}(\text{C}_{23}-\text{C}_{17}-\text{H}_{18})$	1424.9	12.3	1463.4/1458.8
$\delta(\text{CH}_3)\text{s}$	1388.9	4.4	1445.0
$\delta(\text{N-H}) + \nu(\text{NN})\text{t} + \delta(\text{C-H}_{18})$	1350.5	18.0	1351.0
$\delta(\text{C-H}_{18})'' + \nu(\text{CC})\text{ph} + \delta(\text{N-H})$	1332.7	4.0	1334.0
$\delta(\text{C-H}_{18}) + \nu(\text{CC})\text{ph}$	1328.0	34.2	1370.8
$\nu(\text{SO}_2)\text{as}$	1318.1	185.1	1368.4/1361.4
$\delta(\text{C-H}_{18})'$	1294.1	18.2	1304.5
$\nu(\text{CC})\text{ph}$	1282.6	91.0	1297.2/1295.5
$\nu(\text{NN})\text{t} + \delta(\text{N-H})$	1239.9	106.9	1248.1/1245.2/1239.1
$\delta(\text{C-H})\text{ph} + \nu(\text{C}_2-\text{C}_9) + \nu(\text{C}_9-\text{N}_8)$	1236.3	329.2	
$\delta(\text{C-H})\text{ph} + \nu(\text{N}_8-\text{C}_{17})$	1169.6	20.9	1199.0/1189.1/1187.0
$\nu(\text{SO}_2)\text{s} + \delta(\text{C-H})\text{ph}$	1165.8	197.0	
$\delta(\text{C-H})\text{ph} + \nu(\text{SO}_2)\text{s}$	1154.7	81.1	1183.0/1180.6
$\delta(\text{CH}_3)\text{as}'$	1140.2	37.9	1165.1/1161.3
$\delta(\text{CH}_3)\text{as}''$	1120.4	5.7	1152.0
$\delta(\text{CH}_3)\text{as}''' + \delta(\text{NNN})$	1086.3	6.2	n.o.
$\nu(\text{NN})\text{t} + \delta(\text{NNN})\text{t}$	1064.4	20.7	1135.0/1132.6
$\nu(\text{NN})\text{t} + \delta(\text{CH}_3)\text{as}'''$	1056.6	20.2	1117.0
$\delta(\text{C-C})\text{ph}$	1045.9	3.3	n.o.
$\nu(\text{NN})\text{t}$	1038.2	31.7	1091.4
$\delta(\text{C-C})\text{ph}$	1017.8	0.8	n.o.
$\gamma(\text{C-H})\text{ph}$	1003.3	0.0	n.o.
$\gamma(\text{CH}_3)'$	994.3	21.9	1025.0
$\nu(\text{NN})\text{t}$	986.4	5.2	1016.5
$\gamma(\text{C-H})\text{ph}$	968.4	0.4	n.o.
$\delta(\text{C}_{17}\text{C}_{19}\text{C}_{23}\text{H}_{18})$	928.5	38.4	868.6/867.1
$\gamma(\text{C-H})\text{ph}$	886.9	0.2	n.o.
δ Skeletal	865.6	3.8	835.1
$\gamma(\text{CH})\text{ph}$	785.9	8.4	786.0
$\gamma(\text{N-H}_{28})$	766.3	38.3	753.9
$\gamma(\text{C-H})\text{ph}$	750.4	34.1	751.9
$\gamma(\text{NN})\text{t}$	746.2	13.0	749.3
$\delta(\text{CC})\text{ph}$	734.0	13.8	733.4/727.7
$\delta(\text{CC})\text{ph} + \nu(\text{CS})$	691.4	5.2	704.3/703.3
$\gamma(\text{NH}_{28}) + \gamma(\text{NN})\text{t}$	683.1	13.4	674.3
δ Skeletal	675.4	18.9	
δ Skeletal	660.0	7.7	663.0
δ Skeletal	632.0	12.7	611.2/608.8
$\gamma(\text{SO}_2)$	573.2	52.6	592.7
$\omega(\text{SO}_2)$	534.8	38.0	533.6
τ Skeletal	526.7	41.8	524.4
δ Skeletal	497.5	14.7	508.7

^a ν , stretching, δ , bending, γ , rocking, τ , torsion, ω , wagging, sci , scissoring, s , symmetric, as , anti-symmetric, t , tetrazole ring, n.o. , not observed. The infrared region below 500 cm^{-1} was not investigated; extensively delocalised modes are designated generally as skeletal bending (δ skeletal). See Fig. 2 for atom numbering.

also shown in Table 3. Due to the high overlap of bands, the assignment of BZT-DZ has been performed only on the most stable form I. Only in the regions where a doubtless assignment could be made, other forms were also considered [i.e. $\nu(\text{C=N})$, $\nu(\text{C=O})$]. In Pathway (b), the most intense band of azide was observed in the irradiated spectrum: 2142 cm^{-1} : $\nu(\text{N=N=N})\text{as}$. This band was observed in the spectrum of azide isolated in argon matrix at 2140 cm^{-1} [43]. The presence of azide in the photolysed matrix is reinforced by

the observation of the band due to the $\delta(\text{N-H})$ mode at $ca. 1127 \text{ cm}^{-1}$. According to the literature [43], this band occurs at 1150 cm^{-1} in the argon isolated azide. The deviation in the observed azide $\delta(\text{N-H})$ band compared with the literature value for the sole matrix-isolated compound indicates that once produced from fragmentation of 1-TE-BZT, azide interacts in the same matrix cage with the other compounds produced in this path (BZTC=N) and in Pathway (c), where azide is also produced. The

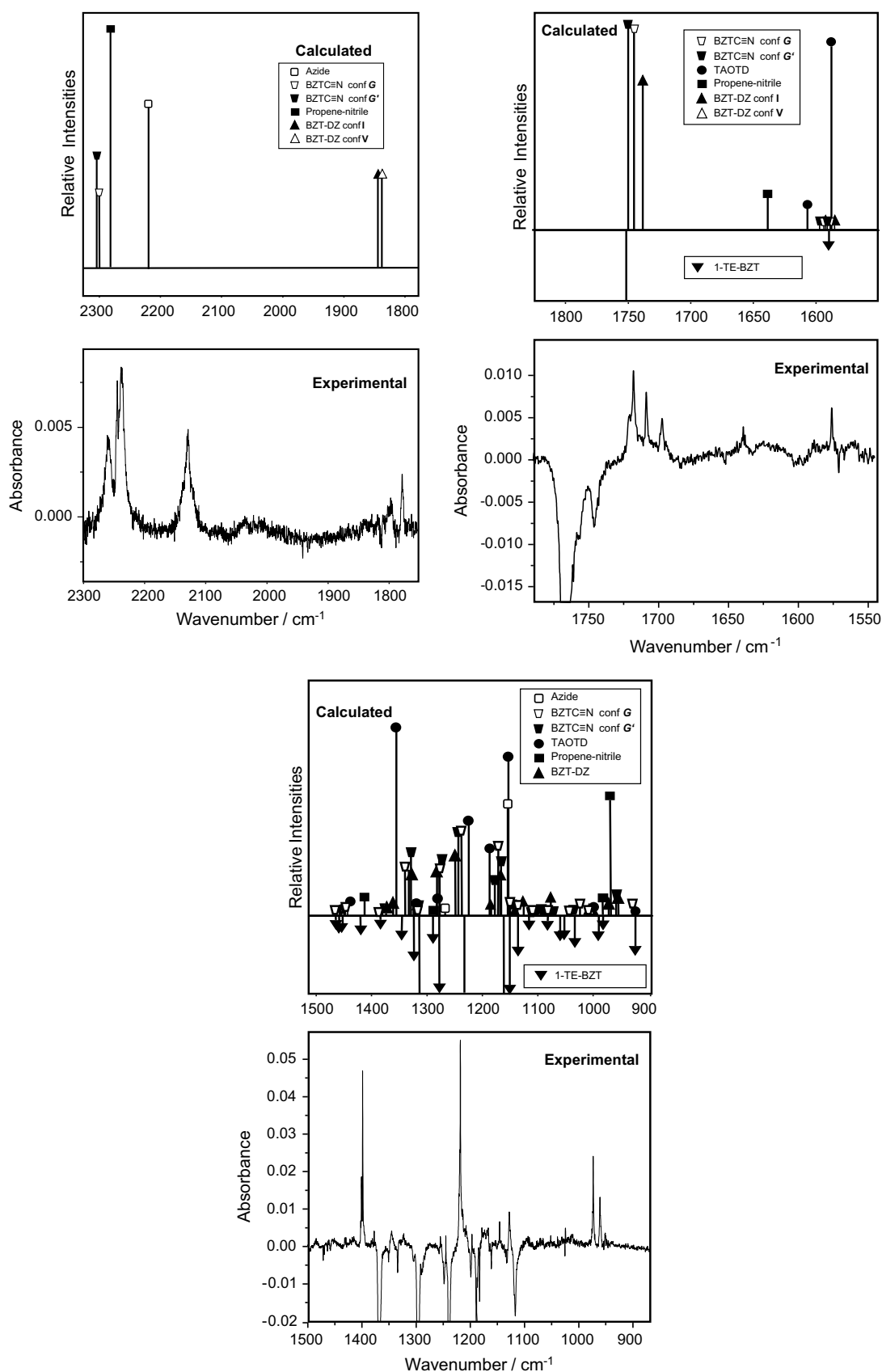


Fig. 5. (Bottom) Infrared difference spectrum [(irradiated matrix by UV light; $\lambda = 275$ nm; 40 min) minus (as-deposited matrix spectrum)] of 1-TE-BTZ in an argon matrix. Assignments for the bands due to photoproducts (pointing up) are given in Table 3. (Top) Simulation of the infrared difference spectrum shown in the bottom panel of the figure, based on the DFT(B3LYP)/6-311++G(3pd,3df) calculated spectra for 1-TE-BTZ (*1H_GSK'*; bands pointing down) and for its photoproducts [Azide, BZTC≡N (conformer *G* and conformer *G'*), TAOTD, propene-nitrile and BZT-DZ (conformer *I* and *V*)]. The intensities of the individual spectra were multiplied by different factors to obtain a better simulation of the experimental difference spectra.

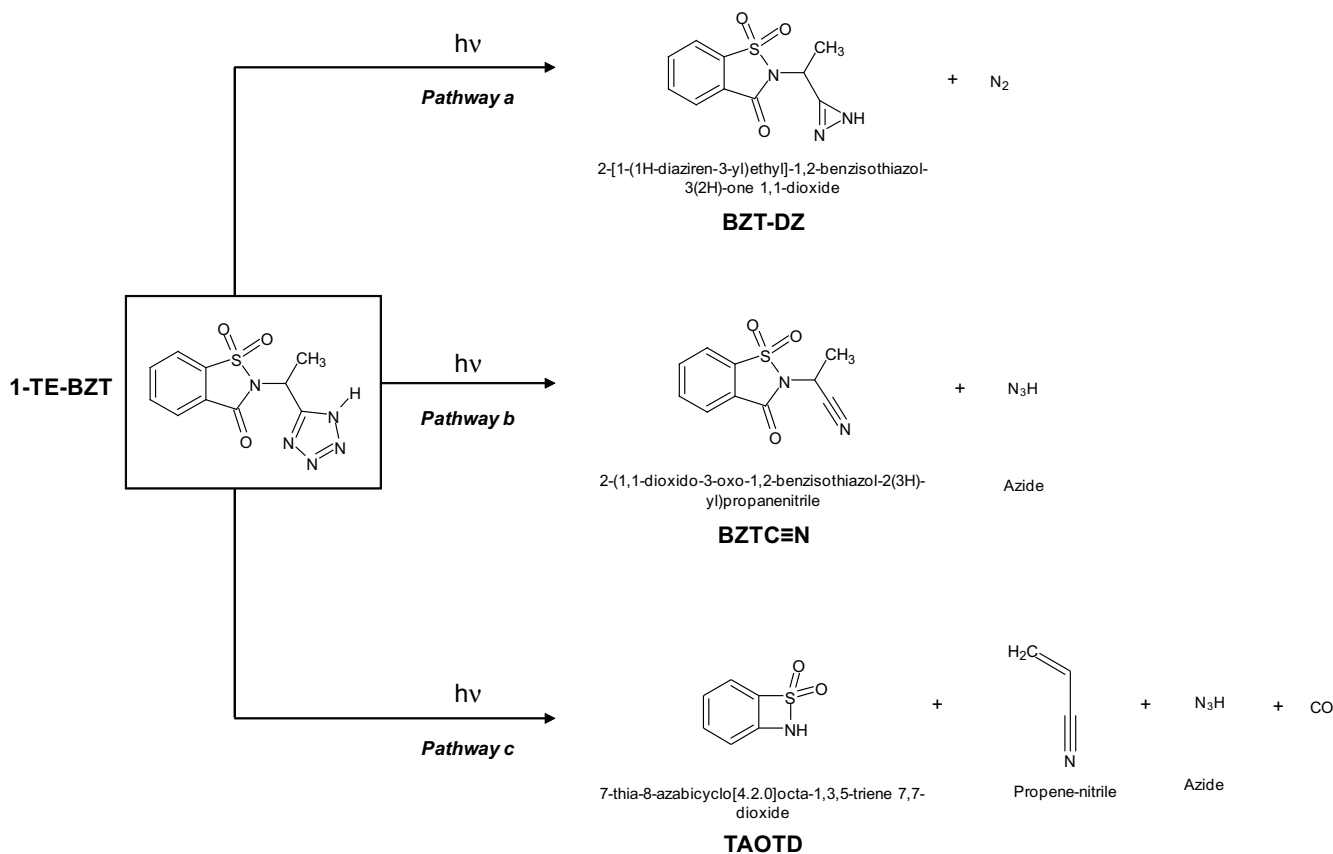


Fig. 6. Proposed reaction pathways resulting from irradiation of 1-TE-BZT monomer isolated in argon matrix.

hydrogen bonds connecting the different complexes, explain the shift of the $\delta(\text{N-H})$ vibrational mode with regard to the matrix isolated pure azide.

The other photoproduct obtained in Pathway (b) is BZTC≡N. According to calculations at the DFT(B3LYP)/6-311++G(3df,3pd) level, only two conformers were found to correspond to minima structures. They differ in the orientation of the CNCC dihedral angle: *G* (CNCC = 91.7) and *G'* (CNCC = -59.5). Their energies are very close (the relative energies of *G* and *G'* forms are 0 and 0.07 kJ mol⁻¹, respectively) and the barrier of interconversion is ca. 20 kJ mol⁻¹. The bands at 2248 and 2241 cm⁻¹ can be assigned to the $\nu(\text{C}\equiv\text{N})$ vibrational mode of these two conformers (Fig. 5 and Table 3). Note that the low experimental intensity of bands intrinsically strong [i.e. $\nu(\text{C}=\text{O})$, $\nu(\text{S}=\text{O})$ symmetric and asymmetric], indicates that Pathway (b) is neither a major photodecomposition Pathway.

In Pathway (c), 1-TE-BZT decarbonylates to give TAOTD, propene-nitrile and azide. The carbon monoxide band is typically observed at 2138 cm⁻¹ in argon matrices and in this case is overlapped with the $\nu(\text{N}=\text{N}=\text{N})$ band of azide, produced in Pathway (b) and also in this Pathway. The available information about propene-nitrile isolated in argon matrices [44] and calculations at the DFT(B3LYP)/6-311++G(3df,3pd) level of theory aided the confirmation of propene-nitrile in the photolysed matrix (see for example experimental bands at 975 and 973 cm⁻¹, ascribed to the $\omega(\text{CH}_2)$ vibrational mode. The opening of the benzisothiazole ring gives TAOTD. The most intense bands of this compound occur in the 1400–950 cm⁻¹ range and fit nicely the calculated spectrum. The experimental intensity of the bands corresponding to the photoproducts generated in Pathway (c) is higher than that of the photoproducts of Pathways (a) and (b). This fact is particularly

evident in the carbonyl region, where only products from (a) and (b) are observed. In the region 1400–950 cm⁻¹, photoproducts obtained in all the three pathways are observed. However, the most intense bands observed in this region in the photolysed matrices can be ascribed to photoproducts of Pathway (c) (Fig. 5 and Table 3). This fact allows us to consider this pathway as the preferred photodecomposition channel for 1-TE-BZT.

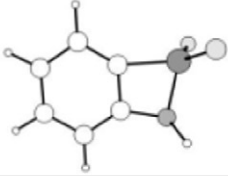
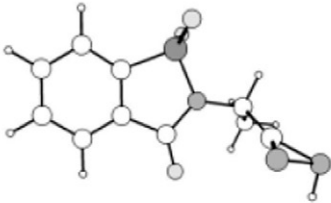
4. Conclusions

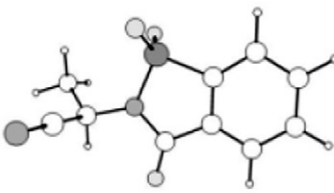
In this work, the alkyl-linked saccharyl-tetrazole conjugate 1-TE-BZT has been synthesised and studied from the view point of its molecular structure and vibrational spectra using matrix isolation FTIR spectroscopy. All experimental results have been supported by quantum chemical calculations at a high level of theory [DFT(B3LYP)/6-311++G(3df,3pd)].

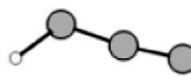
In 1-TE-BZT, the hydrogen atom bound to the tetrazole ring gives rise to two different tautomers, 1*H* and 2*H*. In addition, the two rotational axes of 1-TE-BZT can give rise to different conformational isomers within each tautomeric form. As a whole, the theoretical calculations led to the identification of four conformers 1*H* and two conformers 2*H*. The experimental spectrum obtained from the as deposited compound could be assigned to conformer 1*H*_{GSK'}.

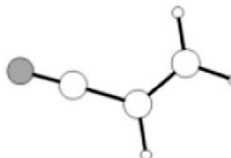
The photochemistry of the saccharyl-tetrazole conjugate 1-TE-BZT has also been addressed. However, the complexity of the studied compound makes difficult the analysis of the experimental information, the interpretations not being conclusive. In this context, considering the high reactivity of the tetrazole ring and the photostability of the benzisothiazole moiety, three photolysis pathways were proposed to interpret the photodecomposition

Table 3
Experimental and calculated [B3LYP/6-311++G(3df,3pd); scaled by 0.978] vibrational frequencies (ν ; cm^{-1}) and calculated IR intensities (I , km mol^{-1}) for the observed photoproducts of 1-TE BZT monomer isolated in argon matrix.^a

Approximate Description	Sym	Conformer	Observed	Calculated		Literature Data								
			ν	ν	I	ν	Ref							
TAOTD	C1													
									$\nu(\text{C-C})_{\text{ph}}$	A	1578	1589.2	40.6	
									$\delta(\text{C-H})_{\text{ph}}$	A	1432/1430	1446.7	18.8	
									$\nu(\text{SO}_2)_{\text{as}}$	A	1402 / 1400 / 1399	1358.9	213.8	
									$\delta(\text{C-H})_{\text{ph}}$	A	1323	1328.7	15.2	
									$\delta(\text{C-H})_{\text{ph}}$	A	1128	1157.2	50.1	
									$\nu(\text{SO}_2)_{\text{s}}$	A		1156.4	133.4	
									$\delta(\text{C-H})_{\text{ph}}$	A	800	755.8	90.2	
									$\delta(\text{C-H})_{\text{ph}}$	A	768	738.7	29.0	
									$\gamma(\text{N-H})$	A	631	628.7	109.0	
									$\gamma(\text{SO}_2)$	A	607	598.2	61.9	
									$\omega(\text{SO}_2)$	A	553	544.9	57.4	
BZT-DZ	C1													
									$\nu(\text{C=N})$	A	I	1822	1845.2	18.7
											V	1803	1839.3	19.1
									$\nu(\text{C=O})$	A	I	1709	1741.4	294.3
											V	1698	1737.2	328.8
									$\nu(\text{SO}_2)_{\text{as}}$	A	I	1377	1338.7	182.8
									$\delta(\text{C-H})_{\text{ph}}$	A	I	1326	1328.8	15.0
									$\delta(\text{N-H})$	A			1324.5	21.7
									$\delta(\text{C-H})_{\text{ph}}$	A	I	1292	1288.4	104.5
													1286.6	87.6
									$\delta(\text{C-H})_{\text{ph}}$	A	I	1255	1254.8	217.3
									$\delta(\text{C-H})_{\text{ph}}$	A	I	1197	1189.8	50.6
									$\nu(\text{SO}_2)_{\text{s}}$	A	I	1167	1175.0	174.3
									$\delta(\text{C-H})_{\text{ph}}$	A	I	1146	1160.0	29.4
									$\delta(\text{N-H})$	A	I	976	978.2	23.1
									$\nu(\text{N-C})$	A	I	959 (sh)	960.4	57.6
									$\gamma(\text{CH})_{\text{ph}}$	A	I	803 (sh)	786.5	7.1
									$\gamma(\text{CH}_3)'$	A	I	803 (sh)	781.0	12.8
$\gamma(\text{C-H})_{\text{ph}}$	A	I	801 (sh) / 800	749.9	39.3									
$\delta(\text{C-C})_{\text{ph}}$	A	I	767 (sh)	733.7	9.4									
C_4 ph out of plane	A	I	662	674.3	24.6									

BZTC≡N		C1				
$\nu(\text{C-N})$	A	G' G	2263	{ 2306.0 2302.5	{ 0.8 0.6	
$\nu\text{C=O}$	A	G' G	1722 1718	1747.3 1745.3	298.9 333.6	
$\nu(\text{SO}_2)\text{as} + \delta(\text{N-C-H})$	A	G	1377	1344.8	148.9	
$\nu(\text{SO}_2)\text{as} + \delta(\text{N-C-H})$	A	G		1341.3	58.2	
$\nu(\text{SO}_2)\text{as}$	A	G'		1337.0	182.6	
$\delta(\text{C-H})\text{ph}$	A	G'	1255	1251.6	257.6	
	A	G	1245	1241.8	294.7	
$\nu(\text{SO}_2)\text{as}$	A	G	1145	1175.8	232.4	
	A	G'		1174.7	149.8	
$\omega(\text{SO}_2)$	A	G	575	568.7	42.2	
	A	G'		567.0	39.6	

Azide		Cs					
$\nu(\text{N=N=N})\text{as}$	A'		2139	2220.0	408.2	2140	[43]
$\delta(\text{N-H})$	A'		1128	1159.0	223.5	1150	[43]

Propene-nitrile		Cs					
$\nu(\text{C-C=N})\text{as}$	A'		2249 / 2242	2281.9	9.6		
$\nu(\text{C=C})$	A'		1639	1638.2	1.5		
$\delta(\text{CH}_2)\text{as}$	A'		1417 / 1415	1418.3	7.2		
$\omega(\text{CH=CH}_2)$	A''		973 / 960	974.8	48.2	974 / 968 / 956 / 954 / 953	[44]
$\gamma(\text{CH}_2) + \nu(\text{C-C})$	A'		856	863.1	1.6		
$\gamma(\text{C-C})$	A''		707	698.3	11.5		

Carbon monoxide						
$\nu(\text{C=O})$	A		2138		2138	[45]

^a Only the investigated bond are shown.

ν , stretching, δ , bending, γ , rocking, s, symmetric, as, anti-symmetric, ph, phenyl; sh, shoulder.

occurred upon matrix irradiation with UV $\lambda = 275$ nm: (a) ejection of molecular nitrogen to give at least six different conformers of BZT-DZ; (b) cleavage of the tetrazole ring to give azide and BZTC≡N, and (c) decarbonylation of 1-TE-BZT to give propene-nitrile, azide and TAOTD. The comparison of the relative intensities of the bands of the photoproducts obtained from the three channels allowed us to conclude that Pathway (c) is the preferred one.

Although with low efficiency, this was the first time that photocleavage of the benzothiazole ring in rare gas matrices

was observed. The pathway proposed opens up several possibilities in the interpretation of the molecular mechanisms leading to photodecomposition of such stable aromatic compounds. The fact that this particular saccharyl derivative is more prone to ring photocleavage than the ones that we previously attempted to photolyse, namely alkyl and allyl saccharyl ethers, may be ascribed to the powerful electron-withdrawing effect of the tetrazole substituent which deviates electron density from the ring, weakening the C–C bond to the carbonyl and subsequently favouring α

cleavage. We now aim at exploring further the photochemistry of benzisothiazoles.

Acknowledgements

The authors are grateful to Fundação para a Ciência e Tecnologia and FEDER (Projects PTDC/QUI/67674/2006 and PTDC/QUI/71203/2006), bilateral cooperation grant (FCT-MinCyT PO/09/18) and CYTED (Network 108RT0362) for financial support. A.G.Z. is member of the Research Career CONICET, Argentina. A.B., B.M.G. and L.D. acknowledge FCT for the award of postdoctoral and doctoral Grants (SFRH/BPD/66154/2009, SFRH/BPD/44689/2008 and SFRH/BD/62090/2009, respectively). We would also like to acknowledge the Milipeia Computer Centre (University of Coimbra), research project "Computação Avançada em Espectroscopia Molecular".

Appendix A. Supplementary material

Supplementary data associated with this article can be found in the online version, at <http://dx.doi.org/10.1016/j.molstruc.2012.04.081>.

References

- [1] Y. Tamura, F. Watanabe, T. Nakatani, K. Yasui, M. Fuji, T. Komurasaki, H. Tsuzuki, R. Maekawa, T. Yoshioka, K. Kawada, K. Sugita, M. Ohtani, *J. Med. Chem.* 41 (1998) 640.
- [2] H. Zhao, Z.-R. Qu, H.-Y. Ye, R.-G. Xiong, *Chem. Soc. Rev.* 37 (2008) 84.
- [3] E.J. Baran, V.T. Yilmaz, *Coord. Chem. Rev.* 250 (2006) 1980.
- [4] M.L.S. Cristiano, R.A.W. Johnstone, P.J. Price, *J. Chem. Soc. Perkin Trans. 1* (1996) 1453.
- [5] N.C.P. Araújo, A.F. Brigas, M.L.S. Cristiano, L.M.T. Frija, E.M.O. Guimarães, R.M.S. Loureiro, *J. Mol. Catal. A: Chem.* 215 (2004) 113.
- [6] L.M.T. Frija, M.L.S. Cristiano, E.M.O. Guimarães, N.C. Martins, R.M.S. Loureiro, J. Bikley, *J. Mol. Catal. A: Chem.* 242 (2005) 241.
- [7] R.A.W. Johnstone, A.H. Wilby, I.D. Entwistle, *Chem. Rev.* 85 (1985) 129.
- [8] J.V. Barkley, M.L.S. Cristiano, R.A.W. Johnstone, R.M.S. Loureiro, *Sect. C: Cryst. Struct. Commun.* 53 (1997) 383.
- [9] M.L.S. Cristiano, A.F. Brigas, R.A.W. Johnstone, R.M.S. Loureiro, P.C.A. Pena, *J. Chem. Res. (S)* (1999) 704.
- [10] N.C.P. Araújo, P.M.M. Barroca, J.F. Bickley, A.F. Brigas, M.L.S. Cristiano, R.A.W. Johnstone, R.M.S. Loureiro, P.C.A. Pena, *J. Chem. Soc. Perkin Trans. 1* (2002) 1213.
- [11] R. Almeida, A. Gómez-Zavaglia, A. Kaczor, M.L.S. Cristiano, M.E.S. Eusébio, T.M.R. Maria, R. Fausto, *Tetrahedron* 64 (2008) 3296.
- [12] A. Kaczor, L. Proniewicz, R. Almeida, A. Gómez-Zavaglia, M.L.S. Cristiano, A.M. Matos Beja, M. Ramos Silva, R. Fausto, *J. Mol. Struct.* 892 (2008) 343.
- [13] L.M.T. Frija, R. Fausto, R.M.S. Loureiro, M.L.S. Cristiano, *J. Mol. Catal. A: Chem.* 305 (2009) 142.
- [14] A. Gómez-Zavaglia, A. Ismael, L.L.L. Cabral, A. Kaczor, J.A. Paixão, R. Fausto, M.L.S. Cristiano, *J. Mol. Struct.* 1003 (2011) 103.
- [15] A. Gómez-Zavaglia, I.D. Reva, L.M.T. Frija, M.L.S. Cristiano, R. Fausto, *J. Phys. Chem. A* 109 (2005) 7967.
- [16] A. Gómez-Zavaglia, I.D. Reva, L.M.T. Frija, M.L.S. Cristiano, R. Fausto, *J. Photochem. Photobiol. A* 179 (2006) 243.
- [17] A. Gómez-Zavaglia, I.D. Reva, L.M.T. Frija, M.L.S. Cristiano, R. Fausto, *J. Mol. Struct.* 786 (2006) 182.
- [18] A. Gómez-Zavaglia, I.D. Reva, L.M.T. Frija, M.L.S. Cristiano, R. Fausto, *J. Photochem. Photobiol. A* 180 (2006) 175.
- [19] L.M.T. Frija, I.D. Reva, A. Gómez-Zavaglia, M.L.S. Cristiano, R. Fausto, *J. Phys. Chem. A* 111 (2007) 2879.
- [20] L.M.T. Frija, I.D. Reva, A. Gómez-Zavaglia, M.L.S. Cristiano, R. Fausto, *Photochem. Photobiol. Sci. (PPS)* 6 (2007) 1170.
- [21] A. Gómez-Zavaglia, I.D. Reva, L.M.T. Frija, M.L.S. Cristiano, R. Fausto, *Chem. Phys. Res. J.* 1 (2009) 221.
- [22] A. Ismael, M.L.S. Cristiano, R. Fausto, A. Gómez-Zavaglia, *J. Phys. Chem. A* 114 (2010) 13076.
- [23] I. Elghamry, D. Döpp, *Tetrahedron Lett.* 42 (2001) 5651.
- [24] D.W. Cho, S.W. Oh, D.U. Kim, H.J. Park, J.Y. Xue, U.C. Yoon, P.S. Mariano, *Bull. Korean Chem. Soc.* 31 (2010) 2453.
- [25] I. Elghamry, D. Döpp, G. Henkel, *Synthesis* 8 (2001) 1223.
- [26] D. Döpp, *Int. J. Photoenergy* 3 (2001) 41.
- [27] R. Krishnan, J.S. Binkley, R. Seeger, J.A. Pople, *J. Chem. Phys.* 72 (1980) 650.
- [28] A.D. McLean, G.S. Chandler, *J. Chem. Phys.* 72 (1980) 5639.
- [29] M.J. Frisch, J.A. Pople, J.S. Binkley, *J. Chem. Phys.* 80 (1984) 3265.
- [30] T. Clark, J. Chandrasekhar, G.W. Spitznagel, P.V.R. Schleyer, *J. Comput. Chem.* 4 (1983) 294.
- [31] P.M.W. Gill, B.G. Johnson, J.A. Pople, M.J. Frisch, *Chem. Phys. Lett.* 197 (1992) 499.
- [32] A.D. Becke, *Phys. Rev. A* 38 (1988) 3098.
- [33] C.T. Lee, W.T. Yang, R.G. Parr, *Phys. Rev. B* 37 (1988) 785.
- [34] P. Pulay, *J. Comput. Chem.* 3 (1982) 556.
- [35] GAMESS, version R1 (1-October-2010), M. Schmidt, K. Baldridge, J. Boatz, S.T. Elbert, M.S. Gordon, J.H. Jensen, S. Koseki, N. Matsunaga, K.A. Nguyen, S.J. Su, T.L. Windus, M. Dupuis, J. Montgomery, *J. Comput. Chem.* 14 (1993) 1347.
- [36] A. Gómez-Zavaglia, A. Kaczor, R. Almeida, M.L.S. Cristiano, M.E.S. Eusébio, T.M.R. Maria, P. Mobili, R. Fausto, *J. Phys. Chem. A* 113 (2009) 3517.
- [37] I.G. Binev, B.A. Stamboliyska, E.A. Velcheva, *Spectrosc. Acta Part A – Mol. Biomol. Spectrosc.* 52 (1996) 1135.
- [38] Y.I. Binev, C.T. Petkov, L. Pejov, *Spectrosc. Acta Part. A – Mol. Biomol. Spectrosc.* 56 (2000) 1949.
- [39] P. Naumov, G. Jovanovski, *Struct. Chem.* 11 (2000) 19.
- [40] G. Jovanovski, S. Tanceva, B. Soptrajanov, *Spectrosc. Lett.* 28 (1995) 1095.
- [41] A. Kaczor, R. Almeida, A. Gomez-Zavaglia, M.L.S. Cristiano, R. Fausto, *J. Mol. Struct.* 876 (2008) 77.
- [42] M. Rozenberg, G. Shoham, I. Reva, R. Fausto, *Phys. Chem. Chem. Phys.* 7 (2005) 2376.
- [43] S. Shen, J.R. Durig, *J. Mol. Struct.* 661–662 (2003) 49.
- [44] W.O. George, E.N. Lewis, D.A. Williams, W.F. Maddams, *Appl. Spectrosc.* 36 (1982) 592.
- [45] F. Duvernay, T. Chiavassa, F. Borget, J.P. Aycard, *Chem. Phys.* 298 (2004) 241.

B Appendix

B.1 Azobenzene Supporting Information

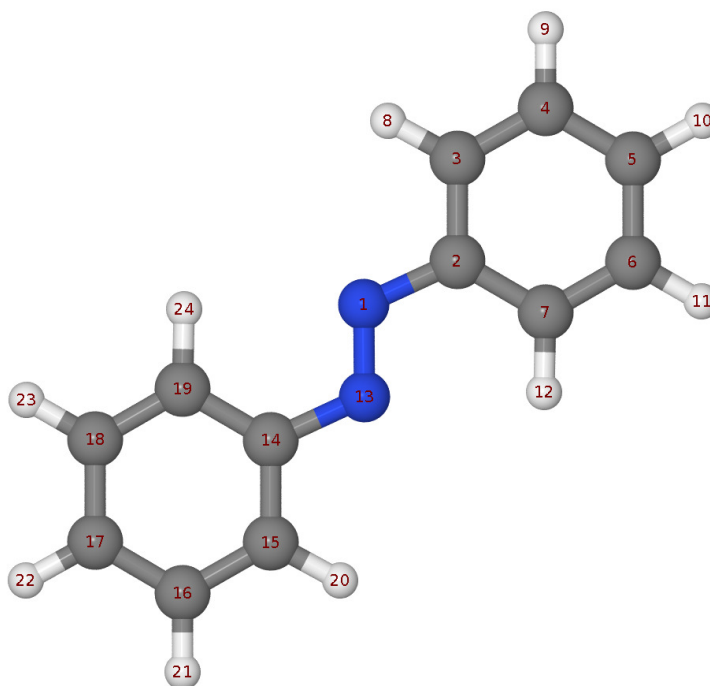


Figure B.1 Atom numbering scheme of azobenzene used in the definition of the internal symmetry coordinates of the normal mode analysis.

Table B.1 Mean unsigned errors (MUE) of each theoretical approach relatively to a set of experimental frequencies of azobenzene.

Method	Basis Set	MUE ^a / cm ⁻¹	References
BP86	6-311++G(3df,3pd)	15	Present work
	cc-pVTZ	10	Present work
	TZVP	15	Ref. Fliegl <i>et al.</i>
PW91	6-311++G(3df,3pd)	12	Present work
	cc-pVTZ	7	Present work
B3LYP	6-311++G(3df,3pd)	25	Present work
	cc-pVTZ	28	Present work
B97-1	6-311++G(3df,3pd)	18	Present work
	cc-pVTZ	22	Ref. Klug <i>et al.</i>
	aug-cc-pVTZ	19	Ref. Klug <i>et al.</i>
OLYP	6-311++G(3df,3pd)	11	Present work
	cc-pVTZ	7	Ref. <i>et al.</i>
MP2	cc-pVTZ	23	Ref. Fliegl <i>et al.</i>

^a Vibrational frequencies of both the *E* and *Z* forms of azobenzene were used in the calculation of the MUE except with the aug-cc-pVTZ basis set where they were only available for the *E* form.

B.1 Azobenzene Supporting Information

Table B.2 Theoretical Frequencies (ν / cm^{-1}) and IR Intensities (I/ km mol^{-1}) of *E*-AB and *Z*-AB forms. The calculated frequencies are not scaled. Raman scattering activities ($S/\text{\AA}^4 \text{ a.m.u.}^{-1}$) calculated at the PW91/cc-pVTZ level are also given.

<i>E</i> -AB							
BP86 / 6-311++G(3df,3pd)		BP86 / cc-pVTZ		B3LYP / 6-311++G(3df,3pd)		B3LYP / cc-pVTZ	
ν	I	ν	I	ν	I	ν	I
3133.9	0.0	3128.6	0.0	3215.7	8.2	3212.4	8.8
3133.9	12.8	3128.6	13.6	3215.6	0.0	3212.3	0.0
3123.0	0.0	3118.2	0.0	3200.1	0.0	3196.9	0.0
3122.8	38.5	3118.0	43.4	3200.0	27.5	3196.7	31.9
3113.2	0.0	3108.6	0.0	3190.2	0.0	3187.1	0.0
3113.1	30.9	3108.5	33.6	3190.1	33.8	3187.0	40.2
3102.5	17.0	3098.4	0.0	3179.3	18.2	3176.3	0.0
3102.5	0.0	3098.4	18.0	3179.2	0.0	3176.3	20.9
3091.4	0.0	3088.3	0.0	3168.0	0.0	3165.9	0.0
3091.3	4.4	3088.2	5.0	3167.9	2.5	3165.8	2.8
1584.8	0.0	1589.2	0.0	1640.1	0.0	1644.7	0.0
1581.4	6.1	1586.2	5.9	1633.9	3.0	1639.1	3.1
1567.7	0.0	1573.3	0.0	1622.6	0.0	1628.6	0.0
1563.7	2.9	1569.4	3.9	1617.0	3.5	1623.1	4.7
1471.5	0.0	1475.3	0.0	1547.9	0.0	1550.9	0.0
1462.3	7.3	1467.4	9.5	1517.1	9.6	1521.9	12.5
1446.5	0.0	1452.4	0.0	1503.6	0.0	1509.0	0.0
1434.4	10.5	1440.6	12.5	1484.0	10.2	1489.8	12.6
1407.9	0.0	1409.5	0.0	1477.1	0.0	1481.7	0.0
1343.5	0.0	1346.0	0.0	1348.9	4.9	1352.3	5.6
1340.3	7.1	1343.0	6.8	1348.3	0.0	1351.1	0.0
1291.6	0.0	1295.1	0.0	1342.6	0.0	1345.6	0.0
1287.3	1.2	1291.4	1.8	1333.7	5.4	1336.9	4.9
1213.1	18.7	1217.1	18.2	1246.9	17.7	1251.5	17.6
1168.4	0.0	1172.0	0.0	1204.5	0.0	1208.0	0.0
1145.9	0.0	1147.9	0.4	1182.5	0.0	1183.7	0.0
1145.9	0.4	1147.9	0.0	1182.4	0.4	1183.7	0.3
1134.5	34.6	1136.5	33.0	1175.7	33.2	1177.5	31.4
1115.8	0.0	1119.5	0.0	1156.4	0.0	1160.5	0.0
1066.8	13.7	1069.0	15.1	1101.1	11.7	1103.2	12.6
1063.0	0.0	1064.8	0.0	1097.5	0.0	1099.2	0.0
1009.8	12.8	1012.6	0.0	1040.1	11.9	1043.5	0.0
1009.7	0.0	1012.0	13.7	1039.6	0.0	1043.2	13.1
965.6	0.0	990.1	3.2	1011.1	0.0	1021.6	2.1
965.5	0.0	989.9	0.0	1010.8	0.1	1021.4	0.0
965.3	0.1	977.9	0.4	1000.9	0.0	1019.7	0.5
964.2	2.8	977.4	0.0	999.5	0.01	1019.2	0.0
955.5	0.0	962.3	0.0	998.3	0.0	1003.8	0.0
953.8	0.03	961.6	0.02	997.2	2.4	1003.0	0.004
913.9	7.8	924.8	7.9	955.5	8.2	964.9	8.0
907.9	0.0	919.0	0.0	949.5	0.0	959.1	0.0
903.9	0.0	909.6	0.0	932.7	0.0	937.6	0.0
826.2	0.0	831.5	0.0	861.7	0.0	866.0	0.0
824.6	0.1	830.1	0.1	860.4	0.1	864.7	0.1
808.3	0.4	815.0	0.5	831.9	0.3	838.1	0.5
764.0	75.5	777.4	52.6	794.2	79.2	806.0	55.5
743.8	0.0	757.0	0.0	773.9	0.0	785.4	0.0
666.1	64.9	683.9	79.6	693.0	67.2	710.2	80.0
660.0	0.0	679.9	0.0	683.5	0.0	705.5	0.0
657.2	0.0	663.1	0.0	683.5	0.0	686.5	0.0
609.0	0.8	611.9	0.6	631.9	0.6	634.7	0.5
602.5	0.0	605.6	0.0	626.1	0.0	629.0	0.0
533.9	12.5	540.4	13.9	557.3	13.4	563.2	14.4
529.1	5.6	530.6	6.5	548.2	5.3	549.7	6.0
512.8	24.4	512.7	23.7	529.0	25.7	528.9	25.3
463.6	0.0	470.7	0.0	486.0	0.0	492.3	0.0
400.9	0.0	405.3	0.0	420.0	0.0	423.6	0.0
397.4	0.0003	401.7	0.0	416.9	0.004	420.4	0.003
298.5	0.0	298.3	0.0	307.5	0.0	309.1	0.6
289.9	0.9	294.3	0.6	305.2	0.8	307.4	0.0
233.6	0.0	238.3	0.0	249.2	0.0	253.2	0.0
216.1	0.0	216.1	0.0	223.5	0.0	223.8	0.0
86.8	0.0	95.3	0.0	92.4	0.0	99.2	0.0
83.0	2.0	82.6	1.9	86.3	2.0	86.3	1.9
60.6	1.5	60.1	1.4	63.5	1.4	63.2	1.3
19.3	0.1	20.4	0.1	21.5	0.04	22.0	0.04

Table B.2 (Cont.)

<i>E-AB</i>									
B97-1 / 6-311++G(3df,3pd)		OLYP / cc-pVTZ		PW91 / 6-311++G(3df,3pd)		PW91 / cc-pVTZ			
ν	I	ν	I	ν	I	ν	I	S	
3208.5	9.6	3176.5	9.6	3149.0	0.0	3142.5	0.0	164.6	
3208.4	0.0	3176.4	0.0	3149.0	13.1	3142.5	13.9	0.0	
3195.9	0.0	3159.6	0.0	3139.6	0.0	3133.5	0.0	597.7	
3195.7	28.7	3159.4	35.0	3139.4	36.1	3133.3	40.5	0.0	
3186.1	0.0	3149.0	0.0	3129.8	0.0	3124.0	0.0	354.0	
3186.0	27.7	3148.9	39.7	3129.8	27.5	3123.9	30.6	0.0	
3175.5	15.1	3136.3	21.3	3119.4	0.0	3113.9	0.0	324.5	
3175.5	0.0	3136.3	0.0	3119.4	15.8	3113.9	17.0	0.0	
3164.2	0.0	3124.1	0.0	3108.3	0.0	3103.9	0.0	88.2	
3164.1	2.5	3124.0	5.5	3108.2	4.4	3103.8	5.0	0.0	
1632.4	0.0	1599.3	0.0	1593.5	0.0	1598.2	0.0	830.8	
1627.0	3.0	1595.1	6.3	1589.8	6.4	1594.8	6.2	0.0	
1616.0	0.0	1579.8	0.0	1575.5	0.0	1581.6	0.0	26.0	
1610.0	3.6	1575.7	2.4	1571.4	2.7	1577.6	3.8	0.0	
1539.2	0.0	1487.6	0.0	1479.4	0.0	1483.1	0.0	727.0	
1506.8	8.6	1473.7	6.3	1467.6	7.0	1472.8	9.4	0.0	
1492.7	0.0	1457.2	0.0	1451.5	0.0	1457.7	0.0	518.4	
1474.6	10.5	1443.3	10.3	1439.5	10.7	1446.0	13.1	0.0	
1468.4	0.0	1425.3	0.0	1417.6	0.0	1419.6	0.0	3851.0	
1342.9	0.0	1355.0	0.0	1353.4	0.0	1355.7	0.0	108.0	
1341.3	7.1	1351.5	7.4	1350.1	6.9	1352.6	6.5	0.0	
1331.6	0.0	1302.3	0.0	1295.1	0.0	1298.8	0.0	319.3	
1324.6	3.0	1297.3	1.3	1290.8	1.0	1295.2	1.7	0.0	
1245.2	20.8	1215.9	17.2	1221.0	20.8	1225.1	20.4	0.0	
1199.2	0.0	1176.9	0.0	1173.0	0.0	1176.9	0.0	868.6	
1175.3	0.4	1156.8	0.0	1148.1	0.0	1149.9	0.4	0.0	
1175.0	0.0	1156.8	0.3	1148.1	0.5	1149.9	0.0	33.8	
1165.7	32.9	1148.8	36.6	1137.9	33.5	1139.6	32.1	0.0	
1151.0	0.0	1122.5	0.0	1121.9	0.0	1125.5	0.0	2514.4	
1091.9	11.8	1079.2	11.9	1070.6	13.8	1072.9	15.2	0.0	
1087.5	0.0	1075.3	0.0	1066.9	0.0	1068.5	0.0	23.9	
1032.3	12.7	1020.4	10.0	1014.9	13.1	1017.8	0.0	28.3	
1032.1	0.0	1019.8	0.0	1014.9	0.0	1017.1	13.5	0.0	
1003.4	0.0	970.5	0.0	968.2	0.0	993.5	0.0	362.9	
1003.2	0.05	970.3	0.04	968.0	0.04	993.4	3.4	0.0	
993.6	0.0	961.7	0.0	967.3	0.0	979.8	0.4	0.0	
992.1	0.01	961.1	0.0	965.6	2.8	979.3	0.0	1.2	
990.5	0.0	960.4	0.02	958.2	0.0	962.7	0.0	0.5	
989.2	2.4	958.4	2.6	956.7	0.02	961.9	0.001	0.0	
948.8	8.0	919.6	7.3	916.7	7.6	927.6	7.2	0.0	
942.9	0.0	913.8	0.0	910.7	0.0	921.7	0.0	0.1	
927.3	0.0	903.5	0.0	906.7	0.0	913.5	0.0	6.9	
857.5	0.0	830.5	0.0	827.5	0.0	832.8	0.0	2.9	
856.1	0.1	829.3	0.1	826.0	0.1	831.3	0.04	0.0	
826.6	0.3	806.2	0.3	812.0	0.4	819.7	0.6	0.0	
789.6	83.6	766.8	76.1	764.8	75.8	780.0	48.3	0.0	
769.6	0.0	745.5	0.0	744.3	0.0	759.1	0.0	0.2	
688.3	65.8	664.3	61.4	664.8	63.1	685.2	76.8	0.0	
677.9	0.0	660.5	0.0	661.5	0.0	681.7	0.0	0.8	
676.8	0.0	654.4	0.0	655.6	0.0	664.7	0.0	7.0	
625.1	0.7	609.0	0.8	610.3	0.8	613.3	0.6	0.0	
618.8	0.0	602.5	0.0	603.6	0.0	606.8	0.0	23.0	
553.9	13.5	537.2	11.8	534.2	12.6	541.3	13.7	0.0	
541.7	3.7	528.9	5.0	530.5	5.4	532.1	6.3	0.0	
523.8	27.1	514.4	25.3	514.6	24.3	514.5	23.5	0.0	
481.5	0.0	465.4	0.0	463.8	0.0	471.3	0.0	0.3	
415.8	0.0	401.1	0.0	401.5	0.0	406.2	0.0	0.01	
412.7	0.01	398.0	0.01	398.0	0.004	402.7	0.001	0.0	
304.6	0.0	299.0	0.0	299.8	0.0	299.6	0.0	1.8	
303.0	0.8	290.7	0.9	290.5	0.9	295.2	0.6	0.0	
247.6	0.0	227.2	0.0	234.2	0.0	239.0	0.0	3.8	
218.2	0.0	214.3	0.0	217.1	0.0	217.1	0.0	1.0	
91.2	0.0	80.7	2.0	86.3	0.0	94.8	0.0	3.3	
80.7	2.0	78.0	0.0	82.4	2.0	82.3	1.9	0.0	
63.7	1.5	60.6	1.4	61.5	1.5	60.9	1.4	0.0	
22.3	0.0	13.0	0.1	15.6	0.03	14.8	0.03	0.0	

Table B.2 (Cont.)

Z-AB							
BP86 / 6-311++G(3df,3pd)		BP86 / cc-pVTZ		B3LYP / 6-311++G(3df,3pd)		B3LYP / cc-pVTZ	
ν	I	ν	I	ν	I	ν	I
3126.6	3.1	3121.5	4.4	3204.6	2.9	3200.6	4.0
3126.6	4.7	3121.4	7.4	3204.5	1.6	3200.5	2.4
3121.4	1.2	3116.7	0.9	3197.3	1.9	3194.0	1.8
3121.1	35.2	3116.5	38.9	3197.0	30.0	3193.8	36.2
3113.3	5.6	3108.7	5.9	3189.3	6.0	3186.0	6.8
3113.3	14.6	3108.7	16.1	3189.2	14.2	3185.9	16.8
3102.1	1.1	3098.2	1.0	3178.2	0.9	3175.2	0.9
3102.0	9.2	3098.1	9.2	3178.2	9.7	3175.2	10.7
3093.6	0.5	3090.5	0.6	3169.5	0.2	3167.1	0.3
3093.5	1.8	3090.4	1.9	3169.4	1.3	3167.0	1.4
1581.9	5.2	1586.3	3.5	1641.1	13.6	1644.9	10.6
1576.2	1.8	1581.4	2.2	1629.0	4.9	1634.6	5.3
1563.8	0.4	1569.1	0.5	1618.3	0.8	1623.9	1.2
1556.9	4.1	1562.1	4.7	1610.9	4.8	1616.3	5.8
1505.5	45.8	1506.6	48.6	1597.1	21.0	1600.3	24.8
1458.3	3.8	1464.2	4.9	1513.5	6.8	1518.7	8.5
1452.0	1.2	1456.9	0.8	1510.7	6.7	1515.6	6.9
1433.1	3.0	1438.9	3.3	1482.9	2.5	1488.2	2.7
1426.6	6.1	1432.3	7.2	1476.5	5.4	1481.7	6.6
1334.1	0.1	1337.1	0.03	1353.3	0.0007	1356.7	0.004
1327.7	2.0	1330.9	1.8	1351.2	0.1	1354.7	0.2
1294.6	0.05	1298.4	0.1	1327.6	0.1	1330.4	0.1
1289.4	1.7	1292.8	2.0	1317.6	2.2	1320.5	2.2
1164.3	0.5	1167.0	0.7	1201.5	0.5	1203.7	0.6
1164.0	0.3	1166.9	0.3	1201.0	0.5	1203.4	0.6
1146.7	0.1	1148.8	0.2	1183.0	0.1	1184.3	0.1
1146.4	0.02	1148.6	0.04	1182.6	0.1	1183.9	0.1
1123.4	2.5	1127.7	1.9	1164.9	0.8	1169.5	0.5
1099.5	0.1	1104.5	0.1	1142.8	0.3	1148.2	0.2
1069.9	1.0	1072.3	1.2	1102.5	0.7	1104.8	0.8
1067.8	12.6	1070.3	12.9	1100.9	11.5	1103.1	11.7
1015.1	2.8	1019.0	2.0	1044.1	4.5	1048.8	1.9
1015.0	4.3	1018.6	4.8	1044.1	2.9	1048.6	5.0
971.7	1.1	989.5	1.1	1011.1	0.5	1020.5	0.9
970.9	0.1	988.8	0.4	1011.0	0.0001	1020.1	0.4
962.4	0.03	965.8	0.05	1002.7	0.1	1008.4	0.1
962.2	0.3	965.8	0.5	1002.6	0.9	1008.2	0.7
947.0	0.2	947.6	0.2	992.5	0.3	990.0	0.2
946.8	0.5	947.2	0.6	992.4	0.2	989.6	0.4
898.9	20.2	903.3	21.1	942.0	21.9	945.8	22.7
894.8	0.2	898.8	0.4	937.4	0.5	940.4	0.7
827.4	4.2	827.9	2.8	865.1	5.8	865.5	4.4
819.2	1.7	821.8	1.5	855.7	1.0	857.5	0.9
816.9	6.1	819.3	6.8	854.3	3.0	856.2	3.3
758.0	14.6	764.6	12.9	790.1	16.0	795.8	14.1
752.2	37.4	755.8	34.2	778.0	46.2	781.2	41.7
738.6	0.2	741.0	0.04	762.2	0.04	764.4	0.01
688.7	95.7	690.7	76.4	716.2	88.6	717.6	82.7
675.5	18.6	686.2	20.4	703.6	19.9	713.1	21.2
668.7	7.1	684.1	23.6	693.5	5.0	708.0	7.9
609.9	0.2	613.2	0.3	634.1	0.3	637.2	0.5
606.7	0.04	609.7	0.1	630.1	0.05	632.8	0.1
585.8	4.8	589.4	5.4	611.7	4.2	615.1	4.6
527.1	0.3	528.9	0.3	548.5	0.4	550.2	0.4
490.5	5.1	492.2	5.0	509.3	4.5	510.9	4.4
434.9	4.8	437.3	4.9	452.5	2.2	454.6	2.3
412.8	3.4	414.3	3.1	434.7	3.6	436.0	3.2
396.7	0.03	399.3	0.02	414.3	0.04	416.6	0.04
392.3	4.6	395.6	4.6	411.5	3.6	414.3	3.6
273.0	5.8	273.6	5.8	290.5	5.4	291.0	5.4
262.8	0.3	263.5	0.3	271.5	0.3	272.1	0.3
168.8	0.2	168.0	0.2	172.9	0.2	172.3	0.2
150.3	3.9	151.0	3.9	156.0	2.7	156.7	2.6
67.9	0.5	67.1	0.5	68.2	0.5	67.8	0.5
49.2	0.02	49.5	0.01	46.8	0.005	46.7	0.001
40.3	1.4	41.1	1.5	42.2	1.2	42.8	1.3

Table B.2 (Cont.)

Z-AB									
B97-1 / 6-311++G(3df,3pd)		OLYP / cc-pVTZ		PW91 / 6-311++G(3df,3pd)		PW91 / cc-pVTZ			
ν	I	ν	I	ν	I	ν	I	S	
3197.7	4.0	3169.6	1.0	3142.2	4.2	3136.0	5.2	469.7	
3197.6	3.3	3169.6	4.1	3142.1	6.8	3135.9	9.8	77.0	
3192.7	1.1	3158.3	2.1	3137.7	0.5	3131.5	0.2	182.0	
3192.4	27.7	3158.1	36.3	3137.4	30.6	3131.3	33.9	22.8	
3184.7	4.6	3150.0	16.8	3130.0	4.6	3124.0	4.9	104.9	
3184.5	11.7	3149.9	7.8	3129.9	12.6	3123.9	14.2	72.8	
3173.5	0.7	3136.7	12.4	3119.0	1.0	3113.6	1.0	168.9	
3173.4	7.7	3136.7	1.3	3118.9	8.1	3113.5	8.4	97.9	
3165.0	0.3	3127.0	0.5	3110.6	0.5	3106.0	0.6	39.7	
3164.9	1.5	3126.9	2.2	3110.4	1.8	3105.9	1.9	19.8	
1633.2	11.2	1599.2	8.5	1591.0	6.3	1595.6	4.2	102.4	
1622.8	4.7	1591.1	2.7	1584.6	1.8	1590.2	2.2	94.3	
1612.5	0.6	1577.1	0.4	1571.7	0.3	1577.3	0.5	3.3	
1605.1	4.7	1570.0	4.0	1564.6	4.0	1570.1	4.7	25.2	
1588.7	22.3	1535.5	40.3	1518.6	44.2	1520.1	47.2	519.0	
1504.2	6.6	1469.7	3.6	1463.2	3.6	1469.2	4.9	0.5	
1501.5	6.6	1464.5	2.2	1457.6	2.0	1462.8	1.7	156.8	
1474.4	2.7	1443.3	2.3	1438.2	2.8	1444.4	3.1	6.2	
1467.9	5.4	1436.3	5.6	1431.6	6.3	1437.6	7.6	3.7	
1343.3	0.002	1345.1	0.04	1343.8	0.1	1346.6	0.05	14.3	
1341.2	0.3	1340.1	1.9	1336.9	2.3	1339.9	2.1	0.1	
1324.2	0.1	1304.4	0.01	1298.1	0.03	1301.9	0.1	1.4	
1314.2	1.9	1298.6	1.9	1293.2	1.6	1296.7	1.9	1.3	
1194.8	0.4	1175.4	0.6	1168.0	0.2	1171.0	0.2	13.7	
1194.8	0.5	1174.8	0.4	1167.6	0.5	1170.2	0.7	12.6	
1175.9	0.1	1157.6	0.1	1148.8	0.1	1150.6	0.2	11.1	
1175.3	0.04	1157.4	0.03	1148.6	0.003	1150.4	0.02	2.9	
1161.6	1.5	1131.1	1.6	1131.1	2.7	1135.0	2.0	43.4	
1140.8	0.1	1106.1	0.2	1107.2	0.2	1111.9	0.2	360.7	
1095.7	0.7	1080.9	0.8	1074.1	1.0	1076.4	1.2	1.7	
1094.5	11.8	1078.8	11.3	1072.0	12.8	1074.4	13.1	4.7	
1038.6	2.8	1024.4	3.7	1020.3	3.0	1024.1	2.1	40.4	
1038.5	4.1	1024.2	2.9	1020.2	4.2	1023.7	4.6	7.3	
1003.4	0.4	971.1	0.6	974.4	1.1	993.2	1.2	9.2	
1003.3	0.0004	970.7	0.001	973.5	0.04	992.5	0.4	105.3	
995.6	0.9	964.6	0.9	966.2	0.03	968.0	0.04	0.4	
995.5	0.04	963.6	0.01	966.1	0.3	967.8	0.6	0.9	
984.6	0.4	953.1	0.5	951.1	0.2	949.2	0.3	4.8	
984.5	0.2	953.0	0.2	951.1	0.4	948.8	0.5	0.0	
936.0	22.7	902.9	18.3	902.4	20.0	906.9	20.8	1.9	
929.9	0.4	899.4	0.4	898.4	0.2	902.2	0.3	2.4	
863.1	6.7	828.2	1.8	830.9	4.2	831.1	2.6	27.9	
850.8	1.1	824.1	1.6	821.5	1.6	824.0	1.4	12.2	
849.5	2.5	819.7	10.3	819.6	5.7	822.0	6.4	16.4	
785.5	15.2	760.5	17.7	760.9	14.8	768.3	12.5	23.8	
773.2	48.2	753.1	31.2	756.0	37.2	760.1	32.8	1.6	
758.6	0.2	736.0	0.3	742.6	0.3	745.4	0.02	9.7	
712.4	91.3	690.2	94.2	690.6	97.8	692.6	71.8	11.6	
699.0	19.5	676.3	19.1	676.1	17.8	688.3	19.2	0.2	
687.3	4.4	666.4	2.9	668.8	6.3	686.6	26.4	0.8	
628.2	0.5	612.3	0.3	611.4	0.2	614.9	0.3	15.1	
622.9	0.1	607.8	0.04	607.9	0.04	611.0	0.1	3.2	
606.5	4.0	590.1	4.2	587.7	4.6	591.7	5.1	84.8	
544.7	0.4	531.4	0.5	528.4	0.2	530.4	0.2	1.1	
504.4	4.8	492.0	4.9	492.7	5.0	494.5	4.7	0.1	
447.2	1.9	435.5	4.5	435.8	4.8	438.7	5.0	2.9	
432.3	3.3	415.4	3.8	415.4	3.5	416.8	3.1	21.7	
409.7	0.1	395.3	0.01	397.7	0.1	400.6	0.04	23.2	
406.3	3.5	393.5	5.2	393.0	4.5	396.7	4.4	1.2	
286.9	5.3	281.2	5.9	274.9	5.8	275.3	5.8	2.2	
271.1	0.3	259.6	0.3	263.9	0.2	264.8	0.2	14.4	
171.2	0.2	163.0	0.2	170.1	0.2	168.9	0.2	30.5	
153.8	2.5	150.3	3.7	150.4	4.0	151.3	4.0	5.4	
68.4	0.4	64.7	0.6	68.8	0.5	68.0	0.5	11.9	
48.1	0.01	47.6	0.001	49.2	0.03	49.9	0.02	24.6	
40.2	1.1	45.8	1.6	40.2	1.4	41.1	1.4	3.0	

Table B.3 Cartesian coordinates of the optimized geometries of *E*-AB and *Z*-AB forms.

Atom	<i>E</i> -AB											
	BP86/6-311++G(3df,3pd)			BP86/cc-pVTZ			B3LYP/6-311++(3df,3pd)			B3LYP/cc-pVTZ		
	x	y	z	x	y	z	x	y	z	x	y	z
N	-0.000884	0.633676	0.000000	-0.002308	0.633516	0.000000	0.000929	0.624347	0.000000	-0.000271	0.624194	0.000000
C	1.284523	1.232570	0.000000	1.284192	1.233287	0.000000	1.279243	1.233610	0.000000	1.278960	1.234135	0.000000
C	1.293411	2.637660	0.000000	1.292884	2.638031	0.000000	1.279243	2.628933	0.000000	1.278960	2.629271	0.000000
C	2.503058	3.333243	0.000000	2.502322	3.333468	0.000000	2.478619	3.328569	0.000000	2.478187	3.328772	0.000000
C	3.710825	2.629036	0.000000	3.709861	2.629245	0.000000	3.683525	2.636217	0.000000	3.682907	2.636325	0.000000
C	3.704878	1.225478	0.000000	3.704050	1.225889	0.000000	3.685524	1.241001	0.000000	3.685009	1.241255	0.000000
C	2.503058	0.524728	0.000000	2.502322	0.525459	0.000000	2.493689	0.537041	0.000000	2.493194	0.537567	0.000000
H	0.335461	3.159251	0.000000	0.334539	3.158787	0.000000	0.328277	3.143435	0.000000	0.327522	3.143012	0.000000
H	2.504555	4.423959	0.000000	2.504077	4.424193	0.000000	2.472889	4.410022	0.000000	2.472703	4.410373	0.000000
H	4.658617	3.169341	0.000000	4.657630	3.169597	0.000000	4.620039	3.177542	0.000000	4.619534	3.177756	0.000000
H	4.650038	0.679885	0.000000	4.649334	0.680474	0.000000	4.625169	0.704677	0.000000	4.624869	0.704994	0.000000
H	2.478719	-0.564254	0.000000	2.476091	-0.563476	0.000000	2.481189	-0.542337	0.000000	2.478968	-0.541861	0.000000
N	0.000884	-0.633676	0.000000	0.002308	-0.633516	0.000000	-0.000929	-0.624347	0.000000	0.000271	-0.624194	0.000000
C	-1.284523	-1.232570	0.000000	-1.284192	-1.233287	0.000000	-1.279243	-1.233610	0.000000	-1.278960	-1.234135	0.000000
C	-1.293411	-2.637660	0.000000	-1.292884	-2.638031	0.000000	-1.279243	-2.628933	0.000000	-1.278960	-2.629271	0.000000
C	-2.503058	-3.333243	0.000000	-2.502322	-3.333468	0.000000	-2.478619	-3.328569	0.000000	-2.478187	-3.328772	0.000000
C	-3.710825	-2.629036	0.000000	-3.709861	-2.629245	0.000000	-3.683525	-2.636217	0.000000	-3.682907	-2.636325	0.000000
C	-3.704878	-1.225478	0.000000	-3.704050	-1.225889	0.000000	-3.685524	-1.241001	0.000000	-3.685009	-1.241255	0.000000
C	-2.503058	-0.524728	0.000000	-2.502322	-0.525459	0.000000	-2.493689	-0.537041	0.000000	-2.493194	-0.537567	0.000000
H	-0.335461	-3.159251	0.000000	-0.334539	-3.158787	0.000000	-0.328277	-3.143435	0.000000	-0.327522	-3.143012	0.000000
H	-2.504555	-4.423959	0.000000	-2.504077	-4.424193	0.000000	-2.472889	-4.410022	0.000000	-2.472703	-4.410373	0.000000
H	-4.658617	-3.169341	0.000000	-4.657630	-3.169597	0.000000	-4.620039	-3.177542	0.000000	-4.619534	-3.177756	0.000000
H	-4.650038	-0.679885	0.000000	-4.649334	-0.680474	0.000000	-4.625169	-0.704677	0.000000	-4.624869	-0.704994	0.000000
H	-2.478719	0.564254	0.000000	-2.476091	0.563476	0.000000	-2.481189	0.542337	0.000000	-2.478968	0.541861	0.000000

Table B.3 (Cont.)

Atom	B97-1/6-311++(3df,3pd)			OLYP/6-311++(3df,3pd)			PW91/6-311++(3df,3pd)			PW91/cc-pVTZ		
	x	y	z	x	y	z	x	y	z	x	y	z
N	0.000771	0.626393	0.000000	0.001006	0.631288	0.000000	-0.000526	0.632020	0.000000	-0.002264	0.631954	0.000000
C	1.284991	1.227353	0.000000	1.284120	1.234003	0.000000	1.280567	1.230998	0.000000	1.280084	1.231851	0.000000
C	1.291863	2.625692	0.000000	1.284120	2.638571	0.000000	1.289495	2.633214	0.000000	1.288755	2.633777	0.000000
C	2.497762	3.320215	0.000000	2.484914	3.345198	0.000000	2.496549	3.327371	0.000000	2.495669	3.327776	0.000000
C	3.701298	2.619376	0.000000	3.698256	2.655189	0.000000	3.701769	2.624530	0.000000	3.700707	2.624862	0.000000
C	3.695797	1.220991	0.000000	3.704427	1.254292	0.000000	3.695899	1.223895	0.000000	3.694972	1.224373	0.000000
C	2.497762	0.521639	0.000000	2.511033	0.542539	0.000000	2.496549	0.524709	0.000000	2.495669	0.525474	0.000000
C	0.341373	3.145843	0.000000	0.327873	3.154504	0.000000	0.333074	3.153345	0.000000	0.331792	3.152977	0.000000
H	2.498138	4.403763	0.000000	2.474328	4.432228	0.000000	2.498122	4.415987	0.000000	2.497536	4.416531	0.000000
H	4.642657	3.156491	0.000000	4.637606	3.202804	0.000000	4.647753	3.163784	0.000000	4.646790	3.164218	0.000000
H	4.634419	0.678671	0.000000	4.650988	0.718415	0.000000	4.639293	0.679432	0.000000	4.638610	0.680033	0.000000
H	2.478426	-0.560037	0.000000	2.507711	-0.541933	0.000000	2.471548	-0.562316	0.000000	2.468477	-0.561581	0.000000
N	-0.000771	-0.626393	0.000000	-0.001006	-0.631288	0.000000	0.000526	-0.632020	0.000000	0.002264	-0.631954	0.000000
C	-1.284991	-1.227353	0.000000	-1.284120	-1.234003	0.000000	-1.280567	-1.230998	0.000000	-1.280084	-1.231851	0.000000
C	-1.291863	-2.625692	0.000000	-1.284120	-2.638571	0.000000	-1.289495	-2.633214	0.000000	-1.288755	-2.633777	0.000000
C	-2.497762	-3.320215	0.000000	-2.484914	-3.345198	0.000000	-2.496549	-3.327371	0.000000	-2.495669	-3.327776	0.000000
C	-3.701298	-2.619376	0.000000	-3.698256	-2.655189	0.000000	-3.701769	-2.624530	0.000000	-3.700707	-2.624862	0.000000
C	-3.695797	-1.220991	0.000000	-3.704427	-1.254292	0.000000	-3.695899	-1.223895	0.000000	-3.694972	-1.224373	0.000000
C	-2.497762	-0.521639	0.000000	-2.511033	-0.542539	0.000000	-2.496549	-0.524709	0.000000	-2.495669	-0.525474	0.000000
H	-0.341373	-3.145843	0.000000	-0.327873	-3.154504	0.000000	-0.333074	-3.153345	0.000000	-0.331792	-3.152977	0.000000
H	-2.498138	-4.403763	0.000000	-2.474328	-4.432228	0.000000	-2.498122	-4.415987	0.000000	-2.497536	-4.416531	0.000000
H	-4.642657	-3.156491	0.000000	-4.637606	-3.202804	0.000000	-4.647753	-3.163784	0.000000	-4.646790	-3.164218	0.000000
H	-4.634419	-0.678671	0.000000	-4.650988	-0.718415	0.000000	-4.639293	-0.679432	0.000000	-4.638610	-0.680033	0.000000
H	-2.478426	0.560037	0.000000	-2.507711	0.541933	0.000000	-2.471548	0.562316	0.000000	-2.468477	0.561581	0.000000

Table B.3 (Cont.)

Atom	Z-AB											
	BP86/6-311++G(3df,3pd)			BP86/cc-pVTZ			B3LYP/6-311++(3df,3pd)			B3LYP/cc-pVTZ		
	x	y	z	x	y	z	x	y	z	x	y	z
N	-0.007786	0.627126	1.933590	-0.008320	0.626774	1.929146	-0.027187	0.619120	1.936520	-0.027550	0.618845	1.932564
C	-0.136152	1.429766	0.752868	-0.136414	1.432195	0.748892	-0.158303	1.419761	0.756544	-0.158471	1.421759	0.753107
C	0.638792	2.600167	0.702810	0.640602	2.601283	0.702221	0.633671	2.565759	0.686383	0.635503	2.566590	0.685612
C	0.485678	3.493179	-0.357061	0.486432	3.500192	-0.352061	0.487932	3.444936	-0.376931	0.488774	3.451189	-0.372759
C	-0.485678	3.260390	-1.337695	-0.486432	3.273241	-1.332278	-0.487932	3.218213	-1.342682	-0.488774	3.229851	-1.337853
C	-1.297248	2.122835	-1.255565	-1.299252	2.136665	-1.254504	-1.313052	2.102589	-1.241292	-1.315202	2.115142	-1.240123
C	-1.121181	1.200382	-0.224306	-1.122852	1.208965	-0.228065	-1.148279	1.197241	-0.202303	-1.149980	1.204894	-0.205458
H	1.359058	2.786963	1.500400	1.361258	2.783261	1.500529	1.358347	2.749754	1.467751	1.360784	2.746036	1.467578
H	1.109094	4.387036	-0.405759	1.110819	4.393555	-0.397401	1.121071	4.319591	-0.440163	1.122972	4.325447	-0.433211
H	-0.623358	3.972106	-2.152429	-0.625107	3.989499	-2.142857	-0.616262	3.915075	-2.159502	-0.618117	3.930948	-2.151081
H	-2.073377	1.951136	-2.002969	-2.076555	1.969665	-2.001761	-2.088619	1.934187	-1.976351	-2.092120	1.951083	-1.974950
H	-1.752847	0.314811	-0.160678	-1.756560	0.324598	-0.167766	-1.790002	0.331803	-0.125693	-1.793634	0.340479	-0.131440
N	0.007786	-0.627126	1.933590	0.008320	-0.626774	1.929146	0.027187	-0.619120	1.936520	0.027550	-0.618845	1.932564
C	0.136152	-1.429766	0.752868	0.136414	-1.432195	0.748892	0.158303	-1.419761	0.756544	0.158471	-1.421759	0.753107
C	-0.638792	-2.600167	0.702810	-0.640602	-2.601283	0.702221	-0.633671	-2.565759	0.686383	-0.635503	-2.566590	0.685612
C	-0.485678	-3.493179	-0.357061	-0.486432	-3.500192	-0.352061	-0.487932	-3.444936	-0.376931	-0.488774	-3.451189	-0.372759
C	0.485678	-3.260390	-1.337695	0.486432	-3.273241	-1.332278	0.487932	-3.218213	-1.342682	0.488774	-3.229851	-1.337853
C	1.297248	-2.122835	-1.255565	1.299252	-2.136665	-1.254504	1.313052	-2.102589	-1.241292	1.315202	-2.115142	-1.240123
C	1.121181	-1.200382	-0.224306	1.122852	-1.208965	-0.228065	1.148279	-1.197241	-0.202303	1.149980	-1.204894	-0.205458
H	-1.359058	-2.786963	1.500400	-1.361258	-2.783261	1.500529	-1.358347	-2.749754	1.467751	-1.360784	-2.746036	1.467578
H	-1.109094	-4.387036	-0.405759	-1.110819	-4.393555	-0.397401	-1.121071	-4.319591	-0.440163	-1.122972	-4.325447	-0.433211
H	0.623358	-3.972106	-2.152429	0.625107	-3.989499	-2.142857	0.616262	-3.915075	-2.159502	0.618117	-3.930948	-2.151081
H	2.073377	-1.951136	-2.002969	2.076555	-1.969665	-2.001761	2.088619	-1.934187	-1.976351	2.092120	-1.951083	-1.974950
H	1.752847	-0.314811	-0.160678	1.756560	-0.324598	-0.167766	1.790002	-0.331803	-0.125693	1.793634	-0.340479	-0.131440

Table B.3 (Cont.)

Atom	Z-AB											
	B97-1/6-311++(3df,3pd)			OLYP/6-311++(3df,3pd)			PW91/6-311++(3df,3pd)			PW91/cc-pVTZ		
	x	y	z	x	y	z	x	y	z	x	y	z
N	-0.029506	0.621005	1.952643	-0.016539	0.624003	1.906325	-0.009675	0.625655	1.934938	-0.009323	0.625356	1.928016
C	-0.160962	1.413208	0.764727	-0.147878	1.442892	0.737749	-0.139046	1.423261	0.756489	-0.137898	1.426844	0.750758
C	0.628858	2.563875	0.690023	0.658246	2.590718	0.679622	0.634401	2.590787	0.701174	0.637330	2.593547	0.701064
C	0.485789	3.434881	-0.384574	0.502032	3.502096	-0.360793	0.483703	3.475697	-0.362018	0.484675	3.487043	-0.354226
C	-0.485789	3.195225	-1.355794	-0.502032	3.315415	-1.315247	-0.483703	3.237604	-1.341117	-0.484675	3.256817	-1.333080
C	-1.309740	2.075131	-1.249028	-1.342700	2.203784	-1.224389	-1.293719	2.102754	-1.254197	-1.295287	2.122247	-1.253071
C	-1.147430	1.177272	-0.199259	-1.165620	1.261869	-0.212760	-1.119984	1.188240	-0.219482	-1.120373	1.199892	-0.225503
H	1.350475	2.756474	1.475221	1.407335	2.746996	1.451265	1.352010	2.781254	1.497519	1.355537	2.777408	1.498486
H	1.117487	4.312818	-0.452409	1.149816	4.373697	-0.414026	1.105942	4.367589	-0.414693	1.107586	4.378934	-0.401612
H	-0.612077	3.885367	-2.181366	-0.640340	4.040794	-2.112671	-0.619535	3.943169	-2.158695	-0.622384	3.969127	-2.144663
H	-2.081993	1.897223	-1.988421	-2.142795	2.065726	-1.947846	-2.066714	1.926935	-2.000851	-2.069704	1.952598	-1.999877
H	-1.786187	0.306943	-0.118093	-1.824943	0.402895	-0.146094	-1.749028	0.303286	-0.152941	-1.751293	0.315821	-0.164092
N	0.029506	-0.621005	1.952643	0.016539	-0.624003	1.906325	0.009675	-0.625655	1.934938	0.009323	-0.625356	1.928016
C	0.160962	-1.413208	0.764727	0.147878	-1.442892	0.737749	0.139046	-1.423261	0.756489	0.137898	-1.426844	0.750758
C	-0.628858	-2.563875	0.690023	-0.658246	-2.590718	0.679622	-0.634401	-2.590787	0.701174	-0.637330	-2.593547	0.701064
C	-0.485789	-3.434881	-0.384574	-0.502032	-3.502096	-0.360793	-0.483703	-3.475697	-0.362018	-0.484675	-3.487043	-0.354226
C	0.485789	-3.195225	-1.355794	0.502032	-3.315415	-1.315247	0.483703	-3.237604	-1.341117	0.484675	-3.256817	-1.333080
C	1.309740	-2.075131	-1.249028	1.342700	-2.203784	-1.224389	1.293719	-2.102754	-1.254197	1.295287	-2.122247	-1.253071
C	1.147430	-1.177272	-0.199259	1.165620	-1.261869	-0.212760	1.119984	-1.188240	-0.219482	1.120373	-1.199892	-0.225503
H	-1.350475	-2.756474	1.475221	-1.407335	-2.746996	1.451265	-1.352010	-2.781254	1.497519	-1.355537	-2.777408	1.498486
H	-1.117487	-4.312818	-0.452409	-1.149816	-4.373697	-0.414026	-1.105942	-4.367589	-0.414693	-1.107586	-4.378934	-0.401612
H	0.612077	-3.885367	-2.181366	0.640340	-4.040794	-2.112671	0.619535	-3.943169	-2.158695	0.622384	-3.969127	-2.144663
H	2.081993	-1.897223	-1.988421	2.142795	-2.065726	-1.947846	2.066714	-1.926935	-2.000851	2.069704	-1.952598	-1.999877
H	1.786187	-0.306943	-0.118093	1.824943	-0.402895	-0.146094	1.749028	-0.303286	-0.152941	1.751293	-0.315821	-0.164092

B.1 Azobenzene Supporting Information

Table B.4 Internal symmetry coordinates used in the normal mode analysis of *E*-azobenzene.^a

Coord.	Definition	Sym.	Appr.	Description
S ₁	$r_{1,13}$	A _g	$\nu(\text{N}=\text{N})$	
S ₂	$r_{1,2} + r_{13,14}$	A _g	$\nu(\text{NC})$	
S ₃	$r_{1,2} - r_{13,14}$	B _u	$\nu(\text{NC})$	
S ₄	$r_{2,3} - r_{3,4} + r_{4,5} - r_{5,6} + r_{6,7} - r_{7,2} + r_{14,15} - r_{15,16}$ $+ r_{16,17} - r_{17,18} + r_{18,19} - r_{19,14}$	A _g	$\nu(\text{CC})_1$	
S ₅	$r_{2,3} - r_{3,4} + r_{4,5} - r_{5,6} + r_{6,7} - r_{7,2} - r_{14,15} + r_{15,16}$ $- r_{16,17} + r_{17,18} - r_{18,19} + r_{19,14}$	B _u	$\nu(\text{CC})_2$	
S ₆	$-r_{2,3} + 2r_{3,4} - r_{4,5} - r_{5,6} + 2r_{6,7} - r_{7,2} - r_{14,15} + 2r_{15,16}$ $- r_{16,17} - r_{17,18} + 2r_{18,19} - r_{19,14}$	A _g	$\nu(\text{CC})_3$	
S ₇	$-r_{2,3} + 2r_{3,4} - r_{4,5} - r_{5,6} + 2r_{6,7} - r_{7,2} + r_{14,15} - 2r_{15,16}$ $+ r_{16,17} + r_{17,18} - 2r_{18,19} + r_{19,14}$	B _u	$\nu(\text{CC})_4$	
S ₈	$r_{2,3} - r_{4,5} + r_{5,6} - r_{7,2} + r_{14,15} - r_{16,17} + r_{17,18} - r_{19,14}$	A _g	$\nu(\text{CC})_5$	
S ₉	$r_{2,3} - r_{4,5} + r_{5,6} - r_{7,2} - r_{14,15} + r_{16,17} - r_{17,18} + r_{19,14}$	B _u	$\nu(\text{CC})_6$	
S ₁₀	$r_{2,3} + 2r_{3,4} + r_{4,5} - r_{5,6} - 2r_{6,7} - r_{7,2} + r_{14,15} + 2r_{15,16}$ $+ r_{16,17} - r_{17,18} - 2r_{18,19} + r_{19,14}$	A _g	$\nu(\text{CC})_7$	
S ₁₁	$r_{2,3} + 2r_{3,4} + r_{4,5} - r_{5,6} - 2r_{6,7} - r_{7,2} - r_{14,15} - 2r_{15,16}$ $- r_{16,17} + r_{17,18} + 2r_{18,19} + r_{19,14}$	B _u	$\nu(\text{CC})_8$	
S ₁₂	$r_{2,3} - r_{4,5} - r_{5,6} + r_{7,2} + r_{14,15} - r_{16,17} - r_{17,18} + r_{19,14}$	A _g	$\nu(\text{CC})_9$	
S ₁₃	$r_{2,3} - r_{4,5} - r_{5,6} + r_{7,2} - r_{14,15} + r_{16,17} + r_{17,18} - r_{19,14}$	B _u	$\nu(\text{CC})_{10}$	
S ₁₄	$r_{2,3} + r_{3,4} + r_{4,5} + r_{5,6} + r_{6,7} + r_{7,2} + r_{14,15} + r_{15,16}$ $+ r_{16,17} + r_{17,18} + r_{18,19} + r_{19,14}$	A _g	$\nu(\text{CC})_{11}$	
S ₁₅	$r_{2,3} + r_{3,4} + r_{4,5} + r_{5,6} + r_{6,7} + r_{7,2} - r_{14,15} - r_{15,16}$ $- r_{16,17} - r_{17,18} - r_{18,19} - r_{19,14}$	B _u	$\nu(\text{CC})_{12}$	
S ₁₆	$r_{7,12} + r_{19,24}$	A _g	$\nu_s(\text{CH})$	
S ₁₇	$r_{7,12} - r_{19,24}$	B _u	$\nu_{as}(\text{CH})$	
S ₁₈	$r_{6,11} + r_{5,10} + r_{4,9} + r_{3,8} + r_{18,23} + r_{17,22} + r_{16,21} + r_{15,20}$	A _g	$\nu(\text{CH})_1$	
S ₁₉	$r_{6,11} + r_{5,10} + r_{4,9} + r_{3,8} - r_{18,23} - r_{17,22} - r_{16,21} - r_{15,20}$	B _u	$\nu(\text{CH})_2$	
S ₂₀	$r_{6,11} + r_{5,10} - r_{4,9} - r_{3,8} + r_{18,23} + r_{17,22} - r_{16,21} - r_{15,20}$	A _g	$\nu(\text{CH})_3$	
S ₂₁	$r_{6,11} + r_{5,10} - r_{4,9} - r_{3,8} - r_{18,23} - r_{17,22} + r_{16,21} + r_{15,20}$	B _u	$\nu(\text{CH})_4$	
S ₂₂	$r_{6,11} - r_{5,10} + r_{4,9} - r_{3,8} + r_{18,23} - r_{17,22} + r_{16,21} - r_{15,20}$	A _g	$\nu(\text{CH})_5$	

S ₂₃	$\Gamma_{6,11} - \Gamma_{5,10} + \Gamma_{4,9} - \Gamma_{3,8} - \Gamma_{18,23} + \Gamma_{17,22} - \Gamma_{16,21} + \Gamma_{15,20}$	B _u	$\nu(\text{CH})_6$
S ₂₄	$\Gamma_{6,11} - \Gamma_{5,10} - \Gamma_{4,9} + \Gamma_{3,8} + \Gamma_{18,23} - \Gamma_{17,22} - \Gamma_{16,21} + \Gamma_{15,20}$	A _g	$\nu(\text{CH})_7$
S ₂₅	$\Gamma_{6,11} - \Gamma_{5,10} - \Gamma_{4,9} + \Gamma_{3,8} - \Gamma_{18,23} + \Gamma_{17,22} + \Gamma_{16,21} - \Gamma_{15,20}$	B _u	$\nu(\text{CH})_8$
S ₂₆	$\beta_{13,1,2} + \beta_{1,13,14}$	A _g	$\delta(\text{NNC})$
S ₂₇	$\beta_{13,1,2} - \beta_{1,13,14}$	B _u	$\delta(\text{NNC})$
S ₂₈	$\beta_{1,2,3} - \beta_{1,2,7} + \beta_{13,14,15} - \beta_{13,14,19}$	A _g	$\delta(\text{NCC})$
S ₂₉	$\beta_{1,2,3} - \beta_{1,2,7} - \beta_{13,14,15} + \beta_{13,14,19}$	B _u	$\delta(\text{NCC})$
S ₃₀	$\beta_{7,2,3} - \beta_{2,3,4} + \beta_{3,4,5} - \beta_{4,5,6} + \beta_{5,6,7} - \beta_{6,7,2} + \beta_{19,14,15}$ $- \beta_{14,15,16} + \beta_{15,16,17} - \beta_{16,17,18} + \beta_{17,18,19} - \beta_{18,19,14}$	A _g	$\delta(\text{ring1})$
S ₃₁	$\beta_{7,2,3} - \beta_{2,3,4} + \beta_{3,4,5} - \beta_{4,5,6} + \beta_{5,6,7} - \beta_{6,7,2} - \beta_{19,14,15}$ $+ \beta_{14,15,16} - \beta_{15,16,17} + \beta_{16,17,18} - \beta_{17,18,19} + \beta_{18,19,14}$	B _u	$\delta(\text{ring2})$
S ₃₂	$2\beta_{7,2,3} - \beta_{2,3,4} - \beta_{3,4,5} + 2\beta_{4,5,6} - \beta_{5,6,7} - \beta_{6,7,2} + 2\beta_{19,14,15}$ $- \beta_{14,15,16} - \beta_{15,16,17} + 2\beta_{16,17,18} - \beta_{17,18,19} - \beta_{18,19,14}$	A _g	$\delta(\text{ring3})$
S ₃₃	$2\beta_{7,2,3} - \beta_{2,3,4} - \beta_{3,4,5} + 2\beta_{4,5,6} - \beta_{5,6,7} - \beta_{6,7,2} - 2\beta_{19,14,15}$ $+ \beta_{14,15,16} + \beta_{15,16,17} - 2\beta_{16,17,18} + \beta_{17,18,19} + \beta_{18,19,14}$	B _u	$\delta(\text{ring4})$
S ₃₄	$\beta_{2,3,4} - \beta_{3,4,5} + \beta_{5,6,7} - \beta_{6,7,2} + \beta_{14,15,16} - \beta_{15,16,17}$ $+ \beta_{17,18,19} - \beta_{18,19,14}$	A _g	$\delta(\text{ring5})$
S ₃₅	$\beta_{2,3,4} - \beta_{3,4,5} + \beta_{5,6,7} - \beta_{6,7,2} - \beta_{14,15,16} + \beta_{15,16,17}$ $- \beta_{17,18,19} + \beta_{18,19,14}$	B _u	$\delta(\text{ring6})$
S ₃₆	$\beta_{8,3,2} - \beta_{8,3,4} - \beta_{9,4,3} + \beta_{9,4,5} - 2\beta_{10,5,4} + 2\beta_{10,5,6} - \beta_{11,6,5}$ $+ \beta_{11,6,7} + \beta_{12,7,6} - \beta_{12,7,2} + \beta_{20,15,14} - \beta_{20,15,16} - \beta_{21,16,15}$ $+ \beta_{21,16,17} - 2\beta_{22,17,16} + 2\beta_{22,17,18} - \beta_{23,18,27} + \beta_{23,18,19}$ $+ \beta_{24,19,18} - \beta_{24,19,14}$	A _g	$\delta(\text{CH})_1$
S ₃₇	$\beta_{8,3,2} - \beta_{8,3,4} - \beta_{9,4,3} + \beta_{9,4,5} - 2\beta_{10,5,4} + 2\beta_{10,5,6} - \beta_{11,6,5}$ $+ \beta_{11,6,7} + \beta_{12,7,6} - \beta_{12,7,2} - \beta_{20,15,14} + \beta_{20,15,16} + \beta_{21,16,15}$ $- \beta_{21,16,17} + 2\beta_{22,17,16} - 2\beta_{22,17,18} + \beta_{23,18,27} - \beta_{23,18,19}$ $- \beta_{24,19,18} + \beta_{24,19,14}$	B _u	$\delta(\text{CH})_2$
S ₃₈	$\beta_{8,3,2} - \beta_{8,3,4} - \beta_{9,4,3} + \beta_{9,4,5} + 2\beta_{10,5,4} - 2\beta_{10,5,6} - \beta_{11,6,5}$ $+ \beta_{11,6,7} + \beta_{12,7,6} - \beta_{12,7,2} + \beta_{20,15,14} - \beta_{20,15,16} - \beta_{21,16,15}$ $+ \beta_{21,16,17} + 2\beta_{22,17,16} - 2\beta_{22,17,18} - \beta_{23,18,27} + \beta_{23,18,19}$ $+ \beta_{24,19,18} - \beta_{24,19,14}$	A _g	$\delta(\text{CH})_3$
S ₃₉	$\beta_{8,3,2} - \beta_{8,3,4} - \beta_{9,4,3} + \beta_{9,4,5} + 2\beta_{10,5,4} - 2\beta_{10,5,6} - \beta_{11,6,5}$ $+ \beta_{11,6,7} + \beta_{12,7,6} - \beta_{12,7,2} - \beta_{20,15,14} + \beta_{20,15,16}$ $+ \beta_{21,16,15} - \beta_{21,16,17} - 2\beta_{22,17,16} + 2\beta_{22,17,18}$	B _u	$\delta(\text{CH})_4$

B.1 Azobenzene Supporting Information

	$+ \beta_{23,18,27} - \beta_{23,18,19} - \beta_{24,19,18} + \beta_{24,19,14}$		
S40	$\beta_{8,3,2} - \beta_{8,3,4} + \beta_{9,4,3} - \beta_{9,4,5} + \beta_{11,6,5} - \beta_{11,6,7} + \beta_{12,7,6}$ $- \beta_{12,7,2} + \beta_{20,15,14} - \beta_{20,15,16} + \beta_{21,16,15} - \beta_{21,16,17}$ $+ \beta_{23,18,27} - \beta_{23,18,19} + \beta_{24,19,18} - \beta_{24,19,14}$	A _g	$\delta(\text{CH})_5$
S41	$\beta_{8,3,2} - \beta_{8,3,4} + \beta_{9,4,3} - \beta_{9,4,5} + \beta_{11,6,5} - \beta_{11,6,7} + \beta_{12,7,6}$ $- \beta_{12,7,2} - \beta_{20,15,14} + \beta_{20,15,16} - \beta_{21,16,15} + \beta_{21,16,17}$ $- \beta_{23,18,27} + \beta_{23,18,19} - \beta_{24,19,18} + \beta_{24,19,14}$	B _u	$\delta(\text{CH})_6$
S42	$\beta_{8,3,2} - \beta_{8,3,4} + \beta_{9,4,3} - \beta_{9,4,5} - \beta_{11,6,5} + \beta_{11,6,7} - \beta_{12,7,6}$ $+ \beta_{12,7,2} + \beta_{20,15,14} - \beta_{20,15,16} + \beta_{21,16,15} - \beta_{21,16,17}$ $- \beta_{23,18,27} + \beta_{23,18,19} - \beta_{24,19,18} + \beta_{24,19,14}$	A _g	$\delta(\text{CH})_7$
S43	$\beta_{8,3,2} - \beta_{8,3,4} + \beta_{9,4,3} - \beta_{9,4,5} - \beta_{11,6,5} + \beta_{11,6,7} - \beta_{12,7,6}$ $+ \beta_{12,7,2} - \beta_{20,15,14} + \beta_{20,15,16} - \beta_{21,16,15} + \beta_{21,16,17}$ $+ \beta_{23,18,27} - \beta_{23,18,19} + \beta_{24,19,18} - \beta_{24,19,14}$	B _u	$\delta(\text{CH})_8$
S44	$\beta_{8,3,2} - \beta_{8,3,4} - \beta_{9,4,3} + \beta_{9,4,5} + \beta_{11,6,5} - \beta_{11,6,7} - \beta_{12,7,6}$ $+ \beta_{12,7,2} - \beta_{20,15,14} + \beta_{20,15,16} + \beta_{21,16,15} - \beta_{21,16,17}$ $- \beta_{23,18,27} + \beta_{23,18,19} + \beta_{24,19,18} - \beta_{24,19,14}$	B _u	$\delta(\text{CH})_9$
S45	$\beta_{8,3,2} - \beta_{8,3,4} - \beta_{9,4,3} + \beta_{9,4,5} + \beta_{11,6,5} - \beta_{11,6,7} - \beta_{12,7,6}$ $+ \beta_{12,7,2} + \beta_{20,15,14} - \beta_{20,15,16} - \beta_{21,16,15} + \beta_{21,16,17}$ $+ \beta_{23,18,27} - \beta_{23,18,19} - \beta_{24,19,18} + \beta_{24,19,14}$	A _g	$\delta(\text{CH})_{10}$
S46	$\tau_{2,1,13,14}$	A _u	$\tau(\text{CNNC})$
S47	$\tau_{13,1,2,3} + \tau_{13,1,2,7} + \tau_{1,13,14,15} + \tau_{1,13,14,19}$	A _u	$\tau(\text{NNCC})$
S48	$\tau_{13,1,2,3} + \tau_{13,1,2,7} - \tau_{1,13,14,15} - \tau_{1,13,14,19}$	B _g	$\tau(\text{NNCC})$
S49	$\tau_{7,2,3,4} - \tau_{2,3,4,5} + \tau_{3,4,5,6} - \tau_{4,5,6,7} + \tau_{5,6,7,2} - \tau_{6,7,2,3}$ $+ \tau_{19,14,15,16} - \tau_{14,15,16,17} + \tau_{15,16,17,18} - \tau_{16,17,18,19}$ $+ \tau_{17,18,19,14} - \tau_{18,19,14,15}$	A _u	$\tau(\text{ring1})$
S50	$\tau_{7,2,3,4} - \tau_{2,3,4,5} + \tau_{3,4,5,6} - \tau_{4,5,6,7} + \tau_{5,6,7,2} - \tau_{6,7,2,3}$ $- \tau_{19,14,15,16} + \tau_{14,15,16,17} - \tau_{15,16,17,18} + \tau_{16,17,18,19}$ $- \tau_{17,18,19,14} + \tau_{18,19,14,15}$	B _g	$\tau(\text{ring2})$
S51	$\tau_{7,2,3,4} - \tau_{3,4,5,6} + \tau_{4,5,6,7} - \tau_{6,7,2,3} + \tau_{19,14,15,16}$ $- \tau_{15,16,17,18} + \tau_{16,17,18,19} - \tau_{18,19,14,15}$	A _u	$\tau(\text{ring3})$
S52	$\tau_{7,2,3,4} - \tau_{3,4,5,6} + \tau_{4,5,6,7} - \tau_{6,7,2,3} - \tau_{19,14,15,16}$ $+ \tau_{15,16,17,18} - \tau_{16,17,18,19} + \tau_{18,19,14,15}$	B _g	$\tau(\text{ring4})$
S53	$- \tau_{7,2,3,4} + 2\tau_{2,3,4,5} - \tau_{3,4,5,6} - \tau_{4,5,6,7} + 2\tau_{5,6,7,2}$ $- \tau_{6,7,2,3} - \tau_{19,14,15,16} + 2\tau_{14,15,16,17} - \tau_{15,16,17,18}$	A _u	$\tau(\text{ring5})$

	$-\tau_{16,17,18,19} + 2\tau_{17,18,19,14} - \tau_{18,19,14,15}$	
S ₅₄	$-\tau_{7,2,3,4} + 2\tau_{2,3,4,5} - \tau_{3,4,5,6} - \tau_{4,5,6,7} + 2\tau_{5,6,7,2}$ $-\tau_{6,7,2,3} + \tau_{19,14,15,16} - 2\tau_{14,15,16,17} + \tau_{15,16,17,18}$ $+ \tau_{16,17,18,19} - 2\tau_{17,18,19,14} + \tau_{18,19,14,15}$	B _g $\tau(\text{ring6})$
S ₅₅	$\tau_{1,3,2,7} + \tau_{13,15,14,19}$	A _u $\gamma(\text{NC})$
S ₅₆	$\tau_{1,3,2,7} - \tau_{13,15,14,19}$	B _g $\gamma(\text{NC})$
S ₅₇	$2\tau_{12,2,7,6} - 3\tau_{11,7,6,5} + 2\tau_{10,6,5,4} - 3\tau_{9,5,4,3} + 2\tau_{8,4,3,2}$ $+ 2\tau_{24,14,19,18} - 3\tau_{23,19,18,17} + 2\tau_{22,18,17,16}$ $- 3\tau_{21,17,16,15} + 2\tau_{20,16,15,14}$	A _u $\gamma(\text{CH})_1$
S ₅₈	$2\tau_{12,2,7,6} - 3\tau_{11,7,6,5} + 2\tau_{10,6,5,4} - 3\tau_{9,5,4,3} + 2\tau_{8,4,3,2}$ $- 2\tau_{24,14,19,18} + 3\tau_{23,19,18,17} - 2\tau_{22,18,17,16}$ $+ 3\tau_{21,17,16,15} - 2\tau_{20,16,15,14}$	B _g $\gamma(\text{CH})_2$
S ₅₉	$\tau_{12,2,7,6} + \tau_{11,7,6,5} + \tau_{10,6,5,4} + \tau_{9,5,4,3} + \tau_{8,4,3,2}$ $+ \tau_{24,14,19,18} + \tau_{23,19,18,17} + \tau_{22,18,17,16}$ $+ \tau_{21,17,16,15} + \tau_{20,16,15,14}$	A _u $\gamma(\text{CH})_3$
S ₆₀	$\tau_{12,2,7,6} + \tau_{11,7,6,5} + \tau_{10,6,5,4} + \tau_{9,5,4,3} + \tau_{8,4,3,2}$ $- \tau_{24,14,19,18} - \tau_{23,19,18,17} - \tau_{22,18,17,16}$ $- \tau_{21,17,16,15} - \tau_{20,16,15,14}$	B _g $\gamma(\text{CH})_4$
S ₆₁	$\tau_{12,2,7,6} + \tau_{11,7,6,5} - \tau_{9,5,4,3} - \tau_{8,4,3,2} + \tau_{24,14,19,18}$ $+ \tau_{23,19,18,17} - \tau_{21,17,16,15} - \tau_{20,16,15,14}$	A _u $\gamma(\text{CH})_5$
S ₆₂	$\tau_{12,2,7,6} + \tau_{11,7,6,5} - \tau_{9,5,4,3} - \tau_{8,4,3,2} - \tau_{24,14,19,18}$ $- \tau_{23,19,18,17} + \tau_{21,17,16,15} + \tau_{20,16,15,14}$	B _g $\gamma(\text{CH})_6$
S ₆₃	$\tau_{12,2,7,6} - \tau_{11,7,6,5} + \tau_{9,5,4,3} - \tau_{8,4,3,2} + \tau_{24,14,19,18}$ $- \tau_{23,19,18,17} + \tau_{21,17,16,15} - \tau_{20,16,15,14}$	A _u $\gamma(\text{CH})_7$
S ₆₄	$\tau_{12,2,7,6} - \tau_{11,7,6,5} + \tau_{9,5,4,3} - \tau_{8,4,3,2} - \tau_{24,14,19,18}$ $+ \tau_{23,19,18,17} - \tau_{21,17,16,15} + \tau_{20,16,15,14}$	B _g $\gamma(\text{CH})_8$
S ₆₅	$\tau_{12,2,7,6} - 2\tau_{10,6,5,4} + \tau_{8,4,3,2} + \tau_{24,14,19,18}$ $- 2\tau_{22,18,17,16} + \tau_{20,16,15,14}$	A _u $\gamma(\text{CH})_9$
S ₆₆	$\tau_{12,2,7,6} - 2\tau_{10,6,5,4} + \tau_{8,4,3,2} - \tau_{24,14,19,18}$ $+ 2\tau_{22,18,17,16} - \tau_{20,16,15,14}$	B _g $\gamma(\text{CH})_{10}$

^aAtom numbering is shown in Figure B.1; $r_{i,j}$ is the distance between atoms A_i and A_j ; $\beta_{i,j,k}$ is the angle between vectors A_kA_i and A_kA_j ; $\tau_{i,j,k,l}$ is the dihedral angle between the plane defined by A_i, A_j, A_k and the plane defined by A_j, A_k, A_l atoms; ν - stretching, δ - in-plane bending, γ - out-of-plane bending, τ - torsion; normalization constants not given.

B.1 Azobenzene Supporting Information

Table B.5 Theoretical wavenumbers (ν/cm^{-1}), Raman scattering activities ($S/\text{\AA}^4$ a.m.u. $^{-1}$) and potential energy distributions (PED, %) for the Raman-active A_g and B_g normal modes of *E*-AB calculated at the PW91/cc-pVTZ level.

ν^a	$S/\text{\AA}^4$ a.m.u. $^{-1}$	Calculated	
		Sym.	PED ^b (%)
3142.5	164.6	A_g	ν_s (CH) (93)
3133.5	597.7	A_g	$\nu(\text{CH})_1$ (83), $\nu(\text{CH})_3$ (12)
3124.0	354.0	A_g	$\nu(\text{CH})_3$ (57), $\nu(\text{CH})_7$ (30)
3113.9	324.5	A_g	$\nu(\text{CH})_7$ (55), $\nu(\text{CH})_3$ (28), $\nu(\text{CH})_5$ (11)
3103.9	88.2	A_g	$\nu(\text{CH})_5$ (82), $\nu(\text{CH})_7$ (14)
1598.2	830.8	A_g	$\nu(\text{CC})_3$ (62), $\delta(\text{CH})_{10}$ (16)
1581.6	26.0	A_g	$\nu(\text{CC})_5$ (66)
1483.1	727.0	A_g	$\nu(\text{N}=\text{N})$ (31), $\delta(\text{CH})_7$ (30), $\nu(\text{CC})_9$ (20)
1457.7	518.4	A_g	$\delta(\text{CH})_1$ (31), $\nu(\text{CC})_7$ (24), $\delta(\text{CH})_7$ (23), $\nu(\text{CC})_9$ (11)
1419.6	3851.0	A_g	$\nu(\text{N}=\text{N})$ (51), $\delta(\text{CH})_1$ (14), $\delta(\text{CH})_7$ (11)
1355.7	108.0	A_g	$\nu(\text{CC})_1$ (89)
1298.8	319.3	A_g	$\delta(\text{CH})_5$ (75)
1176.9	868.6	A_g	$\delta(\text{CH})_{10}$ (41), $\nu(\text{NC})$ (20), $\nu(\text{CC})_3$ (14)
1149.9	33.8	A_g	$\delta(\text{CH})_3$ (77)
1125.5	2514.4	A_g	$\delta(\text{CH})_{10}$ (35), $\nu(\text{NC})$ (27), $\delta(\text{ring}1)$ (11)
1068.5	23.9	A_g	$\delta(\text{CH})_1$ (42), $\nu(\text{CC})_7$ (10)
1017.8	28.3	A_g	$\nu(\text{CC})_9$ (49), $\delta(\text{CH})_7$ (25), $\nu(\text{CC})_{11}$ (23)
993.5	362.9	A_g	$\delta(\text{ring}1)$ (61), $\nu(\text{CC})_{11}$ (35)
979.3	1.2	B_g	$\gamma(\text{CH})_2$ (108), $\gamma(\text{CH})_8$ (14)
962.7	0.5	B_g	$\gamma(\text{CH})_8$ (98), $\gamma(\text{CH})_2$ (14)
921.7	0.1	B_g	$\gamma(\text{CH})_{10}$ (94)
913.5	6.9	A_g	$\delta(\text{NNC})$ (42), $\nu(\text{CC})_{11}$ (17), $\delta(\text{ring}1)$ (12)
832.8	2.9	B_g	$\gamma(\text{CH})_6$ (100)
759.1	0.2	B_g	$\gamma(\text{CH})_4$ (52), $\tau(\text{ring}2)$ (27), $\gamma(\text{NC})$ (18)
681.7	0.8	B_g	$\tau(\text{ring}2)$ (85), $\gamma(\text{CH})_4$ (32)
664.7	7.0	A_g	$\delta(\text{ring}3)$ (60), $\delta(\text{NNC})$ (18)
606.8	23.0	A_g	$\delta(\text{ring}5)$ (87)
471.3	0.3	B_g	$\gamma(\text{NC})$ (45), $\tau(\text{ring}4)$ (49)
406.2	0.01	B_g	$\tau(\text{ring}6)$ (111)
299.6	1.8	A_g	$\delta(\text{NCC})$ (43), $\nu(\text{NC})$ (17), $\delta(\text{ring}3)$ (16)
239.0	3.8	B_g	$\tau(\text{ring}4)$ (47), $\gamma(\text{NC})$ (34), $\tau(\text{NNCC})$ (16)
217.1	1.0	A_g	$\delta(\text{NCC})$ (39), $\delta(\text{NNC})$ (22), $\nu(\text{NC})$ (17), $\delta(\text{ring}3)$ (12)
94.8	3.3	B_g	$\tau(\text{NNCC})$ (82), $\tau(\text{ring}4)$ (16)

^a Theoretical frequencies (ν/cm^{-1}) were not scaled.

^b PED's lower than 10% not included. Definition of symmetry coordinates is given in Table Table B.4.

Table B.6 Internal symmetry coordinates used in the normal mode analysis of *Z*-azobenzene.^a

Coord.	Definition	Sym.	Appr.	Description
S ₁	$r_{1,13}$	A	$\nu(\text{N}=\text{N})$	
S ₂	$r_{1,2} + r_{13,14}$	A	$\nu(\text{NC})$	
S ₃	$r_{1,2} - r_{13,14}$	B	$\nu(\text{NC})$	
S ₄	$r_{2,3} - r_{3,4} + r_{4,5} - r_{5,6} + r_{6,7} - r_{7,2} + r_{14,15} - r_{15,16}$ $+ r_{16,17} - r_{17,18} + r_{18,19} - r_{19,14}$	A	$\nu(\text{CC})_1$	
S ₅	$r_{2,3} - r_{3,4} + r_{4,5} - r_{5,6} + r_{6,7} - r_{7,2} - r_{14,15} + r_{15,16}$ $- r_{16,17} + r_{17,18} - r_{18,19} + r_{19,14}$	B	$\nu(\text{CC})_2$	
S ₆	$-r_{2,3} + 2r_{3,4} - r_{4,5} - r_{5,6} + 2r_{6,7} - r_{7,2} - r_{14,15} + 2r_{15,16}$ $- r_{16,17} - r_{17,18} + 2r_{18,19} - r_{19,14}$	A	$\nu(\text{CC})_3$	
S ₇	$-r_{2,3} + 2r_{3,4} - r_{4,5} - r_{5,6} + 2r_{6,7} - r_{7,2} + r_{14,15} - 2r_{15,16}$ $+ r_{16,17} + r_{17,18} - 2r_{18,19} + r_{19,14}$	B	$\nu(\text{CC})_4$	
S ₈	$r_{2,3} - r_{4,5} + r_{5,6} - r_{7,2} + r_{14,15} - r_{16,17} + r_{17,18} - r_{19,14}$	A	$\nu(\text{CC})_5$	
S ₉	$r_{2,3} - r_{4,5} + r_{5,6} - r_{7,2} - r_{14,15} + r_{16,17} - r_{17,18} + r_{19,14}$	B	$\nu(\text{CC})_6$	
S ₁₀	$r_{2,3} + 2r_{3,4} + r_{4,5} - r_{5,6} - 2r_{6,7} - r_{7,2} + r_{14,15} + 2r_{15,16}$ $+ r_{16,17} - r_{17,18} - 2r_{18,19} + r_{19,14}$	A	$\nu(\text{CC})_7$	
S ₁₁	$r_{2,3} + 2r_{3,4} + r_{4,5} - r_{5,6} - 2r_{6,7} - r_{7,2} - r_{14,15} - 2r_{15,16}$ $- r_{16,17} + r_{17,18} + 2r_{18,19} + r_{19,14}$	B	$\nu(\text{CC})_8$	
S ₁₂	$r_{2,3} - r_{4,5} - r_{5,6} + r_{7,2} + r_{14,15} - r_{16,17} - r_{17,18} + r_{19,14}$	A	$\nu(\text{CC})_9$	
S ₁₃	$r_{2,3} - r_{4,5} - r_{5,6} + r_{7,2} - r_{14,15} + r_{16,17} + r_{17,18} - r_{19,14}$	B	$\nu(\text{CC})_{10}$	
S ₁₄	$r_{2,3} + r_{3,4} + r_{4,5} + r_{5,6} + r_{6,7} + r_{7,2} + r_{14,15} + r_{15,16}$ $+ r_{16,17} + r_{17,18} + r_{18,19} + r_{19,14}$	A	$\nu(\text{CC})_{11}$	
S ₁₅	$r_{2,3} + r_{3,4} + r_{4,5} + r_{5,6} + r_{6,7} + r_{7,2} - r_{14,15} - r_{15,16}$ $- r_{16,17} - r_{17,18} - r_{18,19} - r_{19,14}$	B	$\nu(\text{CC})_{12}$	
S ₁₆	$r_{7,12} + r_{6,11} + r_{5,10} + r_{4,9} + r_{3,8} + r_{19,24} + r_{18,23}$ $+ r_{17,22} + r_{16,21} + r_{15,20}$	A	$\nu(\text{CH})_1$	
S ₁₇	$r_{7,12} + r_{6,11} + r_{5,10} + r_{4,9} + r_{3,8} - r_{19,24} - r_{18,23}$ $- r_{17,22} - r_{16,21} - r_{15,20}$	B	$\nu(\text{CH})_2$	
S ₁₈	$2r_{7,12} - 3r_{6,11} + 2r_{5,10} - 3r_{4,9} + 2r_{3,8} + 2r_{19,24}$ $- 3r_{18,23} + 2r_{17,22} - 3r_{16,21} + 2r_{15,20}$	A	$\nu(\text{CH})_3$	
S ₁₉	$2r_{7,12} - 3r_{6,11} + 2r_{5,10} - 3r_{4,9} + 2r_{3,8} - 2r_{19,24}$ $+ 3r_{18,23} - 2r_{17,22} + 3r_{16,21} - 2r_{15,20}$	B	$\nu(\text{CH})_4$	

B.1 Azobenzene Supporting Information

S ₂₀	$r_{7,12} - r_{6,11} + r_{4,9} - r_{3,8} + r_{19,24} - r_{18,23} + r_{16,21} - r_{15,20}$	A	$\nu(\text{CH})_5$
S ₂₁	$r_{7,12} - r_{6,11} + r_{4,9} - r_{3,8} - r_{19,24} + r_{18,23} - r_{16,21} + r_{15,20}$	B	$\nu(\text{CH})_6$
S ₂₂	$r_{7,12} + r_{6,11} - r_{4,9} - r_{3,8} + r_{19,24} + r_{18,23} - r_{16,21} - r_{15,20}$	A	$\nu(\text{CH})_7$
S ₂₃	$r_{7,12} + r_{6,11} - r_{4,9} - r_{3,8} - r_{19,24} - r_{18,23} + r_{16,21} + r_{15,20}$	B	$\nu(\text{CH})_8$
S ₂₄	$r_{7,12} - 2r_{5,10} + r_{3,8} + r_{19,24} - 2r_{17,22} + r_{15,20}$	A	$\nu(\text{CH})_9$
S ₂₅	$r_{7,12} - 2r_{5,10} + r_{3,8} - r_{19,24} + 2r_{17,22} - r_{15,20}$	B	$\nu(\text{CH})_{10}$
S ₂₆	$\beta_{13,1,2} + \beta_{1,13,14}$	A	$\delta(\text{NNC})$
S ₂₇	$\beta_{13,1,2} - \beta_{1,13,14}$	B	$\delta(\text{NNC})$
S ₂₈	$\beta_{1,2,3} - \beta_{1,2,7} + \beta_{13,14,15} - \beta_{13,14,19}$	A	$\delta(\text{NCC})$
S ₂₉	$\beta_{1,2,3} - \beta_{1,2,7} - \beta_{13,14,15} + \beta_{13,14,19}$	B	$\delta(\text{NCC})$
S ₃₀	$\beta_{7,2,3} - \beta_{2,3,4} + \beta_{3,4,5} - \beta_{4,5,6} + \beta_{5,6,7} - \beta_{6,7,2} + \beta_{19,14,15}$ $- \beta_{14,15,16} + \beta_{15,16,17} - \beta_{16,17,18} + \beta_{17,18,19} - \beta_{18,19,14}$	A	$\delta(\text{ring1})$
S ₃₁	$\beta_{7,2,3} - \beta_{2,3,4} + \beta_{3,4,5} - \beta_{4,5,6} + \beta_{5,6,7} - \beta_{6,7,2} - \beta_{19,14,15}$ $+ \beta_{14,15,16} - \beta_{15,16,17} + \beta_{16,17,18} - \beta_{17,18,19} + \beta_{18,19,14}$	B	$\delta(\text{ring2})$
S ₃₂	$2\beta_{7,2,3} - \beta_{2,3,4} - \beta_{3,4,5} + 2\beta_{4,5,6} - \beta_{5,6,7} - \beta_{6,7,2} + 2\beta_{19,14,15}$ $- \beta_{14,15,16} - \beta_{15,16,17} + 2\beta_{16,17,18} - \beta_{17,18,19} - \beta_{18,19,14}$	A	$\delta(\text{ring3})$
S ₃₃	$2\beta_{7,2,3} - \beta_{2,3,4} - \beta_{3,4,5} + 2\beta_{4,5,6} - \beta_{5,6,7} - \beta_{6,7,2} - 2\beta_{19,14,15}$ $+ \beta_{14,15,16} + \beta_{15,16,17} - 2\beta_{16,17,18} + \beta_{17,18,19} + \beta_{18,19,14}$	B	$\delta(\text{ring4})$
S ₃₄	$\beta_{2,3,4} - \beta_{3,4,5} + \beta_{5,6,7} - \beta_{6,7,2} + \beta_{14,15,16} - \beta_{15,16,17}$ $+ \beta_{17,18,19} - \beta_{18,19,14}$	A	$\delta(\text{ring5})$
S ₃₅	$\beta_{2,3,4} - \beta_{3,4,5} + \beta_{5,6,7} - \beta_{6,7,2} - \beta_{14,15,16} + \beta_{15,16,17}$ $- \beta_{17,18,19} + \beta_{18,19,14}$	B	$\delta(\text{ring6})$
S ₃₆	$\beta_{8,3,2} - \beta_{8,3,4} - \beta_{9,4,3} + \beta_{9,4,5} - 2\beta_{10,5,4} + 2\beta_{10,5,6} - \beta_{11,6,5}$ $+ \beta_{11,6,7} + \beta_{12,7,6} - \beta_{12,7,2} + \beta_{20,15,14} - \beta_{20,15,16} - \beta_{21,16,15}$ $+ \beta_{21,16,17} - 2\beta_{22,17,16} + 2\beta_{22,17,18} - \beta_{23,18,27} + \beta_{23,18,19}$ $+ \beta_{24,19,18} - \beta_{24,19,14}$	A	$\delta(\text{CH})_1$
S ₃₇	$\beta_{8,3,2} - \beta_{8,3,4} - \beta_{9,4,3} + \beta_{9,4,5} - 2\beta_{10,5,4} + 2\beta_{10,5,6} - \beta_{11,6,5}$ $+ \beta_{11,6,7} + \beta_{12,7,6} - \beta_{12,7,2} - \beta_{20,15,14} + \beta_{20,15,16} + \beta_{21,16,15}$ $- \beta_{21,16,17} + 2\beta_{22,17,16} - 2\beta_{22,17,18} + \beta_{23,18,27} - \beta_{23,18,19}$ $- \beta_{24,19,18} + \beta_{24,19,14}$	B	$\delta(\text{CH})_2$
S ₃₈	$\beta_{8,3,2} - \beta_{8,3,4} - \beta_{9,4,3} + \beta_{9,4,5} + 2\beta_{10,5,4} - 2\beta_{10,5,6} - \beta_{11,6,5}$ $+ \beta_{11,6,7} + \beta_{12,7,6} - \beta_{12,7,2} + \beta_{20,15,14} - \beta_{20,15,16} - \beta_{21,16,15}$ $+ \beta_{21,16,17} + 2\beta_{22,17,16} - 2\beta_{22,17,18} - \beta_{23,18,27} + \beta_{23,18,19}$ $+ \beta_{24,19,18} - \beta_{24,19,14}$	A	$\delta(\text{CH})_3$
S ₃₉	$\beta_{8,3,2} - \beta_{8,3,4} - \beta_{9,4,3} + \beta_{9,4,5} + 2\beta_{10,5,4} - 2\beta_{10,5,6}$	B	$\delta(\text{CH})_4$

	$ \begin{aligned} & -\beta_{11,6,5} + \beta_{11,6,7} + \beta_{12,7,6} - \beta_{12,7,2} - \beta_{20,15,14} + \beta_{20,15,16} \\ & + \beta_{21,16,15} - \beta_{21,16,17} - 2\beta_{22,17,16} + 2\beta_{22,17,18} \\ & + \beta_{23,18,27} - \beta_{23,18,19} - \beta_{24,19,18} + \beta_{24,19,14} \end{aligned} $		
S ₄₀	$ \begin{aligned} & \beta_{8,3,2} - \beta_{8,3,4} + \beta_{9,4,3} - \beta_{9,4,5} + \beta_{11,6,5} - \beta_{11,6,7} + \beta_{12,7,6} \\ & - \beta_{12,7,2} + \beta_{20,15,14} - \beta_{20,15,16} + \beta_{21,16,15} - \beta_{21,16,17} \\ & + \beta_{23,18,27} - \beta_{23,18,19} + \beta_{24,19,18} - \beta_{24,19,14} \end{aligned} $	A	$\delta(\text{CH})_5$
S ₄₁	$ \begin{aligned} & \beta_{8,3,2} - \beta_{8,3,4} + \beta_{9,4,3} - \beta_{9,4,5} + \beta_{11,6,5} - \beta_{11,6,7} \\ & + \beta_{12,7,6} - \beta_{12,7,2} - \beta_{20,15,14} + \beta_{20,15,16} - \beta_{21,16,15} \\ & + \beta_{21,16,17} - \beta_{23,18,27} + \beta_{23,18,19} - \beta_{24,19,18} + \beta_{24,19,14} \end{aligned} $	B	$\delta(\text{CH})_6$
S ₄₂	$ \begin{aligned} & \beta_{8,3,2} - \beta_{8,3,4} + \beta_{9,4,3} - \beta_{9,4,5} - \beta_{11,6,5} + \beta_{11,6,7} - \beta_{12,7,6} \\ & + \beta_{12,7,2} + \beta_{20,15,14} - \beta_{20,15,16} + \beta_{21,16,15} - \beta_{21,16,17} \\ & - \beta_{23,18,27} + \beta_{23,18,19} - \beta_{24,19,18} + \beta_{24,19,14} \end{aligned} $	A	$\delta(\text{CH})_7$
S ₄₃	$ \begin{aligned} & \beta_{8,3,2} - \beta_{8,3,4} + \beta_{9,4,3} - \beta_{9,4,5} - \beta_{11,6,5} + \beta_{11,6,7} - \beta_{12,7,6} \\ & + \beta_{12,7,2} - \beta_{20,15,14} + \beta_{20,15,16} - \beta_{21,16,15} + \beta_{21,16,17} \\ & + \beta_{23,18,27} - \beta_{23,18,19} + \beta_{24,19,18} - \beta_{24,19,14} \end{aligned} $	B	$\delta(\text{CH})_8$
S ₄₄	$ \begin{aligned} & \beta_{8,3,2} - \beta_{8,3,4} - \beta_{9,4,3} + \beta_{9,4,5} + \beta_{11,6,5} - \beta_{11,6,7} - \beta_{12,7,6} \\ & + \beta_{12,7,2} - \beta_{20,15,14} + \beta_{20,15,16} + \beta_{21,16,15} - \beta_{21,16,17} \\ & - \beta_{23,18,27} + \beta_{23,18,19} + \beta_{24,19,18} - \beta_{24,19,14} \end{aligned} $	B	$\delta(\text{CH})_9$
S ₄₅	$ \begin{aligned} & \beta_{8,3,2} - \beta_{8,3,4} - \beta_{9,4,3} + \beta_{9,4,5} + \beta_{11,6,5} - \beta_{11,6,7} - \beta_{12,7,6} \\ & + \beta_{12,7,2} + \beta_{20,15,14} - \beta_{20,15,16} - \beta_{21,16,15} + \beta_{21,16,17} \\ & + \beta_{23,18,27} - \beta_{23,18,19} - \beta_{24,19,18} + \beta_{24,19,14} \end{aligned} $	A	$\delta(\text{CH})_{10}$
S ₄₆	$\tau_{2,1,13,14}$	A	$\tau(\text{CNNC})$
S ₄₇	$\tau_{13,1,2,3} + \tau_{13,1,2,7} + \tau_{1,13,14,15} + \tau_{1,13,14,19}$	A	$\tau(\text{NNCC})$
S ₄₈	$\tau_{13,1,2,3} + \tau_{13,1,2,7} - \tau_{1,13,14,15} - \tau_{1,13,14,19}$	B	$\tau(\text{NNCC})$
S ₄₉	$ \begin{aligned} & \tau_{7,2,3,4} - \tau_{2,3,4,5} + \tau_{3,4,5,6} - \tau_{4,5,6,7} + \tau_{5,6,7,2} - \tau_{6,7,2,3} \\ & + \tau_{19,14,15,16} - \tau_{14,15,16,17} + \tau_{15,16,17,18} - \tau_{16,17,18,19} \\ & + \tau_{17,18,19,14} - \tau_{18,19,14,15} \end{aligned} $	A	$\tau(\text{ring1})$
S ₅₀	$ \begin{aligned} & \tau_{7,2,3,4} - \tau_{2,3,4,5} + \tau_{3,4,5,6} - \tau_{4,5,6,7} + \tau_{5,6,7,2} \\ & - \tau_{6,7,2,3} - \tau_{19,14,15,16} + \tau_{14,15,16,17} - \tau_{15,16,17,18} \\ & + \tau_{16,17,18,19} - \tau_{17,18,19,14} + \tau_{18,19,14,15} \end{aligned} $	B	$\tau(\text{ring2})$
S ₅₁	$ \begin{aligned} & \tau_{7,2,3,4} - \tau_{3,4,5,6} + \tau_{4,5,6,7} - \tau_{6,7,2,3} + \tau_{19,14,15,16} \\ & - \tau_{15,16,17,18} + \tau_{16,17,18,19} - \tau_{18,19,14,15} \end{aligned} $	A	$\tau(\text{ring3})$
S ₅₂	$ \begin{aligned} & \tau_{7,2,3,4} - \tau_{3,4,5,6} + \tau_{4,5,6,7} - \tau_{6,7,2,3} - \tau_{19,14,15,16} \\ & + \tau_{15,16,17,18} - \tau_{16,17,18,19} + \tau_{18,19,14,15} \end{aligned} $	B	$\tau(\text{ring4})$
S ₅₃	$ \begin{aligned} & -\tau_{7,2,3,4} + 2\tau_{2,3,4,5} - \tau_{3,4,5,6} - \tau_{4,5,6,7} + 2\tau_{5,6,7,2} \end{aligned} $	A	$\tau(\text{ring5})$

B.1 Azobenzene Supporting Information

	$-\tau_{6,7,2,3} - \tau_{19,14,15,16} + 2\tau_{14,15,16,17} - \tau_{15,16,17,18}$	
	$-\tau_{16,17,18,19} + 2\tau_{17,18,19,14} - \tau_{18,19,14,15}$	
S ₅₄	$-\tau_{7,2,3,4} + 2\tau_{2,3,4,5} - \tau_{3,4,5,6} - \tau_{4,5,6,7} + 2\tau_{5,6,7,2}$	B $\tau(\text{ring6})$
	$-\tau_{6,7,2,3} + \tau_{19,14,15,16} - 2\tau_{14,15,16,17} + \tau_{15,16,17,18}$	
	$+ \tau_{16,17,18,19} - 2\tau_{17,18,19,14} + \tau_{18,19,14,15}$	
S ₅₅	$\tau_{1,3,2,7} + \tau_{13,15,14,19}$	A $\gamma(\text{NC})$
S ₅₆	$\tau_{1,3,2,7} - \tau_{13,15,14,19}$	B $\gamma(\text{NC})$
S ₅₇	$2\tau_{12,2,7,6} - 3\tau_{11,7,6,5} + 2\tau_{10,6,5,4} - 3\tau_{9,5,4,3}$	A $\gamma(\text{CH})_1$
	$+ 2\tau_{8,4,3,2} + 2\tau_{24,14,19,18} - 3\tau_{23,19,18,17}$	
	$+ 2\tau_{22,18,17,16} - 3\tau_{21,17,16,15} + 2\tau_{20,16,15,14}$	
S ₅₈	$2\tau_{12,2,7,6} - 3\tau_{11,7,6,5} + 2\tau_{10,6,5,4} - 3\tau_{9,5,4,3}$	B $\gamma(\text{CH})_2$
	$+ 2\tau_{8,4,3,2} - 2\tau_{24,14,19,18} + 3\tau_{23,19,18,17}$	
	$- 2\tau_{22,18,17,16} + 3\tau_{21,17,16,15} - 2\tau_{20,16,15,14}$	
S ₅₉	$\tau_{12,2,7,6} + \tau_{11,7,6,5} + \tau_{10,6,5,4} + \tau_{9,5,4,3} + \tau_{8,4,3,2}$	A $\gamma(\text{CH})_3$
	$+ \tau_{24,14,19,18} + \tau_{23,19,18,17} + \tau_{22,18,17,16}$	
	$+ \tau_{21,17,16,15} + \tau_{20,16,15,14}$	
S ₆₀	$\tau_{12,2,7,6} + \tau_{11,7,6,5} + \tau_{10,6,5,4} + \tau_{9,5,4,3} + \tau_{8,4,3,2}$	B $\gamma(\text{CH})_4$
	$- \tau_{24,14,19,18} - \tau_{23,19,18,17} - \tau_{22,18,17,16}$	
	$- \tau_{21,17,16,15} - \tau_{20,16,15,14}$	
S ₆₁	$\tau_{12,2,7,6} + \tau_{11,7,6,5} - \tau_{9,5,4,3} - \tau_{8,4,3,2} + \tau_{24,14,19,18}$	A $\gamma(\text{CH})_5$
	$+ \tau_{23,19,18,17} - \tau_{21,17,16,15} - \tau_{20,16,15,14}$	
S ₆₂	$\tau_{12,2,7,6} + \tau_{11,7,6,5} - \tau_{9,5,4,3} - \tau_{8,4,3,2} - \tau_{24,14,19,18}$	B $\gamma(\text{CH})_6$
	$- \tau_{23,19,18,17} + \tau_{21,17,16,15} + \tau_{20,16,15,14}$	
S ₆₃	$\tau_{12,2,7,6} - \tau_{11,7,6,5} + \tau_{9,5,4,3} - \tau_{8,4,3,2} + \tau_{24,14,19,18}$	A $\gamma(\text{CH})_7$
	$- \tau_{23,19,18,17} + \tau_{21,17,16,15} - \tau_{20,16,15,14}$	
S ₆₄	$\tau_{12,2,7,6} - \tau_{11,7,6,5} + \tau_{9,5,4,3} - \tau_{8,4,3,2} - \tau_{24,14,19,18}$	B $\gamma(\text{CH})_8$
	$+ \tau_{23,19,18,17} - \tau_{21,17,16,15} + \tau_{20,16,15,14}$	
S ₆₅	$\tau_{12,2,7,6} - 2\tau_{10,6,5,4} + \tau_{8,4,3,2} + \tau_{24,14,19,18} - 2\tau_{22,18,17,16}$	A $\gamma(\text{CH})_9$
	$+ \tau_{20,16,15,14}$	
S ₆₆	$\tau_{12,2,7,6} - 2\tau_{10,6,5,4} + \tau_{8,4,3,2} - \tau_{24,14,19,18} + 2\tau_{22,18,17,16}$	B $\gamma(\text{CH})_{10}$
	$- \tau_{20,16,15,14}$	

^a Atom numbering is shown in Figure B.1; $r_{i,j}$ is the distance between atoms A_i and A_j ; $\beta_{i,j,k}$ is the angle between vectors A_kA_i and A_kA_j ; $\tau_{i,j,k,l}$ is the dihedral angle between the plane defined by A_i, A_j, A_k and the plane defined by A_j, A_k, A_l atoms; ν - stretching, δ - in-plane bending, γ - out-of-plane bending, τ - torsion; normalization constants not given.

Table B.7 Changes in the vibrational spectra (Max $\Delta\nu/\text{cm}^{-1}$), expected to occur in E -AB molecule undergoing the zero-point vibrations along the τ NNCC coordinates.^a

$E-C_2$ (-3°)		$E-C_{2h}$ (0°)		$E-C_i$ (8.5°)		Max. $\Delta\nu$
ν	I	ν	I	ν	I	
20.31	0.08	14.80	0.03	25.10	0.12	10.30
59.24	1.35	60.89	1.41	57.03	1.38	3.87
78.22	1.91	82.27	1.89	86.84	1.80	8.62
99.16	0.04	94.84	0.00	99.79	0.00	4.95
216.44	0.00	217.13	0.00	216.82	0.00	0.69
239.90	0.24	239.02	0.00	240.52	0.00	1.50
292.71	0.34	295.18	0.62	295.93	1.16	3.23
301.93	0.28	299.61	0.00	300.25	0.00	2.32
403.13	0.00	402.65	0.00	402.44	0.27	0.69
406.68	0.06	406.15	0.00	405.94	0.00	0.74
471.49	0.16	471.35	0.00	472.41	0.00	1.07
514.96	23.52	514.51	23.49	515.30	21.90	0.78
531.22	5.94	532.11	6.25	529.81	8.13	2.30
541.75	13.20	541.30	13.67	542.75	12.77	1.44
606.20	0.00	606.79	0.00	607.56	0.00	1.36
612.57	0.62	613.25	0.65	613.95	0.60	1.38
664.47	0.00	664.71	0.00	664.97	0.00	0.49
682.25	0.12	681.66	0.00	682.25	0.00	0.59
686.00	76.74	685.25	76.76	685.72	77.59	0.75
759.96	0.33	759.14	0.00	758.56	0.00	1.40
780.50	48.44	779.96	48.34	779.42	49.68	1.08
819.22	0.58	819.67	0.57	819.70	0.68	0.47
832.63	0.05	831.34	0.04	830.89	0.97	1.74
834.11	0.06	832.83	0.00	832.36	0.00	1.75
913.01	0.11	913.53	0.00	910.23	0.00	3.30
922.30	0.08	921.74	0.00	924.51	0.00	2.77
928.60	7.23	927.64	7.25	927.05	8.32	1.55
963.05	0.00	961.94	0.00	960.72	0.72	2.33
963.81	0.07	962.71	0.00	961.59	0.00	2.21
980.14	0.08	979.35	0.00	978.29	0.00	1.85
980.65	0.45	979.82	0.42	978.58	1.31	2.06
993.46	3.22	993.43	3.39	993.65	3.05	0.22
993.47	0.00	993.45	0.00	993.66	0.00	0.21
1016.56	13.50	1017.07	13.51	1017.75	12.87	1.19
1017.46	0.00	1017.81	0.00	1018.56	0.00	1.10
1067.92	0.04	1068.55	0.00	1069.03	0.00	1.12
1072.38	15.17	1072.93	15.24	1073.43	15.31	1.05
1125.25	0.00	1125.47	0.00	1125.91	0.00	0.66
1139.69	31.50	1139.64	32.13	1140.23	29.27	0.60
1149.56	0.00	1149.90	0.00	1150.15	0.00	0.59
1149.67	0.36	1149.94	0.45	1150.25	0.35	0.58
1176.80	0.00	1176.86	0.00	1177.12	0.00	0.32
1224.84	20.33	1225.11	20.38	1224.70	18.63	0.41
1295.41	1.77	1295.23	1.69	1295.38	1.58	0.19
1298.70	0.00	1298.84	0.00	1298.56	0.00	0.28
1352.21	6.47	1352.63	6.52	1353.04	6.02	0.82
1355.19	0.01	1355.67	0.00	1356.06	0.00	0.87
1419.50	0.02	1419.60	0.00	1421.61	0.00	2.11
1445.58	13.04	1445.97	13.10	1446.71	12.75	1.12
1457.33	0.02	1457.74	0.00	1458.30	0.00	0.96
1471.96	9.57	1472.78	9.41	1473.28	9.56	1.32
1482.95	0.00	1483.14	0.00	1483.94	0.00	0.99
1577.42	3.92	1577.63	3.82	1578.09	3.73	0.67
1581.47	0.00	1581.57	0.00	1581.55	0.00	0.10
1594.13	5.98	1594.80	6.17	1595.40	5.80	1.28
1597.60	0.00	1598.22	0.00	1598.88	0.00	1.29
3103.99	4.76	3103.81	5.01	3104.05	4.79	0.24
3104.06	0.01	3103.88	0.00	3104.12	0.00	0.25
3114.16	17.29	3113.91	16.99	3113.87	17.10	0.29
3114.17	0.05	3113.94	0.00	3113.88	0.00	0.29
3124.15	30.52	3123.91	30.57	3124.13	30.19	0.24
3124.22	0.01	3123.96	0.00	3124.20	0.00	0.26
3133.55	39.66	3133.31	40.48	3133.33	39.66	0.23
3133.76	0.03	3133.54	0.00	3133.53	0.00	0.23
3141.79	14.46	3142.48	13.87	3141.69	14.14	0.79
3141.82	0.03	3142.51	0.00	3141.73	0.00	0.78

^a Middle column ($E-C_{2h}$) –geometry at the minimum, left ($E-C_2$) and right ($E-C_i$) columns – geometries corresponding to the geometric limits of the zero-point vibrations along the τ NNCC coordinates; IR Intensities (I/ km mol^{-1}) are also given.

B.1 Azobenzene Supporting Information

Table B.8 Changes in the vibrational spectra (Max $\Delta\nu$ / cm^{-1}), expected to occur in *Z*-AB molecule undergoing the zero-point vibrations along the τ NNCC coordinates.^a

<i>Z</i> - <i>C</i> ₂ (42.2°)		<i>Z</i> - <i>C</i> ₂ (49.3°)		<i>Z</i> - <i>C</i> ₂ (57.2°)		Max. $\Delta\nu$
ν	I	ν	I	ν	I	
46.55	1.40	50.37	1.41	54.63	1.45	8.07
51.22	0.02	50.78	0.01	47.79	0.00	3.42
73.28	0.48	68.18	0.48	63.17	0.47	10.11
154.46	4.63	151.43	3.91	146.80	2.93	7.66
180.31	0.15	171.04	0.19	159.94	0.24	20.37
270.46	5.88	265.02	0.23	259.28	0.22	11.18
271.22	0.23	278.54	5.74	287.22	5.61	16.00
398.07	3.77	397.20	4.44	395.86	4.84	2.21
403.43	0.02	400.30	0.05	397.29	0.08	6.14
410.59	2.85	418.29	3.16	426.65	3.52	16.06
444.10	6.91	438.84	4.84	431.81	2.79	12.29
495.83	5.06	494.90	4.68	493.65	4.39	2.18
527.40	0.09	531.77	0.23	535.68	0.47	8.28
590.75	5.49	592.44	5.15	594.03	4.45	3.28
611.61	0.03	612.25	0.04	612.77	0.06	1.16
613.92	0.12	615.87	0.29	618.48	0.53	4.56
686.61	39.33	686.99	31.26	685.46	3.01	1.53
687.65	18.43	688.21	19.56	689.57	20.50	1.92
696.10	58.15	691.69	67.78	689.05	95.74	7.05
748.18	0.03	746.08	0.03	742.78	0.21	5.40
761.64	38.69	760.20	32.06	758.20	26.00	3.45
768.27	11.25	768.51	12.42	768.33	14.23	0.24
822.39	7.87	820.78	5.62	820.80	4.38	1.61
824.26	1.43	822.95	1.50	822.35	1.36	1.91
829.11	2.47	831.57	2.82	833.26	1.71	4.15
903.71	0.17	901.35	0.32	899.75	0.64	3.95
907.88	21.70	906.22	20.45	906.08	18.77	1.80
950.55	0.74	947.99	0.35	946.72	0.26	3.82
950.77	0.27	948.52	0.28	946.83	0.22	3.93
968.79	0.60	967.52	0.60	966.60	0.69	2.19
968.84	0.05	967.68	0.05	966.78	0.05	2.06
992.29	0.41	992.62	0.38	992.91	0.32	0.62
992.81	1.09	993.27	1.18	993.69	1.31	0.88
1023.73	4.41	1024.25	4.52	1024.86	4.92	1.14
1024.38	2.06	1024.80	2.17	1025.27	2.29	0.89
1074.91	13.05	1074.74	13.31	1074.66	13.32	0.25
1076.57	1.49	1076.51	1.15	1076.81	0.84	0.30
1108.07	0.06	1112.68	0.19	1116.78	0.50	8.71
1133.70	2.16	1134.99	1.84	1135.64	1.27	1.94
1150.56	0.00	1150.68	0.03	1150.90	0.09	0.34
1150.87	0.19	1150.85	0.14	1150.95	0.09	0.10
1170.91	0.65	1170.19	0.76	1169.66	0.83	1.26
1172.22	0.17	1171.00	0.18	1169.87	0.29	2.35
1296.67	1.90	1296.26	1.95	1295.90	1.86	0.77
1300.69	0.12	1301.34	0.06	1302.18	0.01	1.49
1340.87	1.72	1340.50	2.34	1340.32	2.46	0.55
1348.55	0.02	1347.14	0.05	1345.89	0.06	2.66
1439.07	8.48	1438.64	7.37	1437.93	6.63	1.14
1445.17	4.09	1445.44	3.01	1445.51	2.13	0.34
1462.07	0.65	1463.36	1.51	1464.77	2.80	2.70
1469.79	5.32	1469.71	4.85	1469.88	4.88	0.17
1512.98	51.47	1520.25	47.36	1528.20	40.64	15.22
1570.34	4.33	1571.00	4.83	1572.25	5.53	1.92
1576.76	0.46	1578.19	0.50	1580.22	0.51	3.46
1590.72	1.54	1590.78	2.22	1590.61	3.49	0.17
1595.62	3.42	1596.13	4.13	1596.29	4.97	0.67
3105.89	2.15	3105.96	1.94	3106.02	1.81	0.13
3106.03	0.62	3106.07	0.61	3106.07	0.59	0.03
3113.70	9.09	3113.48	8.33	3113.25	7.88	0.45
3113.78	1.39	3113.56	0.85	3113.32	0.52	0.47
3124.37	14.92	3123.85	13.91	3123.48	12.76	0.89
3124.41	4.77	3123.93	5.03	3123.59	5.57	0.82
3131.93	36.49	3131.05	33.06	3130.35	30.92	1.58
3132.17	0.53	3131.27	0.23	3130.55	0.26	1.62
3136.59	6.96	3135.76	10.61	3135.56	12.17	1.04
3136.75	4.31	3135.86	5.54	3135.62	6.43	1.13

^a Middle column (49.3°) –geometry at the minimum, left (42.2°) and right (57.2°) columns – geometries corresponding to the geometric limits of the zero-point vibrations along the τ NNCC coordinates; IR Intensities (I/ km mol^{-1}) are also given.

B.2 Azobenzene Paper

Structural and spectroscopic characterization of *E*- and *Z*-isomers of azobenzene†

Cite this: DOI: 10.1039/c4cp00240g

Luis Duarte, Rui Fausto and Igor Reva*

Monomers of azobenzene were isolated in argon matrices at 15 K and characterized by infrared spectroscopy and theoretical calculations. When the equilibrium vapors existing over the azobenzene crystals at room temperature were trapped in the matrix, only the thermodynamically most stable *E*-azobenzene was detected. In an attempt to convert *E*-azobenzene into the *Z* isomer, the matrix-isolated *E*-monomers were irradiated either by broad-band or narrow-band UV-visible light of different wavelengths, in the 600–200 nm range. However, no *E*-to-*Z* transformation was observed under these conditions. In an alternative experiment, *E*-azobenzene was irradiated by UV-visible broad-band light in the gas phase prior to trapping in a matrix. In this case, the *E*-to-*Z* photoisomerization occurred, and both *E*- and *Z*-azobenzene monomers were detected in the matrix sample. Subsequent irradiation of the matrix with narrow-band tunable visible or UV light ($\lambda < 550$ nm) resulted in back conversion of *Z*-azobenzene into the *E*-form. The observed photoinduced *E*-to-*Z* isomerizations allowed for the reliable vibrational characterization of both azobenzene isomers. The two-dimensional potential energy surfaces of *Z*- and *E*-azobenzene were explored as functions of the torsional movement of the two phenyl rings. They exhibit large flat areas around the minima, for both isomers, allowing for large-amplitude zero-point torsional vibrations. For the *Z*-form, these vibrations were found to be responsible for significant changes in the equilibrium NN bond length (up to 0.3 pm). This also allowed to explain the experimentally observed frequency smearing of the N=N stretching vibration in this isomer.

Received 16th January 2014,
Accepted 24th February 2014

DOI: 10.1039/c4cp00240g

www.rsc.org/pccp

Introduction

Azobenzene (AB) and its derivatives are exploited in a wide range of applications. In industry, the azobenzenes account for approximately 50% of all commercial dyes.^{1,2} In addition, they are also frequently employed in the development of photo-responsive biological macromolecules, photoswitchable materials and other photocontrolled molecular devices.^{3–18} Despite the abundance of well-established applications, some aspects concerning the structure, spectra and photochemistry of azobenzene still remain unclear.

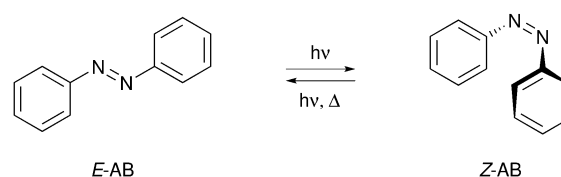
Azobenzene can exist in two configurations, the *E* (*trans*) and *Z* (*cis*) forms (Scheme 1), which have been reported to be interconvertible both photochemically and thermally.^{19–22} Photoisomerization of AB involves excitation in the UV-visible range to either the $S_1(\pi^* \leftarrow n)$ or the $S_2(\pi^* \leftarrow \pi)$ state. It has been

postulated that excitation of *E*-azobenzene (*E*-AB) from the S_0 ground state to the S_2 state is followed by rapid relaxation to S_1 , which then decays back to the S_0 state, either non-radiatively (*via* conical intersection) or by weak fluorescence.^{23–29} The process may however be even more complex, and the involvement of other states has also been suggested.^{30–34} Comparatively, the process following the $\pi^* \leftarrow n$ excitation is simpler, as it involves only the S_1 state.^{25,29,35–37}

The photoisomerization itself has been addressed in a great number of theoretical and experimental studies.^{29–32,37–51} Several mechanisms have been proposed, but the two most commonly discussed ones are rotation and inversion.⁵² The rotational pathway involves torsion around the central NN bond, while in the inversion pathway one of the two NNC angles increases to 180°, resulting in a semi-linear transition state. Additional mixed mechanisms, such as the concerted inversion or the inversion-assisted rotation,

Department of Chemistry, University of Coimbra, P-3004-535 Coimbra, Portugal.
E-mail: reva@qui.uc.pt

† Electronic supplementary information (ESI) available: Complete calculated structural (Cartesian coordinates) and vibrational data (vibrational frequencies, absolute infrared intensities, and Raman activities) for *E*-AB and *Z*-AB optimized geometries, as well as definitions of symmetry coordinates and potential energy distributions resulting from the normal mode analyses. See DOI: 10.1039/c4cp00240g



Scheme 1 Structures of *E* and *Z* isomers of azobenzene.

have also been considered as possible pathways for the photoisomerization of azobenzene. Despite that at present the mechanism is still not consensual, the most recent studies suggest the dominance of the rotational isomerization following excitation of *E*-AB to either S_1 or S_2 , in the gas-phase. In the case of *Z*-azobenzene (*Z*-AB), the available data suggest that photoisomerization occurs by rotation,^{44,49,53,54} following either S_1 or S_2 excitation, whereas thermal isomerization proceeds by inversion.^{40,55}

Vibrational data have been shown to be particularly significant in the elucidation of structural properties and mechanistic questions in azo-based systems.^{35,51,56–60} For example, examination of the NN stretching frequency of *E*-AB in both the ground state and first excited electronic states was used to gain some insight into the photoisomerization mechanism of azobenzene. Fujino and Tahara found that the NN stretching frequency in the S_1 state was very close to that of the ground state and concluded that the double bond nature of the NN bond is retained during the photoisomerization.²⁶ Harabuchi *et al.* reported that the calculated (CASPT2) NN stretching frequency shows a slight decrease along the rotation pathway while it increases rapidly along the inversion pathway.⁵¹ In turn, Ikegami and co-workers studied the thermal isomerization reaction of *Z*-AB by direct molecular dynamics and calculated the vibrational spectra from the obtained trajectories. They showed that skeletal vibrations of the phenyl rings play an important role in the thermal isomerization reaction of the azobenzene molecule.⁴⁰ Likewise, Jiang and Aida found that excitation of similar modes enhances the *Z*-to-*E* isomerization reaction of azodendrimers.⁶¹ Therefore, an accurate description of the vibrations of azobenzene is of value for improving the general understanding of azobenzene and its derivatives.

A few studies dealing with the vibrational analyses of AB can be found in the literature.^{62–66} However, most of these studies rely on comparisons made with experimental spectra obtained for the compound in a KBr pellet or in solution.^{19,67–76} Furthermore, fewer experimental data have been reported for the *Z*-AB form, whose vibrational spectrum remains insufficiently characterized.

In this work, we present the vibrational characterization of both *E* and *Z* monomers of azobenzene isolated in cryogenic matrices. The high-energy *Z* form was generated by UV-visible excitation of the most stable *E* form in the gas phase, followed by deposition in the cryogenic matrix. To the best of our knowledge, this is the first report on the experimental infrared spectra of the isolated monomers of *E*-AB and *Z*-AB. Since the matrix isolation technique permits a direct comparison between the experimental and theoretically calculated spectra and allows attaining a spectral resolution adequate for differentiation of the vibrational signatures of the two isomers of AB, correlations between the observed spectroscopic properties of these molecules and details of their potential energy landscapes could be successfully extracted.

Materials and methods

Experimental section

Commercial azobenzene (*Fluka*, purity 98%) was placed in a Pyrex glass tube connected to the vacuum chamber of the

cryostat through a needle valve, and the compound vapors were deposited, together with a large excess of the matrix gas (argon N60, supplied by Air Liquide), onto a CsI window cooled to 15 K using a closed-cycle helium refrigerator with an APD Cryogenics DE-202A expander. The temperature of the CsI window was measured directly at the sample holder using a silicon diode temperature sensor, connected to a digital temperature controller (Scientific Instruments, Model 9650-1), which provides a stabilization accuracy of 0.1 K. The infrared spectra were recorded in the 4000–400 cm^{-1} range, using a Nicolet 6700 FTIR spectrometer equipped with a deuterated triglycine sulphate (DTGS) detector and a Ge/KBr beam splitter, with 0.5 cm^{-1} resolution.

The matrices were irradiated through an outer quartz window of the cryostat using narrowband tunable (0.2 cm^{-1} spectral width) light provided by a Quanta-Ray MOPO-SL optical parametric oscillator (OPO), pumped with a pulsed (repetition rate = 10 Hz, duration = 10 ns) Nd:YAG laser. In the visible range (440–600 nm) the signal beam of the OPO was used as the light source (pulse energy of 30–40 mJ); in the UV range (230–440 nm), the frequency-doubled signal or idler beam was used (pulse energy \sim 3 mJ). Alternatively, the broad-band visible-UV irradiation was provided by a 500 W Hg(Xe) arc lamp (Spectra-Physics, model 66142), adjusted to have an output power of 200 W.

Computational details

All quantum chemical calculations were performed using the Gaussian 09 program package, and the functionals (PW91, BP86, B97-1, B3LYP and OLYP) and the basis sets (6-311++G(3df,3pd) and cc-pVTZ) were used as defined in Gaussian.⁷⁷ The equilibrium geometries reported here were optimized using the default Berny optimization algorithm.⁷⁸ The geometry optimizations were followed by harmonic frequency calculations at the same theory level, and the nature of the obtained stationary points was checked through analysis of the corresponding Hessian matrices.

The theoretical normal modes were analyzed by carrying out potential energy distribution (PED) calculations. Transformation of the force constants with respect to the Cartesian coordinates into the force constants with respect to the molecule-fixed internal coordinates allowed the PED analyses to be carried out as described by Schachtschneider and Mortimer.⁷⁹ The internal symmetry coordinates used in these analyses were defined as recommended by Pulay *et al.*⁸⁰ In some figures, the theoretical spectra were simulated using Lorentzian profiles centered at the PW91/cc-pVTZ calculated frequencies (not scaled) and having the full-width at half-maximum equal to 4 cm^{-1} . If not stated otherwise, the maxima of these profiles were set to be equal to the absolute calculated infrared intensities.

Results and discussion

Isomeric composition of matrix-isolated AB

Two types of experiments were carried out to obtain the monomers of azobenzene isolated in cryogenic matrices: (a) in the first type of experiment, crystals of AB were placed in a Pyrex glass tube maintained at room temperature, and the equilibrium

vapors were introduced into the cryostat simultaneously with a large excess of argon and condensed together onto the cryostat optical window kept at 15 K. Since the Z - E energy difference in AB is very large [experimentally, it has been reported to be in the range 47–48 kJ mol⁻¹,^{19–22} in agreement with the calculated values obtained at various DFT (over 58 kJ mol⁻¹)⁸¹ and also at CASSCF and MR-CIS (68 kJ mol⁻¹) levels],⁴⁹ the thermodynamically most stable E -AB form should be the only form detectable in the gas phase thermal equilibrium at room temperature. Accordingly, it was the only form observed to be present in the matrices prepared in this type of experiment (Fig. 1a). (b) In the second type of experiment, the experimental layout of the deposition line was the same as in (a); the difference was that the vapors of AB prior to deposition were continuously irradiated through the walls of the Pyrex tube using broad-band UV-visible light coming out of a Hg(Xe) arc lamp. Under these conditions, a set of new bands appeared in the experimental infrared (IR) spectrum of the matrix-isolated compound (Fig. 1b). These new bands could be reliably assigned to the photogenerated Z -AB isomer.⁸² Selected regions of the infrared spectra of matrix-isolated azobenzene obtained in experiments of type (a) and (b) are shown in Fig. 1, along with the theoretical spectra of the E -AB and Z -AB isomers.⁸³

The above described observations deserve two comments, which are important for the following discussion: (i) the Pyrex glass (transmitting light above 290 nm) permits to induce the photochemical reaction and trigger the $E \rightarrow Z$ isomerization of AB in the gas phase. This is in accord with the energies of the lowest singlet excited states of E -AB (peak values: 2.78 and 4.10 eV, equivalent to 446 and 302 nm), measured in the gas phase by electron energy loss spectroscopy.⁸⁴ (ii) The photochemically

generated Z -AB form does not thermally convert back to the E isomer, at room temperature, in the gas phase, on the time scale of the experiments (tens of minutes); it is stable enough to withstand collisions with the walls of the deposition line⁸⁵ and with other AB molecules, and can be successfully trapped in the matrix. This last observation can be reasonably explained by the value of the barrier for the thermal $Z \rightarrow E$ AB conversion, whose experimental^{25,86} measure is about 92–105 kJ mol⁻¹ (calculated DFT values, 80–100 kJ mol⁻¹, stay in the same range).⁸¹

Photoisomerization

The E -AB monomers, trapped in the matrix in the first type of experiment, were irradiated with UV-visible light through an outer quartz window of the cryostat with the objective to induce *in situ* $E \rightarrow Z$ isomerization of azobenzene. Two types of irradiation were applied: (i) narrow-band irradiation with light provided by an optical parametric oscillator (OPO) and tuned from 600 nm to 220 nm wavelength range, or (ii) broad-band irradiation using light coming out of a Hg(Xe) arc lamp equipped with different longpass filters, with cut-off in UV or visible ranges, or without any filters, providing UV output down to 200 nm. The changes in the samples were followed by infrared spectroscopy after each irradiation. All performed irradiations were found not to cause any alteration in the IR spectrum of the irradiated samples.⁸⁷ On the other hand, when a matrix containing both E and Z isomers of azobenzene, obtained in the second type of experiment described above, was irradiated with UV-visible light, an almost complete conversion of the Z form into the E isomer was observed (Fig. 2). In order to find out the longest wavelength at which the photoreaction starts, the samples were irradiated using the tunable output of the OPO, starting from 600 nm and gradually decreasing the wavelength (in steps of 10 nm). The first signs of phototransformation of AB were detected after irradiation at 550 nm, albeit tiny. The onset wavelength of the photo-induced $Z \rightarrow E$ conversion is thus in good agreement with the gas phase electronic absorption spectrum of Z -AB.^{25,88} When the irradiation was performed at 540 nm, the complete $Z \rightarrow E$

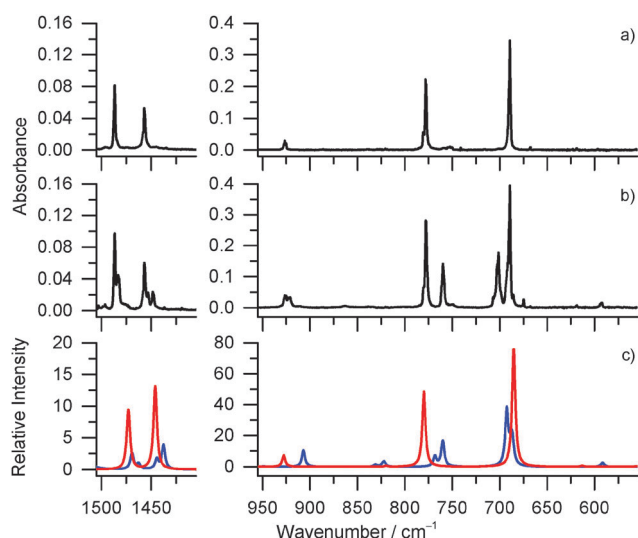


Fig. 1 Selected regions of the experimental infrared spectra of azobenzene isolated in argon matrices at 15 K: (a) shortly after deposition of the equilibrium vapor existing over AB crystals at room temperature; (b) after trapping of the AB vapors subjected prior to deposition to broad-band visible-UV irradiation by a Hg(Xe) lamp. (c) Spectra of E (red) and Z (blue) azobenzene forms simulated on the basis of the PW91/cc-pVTZ calculations. The calculated infrared intensities for Z -AB were scaled by 0.5, while those of E -AB were not scaled.

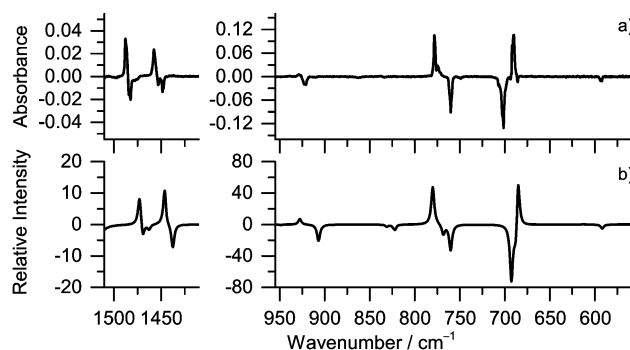


Fig. 2 (a) Changes in the experimental infrared spectrum of AB in an Ar matrix at 15 K (second type of experiment, both E -AB and Z -AB are initially present) after 1 min irradiation at $\lambda = 440$ nm. Negative absorptions correspond to decreasing bands of the initially present Z -AB form. Positive peaks correspond to growing absorptions due to the E -AB form; (b) simulated theoretical difference spectrum, representing quantitative transformation of Z -AB into E -AB, constructed as " E minus Z ".

transformation occurred on a timescale of a few minutes. Irradiation at shorter wavelengths, in separate experiments, also led to consumption of *Z*-AB. When *Z*-AB was totally consumed, all subsequent irradiation at any wavelength, whether using narrow- or broad-band light sources, did not lead to additional changes.

The observed isomerization behavior of AB calls for an obvious conclusion. On the one hand, the *E* → *Z* isomerization was successfully induced in the gas phase by UV-visible irradiation during the deposition of the matrices. On the other hand, no such isomerization could be induced when a similar irradiation was applied to the matrix-isolated *E*-AB monomers. The absence of the photoinduced *E* → *Z* transformation for matrix-isolated AB should then be attributed to the cryogenic matrix, restricting isomerization of the bulky phenyl substituent (C₆H₅) in the solid environment. Such a situation was also recently found to occur for matrix-isolated stilbene, structurally similar to AB.⁸⁹ Interestingly, when one of the substituents linked to a double N=N bond is reduced from phenyl to cyclopropyl (C₃H₅), the photochemical *E* → *Z* transformation could be successfully induced in the matrix.⁹⁰ In this context, it also appears interesting to compare our observations with those from another recently published study, focusing on the photoisomerization of *E*-AB under high external pressures. Singleton *et al.* studied the photo-switching behavior of AB placed inside a diamond-anvil spectroscopic cell as a function of the external pressure.⁹¹ They found that the *Z*-AB content of the photostationary state gradually decreased with pressure, with complete arrest of the *E* → *Z* photoisomerization above 1.5 GPa. The reverse, *Z* → *E* photoisomerization of azobenzene was shown, however, still to be inducible at all the pressures investigated (up to 4 GPa). This was rationalized in terms of isomerization occurring in free volume pockets in the host material (that decrease with an increase of pressure). Apparently, in the cryogenic argon matrix at 15 K, these free volume pockets are smaller than the *E* → *Z* isomerization requirement.⁹²

Choice of the model chemistries

Calculations for the structure and vibrational frequencies of azobenzene have been reported in the literature before. Biswas and Umamathy,⁶⁴ and Kurita *et al.*⁹³ found that the BP86/6-31G* and PW91 (exchange and correlation functionals)/6-31+G* approaches, respectively, gave good results when used in the prediction of azobenzene vibrational frequencies. Fliegel *et al.*⁶⁵ performed RI-MP2 and DFT calculations, and showed that sufficiently extended basis sets have to be employed for the correct description of the azo group. Klug and Burcl^{81,94} found the geometrical parameters calculated using the OLYP and B97-1 functionals to be in excellent agreement with experimental geometries obtained by gas electron diffraction (GED).⁹⁵ Thus, in order to find the most suitable approach for the interpretation of our experimental results, we carried out optimization of the structures of the two AB isomers followed by calculations of their vibrational spectra using the above-mentioned functionals together with more complete basis sets. The widely used B3LYP functional was also included in the set of model chemistries investigated as a reference, and our results were also compared with other

high-level calculations, such as RI-MP2.⁶⁵ A set of well-defined bands in the infrared spectrum of matrix-isolated AB was chosen, and the experimental frequencies were compared with their calculated counterparts, including the data available in the literature. The results are summarized in Table S1 (ESI†). The best overall agreement was found for the PW91/cc-pVTZ and OLYP/cc-pVTZ approaches, both with a mean unsigned error of 7 cm⁻¹. Between these two functionals, the OLYP presents the highest absolute error for the *E* and *Z* forms; hence we chose to use the PW91/cc-pVTZ method to carry out the vibrational calculations and normal mode analyses. From all the theoretical approaches, the B3LYP functional and the second order Møller–Plesset (MP2) approximation gave the less satisfactory results. The Cartesian coordinates and vibrational frequencies of all optimized structures are given in the ESI† (Tables S2 and S3).

Vibrational spectra

The planar *E*-AB structure (C_{2h} symmetry) has 66 normal modes, 33 of which are infrared active (Table 1) while the remaining 33 modes are Raman active (Table S5, ESI†). The most intense infrared absorption bands in the *E*-AB spectrum, situated at 689.2 and 778.3 cm⁻¹, have their calculated counterparts at 685.2 and 780.0 cm⁻¹ (see Fig. 3). They result essentially from the coupling of γ (CH) and τ (ring) modes. The characteristic antisymmetric CN stretching mode was calculated at 1225.1 cm⁻¹ and can be assigned to the experimental band observed at 1221.4 cm⁻¹. The NN stretching vibration is IR-inactive in *E*-AB and, therefore cannot be assessed by our experiment. Frequency of this mode is predicted by our calculations at 1419.6 cm⁻¹ (see Table S2, ESI†), in good agreement with the reported Raman data (~1440 cm⁻¹).²⁶

The planarity of the ground state structure of *E*-AB has been the subject of controversial reports. On the theoretical side, some reports indicate a non-planar structure with C_i symmetry.^{64,93,96} However, it was recently demonstrated that the inversion barrier at the planar structure is an artifact resulting from the use of deficient *ab initio* methods,⁹⁷ and, in accordance with this conclusion, the great majority of the previously described DFT and MP2 theoretical calculations carried out on *E*-AB led to a planar minimum energy structure, with C_{2h} symmetry.^{65,98,99} In our calculations, the optimized ground state *E*-AB geometry was also found to correspond to the planar C_{2h} structure, at all used theory levels (see Table S3 in the ESI† for the Cartesian coordinates of *E*-AB). Experimentally, early GED experiments suggested a non-planar minimum energy structure (with either C₂ or C_i symmetry), with the phenyl groups rotated out of the CNNC plane.¹⁰⁰ However, a more recent GED study of *E*-AB yielded a C_{2h} planar structure for the compound, in agreement with the most recent theoretical results.⁹⁵ The absence of experimental reports on the microwave spectra of azobenzene should be related to the fact that the total molecular dipole moment of *E*-AB is equal to zero (for both the C_i and C_{2h} symmetries). Then, vibrational spectroscopy experiments on this molecule appear as a valuable experimental tool for probing its molecular geometry. Also note that in the previously reported experimental studies on crystalline AB and for the

Table 1 Experimental wavenumbers (ν/cm^{-1}) of the absorption bands observed in the infrared spectrum of *E*-AB isolated in an Ar matrix at 15 K, and the theoretical wavenumbers (ν/cm^{-1}), absolute infrared intensities ($I/\text{km mol}^{-1}$) and potential energy distributions (PED, %) of the infrared-active A_u and B_u normal modes calculated at the PW91/cc-pVTZ level^a

Ar (15 K)	Calculated			
ν	ν	I	Sym.	PED (%)
3104.0	3142.5	13.9	B_u	$\nu_{\text{as}}(\text{CH})$ (93)
3093.1, 3086.7	3133.3	40.5	B_u	$\nu(\text{CH})_2$ (83), $\nu(\text{CH})_4$ (12)
3075.6, 3070.4 , 3057.2	3123.9	30.6	B_u	$\nu(\text{CH})_4$ (57), $\nu(\text{CH})_8$ (30)
3046.35	3113.9	17.0	B_u	$\nu(\text{CH})_8$ (54), $\nu(\text{CH})_4$ (28), $\nu(\text{CH})_6$ (11)
3015.0	3103.8	5.0	B_u	$\nu(\text{CH})_6$ (82), $\nu(\text{CH})_8$ (14)
1595.1, 1592.8	1594.8	6.2	B_u	$\nu(\text{CC})_4$ (64), $\delta(\text{CH})_9$ (17)
1589.3, 1587.9	1577.6	3.8	B_u	$\nu(\text{CC})_6$ (64)
1486.7	1472.8	9.4	B_u	$\delta(\text{CH})_8$ (59), $\nu(\text{CC})_{10}$ (34)
1456.8	1446.0	13.1	B_u	$\delta(\text{CH})_2$ (50), $\nu(\text{CC})_8$ (38)
1307.4	1352.6	6.5	B_u	$\nu(\text{CC})_2$ (88)
1299.8, 1298.2	1295.2	1.7	B_u	$\delta(\text{CH})_6$ (75)
1221.4	1225.1	20.4	B_u	$\nu(\text{NC})$ (49), $\nu(\text{CC})_{12}$ (13), $\delta(\text{CH})_8$ (10)
1158.2	1149.9	0.4	B_u	$\delta(\text{CH})_4$ (76)
1151.6 , 1148.0	1139.6	32.1	B_u	$\delta(\text{CH})_9$ (68), $\nu(\text{CC})_4$ (16)
1071.8	1072.9	15.2	B_u	$\delta(\text{CH})_2$ (43), $\nu(\text{CC})_8$ (42)
1023.6, 1019.3	1017.1	13.5	B_u	$\nu(\text{CC})_{10}$ (50), $\delta(\text{CH})_8$ (27), $\nu(\text{CC})_{12}$ (21)
1000.8	993.4	3.4	B_u	$\delta(\text{ring}2)$ (64), $\nu(\text{CC})_{12}$ (32)
985.9	979.8	0.4	A_u	$\gamma(\text{CH})_1$ (110), $\gamma(\text{CH})_7$ (12)
n.o.	961.9	0.001	A_u	$\gamma(\text{CH})_7$ (99), $\gamma(\text{CH})_1$ (13)
926.6 , 925.1	927.6	7.2	A_u	$\gamma(\text{CH})_9$ (89), $\gamma(\text{NC})$ (10)
n.o.	831.3	0.04	A_u	$\gamma(\text{CH})_5$ (100)
820.6	819.7	0.6	B_u	$\nu(\text{CC})_{12}$ (29), $\nu(\text{NC})$ (26), $\delta(\text{ring}2)$ (19), $\delta(\text{ring}4)$ (11), $\nu(\text{CC})_{10}$ (10)
780.8, 778.3 , 777.5	780.0	48.3	A_u	$\gamma(\text{CH})_3$ (35), $\tau(\text{ring}1)$ (28), $\gamma(\text{NC})$ (23), $\gamma(\text{CH})_9$ (13)
689.2	685.2	76.8	A_u	$\tau(\text{ring}1)$ (67), $\gamma(\text{CH})_3$ (45)
618.8	613.3	0.6	B_u	$\tau(\text{ring}6)$ (79), $\gamma(\text{CC})_6$ (10)
549.9, 547.0, 546.0	541.3	13.7	A_u	$\gamma(\text{NC})$ (31), $\tau(\text{ring}1)$ (25), $\tau(\text{ring}3)$ (22), $\tau(\text{CNCC})$ (19), $\gamma(\text{CH})_3$ (11)
536.4	532.1	6.3	B_u	$\delta(\text{ring}4)$ (66)
521.4	514.5	23.5	B_u	$\delta(\text{NCC})$ (38), $\delta(\text{NNC})$ (24), $\delta(\text{ring}4)$ (13)
n.o.	402.7	0.001	A_u	$\tau(\text{ring}5)$ (112)
n.i.	295.2	0.6	A_u	$\tau(\text{ring}3)$ (80), $\tau(\text{CNCC})$ (24)
n.i.	82.3	1.9	B_u	$\delta(\text{NNC})$ (62), $\delta(\text{NCC})$ (34)
n.i.	60.9	1.4	A_u	$\tau(\text{CNCC})$ (46), $\gamma(\text{NC})$ (41), $\tau(\text{ring}3)$ (10)
n.i.	14.8	0.03	A_u	$\tau(\text{NNCC})$ (95)

^a Theoretical wavenumbers are not scaled. The strongest components of split bands are given in bold. PEDs lower than 10% are not included. Definition of symmetry coordinates is given in Table S4 (ESI); n.o., not observed; n.i., not investigated.

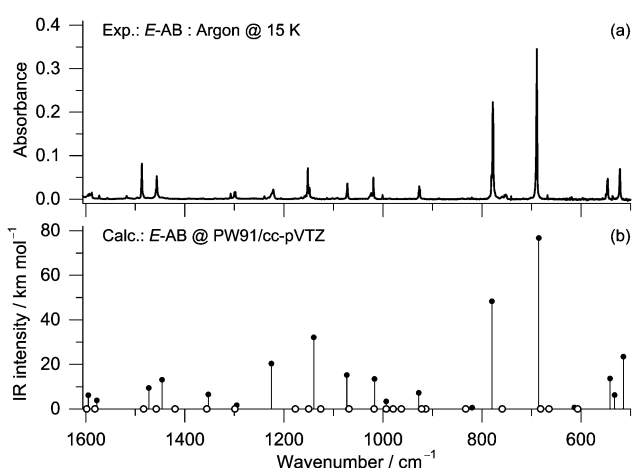


Fig. 3 (a) Experimental infrared spectrum of *E*-AB isolated in an argon matrix at 15 K; (b) theoretical infrared spectrum of the *E*-AB monomer calculated at the PW91/cc-pVTZ level of theory. Black circles represent the infrared-active (A_u and B_u) modes; white circles represent the infrared-inactive (A_g and B_g) modes.

compound in solution,^{100–105} the molecular geometry may suffer significant distortions resulting from the effects of the environment. On the other hand, in the matrix isolation technique the effects of environment are minimized. The excellent agreement of the theoretical spectrum of *E*-AB with that obtained experimentally for the matrix-isolated compound (Fig. 3) can be considered as evidence for the planar structure of this species.

Regarding the *Z*-AB structure (C_2 symmetry), the 66 normal modes span 34 A and 32 B symmetry vibrations, which are both IR and Raman active (Table 2). Despite the fact of all modes being formally IR active, only 10 vibrations have absolute calculated infrared intensities above 10 km mol^{-1} and can be considered medium or strong IR absorbers (see Fig. 4). On the other hand, 16 and 14 vibrations have absolute calculated infrared intensities in the ranges 10–4 and 4–1 km mol^{-1} , respectively, and can be regarded as weak IR absorbers, while almost a half of all vibrations (26 vibrational modes) were predicted to have very weak infrared absorptions (1 km mol^{-1} or less). The experimental spectrum of the *Z*-AB form was obtained as a result of

Table 2 Experimental wavenumbers (ν/cm^{-1}) of the absorption bands observed in the infrared spectrum of Z-AB isolated in an Ar matrix at 15 K, and the PW91/cc-pVTZ calculated wavenumbers (ν/cm^{-1}), absolute infrared intensities ($I/\text{km mol}^{-1}$) and potential energy distributions (PED, %) for the A and B symmetry modes^a

Ar (15 K)	Calculated			
ν	ν	I	Sym.	PED (%)
3095.3	3136.0	5.2	A	$\nu(\text{CH})_1$ (87)
	3135.9	9.8	B	$\nu(\text{CH})_2$ (87)
3085.9	3131.5	0.2	A	$\nu(\text{CH})_7$ (68), $\nu(\text{CH})_9$ (14)
	3131.3	33.9	B	$\nu(\text{CH})_8$ (67), $\nu(\text{CH})_{10}$ (15)
3075.6, 3070.4 , 3057.2	3124.0	4.9	B	$\nu(\text{CH})_{10}$ (77), $\nu(\text{CH})_8$ (17)
	3123.9	14.2	A	$\nu(\text{CH})_9$ (78), $\nu(\text{CH})_7$ (16)
3038.0	3113.6	1.0	A	$\nu(\text{CH})_5$ (90)
	3113.5	8.4	B	$\nu(\text{CH})_6$ (91)
3028.4	3106.0	0.6	A	$\nu(\text{CH})_3$ (93)
	3105.9	1.9	B	$\nu(\text{CH})_4$ (93)
1595.6	1595.6	4.2	A	$\nu(\text{CC})_3$ (61), $\delta(\text{CH})_{10}$ (17), $\nu(\text{N}=\text{N})$ (11)
1593.2	1590.2	2.2	B	$\nu(\text{CC})_4$ (64), $\delta(\text{CH})_9$ (17)
n.o.	1577.3	0.5	A	$\nu(\text{CC})_5$ (70)
1581.6	1570.1	4.7	B	$\nu(\text{CC})_6$ (63)
1514.8, 1512.6	1520.1	47.2	A	$\nu(\text{N}=\text{N})$ (77)
1482.3	1469.2	4.9	B	$\delta(\text{CH})_8$ (62), $\nu(\text{CC})_{10}$ (33)
1477.8	1462.8	1.7	A	$\delta(\text{CH})_7$ (60), $\nu(\text{CC})_9$ (31)
1453.1	1444.4	3.1	A	$\delta(\text{CH})_1$ (51), $\nu(\text{CC})_7$ (38)
1448.4	1437.6	7.6	B	$\delta(\text{CH})_2$ (49), $\nu(\text{CC})_8$ (35)
n.o.	1346.6	0.05	A	$\nu(\text{CC})_1$ (87)
n.o.	1339.9	2.1	B	$\nu(\text{CC})_2$ (82), $\delta(\text{CH})_4$ (11)
n.o.	1301.9	0.1	A	$\delta(\text{CH})_5$ (75)
n.o.	1296.7	1.9	B	$\delta(\text{CH})_6$ (70)
1176.4	1171.0	0.2	B	$\delta(\text{CH})_9$ (56), $\nu(\text{CC})_4$ (19), $\nu(\text{NC})$ (11)
	1170.2	0.7	A	$\delta(\text{CH})_{10}$ (66), $\nu(\text{CC})_3$ (21)
n.o.	1150.6	0.2	A	$\delta(\text{CH})_3$ (78)
n.o.	1150.4	0.02	B	$\delta(\text{CH})_4$ (78)
1151.3	1135.0	2.0	B	$\nu(\text{NC})$ (28), $\delta(\text{CH})_9$ (21), $\delta(\text{ring}2)$ (16), $\nu(\text{CC})_{12}$ (14)
n.o.	1111.9	0.2	A	$\nu(\text{NC})$ (29), $\delta(\text{ring}1)$ (21), $\nu(\text{CC})_{11}$ (18), $\delta(\text{CH})_{10}$ (11)
1074.6	1076.4	1.2	A	$\nu(\text{CC})_7$ (45), $\delta(\text{CH})_1$ (42)
1071.8	1074.4	13.1	B	$\nu(\text{CC})_8$ (45), $\delta(\text{CH})_2$ (40)
1025.3, 1024.1	1024.1	2.1	A	$\nu(\text{CC})_9$ (48), $\delta(\text{CH})_7$ (24), $\nu(\text{CC})_{11}$ (22)
	1023.7	4.6	B	$\nu(\text{CC})_{10}$ (48), $\delta(\text{CH})_8$ (24), $\nu(\text{CC})_{12}$ (22)
1000.7	993.2	1.2	B	$\delta(\text{ring}2)$ (58), $\nu(\text{CC})_{12}$ (38)
	992.5	0.4	A	$\delta(\text{ring}1)$ (58), $\nu(\text{CC})_{11}$ (39)
980.6	968.0	0.04	A	$\gamma(\text{CH})_1$ (118)
	967.8	0.6	B	$\gamma(\text{CH})_2$ (117)
963.1	949.2	0.3	A	$\gamma(\text{CH})_7$ (113)
	948.8	0.5	B	$\gamma(\text{CH})_8$ (111)
920.9	906.9	20.8	B	$\gamma(\text{CH})_{10}$ (78), $\gamma(\text{NC})$ (11)
910.0	902.2	0.3	A	$\gamma(\text{CH})_9$ (90)
862.7	831.1	2.6	B	$\delta(\text{NCC})$ (33), $\gamma(\text{CH})_{10}$ (17), $\nu(\text{NC})$ (13)
833.6	824.0	1.4	A	$\gamma(\text{CH})_5$ (98)
	822.0	6.4	B	$\gamma(\text{CH})_6$ (89)
776.6	768.3	12.5	A	$\gamma(\text{CH})_3$ (30), $\tau(\text{ring}1)$ (23), $\gamma(\text{NC})$ (19)
760.0	760.1	32.8	B	$\nu(\text{NC})$ (19), $\gamma(\text{CH})_4$ (17), $\delta(\text{ring}4)$ (17), $\nu(\text{CC})_{12}$ (11)
748.9	745.4	0.02	A	$\nu(\text{NC})$ (25), $\delta(\text{ring}3)$ (25), $\nu(\text{CC})_{11}$ (11)
701.4	692.6	71.8	B	$\gamma(\text{CH})_4$ (55), $\delta(\text{NCC})$ (21), $\delta(\text{ring}4)$ (11)
693.5	688.3	19.2	A	$\tau(\text{ring}1)$ (68), $\gamma(\text{CH})_3$ (44)
685.7	686.6	26.4	B	$\tau(\text{ring}2)$ (101), $\gamma(\text{CH})_4$ (15)
n.o.	614.9	0.3	A	$\delta(\text{ring}5)$ (65), $\tau(\text{CNCC})$ (10)
n.o.	611.0	0.1	B	$\delta(\text{ring}6)$ (35)
592.2	591.7	5.1	A	$\tau(\text{CNCC})$ (43), $\delta(\text{ring}5)$ (23), $\tau(\text{ring}1)$ (14)
531.3	530.4	0.2	A	$\delta(\text{ring}3)$ (31), $\delta(\text{NCC})$ (15), $\gamma(\text{NC})$ (12), $\tau(\text{ring}3)$ (12)
495.2	494.5	4.7	B	$\delta(\text{ring}4)$ (43), $\gamma(\text{NC})$ (17), $\nu(\text{NC})$ (14), $\tau(\text{ring}4)$ (11)
439.3	438.7	5.0	B	$\tau(\text{ring}4)$ (51), $\gamma(\text{NC})$ (15), $\delta(\text{ring}4)$ (12), $\delta(\text{NCC})$ (12)
419.6	416.8	3.1	A	$\tau(\text{ring}3)$ (29), $\delta(\text{ring}3)$ (18), $\nu(\text{NC})$ (17), $\tau(\text{ring}5)$ (11), $\tau(\text{CNCC})$ (10)
n.o.	400.6	0.04	A	$\tau(\text{ring}5)$ (102)
n.i.	396.7	4.4	B	$\tau(\text{ring}6)$ (112)
n.i.	275.3	5.8	B	$\delta(\text{NCC})$ (67), $\tau(\text{ring}4)$ (16)
n.i.	264.8	0.2	A	$\tau(\text{ring}3)$ (47), $\delta(\text{NCC})$ (20), $\delta(\text{NCC})$ (15), $\tau(\text{CNCC})$ (10)
n.i.	168.9	0.2	A	$\tau(\text{NNCC})$ (55), $\delta(\text{NCC})$ (33), $\delta(\text{NCC})$ (12)
n.i.	151.3	4.0	B	$\gamma(\text{NC})$ (36), $\tau(\text{ring}4)$ (33), $\delta(\text{NCC})$ (13)
n.i.	68.0	0.5	A	$\gamma(\text{NC})$ (33), $\tau(\text{CNCC})$ (27), $\tau(\text{NNCC})$ (21), $\tau(\text{ring}3)$ (11)
n.i.	49.9	0.02	A	$\delta(\text{NCC})$ (40), $\tau(\text{NNCC})$ (35), $\delta(\text{NCC})$ (15), $\gamma(\text{NC})$ (10)
n.i.	41.1	1.4	B	$\tau(\text{NNCC})$ (103)

^a Theoretical wavenumbers are not scaled. The strongest components of split bands are given in bold. PEDs lower than 10% are not included. Definition of symmetry coordinates is given in Table S6 (ESI); n.o., not observed; n.i., not investigated.

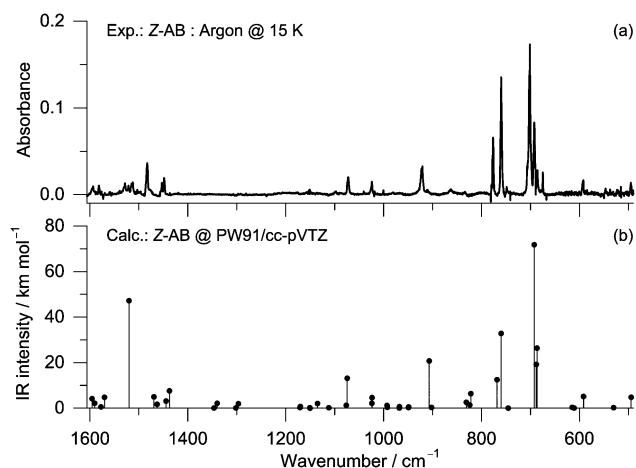


Fig. 4 (a) Extracted experimental infrared spectrum of Z-AB obtained by subtraction of the spectrum recorded in the first type of experiment (deposition which yielded only *E*-AB) from the spectrum recorded in the second type of experiment (deposition which yielded *E*-AB + Z-AB), so that the bands due to *E*-AB are nullified (b) theoretical infrared spectrum of the Z-AB monomer calculated at the PW91/cc-pVTZ level of theory.

post-processing spectra of the two types of experiments performed, where the bands due to *E*-AB were nullified by subtracting the spectrum of the pure *E*-AB form (obtained in experiment type 1) from the spectrum where both *E*-AB and Z-AB forms were present in the matrix (experiment type 2). The resulting spectrum is presented in Fig. 4.

Five of the strongest IR bands of Z-AB are predicted between 780 and 680 cm^{-1} and are due to the $\nu(\text{CH})$ and ring torsion modes. They appear in the experimental spectra as two multiplet features observed at 777–760 and 701–686 cm^{-1} . The $\nu(\text{NN})$ stretching mode is predicted to occur at 1520.1 cm^{-1} and, according to the calculations, should correspond to the second strongest absorption of Z-AB in the infrared region (47 km mol^{-1}). However in the experimental spectrum (Fig. 4), there is no clearly defined band at this position. This apparent contradiction between theory and experiment will be addressed below in detail.

Note that there are much less experimental characterizations available for Z-AB than for the most stable *E*-AB form.^{19,35,67–74} In the previous vibrational analyses reported in the literature, the assignment of modes in the 1600–1570 cm^{-1} and 1200–1100 cm^{-1} regions was uncertain. The calculated bands at 1595.6, 1590.2 and 1570.2 cm^{-1} correspond to the $\nu(\text{CC})$ stretching modes and can be assigned to the experimental absorptions at 1595.6, 1593.2 and 1581.6 cm^{-1} , respectively. In turn, the $\nu(\text{CN})$ stretching vibration calculated at 1135.0 cm^{-1} (B symmetry) was assigned to the weak band at 1151.3 cm^{-1} , while the A-symmetry $\nu(\text{CN})$ stretching mode (calculated at 1111.9 cm^{-1}) has a very weak predicted infrared intensity and was not observed experimentally.

Potential energy surfaces of *E*-AB and Z-AB

A very large number of theoretical studies have been carried out to characterize the potential energy surfaces (PES) connecting the two possible isomers of azobenzene (*E*-AB and Z-AB).^{29–32,37–51}

These potential energy surfaces deal with the necessity of transforming the *trans* CN=NC dihedral angle (in *E*-AB) into the *cis* CN=NC dihedral angle (in Z-AB), related to the *E*-Z isomerization around the central double bond. Such theoretical analyses must inevitably take into account structures very strongly distorted from the equilibrium geometry and enter high-energy regions (over 100 kJ mol^{-1}) of the PES. In such cases, the excited electronic states and conical intersections must be considered, leading to the necessity of multireference calculations. On the other hand, in the context of the present work, we are interested in the characterization of PES in the “low-energy” domain, near the equilibrium geometries. Such analysis can be safely carried out within the single determinant approximation.

Near the energy minima, the PES of azobenzene is considerably flat along the phenyl rings’ torsional coordinates, with large geometrical modifications implying only small energy changes. As shown below, accounting for these geometric changes permits to explain some peculiarities of the vibrational signatures of azobenzene observed in the present work. Considering an independent torsional motion for each phenyl ring, a two-dimensional (2D) PES can be constructed in the vicinity of each isomer, *E*-AB and Z-AB. Each phenyl ring will be named here as a “blade”, while the orientation of this blade relative to the central CNCC fragment can be described by the value of the NNCC dihedral angle, which we shall call here “blade pitch”. To construct the 2D PES described below, two NNCC dihedral angles were incrementally fixed between 0° and 90°, with a step of 10°, while all other remaining geometrical parameters were fully optimized.

The 2D PES map calculated for *E*-AB is presented in Fig. 5. The minimum energy geometry has two blade pitches equal to 0° and is in the center of the map. This structure has the C_{2h} symmetry. If both blades deviate from the equilibrium synchronously, by the same numeric value, and having the same sign of the blade pitch, the resulting set of geometries belongs to the C_2 symmetry point group. In terms of the map shown in Fig. 5, these geometries lie on the diagonal designated C_2 . If the two blades deviate from the equilibrium synchronously, but have the opposite signs of the blade pitch, the resulting set of geometries conserves the C_i symmetry and corresponds to the second diagonal across the map (designated C_i). An important characteristic of the obtained potential energy map is that the central fragment of the map, within the 0–2 kJ mol^{-1} energy range corresponds to large blade pitch variations, up to 25° from the minimum (area of the map colored violet).

It is instructive to analyze the energy of the normal vibrations related to the coordinates of the potential energy map ($\tau(\text{NNCC})$ coordinates), *i.e.* with the change of the blade pitch. According to the normal mode analysis (Table 1 and Table S4, ESI†), there are two vibrations in *E*-AB with contribution from the $\tau(\text{NNCC})$ coordinates. They belong to the B_g and A_u irreducible representations, which in terms of the 2D map (shown in Fig. 5) mean that they describe the vibrational movements along the C_i and C_2 diagonals, respectively. The corresponding vibrational frequencies calculated at the B97-1/cc-pVTZ level are 97.8 (B_g) and 22.0 cm^{-1} (A_u).¹⁰⁶ These frequencies correspond to the zero-point energy vibrations of 0.58 and 0.13 kJ mol^{-1} , respectively.

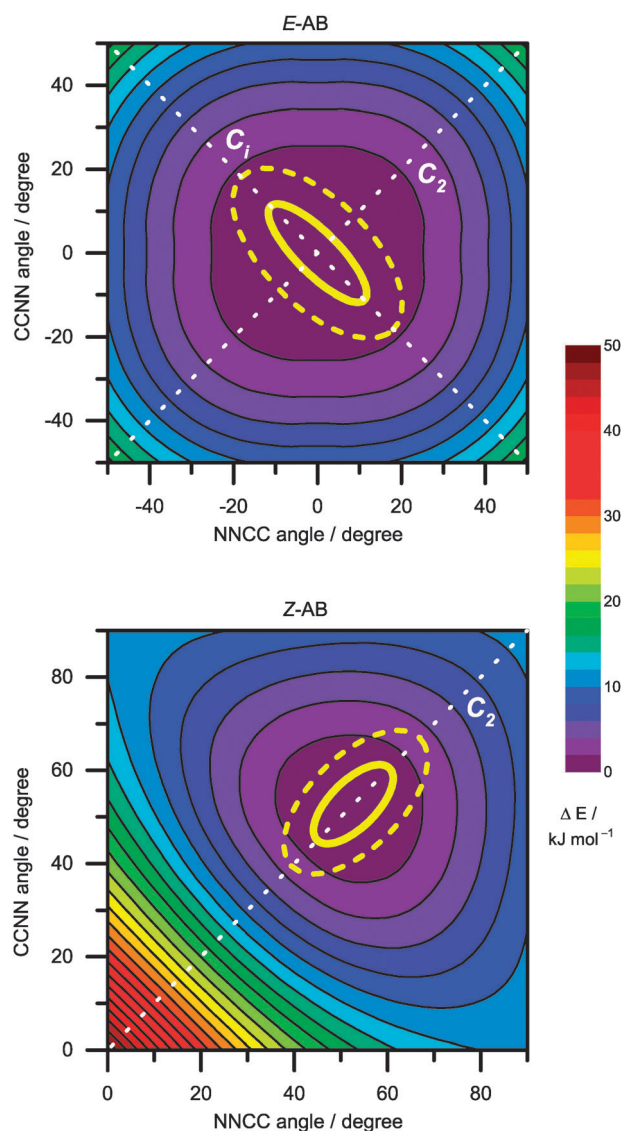


Fig. 5 Relaxed 2D potential energy map of *E*- and *Z*-azobenzene isomers as a function of blade pitch variation, calculated at the B97-1/cc-pVTZ level of theory. The reaction coordinates were chosen as the two CCNN dihedral angles. The central CCNN dihedral angle was in the *trans*- and *cis*-orientations, respectively (and optimized). The relative zeroes were chosen to correspond to the energy of the respective minima. The dotted white diagonal lines indicate the cuts through the surfaces where the molecules conserve a particular overall symmetry (C_1 and C_2 for *E*-AB; C_2 for *Z*-AB). The solid and dashed yellow ellipses indicate the areas accessible to the molecules undergoing the zero-point vibrations and in their first excited vibrational states, respectively. These areas were projected from the frequencies of the two calculated τ (CCNN) vibrations.

The area accessible to the *E*-AB isomer, executing the zero-point vibrational movements, is defined by these two values and is shown in Fig. 5 as a yellow ellipse (continuous line) with the major and minor axes oriented along the C_1 and C_2 diagonals, respectively, and measuring 0.58 and 0.13 kJ mol^{-1} . The larger (dashed) ellipse corresponds to the area on the map accessible to the *E*-AB isomer promoted to the first vibrational excited states (with the principal axes measuring to 1.75 and 0.39 kJ mol^{-1}).

The 2D PES map calculated for *Z*-AB as a function of the two blade pitches is also presented in Fig. 5. The minimum energy geometry has the blade pitches equal to 49° and equal signs. This structure has the C_2 symmetry, and is situated on the C_2 diagonal. As compared to the *E*-AB 2D map, it can be seen that the potential energy surface of *Z*-AB near the minimum has a smaller flat area. This is manifested in larger frequencies of the normal modes related to the phenyl ring torsions in *Z*-AB than in *E*-AB. In *Z*-AB, the two normal modes with dominating contribution from the τ NNCC coordinates belong to the A and B irreducible representations, and have the calculated frequencies equal to 174.0 (A) and 46.3 cm^{-1} (B), about twice as much as in *E*-AB. Similarly, as made above for *E*-AB, these frequencies were used to define the area available for the zero-point vibrational energy movements (solid ellipse in Fig. 5), which extend to 1.04 kJ mol^{-1} along the C_2 diagonal and to 0.28 kJ mol^{-1} in the orthogonal direction. The dashed ellipse designates the area accessible for the *Z*-AB molecule in the first excited vibrational state.

Geometries of *E*-AB and *Z*-AB

It has been previously suggested that the variation of the phenyl dihedral angles is responsible for slight changes observed in the UV absorption spectrum of azobenzene in the 20–120 $^\circ\text{C}$ temperature range.¹⁰⁷ Here, we shall demonstrate that the phenyl ring torsions are also responsible for distinctive peculiarities observed in the vibrational spectra of the compound, even at cryogenic temperatures. The largest deviations of the AB molecule from the equilibrium geometry, related to the τ NNCC coordinates, correspond to the displacements along the C_1 diagonal in *E*-AB, and along the C_2 diagonal in *Z*-AB. The corresponding one-dimensional potential energy scans, calculated now at the PW91/cc-pVTZ level, are shown in Fig. 6. In these scans, the C_1 and C_2 symmetries were conserved for *E*-AB and *Z*-AB, respectively. The blade pitches were incrementally fixed with a step of 5° , and the remaining coordinates were fully optimized. At each point of these scans, the vibrational calculations were carried out. The resulting NN bond distances and NN stretching frequencies are shown in parts (b and e) and (c and f) of Fig. 6. In *E*-AB, the zero-point vibrational energy (ZPE) corresponds to the change in the blade pitch from -8.5° to $+8.5^\circ$ (the points where the ZPE line intersects the energy curve, Fig. 6a). In *Z*-AB, the respective geometry variations within the ZPE energy level comprise the range of dihedral angles from 42° to 57° (Fig. 6d). These pitch variations can be projected to the respective NN geometric and vibrational properties of AB. For *E*-AB, this projection shows that the change in the NN bond length, related to the ZPE vibrations of the pitch angles, is about 0.04 pm, which corresponds to the changes in the ν NN frequency of 2 cm^{-1} . The ZPE vibrations in *Z*-AB result in a change in the NN bond length of about 0.28 pm, which correlates with a change in the ν NN frequency of 15 cm^{-1} . It is then clear that ZPE pitch variations of the same magnitude (17° in *E*-AB, and 15° in *Z*-AB) result in much larger changes of the NN bond length and the ν NN frequency in the *Z*-AB form, as compared to *E*-AB.

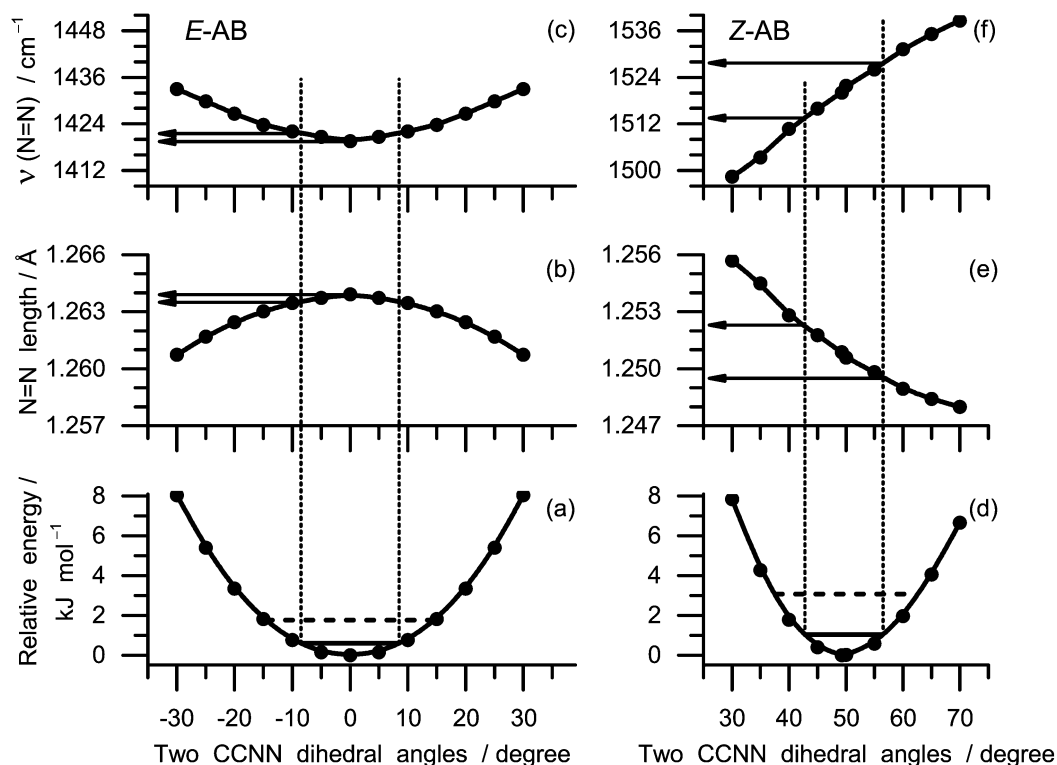


Fig. 6 (a) and (d) Relaxed potential energy scans in azobenzene as functions of the blade pitch variation, calculated at the PW91/cc-pVTZ level of theory for *E*-AB (a) and *Z*-AB (d). The reaction coordinates were chosen as the two CCNN dihedral angles having the same values and opposite signs (for *E*-AB, C_1 symmetry) or the same signs (for *Z*-AB, C_2 symmetry). The solid and dashed horizontal lines indicate energies of the ground states and the first excited vibrational levels along the reaction coordinates, respectively; (b) and (e) the optimized NN bond length; (c) and (f) the ν NN frequency, along the scans shown in parts (a) and (d). Note that the linear ordinate scales in pairs [(a), (d)], [(b), (e)] and [(c), (f)] had chosen the same.

The geometries where the ZPE levels in *E*-AB and *Z*-AB intersect the potential energy profiles were found from the corresponding normal vibrations (τ NNCC) and correspond to the following pitch variations: 8.5° (C_1 symmetry) and 3° (C_2 symmetry) for *E*-AB; 42° and 57° (both C_2 symmetry) for *Z*-AB. For these points the pitch angles were fixed, all the remaining parameters optimized, and the vibrational calculations carried out. The corresponding vibrational frequencies, along with the vibrational data for the minima, are collected in Table S7 (ESI[†]) (*E*-AB) and Table S8 (ESI[†]) (*Z*-AB). These sets of calculations permitted to estimate the changes in the vibrational spectra, expected to occur in an AB molecule undergoing the zero-point vibrations along the τ NNCC coordinates. For *E*-AB, within the frequency range accessible in our experiments (above 400 cm^{-1}) all vibrational modes are predicted to keep their frequencies within 3 cm^{-1} (Table S7, ESI[†]). From the seven calculated modes showing the largest variations of the predicted frequencies (between 2 and 3.3 cm^{-1}), four are infrared inactive and three are weak infrared absorbers (the highest predicted infrared intensity is 6 km mol^{-1}). In practical terms, this means that the effects on other vibrational modes due to the zero-point torsional vibrations of the phenyl rings in *E*-AB are not detectable in the matrix-isolation experiments, where a typical full-width-at-half-maximum of the absorption bands is 2 cm^{-1} . The situation is, however, significantly different for *Z*-AB. For this molecule, sixteen vibrations lying above 400 cm^{-1} are predicted

to have frequency variations above 3 cm^{-1} (as compared to only one, IR inactive mode in *E*-AB). From these 16 vibrations, it is precisely the NN stretching mode (Table S8, ESI[†]) which undergoes the largest frequency shifts along with the zero-point torsional vibrations of the phenyl rings. This has been exemplified graphically in Fig. 7, where the vibrational spectra of the *Z*-AB form, having pitch angles of 42° , 49° and 57° are presented. The uncertainty of the NN stretching frequency with the pitch change in *Z*-AB will result in the smearing of the experimental band over a large frequency range, as designated in Fig. 7a. Thus the broad experimental feature observed at around $1500\text{--}1540\text{ cm}^{-1}$ is assigned to the NN stretching vibration. A similar phenomenon of frequency smearing has been previously observed for dimethyl oxalate.¹⁰⁸ Thus, *Z*-AB is yet another molecule where considering the large amplitude, low frequency vibrations permits a successful explanation of the apparent contradiction between the theory and experiment.

Conclusions

The molecular structures and vibrational properties of the two isomers (*E* and *Z*) of azobenzene were investigated by a combined approach including matrix-isolation IR spectroscopy and theoretical calculations. UV-visible broad-band irradiation of *E*-azobenzene in the gas phase (at room temperature) allows for

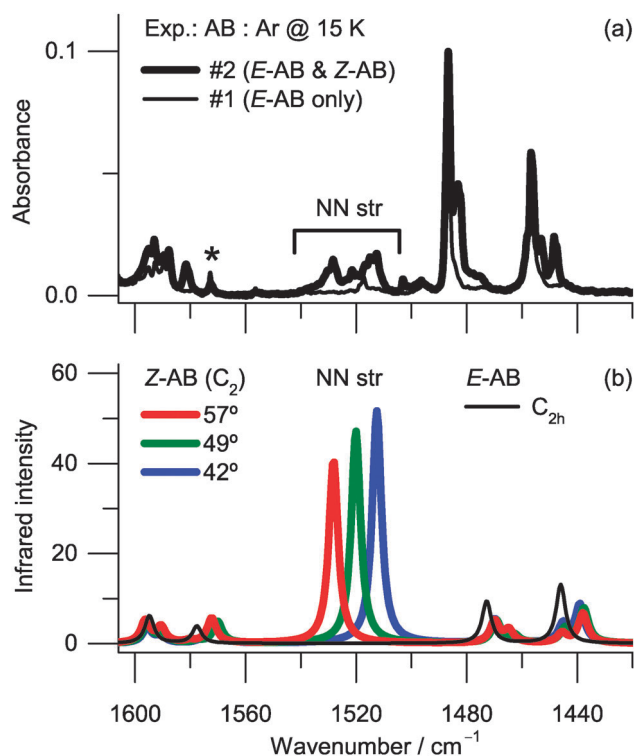


Fig. 7 (a) Fragments of the infrared spectra of azobenzene isolated in argon matrices at 15 K observed in two types of experiment: #1 (thin line) only *E*-AB present; #2 (bold line) both *E*-AB and *Z*-AB present. Experimental intensities (#1 and #2) were normalized to the same amount of *E*-AB. The asterisk designates a band due to matrix-isolated water impurity; (b) simulated spectra of different *Z*-AB and *E*-AB geometries. Black line: *E*-AB at the minimum configuration (C_{2h} symmetry); Red, green, and blue lines: *Z*-AB with the pitch angles fixed at 57° , 49° (minimum), and 42° , respectively, all within the C_2 symmetry. "NN str" refers to the *Z*-AB in both frames.

its partial conversion into the *Z*-isomer and trapping of both species in a cryogenic argon matrix (15 K). On the other hand, for matrix isolated azobenzene, UV-visible ($\lambda < 550$ nm) *in situ* irradiation could only induce the $Z \rightarrow E$ photoconversion, while the $E \rightarrow Z$ process was suppressed, presumably due to matrix steric constraints. The observed photoinduced $E \leftrightarrow Z$ isomerizations, together with a detailed theoretical characterization of the potential energy surfaces of the two isomers allowed for a reliable vibrational characterization of both forms, which appears particularly relevant to the higher energy *Z*-isomer, whose vibrational characterization had not yet been undertaken in detail hitherto. The calculated two-dimensional potential energy surfaces of *Z*-AB and *E*-AB revealed extensive flat areas around the minima, allowing for large-amplitude zero-point torsional movements of the rings. In the case of the *Z*-form, these large amplitude ring torsional movements lead to significant changes in the equilibrium NN bond length (up to 0.3 pm), which, in turn, explain the experimentally observed frequency smearing of the N=N stretching vibration in this isomer. Both the theoretical and experimental results obtained in the present study are consistent with a planar C_{2h} structure for the minimum energy ground state *E*-AB.

Acknowledgements

This work was supported by the Portuguese "Fundação para a Ciência e Tecnologia" (FCT) Research Projects PTDC/QUI-QUI/111879/2009 and PTDC/QUI-QUI/118078/2010, and FCOMP-01-0124-FEDER-021082, co-funded by QREN-COMPETE-UE. L.D. acknowledges FCT for the doctoral Grant No. SFRH/BD/62090/2009. The authors would like to acknowledge the Advanced Computing Laboratory at University of Coimbra for providing computing resources that have contributed to the research results reported within this paper (URL <http://www.lca.uc.pt>), and the Coimbra Chemistry Centre, project PEst-OE/QUI/UI0313/2014.

References

- P. Bamfield, *Chromic Phenomena*, Royal Society of Chemistry, Cambridge, 2nd edn, 2001.
- Industrial Dyes*, ed. K. Hunger, Wiley-VCH Verlag GmbH & Co. KGaA, Weinheim, FRG, 2003.
- Molecular Switches*, ed. B. L. Feringa, Wiley-VCH Verlag GmbH, Weinheim, FRG, 2001.
- A. Natansohn and P. Rochon, *Chem. Rev.*, 2002, **102**, 4139–4175.
- K. G. Yager and C. J. Barrett, *J. Photochem. Photobiol., A*, 2006, **182**, 250–261.
- T. Sasaki and J. M. Tour, *Org. Lett.*, 2008, **10**, 897–900.
- W. R. Browne and B. L. Feringa, *Annu. Rev. Phys. Chem.*, 2009, **60**, 407–428.
- Smart Light-Responsive Materials*, ed. Y. Zhao and T. Ikeda, John Wiley & Sons, Inc., Hoboken, NJ, USA, 2009.
- M.-M. Russew and S. Hecht, *Adv. Mater.*, 2010, **22**, 3348–3360.
- A. A. Beharry and G. A. Woolley, *Chem. Soc. Rev.*, 2011, **40**, 4422–4437.
- E. Merino and M. Ribagorda, *Beilstein J. Org. Chem.*, 2012, **8**, 1071–1090.
- J. Garca-Amorós and D. Velasco, *Beilstein J. Org. Chem.*, 2012, **8**, 1003–1017.
- Z. Mahimwalla, K. G. Yager, J.-i. Mamiya, A. Shishido, A. Priimagi and C. J. Barrett, *Polym. Bull.*, 2012, **69**, 967–1006.
- X. Sun, W. Wang, L. Qiu, W. Guo, Y. Yu and H. Peng, *Angew. Chem., Int. Ed.*, 2012, **51**, 8520–8524.
- D. Iqbal and M. Samiullah, *Materials*, 2013, **6**, 116–142.
- Y. B. Zheng, B. K. Pathem, J. N. Hohman, J. C. Thomas, M. Kim and P. S. Weiss, *Adv. Mater.*, 2013, **25**, 302–312.
- A. A. Beharry, O. Sadovski and G. A. Woolley, *J. Am. Chem. Soc.*, 2011, **133**, 19684–19687.
- S. Samanta, A. A. Beharry, O. Sadovski, T. M. McCormick, A. Babalhavaeji, V. Tropepe and G. A. Woolley, *J. Am. Chem. Soc.*, 2013, **135**, 9777–9784.
- G. S. Hartley, *J. Chem. Soc.*, 1938, 633–642.
- R. J. Corruccini and E. C. Gilbert, *J. Am. Chem. Soc.*, 1939, **61**, 2925–2927.
- E. Wolf and H. K. Cammenga, *Z. Phys. Chem.*, 1977, **107**, 21–38.

- 22 A. W. Adamson, A. Vogler, H. Kunkely and R. Wachter, *J. Am. Chem. Soc.*, 1978, **100**, 1298–1300.
- 23 I. K. Lednev, T.-q. Ye, R. E. Hester and J. N. Moore, *J. Phys. Chem.*, 1996, **100**, 13338–13341.
- 24 T. Nägele, R. Hoche, W. Zinth and J. Wachtveitl, *Chem. Phys. Lett.*, 1997, **272**, 489–495.
- 25 I. Lednev, T. Ye, P. Matousek, M. Towrie, P. Foggi, F. Neuwahl, S. Umaphy, R. Hester and J. Moore, *Chem. Phys. Lett.*, 1998, **290**, 68–74.
- 26 T. Fujino and T. Tahara, *J. Phys. Chem. A*, 2000, **104**, 4203–4210.
- 27 T. Fujino, S. Y. Arzhantsev and T. Tahara, *J. Phys. Chem. A*, 2001, **105**, 8123–8129.
- 28 H. Satzger, C. Root and M. Braun, *J. Phys. Chem. A*, 2004, **108**, 6265–6271.
- 29 C.-W. Chang, Y.-C. Lu, T.-T. Wang and E. W.-G. Diau, *J. Am. Chem. Soc.*, 2004, **126**, 10109–10118.
- 30 T. Schultz, J. Quenneville, B. Levine, A. Toniolo, T. J. Martnez, S. Lochbrunner, M. Schmitt, J. P. Shaffer, M. Z. Zgierski and A. Stolow, *J. Am. Chem. Soc.*, 2003, **125**, 8098–8099.
- 31 A. Cembran, F. Bernardi, M. Garavelli, L. Gagliardi and G. Orlandi, *J. Am. Chem. Soc.*, 2004, **126**, 3234–3243.
- 32 I. Conti, M. Garavelli and G. Orlandi, *J. Am. Chem. Soc.*, 2008, **130**, 5216–5230.
- 33 S. Yuan, Y. Dou, W. Wu, Y. Hu and J. Zhao, *J. Phys. Chem. A*, 2008, **112**, 13326–13334.
- 34 J. Bao and P. M. Weber, *J. Am. Chem. Soc.*, 2011, **133**, 4164–4167.
- 35 P. Hamm, S. M. Ohline and W. Zinth, *J. Chem. Phys.*, 1997, **106**, 519–529.
- 36 H. Satzger, S. Spörlein, C. Root, J. Wachtveitl, W. Zinth and P. Gilch, *Chem. Phys. Lett.*, 2003, **372**, 216–223.
- 37 E. Wei-Guang Diau, *J. Phys. Chem. A*, 2004, **108**, 950–956.
- 38 P. Cattaneo and M. Persico, *Phys. Chem. Chem. Phys.*, 1999, **1**, 4739–4743.
- 39 T. Ishikawa, T. Noro and T. Shoda, *J. Chem. Phys.*, 2001, **115**, 7503–7512.
- 40 T. Ikegami, N. Kurita, H. Sekino and Y. Ishikawa, *J. Phys. Chem. A*, 2003, **107**, 4555–4562.
- 41 C. Ciminelli, G. Granucci and M. Persico, *Chem.–Eur. J.*, 2004, **10**, 2327–2341.
- 42 M. L. Tiago, S. Ismail-Beigi and S. G. Louie, *J. Chem. Phys.*, 2005, **122**, 094311.
- 43 C. R. Crecca and A. E. Roitberg, *J. Phys. Chem. A*, 2006, **110**, 8188–8203.
- 44 J. Shao, Y. Lei, Z. Wen, Y. Dou and Z. Wang, *J. Chem. Phys.*, 2008, **129**, 164111.
- 45 Y. Dou, Y. Hu, S. Yuan, W. Wu and H. Tang, *Mol. Phys.*, 2009, **107**, 181–190.
- 46 H. M. D. Bandara, T. R. Friss, M. M. Enriquez, W. Isley, C. Incarvito, H. A. Frank, J. Gascon and S. C. Burdette, *J. Org. Chem.*, 2010, 4817–4827.
- 47 G. Tiberio, L. Muccioli, R. Berardi and C. Zannoni, *ChemPhysChem*, 2010, **11**, 1018–1028.
- 48 R. J. Maurer and K. Reuter, *J. Chem. Phys.*, 2011, **135**, 224303.
- 49 M. Pederzoli, J. Pittner, M. Barbatti and H. Lischka, *J. Phys. Chem. A*, 2011, **115**, 11136–11143.
- 50 T. Cusati, G. Granucci, E. Martnez-Núñez, F. Martini, M. Persico and S. Vázquez, *J. Phys. Chem. A*, 2012, **116**, 98–110.
- 51 Y. Harabuchi, M. Ishii, A. Nakayama, T. Noro and T. Taketsugu, *J. Chem. Phys.*, 2013, **138**, 064305.
- 52 H. M. D. Bandara and S. C. Burdette, *Chem. Soc. Rev.*, 2012, **41**, 1809–1825.
- 53 P. Sauer and R. E. Allen, *Chem. Phys. Lett.*, 2008, **450**, 192–195.
- 54 Y. Ootani, K. Satoh, A. Nakayama, T. Noro and T. Taketsugu, *J. Chem. Phys.*, 2009, **131**, 194306.
- 55 N. A. Wazzan, P. R. Richardson and A. C. Jones, *Photochem. Photobiol. Sci.*, 2010, **9**, 968–974.
- 56 S. Tanaka, S. Itoh and N. Kurita, *Chem. Phys.*, 2001, **272**, 171–184.
- 57 S. Tanaka and S. Itoh, *Chem. Phys. Lett.*, 2002, **362**, 467–475.
- 58 J. A. Gámez, O. Weingart, A. Koslowski and W. Thiel, *J. Chem. Theory Comput.*, 2012, **8**, 2352–2358.
- 59 V. Furer, A. Vandyukov, J. Majoral, A. Caminade and V. Kovalenko, *Chem. Phys.*, 2013, **421**, 57–67.
- 60 V. Furer, A. Vandyukov, J. Majoral, A. Caminade and V. Kovalenko, *J. Mol. Struct.*, 2013, **1046**, 30–38.
- 61 D.-L. Jiang and T. Aida, *Nature*, 1997, **388**, 454–456.
- 62 M. Klima, A. Kotov and L. Gribov, *J. Struct. Chem.*, 1973, **13**, 987–990.
- 63 D. R. Armstrong, J. Clarkson and W. E. Smith, *J. Phys. Chem.*, 1995, **99**, 17825–17831.
- 64 N. Biswas and S. Umaphy, *J. Phys. Chem. A*, 1997, **101**, 5555–5566.
- 65 H. Fliegl, A. Köhn, C. Hättig and R. Ahlrichs, *J. Am. Chem. Soc.*, 2003, **125**, 9821–9827.
- 66 H. Hacker, *Spectrochim. Acta*, 1965, **21**, 1989–2004.
- 67 J. Le Fevre, M. O'Dwyer and R. Werner, *Aust. J. Chem.*, 1953, **6**, 341.
- 68 R. Kübler, W. Lüttke and S. Weckherlin, *Z. Elektrochem.*, 1960, **64**, 650–658.
- 69 B. Kellerer, H. H. Hacker and J. Brandmüller, *Indian J. Pure Appl. Phys.*, 1971, **9**, 903–909.
- 70 A. Gruger, N. Le Calvé, P. Dizabo and J. Fillaux, *J. Chim. Phys. Phys.-Chim. Biol.*, 1972, **69**, 291–298.
- 71 A. Gruger, N. Le Calvé and J. Fillaux, *J. Chim. Phys. Phys.-Chim. Biol.*, 1972, **69**, 743–750.
- 72 I. K. Barker, V. Fawcett and D. A. Long, *J. Raman Spectrosc.*, 1987, **18**, 71–75.
- 73 H. Okamoto, H.-o. Hamaguchi and M. Tasumi, *Chem. Phys. Lett.*, 1986, **130**, 185–189.
- 74 Z. Meić, G. Baranović, V. Smrečki, P. Novak, G. Keresztury and S. Holly, *J. Mol. Struct.*, 1997, **408**, 399–403.
- 75 C. M. Stuart, R. R. Frontiera and R. A. Mathies, *J. Phys. Chem. A*, 2007, **111**, 12072–12080.
- 76 V. Stepanic, G. Baranović and V. Smrečki, *J. Mol. Struct.*, 2001, **569**, 89–109.
- 77 M. J. Frisch, G. W. Trucks, H. B. Schlegel, G. E. Scuseria, M. A. Robb, J. R. Cheeseman, G. Scalmani, V. Barone,

- B. Mennucci, G. A. Petersson, H. Nakatsuji, M. Caricato, X. Li, H. P. Hratchian, A. F. Izmaylov, J. Bloino, G. Zheng, J. L. Sonnenberg, M. Hada, M. Ehara, K. Toyota, R. Fukuda, J. Hasegawa, M. Ishida, T. Nakajima, Y. Honda, O. Kitao, H. Nakai, T. Vreven, J. A. Montgomery Jr., J. E. Peralta, F. Ogliaro, M. Bearpark, J. J. Heyd, E. Brothers, K. N. Kudin, V. N. Staroverov, R. Kobayashi, J. Normand, K. Raghavachari, A. Rendell, J. C. Burant, S. S. Iyengar, J. Tomasi, M. Cossi, N. Rega, J. M. Millam, M. Klene, J. E. Knox, J. B. Cross, V. Bakken, C. Adamo, J. Jaramillo, R. Gomperts, R. E. Stratmann, O. Yazyev, A. J. Austin, R. Cammi, C. Pomelli, J. W. Ochterski, R. L. Martin, K. Morokuma, V. G. Zakrzewski, G. A. Voth, P. Salvador, J. J. Dannenberg, S. Dapprich, A. D. Daniels, Å. Farkas, J. B. Foresman, J. V. Ortiz, J. Cioslowski and D. J. Fox, *Gaussian 09 Revision A.02*, Gaussian Inc., Wallingford CT, 2009.
- 78 H. B. Schlegel, *J. Comput. Chem.*, 1982, **3**, 214–218.
- 79 J. H. Schachtschneider and F. S. Mortimer, *Vibrational Analysis of Polyatomic-Molecules. VI. FORTRAN IV Programs for Solving the Vibrational Secular Equation and for the Least-Squares Refinement of Force Constants.*, 1969.
- 80 P. Pulay, G. Fogarasi, F. Pang and J. E. Boggs, *J. Am. Chem. Soc.*, 1979, **101**, 2550–2560.
- 81 R. L. Klug and R. Burcl, *J. Phys. Chem. A*, 2010, **114**, 6401–6407.
- 82 Generation of Z-azobenzene in the present work is similar to the method discovered by Hartley, in 1937: when azobenzene placed in a glass bottle was exposed to sunlight for several days, Z-AB was generated. See: G. S. Hartley, *Nature*, 1937, **140**, 281.
- 83 The choice of the model chemistry will be commented in the following section.
- 84 M. Dubecký, R. Derian, L. Horváthová, M. Allan and I. Štich, *Phys. Chem. Chem. Phys.*, 2011, **13**, 20939–20945.
- 85 10–15 cm long, glass and stainless steel.
- 86 S. Monti, G. Orlandi and P. Palmieri, *Chem. Phys.*, 1982, **71**, 87–99.
- 87 The average relaxation time of the electronically excited azobenzene is 121 fs. See, for example: A. J. Neukirch, L. C. Shamberger, E. Abad, B. J. Haycock, H. Wang, J. Ortega, O. V. Prezhdo and J. P. Lewis, *J. Chem. Theory Comput.*, 2014, **10**, 14–23; and collection of references cited therein. For such a fast relaxation, the steady state spectroscopy allows only for detecting spectra of the electronically relaxed molecules.
- 88 J.-A. Andersson, R. Pettersson and L. Tegnér, *J. Photochem.*, 1982, **20**, 17–32.
- 89 O. Ünsalan, N. Kus, S. Jarmelo and R. Fausto, *Spectrochim. Acta, Part A*, 2013, DOI: 10.1016/j.saa.2013.10.050.
- 90 L. Duarte, B. M. Giuliano, I. Reva and R. Fausto, *J. Phys. Chem. A*, 2013, **117**, 10671–10680.
- 91 T. A. Singleton, K. S. Ramsay, M. M. Barsan, I. S. Butler and C. J. Barrett, *J. Phys. Chem. B*, 2012, **116**, 9860–9865.
- 92 A reason for the E to Z reaction suppression could be ascribed to the specific interaction with the matrix cage and the ability of one of the conformers to fit better within the crystal cage than the other one. Such blocked isomerization reaction can sometimes be unblocked by raising the matrix temperature. We plan to carry out such experiments in future.
- 93 N. Kurita, S. Tanaka and S. Itoh, *J. Phys. Chem. A*, 2000, **104**, 8114–8120.
- 94 R. Burcl, *J. Phys. Chem. A*, 2011, **115**, 3605–3606.
- 95 T. Tsuji, H. Takashima, H. Takeuchi, T. Egawa and S. Konaka, *J. Phys. Chem. A*, 2001, **105**, 9347–9353.
- 96 N. Kurita, T. Ikegami and Y. Ishikawa, *Chem. Phys. Lett.*, 2002, **360**, 349–354.
- 97 M. M. Lin, D. Shorokhov and A. H. Zewail, *J. Phys. Chem. A*, 2009, **113**, 4075–4093.
- 98 C. Hättig and K. Hald, *Phys. Chem. Chem. Phys.*, 2002, **4**, 2111–2118.
- 99 L. Briquet, D. P. Vercauteren, E. A. Perpète and D. Jacquemin, *Chem. Phys. Lett.*, 2006, **417**, 190–195.
- 100 M. Traetteberg, I. Hillmo and K. Hagen, *J. Mol. Struct.*, 1977, **39**, 231–239.
- 101 J. J. de Lange, J. M. Robertson and I. Woodward, *Proc. R. Soc. A*, 1939, **171**, 398–410.
- 102 C. J. Brown, *Acta Crystallogr.*, 1966, **21**, 146–152.
- 103 J. A. Bouwstra, A. Schouten and J. Kroon, *Acta Crystallogr., Sect. C: Cryst. Struct. Commun.*, 1983, **39**, 1121–1123.
- 104 J. Harada, K. Ogawa and S. Tomoda, *Acta Crystallogr., Sect. B: Struct. Sci.*, 1997, **53**, 662–672.
- 105 J. Harada and K. Ogawa, *J. Am. Chem. Soc.*, 2001, **123**, 10884–10888.
- 106 The B97-1 and PW91/cc-pVTZ calculated frequencies coincide within 0.1 kJ mol⁻¹ (or within 8 cm⁻¹), and then the choice of either B97-1 or PW91 functional gives similar quantitative results.
- 107 L. De Boni, C. Toro, S. C. Zilio, C. R. Mendonca and F. E. Hernandez, *Chem. Phys. Lett.*, 2010, **487**, 226–231.
- 108 S. B. Lopes, L. Lapinski and R. Fausto, *Phys. Chem. Chem. Phys.*, 2002, **4**, 1014–1020.

C

Appendix

C.1 Hydroxyazobenzene Supporting Information

Table C.1 Cartesian coordinates of the optimized geometries of HAB isomeric forms.

Atom	B3LYP/6-311+G(2df,2p)											
	<i>E</i> -HABt		<i>E</i> -HABc		<i>Z</i> -HABc							
	x	y	z	x	y	z						
C	1.842726	1.055048	0.000000	-1.840286	-1.056665	0.000000	-0.887656	0.171784	-0.801239	0.882363	-0.146515	-0.806589
C	3.212571	1.219591	0.000000	-3.212866	-1.217023	0.000000	-1.955295	1.051460	-0.824601	1.965437	-1.010205	-0.855033
C	4.051712	0.100351	0.000000	-4.052408	-0.097855	0.000000	-3.114283	0.766141	-0.102341	3.127878	-0.723216	-0.139032
C	3.508286	-1.182562	0.000000	-3.508714	1.184734	0.000000	-3.211483	-0.425011	0.615474	3.217359	0.455776	0.599542
C	2.131206	-1.341638	0.000000	-2.133529	1.339200	0.000000	-2.155567	-1.321177	0.601251	2.149488	1.333560	0.610425
C	1.284470	-0.232644	0.000000	-1.284180	0.229156	0.000000	-0.969556	-1.021582	-0.071758	0.957651	1.031284	-0.056548
C	-4.468655	1.125150	0.000000	4.470161	-1.126551	0.000000	3.617304	0.809913	-0.827515	-3.621088	-0.827051	-0.827215
C	-3.090239	1.294353	0.000000	3.091870	-1.297005	0.000000	2.844006	-0.333587	-0.973680	-2.857652	0.326091	-0.945790
C	-2.244275	0.184004	0.000000	2.244902	-0.187445	0.000000	1.898584	-0.663803	-0.001940	-1.908268	0.636728	0.028553
C	-2.789741	-1.106190	0.000000	2.789182	1.103253	0.000000	1.778478	0.119779	1.147922	-1.773948	-0.177673	1.155150
C	-4.165407	-1.267333	0.000000	4.164686	1.265632	0.000000	2.581116	1.242939	1.300982	-2.566682	-1.311382	1.281239
C	-5.009490	-0.155779	0.000000	5.009813	0.154858	0.000000	3.491452	1.601451	0.310873	-3.480972	-1.649424	0.287356
N	-0.857702	0.476230	0.000000	0.858460	-0.480436	0.000000	1.225631	-1.920149	-0.133273	-1.249378	1.903485	-0.075780
N	-0.096718	-0.516577	0.000000	0.097334	0.512213	0.000000	-0.005177	-2.075827	-0.082780	-0.020218	2.072608	-0.034975
O	5.394146	0.329842	0.000000	-5.409943	-0.207097	0.000000	-4.124769	1.678730	-0.153572	4.213086	-1.547157	-0.142833
H	3.659579	2.204316	0.000000	-3.645223	-2.211558	0.000000	-1.908948	1.965736	-1.399841	1.909211	-1.912646	-1.453051
H	4.159259	-2.048940	0.000000	-4.171247	2.038754	0.000000	-4.118775	-0.660462	1.159396	4.131918	0.677675	1.131278
H	1.687958	-2.328159	0.000000	-1.688995	2.325180	0.000000	-2.232265	-2.270347	1.114095	2.216964	2.274233	1.140001
H	-5.118730	1.989976	0.000000	5.121045	-1.990778	0.000000	4.333638	1.072623	-1.594933	-4.341300	-1.072867	-1.596612
H	-2.644629	2.279944	0.000000	2.647417	-2.283125	0.000000	2.955857	-0.978941	-1.834494	-2.984076	0.995315	-1.786470
H	-4.589414	-2.263302	0.000000	4.587609	2.262044	0.000000	2.494868	1.842214	2.198115	-2.470251	-1.934792	2.160733
H	-6.082892	-0.292232	0.000000	6.083094	0.292236	0.000000	4.109080	2.480999	0.432876	-4.091552	-2.536450	0.388871
H	5.873158	-0.504881	0.000000	-5.667529	-1.134184	0.000000	-4.873867	1.373636	0.367622	4.042735	-2.317397	-0.693742
H	1.185236	1.911760	0.000000	-1.184027	-1.914373	0.000000	-0.000757	0.404865	-1.369958	-0.006314	-0.382826	-1.371063
H	-2.126411	-1.958283	0.000000	2.123039	1.954721	0.000000	1.072610	-0.158643	1.918307	-1.065488	0.084534	1.928849

Table C.1 (Cont.)

Atom	B3LYP/cc-pVTZ											
	<i>E</i> -HABt			HAB1c			Z-HABt			Z-HABc		
	x	y	z	x	y	z	x	y	z	x	y	z
C	1.842480	1.054157	0.000000	-1.840047	-1.056229	0.000000	-0.890225	0.172593	-0.796067	0.884056	-0.157283	-0.795343
C	3.211711	1.219001	0.000000	-3.212077	-1.216770	0.000000	-1.963122	1.045054	-0.820405	1.969731	-1.016947	-0.844014
C	4.052034	0.099944	0.000000	-4.052724	-0.098034	0.000000	-3.123661	0.750903	-0.102925	3.137222	-0.720324	-0.139268
C	3.507242	-1.182848	0.000000	-3.507722	1.184745	0.000000	-3.214594	-0.443502	0.610796	3.227099	0.466502	0.587646
C	2.130700	-1.341661	0.000000	-2.133123	1.338812	0.000000	-2.152782	-1.331986	0.597411	2.155938	1.339332	0.598714
C	1.283576	-0.233145	0.000000	-1.283373	0.229172	0.000000	-0.966084	-1.023320	-0.070011	0.959736	1.027453	-0.056116
C	-4.467273	1.126003	0.000000	4.469005	-1.126421	0.000000	3.621444	0.816945	-0.829726	-3.630463	-0.818333	-0.829637
C	-3.089232	1.294325	0.000000	3.091152	-1.296264	0.000000	2.848718	-0.326987	-0.970925	-2.860301	0.330083	-0.944067
C	-2.243401	0.184146	0.000000	2.244084	-0.187049	0.000000	1.902255	-0.653993	0.000836	-1.909858	0.633751	0.031485
C	-2.789998	-1.105310	0.000000	2.789224	1.103053	0.000000	1.780613	0.135940	1.146105	-1.781165	-0.185457	1.155251
C	-4.165320	-1.265921	0.000000	4.164344	1.265170	0.000000	2.582446	1.259961	1.294397	-2.580408	-1.314727	1.277288
C	-5.008648	-0.154332	0.000000	5.008913	0.154521	0.000000	3.493850	1.613864	0.304180	-3.495785	-1.644623	0.282231
N	-0.856675	0.476559	0.000000	0.857582	-0.480593	0.000000	1.232865	-1.912326	-0.127766	-1.247939	1.898724	-0.070486
N	-0.097618	-0.517279	0.000000	0.098086	0.512751	0.000000	0.003237	-2.072902	-0.078310	-0.019187	2.067284	-0.032020
O	5.393950	0.328852	0.000000	-5.409597	-0.207512	0.000000	-4.139257	1.657017	-0.153720	4.224580	-1.540255	-0.143542
H	3.659149	2.203577	0.000000	-3.644302	-2.211536	0.000000	-1.921485	1.961216	-1.393050	1.912495	-1.925047	-1.433588
H	4.158009	-2.049596	0.000000	-4.170713	2.038446	0.000000	-4.122094	-0.686669	1.151227	4.145256	0.696252	1.109869
H	1.686482	-2.327746	0.000000	-1.687380	2.324257	0.000000	-2.223190	-2.283683	1.106462	2.221759	2.285379	1.118862
H	-5.116958	1.991252	0.000000	5.119718	-1.990900	0.000000	4.338039	1.076474	-1.598120	-4.351611	-1.057657	-1.600360
H	-2.642324	2.279314	0.000000	2.645323	-2.281761	0.000000	2.963874	-0.976847	-1.828270	-2.981870	1.003651	-1.781977
H	-4.589761	-2.261822	0.000000	4.587667	2.261528	0.000000	2.494162	1.864216	2.188109	-2.487663	-1.941691	2.154790
H	-6.082221	-0.290224	0.000000	6.082326	0.291649	0.000000	4.111109	2.494261	0.422679	-4.112084	-2.528122	0.380967
H	5.865969	-0.510488	0.000000	-5.659769	1.137323	0.000000	-4.884428	1.338866	0.366569	4.045855	-2.314206	-0.687659
H	1.183662	1.909831	0.000000	-1.182319	-1.912770	0.000000	-0.003114	0.413046	-1.361383	-0.007856	-0.400945	-1.351550
H	-2.126015	-1.956861	0.000000	2.124196	1.953773	0.000000	1.073374	-0.138297	1.916741	-1.071483	0.070445	1.929991

Table C.1 (Cont.)

Atom	PW91/6-311+G(2df,2p)											
	<i>E</i> -HABt		<i>E</i> -HABc		<i>Z</i> -HABc							
	x	y	z	x	y	z						
C	1.838493	1.052499	0.000000	-1.835635	-1.054838	0.000000	-0.876046	0.190144	-0.752575	0.872035	-0.178855	-0.749882
C	3.211024	1.222874	0.000000	-3.210507	-1.220530	0.000000	-1.954904	1.060432	-0.793313	1.964012	-1.034769	-0.812352
C	4.056754	0.101173	0.000000	-4.057440	-0.099138	0.000000	-3.136552	0.749138	-0.107044	3.153521	-0.716719	-0.142027
C	3.515355	-1.189365	0.000000	-3.516778	1.191121	0.000000	-3.243718	-0.461234	0.589288	3.259928	0.489003	0.561510
C	2.135809	-1.354063	0.000000	-2.138553	1.350863	0.000000	-2.177232	-1.349129	0.588177	2.182448	1.359643	0.583105
C	1.280963	-0.242009	0.000000	-1.280776	0.238640	0.000000	-0.968188	-1.025091	-0.046517	0.963847	1.028529	-0.034487
C	-4.477096	1.130559	0.000000	4.478661	-1.131258	0.000000	3.637087	0.817149	-0.842702	-3.652773	-0.813057	-0.841652
C	-3.095319	1.304920	0.000000	3.097045	-1.306895	0.000000	2.856777	-0.326283	-0.986736	-2.871258	0.332379	-0.957812
C	-2.241638	0.192044	0.000000	2.242290	-0.194847	0.000000	1.903542	-0.652055	-0.011302	-1.911510	0.629909	0.020342
C	-2.786976	-1.104553	0.000000	2.786399	1.102289	0.000000	1.786049	0.140809	1.141509	-1.786628	-0.195838	1.149014
C	-4.165950	-1.270125	0.000000	4.165203	1.269117	0.000000	2.600903	1.260146	1.293623	-2.602251	-1.318396	1.273803
C	-5.016024	-0.156788	0.000000	5.016356	0.156609	0.000000	3.516724	1.613351	0.299287	-3.525929	-1.641666	0.276321
N	-0.857949	0.485666	0.000000	0.858776	-0.489370	0.000000	1.236368	-1.907814	-0.135551	-1.250924	1.891943	-0.076894
N	-0.096829	-0.527148	0.000000	0.097242	0.523066	0.000000	-0.003937	-2.074031	-0.052400	-0.011250	2.066329	-0.006535
O	5.401300	0.335678	0.000000	-5.417507	-0.213308	0.000000	-4.156537	1.654041	-0.173224	4.246920	-1.533759	-0.160871
H	3.658479	2.215077	0.000000	-3.643656	-2.222678	0.000000	-1.903946	1.990366	-1.356130	1.898069	-1.959892	-1.387617
H	4.175245	-2.057982	0.000000	-4.188007	2.047012	0.000000	-4.170592	-0.715057	1.105511	4.196995	0.733750	1.056772
H	1.690050	-2.347188	0.000000	-1.691675	2.343527	0.000000	-2.255524	-2.315888	1.082492	2.255746	2.323072	1.084650
H	-5.134493	1.998405	0.000000	5.136902	-1.998471	0.000000	4.357858	-0.970731	-1.616578	-4.380375	-1.048495	-1.616997
H	-2.646927	2.297064	0.000000	2.649723	-2.299540	0.000000	2.965629	-0.979056	-1.851477	-2.986516	1.011506	-1.801080
H	-4.589785	-2.273645	0.000000	4.588018	2.273052	0.000000	2.520189	1.864140	2.196495	-2.516799	-1.948149	2.158471
H	-6.095852	-0.296761	0.000000	6.096045	0.297623	0.000000	4.144810	2.449376	0.421429	-4.156212	-2.523055	0.378191
H	5.873865	-0.512094	0.000000	-5.659097	-1.153321	0.000000	-4.916017	1.316408	0.327862	4.048059	-2.321463	-0.691666
H	1.168346	1.908990	0.000000	-1.166407	-1.912102	0.000000	0.032591	0.442593	-1.292115	-0.041302	-0.438919	-1.277598
H	-2.112035	-1.957186	0.000000	2.110644	1.954269	0.000000	1.071862	-0.134281	1.915583	-1.066703	0.055369	1.925897

Table C.1 (Cont.)

Atom	PW91/cc-pVTZ											
	<i>E</i> -HABt			<i>E</i> -HABc			<i>Z</i> -HABt			<i>Z</i> -HABc		
	x	y	z	x	y	z	x	y	z	x	y	z
C	1.840591	1.055827	0.000000	-1.838266	-1.058314	0.000000	-0.881268	0.205106	-0.736038	0.878400	-0.191230	-0.737808
C	3.212772	1.224088	0.000000	-3.212963	-1.220731	0.000000	-1.963951	1.069732	-0.776790	1.974203	-1.041259	-0.799897
C	4.058115	0.101448	0.000000	-4.059073	-0.098299	0.000000	-3.152427	0.743783	-0.108019	3.168017	-0.711304	-0.141990
C	3.513262	-1.188436	0.000000	-3.514176	1.191260	0.000000	-3.259901	-0.477379	0.569739	3.272529	0.503056	0.547816
C	2.134524	-1.350314	0.000000	-2.136765	1.347048	0.000000	-2.188176	-1.357782	0.569593	2.190324	1.366729	0.569218
C	1.280890	-0.237872	0.000000	-1.280676	0.233952	0.000000	-0.973343	-1.019320	-0.046189	0.968387	1.023411	-0.034790
C	-4.474793	1.130727	0.000000	4.476811	-1.131023	0.000000	3.655458	0.801529	-0.845953	-3.672504	-0.797427	-0.841259
C	-3.093578	1.301317	0.000000	3.095795	-1.303408	0.000000	2.861767	-0.332475	-0.983937	-2.878921	0.339231	-0.953017
C	-2.241785	0.187568	0.000000	2.242545	-0.190802	0.000000	1.905720	-0.644799	-0.006924	-1.913205	0.622843	0.023420
C	-2.789944	-1.107749	0.000000	2.788973	1.105218	0.000000	1.797881	0.155656	1.141502	-1.793994	-0.211404	1.146368
C	-4.168887	-1.269956	0.000000	4.167695	1.269208	0.000000	2.625689	1.265955	1.287660	-2.621193	-1.325539	1.266968
C	-5.016420	-0.155238	0.000000	5.016729	0.155648	0.000000	3.545197	1.603889	0.292173	-3.551200	-1.633368	0.271223
N	-0.858430	0.484726	0.000000	0.858392	-0.489237	0.000000	1.233629	-1.898231	-0.127000	-1.248440	1.882750	-0.071005
N	-0.096335	-0.526804	0.000000	0.096882	0.521900	0.000000	-0.005989	-2.065106	-0.047492	-0.009605	2.058233	-0.003882
O	5.402485	0.333242	0.000000	-5.418558	-0.211133	0.000000	-4.176197	1.643524	-0.171942	4.264544	-1.522907	-0.160676
H	3.663241	2.215055	0.000000	-3.649146	-2.221948	0.000000	-1.912211	2.007877	-1.325805	1.909198	-1.972707	-1.365348
H	4.171455	-2.058581	0.000000	-4.183490	2.048737	0.000000	-4.191588	-0.743967	1.071074	4.212418	0.757984	1.032615
H	1.684888	-2.341763	0.000000	-1.685812	2.337919	0.000000	-2.264134	-2.331766	1.049865	2.259887	2.335914	1.060083
H	-5.130156	2.000282	0.000000	5.133298	-1.999728	0.000000	4.379214	1.048937	-1.621339	-4.405051	-1.020165	-1.615873
H	-2.640965	2.291584	0.000000	2.644711	-2.294378	0.000000	2.963178	-0.991976	-1.844391	-2.989368	1.025588	-1.790988
H	-4.596105	-2.272317	0.000000	4.593468	2.272161	0.000000	-2.551766	1.875567	2.187500	-2.539170	-1.961803	2.147455
H	-6.096605	-0.293403	0.000000	6.096721	0.295250	0.000000	4.184941	2.476505	0.410596	-4.191420	-2.507983	0.370691
H	5.865110	-0.520798	0.000000	-5.651786	1.153997	0.000000	-4.934261	1.287889	0.320149	4.057055	-2.314994	-0.682934
H	1.170379	1.912224	0.000000	-1.169443	-1.915856	0.000000	0.031966	0.469334	-1.261867	-0.037759	-0.460049	-1.256128
H	-2.115492	-1.960724	0.000000	2.113500	1.957376	0.000000	1.080773	-0.107075	1.917097	-1.068972	0.027378	1.922357

Table C.1 (Cont.)

Atom	MP2/cc-pVTZ											
	<i>E</i> -HABt		<i>E</i> -HABc		<i>Z</i> -HABt		<i>Z</i> -HABc					
	x	y	z	x	y	z	x	y	z			
C	-1.821667	-1.049256	0.000000	-1.819233	-1.050539	0.000000	0.817864	0.029048	-0.987154	0.812933	0.068977	-1.005723
C	-3.195191	-1.217856	0.000000	-3.195308	-1.215352	0.000000	1.808251	-0.941860	-0.957612	1.811999	-0.896991	-1.002276
C	-4.041435	-0.103786	0.000000	-4.041961	-0.101448	0.000000	2.869867	-0.832949	-0.057765	2.871371	-0.810726	-0.097399
C	-3.503477	1.182702	0.000000	-3.503875	1.184769	0.000000	2.959110	0.277808	0.781522	2.952505	0.273058	0.777265
C	-2.124424	1.351156	0.000000	-2.126556	1.349080	0.000000	1.988422	1.271470	0.721475	1.976814	1.259721	0.743867
C	-1.275953	0.242505	0.000000	-1.275659	0.239861	0.000000	0.892709	1.131988	-0.129173	0.882167	1.142671	-0.114686
C	4.460979	-1.126551	0.000000	4.461695	-1.130425	0.000000	-3.406685	-0.934584	-0.755885	-3.404716	-0.946796	-0.750236
C	3.080655	-1.301598	0.000000	3.081407	-1.305625	0.000000	-2.797214	0.305890	-0.919581	-2.805098	0.301001	-0.893787
C	2.233444	-0.191139	0.000000	2.234070	-0.195276	0.000000	-1.819758	0.720354	-0.015387	-1.823642	0.704720	0.010951
C	2.768186	1.103242	0.000000	2.768548	1.099216	0.000000	-1.508139	-0.064722	1.097903	-1.495546	-0.101506	1.104253
C	4.146620	1.269828	0.000000	4.146937	1.265935	0.000000	-2.148775	-1.286611	1.274523	-2.125855	-1.331498	1.261073
C	4.995991	0.159944	0.000000	4.996450	0.156166	0.000000	-3.082754	-1.734031	0.339859	-3.066065	-1.765852	0.326416
N	0.848851	-0.490868	0.000000	0.849456	-0.494848	0.000000	-1.274120	2.032340	-0.191033	-1.291348	2.025489	-0.141553
N	0.103909	0.536985	0.000000	0.104822	0.533081	0.000000	-0.026455	2.226556	-0.167449	-0.045441	2.230607	-0.123310
O	-5.383031	-0.344389	0.000000	-5.400412	-0.213386	0.000000	3.797528	-1.833685	-0.062674	3.866838	-1.741993	-0.035083
H	-3.638008	-2.203951	0.000000	-3.621187	-2.211921	0.000000	1.773283	-1.793362	-1.622347	1.765267	-1.722190	-1.702794
H	-4.159663	2.044496	0.000000	-4.173712	2.032883	0.000000	3.796294	0.377262	1.461791	3.792300	0.337122	1.454370
H	-1.682945	2.338176	0.000000	-1.683973	2.335618	0.000000	2.061867	2.156267	1.339104	2.042295	2.124283	1.390435
H	5.115411	-1.987175	0.000000	5.116297	-1.990915	0.000000	-4.146279	-1.268031	-1.470814	-4.148103	-1.270859	-1.465573
H	2.634636	-2.286720	0.000000	2.635478	-2.290791	0.000000	-3.056978	0.955828	-1.744406	-3.076347	0.965703	-1.703030
H	4.565349	2.267083	0.000000	4.565502	2.263438	0.000000	-1.914620	-1.892369	2.139253	-1.879249	-1.953117	2.110980
H	6.068222	0.300673	0.000000	6.068647	0.297078	0.000000	-3.568807	-2.690090	0.475527	-3.545487	-2.727216	0.447650
H	-5.842779	0.502024	0.000000	-5.627188	-1.149649	0.000000	4.474674	-1.621936	0.588593	3.690158	-2.418626	-0.697118
H	-1.157264	-1.900444	0.000000	-1.155679	-1.902450	0.000000	-0.002656	-0.061677	-1.684938	-0.006932	-0.006390	-1.706136
H	2.096796	1.948839	0.000000	2.096876	1.944587	0.000000	-0.779000	0.285783	1.815856	-0.760920	0.237906	1.821912

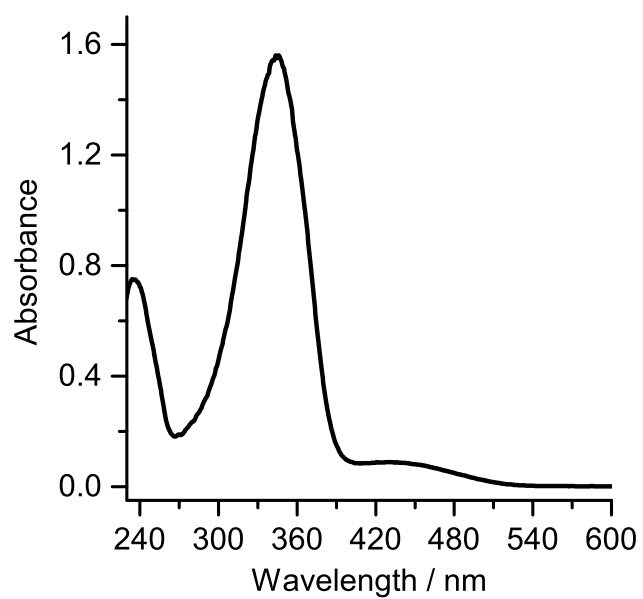


Figure C.1 Experimental UV-visible spectrum of HAB in acetonitrile. The spectrum was obtained in a Shimadzu UV-2100 spectrometer using quartz cuvettes.

Table C.2 Theoretical frequencies (ν/cm^{-1}) and IR intensities ($I/\text{km mol}^{-1}$) of HAB isomeric forms. The calculated frequencies are not scaled.

B3LYP/6-311+G(2df,2p)							
<i>E</i> -HABt		<i>E</i> -HABc		<i>Z</i> -HABt		<i>Z</i> -HABc	
ν	I	ν	I	ν	I	ν	I
3824.5	125.5	3824.5	125.5	3826.8	102.5	3827.4	83.8
3210.1	3.5	3210.1	3.5	3214.5	0.8	3213.7	0.6
3208.1	4.4	3208.1	4.4	3192.3	8.5	3199.5	5.6
3193.5	14.4	3193.5	14.4	3191.7	4.7	3192.5	8.7
3192.5	5.1	3192.5	5.1	3190.2	3.2	3187.4	14.8
3187.5	5.6	3187.5	5.6	3186.9	15.3	3185.1	1.1
3183.9	19.0	3183.9	19.0	3180.5	9.2	3180.9	9.3
3172.9	10.1	3172.9	10.1	3169.7	4.8	3170.0	5.1
3162.8	2.0	3162.8	2.0	3162.5	1.3	3162.7	1.4
3156.5	21.4	3156.5	21.4	3156.2	16.6	3153.7	14.6
1651.1	154.8	1651.1	154.8	1653.6	66.3	1651.1	69.6
1638.5	7.9	1638.5	7.9	1628.0	7.6	1628.5	17.3
1622.4	36.0	1622.4	36.0	1619.7	16.3	1624.1	6.4
1616.9	46.3	1616.9	46.3	1606.8	9.7	1608.1	6.5
1546.7	125.1	1546.7	125.1	1584.6	185.4	1586.1	172.1
1530.5	9.5	1530.5	9.5	1534.4	38.6	1532.6	39.4
1507.0	13.6	1507.0	13.6	1505.4	13.3	1507.9	14.3
1483.4	8.7	1483.4	8.7	1474.9	1.3	1475.7	14.3
1468.3	1.2	1468.3	1.2	1468.9	10.4	1469.4	20.4
1367.6	38.0	1367.6	38.0	1366.4	27.4	1366.8	31.5
1348.8	2.3	1348.8	2.3	1344.5	0.1	1347.6	0.3
1341.2	4.4	1341.2	4.4	1333.2	1.2	1333.1	0.7
1333.0	1.3	1333.0	1.3	1312.3	1.6	1313.6	1.3
1292.0	206.6	1292.0	206.6	1293.1	143.5	1292.0	150.2
1255.4	4.2	1255.4	4.2	1203.2	15.8	1203.3	11.5
1208.5	0.7	1208.5	0.7	1197.3	0.3	1198.9	0.9
1188.1	172.5	1188.1	172.5	1190.5	142.4	1190.1	120.5
1181.0	1.3	1181.0	1.3	1176.1	3.5	1177.5	2.8
1172.1	113.3	1172.1	113.3	1169.1	31.1	1169.1	51.6
1157.6	114.5	1157.6	114.5	1142.7	58.3	1143.4	54.4
1122.4	16.2	1122.4	16.2	1130.6	29.6	1129.1	17.6
1097.9	5.6	1097.9	5.6	1092.6	8.4	1094.0	8.1
1041.0	7.1	1041.0	7.1	1039.7	4.1	1041.7	4.2
1024.1	0.8	1024.1	0.8	1029.7	0.3	1029.0	0.3
1018.3	0.1	1018.3	0.1	1016.1	0.4	1016.4	0.4
1018.0	0.2	1018.0	0.2	1011.5	0.4	1011.3	0.4
1004.0	0.1	1004.0	0.1	993.2	0.1	993.3	0.1
1003.3	0.01	1003.3	0.01	988.0	3.0	992.7	0.2
973.3	2.0	973.3	2.0	973.7	3.3	969.2	7.6
954.6	5.0	954.6	5.0	937.9	13.3	938.0	15.1
934.1	0.2	934.1	0.2	876.4	45.3	879.6	44.8
869.6	50.2	869.6	50.2	855.9	13.6	856.7	25.9
860.5	0.0	860.5	0.04	854.1	16.5	855.1	4.3
857.7	5.3	857.7	5.3	840.9	4.5	840.5	1.7
823.6	11.2	823.6	11.2	824.6	7.1	823.1	13.2
804.0	15.6	804.0	15.6	775.3	35.6	775.3	37.6
790.7	26.2	790.7	26.2	761.0	4.5	761.4	3.6
740.2	7.1	740.2	7.1	730.0	24.1	730.7	20.3
702.6	37.7	702.6	37.7	709.9	35.7	710.3	34.9
658.8	0.5	658.8	0.5	694.9	7.1	694.5	8.6
651.1	0.8	651.1	0.8	653.4	1.2	653.2	0.4
629.2	0.1	629.2	0.1	626.8	0.2	627.9	0.1
561.4	26.6	561.4	26.6	608.7	8.6	608.6	7.1
535.3	4.2	535.3	4.2	540.3	2.0	540.1	3.5
507.9	0.8	507.9	0.8	510.6	9.9	510.9	11.0
505.1	33.7	505.1	33.7	486.5	6.0	486.6	4.1
435.5	0.02	435.5	0.02	431.6	2.5	432.4	4.6
419.9	0.02	419.9	0.02	421.2	13.7	421.6	3.1
411.2	23.3	411.2	23.3	412.8	2.6	413.0	3.5
391.8	2.9	391.8	2.9	405.8	2.8	405.8	13.5
375.7	101.4	375.7	101.4	359.8	92.7	356.3	87.9
286.0	0.5	286.0	0.5	339.5	14.2	339.3	16.6
277.9	0.2	277.9	0.2	266.4	2.4	266.8	3.9
207.3	1.1	207.3	1.1	225.7	0.6	226.1	0.5
197.3	0.2	197.3	0.2	166.4	3.1	167.2	0.5
97.2	0.1	97.2	0.1	119.7	1.1	119.7	1.7
77.2	1.3	77.2	1.3	61.6	0.6	61.8	0.7
47.5	1.1	47.5	1.1	49.6	0.8	49.6	0.2
6.4	0.02	6.4	0.02	30.9	2.1	33.5	0.4

Table C.2 (Cont.)

B3LYP/cc-pVTZ							
<i>E</i> -HABt		<i>E</i> -HABc		<i>Z</i> -HABt		<i>Z</i> -HABc	
ν	I	ν	I	ν	I	ν	I
3808.7	117.7	3811.0	108.1	3809.2	95.9	3810.5	79.2
3209.9	3.6	3208.4	6.7	3214.2	1.1	3213.2	0.8
3208.1	4.3	3208.1	0.4	3191.6	9.5	3198.8	6.3
3193.0	15.8	3199.4	7.2	3190.9	4.8	3191.7	10.2
3191.8	5.7	3192.7	18.2	3189.5	3.7	3186.9	17.2
3186.4	6.2	3184.8	2.2	3186.5	17.5	3184.1	1.3
3183.1	22.7	3183.0	22.0	3179.9	10.3	3180.3	10.8
3171.7	11.5	3171.7	11.3	3168.4	5.4	3168.8	5.9
3161.2	2.3	3161.4	2.0	3160.7	1.3	3161.1	1.3
3154.3	22.9	3146.2	26.2	3154.4	17.8	3151.8	15.9
1655.1	146.5	1651.3	179.6	1657.5	60.8	1655.1	64.7
1642.3	7.7	1641.8	27.4	1631.6	7.2	1632.9	15.6
1625.4	32.2	1629.6	6.1	1622.6	15.9	1626.4	6.7
1620.1	51.2	1621.8	4.9	1609.6	11.1	1611.6	7.2
1549.7	119.8	1552.3	87.6	1589.0	184.7	1590.7	172.7
1533.1	10.1	1529.6	30.5	1537.2	36.8	1535.0	38.1
1510.0	16.6	1507.1	1.3	1507.5	15.0	1511.3	16.2
1485.8	10.3	1484.9	8.1	1477.0	1.4	1478.7	14.9
1471.2	0.8	1471.8	73.5	1471.5	12.5	1472.4	22.8
1371.7	42.2	1373.5	33.3	1370.1	31.3	1369.9	35.7
1351.0	2.8	1350.9	2.4	1346.6	0.1	1351.2	0.3
1343.1	4.3	1343.1	0.9	1335.3	1.6	1335.0	0.9
1334.9	1.5	1332.8	0.6	1314.3	1.5	1316.1	1.4
1297.9	186.9	1293.9	241.9	1298.8	129.8	1297.5	136.7
1256.6	4.8	1257.0	21.9	1204.4	17.8	1204.8	11.2
1209.9	1.1	1209.7	4.1	1198.7	0.6	1201.1	1.3
1192.0	190.3	1198.4	159.6	1194.6	148.0	1193.7	129.9
1181.5	1.2	1181.5	0.7	1176.7	2.7	1179.0	2.0
1173.0	104.1	1172.9	62.1	1170.0	26.8	1170.8	44.2
1158.9	111.2	1157.9	91.8	1143.3	59.3	1144.0	56.7
1123.7	16.6	1122.5	27.3	1131.8	27.8	1130.2	18.1
1099.6	5.6	1099.5	6.4	1094.1	8.5	1096.8	8.4
1043.7	6.5	1043.6	6.6	1042.0	3.6	1045.0	3.8
1026.4	0.6	1025.8	1.2	1032.0	0.4	1031.1	0.4
1020.2	0.3	1020.2	0.3	1017.2	0.4	1017.8	0.4
1016.2	0.2	1016.4	0.2	1003.4	0.5	1003.6	0.5
1008.8	0.04	1000.7	0.04	986.5	0.4	992.4	0.3
1000.8	0.03	992.9	0.1	985.4	3.3	986.8	0.1
974.4	2.1	989.1	1.1	973.6	3.6	965.9	9.0
959.0	3.9	959.0	4.3	937.5	13.6	937.6	15.4
935.5	0.2	937.4	1.0	874.7	40.8	878.4	40.0
870.5	44.3	867.2	51.4	856.1	4.9	856.9	15.6
864.1	0.2	864.1	0.02	854.1	25.2	856.0	12.9
858.4	4.5	858.2	4.3	840.6	6.0	840.6	2.0
822.8	14.2	826.2	5.4	823.3	8.0	820.9	16.0
804.8	14.6	804.9	13.9	775.9	32.8	776.2	34.5
795.1	20.2	795.1	21.3	762.2	3.4	762.8	3.2
747.9	6.4	747.6	6.7	732.6	22.3	733.4	18.4
707.7	35.7	707.7	35.6	712.0	33.7	712.5	32.6
659.9	0.4	659.3	3.5	696.2	6.6	695.6	7.9
651.9	0.7	651.7	0.6	654.4	1.2	654.1	0.3
630.1	0.1	630.0	0.02	627.2	0.2	629.1	0.1
562.3	23.3	562.0	23.9	609.5	8.3	609.6	7.0
535.6	4.5	535.7	11.3	540.7	1.6	540.6	2.9
509.9	0.6	509.3	1.1	511.7	8.2	512.1	9.4
505.6	32.5	505.1	43.5	486.9	5.7	487.6	3.8
436.9	0.1	436.0	0.003	432.3	1.8	433.0	4.6
421.0	0.003	421.0	0.005	421.8	14.1	422.3	2.4
411.9	22.6	412.6	2.8	413.3	2.7	413.7	3.2
396.4	28.6	392.6	0.6	406.9	2.3	406.4	13.9
385.3	73.7	387.5	100.6	374.2	94.6	367.1	91.2
286.2	0.5	285.7	1.0	340.2	10.4	340.3	11.2
278.9	0.2	278.2	0.2	266.1	2.3	266.2	3.8
207.7	1.1	208.0	0.1	226.1	0.7	227.3	0.5
198.5	0.1	198.3	0.1	167.0	3.0	168.0	0.5
97.8	0.1	96.7	0.3	119.7	1.1	120.2	1.6
79.2	1.3	78.9	2.6	61.5	0.6	62.4	0.6
47.6	1.2	47.3	0.5	49.1	0.8	49.5	0.2
12.5	0.04	13.0	0.9	30.8	2.0	35.1	0.4

Table C.2 (Cont.)

PW91/6-311+G(2df,2p)							
<i>E</i> -HABt		<i>E</i> -HABc		<i>Z</i> -HABt		<i>Z</i> -HABc	
ν	I	ν	I	ν	I	ν	I
3714.3	118.8	3714.5	107.9	3714.9	93.5	3715.7	74.4
3141.5	5.0	3139.8	7.3	3147.2	1.1	3146.0	0.7
3139.6	7.5	3139.1	5.5	3131.0	13.8	3138.2	6.2
3131.2	20.7	3138.3	5.5	3129.1	5.2	3131.6	14.3
3128.7	4.8	3131.1	21.6	3127.4	2.9	3124.8	14.3
3123.1	5.4	3122.7	1.3	3123.9	14.8	3123.3	1.0
3121.9	15.0	3121.8	14.7	3119.0	6.2	3120.0	6.3
3111.4	8.4	3111.3	8.2	3108.0	4.2	3108.9	4.7
3101.7	3.6	3101.8	3.5	3101.3	2.2	3102.1	2.2
3093.2	21.9	3082.8	27.1	3093.6	17.6	3089.4	17.7
1606.7	184.9	1603.5	228.9	1611.1	95.5	1607.5	110.6
1593.4	7.3	1593.4	13.4	1581.9	5.8	1585.2	8.6
1578.5	43.7	1583.5	6.4	1574.0	29.3	1580.0	5.4
1575.3	34.0	1576.2	0.8	1559.7	5.3	1562.9	3.5
1491.6	100.1	1490.7	93.6	1509.2	210.3	1510.7	198.9
1475.3	0.3	1474.5	8.0	1483.5	2.5	1481.0	7.1
1456.5	14.1	1453.6	3.3	1452.6	11.6	1458.2	15.0
1440.4	9.2	1439.6	21.1	1435.9	2.1	1435.7	31.4
1408.8	18.7	1410.6	46.7	1427.6	6.2	1431.7	2.7
1370.4	21.2	1371.1	33.1	1361.5	24.1	1362.9	26.2
1351.8	1.8	1352.0	2.2	1329.1	2.3	1332.5	0.5
1294.9	5.1	1295.5	1.2	1299.6	1.9	1299.2	3.6
1289.0	1.9	1286.7	2.7	1289.5	2.3	1294.5	5.4
1264.9	234.9	1263.7	262.3	1268.1	134.3	1267.7	140.2
1228.9	3.3	1230.3	4.8	1172.0	12.7	1172.6	0.7
1178.9	0.01	1178.9	0.2	1164.8	9.6	1168.2	2.3
1157.9	204.1	1161.1	179.4	1163.2	146.5	1162.9	139.5
1148.2	0.1	1148.2	0.1	1141.1	3.5	1145.1	2.4
1134.3	64.9	1134.4	48.9	1135.6	31.1	1137.5	52.9
1122.3	109.5	1121.9	94.6	1109.2	62.3	1110.3	61.1
1084.9	17.6	1084.1	26.5	1097.3	30.1	1096.2	17.0
1068.3	5.9	1068.3	6.6	1063.1	9.6	1067.8	9.3
1015.9	8.1	1015.9	7.6	1014.7	4.4	1019.1	4.7
992.5	0.9	992.4	1.4	999.7	0.3	999.1	0.3
990.4	0.5	990.4	0.4	987.2	0.4	988.4	0.3
978.4	0.1	978.6	0.1	969.3	0.4	969.5	0.4
964.5	0.03	964.3	0.02	951.7	0.2	952.5	0.2
964.1	0.1	952.4	0.1	947.7	3.8	952.0	0.2
931.9	2.2	943.0	1.4	934.3	3.2	931.1	8.5
917.2	3.9	917.3	5.1	897.2	11.5	897.2	12.7
912.3	0.2	913.8	0.7	846.6	33.0	848.9	35.2
839.4	4.3	839.1	4.0	828.7	29.0	830.2	28.6
836.1	46.1	834.0	51.9	820.5	6.2	821.4	3.3
828.1	0.2	828.1	0.02	809.8	9.0	809.6	6.5
789.2	11.6	791.9	3.6	789.7	8.1	789.6	13.7
784.9	16.7	785.0	16.1	751.9	22.2	752.8	24.1
765.2	21.3	765.2	23.0	739.2	11.3	739.8	10.3
716.7	6.3	712.0	7.2	710.3	18.0	711.4	15.8
679.3	35.4	679.2	36.4	685.3	40.0	685.9	39.8
638.8	0.3	638.2	3.5	676.7	11.1	676.3	10.7
631.2	0.8	631.3	1.2	630.9	1.0	630.6	0.7
609.2	0.1	609.3	0.03	602.8	0.2	606.1	0.1
539.2	24.1	539.0	24.7	583.2	9.0	583.6	7.6
520.4	4.0	520.6	9.9	519.9	1.3	520.5	2.5
490.0	33.4	489.7	43.6	491.6	9.2	492.1	10.1
487.9	0.7	487.2	1.5	470.7	6.6	471.7	5.2
420.9	0.4	420.4	0.001	415.5	2.0	416.2	5.9
403.9	0.1	403.8	0.02	407.3	18.0	408.2	2.2
397.2	21.6	397.6	4.0	394.8	5.0	395.2	7.4
394.5	79.7	388.6	91.4	392.5	4.7	392.6	17.2
372.3	17.9	372.8	5.3	386.0	86.4	380.1	84.8
279.8	0.7	279.6	1.1	325.7	10.5	326.0	9.4
266.1	0.3	265.5	0.3	253.6	2.3	253.4	3.8
202.5	1.2	202.8	0.1	216.9	0.7	218.9	0.6
189.5	0.2	188.9	0.05	162.4	3.3	163.8	0.6
97.5	0.1	96.5	0.4	113.8	1.6	115.0	2.4
77.8	1.3	78.1	2.5	59.3	0.4	60.5	0.6
48.4	1.3	48.3	0.8	48.3	1.1	48.4	0.4
23.1	0.1	22.9	0.9	29.6	2.0	36.1	0.4

Table C.2 (Cont.)

PW91/cc-pVTZ							
<i>E</i> -HABt		<i>E</i> -HABc		<i>Z</i> -HABt		<i>Z</i> -HABc	
ν	I	ν	I	ν	I	ν	I
3697.3	110.4	3699.0	100.8	3697.8	86.4	3698.1	65.5
3141.8	5.1	3139.7	7.7	3148.2	1.2	3146.5	0.8
3139.6	8.2	3139.2	5.7	3131.7	15.1	3138.4	6.8
3131.7	20.7	3138.9	4.7	3129.4	5.2	3132.2	15.7
3129.3	6.9	3131.4	24.4	3127.6	3.6	3126.1	15.7
3123.8	6.1	3123.4	2.0	3125.1	16.5	3123.5	1.1
3122.2	16.6	3122.2	16.7	3120.2	7.1	3121.2	7.2
3111.5	9.7	3111.5	9.4	3108.5	5.0	3109.4	5.5
3101.2	3.7	3101.4	3.8	3101.4	2.3	3102.3	2.4
3092.8	23.1	3081.0	29.1	3092.3	18.8	3088.2	17.5
1614.2	167.5	1609.6	219.0	1615.1	88.4	1611.9	103.4
1599.6	6.0	1599.4	11.5	1587.3	5.7	1590.9	7.5
1578.9	51.9	1584.8	3.0	1576.7	29.6	1582.3	6.2
1575.4	35.3	1576.2	1.5	1563.8	6.1	1567.7	3.8
1496.8	90.0	1496.1	79.0	1513.3	204.4	1515.0	192.0
1479.8	0.03	1478.5	10.9	1486.6	2.5	1484.1	8.0
1457.7	14.7	1453.7	3.9	1457.8	13.4	1463.7	16.3
1444.8	7.0	1442.8	30.8	1439.2	2.6	1439.8	28.9
1413.0	23.6	1414.1	48.5	1431.9	7.1	1436.2	7.2
1373.4	24.4	1374.8	41.6	1365.4	28.2	1366.5	30.2
1352.8	1.7	1352.9	2.0	1332.9	2.3	1337.0	0.5
1299.7	5.1	1300.0	1.1	1301.1	2.1	1301.8	0.6
1294.7	2.1	1292.1	3.0	1294.1	2.7	1297.7	9.1
1273.1	198.5	1270.4	241.0	1273.7	120.4	1273.7	124.9
1230.8	4.2	1231.4	8.1	1173.3	21.1	1174.3	0.4
1181.0	1.1	1180.1	0.9	1167.8	62.5	1171.3	3.6
1165.0	228.0	1171.7	185.6	1166.6	93.3	1166.7	147.6
1147.9	0.1	1147.8	0.005	1143.6	1.5	1148.1	1.0
1135.2	74.2	1134.7	47.7	1137.3	26.5	1139.3	43.8
1125.6	99.0	1124.2	87.2	1109.1	66.5	1110.3	64.3
1088.1	18.0	1087.0	31.5	1098.0	28.0	1097.0	18.2
1069.2	5.6	1069.0	6.7	1067.2	10.2	1072.5	9.9
1018.1	7.5	1017.8	7.3	1019.1	3.9	1023.7	4.3
996.3	0.7	995.5	1.4	1001.7	0.4	1001.2	0.3
992.7	0.5	992.7	0.6	989.7	0.5	991.1	0.3
977.8	0.2	978.0	0.2	962.2	0.4	962.6	0.4
971.2	0.1	961.7	0.03	946.2	3.8	953.5	0.4
961.9	0.02	953.5	0.4	944.9	1.0	945.5	0.2
935.8	2.4	952.5	0.9	935.1	3.1	927.1	9.9
922.5	3.5	922.6	4.0	896.7	11.3	896.9	12.3
912.0	0.1	913.6	0.6	845.5	28.8	848.3	30.7
840.1	3.4	839.7	3.2	828.0	28.7	830.4	26.7
838.9	38.5	835.0	45.9	821.9	6.6	822.9	2.9
833.2	0.3	833.1	0.1	808.8	9.5	808.8	6.5
789.4	15.6	793.4	5.6	788.4	9.2	787.1	17.0
785.6	15.4	785.6	14.8	753.0	20.3	754.1	22.4
769.6	15.8	769.7	17.7	740.6	9.0	741.5	8.7
725.6	5.4	725.4	5.6	713.8	18.1	714.6	15.4
684.7	34.8	684.6	34.8	687.9	36.0	688.5	36.1
640.2	0.3	639.2	3.2	678.1	10.4	677.4	10.2
631.3	0.8	631.4	1.2	631.8	1.0	631.8	0.5
608.4	0.1	608.2	0.03	605.1	0.1	609.0	0.01
540.2	21.0	539.8	22.3	584.5	8.8	585.0	7.4
520.0	3.7	520.1	9.1	520.7	0.9	521.3	1.9
490.6	31.7	489.9	42.2	492.9	7.3	493.3	8.2
489.7	0.3	489.0	1.4	471.9	6.1	473.0	4.8
422.9	16.1	424.0	28.6	416.7	2.3	417.1	6.5
414.3	72.7	414.8	64.8	408.7	34.6	409.9	3.0
403.9	0.0004	403.9	0.2	402.2	63.9	396.1	9.5
399.0	21.5	399.5	3.4	395.5	2.2	395.7	63.4
374.3	7.1	375.1	0.5	392.7	11.5	391.0	32.9
279.8	0.5	279.3	0.9	326.2	9.8	326.9	8.5
265.8	0.2	265.2	0.2	252.5	2.1	252.5	3.5
201.7	1.1	201.7	0.1	218.7	0.8	221.1	0.6
190.1	0.1	190.2	0.1	163.1	3.0	164.3	0.5
95.6	0.1	94.8	0.3	114.8	1.6	116.4	2.3
78.4	1.3	77.0	2.5	59.6	0.4	61.4	0.6
46.0	1.4	45.3	0.5	48.0	1.4	48.4	0.4
3.5	0.0	6.3	1.1	32.6	1.6	39.6	0.3

Table C.2 (Cont.)

MP2/cc-pVTZ							
<i>E</i> -HABt		<i>E</i> -HABc		<i>Z</i> -HABt		<i>Z</i> -HABc	
ν	I	ν	I	ν	I	ν	I
3835.2	119.2	3836.4	111.5	3837.1	94.9	3838.5	81.7
3250.1	3.1	3249.6	4.0	3240.3	0.8	3240.7	2.1
3249.5	2.5	3247.2	1.3	3239.0	9.3	3238.7	9.4
3238.3	12.4	3243.0	2.5	3230.4	8.1	3231.0	0.4
3232.9	2.1	3238.4	12.8	3228.3	2.9	3230.2	9.2
3229.6	2.2	3228.7	9.3	3224.0	1.3	3223.8	2.4
3228.6	9.2	3225.7	0.9	3223.7	2.3	3221.7	1.9
3219.0	5.4	3219.1	5.2	3215.2	1.4	3215.1	1.6
3208.2	0.7	3208.3	0.6	3207.9	0.7	3207.7	0.6
3200.9	13.3	3195.5	15.0	3199.7	10.2	3198.2	9.4
1658.9	106.7	1654.6	166.8	1655.9	60.2	1653.6	74.3
1640.3	14.4	1644.3	12.2	1634.9	35.5	1637.9	14.5
1637.2	75.5	1639.8	0.6	1634.1	1.9	1634.1	3.2
1629.0	4.3	1629.0	0.9	1623.4	5.1	1623.6	2.8
1538.6	61.9	1536.3	70.4	1533.0	64.4	1531.4	76.8
1510.4	0.8	1510.8	3.3	1506.5	10.7	1506.5	10.1
1495.5	1.7	1494.4	0.4	1492.2	2.6	1492.2	2.1
1486.8	11.5	1486.3	6.5	1481.3	2.6	1481.3	1.3
1478.3	8.8	1478.1	7.3	1468.4	16.4	1469.1	1.3
1465.4	13.6	1466.5	45.4	1462.0	26.1	1462.2	20.2
1409.4	1.2	1409.7	21.4	1452.6	25.2	1453.6	42.6
1328.6	3.3	1329.8	0.4	1331.3	4.8	1331.0	2.4
1326.4	3.7	1324.9	1.2	1329.1	0.8	1328.2	8.7
1306.2	192.1	1305.9	192.7	1301.2	108.0	1301.8	101.0
1266.6	6.2	1267.8	5.5	1207.0	10.8	1206.5	12.0
1213.7	3.6	1213.2	0.2	1200.8	119.5	1200.6	127.9
1198.9	212.4	1201.6	186.6	1197.2	33.6	1198.4	21.9
1177.1	0.03	1177.1	0.1	1178.9	6.2	1179.4	14.8
1169.6	22.9	1169.7	21.3	1176.3	14.4	1176.7	13.2
1163.0	66.1	1162.5	61.6	1164.5	12.1	1165.0	11.0
1112.3	15.0	1111.5	21.2	1117.2	19.2	1115.9	13.3
1095.2	4.6	1095.1	4.4	1097.7	7.1	1097.8	7.1
1041.0	8.7	1041.0	8.7	1044.5	3.1	1044.5	3.1
1022.4	4.0	1022.2	4.8	1025.8	1.4	1026.0	1.1
1013.3	3.3	1013.4	3.3	1013.9	1.1	1013.9	0.9
978.6	0.02	979.0	0.03	967.5	0.2	967.3	0.2
974.5	0.1	968.6	0.001	961.5	0.04	961.8	0.1
968.8	0.0	962.0	0.1	950.7	0.3	955.4	1.3
936.9	5.6	944.3	2.6	935.1	19.8	930.9	26.3
932.9	0.6	936.1	3.1	924.5	3.1	921.1	0.7
931.5	0.8	934.3	1.8	890.7	8.1	892.9	7.6
857.3	13.7	856.8	0.4	850.8	0.5	851.0	0.4
855.6	28.4	855.0	9.6	843.4	12.1	844.8	26.8
855.4	10.2	853.5	49.0	835.7	33.5	840.3	8.8
819.1	16.3	821.8	7.5	817.6	7.0	811.0	16.7
801.4	7.8	801.5	7.3	769.3	39.8	769.1	44.4
779.8	32.1	779.8	33.5	760.1	27.2	760.9	24.3
717.5	11.5	716.7	11.7	715.5	10.3	715.7	10.1
686.2	23.6	686.1	23.4	702.0	36.2	701.9	34.6
649.2	0.2	648.6	3.0	676.9	3.4	676.4	4.3
641.5	0.6	641.6	0.8	643.2	1.2	643.5	0.4
615.7	0.2	615.7	0.1	617.5	0.1	617.4	0.1
554.5	23.3	554.3	23.8	596.4	6.9	596.3	5.8
527.8	5.2	527.9	11.6	535.9	4.6	535.7	5.8
502.5	0.3	502.0	0.8	501.0	5.8	500.4	5.8
499.4	16.4	498.8	23.4	476.5	1.9	476.0	1.9
426.9	0.2	425.4	0.7	427.0	3.4	428.8	4.0
412.3	0.0	412.2	0.001	411.3	4.8	411.5	3.0
404.9	20.8	406.0	4.3	406.0	1.4	406.1	1.9
388.4	0.01	389.1	0.0004	397.6	4.6	395.7	9.7
355.8	100.8	350.6	99.7	348.5	2.8	348.6	1.5
283.5	0.7	282.9	0.9	338.3	95.9	335.5	95.1
275.1	0.1	274.5	0.1	271.5	3.3	272.4	5.6
209.2	0.8	209.6	0.0	219.9	0.7	219.4	0.7
191.1	0.1	190.7	0.1	163.6	1.8	162.9	0.3
89.2	0.1	87.8	0.3	124.5	1.5	124.0	1.1
77.5	1.1	77.6	2.4	60.7	0.7	60.9	0.3
49.8	1.0	49.8	0.8	52.8	1.0	52.6	0.1
18.2	0.2	17.4	0.6	37.3	0.4	37.0	0.02

D

Appendix

D.1 CPDP Supporting Information

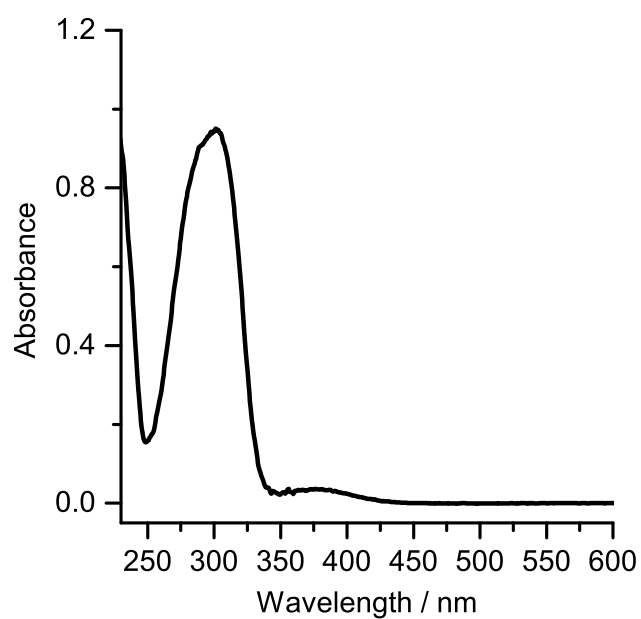


Figure D.1 Experimental UV-visible spectrum of CPDP in acetonitrile. The spectrum was obtained in a Shimadzu UV-2100 spectrometer using quartz cuvettes.

Table D.1 Cartesian coordinates of the optimized geometries of CPDP isomeric forms.

Atom	B3LYP/6-311+G(2df,2p)											
	CPDP1t			CPDP1c			CPDP2t			CPDP2c		
	x	y	z	x	y	z	x	y	z	x	y	z
C	0.734270	0.931650	0.000000	1.299714	1.395842	0.000000	-0.889976	1.137736	0.000000	-0.962466	1.260876	0.000000
C	2.078680	1.246960	0.000000	2.648016	1.074444	0.000000	-2.270355	1.170470	0.000000	-2.347796	1.223545	0.000000
C	3.034670	0.227190	0.000000	3.032843	-0.263053	0.000000	-2.998329	-0.023224	0.000000	-2.998536	-0.006836	0.000000
C	2.633890	-1.105820	0.000000	2.064462	-1.271177	0.000000	-2.333736	-1.246423	0.000000	-2.257145	-1.192226	0.000000
C	1.280380	-1.415800	0.000000	0.720633	-0.943554	0.000000	-0.945710	-1.272333	0.000000	-0.874900	-1.148156	0.000000
C	0.320340	-0.406490	0.000000	0.324908	0.397398	0.000000	-0.2111728	-0.088271	0.000000	-0.212824	0.083722	0.000000
N	-1.034160	-0.833200	0.000000	-1.024533	0.840582	0.000000	1.198994	-0.229805	0.000000	1.196779	0.239346	0.000000
O	4.345980	0.602000	0.000000	4.369208	-0.536034	0.000000	-4.358001	0.076670	0.000000	-4.362260	-0.000668	0.000000
N	-1.885800	0.075090	0.000000	-1.887970	-0.056360	0.000000	1.852631	0.828069	0.000000	1.861159	-0.811729	0.000000
C	-3.229270	-0.391010	0.000000	-3.225032	0.428157	0.000000	3.279095	0.664644	0.000000	3.285902	-0.634122	0.000000
C	-4.224160	0.472600	0.746570	-4.232475	-0.420477	-0.746641	3.938677	-0.477386	0.745628	3.934375	0.514317	-0.745601
C	-4.224160	0.472600	-0.746570	-4.232475	-0.420477	0.746641	3.938677	-0.477386	-0.745628	3.934375	0.514317	0.745601
H	-0.011900	1.712640	0.000000	0.979769	2.428996	0.000000	-0.317692	2.053943	0.000000	-0.437750	2.206728	0.000000
H	2.412190	2.275620	0.000000	3.409305	1.841860	0.000000	-2.807444	2.109076	0.000000	-2.935712	2.130642	0.000000
H	3.375470	-1.896170	0.000000	2.369609	-2.311622	0.000000	-2.897549	-2.171942	0.000000	-2.769736	-2.147763	0.000000
H	0.949480	-2.445470	0.000000	-0.033445	-1.716935	0.000000	-0.411852	-2.212999	0.000000	-0.293827	-2.058824	0.000000
H	4.912390	-0.175760	0.000000	4.512412	-1.487432	0.000000	-4.755169	-0.799714	0.000000	-4.696333	-0.902913	0.000000
H	-3.358810	-1.467220	0.000000	-3.339938	1.505991	0.000000	3.779987	1.620716	0.000000	3.796128	-1.585254	0.000000
H	-3.821060	1.337980	1.251890	-3.842794	-1.292734	-1.250753	3.257114	-1.156079	1.238813	3.246391	1.186455	-1.238835
H	-3.821060	1.337980	-1.251890	-3.842794	-1.292734	1.250753	3.257114	-1.156079	-1.238813	3.246391	1.186455	1.238835
H	-5.016800	-0.039900	1.272520	-5.016753	0.103484	-1.273820	4.855475	-0.261692	1.275971	4.853264	0.307320	-1.275757
H	-5.016800	-0.039900	-1.272520	-5.016753	0.103484	1.273820	4.855475	-0.261692	-1.275971	4.853264	0.307320	1.275757

Table D.1 (Cont.)

Atom	B3LYP/6-311+G(2df,2p)						B3LYP/cc-pVTZ					
	CPDPZ1t			CPDPZ1c			CPDP1t			CPDP1c		
	x	y	z	x	y	z	x	y	z	x	y	z
C	0.541233	-0.614949	-0.826726	-0.529450	0.567318	-0.875804	0.734096	0.931758	0.000000	1.298767	1.395151	0.000000
C	1.792678	-1.141710	-0.546175	-1.797225	1.078066	-0.623489	2.077861	1.247115	0.000000	2.646601	1.074741	0.000000
C	2.728582	-0.378606	0.147709	-2.701803	0.351818	0.146642	3.034818	0.227425	0.000000	3.032971	-0.263090	0.000000
C	2.412657	0.923167	0.532164	-2.341562	-0.900705	0.640946	2.632596	-1.105625	0.000000	2.063763	-1.270869	0.000000
C	1.169519	1.456096	0.222223	-1.087834	-1.418271	0.361268	1.279503	-1.414900	0.000000	0.720411	-0.943442	0.000000
C	0.210515	0.683222	-0.428729	-0.158772	-0.678520	-0.371868	0.319311	-0.405960	0.000000	0.323783	0.396909	0.000000
N	-1.012798	1.329161	-0.812100	1.077000	-1.319396	-0.725337	-1.034747	-0.833234	0.000000	-1.025246	0.840722	0.000000
O	3.941070	-0.952314	0.408742	-3.956741	0.807457	0.438936	4.345677	0.601440	0.000000	4.368708	-0.535864	0.000000
N	-2.136204	0.883020	-0.526102	2.190743	-0.838725	-0.460152	-1.884491	0.076532	0.000000	-1.886757	-0.057714	0.000000
C	-2.322637	-0.268806	0.306156	2.351509	0.354735	0.316403	-3.227773	-0.391123	0.000000	-3.223721	0.428460	0.000000
C	-3.627769	-0.263585	1.074249	3.638978	0.394585	1.113988	-4.222890	0.471552	0.746539	-4.230814	-0.419946	-0.746597
C	-3.475566	-1.165543	-0.101693	3.508930	1.237283	-0.107403	-4.222890	0.471552	-0.746539	-4.230814	-0.419946	0.746597
H	-0.177227	-1.208266	-1.376031	0.164806	1.132529	-1.483034	-0.013542	1.711319	0.000000	0.976261	2.427517	0.000000
H	2.059260	-2.141667	-0.859973	-2.081347	2.042790	-1.028474	2.412185	2.275575	0.000000	3.408095	1.841998	0.000000
H	3.143906	1.526519	1.057739	-3.058270	-1.461912	1.224361	3.373899	-1.896444	0.000000	2.368948	-2.311473	0.000000
H	0.930245	2.477306	0.487155	-0.813974	-2.405096	0.710121	0.946102	-2.443788	0.000000	-0.034988	-1.715525	0.000000
H	4.506393	-0.329083	0.874845	-4.099901	1.665453	0.028462	4.905723	-0.181742	0.000000	4.504161	-1.489052	0.000000
H	-1.462523	-0.725505	0.775474	1.477790	0.826575	0.743836	-3.356649	-1.467304	0.000000	-3.337256	1.506320	0.000000
H	-4.246642	0.614937	0.962450	4.263294	-0.485471	1.060522	-3.818679	1.337174	1.250716	-3.838295	-1.290558	-1.251491
H	-3.991886	-0.897555	-1.012029	4.046632	0.929686	-0.992585	-3.818679	1.337174	-1.250716	-3.838295	-1.290558	1.251491
H	-3.601834	-0.689824	2.066824	3.586045	0.868136	2.083774	-5.016101	-0.040902	1.271931	-5.016693	0.103750	-1.271912
H	-3.345881	-2.226367	0.059533	3.371173	2.303770	0.000774	-5.016101	-0.040902	-1.271931	-5.016693	0.103750	1.271912

Table D.1 (Cont.)

Atom	B3LYP/cc-pVTZ											
	CPDP2t		CPDP2c		CPDP2i		CPDP2ic					
	x	y	z	x	y	z	x	y	z			
C	-0.888587	1.136410	0.000000	-0.962673	1.261754	0.000000	0.541915	-0.617281	-0.823124	-0.526921	0.569895	-0.867998
C	-2.268301	1.170718	0.000000	-2.347359	1.223639	0.000000	1.794135	-1.142026	-0.544658	-1.794961	1.079939	-0.618105
C	-2.998262	-0.022460	0.000000	-2.998522	-0.007321	0.000000	2.731348	-0.378016	0.147730	-2.703329	0.352057	0.146662
C	-2.333338	-1.245985	0.000000	-2.255106	-1.191872	0.000000	2.413385	0.924136	0.530601	-2.344338	-0.903570	0.635830
C	-0.945872	-1.272860	0.000000	-0.873437	-1.146427	0.000000	1.169695	1.454897	0.221600	-1.090800	-1.420517	0.356910
C	-0.210854	-0.089683	0.000000	-0.211936	0.085398	0.000000	0.209868	0.681231	-0.427063	-0.158227	-0.678874	-0.369837
N	1.199983	-0.231416	0.000000	1.197782	0.241251	0.000000	-1.013041	1.328683	-0.808687	1.077485	-1.321051	-0.720124
O	-4.357349	0.077657	0.000000	-4.361616	-0.002367	0.000000	3.944266	-0.949607	0.407976	-3.958378	0.807090	0.436171
N	1.850450	0.828095	0.000000	1.858775	-0.811638	0.000000	-2.136513	0.881772	-0.526797	2.191013	-0.840063	-0.457215
C	3.277150	0.664949	0.000000	3.283803	-0.634695	0.000000	-2.324081	-0.273624	0.300719	2.352052	0.356490	0.315257
C	3.937347	-0.476339	0.745457	3.933168	0.512835	-0.745440	-3.624659	-0.262428	1.076214	3.639970	0.397500	1.110953
C	3.937347	-0.476339	-0.745457	3.933168	0.512835	0.745440	-3.484782	-1.160491	-0.104158	3.509301	1.236342	-0.113175
H	-0.313045	2.050520	0.000000	-0.437442	2.207338	0.000000	-0.176427	-1.211871	-1.371270	0.169777	1.137110	-1.470600
H	-2.805382	2.109385	0.000000	-2.936419	2.130053	0.000000	2.062134	-2.141829	-0.857888	-2.076916	2.046974	-1.019497
H	-2.897691	-2.171375	0.000000	-2.766789	-2.148077	0.000000	3.144807	1.529568	1.053881	-3.063354	-1.466679	1.214616
H	-0.411412	-2.213208	0.000000	-0.289034	-2.054917	0.000000	0.928882	2.476342	0.484344	-0.818121	-2.409042	0.701906
H	-4.747515	-0.802609	0.000000	-4.687715	-0.908213	0.000000	4.502909	-0.319749	0.874593	-4.090756	1.669075	0.028847
H	3.778261	1.621010	0.000000	3.794029	-1.585938	0.000000	-1.464897	-0.738086	0.763846	1.479865	0.832460	0.741022
H	3.254426	-1.154608	1.237586	3.243981	1.184718	-1.237574	-4.236391	0.621852	0.969709	4.261970	-0.484319	1.057400
H	4.854650	-0.260710	1.275205	4.852500	0.305657	-1.275016	-3.596387	-0.693746	2.066621	3.590901	0.875573	2.078835
H	4.854650	-0.260710	-1.275205	4.852500	0.305657	1.275016	-3.362731	-2.222909	0.053187	3.373020	2.303295	-0.006511

Table D.1 (Cont.)

Atom	PW91/6-311+G(2df,2p)						CPDP1c			CPDP2t			CPDP2c		
	x	y	z	x	y	z	x	y	z	x	y	z	x	y	z
C	0.726019	0.926756	0.000000	1.306131	1.406756	0.000000	-0.884531	1.139358	0.000000	-0.961213	1.270028	0.000000	-0.961213	1.270028	0.000000
C	2.071964	1.251280	0.000000	2.656341	1.078247	0.000000	-2.268453	1.174882	0.000000	-2.349973	1.230538	0.000000	-2.349973	1.230538	0.000000
C	3.037093	0.232239	0.000000	3.035739	-0.266918	0.000000	-3.000606	-0.023017	0.000000	-3.000902	-0.006460	0.000000	-3.000902	-0.006460	0.000000
C	2.641952	-1.108891	0.000000	2.058228	-1.274669	0.000000	-2.334801	-1.252723	0.000000	-2.254218	-1.195783	0.000000	-2.254218	-1.195783	0.000000
C	1.287211	-1.427695	0.000000	0.712955	-0.939800	0.000000	-0.943803	-1.281145	0.000000	-0.868961	-1.149373	0.000000	-0.868961	-1.149373	0.000000
C	0.316887	-0.418725	0.000000	0.321488	0.408863	0.000000	-0.204443	-0.092185	0.000000	-0.205604	0.088902	0.000000	-0.205604	0.088902	0.000000
N	-1.038554	-0.851323	0.000000	-1.023645	0.857558	0.000000	1.203396	-0.234912	0.000000	1.201061	0.245463	0.000000	1.201061	0.245463	0.000000
O	4.349453	0.615099	0.000000	4.373809	-0.547611	0.000000	-4.363366	0.078874	0.000000	-4.367828	-0.003198	0.000000	-4.367828	-0.003198	0.000000
N	-1.889770	0.073167	0.000000	-1.892244	-0.055163	0.000000	1.856435	0.840975	0.000000	1.864492	-0.823965	0.000000	1.864492	-0.823965	0.000000
C	-3.230797	-0.391230	0.000000	-3.226657	0.428654	0.000000	3.280145	0.674152	0.000000	3.286549	-0.644124	0.000000	3.286549	-0.644124	0.000000
C	-4.223562	0.485930	0.746884	-4.232652	-0.433056	-0.746914	3.931743	-0.481095	0.745643	3.928045	0.516796	-0.745626	3.928045	0.516796	-0.745626
C	-4.223562	0.485930	-0.746884	-4.232652	-0.433056	0.746914	3.931743	-0.481095	-0.745643	3.928045	0.516796	0.745626	3.928045	0.516796	0.745626
H	-0.033571	1.705251	0.000000	0.985841	2.447180	0.000000	-0.301762	2.057861	0.000000	-0.431638	2.221268	0.000000	-0.431638	2.221268	0.000000
H	2.402919	2.288125	0.000000	3.427046	1.845948	0.000000	-2.809065	2.119555	0.000000	-2.944248	2.141689	0.000000	-2.944248	2.141689	0.000000
H	3.394155	-1.899051	0.000000	2.362318	-2.323084	0.000000	-2.905240	-2.182589	0.000000	-2.770570	-2.157661	0.000000	-2.770570	-2.157661	0.000000
H	0.956769	-2.464922	0.000000	-0.054157	-1.710952	0.000000	-0.404464	-2.226842	0.000000	-0.276975	-2.061984	0.000000	-0.276975	-2.061984	0.000000
H	4.911931	-0.175613	0.000000	4.496670	-1.510168	0.000000	-4.750249	-0.811136	0.000000	-4.686994	-0.919568	0.000000	-4.686994	-0.919568	0.000000
H	-3.371695	-1.473758	0.000000	-3.350763	1.513170	0.000000	3.791908	1.632175	0.000000	3.806917	-1.597515	0.000000	3.806917	-1.597515	0.000000
H	-3.803095	1.349816	1.254462	-3.825260	-1.303391	-1.254229	3.226473	-1.147403	1.238464	3.217286	1.177088	-1.238638	3.217286	1.177088	-1.238638
H	-3.803095	1.349816	-1.254462	-3.825260	-1.303391	1.254229	3.226473	-1.147403	-1.238464	3.217286	1.177088	1.238638	3.217286	1.177088	1.238638
H	-5.021263	-0.026738	1.277899	-5.021934	0.091519	-1.278882	4.853996	-0.273341	1.282464	4.852126	0.316726	-1.282198	4.852126	0.316726	-1.282198
H	-5.021263	-0.026738	-1.277899	-5.021934	0.091519	1.278882	4.853996	-0.273341	-1.282464	4.852126	0.316726	1.282198	4.852126	0.316726	1.282198

Table D.1 (Cont.)

Atom	B3LYP/6-311+G(2df,2p)						PW91/cc-PVTZ					
	CPDPZ1t		CPDPZ1c		CPDP1t		CPDP1c		CPDP1c		CPDP1c	
	x	y	z	x	y	z	x	y	z	x	y	z
C	0.520261	-0.622239	-0.783742	-0.495741	0.585466	-0.802214	0.725725	0.926791	0.000000	1.305095	1.406013	0.000000
C	1.776302	-1.154987	-0.517131	-1.769054	1.102161	-0.573975	2.070894	1.251465	0.000000	2.654800	1.078461	0.000000
C	2.735778	-0.382308	0.144830	-2.711911	0.355133	0.139517	3.037169	0.232643	0.000000	3.035763	-0.267020	0.000000
C	2.437963	0.937269	0.505040	-2.383275	-0.927455	0.593997	2.640476	-1.108515	0.000000	2.057225	-1.274308	0.000000
C	1.192460	1.477279	0.203544	-1.125418	-1.452746	0.330928	1.286265	-1.426627	0.000000	0.712577	-0.939568	0.000000
C	0.206496	0.695306	-0.410652	-0.155060	-0.693447	-0.338880	0.315876	-0.418131	0.000000	0.320488	0.408465	0.000000
N	-1.010308	1.348558	-0.788101	1.073708	-1.343740	-0.681997	-1.034267	-0.851800	0.000000	-1.024464	0.858383	0.000000
O	3.950657	-0.962301	0.396273	-3.973217	0.815878	0.408280	4.349074	0.614418	0.000000	4.373024	-0.547755	0.000000
N	-2.147221	0.888413	-0.521489	2.202127	-0.849236	-0.444156	-1.888184	0.074610	0.000000	-1.890842	-0.056189	0.000000
C	-2.326334	-0.272023	0.298200	2.360607	0.355891	0.312727	-3.229268	-0.391414	0.000000	-3.225329	0.429291	0.000000
C	-3.643671	-0.284072	1.056782	3.674506	0.425745	1.074605	-4.221974	0.484980	0.746913	-4.230393	-0.432843	-0.746896
C	-3.474278	-1.177118	-0.124871	3.496788	1.254864	-0.151688	-4.221974	0.484980	-0.746913	-4.230393	-0.432843	0.746896
H	-0.218101	-1.223251	-1.311862	0.229012	1.167340	-1.369229	-0.035555	1.703644	0.000000	0.982065	2.445625	0.000000
H	2.031972	-2.169351	-0.817512	-2.032093	2.090853	-0.954055	2.402489	2.288178	0.000000	3.425776	1.845972	0.000000
H	3.190730	1.548613	1.005249	-3.131595	-1.504951	1.132887	3.392437	-1.899191	0.000000	2.361229	-2.322977	0.000000
H	0.963711	2.513363	0.447650	-0.871974	-2.463635	0.646215	0.953098	-2.463016	0.000000	-0.056342	-1.708938	0.000000
H	4.522211	-0.318075	0.842809	-4.075705	1.701922	0.026893	4.903966	-0.182554	0.000000	4.486881	-1.512121	0.000000
H	-1.460149	-0.729068	0.775349	1.485435	0.823434	0.762721	-3.369951	-1.473734	0.000000	-3.349872	1.513504	0.000000
H	-4.268349	0.598524	0.943742	4.310346	-0.453631	1.009916	-3.799747	1.348943	1.252935	-3.820272	-1.302649	-1.252965
H	-3.983242	-0.900284	-1.044727	4.013784	0.941316	-1.055192	-3.799747	1.348943	-1.252935	-3.820272	-1.302649	1.252965
H	-3.615334	-0.716604	2.053467	3.635246	0.908634	2.047502	-5.020554	-0.027250	1.277213	-5.021634	0.090097	-1.277772
H	-3.332882	-2.244305	0.027624	3.339391	2.325989	-0.051266	-5.020554	-0.027250	-1.277213	-5.021634	0.090097	1.277772

Table D.1 (Cont.)

Atom	PW91/cc-pVTZ											
	CPDP2t			CPDP2c			CPDPZ1t			CPDPZ1c		
	x	y	z	x	y	z	x	y	z	x	y	z
C	-0.882833	1.137658	0.000000	-0.961526	1.271215	0.000000	0.519095	-0.625691	-0.774404	-0.494155	0.589699	-0.791070
C	-2.265974	1.175074	0.000000	-2.349612	1.230670	0.000000	1.775805	-1.156890	-0.510744	-1.768102	1.104501	-0.565609
C	-3.000514	-0.022135	0.000000	-3.000850	-0.006969	0.000000	2.739091	-0.381936	0.144292	-2.715438	0.354191	0.139179
C	-2.334337	-1.252140	0.000000	-2.251696	-1.195188	0.000000	2.441321	0.939770	0.498389	-2.387666	-0.932004	0.586187
C	-0.943955	-1.281737	0.000000	-0.867180	-1.147050	0.000000	1.195338	1.477763	0.198671	-1.129272	-1.454884	0.324917
C	-0.203504	-0.093881	0.000000	-0.204732	0.091164	0.000000	0.206026	0.693678	-0.407227	-0.154754	-0.692125	-0.334909
N	1.204605	-0.236668	0.000000	1.202274	0.247735	0.000000	-1.010571	1.349666	-0.780589	1.073994	-1.344803	-0.672884
O	-4.362498	0.079991	0.000000	-4.367059	-0.005619	0.000000	3.954375	-0.959746	0.394173	-3.976908	0.813749	0.404663
N	1.853663	0.841300	0.000000	1.861423	-0.824002	0.000000	-2.147661	0.889078	-0.519035	2.202538	-0.849695	-0.440727
C	3.277912	0.674414	0.000000	3.284096	-0.644796	0.000000	-2.328533	-0.277208	0.293007	2.362969	0.361390	0.307491
C	3.930091	-0.479880	0.745542	3.926744	0.514859	-0.745526	-3.643074	-0.286015	1.055844	3.675010	0.428529	1.072079
C	3.930091	-0.479880	-0.745542	3.926744	0.514859	0.745526	-3.482601	-1.172367	-0.132146	3.504739	1.250460	-0.160260
H	-0.296536	2.053878	0.000000	-0.431771	2.222404	0.000000	-0.220911	-1.229651	-1.296779	0.232576	1.175014	-1.351922
H	-2.806045	2.120118	0.000000	-2.945203	2.141027	0.000000	2.030801	-2.172690	-0.807009	-2.029475	2.095825	-0.940578
H	-2.905375	-2.181888	0.000000	-2.766656	-2.158043	0.000000	3.196154	1.554148	0.992202	-3.138717	-1.513014	1.117539
H	-0.404278	-2.227292	0.000000	-0.271534	-2.057243	0.000000	0.966258	2.515013	0.437630	-0.876245	-2.467831	0.633985
H	-4.741431	-0.814224	0.000000	-4.676352	-0.926114	0.000000	4.520098	-0.306747	0.836882	-4.068831	1.702220	0.024455
H	3.790519	1.632053	0.000000	3.804819	-1.598066	0.000000	-1.464619	-0.743490	0.764832	1.490338	0.838130	0.752226
H	3.223690	-1.146376	1.236586	3.215153	1.175655	-1.236760	-4.261103	0.602064	0.948635	4.304648	-0.455710	1.012142
H	3.223690	-1.146376	-1.236586	3.215153	1.175655	1.236760	-3.992353	-0.885316	-1.048498	4.021700	0.926003	-1.059959
H	4.852930	-0.272171	1.281595	4.851317	0.314408	-1.281332	-3.615076	-0.726189	2.049258	3.637945	0.919156	2.041261
H	4.852930	-0.272171	-1.281595	4.851317	0.314408	1.281332	-3.348042	-2.241311	0.014623	3.354726	2.323236	-0.066002

Table D.1 (Cont.)

Atom	CPDP1t			CPDP1c			MP2/cc-pVTZ			CPDP2t			CPDP2c		
	x	y	z	x	y	z	x	y	z	x	y	z	x	y	z
C	0.720586	0.932841	0.000000	1.292684	1.399782	0.000000	-0.869421	1.137574	0.000000	-0.945205	1.265907	0.000000			
C	2.069701	1.246037	0.000000	2.642074	1.074523	0.000000	-2.253797	1.168018	0.000000	-2.332742	1.225949	0.000000			
C	3.027697	0.227635	0.000000	3.025188	-0.265568	0.000000	-2.983546	-0.024888	0.000000	-2.983958	-0.006310	0.000000			
C	2.627249	-1.107591	0.000000	2.053568	-1.271225	0.000000	-2.318860	-1.250185	0.000000	-2.240636	-1.190987	0.000000			
C	1.272494	-1.419683	0.000000	0.705576	-0.944017	0.000000	-0.928822	-1.278890	0.000000	-0.854433	-1.149345	0.000000			
C	0.314442	-0.407102	0.000000	0.318994	0.399489	0.000000	-0.198303	-0.091505	0.000000	-0.199216	0.085881	0.000000			
N	-1.035183	-0.847232	0.000000	-1.025498	0.856130	0.000000	1.211627	-0.241388	0.000000	1.209465	0.250122	0.000000			
O	4.338146	0.607254	0.000000	4.362285	-0.537351	0.000000	-4.343726	0.079095	0.000000	-4.348143	0.003602	0.000000			
N	-1.880821	0.092226	0.000000	-1.882879	-0.072482	0.000000	1.845290	0.850809	0.000000	1.854739	-0.835149	0.000000			
C	-3.215749	-0.391938	0.000000	-3.211554	0.428711	0.000000	3.267376	0.677157	0.000000	3.274870	-0.646235	0.000000			
C	-4.204663	0.471757	0.747343	-4.212165	-0.421203	-0.747399	3.888671	-0.481297	0.746197	3.883493	0.519009	-0.746164			
C	-4.204663	0.471757	-0.747343	-4.212165	-0.421203	0.747399	3.888671	-0.481297	-0.746197	3.883493	0.519009	0.746164			
H	-0.029190	1.709997	0.000000	0.968418	2.431241	0.000000	-0.292335	2.050278	0.000000	-0.416621	2.209253	0.000000			
H	2.405866	2.273395	0.000000	3.406517	1.838149	0.000000	-2.792901	2.104932	0.000000	-2.923333	2.130761	0.000000			
H	3.369769	-1.896263	0.000000	2.358452	-2.311228	0.000000	-2.884637	-2.173869	0.000000	-2.753542	-2.145686	0.000000			
H	0.935949	-2.447178	0.000000	-0.053371	-1.712298	0.000000	-0.390898	-2.216914	0.000000	-0.268388	-2.056383	0.000000			
H	4.882331	-0.187264	0.000000	4.475758	-1.493628	0.000000	-4.714565	-0.809712	0.000000	-4.656628	-0.908654	0.000000			
H	-3.338567	-1.466991	0.000000	-3.320494	1.505243	0.000000	3.788126	1.620435	0.000000	3.805838	-1.583810	0.000000			
H	-3.791920	1.334007	1.246394	-3.811866	-1.289410	-1.246263	3.174685	-1.130653	1.230379	3.162447	1.160591	-1.230259			
H	-3.791920	1.334007	-1.246394	-3.811866	-1.289410	1.246263	3.174685	-1.130653	-1.230379	3.162447	1.160591	1.230259			
H	-4.999634	-0.041645	1.264705	-4.999828	0.103246	-1.264847	4.813724	-0.293617	1.268591	4.810545	0.341424	-1.268544			
H	-4.999634	-0.041645	-1.264705	-4.999828	0.103246	1.264847	4.813724	-0.293617	-1.268591	4.810545	0.341424	1.268544			

Table D.1 (Cont.)

Atom	MP2/cc-pVTZ					
	CPDPZ1t			CPDPZ1c		
	x	y	z	x	y	z
C	0.506300	-0.576421	-0.890206	-0.486881	0.527438	-0.925379
C	1.741342	-1.131472	-0.578963	-1.736279	1.072748	-0.643654
C	2.666468	-0.399043	0.164516	-2.637536	0.377258	0.162115
C	2.358404	0.898940	0.572489	-2.293923	-0.877356	0.665931
C	1.132777	1.463824	0.234198	-1.058140	-1.432571	0.359803
C	0.190770	0.718876	-0.471551	-0.138664	-0.721933	-0.411900
N	-1.019569	1.368459	-0.877471	1.085310	-1.368520	-0.780959
O	3.858519	-1.001984	0.449683	-3.872950	0.864453	0.482437
N	-2.139070	0.893658	-0.542261	2.193590	-0.855184	-0.466354
C	-2.228105	-0.234046	0.332772	2.255217	0.318485	0.348542
C	-3.534034	-0.281312	1.091138	3.549325	0.421828	1.121985
C	-3.315264	-1.214694	-0.052374	3.336647	1.290786	-0.072227
H	-0.212102	-1.140760	-1.470358	0.212408	1.063484	-1.553718
H	2.003721	-2.128352	-0.904062	-2.008825	2.038722	-1.051868
H	3.081874	1.474303	1.137510	-3.009696	-1.408829	1.276822
H	0.896852	2.480027	0.519032	-0.793972	-2.417567	0.719713
H	4.399412	-0.380236	0.947520	-3.979431	1.721227	0.056249
H	-1.337994	-0.615338	0.811949	1.353381	0.712418	0.794383
H	-4.194954	0.555772	0.931276	4.221650	-0.414699	1.015997
H	-3.831743	-1.001456	-0.974924	3.868984	1.035558	-0.974883
H	-3.492715	-0.677253	2.093573	3.488487	0.869484	2.101376
H	-3.119056	-2.255011	0.155643	3.126032	2.338135	0.078438

Table D.2 Theoretical frequencies (ν/cm^{-1}) and IR intensities ($I/\text{km mol}^{-1}$) of CPDP isomeric forms. The calculated frequencies are not scaled.

B3LYP/6-311+G(2df,2p)							
CPDP1t		CPDP1c		CPDP2t		CPDP2c	
ν	I	ν	I	ν	I	ν	I
3828.2	100.6	3827.7	90.4	3828.3	108.3	3826.8	89.8
3230.1	4.7	3229.3	6.8	3225.7	10.5	3226.1	10.4
3216.9	0.003	3216.0	0.1	3212.4	0.5	3212.7	0.6
3207.5	2.9	3205.7	2.2	3206.8	11.1	3205.5	2.4
3190.8	3.3	3199.0	3.1	3189.6	2.2	3198.3	6.3
3185.5	5.1	3184.5	4.7	3185.7	17.1	3185.3	17.2
3154.5	18.7	3149.2	20.2	3185.2	5.9	3183.2	10.8
3140.3	18.7	3140.3	24.1	3154.3	17.6	3148.7	22.2
3136.5	12.5	3136.2	14.7	3130.8	15.8	3131.1	15.8
3131.3	15.3	3132.1	12.9	3129.9	14.4	3130.1	14.5
1648.8	100.9	1648.7	129.4	1648.5	89.7	1647.8	122.8
1629.3	49.4	1633.0	21.0	1627.5	36.3	1631.2	12.3
1570.8	59.4	1573.4	40.7	1579.5	86.6	1582.0	62.5
1534.0	50.8	1530.5	49.3	1531.1	69.0	1528.0	45.1
1496.4	4.7	1495.1	7.3	1486.8	3.5	1487.9	12.6
1468.7	8.7	1472.1	37.4	1467.8	8.5	1470.1	37.0
1463.5	4.9	1462.1	3.1	1457.6	4.5	1458.6	4.4
1373.0	4.6	1377.0	0.6	1374.2	2.2	1373.3	3.1
1364.6	27.0	1365.3	18.9	1362.4	42.7	1363.3	13.4
1332.9	9.2	1333.8	0.9	1330.4	13.4	1331.3	1.6
1286.5	150.1	1284.5	194.0	1286.1	134.4	1283.7	200.9
1228.7	9.0	1228.9	6.9	1242.1	0.6	1242.9	4.2
1215.0	8.4	1216.2	5.4	1216.0	3.9	1215.8	10.3
1205.2	1.1	1203.6	0.4	1206.1	0.7	1206.7	0.7
1195.1	8.0	1196.6	19.2	1186.2	149.8	1183.0	144.6
1186.2	142.9	1184.9	147.9	1172.7	74.6	1175.4	38.1
1161.5	139.5	1163.2	80.4	1138.9	79.7	1138.9	46.1
1120.2	16.4	1120.4	23.4	1130.0	1.2	1130.0	1.1
1119.0	0.1	1118.7	0.3	1118.3	2.2	1117.9	51.4
1078.7	4.7	1075.9	4.1	1085.5	4.7	1085.4	4.5
1054.0	8.3	1051.2	9.6	1058.0	13.1	1057.9	14.0
1024.3	0.5	1026.9	0.3	1022.1	1.3	1023.9	0.3
1000.5	0.1	990.8	0.1	1003.2	0.02	992.9	0.02
968.3	1.2	979.7	1.1	988.3	74.0	988.9	55.9
956.2	85.2	955.2	82.1	971.5	1.2	981.8	0.8
929.3	20.8	929.9	20.3	908.1	2.6	908.3	2.8
908.4	4.3	906.1	5.4	891.2	33.3	892.6	38.7
863.6	47.3	863.5	49.2	867.7	47.7	865.8	52.9
857.5	4.9	857.6	5.5	838.5	7.8	838.7	11.9
822.0	13.6	823.1	4.9	824.2	10.0	828.0	4.3
819.8	1.0	819.2	6.2	822.2	12.8	822.8	4.9
801.7	1.6	800.0	1.5	817.5	5.0	817.6	4.8
780.0	15.4	778.7	10.6	777.6	20.0	778.5	17.4
740.8	0.1	739.2	0.1	742.8	0.1	740.4	0.1
656.7	1.2	657.9	3.2	653.5	0.5	654.4	2.3
587.4	22.4	585.6	30.5	629.0	7.3	628.8	6.4
550.0	14.4	550.1	15.0	551.9	14.1	551.6	14.3
523.8	4.6	525.0	4.4	514.7	15.6	513.7	38.1
462.7	3.5	461.0	6.6	460.9	2.5	459.6	4.3
433.2	1.1	432.3	0.1	430.5	1.1	429.9	0.2
414.9	14.7	416.3	6.1	426.3	20.3	427.7	0.4
385.1	2.8	384.0	3.3	373.8	9.7	372.9	4.7
363.9	101.1	361.4	98.5	358.8	36.0	356.9	10.0
311.1	7.6	310.8	5.8	348.6	69.0	334.7	92.9
282.4	1.2	280.9	1.2	215.1	0.3	215.5	0.1
225.0	0.1	224.7	0.05	191.5	0.1	191.4	0.0
131.0	0.9	128.4	0.6	152.1	0.7	152.9	0.9
100.0	1.9	101.0	4.2	110.5	3.0	112.3	4.6
88.5	1.0	83.7	1.0	64.3	0.8	64.8	0.2
40.6	0.9	35.4	0.1	35.7	0.002	35.8	1.5

D.1 CPDP Supporting Information

Table D.2 (Cont.)

B3LYP/6-311+G(2df,2p)				B3LYP/cc-pVTZ			
CPDPZ1t		CPDPZ1c		CPDP1t		CPDP1c	
ν	I	ν	I	ν	I	ν	I
3830.8	83.5	3833.9	97.9	3810.8	94.1	3810.4	82.7
3227.9	5.6	3229.5	5.4	3229.3	7.7	3228.6	7.8
3214.6	0.1	3216.1	0.3	3215.9	0.1	3215.1	0.1
3194.1	4.2	3195.4	5.4	3207.4	3.0	3205.5	2.1
3186.2	4.8	3182.4	3.1	3189.7	4.0	3198.2	7.2
3178.5	2.8	3179.2	1.6	3184.3	5.7	3183.4	2.5
3161.6	5.7	3161.7	5.1	3152.4	19.7	3146.8	22.0
3152.7	16.7	3148.6	18.0	3139.0	24.3	3139.1	25.3
3136.4	10.4	3138.5	11.3	3134.5	15.8	3134.1	15.9
3134.8	12.5	3135.9	11.3	3130.4	12.7	3131.2	11.2
1649.2	47.0	1644.4	56.8	1652.4	94.4	1652.5	116.5
1620.8	18.0	1623.1	5.4	1632.2	49.3	1635.7	15.1
1595.8	55.1	1598.8	47.5	1575.0	58.7	1577.8	41.3
1530.1	86.4	1527.2	98.7	1536.6	49.8	1533.2	59.3
1496.6	0.9	1503.0	0.8	1496.4	2.7	1494.9	8.0
1463.2	14.1	1471.4	3.5	1471.5	10.2	1474.9	38.1
1458.6	3.0	1460.9	18.6	1462.2	3.0	1460.8	3.0
1368.1	0.1	1369.6	0.4	1375.5	6.2	1379.4	1.7
1359.8	25.5	1359.0	29.5	1368.5	29.3	1369.2	27.5
1322.7	2.8	1319.8	1.9	1334.5	10.0	1335.2	1.6
1282.2	135.1	1281.6	118.9	1291.8	137.7	1290.1	161.8
1221.4	1.1	1222.9	0.9	1230.4	10.6	1230.6	8.4
1199.5	3.4	1203.6	0.3	1216.4	8.1	1217.6	2.7
1196.7	24.3	1194.4	112.4	1207.0	0.3	1205.5	0.3
1184.3	135.8	1190.7	60.1	1195.9	9.0	1197.4	25.7
1167.4	8.7	1169.4	2.4	1189.2	149.5	1188.4	146.3
1156.3	18.6	1156.1	26.2	1162.4	129.9	1164.2	100.5
1124.9	18.5	1124.0	2.8	1121.2	0.1	1121.2	20.3
1123.4	8.5	1121.4	14.7	1121.1	16.9	1120.9	0.1
1084.0	3.3	1089.1	4.2	1078.2	3.4	1075.6	3.4
1052.3	0.8	1062.1	0.4	1053.9	8.5	1051.8	9.7
1027.2	0.2	1025.6	0.3	1026.6	0.4	1029.2	0.5
984.2	0.9	985.5	0.2	1011.3	0.2	996.3	0.6
967.8	0.8	960.4	1.1	973.8	1.5	990.2	0.6
926.1	45.9	925.2	51.5	958.3	88.8	957.0	79.3
914.4	13.3	921.0	1.4	931.0	14.9	931.8	16.8
888.8	104.0	893.8	104.5	909.6	4.5	908.0	5.3
857.6	24.2	862.5	18.7	865.4	41.0	864.5	44.3
846.7	4.6	847.0	12.2	858.5	4.2	858.4	5.3
830.5	10.6	832.0	5.1	823.1	17.3	824.1	6.5
826.2	3.9	820.7	11.5	821.2	0.2	820.7	6.1
782.3	6.6	790.1	6.1	802.8	1.6	800.9	1.6
762.8	2.6	765.0	2.7	781.2	12.5	780.2	12.2
715.7	13.7	715.2	11.2	749.4	0.5	749.4	0.5
676.6	6.0	674.4	10.4	657.6	1.3	658.8	4.3
645.1	3.7	645.0	2.4	588.0	22.5	586.2	32.9
611.2	4.8	612.6	3.8	551.6	11.9	551.7	13.0
516.0	16.1	515.0	16.7	524.1	5.3	525.5	6.7
466.3	0.4	466.5	0.03	464.0	2.8	462.4	4.9
425.1	1.5	424.1	5.5	434.2	0.5	434.1	0.4
417.9	14.8	418.2	3.6	415.5	14.5	417.0	6.1
356.3	2.3	357.5	3.6	387.8	20.7	385.9	6.9
335.4	3.8	340.8	13.5	377.3	82.3	374.2	93.8
322.5	97.5	338.1	73.5	311.4	6.8	311.4	4.3
290.0	1.8	299.8	0.7	282.5	1.3	281.1	0.5
190.9	0.3	197.4	0.5	226.4	0.04	226.4	0.02
171.5	2.0	170.4	0.9	131.8	0.5	129.7	0.5
79.0	3.3	97.4	1.6	100.7	1.5	102.1	2.9
66.3	0.6	72.4	0.7	89.6	0.6	84.8	1.0
34.2	1.8	28.4	0.6	41.9	0.9	37.8	0.02

Table D.2 (Cont.)

B3LYP/cc-pVTZ							
CPDP2t		CPDP2c		CPDPZ1t		CPDPZ1c	
v	I	v	I	v	I	v	I
3810.4	89.3	3809.4	86.1	3813.1	76.5	3816.2	70.3
3224.8	11.1	3225.3	10.8	3227.0	6.6	3228.6	6.4
3211.5	0.6	3211.8	0.6	3213.6	0.1	3214.9	0.3
3206.9	3.2	3205.5	2.2	3193.2	4.1	3194.5	6.4
3188.9	3.0	3197.3	6.4	3185.2	5.6	3181.4	4.7
3184.2	6.4	3183.0	18.7	3177.2	3.2	3178.1	1.9
3183.3	18.7	3182.1	2.7	3161.5	5.8	3161.4	5.4
3151.9	19.5	3146.5	23.7	3150.4	18.2	3146.4	18.8
3128.9	17.3	3129.0	17.2	3134.7	12.1	3136.7	12.7
3128.1	14.9	3128.4	14.6	3133.0	13.8	3133.9	13.0
1651.8	87.4	1651.4	110.3	1653.0	43.3	1648.1	53.5
1630.3	41.4	1633.7	11.3	1623.3	18.5	1625.4	6.0
1583.0	86.6	1585.7	60.9	1600.5	55.9	1603.3	47.4
1533.4	50.8	1530.3	57.4	1532.4	82.2	1529.3	92.4
1487.0	2.5	1488.3	13.9	1496.5	0.8	1502.4	0.5
1470.2	10.1	1472.7	35.9	1465.8	15.6	1469.5	3.6
1456.4	4.4	1457.5	4.4	1457.7	3.1	1463.4	20.9
1375.8	3.6	1374.8	6.7	1369.5	0.4	1370.7	0.3
1365.9	37.7	1367.1	18.6	1362.7	28.8	1362.2	34.3
1332.2	5.6	1333.1	1.8	1324.9	3.2	1321.9	2.3
1291.4	135.8	1289.6	163.1	1288.0	122.2	1287.1	111.8
1242.9	0.4	1243.8	5.4	1223.6	1.2	1224.9	1.0
1218.8	4.1	1218.6	10.3	1201.8	2.8	1205.4	0.3
1208.3	0.6	1208.9	0.6	1198.1	26.8	1196.9	161.3
1189.2	172.1	1186.9	148.6	1188.5	142.7	1193.0	13.5
1174.0	49.1	1176.9	45.9	1168.0	7.0	1169.6	2.8
1139.8	73.2	1139.7	57.4	1156.5	16.8	1156.1	22.8
1131.6	1.2	1131.6	1.2	1126.0	21.3	1124.9	2.8
1119.3	11.8	1119.0	27.8	1123.9	5.6	1122.5	15.5
1086.2	4.1	1086.1	4.1	1084.2	2.9	1088.5	3.5
1059.0	14.1	1058.9	14.7	1052.7	0.8	1061.7	0.4
1024.0	0.1	1026.0	0.3	1028.8	0.2	1027.0	0.2
1011.4	0.1	996.5	0.3	980.8	1.1	983.8	0.1
990.2	70.9	990.9	56.3	965.7	0.9	956.4	1.1
973.8	1.4	989.7	0.6	927.6	49.4	927.0	51.7
909.7	2.0	909.9	2.2	915.8	11.7	921.6	3.2
892.7	31.7	894.2	39.1	887.9	97.5	892.8	97.7
868.9	41.7	865.7	49.0	856.0	24.4	861.4	17.0
840.6	7.7	840.9	9.0	847.2	4.1	847.5	11.9
823.3	14.2	828.8	5.6	830.9	10.9	833.1	5.9
823.2	7.7	823.8	6.9	825.2	4.6	818.6	13.2
819.4	4.0	819.6	4.7	784.4	6.5	791.3	6.4
779.9	17.4	780.9	18.0	764.9	2.9	766.2	3.1
749.3	0.4	749.2	0.6	717.3	12.4	716.5	10.2
654.1	0.8	655.2	2.4	678.0	6.0	675.4	11.2
629.7	6.6	629.6	6.9	645.7	3.6	645.5	2.0
552.9	12.0	553.0	12.2	611.6	4.3	612.8	3.5
515.4	18.4	514.3	39.9	517.1	13.4	516.1	14.1
462.1	1.8	461.0	3.0	466.6	0.3	466.7	0.1
431.0	0.4	431.1	0.4	425.6	1.4	424.6	6.5
426.5	18.3	428.6	0.6	418.1	14.5	418.5	3.4
374.4	8.3	373.3	3.8	357.9	3.9	359.6	16.8
367.7	85.7	360.9	33.5	336.7	95.2	351.8	79.2
355.1	17.4	350.3	68.0	334.9	3.3	339.6	14.4
216.1	0.4	216.8	0.1	290.1	1.4	299.2	0.9
192.7	0.1	193.0	0.003	191.8	0.3	198.1	0.4
154.2	0.4	155.3	0.5	171.5	1.9	170.4	0.8
111.3	1.6	113.5	3.6	80.0	3.1	97.4	1.3
65.3	0.9	66.2	0.3	67.3	0.6	72.3	0.4
34.9	0.01	35.3	1.3	34.5	1.9	30.3	0.6

D.1 CPDP Supporting Information

Table D.2 (Cont.)

PW91/6-311+(2df,2p)							
CPDP1t		CPDP1c		CPDP2t		CPDP2c	
v	I	v	I	v	I	v	I
3717.2	89.8	3715.6	78.4	3716.3	125.1	3714.6	82.5
3178.5	4.8	3177.6	5.0	3169.5	8.2	3169.7	7.7
3165.4	0.1	3164.3	0.05	3155.9	0.8	3156.1	0.9
3140.1	4.3	3137.7	6.2	3139.8	11.8	3137.9	3.8
3127.6	3.8	3137.4	3.4	3127.1	14.2	3136.7	6.2
3122.0	4.6	3122.1	1.6	3126.0	4.3	3126.7	15.6
3091.8	19.2	3083.8	15.4	3121.6	5.4	3120.4	1.2
3083.9	14.0	3083.5	22.2	3091.2	18.1	3083.0	24.7
3082.4	13.3	3082.0	13.4	3072.4	15.0	3072.6	14.8
3062.2	26.0	3063.7	25.7	3069.2	14.0	3069.5	13.3
1606.9	113.7	1607.4	138.0	1604.4	103.7	1604.1	135.9
1586.6	56.1	1591.1	16.0	1582.7	50.7	1588.1	11.0
1499.2	87.7	1501.7	67.3	1503.8	100.0	1506.9	72.1
1480.0	2.2	1474.3	21.9	1480.6	27.2	1475.3	32.7
1444.7	2.2	1443.4	23.0	1437.2	2.1	1439.2	30.5
1427.6	7.0	1432.3	14.4	1424.7	6.8	1427.9	11.4
1412.0	3.8	1410.0	3.9	1405.5	5.4	1406.4	5.3
1370.7	17.5	1371.8	21.6	1368.1	21.5	1369.1	20.0
1323.0	2.5	1326.8	5.4	1320.0	0.5	1319.4	0.2
1290.8	11.7	1291.4	2.4	1286.9	13.4	1288.0	3.4
1259.8	157.9	1259.8	160.6	1259.6	154.4	1259.8	168.4
1196.5	8.0	1197.0	9.7	1214.5	2.0	1216.2	5.1
1185.8	1.7	1186.7	2.3	1190.1	4.7	1189.9	4.8
1169.1	0.5	1167.2	0.5	1169.0	0.8	1169.4	0.8
1164.3	7.5	1166.5	10.2	1156.2	153.8	1153.9	151.6
1157.6	166.3	1156.4	166.8	1135.1	57.3	1138.7	51.8
1126.3	114.1	1128.1	99.3	1104.9	65.7	1105.0	49.5
1086.6	18.4	1086.6	19.7	1084.8	1.9	1084.7	2.1
1073.7	0.5	1072.8	0.5	1083.5	3.9	1083.9	24.2
1034.1	4.4	1031.0	4.4	1039.8	4.6	1039.4	4.7
1013.2	9.3	1010.3	10.3	1022.2	13.6	1021.9	12.8
995.2	0.6	998.3	0.7	990.9	1.6	993.6	0.8
960.8	0.1	949.9	0.1	963.4	0.1	961.8	86.8
939.1	135.4	940.2	1.2	961.4	102.5	952.1	0.1
927.4	1.5	938.2	126.6	930.6	1.3	942.4	0.9
907.1	2.2	906.9	2.0	873.9	40.1	875.2	46.9
872.4	2.6	869.7	3.6	871.3	1.0	871.3	1.1
841.4	4.8	841.3	6.0	834.4	44.2	832.0	50.4
829.9	43.4	829.2	46.2	825.9	9.8	826.1	11.9
801.9	5.7	800.1	5.0	803.6	8.7	804.0	5.1
786.7	8.0	789.2	3.7	797.4	4.9	797.9	6.0
782.9	2.3	781.2	2.5	789.2	8.9	793.6	1.0
763.8	11.9	762.0	11.2	761.1	18.2	762.0	16.8
717.5	0.1	715.4	0.05	720.0	0.0	717.1	0.1
636.8	1.7	638.2	5.6	631.7	0.6	633.2	3.0
572.4	23.8	570.8	33.7	614.4	7.7	614.4	8.6
528.2	12.0	528.3	13.4	530.6	12.2	530.5	12.5
509.5	5.0	510.7	6.0	501.5	18.0	500.7	40.5
447.8	3.6	446.1	6.5	446.3	2.3	445.2	4.0
418.2	0.3	416.9	0.3	414.7	0.2	415.0	0.4
402.2	14.7	403.6	6.7	413.3	16.1	413.2	0.6
386.5	92.9	381.5	90.6	370.6	98.6	363.2	4.3
371.6	5.9	370.2	4.6	364.0	9.1	361.2	91.2
305.2	6.8	304.9	4.4	342.6	2.1	341.4	4.9
276.3	1.6	274.3	0.5	211.2	0.3	211.6	0.1
219.4	0.1	219.1	0.04	185.5	0.1	185.6	0.01
129.6	0.8	126.6	0.8	157.8	0.7	158.6	0.8
100.5	1.9	101.6	3.2	109.4	3.6	111.9	4.0
92.7	0.6	86.3	1.2	66.1	0.9	66.7	0.3
41.9	1.0	37.4	0.0	38.5	0.1	37.7	1.7

Table D.2 (Cont.)

PW91/6-311+G(2df,2p)				PW91/cc-pVTZ			
CPDPZ1t		CPDPZ1c		CPDP1t		CPDP1c	
ν	I	ν	I	ν	I	ν	I
3719.9	72.6	3723.2	88.7	3699.5	82.0	3698.6	71.5
3172.6	4.7	3174.2	4.6	3178.8	5.8	3177.8	5.4
3159.3	0.1	3160.3	0.3	3165.5	0.1	3164.5	0.05
3131.4	4.0	3134.3	6.1	3140.6	4.7	3137.9	5.5
3124.1	5.5	3121.0	3.1	3127.6	4.1	3137.6	4.8
3114.8	2.8	3118.0	1.4	3122.2	4.7	3122.1	1.7
3089.6	18.0	3085.0	12.0	3090.5	19.4	3083.0	11.3
3084.8	8.1	3084.6	17.1	3083.4	15.4	3082.2	27.7
3078.9	11.9	3080.7	9.9	3081.6	14.2	3081.2	13.8
3076.9	8.4	3076.9	8.8	3063.0	25.6	3064.7	25.4
1605.2	55.2	1598.7	78.1	1610.6	105.5	1611.2	125.9
1575.4	31.0	1579.7	3.7	1589.2	56.7	1593.7	16.7
1514.2	72.9	1515.5	68.8	1501.8	88.0	1504.7	61.5
1478.5	54.2	1476.2	68.7	1483.2	1.5	1477.1	22.2
1442.7	1.9	1446.7	1.8	1445.7	2.5	1444.9	26.1
1424.9	12.2	1422.6	17.4	1430.3	8.2	1434.8	13.9
1404.0	3.3	1416.7	4.0	1411.8	3.7	1409.8	3.8
1351.3	25.6	1352.2	19.6	1374.4	21.8	1375.7	25.7
1316.5	1.4	1317.5	2.8	1325.0	2.2	1328.5	4.7
1294.7	2.1	1292.3	5.6	1293.0	10.5	1293.0	2.9
1256.0	120.5	1256.3	104.3	1265.2	149.4	1266.2	139.8
1192.5	1.6	1193.4	1.6	1198.0	8.8	1198.2	10.4
1163.7	28.9	1165.5	169.1	1187.4	1.2	1188.4	1.2
1158.9	2.0	1161.8	9.2	1171.5	0.3	1169.9	0.4
1156.7	138.2	1159.7	1.9	1163.9	11.5	1165.9	16.6
1134.4	8.5	1136.1	7.6	1160.5	169.9	1159.8	168.9
1120.0	15.7	1119.7	23.0	1126.8	107.1	1128.6	95.9
1092.2	27.3	1090.5	15.6	1087.2	20.1	1087.2	22.1
1080.5	2.2	1079.3	2.1	1076.7	0.3	1075.7	0.3
1035.0	3.5	1036.4	4.1	1033.3	3.5	1030.7	3.6
1006.4	1.1	1011.8	0.8	1012.6	9.1	1010.2	9.9
995.9	0.2	994.1	0.3	997.5	0.6	1000.7	0.6
942.3	0.8	945.5	0.6	973.4	0.2	957.8	0.9
928.5	5.3	925.2	6.0	941.2	128.3	951.7	0.4
913.6	75.0	912.7	74.1	934.0	1.6	940.3	120.3
879.5	10.9	883.5	0.7	908.2	1.8	908.3	1.5
857.1	86.9	862.8	92.5	873.9	2.6	871.6	3.5
827.2	28.9	834.6	6.0	842.3	5.0	842.1	5.8
826.5	1.3	825.3	27.0	832.6	36.0	831.1	40.1
811.5	10.9	811.5	6.3	804.0	6.3	802.0	5.2
792.8	5.8	788.2	12.4	787.5	10.4	790.7	5.4
755.2	6.1	762.1	5.1	783.9	1.9	782.3	2.0
739.3	3.5	741.2	2.6	764.9	10.8	763.4	10.2
697.4	12.6	697.5	10.4	727.2	0.4	727.3	0.5
659.9	4.5	658.2	9.0	637.6	1.5	639.1	5.3
622.4	2.6	622.2	1.3	572.9	23.1	571.3	32.2
589.3	5.5	590.9	5.0	530.4	10.0	530.5	11.2
495.8	14.6	496.3	13.9	509.6	4.1	511.1	6.8
452.7	0.5	452.9	0.1	449.3	2.0	447.8	4.2
408.4	1.5	408.5	6.4	420.0	1.2	419.3	2.7
401.5	17.4	401.6	5.3	402.7	15.1	404.4	6.8
351.1	80.0	369.3	71.0	402.7	94.8	394.4	91.9
341.9	13.6	342.7	5.0	373.2	1.7	373.0	0.1
322.6	4.5	327.6	11.7	305.3	7.0	305.1	3.5
278.6	1.1	285.7	1.1	276.1	1.7	274.4	0.6
185.1	0.4	192.9	0.4	221.0	0.05	221.0	0.01
167.0	2.1	167.0	1.0	130.5	0.6	128.0	0.6
79.7	4.3	94.3	2.4	101.1	1.4	102.9	3.1
67.0	0.7	69.4	0.5	94.1	0.5	88.1	1.2
35.2	1.3	40.4	0.6	42.9	1.1	39.8	0.0

D.1 CPDP Supporting Information

Table D.2 (Cont.)

PW91/cc-pVTZ							
CPDP2t		CPDP2c		CPDPZ1t		CPDPZ1c	
ν	I	ν	I	ν	I	ν	I
3698.8	80.8	3697.8	77.6	3703.3	69.5	3706.4	61.7
3169.7	8.5	3169.9	8.4	3172.7	5.0	3174.5	5.2
3156.0	0.8	3156.3	0.8	3159.2	0.1	3160.3	0.4
3140.6	4.8	3138.6	3.3	3131.9	4.2	3134.9	6.3
3126.1	0.5	3137.0	5.9	3124.3	5.7	3121.7	3.3
3125.6	20.1	3125.3	17.8	3115.1	2.4	3118.2	1.3
3121.8	6.2	3120.4	2.0	3088.4	17.8	3085.6	8.9
3089.7	19.6	3081.7	25.7	3085.5	7.0	3083.3	17.8
3071.5	16.0	3071.7	15.8	3078.2	12.6	3080.3	10.7
3068.3	15.1	3068.8	14.3	3076.6	10.8	3076.6	11.3
1607.7	99.0	1607.9	126.6	1609.0	51.3	1602.6	74.0
1585.2	56.6	1590.6	12.6	1577.4	32.4	1581.6	4.2
1506.1	90.1	1509.5	66.9	1517.6	71.5	1518.8	67.4
1483.4	16.8	1478.0	31.5	1481.6	52.2	1479.1	65.1
1438.8	1.4	1441.2	35.4	1443.0	1.7	1447.0	1.4
1426.6	7.5	1429.8	10.0	1428.0	14.2	1425.7	20.1
1405.1	5.5	1406.1	5.5	1404.1	3.4	1414.9	4.1
1371.6	23.9	1373.1	23.6	1354.8	30.0	1355.8	23.5
1320.9	0.7	1320.4	0.2	1318.4	0.8	1319.0	2.5
1289.0	5.3	1290.1	3.0	1296.1	2.3	1293.6	6.2
1264.9	149.0	1266.1	150.9	1263.0	104.5	1262.8	95.3
1214.8	1.6	1216.7	6.4	1194.5	1.8	1195.2	1.9
1192.5	4.7	1192.5	4.8	1165.4	39.3	1168.7	169.9
1171.7	0.6	1172.1	0.6	1161.9	10.8	1164.4	6.6
1158.7	178.5	1158.5	163.3	1161.2	125.2	1161.3	4.1
1136.2	38.3	1140.2	44.7	1134.3	7.9	1136.0	8.1
1105.4	59.6	1105.6	51.1	1119.5	13.8	1119.0	20.1
1087.0	1.9	1086.9	1.9	1093.1	28.3	1091.6	17.0
1084.2	16.0	1084.9	26.7	1081.4	2.1	1080.6	2.2
1040.4	4.0	1040.1	4.0	1034.2	2.9	1036.4	3.4
1022.7	13.6	1022.5	12.9	1006.0	1.0	1011.1	0.7
993.0	0.1	996.0	0.3	997.5	0.2	995.5	0.3
973.0	0.1	963.3	86.5	939.6	0.9	945.2	0.6
962.8	100.9	957.5	0.6	927.5	8.2	922.6	15.8
933.5	1.5	950.8	0.4	914.7	68.6	912.3	60.3
875.3	38.3	876.9	45.3	880.7	10.4	884.5	1.0
873.0	0.6	872.9	0.7	855.5	85.7	861.9	90.9
836.5	37.2	832.7	45.3	827.3	20.1	834.7	3.7
828.2	8.4	828.5	9.3	825.8	9.2	825.6	25.6
804.7	4.3	805.1	3.8	812.1	12.2	811.6	7.2
799.8	5.2	800.3	6.3	791.5	6.4	785.4	14.8
788.4	11.8	794.9	2.0	757.1	6.2	763.6	5.2
763.4	15.5	764.2	16.0	741.4	3.4	742.3	3.1
727.2	0.3	727.2	0.5	699.3	12.0	698.9	9.9
632.2	0.9	634.0	2.8	661.8	4.7	659.6	9.7
615.2	6.9	615.1	7.8	622.9	2.5	622.7	1.1
532.3	10.0	532.5	10.5	589.8	5.2	591.1	4.7
502.1	19.7	501.2	39.3	497.4	11.8	497.7	11.0
447.6	1.4	446.8	2.3	453.0	0.4	453.1	0.1
415.9	0.6	416.0	0.5	409.0	1.0	409.1	7.5
413.3	15.9	415.0	2.1	401.9	17.6	401.8	5.9
384.8	95.4	380.2	93.2	368.1	87.2	382.6	87.2
364.3	9.4	363.8	3.9	343.7	4.5	343.5	4.6
344.9	1.1	345.2	0.5	321.9	4.2	326.5	12.7
212.0	0.4	212.6	0.1	278.2	1.1	284.6	1.2
187.0	0.1	187.6	0.02	186.5	0.4	193.9	0.4
159.5	0.4	160.4	0.4	167.1	2.0	166.7	0.8
110.0	1.6	113.2	3.6	81.0	4.0	95.3	2.0
67.2	1.0	68.2	0.3	67.7	0.5	69.9	0.3
37.4	0.1	36.9	1.5	36.1	1.4	42.3	0.6

Table D.2 (Cont.)

M2P/cc-pVTZ							
CPDP1t		CPDP1c		CPDP2t		CPDP2c	
v	I	v	I	v	I	v	I
3837.9	99.9	3838.5	91.7	3837.3	97.4	3838.3	96.0
3301.2	1.9	3301.1	1.9	3295.0	4.9	3295.1	4.9
3289.5	0.1	3289.4	0.1	3283.3	0.8	3283.5	0.9
3248.8	1.7	3245.8	1.4	3249.7	7.9	3249.2	12.0
3233.2	1.7	3242.8	2.5	3249.2	5.2	3246.7	0.9
3229.1	2.0	3225.8	0.9	3231.8	1.4	3242.5	2.3
3202.6	13.8	3202.8	13.4	3229.3	2.6	3224.5	1.0
3200.5	12.6	3194.8	13.7	3200.7	11.7	3195.2	13.9
3192.4	2.4	3192.4	2.5	3181.9	7.8	3181.9	7.7
3191.3	6.8	3191.3	6.8	3181.7	5.9	3181.8	5.9
1661.1	59.5	1655.9	107.5	1660.5	61.2	1655.8	108.0
1640.4	74.5	1647.4	8.7	1640.2	73.4	1646.9	9.6
1539.7	64.8	1537.4	70.3	1539.7	68.5	1537.7	74.7
1508.0	4.0	1508.0	3.9	1504.0	11.0	1503.5	4.6
1492.3	1.6	1491.4	0.7	1492.6	2.9	1491.8	0.5
1478.5	17.9	1479.0	32.4	1478.4	11.0	1478.9	27.7
1468.2	3.1	1468.2	3.1	1455.7	5.0	1455.7	5.1
1447.6	2.9	1447.9	29.0	1451.9	5.0	1452.2	33.8
1386.7	2.1	1386.5	5.4	1368.7	0.9	1368.8	0.8
1327.2	16.5	1328.2	1.8	1326.4	9.8	1327.2	1.0
1303.1	130.4	1301.9	130.0	1304.6	134.5	1303.2	139.2
1243.8	2.4	1243.2	6.7	1255.7	1.7	1256.6	3.4
1228.5	1.4	1229.8	4.9	1235.5	7.5	1235.4	5.1
1213.1	8.5	1213.3	6.8	1215.0	0.6	1215.1	0.6
1208.1	0.4	1208.1	0.4	1199.4	193.0	1201.7	171.1
1199.1	192.6	1201.6	171.9	1171.2	21.7	1171.2	21.6
1164.1	55.4	1163.4	49.4	1146.2	31.9	1146.0	26.5
1126.8	0.6	1127.1	0.6	1132.5	2.2	1132.4	2.3
1111.4	12.3	1110.6	19.4	1111.0	11.9	1110.0	22.1
1068.4	3.7	1068.2	3.7	1077.9	4.1	1078.2	4.1
1049.9	8.3	1049.6	8.6	1059.9	16.7	1060.2	15.6
1024.6	1.7	1024.4	2.4	1024.1	0.8	1023.9	1.5
979.6	0.1	977.1	71.7	1004.1	58.7	1004.5	50.6
977.2	78.6	967.2	0.1	979.0	0.1	965.9	0.3
941.2	4.4	952.2	3.1	935.7	3.5	949.0	2.2
937.5	4.3	938.3	5.7	916.9	1.6	917.2	2.2
918.7	4.1	919.1	5.0	897.3	25.9	898.4	31.9
859.7	7.0	859.8	8.1	856.1	38.2	852.6	44.8
856.1	34.1	854.0	40.2	852.1	5.0	851.8	5.0
842.9	8.8	843.1	8.0	837.6	5.1	837.7	6.6
820.9	14.5	823.0	8.7	819.3	6.7	822.8	6.5
797.3	3.9	797.5	3.0	819.2	15.2	819.3	6.2
780.7	6.4	780.5	6.6	786.4	10.4	786.5	10.1
721.4	1.0	720.5	1.0	719.9	0.9	719.5	0.9
646.1	1.1	646.0	5.2	644.1	0.6	644.3	2.9
583.4	12.6	581.5	18.4	627.1	3.2	626.5	3.4
548.2	11.9	547.9	12.5	548.7	12.2	548.5	12.7
518.2	5.7	519.2	7.4	511.7	13.1	510.2	29.2
459.8	3.2	458.7	5.7	460.7	2.6	459.5	5.0
423.6	2.1	423.3	0.0	420.7	1.8	422.9	0.9
408.3	15.3	408.6	6.4	420.3	14.4	421.1	0.02
382.4	0.9	382.5	2.0	372.9	9.4	371.6	3.5
347.4	99.0	342.7	97.3	358.3	12.1	357.9	8.5
311.2	5.1	311.7	3.0	348.0	87.9	343.2	91.0
278.9	1.1	278.4	0.7	218.2	0.3	218.5	0.1
221.2	0.03	221.2	0.03	189.9	0.1	189.8	0.1
124.2	0.3	123.6	0.4	171.7	0.5	170.5	0.5
98.2	1.3	98.3	2.5	113.5	1.5	113.5	3.3
81.1	0.8	80.8	1.1	63.3	0.8	63.1	0.4
35.4	0.7	34.4	0.1	31.5	0.002	30.5	1.0

Table D.2 (Cont.)

MP2/cc-pVTZ			
CPDPZ1t		CPDPZ1c	
ν	I	ν	I
3841.1	86.7	3840.9	80.3
3300.5	1.1	3300.7	1.1
3288.5	0.2	3288.6	0.3
3236.7	1.5	3240.0	2.2
3228.9	2.3	3222.1	1.0
3213.7	0.9	3219.1	1.6
3212.2	3.8	3212.9	3.2
3198.6	10.8	3195.8	10.8
3192.5	4.7	3192.6	4.9
3189.2	5.5	3189.1	5.6
1658.4	40.3	1656.2	49.8
1635.5	26.2	1638.1	10.6
1535.0	85.8	1533.3	95.6
1506.7	1.2	1506.7	1.2
1490.8	10.0	1490.7	10.6
1480.6	11.2	1481.6	7.0
1466.8	3.3	1466.8	3.7
1452.2	35.8	1453.4	31.2
1372.8	1.4	1372.3	2.3
1328.8	6.6	1328.2	8.7
1298.8	96.0	1298.6	93.1
1238.6	0.5	1238.5	0.5
1209.2	1.4	1209.2	0.3
1202.7	77.2	1203.1	91.9
1199.0	91.5	1198.6	78.9
1178.1	3.3	1178.5	3.1
1173.6	21.2	1174.0	23.2
1122.1	1.3	1121.6	2.3
1113.7	18.2	1113.3	15.2
1073.5	3.4	1073.4	3.6
1052.5	3.6	1052.5	3.8
1028.1	1.3	1028.3	1.1
956.4	20.2	956.4	8.9
951.9	29.0	953.5	36.7
932.9	16.9	929.8	20.7
919.4	11.7	919.4	17.1
906.2	31.8	906.2	26.0
855.9	7.6	857.1	9.4
844.8	15.0	846.2	18.5
842.0	23.1	843.2	10.3
821.2	5.4	816.3	10.1
789.4	8.2	789.2	9.6
766.3	10.0	767.3	9.3
712.0	7.5	711.8	6.9
669.2	2.1	667.3	6.7
636.2	3.9	636.7	2.0
603.8	4.3	603.6	3.8
512.3	14.2	512.3	14.2
459.7	0.5	459.3	0.2
418.0	5.4	417.9	7.3
411.9	7.3	412.2	2.5
361.0	1.9	361.4	1.6
336.1	5.8	336.6	10.6
325.9	94.1	325.4	95.7
286.0	1.4	286.2	1.0
191.5	0.1	190.3	0.2
167.2	1.7	166.1	0.8
91.4	1.7	90.4	1.0
61.2	0.6	60.8	0.3
33.4	1.9	30.9	0.3

E

Appendix

E.1 CPDNO Supporting Information

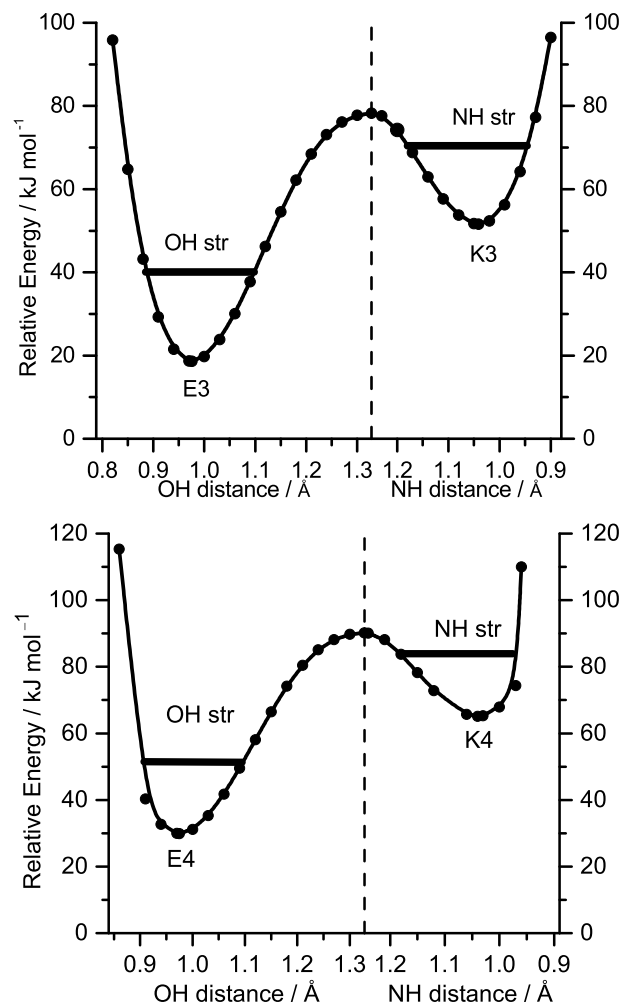


Figure E.1 Relaxed potential energy surface for the proton shift between the E3-K3 (top) and E4-K4 (bottom) minima in CPDNO calculated at the B3LYP/6-311+G(2df,2p) level of theory. The lowest energy vibrational levels are designated by horizontal lines. The change in the reaction coordinate (OH vs. NH distance) is designated by the vertical dashed line. The energy of E1 form was chosen as the relative zero.

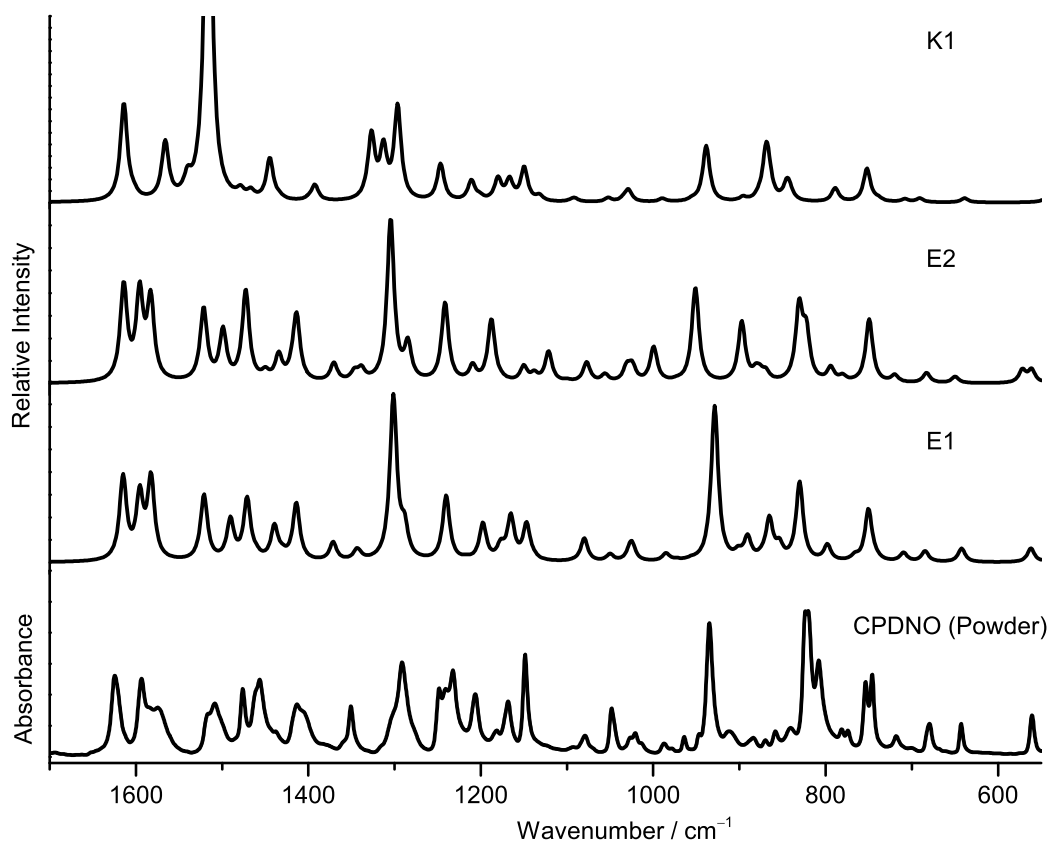


Figure E.2 Experimental infrared spectrum of CPDNO in a KBr pellet compared with the calculated infrared spectra of CPDNO most stable isomeric forms. The calculated frequencies were scaled by a factor of 0.975. The calculated infrared spectra were simulated by fitting to a Lorentzian function (FWHM = 10 cm^{-1}).

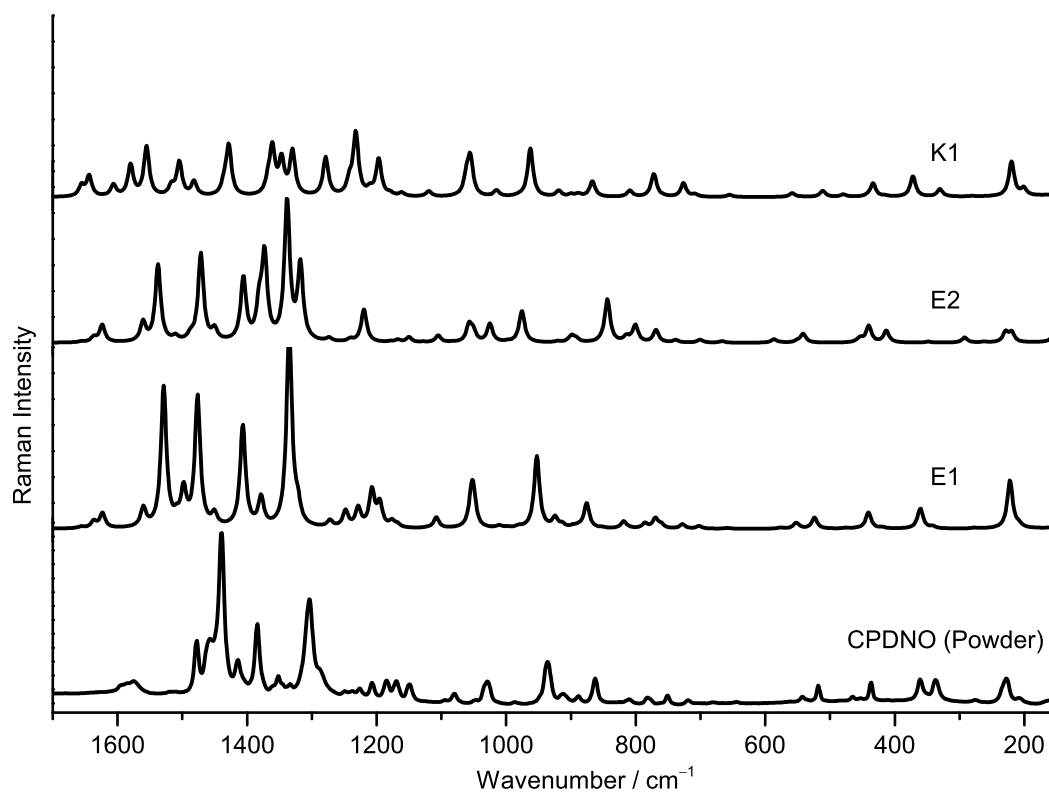


Figure E.3 Experimental Raman spectrum of CPDNO in the solid state (powder) compared with the calculated Raman spectra of CPDNO most stable isomeric forms. The Raman spectrum of the sample was recorded with a DXR SmartRaman Spectrometer in the $3300\text{--}50\text{ cm}^{-1}$ range with excitation provided by a Nicolet DXR 780 nm laser (14 mW). The Raman activities were calculated at the B3LYP/6-311+G(2df,2p) level of theory and converted to relative Raman intensities using relations derived from the intensity theory of Raman scattering (see additional references given at the end). The calculated Raman spectra were simulated by fitting to a Lorentzian function ($\text{FWHM} = 10\text{ cm}^{-1}$) and the calculated frequencies were scaled by a factor of 0.975.

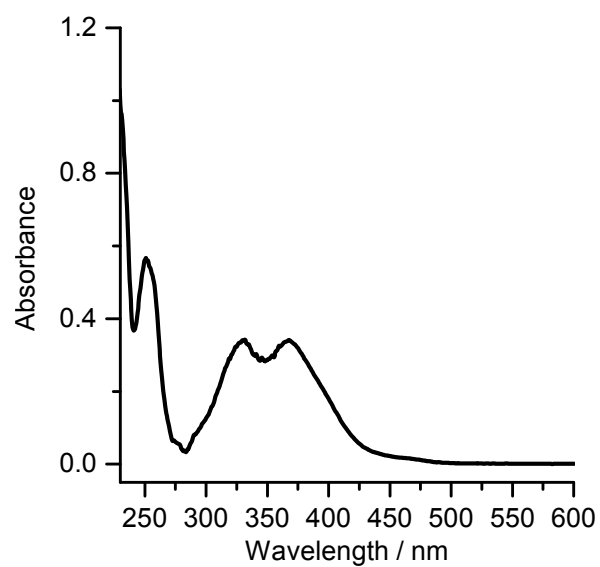


Figure E.4 Experimental UV-visible spectrum of CPDNO in acetonitrile. The spectrum was obtained in a Shimadzu UV-2100 spectrometer using quartz cuvettes.

Table E.1 Cartesian coordinates of the optimized geometries of CPDNO isomeric forms. All calculations were carried out at the B3LYP/6-311+G(2df,2p) level of theory.

Atom	E1			E2			E3			E4		
	x	y	z	x	y	z	x	y	z	x	y	z
C	-2.758860	-2.286090	0.000000	2.157790	-2.519680	0.000000	1.395760	-2.763600	0.000000	-2.264530	-2.439050	0.000000
C	-3.892860	-1.451430	0.000000	3.426980	-1.910830	0.000000	2.780690	-2.531350	0.000000	-3.503210	-1.777780	0.000000
C	-3.731150	-0.088870	0.000000	3.521250	-0.541730	0.000000	3.244260	-1.239170	0.000000	-3.531010	-0.405250	0.000000
C	-2.440880	0.488900	0.000000	2.361280	0.266020	0.000000	2.352840	-0.144000	0.000000	-2.336960	0.348480	0.000000
C	-1.293130	-0.355090	0.000000	1.076420	-0.349300	0.000000	0.940280	-0.375610	0.000000	-1.071730	-0.321050	0.000000
C	-1.490820	-1.755210	0.000000	1.010840	-1.761550	0.000000	0.496640	-1.720020	0.000000	-1.079310	-1.736730	0.000000
C	0.014660	0.242750	0.000000	-0.097040	0.482230	0.000000	0.069690	0.770120	0.000000	0.118740	0.488840	0.000000
C	0.138080	1.640370	0.000000	0.042020	1.879710	0.000000	0.622420	2.057460	0.000000	0.002790	1.884970	0.000000
C	-1.014900	2.457550	0.000000	1.327950	2.466910	0.000000	2.016150	2.263410	0.000000	-1.252420	2.523900	0.000000
C	-2.258990	1.896880	0.000000	2.445080	1.683710	0.000000	2.851470	1.185840	0.000000	-2.386950	1.767790	0.000000
N	1.098050	-0.633760	0.000000	-1.325780	-0.169990	0.000000	-1.327780	0.828820	0.000000	1.460090	0.094660	0.000000
N	2.253960	-0.137210	0.000000	-2.364540	0.538420	0.000000	-2.019350	-0.212960	0.000000	1.772060	-1.114710	0.000000
O	1.326470	2.253160	0.000000	-1.010860	2.700020	0.000000	-0.163770	3.148990	0.000000	1.095320	2.671460	0.000000
C	3.306110	-1.095020	0.000000	-3.610020	-0.172490	0.000000	-3.419510	0.036230	0.000000	3.182720	-1.382380	0.000000
C	4.567810	-0.722900	0.747460	-3.766830	-1.479710	-0.746640	-4.276600	-0.964590	-0.746590	4.163280	-0.501200	-0.746110
C	4.567810	-0.722900	-0.747460	-3.766830	-1.479710	0.746640	-4.276600	-0.964590	0.746590	4.163280	-0.501200	0.746110
H	-2.887150	-3.360840	0.000000	2.083600	-3.599520	0.000000	1.024460	-3.780420	0.000000	-2.236400	-3.521130	0.000000
H	-4.884020	-1.884800	0.000000	4.320200	-2.520990	0.000000	4.308500	-1.037780	0.000000	-4.424200	-2.345260	0.000000
H	-4.593220	0.566780	0.000000	4.490250	-0.057950	0.000000	3.472850	-3.362690	0.000000	-4.475530	0.124850	0.000000
H	-0.626820	-2.401790	0.000000	0.442390	-2.237580	0.000000	2.388080	-1.919020	0.000000	-0.140740	-2.261600	0.000000
H	-0.872870	3.529480	0.000000	1.388640	3.546500	0.000000	0.560050	3.278180	0.000000	-1.281950	3.604250	0.000000
H	-3.135650	2.532890	0.000000	3.425100	2.144810	0.000000	3.924220	1.333980	0.000000	-3.356910	2.249370	0.000000
H	2.014390	-1.535700	0.000000	-1.821340	2.118480	0.000000	-1.079990	2.813430	0.000000	1.856450	2.062650	0.000000
H	2.981410	-2.128280	0.000000	-4.445300	0.511110	0.000000	-3.716410	1.079450	0.000000	3.369870	-2.445480	0.000000
H	5.075920	-1.518560	1.273200	-4.695270	-1.641930	-1.275520	-5.136190	-0.573160	-1.271630	4.970170	-0.989820	-1.273570
H	5.075920	-1.518560	-1.273200	-4.695270	-1.641930	1.275520	-5.136190	-0.573160	1.271630	4.970170	-0.989820	1.273570
H	4.568210	0.231270	1.254470	-2.875800	-1.837220	-1.243180	-3.753370	-1.761670	-1.254260	3.730400	0.352030	-1.249510
H	4.568210	0.231270	-1.254470	-2.875800	-1.837220	1.243180	-3.753370	-1.761670	1.254260	3.730400	0.352030	1.249510

Table E.1 (Cont.)

Atom	E5			E6			E7			E8		
	x	y	z	x	y	z	x	y	z	x	y	z
C	2.573380	-2.381140	-0.051340	2.056460	-2.574100	0.034710	1.241090	-2.766200	-0.046100	-2.222200	-2.451710	0.000000
C	3.754390	-1.629460	0.117570	3.350130	-2.014780	0.000800	2.638740	-2.604010	-0.024430	-3.472440	-1.810140	0.000000
C	3.684910	-0.262490	0.188720	3.498990	-0.652590	-0.024160	3.165530	-1.339690	0.006490	-3.519220	-0.440060	0.000000
C	2.441620	0.407850	0.096420	2.371180	0.202620	-0.014750	2.328050	-0.199230	0.023080	-2.333980	0.330600	0.000000
C	1.244630	-0.351010	-0.065120	1.061030	-0.359880	0.029420	0.904460	-0.356860	0.024450	-1.055110	-0.314860	0.000000
C	1.350980	-1.762690	-0.136490	0.942580	-1.772110	0.052750	0.398200	-1.681140	-0.018210	-1.048310	-1.733290	0.000000
C	-0.019510	0.317990	-0.136500	-0.085290	0.499880	0.062410	0.078280	0.821670	0.020910	0.134230	0.504090	0.000000
C	-0.058310	1.706550	-0.083520	0.098610	1.878620	0.011180	0.685550	2.075490	-0.001960	-0.005550	1.894290	0.000000
C	1.139070	2.443550	0.056100	1.403660	2.416770	-0.054180	2.088850	2.207740	0.015380	-1.276510	2.506140	0.000000
C	2.350260	1.818120	0.151540	2.505910	1.609690	-0.057910	2.886810	1.100280	0.029610	-2.407200	1.744210	0.000000
N	-1.143680	-0.503230	-0.381540	-1.342490	-0.140960	0.030410	-1.329870	0.875780	-0.043960	1.479600	0.099350	0.000000
N	-2.221560	-0.147390	0.131870	-2.287850	0.442060	0.592040	-1.984050	-0.074810	0.428710	1.761810	-1.115480	0.000000
O	-1.241820	2.367110	-0.209780	-0.971280	2.716440	-0.020600	-0.099900	3.184910	-0.007850	1.107860	2.672110	0.000000
C	-3.314620	-0.993830	-0.199410	-3.557340	-0.220460	0.485790	-3.392060	0.092820	0.287790	3.172840	-1.391930	0.000000
C	-4.367160	-1.155400	0.877860	-3.945780	-0.986940	-0.761590	-4.202860	-1.172880	0.109990	4.148970	-0.504900	-0.745710
C	-4.660220	-0.308160	-0.314850	-3.666440	-1.732440	0.498660	-4.237580	-0.453640	1.418350	4.148970	-0.504900	0.745710
H	2.632030	-3.460110	-0.113420	1.940500	-3.650120	0.048090	0.819610	-3.762530	-0.082130	-2.177030	-3.533260	0.000000
H	4.709450	-2.132750	0.188330	4.218190	-2.660340	-0.007570	3.287520	-3.469580	-0.038170	-4.384710	-2.391630	0.000000
H	4.583990	0.327890	0.316110	4.486130	-0.207840	-0.052810	4.238330	-1.190610	0.011420	-4.470290	0.078250	0.000000
H	0.451230	-2.344670	-0.265460	-0.043240	-2.209390	0.079070	-0.666340	-1.833260	-0.012980	-0.103610	-2.245490	0.000000
H	1.079020	3.525870	0.093580	1.516240	3.494790	-0.093930	2.523560	3.200860	0.020310	-1.339900	3.588370	0.000000
H	3.254320	2.402300	0.267240	3.496400	2.044720	-0.098360	3.964050	1.207070	0.041600	-3.381000	2.217440	0.000000
H	-1.065990	3.307040	-0.318860	-0.666100	3.608230	-0.216180	0.456570	3.967860	-0.061490	0.845540	3.597910	0.000000
H	-3.092170	-1.831090	-0.851610	-4.327920	-0.340480	0.992190	-3.710130	0.997540	-0.217250	3.359780	-2.455290	0.000000
H	-4.831850	-2.127590	0.958950	-4.966070	-0.892460	-1.105710	-5.059620	-1.113440	-0.545980	4.956550	-0.989680	-1.276130
H	-5.331140	-0.683710	-1.074180	-4.488060	-2.164710	1.052030	-5.118740	0.112490	1.684230	4.956550	-0.989680	1.276130
H	-4.171860	-0.657740	1.816410	-3.189400	-1.018500	-1.533450	-3.650790	-2.099980	0.057610	3.705290	0.350230	-1.236160
H	-4.661610	0.764100	-0.186270	-2.726910	-2.261950	0.565060	-3.703340	-0.890450	2.249450	3.705290	0.350230	1.236160

Table E.1 (Cont.)

Atom	E9			E10			E11			K1		
	x	y	z	x	y	z	x	y	z	x	y	z
C	3.358010	1.871090	-0.597980	2.721147	2.103629	0.210281	-2.611167	1.930670	-0.310506	2.799740	2.295070	0.000000
C	4.017000	2.458570	0.500730	3.706996	1.268394	-0.355476	-3.542780	1.057554	0.289400	3.918880	1.454120	0.000000
C	3.768960	1.997040	1.768010	3.423562	-0.048677	-0.610195	-3.184624	-0.235038	0.572246	3.737410	0.086550	0.000000
C	2.867580	0.930230	1.995240	2.148490	-0.588792	-0.316355	-1.886242	-0.714736	0.274116	2.446880	-0.470330	0.000000
C	2.227730	0.309120	0.876700	1.146896	0.261037	0.242565	-0.938855	0.174970	-0.319965	1.314730	0.380110	0.000000
C	2.487440	0.824910	-0.417510	1.471365	1.616262	0.499662	-1.341398	1.503546	-0.606637	1.521800	1.769270	0.000000
C	1.324590	-0.766130	1.124580	-0.147480	-0.268579	0.517841	0.372286	-0.300833	-0.604972	-0.014690	-0.218670	0.000000
C	0.998800	-1.114300	2.425800	-0.404282	-1.604831	0.280279	0.698308	-1.616257	-0.350667	-0.175870	-1.671600	0.000000
C	1.645240	-0.507740	3.520290	0.596361	-2.442943	-0.256360	-0.241668	-2.487882	0.234975	1.032230	-2.469600	0.000000
C	2.566650	0.479280	3.304640	1.837551	-1.949182	-0.552222	-1.501807	-2.049688	0.542821	2.256000	-1.895860	0.000000
N	0.524140	-1.408900	0.124900	-1.065707	0.555263	1.249251	1.256064	0.505568	-1.401210	-1.053180	0.614570	0.000000
N	0.986610	-2.073820	-0.820910	-2.168125	0.912529	0.807156	2.087911	1.313519	-0.983440	-2.256030	0.148260	0.000000
O	0.067120	-2.064200	2.690500	-1.644843	-2.093431	0.584203	1.966322	-2.034993	-0.659641	-1.309500	-2.210310	0.000000
C	2.383340	-2.322330	-0.967270	-2.596257	0.595879	-0.517117	2.408972	1.592121	0.400444	-3.361180	1.049670	0.000000
C	2.868740	-2.408190	-2.402960	-3.503436	1.642040	-1.137380	3.258204	0.612237	1.183386	-4.611780	0.680020	0.753030
C	2.693600	-3.659070	-1.618870	-4.084613	0.357683	-0.658153	1.898173	0.990806	1.691686	-4.611780	0.680020	-0.753030
H	3.534860	2.253580	-1.594780	2.954567	3.139483	0.419120	-2.902498	2.946875	-0.541496	2.934510	3.369000	0.000000
H	4.704240	3.278740	0.342350	4.685937	1.668996	-0.582757	-4.539260	1.409863	0.520212	4.915930	1.873480	0.000000
H	4.253520	2.454170	2.622040	4.175879	-0.698568	-1.040040	-3.895310	-0.913915	1.027348	4.592570	-0.578210	0.000000
H	1.980670	0.400280	-1.271900	0.721602	2.259573	0.937622	-0.639146	2.179794	-1.072927	0.664130	2.425490	0.000000
H	1.388430	-0.839050	4.516960	0.364315	-3.486861	-0.436402	0.049466	-3.511334	0.443650	0.903280	-3.543460	0.000000
H	3.065200	0.946810	4.144120	2.595593	-2.600257	-0.968025	-2.217286	-2.725422	0.992832	3.142160	-2.520640	0.000000
H	-0.383280	-2.283770	1.860820	-1.656102	-3.047731	0.467029	2.031720	-2.987351	-0.543193	-3.032780	2.078260	0.000000
H	3.065170	-1.950090	-0.215560	-1.922087	0.050274	-1.164062	2.742612	2.619025	0.458281	-4.622120	-0.278180	1.254010
H	3.865980	-2.038670	-2.592830	-3.391378	1.805387	-2.199639	4.143349	0.996713	1.669657	-4.622120	-0.278180	-1.254010
H	2.138990	-2.184760	-3.167440	-3.679851	2.529950	-0.548169	1.833873	1.679162	2.524042	-5.131710	1.468090	1.278980
H	1.844710	-4.286650	-1.846740	-4.656055	0.370179	0.258172	3.362970	-0.371867	0.749036	-5.131710	1.468090	-1.278980
H	3.568040	-4.175490	-1.250040	-4.385649	-0.387634	-1.380012	1.125368	0.243204	1.671207	-2.345900	-0.885410	0.000000

Table E.1 (Cont.)

Atom	K2			K3			K4			K5		
	x	y	z	x	y	z	x	y	z	x	y	z
C	2.215730	-2.519260	0.000000	1.574610	2.736720	0.000000	-2.414600	-2.349930	0.000000	3.132933	1.882621	-0.062901
C	3.467820	-1.894140	0.000000	2.935210	2.426850	0.000000	-3.604540	-1.621240	0.000000	3.977207	0.852941	0.358812
C	3.535830	-0.515940	0.000000	3.328220	1.100220	0.000000	-3.553650	-0.238380	0.000000	3.463638	-0.420156	0.516679
C	2.367380	0.264570	0.000000	2.384840	0.065660	0.000000	-2.329020	0.440310	0.000000	2.112853	-0.690851	0.251520
C	1.100270	-0.367320	0.000000	0.995280	0.379970	0.000000	-1.113390	-0.302320	0.000000	1.255666	0.351383	-0.168335
C	1.053770	-1.770860	0.000000	0.615930	1.736160	0.000000	-1.186180	-1.708600	0.000000	1.793149	1.638067	-0.310536
C	-0.099860	0.461760	0.000000	0.078940	-0.724220	0.000000	0.107730	0.450740	0.000000	0.174997	0.064770	-0.396815
C	0.005330	1.921660	0.000000	0.509310	-2.124340	0.000000	0.146950	1.914660	0.000000	-0.611614	-1.360134	-0.452026
C	1.338940	2.487500	0.000000	1.941380	-2.347860	0.000000	-1.136720	2.585880	0.000000	0.319021	-2.347265	0.087069
C	2.438020	1.701770	0.000000	2.807400	-1.311360	0.000000	-2.288870	1.880290	0.000000	1.587033	-2.027350	0.404493
N	-1.271540	-0.166970	0.000000	-1.269960	-0.654480	0.000000	1.364010	-0.045170	0.000000	-0.914686	1.112487	-0.657932
N	-2.372730	0.504140	0.000000	-2.050610	0.353960	0.000000	1.772570	-1.253210	0.000000	-2.226097	1.152265	-0.683309
O	-1.010410	2.655790	0.000000	-0.324850	-3.048940	0.000000	1.235850	2.521220	0.000000	-1.648841	-1.712414	-1.014674
C	-3.639030	-0.166060	0.000000	-3.427600	0.015630	0.000000	3.187710	-1.436220	0.000000	-3.172297	0.289437	-0.028369
C	-3.832860	-1.454560	0.752480	-4.362880	0.943380	-0.747670	4.156250	-0.538510	0.748550	-4.246375	0.953986	0.776277
C	-3.832860	-1.454560	-0.752480	-4.362880	0.943380	0.747670	4.156250	-0.538510	-0.748550	-3.140370	0.197423	1.473486
H	2.154270	-3.599860	0.000000	1.258510	3.771830	0.000000	-2.446070	-3.431730	0.000000	3.525703	2.882548	-0.194143
H	4.372900	-2.486380	0.000000	3.675590	3.215330	0.000000	-4.558090	-2.131780	0.000000	5.021578	1.049960	0.560095
H	4.496890	-0.016420	0.000000	4.380740	0.844470	0.000000	-4.469420	0.340010	0.000000	4.103671	-1.230027	0.844636
H	0.092280	-2.262470	0.000000	-0.430300	1.991550	0.000000	-0.275450	-2.283630	0.000000	1.142960	2.442145	-0.621151
H	1.406380	3.566960	0.000000	2.276810	-3.375700	0.000000	-1.125870	3.666980	0.000000	-0.049953	-3.361997	0.152607
H	3.422820	2.155390	0.000000	3.874510	-1.502910	0.000000	-3.238770	2.402830	0.000000	2.265284	-2.794568	0.761112
H	-4.444140	0.553330	0.000000	-3.667620	-1.045180	0.000000	3.415540	-2.491070	0.000000	-3.402312	-0.616964	-0.567733
H	-2.957110	-1.852940	1.244640	-3.901660	1.778120	-1.254620	3.743250	0.324060	1.256110	-5.236507	0.523124	0.740243
H	-2.957110	-1.852940	-1.244640	-3.901660	1.778120	1.254620	3.743250	0.324060	-1.256110	-4.232584	2.033144	0.859568
H	-4.765570	-1.596040	1.279800	-5.190180	0.487200	-1.272550	4.968510	-1.016730	1.277070	-2.397548	0.781418	1.997844
H	-4.765570	-1.596040	-1.279800	-5.190180	0.487200	1.272550	4.968510	-1.016730	-1.277070	-3.361314	-0.761543	1.919365
H	-2.284770	1.534010	0.000000	-1.644340	-1.625640	0.000000	2.015520	0.765620	0.000000	-2.556441	2.079806	-0.899092

Table E.1 (Cont.)

Atom	K6			K7			K8			K9		
	x	y	z	x	y	z	x	y	z	x	y	z
C	1.679100	2.668520	-0.456180	-2.274796	-2.406116	-0.378528	3.275670	1.851420	-0.103730	-0.603091	-2.788569	0.564597
C	2.961730	2.358980	-0.019580	-3.416197	-1.816609	0.152407	4.136040	0.782840	0.158040	-1.892766	-2.937907	0.049493
C	3.267100	1.046850	0.310690	-3.393440	-0.467911	0.474359	3.611570	-0.488080	0.297570	-2.587917	-1.814274	-0.355317
C	2.302040	0.039280	0.238590	-2.237812	0.298500	0.303297	2.233340	-0.717470	0.171800	-2.012623	-0.537654	-0.288787
C	0.971070	0.360310	-0.133930	-1.045167	-0.312220	-0.166262	1.360520	0.363650	-0.087260	-0.665013	-0.390628	0.151808
C	0.698900	1.683670	-0.511790	-1.108599	-1.665673	-0.535245	1.910980	1.646490	-0.213540	-0.002349	-1.543644	0.619739
C	-0.025120	-0.722300	-0.149770	0.159355	0.518735	-0.286872	-0.092470	0.116090	-0.175370	-0.134548	0.945616	0.206074
C	0.453590	-2.148130	-0.199890	0.021994	2.013727	-0.293520	-0.571760	-1.294570	-0.244290	-0.990239	2.129180	0.082612
C	1.830940	-2.366560	0.264820	-1.238315	2.535480	0.251197	0.391830	-2.329250	0.121440	-2.348281	1.886271	-0.368083
C	2.671460	-1.342820	0.482700	-2.270017	1.727857	0.544825	1.695640	-2.051400	0.305670	-2.801251	0.631749	-0.576581
N	-1.314820	-0.631630	-0.009130	1.405573	0.131613	-0.288451	-0.829540	1.189610	-0.307980	1.138506	1.341268	0.517050
N	-1.960070	0.507800	0.175290	1.801582	-1.109693	-0.160964	-2.135240	1.277660	-0.218940	2.331459	0.903366	0.378907
O	-0.250630	-3.075840	-0.557760	0.905160	2.763975	-0.677252	-1.687690	-1.585680	-0.670420	-0.545667	3.268171	0.309670
C	-3.305160	0.415380	0.674850	3.192197	-1.362108	0.133054	-3.049060	0.435090	0.513100	2.557733	-0.245094	-0.406304
C	-4.389850	0.025670	-0.280490	3.922747	-0.598734	1.210754	-4.199760	-0.242780	-0.163920	3.620940	-1.218436	0.086869
C	-4.286970	1.448960	0.201780	4.239435	-0.368204	-0.246860	-4.443970	0.966770	0.698660	3.942423	-0.294818	-1.034514
H	1.438130	3.677200	-0.764470	-2.290543	-3.444077	-0.683507	3.675760	2.850520	-0.218210	-0.067509	-3.652045	0.937324
H	3.721100	3.126880	0.038620	-4.319586	-2.395346	0.288762	5.200930	0.948150	0.251370	-2.352125	-3.915460	-0.002429
H	4.273680	0.784620	0.612130	-4.288073	0.014681	0.848049	4.263920	-1.328020	0.502710	-3.607703	-1.903997	-0.790958
H	-0.265920	1.946420	-0.918870	-0.268505	-2.140356	-1.019648	1.250630	2.479700	-0.401680	0.979349	-1.461837	1.058163
H	2.136510	-3.397170	0.384650	-1.294517	3.608204	0.377728	0.007470	-3.339060	0.174310	-2.969060	2.755937	-0.534020
H	3.689930	-1.532970	0.802330	-3.193451	2.143198	0.932631	2.391560	-2.850360	0.536520	-3.815226	0.474860	-0.926414
H	-3.391030	0.064590	1.697880	3.417966	-2.412681	0.013446	-2.576070	-0.076770	1.340290	1.103440	2.316926	0.846476
H	-5.188330	-0.596010	0.097020	4.629486	-1.134573	1.828914	-4.483860	-1.218860	0.199880	1.737851	-0.647441	-0.982504
H	-4.089830	-0.187380	-1.295680	3.364402	0.178541	1.713396	-4.264590	-0.124510	-1.235080	3.453556	-2.265035	-0.123486
H	-3.929990	2.188570	-0.501450	3.890939	0.557897	-0.679361	-4.695060	1.895780	0.200960	4.046137	-1.004579	1.056348
H	-5.014150	1.816270	0.911330	5.168569	-0.749429	-0.646059	-4.906740	0.846530	1.667960	4.584826	0.549186	-0.832536
H	-1.434890	1.330680	0.454180	1.146938	-1.812730	0.166499	-2.423900	2.241830	-0.288350	3.994861	-0.689838	-2.038994

Table E.1 (Cont.)

Atom	K10			K11			K12			K13		
	x	y	z	x	y	z	x	y	z	x	y	z
C	3.049470	2.007340	-0.000824	-2.600556	-2.394026	0.079883	0.214263	2.675928	-0.847159	2.208300	-2.499004	-0.464880
C	4.008228	1.012321	0.208367	-3.770889	-1.648069	-0.077852	-0.870004	3.224808	-0.169116	3.437231	-1.934356	-0.117847
C	3.604663	-0.306517	0.301172	-3.686230	-0.270268	-0.140509	-1.794680	2.382252	0.430230	3.500308	-0.583146	0.165298
C	2.257592	-0.667891	0.160231	-2.451466	0.390048	-0.074084	-1.638918	0.994093	0.383011	2.354603	0.223648	0.134185
C	1.280866	0.336879	-0.081674	-1.252798	-0.363580	0.049834	-0.486802	0.437043	-0.223685	1.094926	-0.350266	-0.183283
C	1.711279	1.680149	-0.123767	-1.371202	-1.765323	0.156574	0.402465	1.300114	-0.871265	1.065281	-1.721107	-0.510193
C	-0.093652	-0.059668	-0.234046	0.003267	0.350576	0.086301	-0.357353	-1.029719	-0.279582	0.021209	0.510577	-0.180880
C	-0.517986	-1.450781	-0.191646	0.080603	1.811531	0.103475	-1.624130	-1.847880	-0.157429	0.021209	0.510577	-0.180880
C	0.542208	-2.404079	0.125705	-1.208588	2.492399	-0.021580	-2.707143	-1.197966	0.598767	1.364011	2.447310	0.351448
C	1.832223	-2.036311	0.271122	-2.376786	1.827339	-0.111180	-2.691956	0.118462	0.863689	2.437976	1.636992	0.403069
N	-0.962502	0.904788	-0.711020	1.142855	-0.387161	-0.012264	0.692523	-1.780355	-0.405903	-1.284450	-0.085552	-0.270912
N	-2.213170	1.116970	-0.576449	2.353279	-0.022697	0.155300	-1.966575	-1.406302	-0.292926	-2.437568	0.442117	-0.424168
O	-1.665222	-1.825461	-0.477881	1.139044	2.439559	0.171029	-1.741810	-2.980798	-0.586246	-0.948580	2.714838	-0.002359
C	-2.920089	0.429190	0.414270	3.305365	-1.015934	-0.160836	2.470654	-0.365459	0.579061	-3.520286	-0.495558	-0.349884
C	-4.347020	0.036889	0.069848	4.603279	-0.981610	0.620362	3.413357	0.696550	0.077505	-4.330925	-0.611841	0.909009
C	-4.125358	1.203093	0.959482	4.594913	-0.540538	-0.806219	3.925090	-0.428887	0.937293	-3.499474	-1.784410	0.443767
H	3.349499	3.046205	-0.042936	-2.652725	-3.471519	0.164700	0.913876	3.320129	-1.363464	2.147537	-3.548454	-0.721263
H	5.051768	1.274520	0.316098	-4.731187	-2.142279	-0.130395	-1.007930	4.297103	-0.134485	4.330266	-2.543354	-0.089788
H	4.333626	-1.085988	0.486513	-4.585566	0.325275	-0.238829	-2.669591	2.795057	0.917093	4.449192	-0.123924	0.413772
H	0.992369	2.485139	-0.210907	-0.503505	-2.386966	0.342331	1.233985	0.890326	-1.421874	0.150726	-2.196634	-0.843422
H	0.234823	-3.439035	0.193086	-1.164288	3.572975	-0.040066	-3.538271	-1.831272	0.878328	1.439391	3.509011	0.543594
H	2.589732	-2.784718	0.474532	-3.307856	2.374972	-0.203811	-3.522922	0.578950	1.386440	3.414155	2.043602	0.642016
H	-0.533602	1.593475	-1.324823	2.922772	-1.990278	-0.468505	2.543289	-2.234234	-0.293544	-4.096597	-0.494723	-1.268573
H	-2.380654	-0.218406	1.086112	5.047989	-1.934127	0.871692	1.769180	-0.086598	1.354282	-5.406374	-0.658513	0.816888
H	-4.679620	-0.901705	0.486706	4.673014	-0.221857	1.384605	3.337282	1.687037	0.503127	-3.970898	-0.067187	1.770390
H	-4.650642	0.220785	-0.949420	4.653768	0.518137	-1.010120	3.670836	0.670401	-0.972160	-2.637983	-2.034992	1.049342
H	-4.280533	2.193772	0.558940	5.031220	-1.184045	-1.557088	4.524273	-1.190547	0.454086	-3.995689	-2.646099	0.020343
H	-4.300935	1.098723	2.020917	0.981774	-1.361777	-0.289764	4.206049	-0.227498	1.960989	-1.259606	-1.106234	-0.174102

Table E.2 Theoretical frequencies (ν/cm^{-1}) and IR intensities ($I/\text{km mol}^{-1}$) of all considered isomeric forms. All calculations were carried out at the B3LYP/6-311+G(2df,2p) level of theory. The calculated frequencies are not scaled.

E1		E2		E3		E4		E5	
ν	I	ν	I	ν	I	ν	I	ν	I
3226.9	4.8	3225.5	10.0	3588.6	98.7	3603.7	93.4	3817.6	70.7
3213.2	0.1	3213.2	0.6	3253.8	5.9	3251.9	6.2	3230.2	5.8
3212.9	4.7	3212.2	5.2	3228.4	6.5	3222.9	12.5	3217.0	0.1
3193.4	9.4	3193.6	8.3	3215.0	0.1	3209.0	0.4	3210.8	3.7
3186.1	24.1	3186.7	8.8	3198.9	6.8	3199.2	6.1	3185.2	24.4
3168.9	12.0	3186.3	28.3	3186.2	23.0	3186.3	23.7	3174.5	16.3
3165.6	3.9	3169.0	15.4	3168.6	20.7	3184.1	15.2	3168.5	10.6
3159.0	1.1	3165.1	1.3	3166.3	0.4	3169.1	20.3	3158.4	1.3
3157.1	163.7	3159.3	0.7	3158.5	0.9	3166.7	0.4	3143.5	11.1
3145.2	92.5	3131.7	9.5	3139.1	17.4	3158.5	1.0	3140.1	19.4
3135.7	5.2	3131.7	13.7	3135.9	13.5	3129.7	14.8	3136.8	13.4
3135.2	12.6	3089.1	216.7	3121.8	24.7	3129.1	11.2	3127.0	14.7
1656.5	57.5	1655.8	65.8	1653.2	77.4	1653.1	72.9	1658.6	32.9
1636.7	43.3	1636.8	59.6	1635.4	61.5	1635.3	50.9	1640.9	13.5
1623.3	55.9	1623.7	55.4	1616.2	31.3	1617.2	19.8	1614.8	15.8
1560.2	45.4	1560.6	50.3	1565.2	23.6	1568.2	33.7	1568.3	2.1
1528.8	27.5	1537.6	34.6	1549.2	67.4	1551.7	71.9	1543.6	41.4
1508.9	42.1	1510.5	63.0	1497.8	38.2	1496.6	32.5	1503.0	4.5
1498.0	2.7	1487.2	5.4	1495.9	11.7	1483.9	9.5	1494.3	1.8
1476.4	22.9	1471.3	17.3	1478.7	11.3	1477.9	7.7	1466.6	19.5
1467.1	3.3	1454.9	4.9	1464.0	3.3	1456.2	4.7	1461.9	3.2
1450.4	39.6	1450.1	44.9	1425.4	54.7	1424.9	43.4	1418.3	4.0
1406.6	12.6	1405.7	12.7	1403.7	21.8	1402.7	15.3	1396.2	5.7
1378.5	6.2	1381.2	6.1	1379.9	0.8	1372.5	4.6	1377.2	16.3
1375.1	1.8	1373.0	7.8	1368.8	3.2	1370.6	1.3	1372.1	30.5
1334.9	114.0	1338.2	112.7	1311.3	37.7	1313.6	35.4	1303.9	23.8
1321.7	19.8	1317.7	24.6	1301.5	25.0	1302.7	27.0	1276.4	104.3
1272.1	45.1	1273.4	54.7	1255.3	157.5	1251.0	173.6	1244.8	1.6
1248.0	1.1	1240.6	10.3	1236.1	28.9	1236.4	29.9	1231.0	27.1
1228.4	25.5	1219.6	3.9	1218.8	18.9	1213.1	15.8	1220.5	4.5
1207.2	9.2	1218.1	39.6	1199.8	0.6	1205.2	0.7	1200.8	0.7
1199.7	0.5	1206.2	0.8	1197.3	39.4	1202.5	14.5	1196.9	13.8
1195.1	29.9	1179.8	10.4	1183.2	4.9	1182.0	15.4	1192.3	11.9
1176.4	24.9	1167.3	5.1	1178.7	73.3	1167.6	3.5	1174.8	9.6
1167.8	1.4	1150.3	21.1	1167.3	5.7	1147.6	38.0	1167.8	8.2
1122.5	0.3	1128.0	1.1	1119.5	0.2	1129.7	0.8	1122.8	0.2
1107.8	16.0	1105.0	13.9	1095.8	11.0	1088.9	12.3	1091.1	40.6
1077.1	4.8	1083.2	5.2	1075.8	4.0	1075.5	4.4	1076.3	3.5
1053.5	6.3	1057.3	9.8	1061.5	7.1	1065.1	0.8	1052.5	6.0
1050.7	9.0	1050.8	10.5	1047.1	4.8	1048.2	15.5	1047.5	3.5
1014.6	0.2	1025.2	24.2	1022.2	0.4	1023.6	0.6	1013.0	0.3
1010.5	5.1	1012.8	0.1	1016.0	11.6	1022.9	19.7	991.5	30.9
998.2	0.9	998.1	0.8	999.0	0.7	998.5	0.8	987.2	3.2
980.3	0.8	979.4	0.8	981.9	0.8	982.0	0.8	964.2	0.1
952.6	107.8	975.5	65.4	949.7	114.7	960.7	75.9	938.1	140.8
924.6	4.7	920.4	41.7	910.4	0.3	904.3	0.8	923.0	1.0
913.5	15.4	903.5	6.3	905.0	1.0	900.3	0.2	903.0	4.8
896.4	2.0	898.7	4.7	900.4	0.5	894.2	5.6	887.6	0.9
887.5	28.3	891.7	5.8	870.4	2.0	849.7	46.0	872.6	5.7
875.7	9.4	852.2	50.4	850.3	44.0	828.2	18.7	825.3	54.7
851.6	54.8	843.6	31.9	818.0	7.2	815.2	1.6	821.5	13.2
818.6	10.9	814.6	9.5	811.6	3.0	809.7	6.7	803.6	1.6
810.3	0.0	806.9	0.0	780.1	3.1	791.0	9.8	783.6	2.7
785.7	3.1	800.4	3.7	770.3	30.9	770.3	31.9	764.7	24.9
769.7	36.3	768.9	36.0	753.3	7.8	762.2	4.1	756.2	3.0
760.8	1.5	768.3	8.1	726.0	51.4	735.0	7.1	724.6	4.5
727.9	6.0	738.3	4.9	722.3	5.6	715.7	26.8	687.8	18.6
702.3	7.4	700.6	7.0	697.5	32.8	692.6	47.5	654.4	8.8
658.8	9.4	666.6	4.4	630.4	2.7	655.3	5.7	584.8	8.4
576.4	9.6	586.5	8.8	595.7	19.8	583.8	5.3	559.3	2.7
552.7	2.3	575.6	8.8	584.5	4.7	578.3	12.2	541.5	1.8
550.1	0.0	550.3	0.0	548.3	1.4	547.4	1.6	525.3	4.1
524.0	2.7	541.4	5.4	532.5	4.2	542.9	5.2	466.3	2.7
475.9	16.1	458.0	4.2	460.0	20.4	491.0	25.6	452.2	0.9
459.1	3.8	453.1	23.6	458.2	2.8	455.6	3.8	434.9	2.1
440.7	2.7	440.1	4.1	439.6	0.9	439.2	1.2	418.0	3.4
419.1	0.3	413.5	0.2	419.8	2.0	413.4	0.8	360.9	26.0
363.9	0.1	413.1	2.7	356.5	2.3	350.4	7.7	349.5	39.4
360.4	3.3	348.6	0.2	346.9	7.4	336.1	1.7	338.1	34.7
341.2	9.4	292.2	5.6	274.7	0.7	314.9	1.5	301.7	0.5
277.1	0.0	262.4	0.0	271.4	1.1	256.2	1.5	267.2	0.6
222.2	2.3	228.9	0.6	263.4	1.3	199.3	0.1	224.6	4.5
208.4	2.9	219.6	2.8	197.6	0.6	191.9	0.0	166.9	3.2
139.1	0.3	155.0	0.6	141.1	0.3	155.2	0.9	137.1	0.7
125.3	0.1	120.1	0.3	106.6	1.0	118.7	0.6	117.9	2.2
96.8	1.1	97.2	0.8	85.9	1.1	100.1	1.3	75.5	1.3
71.4	0.4	78.2	0.7	72.2	0.6	62.8	0.1	67.9	0.7
49.1	0.5	38.6	0.2	39.8	0.0	34.9	0.5	32.7	0.7

E.1 CPDNO Supporting Information

Table E.2 (Cont.)

E6		E7		E8		E9		E10	
ν	I	ν	I	ν	I	ν	I	ν	I
3814.8	72.6	3826.4	89.4	3822.8	82.1	3706.5	75.4	3837.6	90.3
3225.0	10.6	3249.2	3.8	3257.8	10.1	3232.7	4.0	3231.1	5.5
3215.6	4.7	3227.5	7.5	3224.0	10.2	3219.6	0.1	3218.1	0.1
3211.5	0.6	3213.8	0.3	3210.8	0.8	3198.9	6.6	3198.0	5.5
3186.7	6.3	3185.8	23.0	3185.6	24.1	3194.8	7.1	3184.9	21.5
3185.7	32.5	3175.2	16.4	3181.1	18.1	3186.0	20.1	3176.9	13.7
3174.6	16.3	3168.0	12.2	3174.4	16.2	3170.6	14.0	3169.7	9.4
3168.8	10.0	3158.2	1.3	3167.3	12.7	3168.8	1.7	3158.8	1.7
3159.1	1.1	3149.0	11.7	3157.6	1.2	3167.3	3.4	3153.8	6.9
3143.5	11.7	3140.4	25.4	3149.0	10.1	3159.5	1.7	3146.2	10.5
3132.3	15.7	3135.4	14.5	3128.0	16.3	3140.0	8.3	3139.1	11.0
3127.8	15.1	3132.7	9.1	3127.0	17.1	3139.0	8.3	3137.4	11.2
1658.4	31.9	1657.0	47.6	1656.4	57.3	1654.4	33.9	1658.4	26.8
1641.5	19.3	1642.9	17.1	1642.0	9.9	1635.0	68.9	1641.1	13.5
1617.1	11.0	1612.7	16.6	1612.9	22.7	1615.0	9.2	1616.5	16.5
1573.5	2.7	1569.5	7.1	1570.9	22.3	1580.4	22.5	1596.8	18.1
1543.7	48.8	1541.7	53.8	1541.0	55.0	1552.3	33.4	1544.1	33.0
1502.4	6.6	1505.1	9.2	1504.4	9.4	1499.1	37.7	1504.1	4.7
1480.7	2.3	1495.6	2.9	1479.2	5.6	1493.9	3.0	1494.0	1.0
1468.1	22.7	1464.4	28.4	1463.6	29.3	1473.7	1.9	1465.5	14.1
1453.9	3.9	1463.5	2.7	1450.1	4.5	1463.6	3.6	1462.6	2.7
1417.1	4.7	1420.2	3.8	1424.1	3.2	1414.4	65.7	1415.6	6.0
1395.5	6.5	1383.6	17.6	1380.4	65.5	1385.2	16.8	1392.5	3.9
1375.9	36.9	1375.2	46.8	1372.6	28.9	1379.0	5.3	1371.8	34.6
1371.2	8.0	1372.6	28.4	1367.3	1.3	1370.6	4.0	1366.9	11.8
1305.4	18.6	1304.2	17.9	1309.2	6.3	1316.0	6.7	1298.4	34.6
1278.6	130.1	1274.9	122.5	1276.8	104.3	1292.7	9.8	1273.3	110.1
1244.3	2.4	1243.8	8.0	1243.8	1.1	1237.0	14.3	1238.4	3.9
1235.6	30.8	1229.8	60.3	1231.3	50.3	1235.0	206.9	1222.8	25.5
1216.3	9.8	1219.2	9.8	1214.3	19.7	1218.4	7.0	1217.6	30.3
1206.1	1.2	1199.4	0.5	1208.1	0.7	1203.9	0.6	1201.3	0.2
1195.1	16.3	1196.4	12.2	1196.9	17.3	1182.1	10.5	1184.7	2.7
1176.4	7.4	1189.2	7.1	1181.5	3.9	1173.0	8.1	1174.2	2.9
1171.9	6.9	1179.8	14.3	1174.7	26.6	1168.0	2.2	1170.5	7.1
1154.3	9.2	1171.6	11.4	1151.3	22.4	1166.0	32.6	1165.3	11.9
1129.7	1.0	1125.6	0.3	1127.5	1.0	1119.1	1.1	1115.4	0.3
1086.8	47.3	1087.5	17.7	1083.1	9.3	1084.8	4.2	1079.8	2.9
1081.0	5.9	1075.5	4.0	1082.9	4.4	1061.9	0.2	1059.4	26.8
1050.5	6.9	1057.5	1.7	1067.2	20.4	1057.1	2.4	1055.9	1.1
1046.8	8.9	1050.5	3.8	1051.6	19.3	1050.4	2.6	1045.4	5.1
1011.7	0.4	1013.6	0.3	1026.9	0.6	1008.6	0.0	1011.5	0.1
1001.2	35.6	1005.2	72.8	1019.3	70.8	996.6	14.1	986.3	2.7
987.1	1.6	988.0	1.6	992.5	1.6	989.8	1.0	977.5	52.8
964.8	0.3	966.0	0.1	968.8	0.0	974.8	1.1	960.3	0.1
952.1	90.0	946.7	105.8	953.2	77.2	924.3	72.1	925.1	94.1
903.1	6.2	913.3	3.3	903.5	0.3	909.8	13.2	909.8	10.2
895.7	5.1	900.5	2.0	896.0	0.1	888.9	26.5	893.8	24.9
886.0	0.6	887.1	3.4	891.7	12.0	886.2	26.7	882.3	15.9
838.8	28.6	869.6	4.4	829.5	14.7	855.5	14.7	857.9	8.2
822.7	47.5	827.8	50.5	828.5	58.2	841.7	45.1	826.0	6.1
816.3	10.5	821.7	14.9	815.1	10.8	824.5	3.2	823.5	51.3
803.4	3.5	799.1	1.5	801.5	0.7	808.0	1.8	813.1	6.2
794.1	2.5	778.6	2.6	791.5	13.7	782.8	0.6	779.6	0.2
766.0	10.7	764.2	27.0	767.4	25.0	764.8	25.9	762.9	18.6
764.0	21.2	749.9	8.0	762.1	2.8	747.8	15.2	745.5	15.0
735.5	4.8	721.5	4.6	735.6	6.6	736.4	4.8	734.8	11.9
684.6	13.9	691.0	10.2	690.3	10.1	687.6	7.8	686.3	8.2
664.9	4.8	626.2	7.7	654.2	5.9	660.8	6.5	659.1	2.6
582.2	10.0	596.5	15.2	584.2	7.3	627.7	9.3	625.9	1.1
578.5	12.7	574.5	5.8	576.2	10.3	572.8	1.6	556.3	2.3
544.4	0.5	543.4	2.0	546.4	2.4	565.4	67.5	539.9	2.8
541.8	2.6	532.5	0.3	544.9	0.9	534.7	14.3	530.0	1.9
459.6	5.1	461.4	2.0	487.8	17.9	529.5	18.3	518.1	6.1
442.2	5.2	451.4	4.0	455.9	3.3	518.0	5.9	463.8	1.6
439.6	2.5	437.8	3.3	437.8	3.0	461.5	1.7	438.4	2.8
420.5	0.6	418.1	2.0	409.4	0.6	441.4	1.4	427.3	4.4
383.3	9.0	367.3	39.7	366.8	66.7	429.9	2.3	356.0	5.0
363.1	71.9	356.1	38.7	341.5	0.6	355.1	3.7	334.3	2.5
318.9	11.0	332.4	16.8	325.7	14.0	311.7	10.6	310.0	40.9
289.4	5.9	282.9	1.9	319.9	6.5	309.1	2.8	304.8	42.4
244.5	3.8	265.0	3.1	232.8	3.0	265.8	1.2	267.4	2.7
207.7	2.3	236.8	3.3	197.1	0.1	237.5	3.2	227.1	8.6
156.2	2.6	175.8	5.0	157.9	3.0	167.1	0.9	159.8	0.5
140.6	3.5	139.6	1.2	126.9	0.0	163.9	1.5	150.3	1.0
115.6	2.0	112.4	1.8	112.0	1.6	112.7	0.2	125.0	0.6
89.9	0.6	76.2	1.7	100.6	1.8	90.0	1.1	83.0	0.5
54.8	1.5	61.5	1.1	51.4	0.4	66.9	0.4	68.1	0.7
16.2	0.5	19.2	1.7	12.6	0.4	42.4	1.5	31.7	1.4

Table E.2 (Cont.)

E11		K1		K2		K3		K4	
v	I	v	I	v	I	v	I	v	I
3836.1	148.2	3221.8	8.5	3227.3	10.5	3238.3	1.9	3236.9	2.3
3255.4	0.7	3207.1	0.6	3214.2	0.7	3230.6	1.7	3215.8	8.6
3219.8	2.2	3204.5	5.7	3204.4	6.1	3217.0	2.6	3200.5	0.3
3197.5	5.2	3190.2	2.7	3190.0	9.3	3194.5	9.3	3194.9	6.7
3185.1	17.2	3189.6	11.5	3187.0	19.1	3188.0	17.3	3188.2	40.0
3178.6	10.8	3186.8	22.9	3186.7	9.7	3169.8	6.9	3187.4	15.6
3170.5	8.5	3168.5	12.6	3168.8	10.2	3160.6	6.2	3170.6	22.8
3162.5	11.6	3159.7	5.7	3160.0	7.0	3151.9	8.1	3160.8	6.1
3159.3	0.8	3151.0	5.9	3156.5	106.9	3149.9	80.2	3156.3	50.7
3148.4	9.6	3132.3	6.3	3150.8	6.9	3137.9	11.2	3152.4	2.2
3139.8	13.0	3130.1	11.2	3135.0	8.1	3135.9	11.3	3123.7	6.8
3133.7	12.4	3098.2	93.6	3133.2	12.5	3087.5	24.3	3122.4	1.8
1658.4	19.2	1655.6	131.3	1655.4	133.9	1670.2	377.7	1668.8	338.4
1654.1	34.1	1643.9	6.2	1643.3	9.3	1646.0	10.0	1645.1	10.4
1642.1	16.7	1606.3	76.6	1607.1	89.6	1620.6	47.5	1619.7	38.0
1607.8	4.5	1579.8	22.7	1580.5	24.2	1583.2	19.3	1583.9	17.1
1545.2	38.7	1555.3	592.3	1552.5	485.9	1566.3	167.8	1564.0	84.6
1505.9	8.0	1516.8	10.6	1516.6	14.0	1512.6	75.9	1514.9	5.5
1497.3	0.6	1504.6	9.9	1495.4	4.1	1498.3	268.0	1503.0	115.6
1470.9	5.7	1481.9	56.1	1482.3	47.4	1494.7	56.3	1497.4	264.0
1464.5	13.3	1470.4	3.3	1457.4	4.8	1463.4	16.4	1479.6	3.9
1416.6	11.0	1435.5	2.1	1434.6	1.6	1458.8	239.5	1458.3	200.3
1389.3	4.0	1428.3	21.1	1431.6	5.9	1432.6	16.2	1430.9	26.1
1384.2	1.6	1367.5	1.7	1411.8	48.1	1424.8	65.0	1425.4	19.8
1365.7	50.2	1361.0	86.2	1352.2	8.2	1369.3	22.6	1372.9	29.8
1298.3	30.1	1346.7	65.4	1344.0	23.8	1348.1	2.9	1348.3	0.4
1275.2	138.5	1329.8	125.1	1314.5	274.6	1324.8	34.2	1324.1	47.9
1238.0	3.2	1278.7	49.9	1277.4	44.9	1281.3	111.9	1279.0	176.4
1223.6	53.8	1242.1	27.0	1245.3	16.8	1240.1	65.0	1240.4	71.2
1216.0	34.8	1232.1	4.8	1236.5	67.4	1226.1	23.6	1227.5	4.3
1203.4	2.1	1210.5	29.5	1222.9	15.6	1209.8	12.5	1209.6	9.3
1184.5	0.4	1197.5	0.5	1201.4	0.6	1200.0	5.5	1203.8	2.9
1174.7	5.7	1196.7	26.8	1183.6	10.0	1198.8	16.9	1186.5	13.1
1168.2	16.9	1179.2	45.0	1160.3	7.6	1184.9	4.6	1160.3	17.4
1150.3	9.5	1161.1	7.2	1138.3	27.7	1159.6	23.9	1147.6	22.3
1132.5	6.8	1124.0	1.3	1119.1	0.9	1115.8	0.7	1130.4	2.7
1086.9	8.1	1119.4	5.0	1103.2	0.5	1109.3	1.3	1112.4	5.8
1055.2	28.2	1079.4	5.2	1081.0	4.3	1073.6	0.0	1074.0	4.4
1053.2	9.7	1061.4	3.2	1061.5	7.3	1071.7	7.7	1072.3	14.1
1045.6	10.2	1055.3	16.4	1054.9	26.2	1054.1	6.4	1049.5	15.6
1009.8	2.9	1015.7	0.1	1030.1	4.1	1050.8	28.6	1035.9	90.9
985.0	4.3	1015.1	4.1	1015.7	0.1	1033.2	38.3	1034.6	20.2
975.4	53.1	1011.6	0.3	1010.6	0.1	1015.6	1.7	1016.1	0.2
958.2	0.8	979.5	2.4	981.8	59.7	1012.2	0.7	1013.8	0.3
942.0	34.7	962.7	75.8	978.7	2.3	977.9	2.4	979.4	3.1
896.7	36.5	918.9	4.9	922.1	7.1	956.6	146.2	966.7	62.7
887.1	0.5	899.8	3.8	897.5	0.0	909.8	2.1	903.8	1.4
861.3	1.1	891.4	64.8	881.6	28.3	902.1	1.1	894.3	1.4
844.7	21.3	888.1	20.2	878.1	83.0	896.8	1.1	890.5	7.8
834.6	9.0	867.1	19.7	856.3	1.1	870.0	10.9	859.1	49.0
815.8	43.8	863.7	12.9	814.7	4.3	859.1	54.8	829.8	13.1
793.8	3.4	810.4	3.8	811.3	17.2	809.7	0.9	810.5	0.4
770.8	24.9	809.0	14.8	798.6	0.5	803.5	11.6	799.3	6.6
761.5	20.9	772.9	2.4	786.8	0.3	780.5	6.9	786.0	10.9
738.2	5.3	771.4	42.8	770.6	40.4	771.7	41.4	772.7	40.8
718.8	8.1	758.0	3.7	760.9	13.9	753.8	14.2	755.5	9.0
683.8	6.4	726.2	3.9	736.1	4.4	726.3	1.2	735.7	2.2
660.3	3.8	708.6	5.3	705.2	5.6	699.3	0.7	698.9	0.3
628.9	3.9	655.3	5.8	661.4	4.4	622.1	9.4	644.0	2.6
569.4	6.1	558.6	1.0	587.4	3.2	605.0	14.8	598.2	10.7
550.4	1.6	557.2	5.0	557.1	3.6	572.3	2.9	571.8	1.8
537.0	1.8	541.8	16.8	537.1	19.0	544.6	5.9	543.6	2.5
511.8	4.0	511.4	5.4	536.2	6.3	527.2	12.1	535.3	8.5
452.0	4.1	479.6	0.6	472.0	12.2	474.4	0.3	479.3	34.8
438.7	2.1	441.3	0.2	443.3	2.0	440.5	1.3	443.0	3.8
430.7	1.3	433.5	6.3	432.7	6.3	437.9	10.3	440.4	8.5
362.9	3.4	414.8	2.0	431.6	0.5	412.1	9.2	411.2	2.6
318.5	20.1	373.8	3.5	416.2	1.6	364.4	12.0	354.5	3.0
307.1	80.2	371.9	3.6	369.4	3.0	352.1	3.0	353.6	4.5
306.3	0.8	330.3	14.1	287.9	1.3	264.1	7.2	329.4	3.9
270.6	8.6	280.9	0.8	282.5	0.7	263.3	0.7	263.5	8.8
233.6	9.4	219.8	2.3	218.5	2.9	257.4	7.6	213.8	0.6
161.3	3.7	200.9	4.8	205.7	4.1	202.8	2.6	185.5	0.0
146.8	1.7	128.4	0.1	137.0	0.4	142.4	1.6	151.0	2.6
119.8	0.9	111.8	0.0	109.9	0.0	98.6	0.8	105.5	0.1
69.6	0.5	92.6	0.9	92.7	0.5	84.3	2.6	95.8	2.3
41.5	1.0	52.6	1.4	62.3	1.4	68.8	2.4	65.2	1.8
32.2	1.1	17.6	0.1	27.1	0.2	45.9	0.4	10.9	1.9

E.1 CPDNO Supporting Information

Table E.2 (Cont.)

K5		K6		K7		K8		K9	
ν	I	ν	I	ν	I	ν	I	ν	I
3586.8	73.7	3463.8	3.0	3467.4	5.9	3569.5	62.0	3293.5	112.1
3223.7	8.0	3230.4	10.5	3229.9	6.0	3232.6	11.1	3234.5	2.6
3206.5	5.1	3211.7	4.9	3213.4	5.3	3206.6	4.5	3220.3	0.3
3204.9	4.2	3200.7	5.8	3199.5	5.9	3198.5	7.8	3217.9	3.8
3188.0	7.6	3191.1	7.4	3190.7	7.7	3187.3	8.0	3193.6	8.5
3187.0	21.8	3189.2	16.9	3189.0	17.2	3186.9	30.0	3189.9	18.6
3179.8	4.0	3173.0	6.3	3172.5	7.0	3169.1	15.0	3177.9	4.3
3169.4	12.7	3163.1	6.9	3165.5	13.9	3159.8	5.4	3169.7	9.9
3160.2	5.1	3150.0	8.1	3162.7	7.9	3155.2	4.0	3161.4	8.0
3149.2	7.6	3145.2	6.4	3149.6	8.1	3148.5	8.8	3152.7	6.0
3137.5	3.7	3133.4	10.7	3137.7	11.8	3146.8	11.5	3140.0	7.4
3125.0	13.6	3112.4	30.1	3129.3	10.8	3116.4	18.7	3137.6	8.2
1674.5	323.9	1719.5	295.8	1710.4	305.2	1681.6	318.8	1662.2	328.2
1654.3	7.2	1659.9	9.7	1659.4	8.3	1654.7	15.5	1644.8	7.2
1631.4	38.7	1629.7	4.7	1629.0	7.1	1632.2	27.3	1618.2	58.4
1586.3	7.4	1593.3	3.7	1592.4	2.9	1592.2	50.1	1582.3	50.7
1580.4	77.7	1563.2	234.1	1559.7	315.8	1585.7	23.0	1555.2	80.4
1511.9	10.1	1519.5	15.1	1521.0	121.4	1511.8	12.5	1519.9	75.9
1504.6	3.0	1502.0	60.3	1503.0	1.4	1503.0	7.4	1504.0	176.1
1486.4	26.6	1487.7	12.5	1484.8	8.5	1488.0	69.2	1490.8	151.4
1471.1	31.3	1480.7	5.2	1477.5	16.0	1471.2	273.4	1480.1	9.2
1467.0	247.6	1467.5	3.1	1458.0	5.1	1468.4	38.2	1464.7	3.5
1430.3	21.4	1425.5	8.7	1426.4	12.2	1430.2	21.0	1429.1	43.5
1365.6	42.7	1388.9	150.9	1416.1	4.2	1385.2	60.6	1400.6	90.2
1351.4	40.3	1338.2	0.4	1339.5	3.8	1351.1	17.4	1384.6	81.3
1323.3	25.0	1323.7	9.6	1325.3	20.8	1321.9	13.3	1347.9	3.4
1310.9	2.2	1288.6	25.1	1308.5	48.3	1310.0	1.0	1317.0	23.7
1260.7	16.2	1256.4	82.7	1259.1	65.9	1260.5	17.7	1284.1	28.7
1239.3	14.7	1243.4	24.3	1240.2	15.0	1237.7	14.4	1237.7	56.4
1230.6	16.8	1232.3	14.9	1229.9	6.5	1225.2	2.5	1215.0	2.1
1200.9	61.8	1196.8	16.4	1202.5	97.2	1210.4	58.9	1204.8	0.3
1191.5	3.8	1193.6	1.3	1200.0	21.8	1192.9	1.4	1193.6	57.0
1183.5	5.8	1190.2	0.8	1190.6	9.3	1185.2	2.9	1187.4	0.9
1171.7	0.2	1171.2	90.2	1154.6	15.1	1182.7	12.1	1168.5	6.1
1155.4	5.3	1153.2	26.3	1139.9	9.9	1155.4	6.6	1158.6	39.3
1122.3	4.9	1132.5	0.8	1119.4	11.0	1120.5	2.8	1119.1	0.3
1105.8	28.0	1115.2	43.8	1099.5	12.5	1106.7	22.6	1099.6	10.2
1079.0	3.7	1080.4	1.5	1089.7	7.2	1075.7	7.7	1082.9	5.5
1062.6	2.3	1077.2	20.2	1079.1	5.9	1062.7	4.1	1071.0	4.6
1053.4	16.3	1058.3	10.1	1053.7	13.7	1057.8	5.0	1052.3	7.4
1022.7	17.7	1045.6	3.1	1043.5	19.4	1017.7	1.6	1033.3	15.4
1016.8	0.4	1021.1	0.6	1020.8	0.5	1013.4	0.2	1013.8	0.1
1013.3	0.6	1012.4	1.1	1010.4	0.6	1008.6	10.5	1005.7	0.7
988.6	2.6	986.2	4.4	984.4	0.4	980.4	2.2	995.8	38.7
981.1	2.3	980.2	4.7	976.1	5.0	976.5	7.0	972.7	4.4
943.5	5.0	955.6	6.4	929.2	16.7	931.7	27.4	933.3	241.9
901.8	0.7	909.3	4.8	907.2	3.6	901.5	0.5	901.6	11.7
866.3	36.5	882.4	14.3	884.4	16.2	873.1	39.4	892.2	17.0
860.9	10.4	862.0	39.2	862.4	40.2	860.6	28.3	882.8	16.2
851.6	20.3	851.5	7.2	823.8	15.2	852.2	6.2	858.0	39.3
834.0	1.2	830.8	5.2	817.8	7.2	827.2	11.0	851.6	27.9
814.6	10.5	818.3	9.7	809.0	3.3	813.4	6.0	811.0	8.5
777.5	3.3	779.4	16.1	781.0	9.6	772.1	42.0	797.7	1.3
772.6	37.9	772.7	14.9	771.0	20.8	762.5	14.9	781.4	7.1
754.1	3.8	753.2	8.3	755.0	8.8	752.8	2.6	766.1	41.3
722.9	23.8	722.8	1.2	730.2	1.5	716.8	17.8	749.6	17.9
700.7	19.0	701.0	4.6	701.0	4.5	694.4	14.5	725.2	13.4
687.1	2.9	648.8	106.6	643.0	104.1	686.3	10.1	697.9	0.5
644.8	35.6	627.7	10.6	639.8	3.6	649.0	73.9	674.1	31.7
560.4	11.0	587.3	1.8	589.8	5.1	555.2	0.9	593.4	7.6
555.8	1.6	559.5	45.0	556.6	31.1	552.1	5.5	584.6	42.2
539.0	14.6	524.1	18.1	535.5	5.5	535.9	20.0	553.1	1.6
509.2	18.4	513.1	41.5	509.6	65.7	513.4	72.9	539.7	7.7
468.4	41.3	468.4	4.9	484.4	26.9	467.9	21.8	492.8	11.3
452.8	0.9	446.8	1.7	439.8	4.6	452.5	31.4	466.7	6.5
432.1	4.1	436.5	2.9	434.6	5.5	429.9	3.2	442.5	10.8
414.3	5.0	417.5	1.6	421.4	14.3	402.6	1.9	416.2	3.3
355.1	2.0	353.4	3.0	359.1	3.4	352.4	10.5	364.0	14.5
335.8	14.0	329.1	13.2	328.0	0.6	342.1	19.2	327.5	4.4
291.3	3.9	289.9	4.0	317.4	7.4	292.4	1.1	296.2	2.5
281.3	3.4	238.7	3.7	235.7	1.0	278.3	1.9	276.1	2.0
212.1	4.5	219.5	8.6	198.9	4.5	208.4	4.4	218.3	5.1
189.4	8.7	179.9	2.5	187.5	2.0	171.5	7.5	181.6	0.9
169.3	0.5	145.4	0.4	151.1	1.3	164.9	1.6	177.3	0.3
116.0	0.7	92.2	0.9	90.1	1.7	116.5	1.3	106.2	1.8
85.4	1.9	85.8	2.4	87.8	2.0	78.7	0.8	85.9	0.5
45.0	0.8	49.2	1.9	57.3	2.0	49.6	2.5	63.5	0.4
39.9	0.5	36.5	0.2	35.4	0.6	48.2	3.5	58.5	0.6

Table E.2 (Cont.)

K10		K11		K12		K13	
v	I	v	I	v	I	v	I
3460.0	21.4	3324.0	0.4	3564.0	52.1	3334.9	9.4
3240.8	2.6	3233.9	2.4	3220.0	3.4	3222.9	9.5
3222.8	1.0	3220.6	0.5	3218.6	7.7	3200.0	3.7
3204.4	6.4	3191.7	17.9	3202.0	1.3	3192.1	16.3
3191.1	19.5	3190.1	9.7	3189.8	7.2	3191.1	8.7
3188.4	9.1	3174.6	13.8	3188.3	18.6	3175.5	13.4
3175.1	14.8	3162.1	7.5	3171.1	9.8	3163.0	6.7
3161.8	6.0	3149.9	8.5	3161.6	5.5	3150.5	8.6
3154.8	8.5	3143.7	12.2	3153.8	2.3	3146.1	11.3
3150.6	7.3	3138.6	11.9	3148.7	8.8	3136.3	11.7
3150.0	5.6	3136.7	10.1	3130.2	5.3	3125.1	9.0
3137.2	9.7	3043.8	36.0	3122.2	12.3	3123.9	9.3
1655.4	163.8	1671.6	247.3	1726.6	306.0	1674.4	286.4
1641.3	10.1	1649.1	0.3	1656.2	12.2	1651.4	0.6
1613.9	114.2	1631.7	26.5	1631.2	10.0	1631.3	33.9
1583.0	36.4	1602.9	78.0	1613.9	162.4	1599.7	27.3
1563.5	39.3	1573.1	90.4	1589.9	26.8	1571.1	90.9
1523.1	2.9	1517.7	52.7	1513.7	46.2	1519.5	31.1
1498.3	80.2	1494.4	3.6	1503.8	3.0	1502.1	3.4
1480.4	50.2	1483.7	4.5	1493.8	155.0	1485.0	6.0
1478.3	124.1	1463.0	4.0	1482.0	8.8	1469.3	14.3
1464.7	3.6	1441.4	514.6	1467.1	4.4	1433.2	403.5
1428.0	11.7	1427.5	77.3	1422.3	9.6	1427.5	208.5
1396.1	6.3	1409.5	51.2	1385.9	55.2	1397.1	11.0
1360.4	13.1	1371.9	21.1	1336.8	1.9	1367.1	81.1
1356.8	44.0	1361.1	63.8	1318.8	1.3	1351.4	131.0
1336.2	95.1	1341.8	42.6	1280.3	20.2	1339.1	83.4
1279.3	54.2	1276.7	23.6	1248.7	32.9	1277.2	14.0
1238.2	29.1	1235.6	43.0	1232.7	43.3	1236.9	47.3
1218.3	6.4	1227.7	21.0	1223.5	1.2	1224.8	0.3
1209.3	41.9	1206.5	5.6	1200.9	10.2	1207.8	9.4
1200.4	0.6	1202.0	0.4	1195.2	13.4	1194.2	6.2
1188.7	9.0	1197.3	4.7	1187.2	0.4	1193.6	5.9
1178.6	12.8	1191.9	5.3	1170.5	30.5	1161.9	10.1
1161.3	6.6	1161.5	8.0	1147.5	17.3	1151.0	9.8
1100.7	5.0	1110.2	4.8	1125.2	2.0	1127.3	7.7
1098.1	1.0	1102.4	0.1	1092.5	52.0	1111.5	2.5
1069.6	2.2	1074.2	5.7	1083.9	2.7	1081.9	4.2
1068.7	3.9	1072.6	5.2	1066.8	1.5	1073.5	3.6
1047.7	9.4	1057.2	13.8	1060.5	8.7	1047.5	14.0
1011.7	0.8	1018.8	20.5	1019.3	0.7	1028.8	0.8
1005.9	6.8	1013.8	0.1	1016.3	4.5	1015.5	0.1
998.9	0.0	996.8	0.1	1010.2	2.5	999.0	0.1
966.1	2.9	963.4	3.0	982.2	1.6	972.2	3.2
936.3	128.3	951.7	148.2	978.5	4.2	965.2	8.2
914.2	231.1	934.6	70.7	935.1	35.1	957.2	59.4
891.5	53.4	895.3	3.4	904.5	3.4	925.3	19.2
880.9	2.8	879.1	22.0	879.7	27.7	877.8	11.0
857.9	16.2	874.7	7.9	858.8	29.9	867.0	3.7
851.7	17.5	864.3	25.5	851.2	9.6	854.8	33.3
837.3	123.7	852.7	33.1	822.4	6.0	830.3	10.1
798.3	13.3	800.0	7.1	817.4	6.8	811.3	12.1
788.0	2.4	792.4	4.2	775.6	16.7	793.5	0.1
776.8	19.8	784.1	1.4	772.3	12.3	780.4	3.2
765.1	39.5	760.7	24.9	753.1	15.4	760.2	44.1
755.8	18.9	756.1	27.9	714.0	28.9	754.8	6.3
726.4	16.4	721.6	0.8	701.0	2.0	724.9	1.7
692.0	23.4	695.5	0.5	690.9	24.3	697.2	0.4
680.0	3.1	656.5	8.1	609.6	115.1	658.5	8.3
588.7	15.3	559.6	0.5	598.6	32.1	570.5	2.1
560.3	3.1	549.1	0.9	564.3	8.2	549.6	0.1
552.0	3.0	532.4	5.4	534.1	9.3	541.0	7.8
535.3	0.8	507.9	7.5	524.4	37.3	520.3	4.7
497.3	17.3	474.9	7.2	477.4	9.2	458.4	10.0
464.0	17.9	437.4	3.2	436.0	4.1	443.6	4.3
435.1	5.3	430.2	5.6	425.4	23.6	430.0	6.8
407.8	1.0	398.4	2.3	405.7	0.7	404.0	3.3
352.0	3.4	360.2	2.6	358.5	9.3	370.8	1.0
348.1	10.6	326.8	6.4	323.3	10.7	330.0	11.3
305.2	4.8	297.1	6.4	290.9	1.6	303.0	2.4
277.6	0.2	261.4	6.5	269.1	5.2	262.1	1.6
213.6	7.7	217.5	2.8	203.6	2.0	217.4	7.0
173.8	1.2	173.5	0.3	175.4	1.6	166.3	2.6
164.3	0.1	127.9	2.1	162.0	0.6	127.5	2.4
133.5	1.2	98.0	0.8	91.8	1.4	95.2	1.8
77.9	2.1	72.4	1.6	82.3	1.3	72.1	3.2
54.2	0.8	48.5	3.2	63.2	1.2	40.8	2.9
52.8	1.3	43.9	1.5	52.5	0.9	32.9	1.2

Additional References

Polavarapu, P. L. *J. Phys. Chem.* **1990**, *94*, 8106–8112.

Michalska, D.; Wysokiński, R. *Chem. Phys. Lett.* **2005**, *403*, 211–217.

E.2 CPDNO Paper

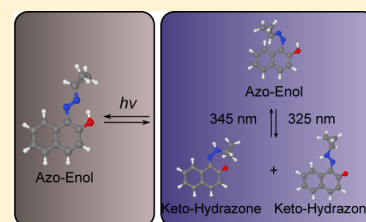
Tautomers and UV-Induced Photoisomerization of a Strongly Intramolecularly H-Bonded Aromatic Azo-Dye: 1-(Cyclopropyl)diazo-2-naphthol

Luis Duarte,* Barbara Michela Giuliano, Igor Reva, and Rui Fausto

Department of Chemistry, University of Coimbra, P-3004-535 Coimbra, Portugal

Supporting Information

ABSTRACT: Aromatic azo compounds have a wide range of industrial applications as dyes in optical and color-changing materials and can also be exploited in the design of new photodynamic molecular systems. The azo derivative 1-(cyclopropyl)diazo-2-naphthol was isolated in low-temperature cryogenic matrices, and its molecular structure, tautomeric equilibrium, and photochemical transformations were characterized by infrared spectroscopy and theoretical calculations. Only azo–enol forms having the OH group involved in a strong intramolecular hydrogen bond, forming a six-membered ring with the azo group, were found experimentally. Irradiation with a narrowband source in the near-UV range generates different rotameric and tautomeric azo–enol and keto–hydrazone forms that can be interconverted at different irradiation wavelengths.



INTRODUCTION

Aromatic azo compounds have a wide range of industrial applications as dyes in optical and color-changing materials such as sunglasses, textiles, paints, cosmetics, and food additives.¹ These compounds usually undergo reversible *E–Z* (“Entgegen”–“Zusammen”) photoisomerization which can also be exploited in the design of new dynamic molecular systems (photo-switches, molecular motors, etc.),^{2–5} and even in the development of potential photothermal sensitizers in the photodynamic therapy of some forms of cancer and other diseases.^{6,7} The aromatic compounds having azo ($-\text{N}=\text{N}-$) and hydroxyl groups in ortho or para positions may give rise to two distinct tautomeric structures: azo–enol (OH) or keto–hydrazone (NH), which may coexist under certain experimental conditions. These tautomeric structures can be stabilized by intramolecular hydrogen bonds, and the equilibrium between the two can be further explored in signaling and switching.^{8,9} Thus, detailed knowledge on the structures and photochemical behavior of such compounds is crucial for understanding their reactivity and particularly important from the viewpoint of their applications.

Several theoretical and experimental studies on the azo–hydrazone tautomeric equilibrium can be found in the literature.^{10–18} However, due to the dependence of the tautomeric forms on the surrounding chemical environment, their structural and spectroscopic characterizations are not trivial. Indeed, many issues concerning the relative stability of these species and related with the intramolecular proton transfer that interconvert them into each other remain unclear. Thereby, the matrix isolation technique emerges as a convenient way of obtaining information on the conformational and tautomeric preferences in such systems. In this method, the molecules under study are embedded in a solidified noble gas (usually argon at 10–15 K); under these conditions, the effects of

external factors like solvent–solute or solute–solute intermolecular interactions on the structures and chemical behavior of the possible conformers and tautomers are usually less prominent. In addition, due to the almost absent interaction with the environment, the experimental spectra can then be directly compared with theoretical calculations performed for the individual solute molecule in vacuo. This allows attaining a solid theoretical basis for the interpretation of the experimental data. Moreover, due to the absence of molecular diffusion, the photochemical rearrangements taking place upon in situ excitation of a matrix-isolated species are in general reduced to unimolecular transformations. Such a fact introduces a very useful simplification in the study of mechanistic details of the observed photochemical processes and facilitates the identification of the formed photoproducts.

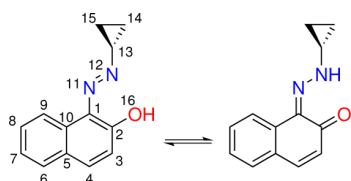
In this work, we studied and characterized, by infrared (IR) spectroscopy, the structure and UV-induced phototransformations of a cycloalkyl azo naphthol: 1-(cyclopropyl)diazo-2-naphthol¹⁹ (or 1-(cyclopropyldiazenyl)naphthalen-2-ol; CPDNO; Scheme 1) isolated in cryogenic rare gas matrices. The amount of information available concerning the photochemical behavior of this type of mixed aliphatic–aromatic azo compounds is considerably less than for other typical azo compounds with aromatic substituents. This particular compound, which has a cyclopropyl group instead of the more usual rigid aromatic substituents, can exhibit a different range of conformational possibilities that, together with the azo/hydrazone tautomerism, could be pertinent for the development of new azo-based systems. The structures of the starting compound and of the generated photoproducts were established with help of theoretical

Received: May 22, 2013

Revised: September 20, 2013

Published: September 23, 2013

Scheme 1. Structures for the Azo–Enol (E) and Keto–Hydrazone (K) Forms of CPDNO, with Numbering of Heavy Atoms



calculations carried on at the density functional theory (DFT) (B3LYP)/6-311+G(2df,2p) level of approximation.

MATERIALS AND METHODS

Experimental Section. The studied compound was sublimated from a miniature glass oven placed in the vacuum chamber of the cryostat, and the vapor of the compound deposited together with a large excess of matrix gas (argon N60 or xenon N48; both supplied by Air Liquide), onto a CsI window cooled to 15 K (Ar) or 30 K (Xe) by a closed-cycle helium refrigerator with an APD Cryogenics DE-202A expander. The temperature of the CsI window was measured directly at the sample holder by a silicon diode temperature sensor connected to a digital temperature controller (Scientific Instruments, model 9650-1), which provides an accuracy of 0.1 K. The matrix isolation infrared spectra were recorded in the 4000–400 cm^{-1} range, using a Nicolet 6700 FTIR spectrometer equipped with a deuterated triglycine sulfate (DTGS) detector and a Ge/KBr beam splitter, with 0.5 cm^{-1} spectral resolution. The matrices were irradiated through an outer quartz window of the cryostat using narrowband tunable (0.2 cm^{-1} spectral width) frequency-doubled signal beam provided by a Quanta-Ray MOPO-SL optical parametric oscillator, pumped with a pulsed (repetition rate = 10 Hz, pulse energy \approx 1 mJ, duration = 10 ns) Nd:YAG laser.

Computational Details. The quantum chemical calculations were performed at the B3LYP^{20,21} level of theory, using the 6-311+G(2df,2p) basis set. Geometrical parameters were optimized using the Lebedev angular (nrad = 96, nleb = 590) grid²² and the quadratic approximation optimization algorithm together with an SCF density convergence criterion of 1×10^{-6} Hartree and an gradient convergence criterion of 1×10^{-5} Hartree/Bohr. The geometry optimization was followed by harmonic frequency calculation at the same theory level, and the nature of the obtained stationary points was checked through analysis of the corresponding Hessian matrix. No imaginary frequencies were found. Anharmonic corrections for selected modes of isomers E1 and K1 were carried out with the vibrational self-consistent field method (VSCF)²³ combined with the quartic force field approximation (QFF).²⁴ All calculations were carried out using the 11 Aug 2011 (R1) version of the Gamess-US program.^{25,26}

RESULTS AND DISCUSSION

Potential Energy Surface of CPDNO. The studied molecule, CPDNO, has two rigid units, the aromatic naphthol ring and the alkyl (cyclopropane) ring. The molecule may adopt azo–enol (E) or keto–hydrazone (K) tautomeric forms (Scheme 1). For each tautomer, several conformers are possible due to the different relative arrangements of the two rings around the azo (or hydrazone) group. Additionally, in the case of the E tautomer, several conformers may arise due to the

internal rotation of the hydroxyl group. Hereafter, the conformers will be named by letters E or K designating the respective tautomer, followed by numbers (in the increasing energy order) designating conformers within each tautomer.

Taking into account both E and K tautomeric forms, the performed theoretical calculations predicted more than 20 minima on the ground electronic state potential energy surface of CPDNO. The optimized geometries and relative energies of the CPDNO isomers most relevant for the present discussion are shown in Figure 1. All of the optimized structures, their energies, and Cartesian coordinates are given in the Supporting Information (Figures S1, S2 and Table S1).

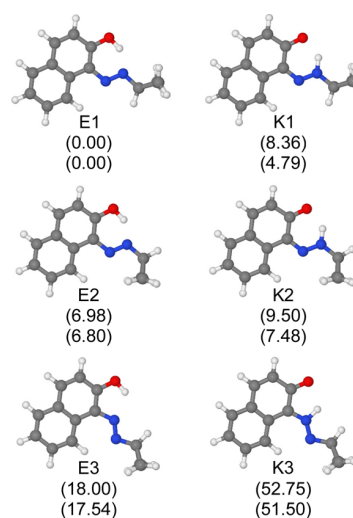


Figure 1. Most stable isomeric forms of CPDNO calculated at the B3LYP/6-311+G(2df,2p) level of theory. The relative energies, in kJ mol^{-1} , with the zero point correction (top) and with thermal correction to Gibbs free energy at 298 K (bottom) are given below each structure.

The two-dimensional potential-energy landscape of E-form of CPDNO as a function of the C–C–O–H and C–C–N=N dihedal angles is shown in Figure 2. This surface was calculated

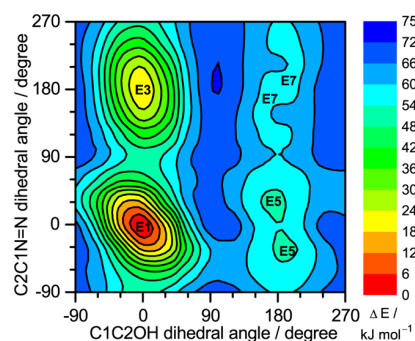


Figure 2. Contour map of the relaxed potential energy surface of CPDNO calculated at the B3LYP/6-311+G(2df,2p) level of theory as a function of the C–C–O–H and C–C–N=N dihedal angles. Relative energy is calculated with respect to the lowest energy ground state (E1) form. Atom numbering is shown in Scheme 1.

on a two-dimensional grid of 144 points where the reaction coordinates (the two dihedal angles specified above) assumed

all values between 0 and 360°, with an increment of 30°. With the two dihedral angles incrementally fixed, all remaining parameters were optimized. Before focusing on these two structurally most relevant internal rotation degrees of freedom, we shall consider the relative energies of possible minimum energy structures differing in the arrangements about the CNNC and NNCH fragments.

The optimized values of the CNNC and NNCH dihedral angles conserved trans and cis orientations, respectively. Structures E1, E3, E5, and E7 have the NNCH dihedral angle in the cis orientation. Their less stable E2, E4, E6, and E8 counterparts (not shown in Figure 2) have the NNCH dihedral angle in the trans orientation (i.e., have the cyclopropane group rotated by $\approx 180^\circ$; see Figure 1 and Figure S1 in the Supporting Information). The higher stability of the NNCH cis forms can be explained by taking into account two factors: (i) negative hyperconjugation (Bohlmann effect). It occurs when the lone pair on the nitrogen is anti coplanar to a *geminal* CH bond (i.e., both N and H atoms are attached to the same carbon atom);^{27,28} (ii) the additional stabilizing interaction between the lone pair of the nitrogen atom *vicinal* to the CH group and the positively charged hydrogen atom of the latter moiety. These two stabilizing interactions are present in E1, E3, E5, and E7 and absent in E2, E4, E6, and E8.

Regarding the CNNC dihedral angle: the azo group can adopt two orientations around the N=N bond, trans (or “entgegen”) and cis (“zusammen”). The cis structures are energetically unfavorable because of two reasons. First, the two adjacent nitrogen atoms having the same hybridization create repulsion of the lone electron pairs at both nitrogen atoms, inevitably augmenting the internal energy.²⁹ Second, the cis arrangement brings the naphthol and cyclopropane rings into a close geometrical proximity, thus creating sterically crowded structures. To avoid the crowded geometries, the cyclopropane ring must be then moved away from the plane of the naphthol ring, at the expense of breaking the π -conjugation in the molecule. Though a few minima with a cis CNNC dihedral angle were indeed located for CPDNO, all of them have very high relative energies (≈ 65 kJ mol⁻¹ or above; see Figure S1 in the Supporting Information).

The analysis of Figure 2 allows to extract the following conclusions regarding the dependence of the molecule's energy on the C–C–O–H and C–C–N=N dihedral angles: (i) all potential energy minima located on this surface are grouped along the two valleys where the CCOH dihedral angle assumes the cis (0°) or trans ($\approx 180^\circ$) orientations with respect to the C(1)C(2) bond. This means that hydroxyl group is essentially coplanar with the aromatic naphthol ring. This is also true for all other minima of the E-tautomer of CPDNO; (ii) the trans-OH minima (E5 and E7) have very high relative energies (≈ 50 kJ mol⁻¹ or above). This is explained by the unfavorable vicinity of the lone electron pair of the oxygen with the lone electron pairs of the azo group; (iii) the cis-OH minima (E1 and E3) are stabilized due to the favorable orientation of the hydroxyl group establishing an intramolecular hydrogen bond with one of the nitrogen atoms of the azo group; (iv) the minima along the CCNN dihedral angle also adopt positions close to the cis and trans orientations. This is dictated by the fact that the π -electron system of the N=N bond is stabilized due to the conjugative interaction with the π -electron system of the naphthol ring, which is maximized for coplanar arrangements of these two moieties.

Formation of the keto–hydrazone tautomer of CPDNO implies migration of labile hydrogen from the OH group to one of the two nitrogen atoms. These two possibilities are depicted in Figure 1, where the azo–enol forms E1 and E2 forming an intramolecular six-membered ring via OH \cdots N bond give rise to the keto–hydrazone forms K1 and K2, bearing a six-membered ring with an O \cdots HN bond. Similarly, the E3 form on one side and the K3 form on the other side are the counterparts having a five-membered ring stabilized by an intramolecular OH \cdots N/O \cdots HN interaction. The azo–enol and keto–hydrazone isomers having the intramolecular H-bond inserted in a six-membered ring were found to be more stable by approximately 20 kJ mol⁻¹ and 50 kJ mol⁻¹, respectively, than their five-membered ring counterparts.

On the whole, the most stable isomer of CPDNO corresponds to E1. Among all of the calculated minima, only three other structures (K1, E2, and K2) fit into the 0–10 kJ mol⁻¹ interval of relative energies (see Figure 1). The relative populations of E1, K1, E2, and K2 at room temperature, estimated from the calculated Gibbs free energies at 298.15 K and the Boltzmann distribution (79, 12, 5, and 4%, respectively) suggest that only these four forms contribute non-negligibly to the gas phase equilibrium and, consequently, may be expected to appear in the deposited low-temperature matrices. All of the remaining structures have calculated energies above 17 kJ mol⁻¹, and their populations can be neglected from the viewpoint of the thermal equilibrium.

As it will be shown below in this work, only the signatures of two azo–enol conformers, E1 and E2, were in fact identified in the experimental spectra. The nonobservation of the keto–hydrazone forms can be explained with the aid of the potential energy surfaces describing the displacement of the hydrogen atom in the [E1, K1] and [E2, K2] pairs (see Figure 3). The transition states for the proton shift in these two pairs were fully optimized, and the remaining points were calculated with incrementally fixed OH distances on the E-side for E1 and E2 and with incrementally fixed NH distances on the K-side for K1 and K2. Thus, each graph consists of two parts having two different abscissas (OH vs NH distance) that alternate at the transition state. The conclusions from these two surfaces are the following: (i) both E1 and E2 azo–enol minima are lower in energy than their K1 and K2 keto–hydrazone counterparts; (ii) even more important, the lowest (zero point) vibrational levels of these E forms are lower in energy than those in the respective K forms, that is, in both pairs the E-forms have lower internal energy (see Figures 1 and 3); (iii) both transition states for the proton movement in the [E1, K1] and [E2, K2] pairs are below the lowest vibrational states in K1 and K2, which means these two K-forms cannot be treated as independent species (see Figure 3). This dynamic behavior of the proton and its importance to the characterization of azo–enol/keto–hydrazone tautomeric forms was pointed out before by Gilli and co-workers in a series of X-ray crystallography and theoretical studies of phenyl-substituted 1-arylaazo-2-naphthols.^{10,12}

From the viewpoint of the present experiments, at cryogenic temperatures, only the lowest vibrational states are relevant, and the system barrierlessly relaxes to the more stable E1 and E2 structures.³⁰ However, the geometries of these E tautomers shall be characterized by a very-large-amplitude motion of the labile proton between the O and N atoms. As a consequence, the corresponding vibrational frequencies (primarily due to the OH stretching) should then experience a large uncertainty,

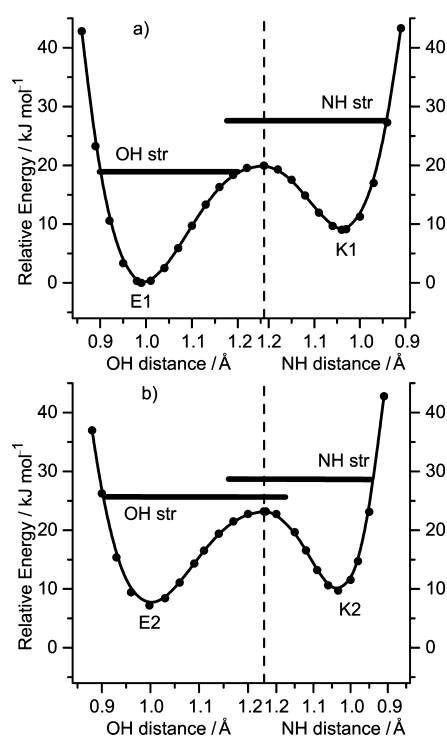


Figure 3. Relaxed potential energy surface for the proton shift between the E1–K1 (a) and E2–K2 (b) minima in CPDNO calculated at the B3LYP/6-311+G(2df,2p) level of theory. The lowest energy vibrational levels along the reaction coordinate are designated by horizontal lines. The change in the reaction coordinate (OH vs NH distance) is designated by the vertical dashed line. The energy of E1 form was chosen as the relative zero.

manifested by the broadening of absorptions in the experiment. It is indeed the fact, as will be shown below.

CPDNO Structure in a Matrix Shortly after Deposition.

The experimental FTIR spectra of CPDNO isolated in argon (15 K) and xenon (30 K) matrices are presented in Figure 4

together with the theoretical spectrum of the azo-enol form E1. With exception of the ν OH stretching region, there is a relatively good agreement between the experimental spectra and the theoretical spectrum predicted for the E1 conformer. The absence of an absorption characteristic of a free OH group in the region around 3700–3600 cm^{-1} , together with the appearance of a broad absorption feature, with a large integrated intensity, between 2950 and 2570 cm^{-1} , indicates that the OH group of the E1 azo-enol form is involved in a very strong intramolecular OH \cdots N hydrogen bond. Due to this strong intramolecular bond, the H \cdots N equilibrium distance in E1 shortens to ≈ 1.69 Å (calculated value). This H \cdots N distance characterizes the strength of a hydrogen bond and can be related to the frequency shift of the OH stretching vibration in the H bonded OH group (relatively to the unperturbed OH group). According to the empirical relationship^{31,32} such a frequency shift in E1 should amount to no less than 600–700 cm^{-1} , that is, fall below 3000 cm^{-1} (if the OH stretching mode of phenol 3634 cm^{-1} is considered as an unperturbed reference).³³ The OH stretching frequency in E1 is predicted by the present harmonic calculations as low as at 3157.1 cm^{-1} . The anharmonic VSCF approximation was used also to locate the frequency for this particular mode more precisely. The calculated anharmonic OH stretching frequency (ca. 2701.6 cm^{-1}), even though obtained without taking in consideration the coupling between modes, still gives quite satisfactory agreement with the position of the broad absorption feature. This particular type of interactions in which the H-bond encloses a pseudoaromatic ring and the coupling of the proton motion with the π -electron causes the appearance of lower frequency ν (OH) bands with huge integrated intensity has been reported before.^{34,35} Also, as suggested by the analysis of the potential energy surfaces for the proton shifts discussed above, there is no spectral evidence that the keto-hydrazone K1 and K2 (the calculated frequencies are given in the Table S2 of the Supporting Information) tautomers are present in the deposited matrices. According to the calculations, if any of the K-forms (K1 and/or K2) were to be present, two relatively strong absorptions due to C=O stretching (involved in the

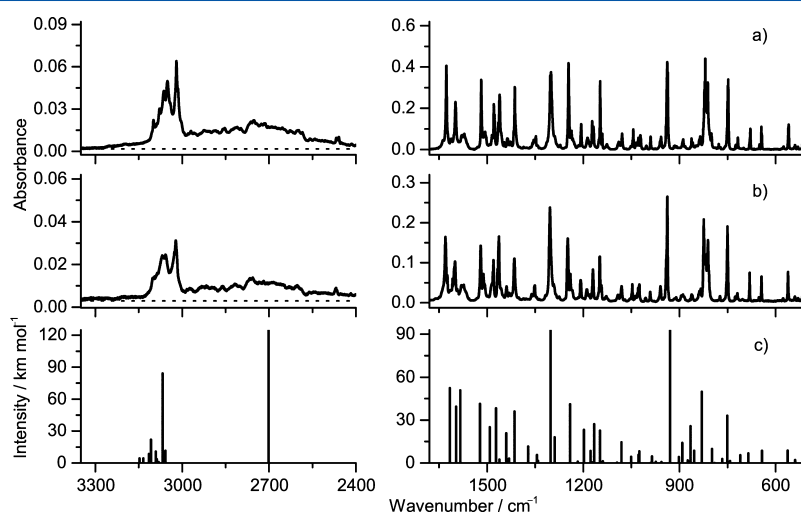


Figure 4. Selected regions of the experimental infrared spectra of monomeric CPDNO isolated in xenon at 30 K (a) and argon at 15 K (b) matrices compared with the theoretical spectrum of azo-enol form E1 (c). The calculated harmonic frequencies were scaled by a factor of 0.976 obtained by least-squares linear fitting. The OH stretching frequency at ≈ 2700 cm^{-1} was calculated within the VSCF anharmonic approximation and was not scaled.

Table 1. Selected Experimental Wavenumbers for the E1 and E2 Azo–Enol Isomers^a

E1				E2			
Ar (15 K)	Xe (30 K)	calculated		Ar (15 K)	Xe (30 K)	calculated	
ν	ν	ν	I	ν	ν	ν	I
2850–2570	2850–2570	3079.7	163.7	2850–2570	2850–2570	3013.4	216.7
1630.0	1627.0	1615.9	57.5	1630 ^c	1627.8 ^b	1615.2	65.8
1599.9	1598.6	1596.6	43.3	1600 ^c	1599.8 ^b	1596.7	59.6
1520.0 , 1511.4	1518.1 , 1508.8, 1505.9	1522.0	45.4	1579.5	1579.4 ^b	1583.9	55.4
1481.9, 1480.1	1478.9 , 1476.9	1491.3	27.5	1520 ^c	1518.5 ^b	1522.4	50.3
1467.6, 1463.0	1464.9, 1461.0	1471.9	42.1	1485.0	1484.5 ^b	1499.9	34.6
1439.3	1437.0	1440.2	22.9	1467.6	1465.0 ^b	1473.5	63.0
1415.1	1413.4	1414.9	39.6	1430.3	1427.5 ^b	1435.3	17.3
1304.0	1302.6, 1300.8	1302.2	114.0	1304 ^c	1303.6 ^b	1305.4	112.7
1248.5 , 1240.3	1246.1 , 1237.9, 1236.4	1240.9	45.1	1249 ^c	1247.1 ^b	1242.2	54.7
1208.3	1206.6	1198.3	25.5	1215.2	1213.7 ^b	1210.2	10.3
1170.0	1172.2 , 1168.7	1165.8	29.9	1188 ^c	1186.7 ^b	1188.3	39.6
1149.5, 1148.3	1147.4	1147.6	24.9	1149 ^c	1151.0 ^b	1150.8	10.4
1080.7	1078.9	1080.7	16.0	1128 ^c	1126.3	1122.1	21.1
991.2	990.2	985.8	5.1	1053.4	1051.5 ^b	1056.7	5.2
937.8	938.0 , 936.6	929.3	107.8	1037.7	1035.2 ^b	1031.4	9.8
750.4	749.2 , 747.8	750.8	36.3	1005.7	1003.2	1000.1	24.2
719.4	720.6, 718.1	710.1	6.0	959.4	957.5	951.6	65.4
681.2	678.8	685.1	7.4	725.5	724.6	720.2	4.9
644.2	644.7 , 643.3	642.7	9.4	651.5	650.8	650.2	4.4
561.5	560.1, 559.3	562.3	9.6	577.2	575.3	572.1	8.8
464.7	465.4, 466.4, 464.2	464.2	16.1	530.2	530.8	528.1	5.4

^aB3LYP/6-311+G(2df,2p) calculated wavenumbers (ν) in cm^{-1} and intensities (I) in km mol^{-1} are also given. The theoretical wavenumbers are scaled by a factor of 0.976. The strongest components of split bands are given in bold. The OH stretching frequencies of E1 and E2 calculated within the VSCF anharmonic approximation are 2701.6 and 2657.9 cm^{-1} , respectively. ^bBands assigned based on annealing experiments. ^cEstimated values for E2 bands masked by E1 absorptions.

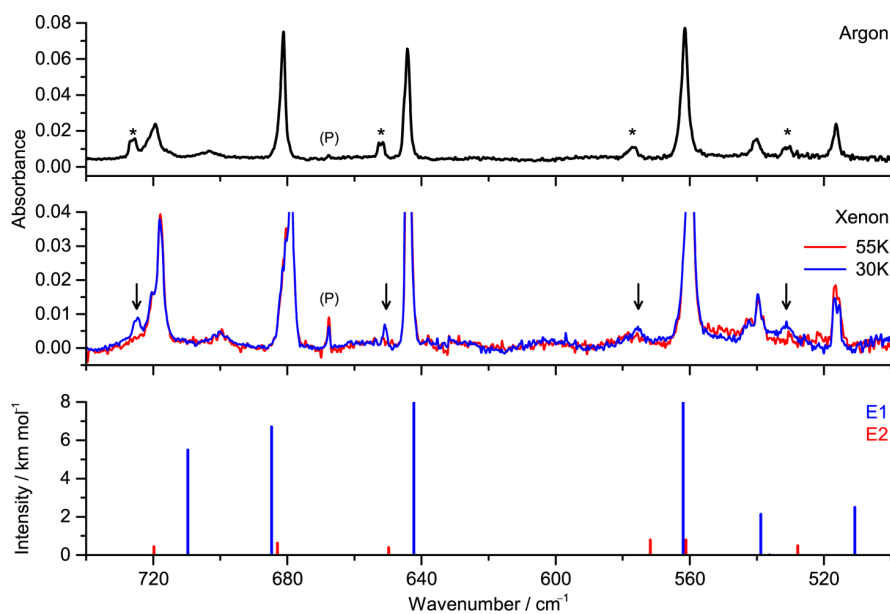


Figure 5. Selected region of the experimental infrared spectrum of CPDNO in argon (15 K) and xenon (30 K) matrices, compared with the theoretical spectra of azo–enol forms E1 (blue) and E2 (red). An asterisk (*) indicates the peaks corresponding to absorptions due to the E2 form in an argon matrix. A downward arrow (↓) indicates the decreasing bands of E2 form upon annealing in a xenon matrix. The band at 667 cm^{-1} , marked as (P), is due to atmospheric CO_2 . The calculated intensities of E1 and E2 were scaled by 0.9 and 0.1, respectively. All calculated frequencies were scaled by a factor of 0.976.

extensive conjugation and hydrogen bonding mentioned before) and N–H in-plane bending vibrations should be identifiable in the 1580–1505 cm^{-1} spectral region. Therefore,

based on the absence of these characteristic absorptions in this particular region, the presence of the K1 and K2 forms can be ruled out.

The overall correspondence of the experimental spectrum and that calculated for the E1 conformer is quite satisfactory. However, based on the theoretical predictions, it can be expected that the E2 form contributes to the thermal equilibrium too. Its contribution should be about 6% if only E1 and E2 are participating in the thermal equilibrium. Alternatively, if K1 and K2 are also contributing to the thermal equilibrium at room temperature, and then collapse to E1 and E2, respectively, upon deposition of the matrix, the E2 fraction should be about 9%. Such an amount of E2 (6–9%) should be detectable experimentally. The barrier for intramolecular rotation of the cyclopropane moiety transforming E2 to E1 forms into each other was calculated to be $\approx 14 \text{ kJ mol}^{-1}$ from E2 to E1. Such a high barrier can be overcome at relatively high temperatures, above 50 K.^{36,37} Among noble gases, only Xe matrix permits attaining of such temperatures. Indeed, after annealing the xenon matrix to 55 K, a set of bands (see Table 1 and Tables S3/S4 for tentative assignments) present in the spectrum of the deposited sample disappeared (see bands marked by arrows in Figure 5). These disappearing bands have frequencies that match infrared absorptions in the calculated spectrum of the E2 conformer (and do not overlap with the E1

absorptions). Annealing of argon matrices should not lead to relaxation of form E2, since a barrier of $\approx 14 \text{ kJ mol}^{-1}$ cannot be overcome in the temperature interval where argon is still rigid enough (up to 35 K). Then the population of E2 should be efficiently trapped in an argon matrix, and the ratio of forms E1/E2 trapped in argon should be similar to their ratio in the gas phase prior to deposition. In fact, if the calculated intensities of E1 and E2 are scaled as 9:1 (as in the gas-phase equilibrium during sublimation), the simulated spectrum (Figure 5, bottom) provides a good match with the experiment (Figure 5, top). In such way, the presence of the E2 conformer in the samples before annealing was reliably confirmed and some of its most prominent bands identified. As a complement, the experimental infrared (in a KBr pellet) and the Raman spectrum of CPDNO powder was also obtained (see Figure S5 and S6 in the Supporting Information). However, several factors, such as the presence of intermolecular interactions, contribute to the complexity of the experimental pattern of bands displayed and limit the amount of information that can be retrieved. Nevertheless, there is a fairly reasonable good overall agreement with the spectrum simulated for azo-enol form E1, further suggesting that this form is also the predominant one in the solid state.

Photochemistry. CPDNO isolated in the cryogenic matrices was irradiated with a narrowband UV laser light source. The series of UV irradiations started at $\lambda = 375 \text{ nm}$ and continued at shorter wavelengths (UV–visible spectrum of CPDNO is given in Figure S7). After each irradiation, the reaction was monitored by analysis of the IR spectrum. Immediately after the first irradiation at 375 nm the bands due to CPDNO decreased in intensity, and several new bands emerged in the spectrum (the new bands remained stable in the absence of irradiation). The bands due to E1 and E2 forms continued to decrease with irradiations at shorter wavelengths. The decrease of the broad absorption feature in the $3000\text{--}2400 \text{ cm}^{-1}$ range (see Figure 6) suggests that the initial E1/E2 structures stabilized by the $\text{OH}\cdots\text{N}$ hydrogen bond involved in a six-membered ring are consumed. Simultaneously, the appearance of bands in the $3600\text{--}3400 \text{ cm}^{-1}$ range of the spectrum indicates that new structures bearing OH or NH group not involved in a six-membered intramolecular interaction are generated. A similar spectroscopic behavior

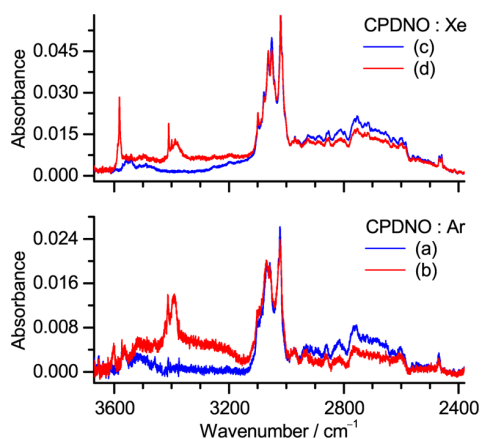


Figure 6. Experimental spectra of CPDNO isolated in argon (bottom) and xenon (top) matrices, before (blue) and after (red) 3 min of UV-irradiation at $\lambda = 340\text{--}345 \text{ nm}$.

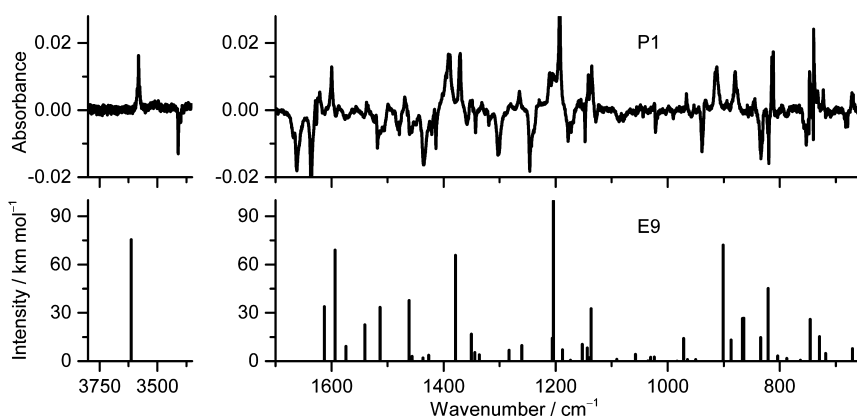


Figure 7. Changes in the experimental infrared spectrum of CPDNO isolated in a xenon matrix (top) after initial 6 min irradiation at $\lambda = 375 \text{ nm}$ and subsequent 3 min of UV irradiation ($\lambda = 345 \text{ nm}$), compared with the theoretical infrared spectrum of the E9 form calculated at the B3LYP/6-311+G(2df,2p) level. Negative absorptions correspond to decreasing bands of the initially present E1 (and E2) form and to set P2 of photoproducts. Positive peaks correspond to growing absorptions due to the set P1 of photoproducts. Theoretical wavenumbers were scaled by a factor of 0.976.

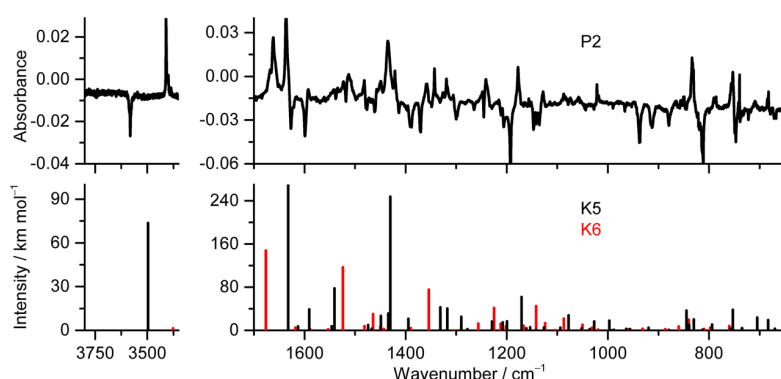


Figure 8. Changes in the experimental infrared spectrum of CPDNO isolated in a xenon matrix (top) after 6 min of UV irradiation ($\lambda = 325$ nm, preceded by irradiations described in caption of Figure 7) compared with the theoretical infrared spectra of forms K5 and K6 calculated at the B3LYP/6-311+G(2df,2p) level. Negative absorptions correspond to decreasing bands of the initially present E1 (and E2) form and to set P1 of photoproducts. Positive peaks correspond to growing absorptions due to the set P2 of photoproducts. Theoretical wavenumbers were scaled by a factor of 0.976. The calculated intensities of forms K5 and K6 were scaled by 1 and 0.5, respectively.

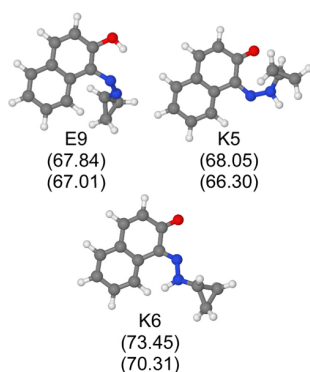
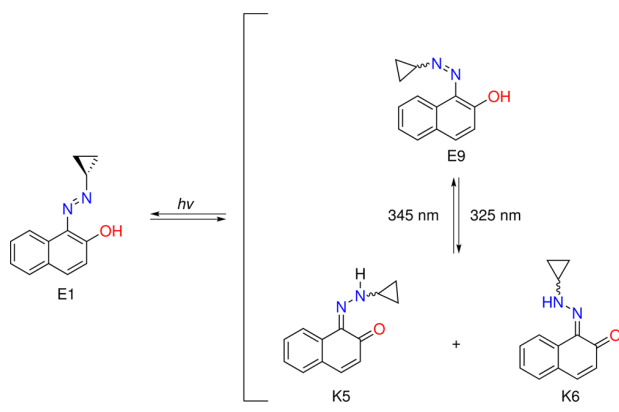


Figure 9. Structures of the photogenerated products. The relative energies, in kJ mol^{-1} , with the zero point correction (top) and with thermal correction to Gibbs free energy at 298 K (bottom) are given below each structure.

Scheme 2. Photoisomerization Reactions of CPDNO



was observed for matrix-isolated *o*-hydroxybenzaldehyde (salicylaldehyde) and *o*-hydroxyacetophenone when new, non-hydrogen-bonded conformers of these compounds were photogenerated by UV irradiation.³⁸

With the aid of irradiations at shorter wavelengths, it was possible to group the new bands in two distinct sets indicated as P1 and P2 in Figures 7 and 8, respectively. Upon irradiation at 345 nm, the intensity of bands belonging to the P1 set

Table 2. Observed Experimental and Calculated Wavenumbers for the E9 Azo–Enol Photoproduct^a

E9			
Ar (15 K)	Xe (30 K)	calculated	
ν	ν	ν	<i>I</i>
3601.8	3581.5	3615.7	75.4
1631.0	1628.9, 1625.7	1613.9	33.9
1602.1	1599.7	1594.9	68.9
1540.9	1534.9	1541.7	22.5
1522.7	1519.3	1514.2	33.4
1467.5	1465.3	1462.4	37.7
1401.4, 1395.4	1395.1, 1391.4	1379.7	65.7
1370.3	1370.2	1351.3	16.8
1211.1 , 1196.0	1209.9 , 1192.8	1204.7	206.9
n.o.	966.7	972.2	14.1
912.2 , 909.4	915.2, 912.4	901.7	72.1
896.5	894.3	887.5	13.2
880.7	879.5	867.2	26.5
		864.5	26.7
815.9	814.2, 811.6	821.1	45.1
747.1	747.0	746.1	25.9
733.3	732.4	729.4	15.2
725.5	722.3	718.4	4.8
672.8	671.3 , 668.9	670.8	7.8

^aB3LYP/6-311+G(2df,2p) calculated wavenumbers (ν) in cm^{-1} and intensities (*I*) in km mol^{-1} are also given. The theoretical wavenumbers are scaled by a factor of 0.976. The strongest components of split bands are given in bold.

increased, while the bands of the P2 set showed a decrease in intensity. For irradiations at 325 nm, the opposite behavior is observed with the intensity of the bands of the P2 and P1 sets increasing and decreasing, respectively. This behavior clearly indicates a reversible phototransformation between, at least, two different forms. After comparing the experimental difference IR spectra with the spectra calculated for several rotameric and tautomeric forms (see Table S2 of the Supporting Information), the P1 set of photoproduct bands could be assigned to the E9 azo–enol form (see Figure 9 and Scheme 2). The E9 azo–enol form most characteristic vibrations situated at ca. 3582, 1600, 1393, 1200, and 914 cm^{-1} (just to name a few) can be promptly identified (see Table 2).

Table 3. Observed Experimental and Calculated Wavenumbers for the K5 and K6 Keto–Hydrazone Photoproducts^a

K5				K6			
Ar (15 K)		Xe (30 K)		Ar (15 K)		Xe (30 K)	
calculated		calculated		calculated		calculated	
ν	ν	ν	I	ν	ν	ν	I
3414.1, 3412.6	3410.3 , 3399.82	3498.9	73.7	1674.4, 1666.4	1667.6, 1661.7	1677.3	295.8
1639.6	1636.4	1633.4	323.9	1526.7	1523.1	1524.9	234.1
1595.8	1592.5	1591.4	38.7	1360.1	1357.9	1354.9	150.9
1544.5	1540.8	1541.7	77.7	1243.3	1241.2	1225.7	82.7
1454.6	1449.1	1450.0	26.6	1133.2	1128.2	1142.5	90.2
1436.1 , 1427.3	1435.3 , 1421.1	1431.0	247.6	621.9	622.1	632.9	106.6
1339.8	1343.0	1332.1	42.7	n.o.	602.0	612.3	10.6
1317.5	1319.3	1318.3	40.3				
1177.6	1177.7	1171.5	61.8				
834.8	833.7	845.0	36.5				
788.6	786.1	794.7	10.5				
753.1	756.3, 753.1	753.6	37.9				
711.4	709.1	705.1	23.8				
684.6	682.4	683.5	19.0				
n.o.	616.5	629.0	35.6				

^aB3LYP/6-311+G(2df,2p) calculated wavenumbers (ν) in cm^{-1} and intensities (I) in km mol^{-1} are also given. The theoretical wavenumbers are scaled by a factor of 0.976. The strongest components of split bands are given in bold.

The photoinduced generation of conformer E9 (N=N cis) from E1 (N=N trans) can be considered as another variant of the largely explored characteristic “entgegen”–“zusammen” (E–Z) isomerization of azo compounds.^{39,40} Upon such isomerization, the intramolecular OH⋯N hydrogen bond is broken, and therefore a band due to the OH stretching vibration emerges in the spectral range characteristic of free OH groups.²⁹

On the other hand, the P2 set of photoproduct bands can be interpreted assuming the presence of two different keto–hydrazone forms. This is suggested by the observation of a band around 3410 cm^{-1} characteristic of a free NH stretching vibration.²⁹ The most intense bands at ca. 3410, 1636, 1541, 1435, and 1178 cm^{-1} can be assigned to the K5 form, while the bands at ca. 1662, 1523, 1355 cm^{-1} suggest the presence of form K6 (see Figure 9, Scheme 2, and Table 3). The NH str vibration of form K6 was not observed. The calculated intensity ($\approx 3 \text{ km mol}^{-1}$) for this frequency is very low, and its experimental observation should be considered tentative. Generation and stabilization of keto–hydrazone forms K5 and K6 appears possible due to the internal rotation around the C(1)N(11) bond which puts the newly formed N(12)H moiety away from the oxygen atom. The stability of keto–hydrazone tautomers, as individual structures, is already possible for forms where the O⋯HN bond is involved in a five-membered ring (like for K3 and K4, see Figure S3 and S4 in the Supporting Information), and even more so, when the NH bond is completely free from donor/acceptor interactions.

The fact that P1 and P2 photoproducts are structural isomers of CPDNO and not decomposition products was confirmed by carrying out further irradiations of the sample using UV light in the 310–280 nm range. After these irradiations, the photoproducts P1 and P2 are consumed, and bands due to the E1 and E2 starting forms are partially growing back. However, most probably, some other new photoproducts⁴¹ are also appearing in the samples, and their experimental identification becomes complicated, since upon many irradiations the spectrum becomes very congested. The reversibility of the starting material (E1 and E2-forms) upon UV-irradiations with shorter wavelengths in the present experiments is similar to the

reversibility observed previously for salicylaldehyde and *o*-hydroxyacetophenone under similar conditions.³⁸

CONCLUSIONS

In the present study, we investigated the structure and photochemistry of a matrix-isolated azo derivative, 1-(cyclopropyl)-diaz-2-naphthol. The compound was isolated in cryogenic gas matrices and characterized by IR spectroscopy. Among the several possible isomers, only the azo–enol forms having the OH group involved in a strong intramolecular hydrogen bond, forming a six-membered ring with the azo group (E1 and E2) were found in the experiment. The nonobservation of the keto–hydrazone tautomers was explained with the aid of quantum chemical calculations [B3LYP/6-311+G(2df,2p)] describing the displacement of the hydrogen atom in the tautomeric azo–enol/keto–hydrazone systems. Different rotameric and tautomeric forms without intramolecular H-bonding were photogenerated by UV irradiation of CPDNO at different wavelengths in the near-UV range. Irradiation at 345 nm generates the E9 azo–enol (cis) form, while upon irradiation at 325 nm, two keto–hydrazone forms (K5 and K6) are produced. These phototransformations were shown to be reversible, and depending on the excitation light, the azo–enol or the keto–hydrazone forms can be produced. Further irradiations using UV light in the 310–280 nm range partially regenerate the initial forms.

ASSOCIATED CONTENT

Supporting Information

Figures S1 and S2 showing all optimized structures and their respective energies; Figures S3 and S4 showing the relaxed potential energy surface for the proton shift between E3–K3 and E4–K4 minima, respectively; Figure S5 showing the experimental infrared spectrum of CPDNO powder in a KBr pellet; Figure S6 showing the experimental Raman spectrum of CPDNO powder; Figure S7 showing the experimental UV–visible spectrum of CPDNO in acetonitrile; Table S1 showing the Cartesian coordinates of all optimized structures; Table S2 showing the calculated frequencies of all considered isomeric

forms; Table S3 and S4 showing the tentative assignments for the E1 and E2 azo-enol isomers isolated in argon and xenon matrices, respectively. This material is available free of charge via the Internet at <http://pubs.acs.org>.

AUTHOR INFORMATION

Corresponding Author

*E-mail: lduarte@qui.uc.pt.

Present Address

B.M.G.: Centro de Astrobiología, INTA-CSIC, Carretera de Ajalvir, km 4, Torrejón de Ardoz, 28850 Madrid, Spain.

Notes

The authors declare no competing financial interest.

ACKNOWLEDGMENTS

This work was supported by the Portuguese “Fundação para a Ciência e Tecnologia” (FCT) Research Projects PTDC/QUI-QUI/111879/2009 and PTDC/QUI-QUI/118078/2010, FCOMP-01-0124-FEDER-021082, cofunded by QREN-COMPETE-UE. L.D. acknowledges FCT for the doctoral grant no. SFRH/BD/62090/2009. B.M.G. acknowledges FCT for the postdoctoral grant no. SFRH/BPD/44689/2008. The authors thank Prof. Ana Maria Oliveira-Campos (University of Minho) for providing the compound studied and the Advanced Computing Laboratory at University of Coimbra for providing computing resources that have contributed to the research results reported within this paper.

REFERENCES

- (1) Hunger, K., Ed. *Industrial Dyes*; Wiley-VCH Verlag GmbH & Co. KGaA: Weinheim, FRG, 2003.
- (2) Feringa, B. L., Ed. *Molecular Switches*; Wiley-VCH Verlag GmbH: Weinheim, FRG, 2001.
- (3) Kumar, A. S.; Ye, T.; Takami, T.; Yu, B.-C.; Flatt, A. K.; Tour, J. M.; Weiss, P. S. Reversible Photo-Switching of Single Azobenzene Molecules in Controlled Nanoscale Environments. *Nano Lett.* **2008**, *8*, 1644–1648.
- (4) Sasaki, T.; Tour, J. M. Synthesis of a New Photoactive Nanovehicle: A Nanoworm. *Org. Lett.* **2008**, *10*, 897–900.
- (5) Browne, W. R.; Feringa, B. L. Light Switching of Molecules on Surfaces. *Annu. Rev. Phys. Chem.* **2009**, *60*, 407–428.
- (6) Isak, S.; Eyring, E.; Spikes, J.; Meekins, P. Direct Blue Dye Solutions: Photo Properties. *J. Photochem. Photobiol., A* **2000**, *134*, 77–85.
- (7) Li, Y.; Patrick, B. O.; Dolphin, D. Near-Infrared Absorbing Azo Dyes: Synthesis and X-ray Crystallographic and Spectral Characterization of Monoazopyrroles, Bisazopyrroles, and a Boron-Azopyrrole Complex. *J. Org. Chem.* **2009**, *74*, 5237–5243.
- (8) Antonov, L.; Deneva, V.; Simeonov, S.; Kurteva, V.; Nedeltcheva, D.; Wirz, J. Exploiting Tautomerism for Switching and Signaling. *Angew. Chem., Int. Ed.* **2009**, *48*, 7875–7878.
- (9) Burdette, S. C. Molecular Switches: Hydrazones Double Down on Zinc. *Nat. Chem.* **2012**, *4*, 695–696.
- (10) Gilli, P.; Bertolasi, V.; Pretto, L.; Lyčka, A.; Gilli, G. The Nature of Solid-State N-H...O/O-H...N Tautomeric Competition in Resonant Systems. Intramolecular Proton Transfer in Low-Barrier Hydrogen Bonds Formed by the ..O=C-C=N-NH... ↔ ..HO-C=C-N=N... Ketohydrazone-Azoenol System. A Variable-Temperature X-ray Crystallographic and DFT Computational Study. *J. Am. Chem. Soc.* **2002**, *124*, 13554–13567.
- (11) Nedeltcheva, D.; Damyanova, B.; Popov, S. Gas Phase Tautomerism of Tautomeric Azo Naphthols and Related Schiff Bases Studied by Mass Spectrometry. *J. Mol. Struct.* **2005**, *749*, 36–44.
- (12) Gilli, P.; Bertolasi, V.; Pretto, L.; Antonov, L.; Gilli, G. Variable-Temperature X-ray Crystallographic and DFT Computational Study of the N-H...O/N...H-O Tautomeric Competition in 1-(Arylazo)-2-Naphthols. Outline of a Transition-State Hydrogen-Bond Theory. *J. Am. Chem. Soc.* **2005**, *127*, 4943–4953.
- (13) Filarowski, A.; Kochel, A.; Kluba, M.; Kamounah, F. S. Structural and Aromatic Aspects of Tautomeric Equilibrium in Hydroxy Aryl Schiff Bases. *J. Phys. Org. Chem.* **2008**, *21*, 939–944.
- (14) Nedeltcheva, D.; Kamounah, F. S.; Mirolo, L.; Fromm, K. M.; Antonov, L. Solid State Tautomerism in 2-((Phenylimino)methyl)naphthalene-1-ol. *Dyes Pigm.* **2009**, *83*, 121–126.
- (15) Nedeltcheva, D.; Kurteva, V.; Topalova, I. Gas-Phase Tautomerism in Hydroxy Azo Dyes - from 4-Phenylazo-1-Phenol to 4-Phenylazo-Anthracen-1-ol. *Rapid Commun. Mass Spectrom.* **2010**, *24*, 714–720.
- (16) Almeida, M. R.; Stephani, R.; Dos Santos, H. F.; de Oliveira, L. F. C. Spectroscopic and Theoretical Study of the “Azo”-Dye E124 in Condensate Phase: Evidence of a Dominant Hydrazone Form. *J. Phys. Chem. A* **2010**, *114*, 526–534.
- (17) Kurteva, V. B.; Antonov, L. M.; Nedeltcheva, D. V.; Crochet, A.; Fromm, K. M.; Nikolova, R. P.; Shivachev, B. L.; Nikiforova, M. S. Switching Azonaphthols Containing a Side Chain With Limited Flexibility. Part 1. Synthesis and Tautomeric Properties. *Dyes Pigm.* **2012**, *92*, 1266–1277.
- (18) Ferreira, G. R.; Garcia, H. C.; Couri, M. R. C.; Dos Santos, H. F.; de Oliveira, L. F. C. On the Azo/Hydrazone Equilibrium in Sudan I Azo Dye Derivatives. *J. Phys. Chem. A* **2013**, *117*, 642–649.
- (19) Tomilov, Y.; Kostyuchenko, L.; Shulishov, E.; Nefedov, O. Formation of Cyclopropylazoarenes in the Azo Coupling Reactions of the Cyclopropanediazonium Ion With Active Aromatic Compounds. *Mendeleev Commun.* **2002**, *12*, 104–105.
- (20) Becke, A. D. Density-Functional Thermochemistry. III. The Role of Exact Exchange. *J. Chem. Phys.* **1993**, *98*, 5648–5652.
- (21) Stephens, P. J.; Devlin, F. J.; Chabalowski, C. F.; Frisch, M. J. Ab Initio Calculation of Vibrational Absorption and Circular Dichroism Spectra Using Density Functional Force Fields. *J. Phys. Chem.* **1994**, *98*, 11623–11627.
- (22) Lebedev, V. I.; Laikov, D. N. A Quadrature Formula for the Sphere of the 131st Algebraic Order of Accuracy. *Dokl. Math.* **1999**, *59*, 477–481.
- (23) Chaban, G. M.; Jung, J. O.; Gerber, R. B. Ab Initio Calculation of Anharmonic Vibrational States of Polyatomic Systems: Electronic Structure Combined with Vibrational Self-Consistent Field. *J. Chem. Phys.* **1999**, *111*, 1823–1829.
- (24) Yagi, K.; Hirao, K.; Taketsugu, T.; Schmidt, M. W.; Gordon, M. S. Ab Initio Vibrational State Calculations With a Quartic Force Field: Applications to H₂CO, C₂H₄, CH₃OH, CH₃CCH, and C₆H₆. *J. Chem. Phys.* **2004**, *121*, 1383–1389.
- (25) Schmidt, M. W.; Baldrige, K. K.; Boatz, J. A.; Elbert, S. T.; Gordon, M. S.; Jensen, J. H.; Koseki, S.; Matsunaga, N.; Nguyen, K. A.; Su, S.; et al. General Atomic and Molecular Electronic Structure System. *J. Comput. Chem.* **1993**, *14*, 1347–1363.
- (26) Gordon, M.; Schmidt, M. In *Theory and Applications of Computational Chemistry: The First Forty Years*; Dykstra, C., Frenking, G., Kim, K., Scuseria, G., Eds.; Elsevier: Amsterdam, 2005; pp 1167–1189.
- (27) Wolfe, S.; Schlegel, H. B.; Whangbo, M.-H.; Bernardi, F. On the Origin of the Bohlmann Bands. *Can. J. Chem.* **1974**, *52*, 3787–3792.
- (28) Lü, J.-H.; Chen, K.-H.; Allinger, N. L. Alcohols, Ethers, Carbohydrates, and Related Compounds Part V. 2 The Bohlmann Torsional Effect. *J. Phys. Chem. A* **2004**, *108*, 3006–3015.
- (29) Reva, I.; Almeida, B. J.; Lapinski, L.; Fausto, R. UV-Induced Photoisomerization of Maleic Hydrazone. *J. Mol. Struct.* **2012**, *1025*, 74–83.
- (30) Estimative C-PCM calculations indicate that the relative energy of a more polar K1 form with respect to E1 decreases only slightly, from ≈ 9.06 (*in vacuo*) to 6.40 kJ mol⁻¹ (in xenon). Therefore a solvation difference of the molecules with noticeably different dipole moments does not have an impact on our results.
- (31) Rozenberg, M.; Shoham, G.; Reva, I.; Fausto, R. A Correlation Between the Proton Stretching Vibration Red Shift and the Hydrogen

Bond Length in Polycrystalline Amino Acids and Peptides. *Phys. Chem. Chem. Phys.* **2005**, *7*, 2376–2383.

(32) Rostkowska, H.; Nowak, M. J.; Lapinski, L.; Adamowicz, L. IR Spectral and Theoretical Characterization of Intramolecular Hydrogen Bonds Closing Five-Membered Rings. *Phys. Chem. Chem. Phys.* **2001**, *3*, 3012–3017.

(33) Giuliano, B. M.; Reva, I.; Lapinski, L.; Fausto, R. Infrared Spectra and Ultraviolet-Tunable Laser Induced Photochemistry of Matrix-Isolated Phenol and Phenol-d5. *J. Chem. Phys.* **2012**, *136*, 024505.

(34) Pajak, J.; Rospenk, M.; Ramaekers, R.; Maes, G.; Glowiak, T.; Sobczyk, L. DFT Theoretical, X-ray Diffraction and IR Matrix-Isolated Studies on 4-Chloro-2'-Hydroxy-4'-Ethoxyazobenzene. *Chem. Phys.* **2002**, *278*, 89–100.

(35) Pajak, J.; Ramaekers, R.; Rospenk, M.; Alexandrov, V.; Stepanian, S.; Adamowicz, L.; Maes, G. Matrix-Isolation FT-IR Studies and Theoretical Calculations of the Vibrational Properties of 4-Methyl-2'-Hydroxy-4'-Ethoxyazobenzene. *Chem. Phys.* **2003**, *286*, 193–204.

(36) Reva, I.; Simão, A.; Fausto, R. Conformational Properties of Trimethyl Phosphate Monomer. *Chem. Phys. Lett.* **2005**, *406*, 126–136.

(37) Jesus, A. J. L.; Rosado, M. T. S.; Reva, I.; Fausto, R.; Eusébio, M. E. S.; Redinha, J. S. Structure of Isolated 1,4-Butanediol: Combination of MP2 Calculations, NBO Analysis, and Matrix-Isolation Infrared Spectroscopy. *J. Phys. Chem. A* **2008**, *112*, 4669–4678.

(38) Lapinski, L.; Rostkowska, H.; Reva, I.; Fausto, R.; Nowak, M. J. Positive Identification of UV-Generated, Non-Hydrogen-Bonded Isomers of o-Hydroxybenzaldehyde and o-Hydroxyacetophenone. *J. Phys. Chem. A* **2010**, *114*, 5588–5595.

(39) Beharry, A. A.; Woolley, G. A. Azobenzene Photoswitches for Biomolecules. *Chem. Soc. Rev.* **2011**, *40*, 4422–4437.

(40) Merino, E.; Ribagorda, M. Control Over Molecular Motion Using the Cis-Trans Photoisomerization of the Azo Group. *Beilstein J. Org. Chem.* **2012**, *8*, 1071–1090.

(41) These new photoproducts probably result from partial decomposition.

List of Figures

1.1	Structural formula of diimide, a general azo compound, and the most common aromatic azo compound - azobenzene.	1
1.2	Schematic representation of some azo-based molecular applications. .	2
1.3	Photoisomerization of azobenzene.	3
1.4	Electronic absorption spectra of the <i>E</i> - and <i>Z</i> - isomers of azobenzene dissolved in ethanol.	5
1.5	Proposed photoisomerization mechanisms for azobenzene.	7
1.6	Compounds studied in this work.	9
1.7	Schematic representation of a species isolated in a matrix host (usually neon, argon, and xenon).	10
1.8	Schematic representation of a matrix isolation setup.	11
1.9	Potential energy diagrams for the harmonic and anharmonic oscillator. 13	
2.1	Matrix isolation experimental setup used during this work.	34
2.2	Schematic representation of a spectrometer layout.	35
2.3	Quanta-Ray Pro Pulsed Nd:YAG laser and MOPO-SL Optical Parametric Oscillator.	36
2.4	Simplified energy-level scheme of a Nd:YAG laser.	37
3.1	Structures of <i>E</i> and <i>Z</i> isomers of azobenzene.	41
3.2	Selected regions of the experimental and theoretical infrared spectra of azobenzene.	43
3.3	Changes in the experimental infrared spectrum of azobenzene in an Ar matrix at 15 K after UV irradiation.	45
3.4	Experimental infrared spectrum of <i>E</i> -AB monomer isolated in an argon matrix at 15 K.	49
3.5	Extracted experimental infrared spectrum of <i>Z</i> -AB monomer isolated in an argon matrix at 15 K.	50

3.6	Relaxed 2D potential energy map of <i>E</i> - and <i>Z</i> -azobenzene isomers as a function of blade pitch variation.	53
3.7	Relaxed potential energy scans in azobenzene as functions of the blade pitch variation.	56
3.8	Fragments of the infrared spectra of azobenzene isolated in argon matrices at 15 K observed in two types of experiments.	58
3.9	Structure of 4-hydroxyazobenzene (HAB).	59
3.10	Most stable structures of HAB.	60
3.11	Experimental and theoretical infrared spectra of HAB.	62
3.12	Changes in the experimental infrared spectrum of HAB in an Xe matrix at 60 K after UV irradiation.	65
3.13	Structure of 4-(cyclopropyldiazenyl)phenol (CPDP).	67
3.14	Contour map of the relaxed potential energy surface of CPDP.	68
3.15	Most stable structures of CPDP.	69
3.16	Experimental and theoretical infrared spectra of CPDP.	71
3.17	Selected region of the experimental infrared spectrum of CPDP in a xenon (30 K) matrix.	74
3.18	Extracted experimental infrared spectrum of CPDP2.	77
3.19	Extracted experimental infrared spectrum of CPDPZ.	78
3.20	Structures for the azo-enol (E) and keto-hydrazone (K) forms of 1-(cyclopropyldiazenyl)naphthalen-2-ol (CPDNO).	81
3.21	Structures of the calculated azo-enol forms of CPDNO.	82
3.22	Structures of the calculated keto-hydrazone forms of CPDNO.	83
3.23	Contour map of the relaxed potential energy surface of CPDNO.	85
3.24	Relaxed potential energy surface for the proton shift between the E1-K1 and E2-K2 minima in CPDNO.	87
3.25	Selected regions of the experimental and theoretical infrared spectra of CPDNO.	89
3.26	Selected regions of the experimental infrared spectra of CPDNO upon annealing in a xenon matrix.	90
3.27	Experimental spectra of CPDNO isolated in argon and xenon matrices, before and after UV irradiation.	94
3.28	Changes in the experimental infrared spectrum of CPDNO isolated in a xenon matrix after UV irradiation at $\lambda = 345$ nm.	95
3.29	Changes in the experimental infrared spectrum of CPDNO isolated in a xenon matrix after UV irradiation at $\lambda = 325$ nm.	96

4.1	Experimentally observed photoisomerization behavior of AB.	105
4.2	Experimentally observed photoisomerization behavior of HAB.	106
4.3	Photoisomerization reactions of CPDP.	107
4.4	Photoisomerization reactions of CPDNO.	108
B.1	Atom numbering scheme of azobenzene used in the definition of the internal symmetry coordinates.	131
C.1	Experimental UV-visible spectrum of HAB in acetonitrile.	171
D.1	Experimental UV-visible spectrum of CPDP in acetonitrile.	177
E.1	Relaxed potential energy surface for the proton shift between the E3- K3 and E4-K4 minima in CPDNO.	196
E.2	Experimental infrared spectrum of CPDNO in a KBr pellet.	197
E.3	Experimental Raman spectrum of CPDNO powder.	198
E.4	Experimental UV-visible spectrum of CPDNO in acetonitrile.	199

List of Tables

3.1	Experimental wavenumbers of the absorption bands observed in the infrared spectrum of <i>E</i> -AB.	48
3.2	Experimental wavenumbers of the absorption bands observed in the infrared spectrum of <i>Z</i> -AB.	51
3.3	Calculated relative energies, with zero-point vibrational energy correction, of HAB conformers.	61
3.4	Experimental observed wavenumbers of the <i>E</i> -HAB conformers.	63
3.5	Calculated relative energies, with zero-point vibrational energy correction, of CPDP conformers.	70
3.6	Experimental observed wavenumbers of the CPDP1 conformers.	72
3.7	Experimental observed wavenumbers of the CPDP2 conformers.	75
3.8	Experimental observed wavenumbers of the CPDPZ conformers.	79
3.9	Experimental observed wavenumbers of the E1 azo-enol isomer.	91
3.10	Selected experimental wavenumbers of the absorption bands observed for the E1 and E2 azo-enol isomers	93
3.11	Observed experimental and calculated wavenumbers for the E9 azo-enol photoproduct.	96
3.12	Observed experimental and calculated wavenumbers for the K5 and K6 keto-hydrazone photoproducts.	97
B.1	Mean unsigned errors of each theoretical approach relatively to a set of experimental frequencies of azobenzene.	132
B.2	Theoretical frequencies and IR intensities of <i>E</i> -AB and <i>Z</i> -AB forms.	133
B.3	Cartesian coordinates of the optimized geometries of <i>E</i> -AB and <i>Z</i> -AB forms.	137
B.4	Internal symmetry coordinates used in the normal mode analysis of <i>E</i> -azobenzene.	141

B.5	Theoretical wavenumbers, Raman scattering activities and potential energy distributions for the Raman-active A_g and B_g normal modes of E -AB.	145
B.6	Internal symmetry coordinates used in the normal mode analysis of Z -azobenzene.	146
B.7	Changes in the vibrational spectra, expected to occur in E -AB molecule undergoing the zero-point vibrations along the τ NNCC coordinates.	150
B.8	Changes in the vibrational spectra, expected to occur in Z -AB molecule undergoing the zero-point vibrations along the τ NNCC coordinates.	151
C.1	Cartesian coordinates of the optimized geometries of HAB isomeric forms.	166
C.2	Theoretical frequencies and IR intensities of HAB isomeric forms.	172
D.1	Cartesian coordinates of the optimized geometries of CPDP isomeric forms.	178
D.2	Theoretical frequencies and IR intensities of CPDP isomeric forms.	186
E.1	Cartesian coordinates of the optimized geometries of CPDNO isomeric forms.	200
E.2	Theoretical frequencies and IR intensities of all considered CPDNO isomeric forms.	206